

# **Kubische Mesophasen und spontaner Symmetriebruch polycatenarer Bithiophen- und Benzilderivate**

Dissertation

zur Erlangung des Doktorgrades der Naturwissenschaften  
(Dr. rer. nat.)

der

Naturwissenschaftlichen Fakultät II  
Chemie, Physik und Mathematik

der Martin-Luther-Universität  
Halle-Wittenberg

vorgelegt von

Herrn Tino Reppe  
geb. am 06.09.1990 in Halle/Saale

Gutachter

- 1.) Prof. Dr. Carsten Tschierske
- 2.) Prof. Dr. Wolfgang Weigand

Datum der Verteidigung: 15.03.2023





## Abstract

Since liquid crystals were first mentioned in 1888 field of research developed due to the increased demands of LC-Display industry during the last decades. Nowadays the interest in 3D-self-assembled more complex systems rises for organic semiconductors<sup>[1,2]</sup>, drug delivery (cubosomes)<sup>[3-5]</sup>, protein crystallization<sup>[6-8]</sup>, templates for the preparation of porous materials<sup>[9]</sup>, enantioselective catalysis<sup>[10,11]</sup> and many more applications. The bicontinuous cubic phases with their three-dimensional ordered networks may be key factor to accomplish these tasks.

For this aim new symmetric and nonsymmetric polycatenar thiophene- and benzil-based mesogens which are able to form thermotropic liquid crystalline phases were synthesized. These rod-like molecules were modified by changing the length of their core units, number of flexible chains, introducing electron donors and acceptors or a variety of aromatic rings. These substances were able to form lamellar, columnar and three-dimensional liquid crystalline phases. Characterizations of the mesophases were performed by using polarization microscopy, differential scanning calorimetry and XRD-diffraction.

The majority of the synthesized mesogens, especially nonsymmetric, displayed the three-dimensional bicontinuous cubic phases with the space groups  $Ia3d$  and  $I23$ . Crucial for the appearance of these phases is the existence of energy-minimized helical molecular conformers in these achiral thiophene- and benzil-based mesogens. Helical self-assembly of these conformers leads to the development of chirality which is important to the formation of the achiral  $Ia3d$  and the chiral conglomerates in the  $I23$  superstructures. In connection with increasing volumes of substituents the sequence  $Ia3d_{(L)}-I23-Ia3d_{(S)}$  is observed. The double network  $Ia3d$ -phase can be divided into a long and a short pitch range, while the triple network  $I23$ -phase is in the intermediate pitch range.

It was observed that mirror-symmetry breaking can spontaneously take place in the liquid state ( $Iso_1^{[*]}$ ), in the liquid crystalline state ( $Cub_{bi}^{[*]}/I23$ ) and in the crystalline state ( $Cr_{Iso}^*$ ). In the liquid state a cybotactic isotropic liquid with a fluctuating local network structure ( $Iso_1$ ) has been found. The achiral liquid shows an increasing connection between local ordered clusters with decreasing temperature in all benzil-based mesogens and for some thiophenes as well.

This work provides an understanding of the molecular requirements for the formation of the bicontinuous cubic phases ( $Ia3d$ ,  $I23$ ) in thiophene- and benzil-based mesogens.



## Danksagung

Mein besonderer Dank gilt Herrn Prof. Dr. C. TSCHERSKE, der es mir ermöglichte in seiner Arbeitsgruppe die Arbeit zu dem äußerst interessanten Thema anzufertigen. Ich danke ihm für seine allzeit gewährende Unterstützung und Diskussionsbereitschaft.

Bei Herrn Prof. Dr. F. LIU, State Key Laboratory for Mechanical Behavior of Materials der Xi'an Jiatong University danke ich für die Durchführung und Auswertung von Synchrotron-XRD Experimente. Bei Herrn Dr. S. POPPE bedanke ich mich für Durchführung und Auswertung zahlreicher hausinterner röntgenographischer Untersuchungen.

Für die Aufnahmen von unzähligen differentialkalorimetrischen Messungen bedanke ich mich bei Herrn R. GYGER. Für die Aufnahmen hochauflösender Massespektren danke ich Frau S. TANNER aus der Makromolekularen Chemie. Des Weiteren danke ich Frau M. MANND aus dem pharmazeutischen Institut der MLU und den Mitarbeitern aus dem Chemie-Institut für die Durchführungen der Elementaranalysen.

Herrn Dr. D. STRÖHL und seinem Team danke ich für Messung zahlreichen NMR-Spektren und die Diskussionsbereitschaft bei der Analyse dieser.

Ein besonderer Dank gebührt den Mitgliedern der AG Tschierske für die schöne gemeinsame Zeit und vor allem ständige Unterstützung bei Fragestellungen jeglicher Art.



---

# Inhaltsverzeichnis

<b>1. Einleitung und Motivation</b> .....	1
1.1 Flüssigkristalliner Zustand.....	1
1.2 Kubische Phasen und spontaner Symmetriebruch.....	4
1.3 Flüssige isotrope Mesophasen und spontaner Symmetriebruch.....	9
1.4 Zielstellung .....	10
<b>2. Synthese</b> .....	11
2.1 Nomenklatur der Zielverbindungen.....	12
<b>3. Thermotrope Selbstorganisation der polycatenaren Bithiophene</b> .....	15
3.1 Effekte der Kettenzahl und Kettenposition (Publikation C).....	15
3.2 Einfluss von Substituenten am unsubstituierten Ende tricarbonarer Mesogene (Publikation A) .....	16
3.3 Ergänzungen zu Publikation A: Einfluss von Fluorsubstituenten am aromatischen Ring.....	20
3.4 Polycatenare Bithiophene mit cycloaliphatischen Endgruppen (Publikation B).....	21
3.5 Ergänzungen zu Publikation B .....	22
3.6 Untersuchung der tricarbonaren Bithiophene mit einem 3,5-substituierten Ende (Publikation C).....	24
3.7 Ergänzungen zu Publikation C: Vergleich mit tetracatenaren Bithiophenen mit einem 3,4,5-trisubstituierten Ende .....	28
<b>4. Thermotrope Selbstorganisation der polycatenaren Benzile (Publikation D und E)</b> ..	31
4.1 Einfluss der Kernlänge sowie Anzahl und Länge der Alkoxyketten.....	31
4.2 Einführung polarer Substituenten (Publikation E).....	35
4.3 Ergänzungen zu Publikationen D und E .....	37
4.3.1 Homologe Reihe symmetrischer tetracatenarer Verbindungen.....	37
4.3.2 Benzilbasierte Polycatenare mit einer verzweigten Endgruppe .....	38
<b>5. Zusammenfassung der Ergebnisse</b> .....	41
<b>6. Experimenteller Teil</b> .....	45
6.1 Charakterisierungsmethoden .....	45
6.2 Synthetischer Teil .....	46

6.3 Allgemeine Arbeitsvorschriften .....	49
6.4 Synthese und analytische Daten .....	51

<b>Literaturverzeichnis.....</b>	<b>69</b>
----------------------------------	-----------

**Anhang**

## Abkürzungsverzeichnis

### Phasenbezeichnungen

LC	flüssigkristallin
Cr	kristallin
CrG	kristalline lamellare G-Phase
Cr <sub>Iso</sub>	optisch isotrope kristalline Phase (achiral)
Cr <sub>Iso</sub> <sup>[*]</sup>	optisch isotrope kristalline Phase mit Konglomeratstruktur (chiral)
N	nematische Phase
SmA	smektische A-Phase ohne einheitlich Neigung der Moleküle
SmC <sub>s</sub>	synklone smektische C-Phase
SmC <sub>a</sub>	antikline smektische C-Phase
SmQ	smektische Q-Phase
HexB	hexatische B-Phase
HexF	hexatische F-Phase
HexI	hexatische I-Phase
HexI <sub>s</sub> <sup>dis</sup>	synklone hexatische I-Phase mit HexI <sub>s</sub> Ordnung der Alkylketten und SmC <sub>s</sub> Ordnung der aromatischen Kerne
Cub <sub>bi</sub> / <i>Ia3d</i>	bikontinuierlich kubische Phase mit <i>Ia3d</i> Raumgruppe (achiral)
Cub <sub>bi</sub> / <i>Ia3d</i> <sub>(L)</sub>	long pitch <i>Ia3d</i> -Phase (achiral)
Cub <sub>bi</sub> / <i>Ia3d</i> <sub>(S)</sub>	short pitch <i>Ia3d</i> -Phase (achiral)
Cub <sub>bi</sub> <sup>[*]</sup> / <i>I23</i>	bikontinuierlich kubische Phase mit <i>I23</i> Raumgruppe (chiral)
Col <sub>hex</sub>	hexagonal kolumnare LC-Phase
Col <sub>ob</sub>	schiefwinkliger kolumnare Phase
Iso	achirale isotrope Flüssigkeit
Iso <sub>1</sub>	achirale isotrope Flüssigkeit mit cybotaktischer Struktur
Iso <sub>1</sub> <sup>[*]</sup>	chirale isotrope Flüssigkeit mit Konglomeratstruktur achiraler Moleküle
M	unbekannte Mesophase (M, M1, M2)

### Substanzbezeichnungen

ANBC- <i>n</i>	4'- <i>n</i> -Alkoxy-3'-nitrobiphenyl-4-carbonsäuren
BABH- <i>n</i>	1,2-Bis-(4- <i>n</i> -alkoxybenzoyl)hydrazide
DCC	<i>N,N'</i> -Dicyclohexylcarbodiimid
DMAP	4- <i>N,N</i> -Dimethylaminopyridin
DMF	<i>N,N</i> -Dimethylformamid
NBS	<i>N</i> -Bromsuccinimid
THF	Tetrahydrofuran
TBAI	Tetra- <i>n</i> -butylammoniumiodid
MEK	Methylethylketon

### Sonstige Abkürzungen

RT	Raumtemperatur
$\phi$	Verdrillungswinkel benachbarter Moleküle





# 1. Einleitung und Motivation

## 1.1 Flüssigkristalliner Zustand

Flüssigkristalline Systeme bestehen aus unzähligen einzelnen Molekülen, die über attraktive und repulsive Wechselwirkungen (Dispersions-WeWi) interagieren <sup>[12]</sup> und sich zu supramolekularen Überstrukturen organisieren können. Moleküle, die befähigt sind einen solchen Zustand auszubilden, stellen eine besondere Form der Materie dar. Sie sind in der Lage verschiedenste flüssigkristalline Phasen (LC-Phasen) auszubilden. Jener nichtklassische Aggregatzustand befindet sich zwischen dem hoch geordneten festen (Cr) und dem ungeordneten flüssigen Aggregatzustand (Iso), dabei vereinen diese Systeme Eigenschaften beider Zustände (Abb. 1.1). Aufgrund dessen werden solche Verbindungen als „Mesogene“ bezeichnet. Substanzen mit flüssigkristallin mesomorphen Charakter zeigen anisotrope Eigenschaften eines Feststoffes, wie der Doppelbrechung, bei zeitgleicher Fluidität von Flüssigkeiten. <sup>[13,14]</sup> Dieses Verhalten kann bei einer großen Bandbreite von Molekülen beobachtet werden (Abb. 1.4), dennoch ist die Bildung flüssigkristalliner Phasen allgemein auf zwei grundlegende Konzepte zurückzuführen - die Formanisotropie und die Amphiphilie. Bei der anisometrischen Raumausdehnung eines Moleküls in verschiedene Raumrichtungen entsteht eine Abhängigkeit der Ordnung der Moleküle untereinander aufgrund attraktiver und repulsiver Wechselwirkungen. <sup>[15]</sup> Dies resultiert in einer Orientierungsfernordnung der Mesogene, welche charakteristisch für nematische Phasen (N) ist und bevorzugt von stäbchenförmigen (kalamitsisch) <sup>[16]</sup> und scheibenförmigen (diskotisch) <sup>[17]</sup> Molekülen gebildet wird. Die Ausbildung flüssigkristalliner Mesophasen kann auf zwei Wegen erreicht werden, durch eine Temperaturänderung (thermotrop) oder durch die Zugabe eines Lösungsmittels und zusätzlicher Temperaturänderung (lyotrop). <sup>[18]</sup>

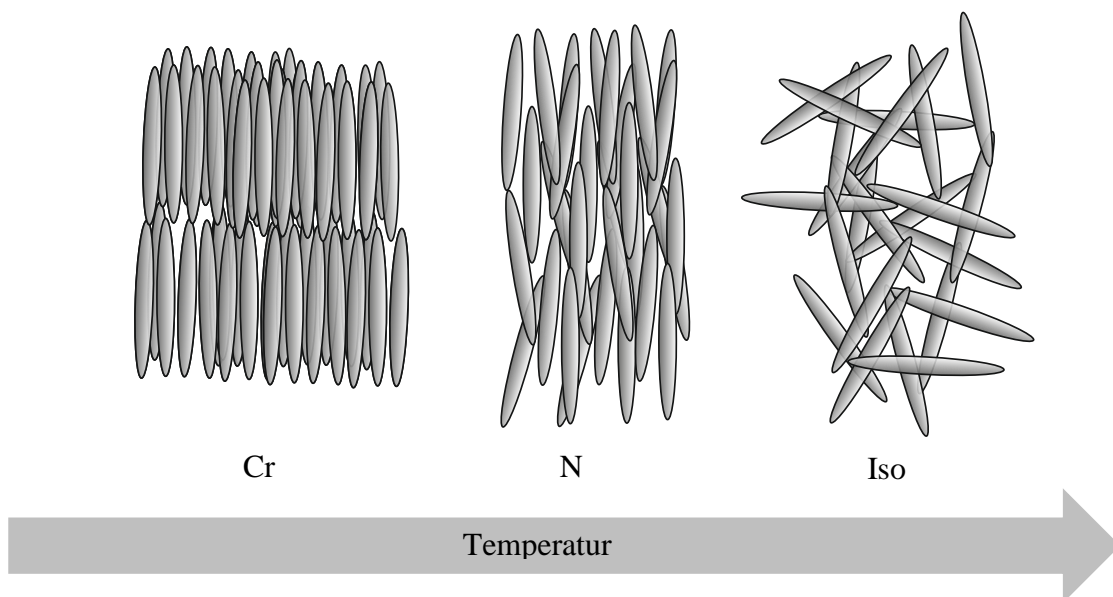


**Abbildung 1.1** Schematische Darstellung der Organisation kalamitischer Moleküle während des Übergangs vom geordneten kristallinen (Cr) über den flüssigkristallinen (nematisch, N) in den ungeordneten flüssigen Zustand (Iso) mit steigender Temperatur.

Darüber hinaus können Mesogene eine große Vielfalt an LC-Phasen ausbilden, bei denen neben der Orientierungsfernordnung noch eine Positionsfernordnung in einer, zwei oder drei Raumrichtungen hinzukommt. Dies gelingt durch das Hinzufügen mindestens eines inkompatiblen Molekülteils zum rigiden Gerüst, die aufgrund ihrer Eigenschaften miteinander unverträglich sind. Aufgrund dessen, dass diese Segmente dennoch kovalent gebunden sind, resultiert eine Segregation jener Molekülteile in getrennte Nanodomänen, das letztendlich zu der Ausbildung flüssigkristalliner Phasen mit 1-, 2- oder 3-dimensionaler Fernordnung, die als smektische (Sm), kolumnare (Col) bzw. 3D-Phasen (zumeist kubische Phasen = Cub) bezeichnet werden, führt. Damit ist die Ausbildung dieser positionsferngeordneten Phasen mit dem fundamentalen Konzept der Amphiphilie verknüpft.<sup>[19,20]</sup> Die Segregation kann durch die Kombination von aromatischen/aliphatischen (polycatenare Moleküle<sup>[21,22]</sup>), polaren/unpolaren (klassische Amphiphile, z.B.: Polyhydroxy-Verbindungen<sup>[23]</sup>) oder rigiden/flexiblen Molekülteilen hervorgerufen werden. Entscheidend bei der Ausbildung der LC-Phasen ist das Volumenverhältnis zwischen den nicht mischbaren Molekülsegmenten. Durch die Entmischung der Segmente in Nanodomänen entstehen zwischen diesen Domänen Grenzflächen (Intermaterial dividing surface = IMDS)<sup>[24]</sup>, die für die jeweiligen Phasen spezifisch sind.

Im Folgenden werden sich die Beschreibungen nur auf kalamitische polycatenare Mesogene beschränken. Bei Amphiphilen mit annähernder gleicher Verteilung zwischen dem starren aromatischen Gerüst und den flexiblen Alkylketten bilden sich vor allem Schichtstrukturen mit flachen Grenzflächen aus. Zu diesen Phasen gehören die lamellaren Phasen wie die smektische Phase (Sm). In diesen ungeordneten Schichtstrukturen richten sich die Moleküle parallel zueinander aus, dabei können die Moleküllängsachsen zur Schichtebene senkrecht (SmA), geneigt (SmC) oder parallel (Lam) ausgerichtet sein. Hexatische Phasen (Hex) bilden zusätzlich eine hexagonale Positionsfernordnung in den einzelnen Schichten aus, in der die Moleküle ebenfalls senkrecht (HexB) oder geneigt (HexI, HexF) vorliegen können (Abb. 1.2). Zwischen den Schichten gibt es aber keine Fernordnung, sondern nur eine sogenannte „Bindungsorientierungsordnung“.<sup>[24,25]</sup> Betrachtet man die Ausrichtung der Moleküle in den benachbarten Schichtebenen der geneigten Phasen kann zusätzlich noch zwischen synklin (Index s), gleiche Ausrichtung, und antiklin (Index a), alternierende Ausrichtung, unterschieden werden.

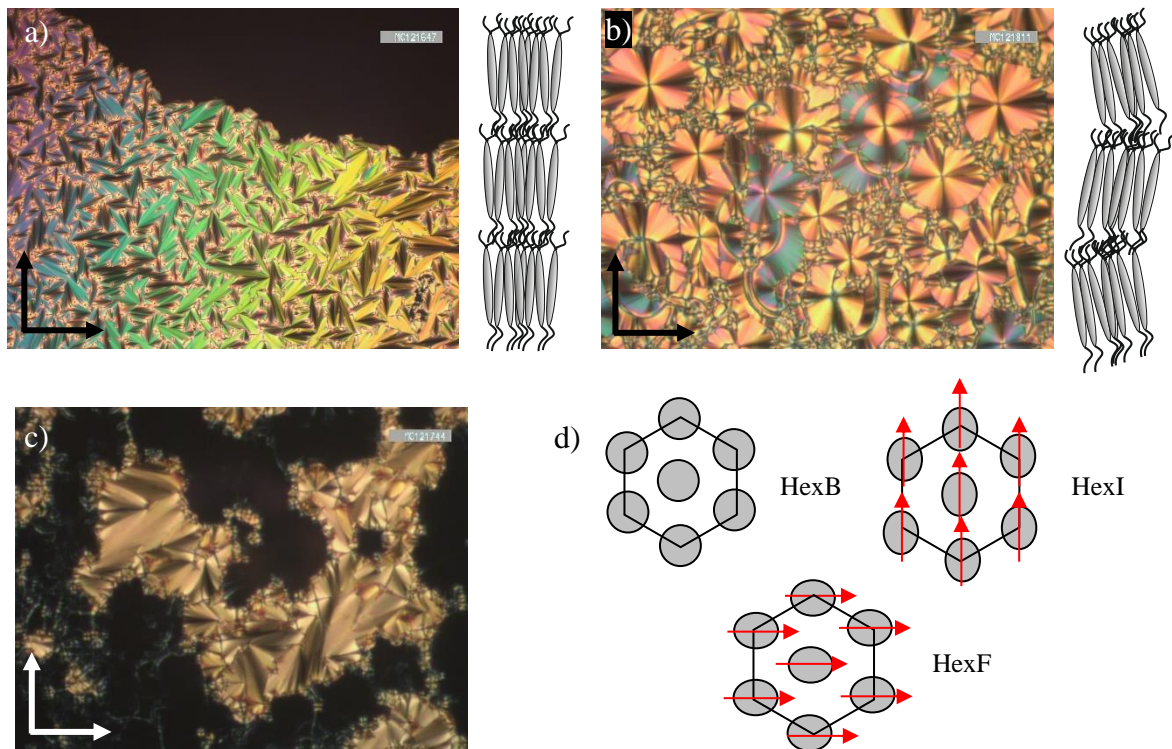


**Abbildung 1.2** Polarisationsmikroskopische Aufnahmen der Texturen und Strukturen von (a) einer smektischen A-Phase ( $SmA$ ), (b) einer antiklinen smektische C-Phase ( $SmC_a$ ) und (c) einer hexatischen B-Phase ( $Hex_B$ ). (d) Schematische Darstellung verschiedener hexatischer Phasen mit Blickrichtung parallel zur Schichtnormalen. Die grauen Ellipsen representieren die Querschnitte durch die Moleküle und die Pfeile geben die Tilt-Richtung an. [27]

Wird das Volumen nur eines inkompatiblen Molekülsegmentes stetig erhöht, nimmt die Grenzflächenkrümmung zwischen den Domänen zu und die Ausbildung bikontinuierlicher kubischer ( $Cub_V$ ), kolumnarer ( $Col$ ) bis hin zu mizellar kubischen Phasen ( $Cub_I$ ) kann beobachtet werden. [28] Die Phasensequenz  $Sm-Cub_V-Col-Cub_I$  kann für amphiphile Substanzen allgemein beobachtet werden (Abb. 1.3). Zusätzlich kann zwischen Normalphasen (polarer Anteil nimmt zu) und inversen Phasen (lipophiler Anteil nimmt zu) unterschieden werden.

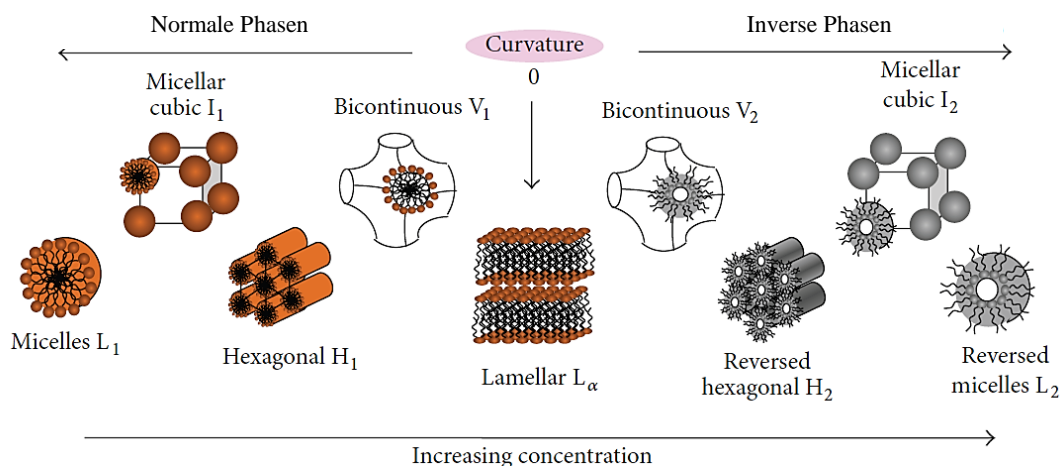


**Abbildung 1.3** Allgemeine Phasensequenz amphiphiler Moleküle in Abhängigkeit von der Konzentration des Amphiphils in einem polaren Lösungsmittel. [29] Copyright 2015 Domenico Lombardo et al.

## 1.2 Kubische Phasen und spontaner Symmetriebruch

Kubische Phasen nehmen einen besonderen Stellenwert in dieser Arbeit ein, einerseits entsprechen sie nicht dem klassischen Konzept der Formanisotropie als Ursache flüssigkristalliner Phasen und andererseits treten diese bei einer Vielzahl von Molekülen unterschiedlicher Struktur, zumeist nur in kleinen Temperaturbereichen, auf (Abb. 1.4).

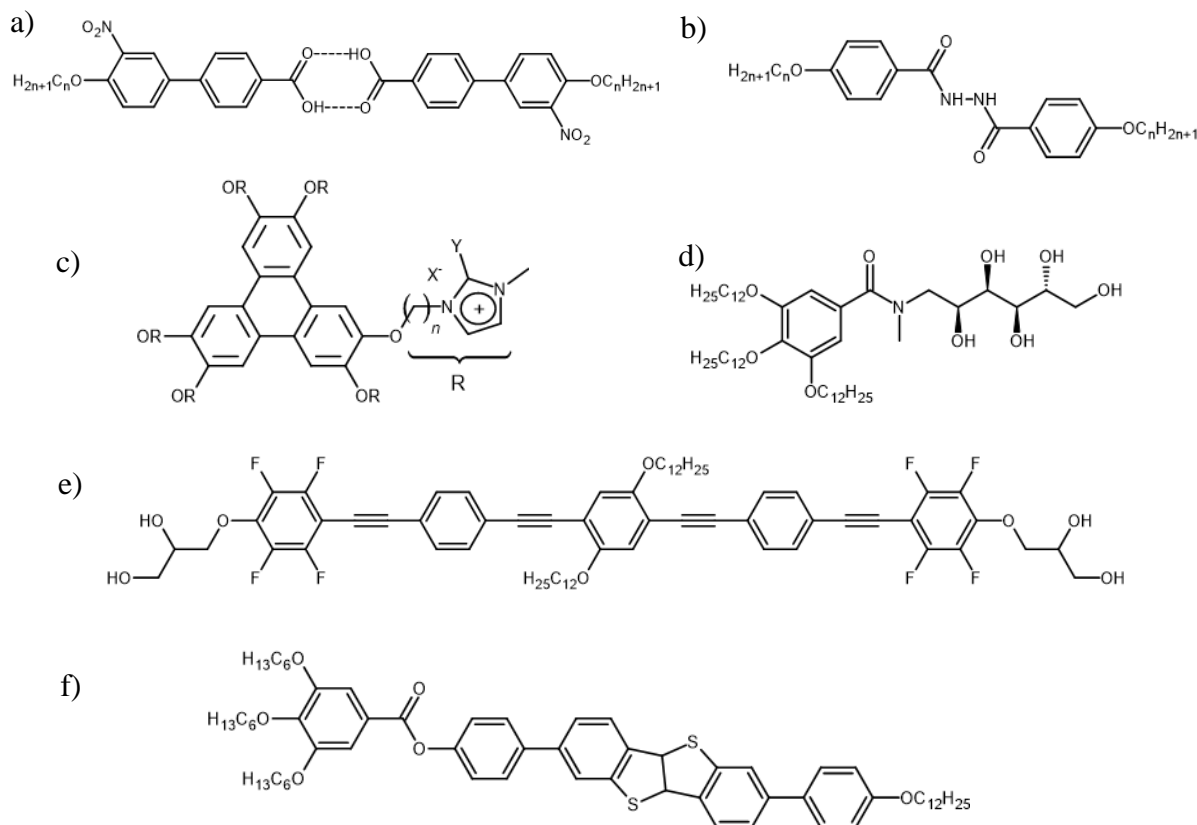


**Abbildung 1.4** Ausgewählte Beispiele von Verbindungen mit thermotropen kubischen Mesophasen: (a) ANBC-*n* <sup>[30-33]</sup>, (b) BABH-*n* <sup>[33-35]</sup>, (c) diskotische Triphenylene <sup>[36]</sup>, (d) 3,4,5-Tridodecyloxybenzoyl-*N*-methylglucamid <sup>[37]</sup>, (e) fluoriertes Oligo(*p*-phenylenethinylene) basierte Bolapolyphile <sup>[38]</sup> und (f) polycatenare [1]benzothieno[3,2-b]benzothiophene <sup>[39]</sup>.

Ihre Sonderstellung beruht zunächst auf visuellen Besonderheiten, da sie eine hohe Viskosität aufweisen und optisch isotrop unter dem Polarisationsmikroskop erscheinen aufgrund ihrer kubischen dreidimensionalen Struktur. Dennoch verdeutlichen röntgenographische Untersuchungen, dass sie dem flüssigkristallinen Zustand zu zuschreiben sind. Denn es zeigt sich neben den scharfen Bragg-Reflexen im Kleinwinkelbereich auch die typische diffuse Streuung bei ca. 0.45 nm im Weitwinkelbereich, weshalb sie eindeutig den Flüssigkristallen zu zuordnen sind. Die voranschreitende Forschung auf dem Gebiet der Flüssigkristalle hat in den letzten Jahren auch die Aufklärung der verschiedenen Strukturen der kubischen Phasen vorangetrieben. Kubische Phasen sind bereits seit mehr als 60 Jahren bekannt (ANBC-*n* von GRAY et. al <sup>[30-33]</sup>, BABH-*n* von DEMUS et.al <sup>[33-35]</sup>), doch die Aufklärung hält bis heute an. Iniziiert wurde die Forschung zunächst in lyotropen Systemen durch die Untersuchung von Lipiden oder Tensiden. <sup>[28,40]</sup> Die fortschreitende Forschung führte zu dem Ergebnis, dass das Verhalten nicht exklusiv für lyotrope Systeme gültig ist, auch wasserfreie Amphiphile

(dendritische und stäbchenförmige Moleküle) können kubische Phasen ausbilden. [30,34,41,81] Bekannte thermotrope homologe Reihen der BABH-*n* und ANBC-*n* zeigten ebenfalls die Phasensequenz Sm-Cub<sub>v</sub>-Col.

Wie bereits erwähnt werden kubische Phasen in zwei Kategorien eingeteilt: den mizellar kubischen Phasen (Cub<sub>I</sub> bzw. Cub<sub>mic</sub>) [28,42,43] und den bikontinuierlichen kubischen Phasen (Cub<sub>v</sub> bzw. Cub<sub>bi</sub>) [33,44]. Der Unterschied liegt in der Ausbildung unterschiedlicher Aggregate bei der Separation der Molekülsegmente. Mizellar kubische Phasen (Cub<sub>mic</sub>) bilden geschlossene sphärische Aggregate aus, in denen ein Molekülsegment den Innenraum einer Mizelle füllt und das andere das Kontinuum bildet. Durch verschiedene Anordnungen der Mizellen im Raum können kubische Gitter mit unterschiedlicher Symmetrie entstehen, wie *Im3m* (innenzentriert), *Fm3m* (flächenzentriert) oder das komplexe *Pn3m*-Gitter (Abb. 1.5).

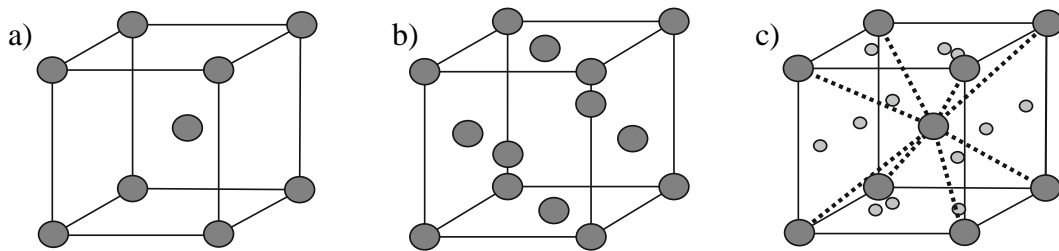


**Abbildung 1.5** Einheitszellen der mizellar kubischen Phasen (Cub<sub>mic</sub>) mit den Raumgruppen (a) *Im3m*, (b) *Fm3m* und (c) *Pn3m*.

Die bikontinuierlichen kubischen Phasen (Cub<sub>bi</sub>) bilden hingegen mindestens zwei interpenetrierende kontinuierliche dreidimensionale Netzwerke aus. Die Netzwerke befinden sich in einem Kontinuum und sind durch eine Minimalgrenzfläche (infinite periodic minimal surface, IPMS [45]) getrennt. In lyotropen als auch thermotropen Systemen werden die Raumgruppen *Ia3d* (Doppelgyroid, DG) [46,47], *Im3m* (Doppelprimitiv, DP) [47-49] und *Pn3m* (Doppeldiamant, DD) [50,51] gefunden. Die Strukturen der Raumgruppen unterscheiden sich durch Art der Minimalfläche zwischen den Netzwerken als auch in der Zahl der Verzweigungen der Netzwerke an den Knoten (DG: 3, DD: 4, DP: 6). [33,52]

Die in thermotropen als auch lyotropen Systemen am häufigsten auftretende Raumgruppe mit *Ia3d*-Symmetrie (Cub<sub>bi</sub>/*Ia3d*) besteht aus zwei interpenetrierenden spiegelbildlichen Netzwerken, die durch eine Schoen-Gyroid-Grenzfläche getrennt sind, deren Knotenpunkte eine Valenz von drei besitzen. Eine gleichmäßige Besetzung der beiden chiralen Netzwerke entgegengesetzter Händigkeit führt zu einer achiralen Gesamtstruktur, weshalb die Phase unter dem Polarisationsmikroskop optisch inaktiv ist. Dies zeigt sich während des Entkreuzens des Analysators um wenige Grad (1-5°) im und gegen den Uhrzeigersinn, wobei keine optische Aktivität beobachtet werden kann. Darüber hinaus ist die Viskosität der Phase stark erhöht gegenüber einer isotropen Flüssigkeit, was in der Abbildung 1.6 a, c an der Gestalt der Phasengrenze Luft/Probe deutlich zu erkennen ist. Das hochaufgelöste SAXS-Diffraktogramm der *Ia3d*-Phase ist in Abbildung 1.6 g dargestellt. In den hausinternen röntgenographischen Untersuchungen der Phase werden neben dem diffusen Weitwinkelreflex auch die intensivsten (211) und (220) Kleinwinkelbereichreflexe (zusätzlich (332)) des *Ia3d*-Gitters gefunden (Abb. 1.6 f). Dieses Diffraktogramm zusammen mit dem Nachweis der optischen Inaktivität erlauben eine sichere Zuordnung der kubischen *Ia3d*-Phase bei polycatenaren Systemen.

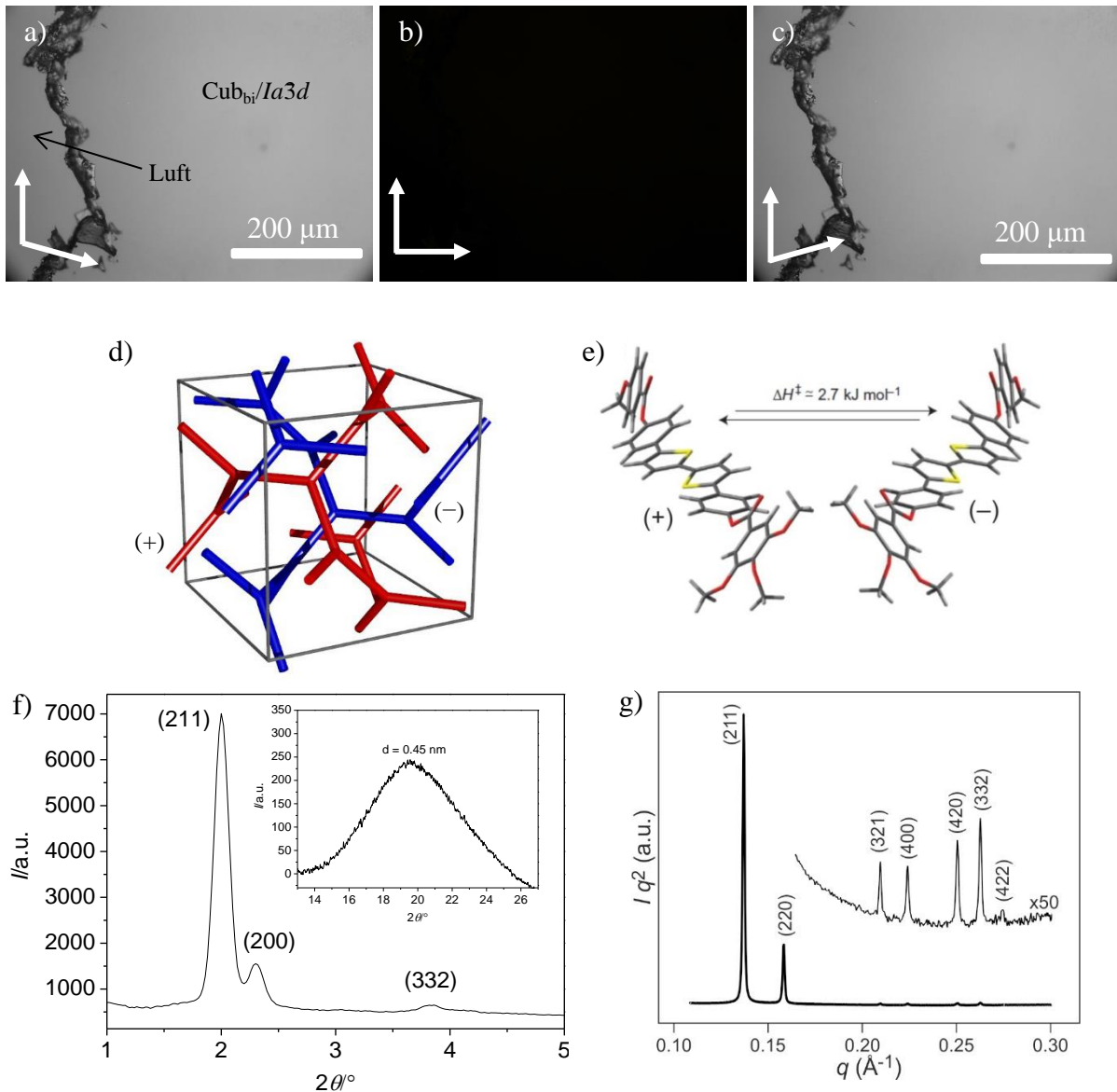


**Abbildung 1.6** Polarisationsmikroskopische Aufnahme der achiralen bikontinuierlichen kubischen  $\text{Cub}_{\text{bi}}/\text{Ia}3d$ -Phase an der Phasengrenze Luft/Probe bei entkreuzten Polarisatoren (a) im Uhrzeigersinn, (c) entgegen des Uhrzeigersinns und (b) bei gekreuzten Polarisatoren. Die Aufnahmen wurden nachträglich in Graustufen umgewandelt. (d) Darstellung der enantiomorphen Netzwerke der kubischen  $\text{Cub}_{\text{bi}}/\text{Ia}3d$ -Phase.<sup>[52]</sup> (e) Modellverbindung der chiralen Konformere eines Bithiophens.<sup>[61]</sup> (f) SAXS und WAXS der  $\text{Cub}_{\text{bi}}/\text{Ia}3d$ -Phase mit hausinternen Röntgendiffraktometer (XRD) und (g) hochauflösendes SAXS der  $\text{Cub}_{\text{bi}}/\text{Ia}3d$ -Phase mit Synchrotronstrahlung.

Darüber hinaus wird bei polycatenaren und anderen Molekülen mit starren Segmenten (z.B. ANBC- $n$  und BABH- $n$ ) eine weitere kubische Phase beobachtet, welche zunächst der Raumgruppe  $Im\bar{3}m$  zugeordnet wurde. Bei Untersuchungen der  $Im\bar{3}m$ -Phase in diesen thermotropen Systemen stellte man jedoch im Unterschied zu lyotropen Systemen fest, dass die ermittelten Gitterparameter in den röntgenographischen Analysen um ca. 50 % größer sind als erwartet. Folglich konnte die Struktur der thermotropen  $Im\bar{3}m$ -Phase nicht mit der aus den lyotropen Systemen übereinstimmen. Des Weiteren zeigten polarisationsmikroskopische Aufnahmen der Phase, dass diese im Gegensatz zur  $\text{Ia}3d$ -Phase mit um einen kleinen Winkel entkreuzten Polarisator optisch aktiv sind.<sup>[82]</sup> Das heißt, es tritt ein spontaner Symmetriebruch auf, der sich durch die Bildung einer Konglomeratstruktur von Domänen mit



unterschiedlicher Helligkeit (= entgegengesetzte Chiralität) äußert, welche bei entgegengesetzter Stellung der Polarisatoren invertiert werden (Abb. 1.7 a, c).

Die Grundlage für den spontanen Symmetriebruch ist die chirale Selbsterkennung (chiral self-sorting) <sup>[53]</sup>, erstmals bekannt durch die Entdeckung der Kristallisation der spiegelbildlichen Weinsäuresalze durch PASTEUR <sup>[54]</sup>. Voraussetzung für den spontanen Symmetriebruch auf makroskopischer Ebene sind Moleküle mit konfigurativer oder konformativer Chiralität. Dabei können sich Enantiomere entweder entmischen, Bildung von Konglomeraten, oder Racemate bilden. Die hier betrachteten achiralen Moleküle liegen in einem Gleichgewicht verschiedener zumeist chiraler Konformere vor, deren Enantiomerisierungsbarriere nur sehr gering ist und diese somit im thermodynamischen Gleichgewicht vorliegen. Eine spontane Synchronisation der helikalen Konformere in helikalen Überstrukturen wird hier als Ursache der Konglomeratbildung in den kubischen *Im3m*-Phasen angesehen. <sup>[55,56]</sup>

Anhand dieser Überlegungen wurden alternative Modelle der Struktur der chiralen „*Im3m*-Phase“ in thermotropen Systemen durch LEVELUT und CLERC <sup>[57]</sup>, KUTSUMIZU <sup>[58]</sup> und SAITO <sup>[59]</sup> postuliert. Allerdings konnten diese nicht alle Merkmale der Phase grundlegend erklären. Die Chiralität der Phase widerlegt bereits, dass es sich um die *Im3m*-Phase handeln kann, da sie intrinsisch achiral ist. Erst kürzlich wurde eine neue Struktur durch ZENG und UNGAR vorgeschlagen, welche alle Merkmale der Struktur vereint. <sup>[60]</sup> Es handelt sich dabei um eine bikontinuierliche kubische Phase bestehend aus drei Netzwerken mit *I23* Raumgruppe, deren Knotenpunkte ausschließlich dreiwertige Verknüpfungen besitzen. Diese Tatsache erklärt zunächst den deutlich größeren Raumanspruch des Gitters im Gegensatz zu der *Im3m*-Phase. Durch eine helikale Organisation der Moleküle kann die Helicität der Einzelnetzwerke nicht kompensiert werden und damit ist die makroskopische Chiralität erklärbar (Abb. 1.7 a, c). Die Abbildung 1.7 g zeigt das hochauflösende SAXS-Diffraktogramm einer *I23*-Phase, aufgenommen am Synchrotron. In den hausinternen Röntgendiffraktogrammen werden neben der diffusen Weitwinkelstreuung die intensivsten (321), (400) und (420) Kleinwinkelreflexe gefunden (Abb. 1.7 f). Zusammen mit dem Nachweis der optischen Aktivität (Konglomeratstruktur) ist die sichere Identifizierung der *I23*-Phase möglich. Im Gegensatz zur *I23*-Phase ist die *Ia3d*-Phase immer achiral, auch wenn die Moleküle entlang der einzelnen Netzwerke helikal organisiert sind. Dies liegt daran, dass die beiden Netzwerke enantiomorph sind und damit auch der Helixsinn in den beiden Netzwerken entgegengesetzt ist. Es handelt sich also um eine supramolekulare *meso*-Struktur.

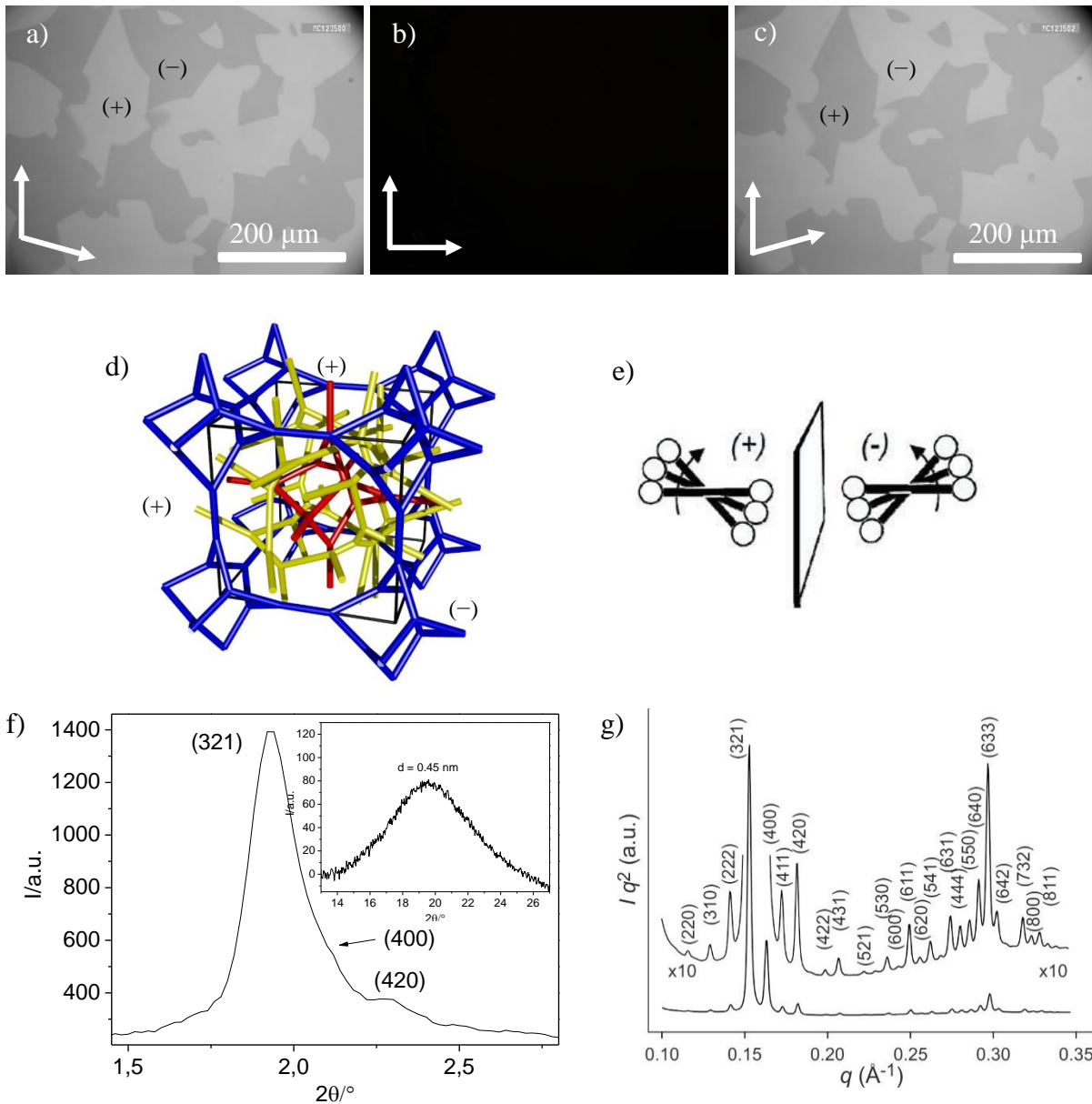


**Abbildung 1.7** Polarisationsmikroskopische Aufnahme eines Konglomerates der chiralen bikontinuierlichen kubischen  $\text{Cub}_{\text{bi}}^{[*]}/I23$  bei entkreuzten Polarisatoren (a) im Uhrzeigersinn, (c) entgegen des Uhrzeigersinns und (b) bei gekreuzten Polarisatoren. Die Aufnahmen wurden nachträglich in Graustufen umgewandelt. (d) Darstellung der Netzwerke der kubischen  $\text{Cub}_{\text{bi}}^{[*]}/I23$ -Phase. <sup>[52]</sup> (e) Schematische Darstellung der Entwicklung des helikalen Twists entlang der Netzwerke, verursacht durch die Abstoßung voluminöser Endgruppen. (f) SAXS und WAXS der  $\text{Cub}_{\text{bi}}^{[*]}/I23$ -Phase vom hausinternen Röntgendiffraktometer (XRD) und (g) hochauflösendes SAXS der  $\text{Cub}_{\text{bi}}^{[*]}/I23$ -Phase mit Synchrotronstrahlung.



### 1.3 Flüssige isotrope Mesophasen und spontaner Symmetriebruch

Eine Sonderstellung nehmen die isotropen Flüssigkeiten polycatenarer Moleküle in Nachbarschaft zu den  $\text{Cub}_{\text{bi}}$ -Phasen ein. In früheren Arbeiten konnte bereits gezeigt werden, dass neben der normalen achiralen isotropen Flüssigkeit (Iso) noch eine weitere chirale isotrope Flüssigkeit ( $\text{Iso}_1^{[*]}$ ) existiert.<sup>[61]</sup> Der spontane Symmetriebruch achiraler Moleküle in diesen Flüssigkeiten äußert sich in der Ausbildung einer Konglomeratstruktur mit chiralen Domänen (Abb. 1.8 a-c). Auf molekularer Ebene gesehen bleibt offensichtlich die helikale Überstruktur der kubischen Phasen zumindest lokal erhalten, wobei die chirale Information über makroskopische Distanzen weitergegeben wird. Der Iso- $\text{Iso}_1^{[*]}$  Übergang kann in DSC-Untersuchungen als ein breites Endotherm ( $\Delta H \sim 0.1$  kJ/mol) beobachtet werden. Die Bildung der chiralen isotropen Phase findet nicht ausschließlich am Cub-Iso Übergang statt, auch der  $\text{SmC}$ - $\text{Iso}_1^{[*]}$  Übergang ist bekannt.

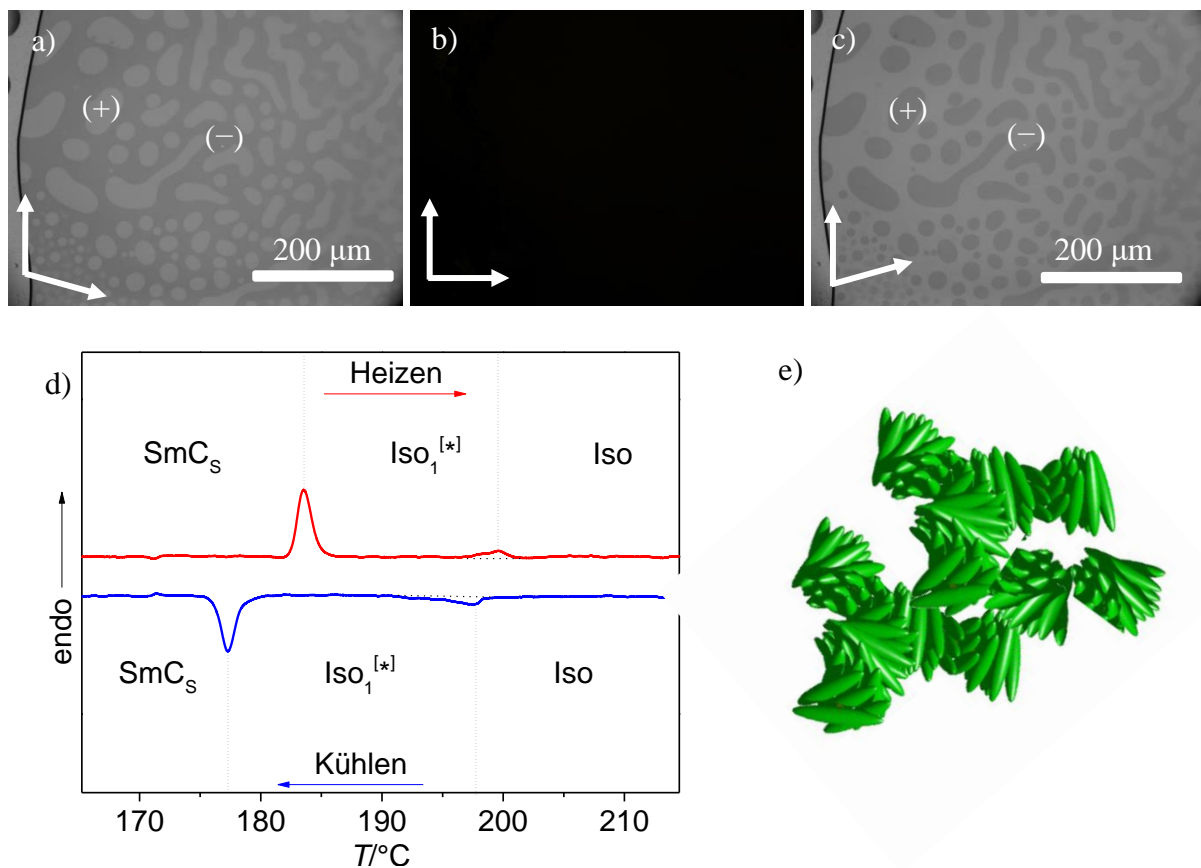


**Abbildung 1.8** Polarisationsmikroskopische Aufnahme des spontanen Symmetriebruchs der chiralen Flüssigkeit  $\text{Iso}_1^{[*]}$  bei entkreuzten Polarisatoren (a) im Uhrzeigersinn, (c) entgegen des Uhrzeigersinns und (b) bei gekreuztem Polarisatoren. Die Aufnahmen wurden nachträglich in Graustufen umgewandelt. (d) Differentialkalorimetrische Aufnahme des  $\text{SmC}_s$ - $\text{Iso}_1^{[*]}$ -Iso-Übergangs. (e) Schematische Darstellung eines helikal verdrillten Clusters calamitischer Mesogene in der chiralen  $\text{Iso}_1^{[*]}$ -Phase.<sup>[62]</sup>

## 1.4 Zielstellung

In dem ersten Teil der Arbeit ist es Ziel den bisherigen Kenntnisstand <sup>[52,61,63,64]</sup> auf dem Gebiet der polycatenaren 5,5'-Diphenyl-2,2'-bithiophen zu vervollständigen. Durch systematische Variationen der Struktur soll ein detailliertes Verständnis der Struktur/Eigenschaft-Beziehung gewonnen werden. Dabei liegt ein besonderes Augenmerk auf der Ausbildung der bikontinuierlichen kubischen Phasen ( $Cub_{bi}/Ia3d$ ,  $Cub_{bi}^{[*]}/I23$ ), den isotropen Flüssigkeiten ( $Iso_1$ ,  $Iso_1^{[*]}$ ) und dem in diesen Mesophasen auftretenden Spiegelsymmetriebruch.

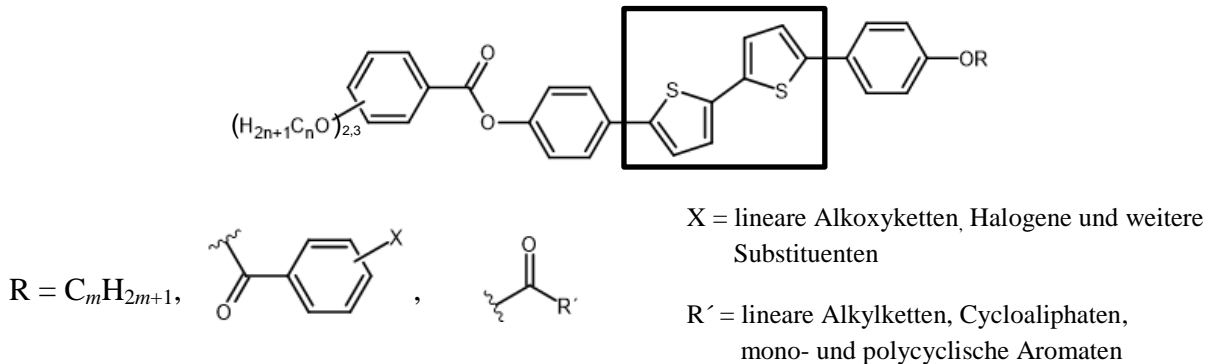


Abbildung 1.9 Strukturen der polycatenare Bithiophene.

In dem zweiten Teil der Arbeit ist es Ziel die bisherigen Kenntnisse zum Design-Konzept kubischer Phasen auf die Substanzklasse der Benzile als Grundgerüst zu übertragen. Benzile sind vom großen Interesse, da sie wie die 5,5'-Diphenyl-2,2'-bithiophene leicht eine helikale Konformation einnehmen können. Das Ziel ist es erste Beispiele flüssigkristalliner Benzile zu synthetisieren, insbesondere solche, die in der Lage sind kubischen Phasen ( $Cub_{bi}/Ia3d$ ,  $Cub_{bi}^{[*]}/I23$ ) als auch die isotropen Mesophasen ( $Iso_1$ ,  $Iso_1^{[*]}$ ) zu bilden. Wie bei den Bithiophenen ist der Spiegelsymmetriebruch innerhalb der Phasen von besonderem Interesse.

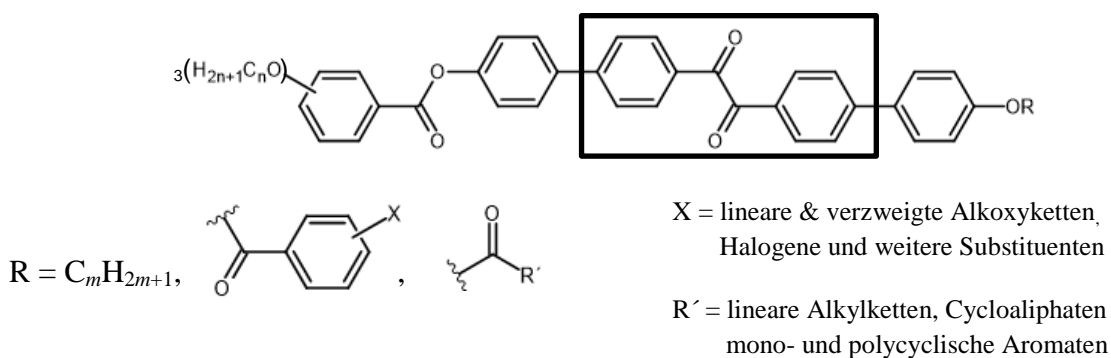
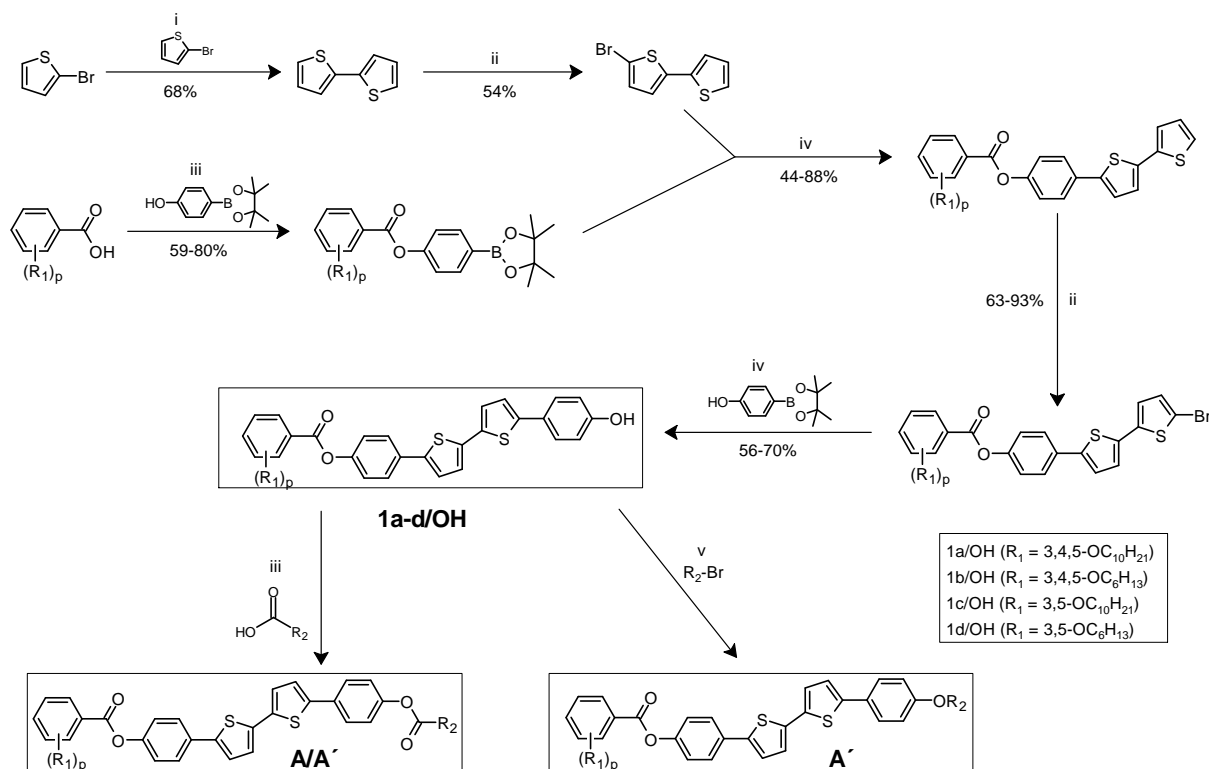


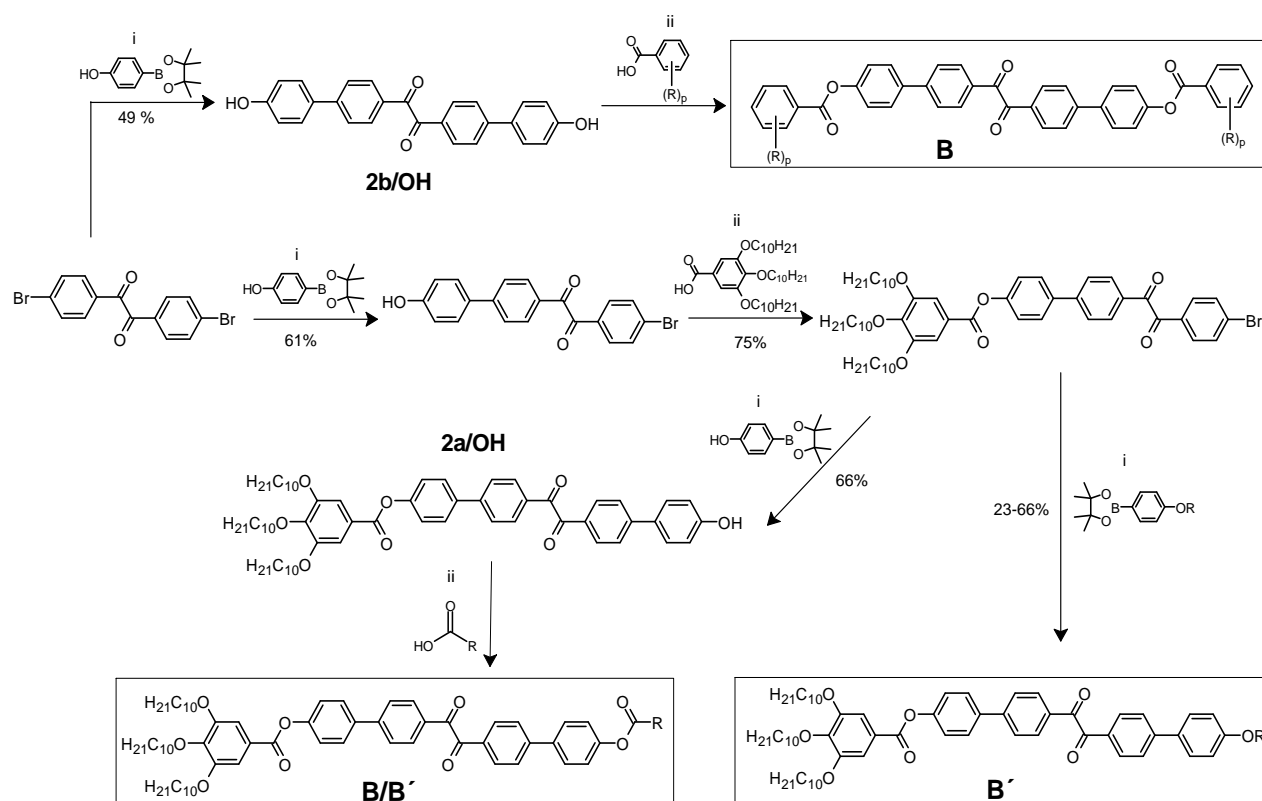
Abbildung 1.10 Strukturen der polycatenaren Benzilderivate.

## 2. Synthese

Die Synthese der 5,5'-Diphenyl-2,2'-bithiophene **A/A'** und der Benzilderivate **B/B'** sind in den „Supporting Information“ der Publikationen **C** [27], **D** [62] und in der Referenz [52] beschrieben und in den Schemata 2.1 und 2.2 nochmals zusammenfassend dargestellt. Diese basieren auf SUZUKI-Kopplungen [87] zum Aufbau des polyaromatischen Grundgerüsts, gefolgt von Alkylierungen und Acylierungen der intermediären Phenole **1a-d/OH** bzw. **2a-b/OH**. Die Synthesestrategie der Bithiophene wurde bereits in früheren Arbeiten entwickelt [52,63,64] und auf die Synthese der neuen Verbindungen angewandt. Für die Synthese der Benzile **B/B'** wurde eine Synthesestrategie ausgehend von 4,4'-Dibrombenzil entwickelt. Details der Synthesen und die analytischen Daten der neuen Verbindungen finden sich in den SI der Publikationen (**D**, **E**). Für die symmetrischen Benzile wird 4,4'-Dibrombenzil mit zwei äquivalenten 4-Hydroxyphenylboronsäurepinacolester zum zweiwertigen Phenol **2b/OH** umgesetzt. Zur Synthese der unsymmetrischen Benzile wird 4,4'-Dibrombenzil lediglich mit einem äquivalent 4-Hydroxyphenylboronsäurepinacolester umgesetzt und nach Acylierung mit 3,4,5-Tri-*n*-decyloxybenzoylchlorid erfolgt eine zweite SUZUKI-Kopplung, entweder mit einem 4-Alkyloxyphenylboronsäurepinacolester zu den Verbindungen **B'** oder mit 4-Hydroxyphenylboronsäurepinacolester zum Phenol **2a/OH**. Das zweiwertige Phenol **2b/OH** bzw. das Phenol **2a/OH** werden acyliert, was zu den symmetrischen bzw. unsymmetrischen polycatenaren Verbindungen **B** führt. Die Synthesen und die analytischen Daten der nicht-publizierten Verbindungen sind im experimentellen Teil in Kapitel 6 zusammengefasst.



**Schema 2.1** Synthese der polycatenaren 5,5'-Diphenyl-2,2'-bithiophen basierten Zielverbindungen **A** und **A'**. Reagenzien und Bedingungen: i) Mg, abs. Et<sub>2</sub>O, Rückfluss, anschließend [Ni(dppp)]Cl<sub>2</sub>, 0°C; ii) NBS, abs. THF, RT [75]; iii) DCC, DMAP, CH<sub>2</sub>Cl<sub>2</sub>, RT oder SOCl<sub>2</sub>, Py, DMAP, CH<sub>2</sub>Cl<sub>2</sub>, RT; iv) [Pd(PPh<sub>3</sub>)<sub>4</sub>], THF, NaHCO<sub>3</sub>-gesättigt, Rückfluss; v) K<sub>2</sub>CO<sub>3</sub>, TBAI, MEK, Rückfluss. [52,63,64] *p* = 1-3 (Abb. 2.1).



**Schema 2.2** Synthese der 1,2'-Biphenyl-1,2-ethandion basierten Zielmoleküle **B** und **B'**. Reagenzien und Bedingungen: i)  $[\text{Pd}(\text{PPh}_3)_4]$ , THF,  $\text{NaHCO}_3$ -gesättigt, Rückfluss; ii)  $\text{SOCl}_2$ , Py, DMAP,  $\text{CH}_2\text{Cl}_2$ , RT. <sup>[65]</sup>  $p = 1-3$  (Abb. 2.1).

## 2.1 Nomenklatur der Zielverbindungen

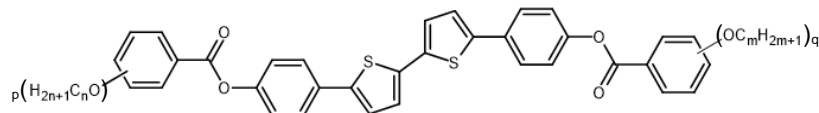
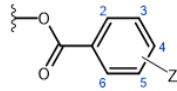
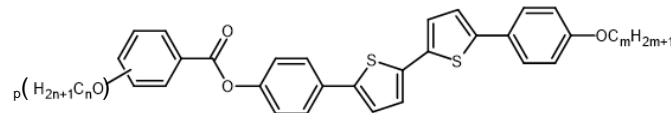
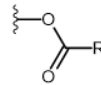
In den Publikationen **A** bis **E** wurden für die Substanzen unterschiedliche Nomenklaturen verwendet. In der zusammenfassenden Darstellung der wichtigsten Ergebnisse wird eine von der in den Publikationen verwendete abweichende, aber einheitliche Substanzbezeichnung angewendet, die im Folgenden erläutert wird (Abb. 2.1).

Die sechskernigen Verbindungen mit einem 5,5'-Diphenyl-2,2'-bithiophen Grundgerüst und zwei terminal gebundenen Benzoatgruppen erhalten die Abkürzung **A**. Die Kleinbuchstaben **a-d** kennzeichnen die Anzahl und Position der Alkoxyketten gefolgt von einer tiefgestellten Zahl  $n/m$ , welche die Kettenlänge beschreibt (Abb. 2.1 c). Bei anderen Substituenten wird eine geeignete Abkürzung verwendet und deren Position durch eine vorangestellte Zahl in Klammern gekennzeichnet. Die fünfkernigen Substanzen mit lediglich einer terminal gebundenen Benzoateinheit und einem davon verschiedenen zweiten Molekülende werden als **A'** bezeichnet (Abb. 2.1 a). Bei diesen Substituenten handelt es um lineare (lin), verzweigte (br), cyclische (cy, Ada, Npht, Anth, Biph) oder heterocyclische (Th) Acyloxygruppen.

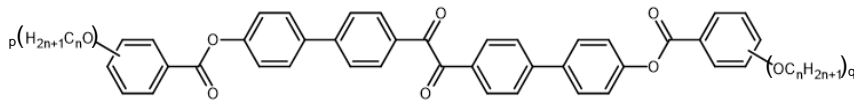
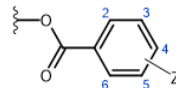
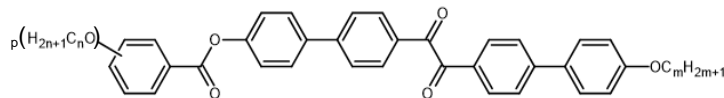
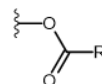
Analog zu den Bithiophenen **A** und **A'** erhalten Mesogene mit einem 1,2-Bis-(1,1'-biphenyl-4-yl)-1,2-ethandion Grundkörper in Abhängigkeit von der terminal gebundenen Benzoateinheiten die Bezeichnung **B** oder **B'** (Abb. 2.1 b).

Substanzen, welche noch nicht publiziert wurden und mit dieser Nomenklatur nicht erfasst werden können, werden an gegebener Stelle erläutert. Zur Kennzeichnung der Mesogene, welche von DRESSEL <sup>[63]</sup> synthetisiert wurden sind, werden diese *kursiv* geschrieben.

a)

 $\mathbf{Ax}_n/y_m$  $\mathbf{Ax}_n/^{(r)}\mathbf{Z}$ (Z = H, F, Br, I, CN, NO<sub>2</sub>) $\mathbf{A}'x_n/m$  $\mathbf{A}'x_n/\mathbf{R}$ 

b)

 $\mathbf{Bx}_n/y_m$  $\mathbf{Bx}_n/^{(r)}\mathbf{Z}$ (Z = H, F, Br, I, CN, NO<sub>2</sub>) $\mathbf{B}'x_n/m$  $\mathbf{B}'x_n/\mathbf{R}$ 

c)

$$x,y = \begin{cases} \mathbf{a} = 3,4,5\text{-Trialkoxysubstitution} & (p,q = 3) & \mathbf{R} = \text{linm, cym, brm} \\ \mathbf{b} = 3,5\text{-Dialkoxysubstitution} & (p,q = 2) & \\ \mathbf{c} = 3,4\text{-Dialkoxysubstitution} & (p,q = 2) & \mathbf{R} = \text{Ada, Npht, Anth, Biph, Th} \\ \mathbf{d} = 4\text{-Alkoxysubstitution} & (p,q = 1) & \end{cases}$$

**Abbildung 2.1** Schema zur Benennung der polycatenaren (a) 5,5'-Diphenyl-2,2'-bithiophene ( $\mathbf{Ax}_n/y_m$ ,  $\mathbf{Ax}_n/^{(r)}\mathbf{Z}$ ,  $\mathbf{A}'x_n/m$ ,  $\mathbf{A}'x_n/\mathbf{R}$ ) und (b) der 1,2-Diphenyl-1,2-ethandione ( $\mathbf{Bx}_n/y_m$ ,  $\mathbf{Bx}_n/^{(r)}\mathbf{Z}$ ,  $\mathbf{B}'x_n/m$ ,  $\mathbf{B}'x_n/\mathbf{R}$ ). (c) Erklärung der Kürzel für die Beschreibung der Kettenverteilung und -anzahl an den Grundkörpern.



### 3. Thermotrope Selbstorganisation der polycatenaren Bithiophene

Dieses Kapitel beschäftigt sich mit den flüssigkristallinen Eigenschaften der 5,5'-Diphenyl-2,2'-bithiophen basierten Mesogene und vervollständigt frühere Arbeiten. <sup>[52,61,63,64]</sup> Die Publikationen A–C werden zunächst zusammenfassend diskutiert und an gegebener Stelle werden weitere nicht publizierte Verbindungen beschrieben.

#### 3.1 Effekte der Kettenzahl und Kettenposition (Publikation C)

In der Publikation C <sup>[27]</sup> wurde das Phasenverhalten der polycatenaren Bithiophene in Abhängigkeit von Kettenanzahl und -position beleuchtet, wobei es sich ausschließlich um *n*-Decyloxyketten handelt, die an die terminalen Benzoateinheiten des Moleküls  $Ax_{10}/y_{10}$  geknüpft sind. Die Ergebnisse sind in dem Balkendiagramm der Abbildung 3.1 zusammengefasst.

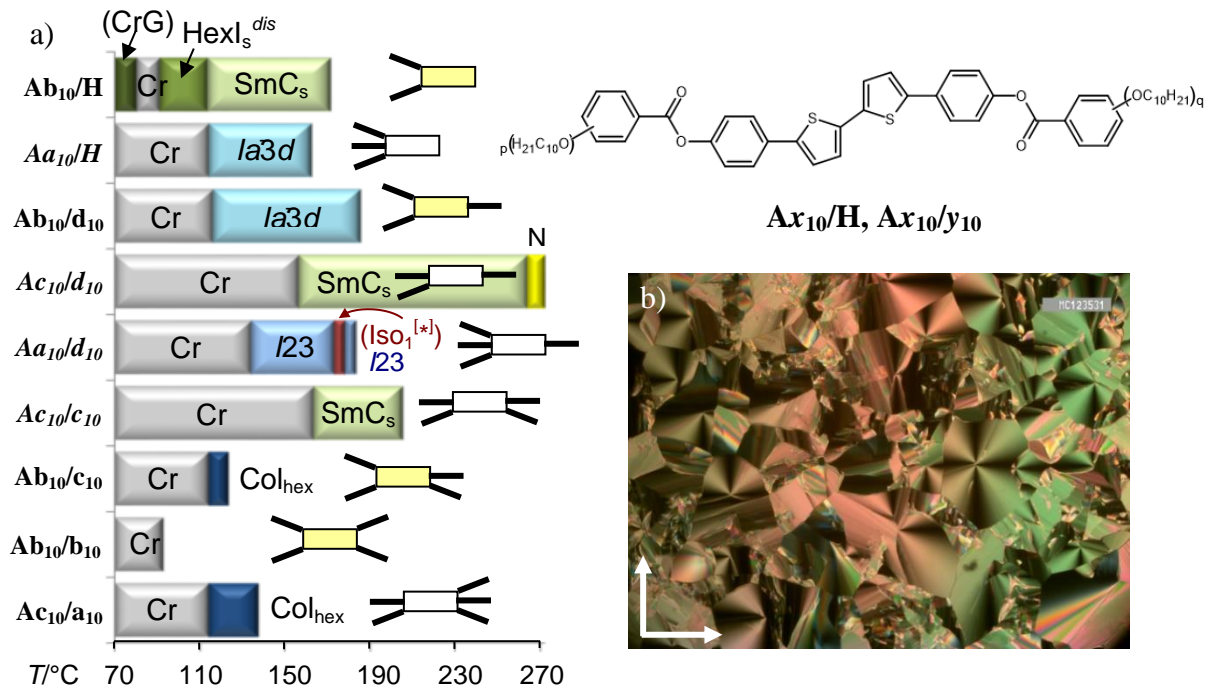


**Abbildung 3.1** (a) Mesophasen der polycatenaren Bithiophene  $Ax_{10}/y_{10}$  in Abhängigkeit von der Kettenanzahl und -position während des Heizzyklus. <sup>[27]</sup> (b) Polarisationsmikroskopische Aufnahme der hexagonal kolumnaren Phase (Col<sub>hex</sub>) der Verbindung  $Ab_{10}/c_{10}$  bei  $T = 120^\circ\text{C}$ . Abkürzungen: Cr = kristalliner Feststoff; CrG = kristalline lamellare G-Phase; HexI<sub>s</sub><sup>dis</sup> = synklone hexatische I-Phase (Kap. 3.2 in Publ. C) <sup>[27]</sup>; SmC<sub>s</sub> = synklone smektische C-Phase; Ia3d = achirale Cub<sub>bi</sub>-Phase mit Ia3d-Symmetrie (Cub<sub>bi</sub>/Ia3d); I23 = chirale Cub<sub>bi</sub>-Phase mit I23-Symmetrie (Cub<sub>bi</sub><sup>[\*]</sup>/I23); Col<sub>hex</sub> = hexagonale kolumnare Phase; Iso<sub>1</sub><sup>[\*]</sup> = spiegel-symmetriegebrochene isotrope Flüssigkeit mit Konglomeratstruktur chiraler Domänen.

Es zeigt sich, dass bei der Erhöhung der Kettenzahl von zwei auf fünf ein Übergang von lamellaren Strukturen (smektisch Sm, hexatisch Hex) über die beiden bikontinuierlichen kubischen Phasen ( $\text{Cub}_{\text{bi}}/Ia3d$ ,  $\text{Cub}_{\text{bi}}^{[*]}/I23$ ) zu den hexagonal kolumnaren Phasen ( $\text{Col}_{\text{hex}}$ ) stattfindet. Verbindungen mit zwei Ketten sind lediglich smektisch, mit drei und vier Ketten smektisch, kubisch und kolumnar und mit fünf ausschließlich kolumnar. Dies stimmt mit Beobachtungen in anderen Reihen polycatenarer Verbindungen überein. <sup>[21]</sup> Die Verteilung der Ketten weist darauf hin, dass vor allem bei den tri- und tetracatenaren Verbindungen die Symmetrie des Moleküls einen Einfluss auf die gebildeten Mesophasen hat. So bilden unsymmetrische Moleküle bevorzugt bikontinuierliche kubische Phasen ( $\text{Cub}_{\text{bi}}$ ) und symmetrisch substituierte Verbindungen tendieren zur Bildung von geeigneten smektischen Phasen (SmC). Ausgehend von diesen Erkenntnissen rückten die unsymmetrischen tricatenaren und tetracatenaren Bithiophene in den Mittelpunkt. Im Folgenden wird zunächst auf die tri- und tetracatenaren 3,4,5-Trialkoxybenzoate eingegangen (Publ. **A**, **B**) und am Ende des Abschnitts die tricatenaren Verbindungen mit 3,5-Dialkoxybenzoat-Einheiten (Publ. **C**) beschrieben.

### 3.2 Einfluss von Substituenten am unsubstituierten Ende tricatenarer Mesogene (Publikation A)

Daher wurde der Einfluss verschiedenster Substituenten und deren Substitutionsmuster auf die bikontinuierlichen kubischen Phasen detailliert untersucht und in der Publikation **A** <sup>[65]</sup> zusammengefasst. Die Publikation stellt ein Resümee zum Design-Konzept der beiden kubischen Phasen mit  $Ia3d$ - und  $I23$ -Raumgruppe in Abhängigkeit des Substitutionsmusters dar. Ausgangspunkt der Betrachtung ist die Verbindung  $\text{Aa}_{10}/\mathbf{H}$  <sup>[63]</sup> mit einem 5,5'-Diphenyl-2,2'-bithiophen-Gerüst und drei Decyloxyketten in den 3,4,5-Positionen an einem Ende und ohne Substituenten am anderen. Die Verbindung wies eine enantiotrope achirale  $\text{Cub}_{\text{bi}}/Ia3d$ -Phase auf.

Die Einführung von sphärischen Substituenten in der para-Position ( $\text{Aa}_{10}/^{(4)}\mathbf{Z}$ ), führt zu einer Stabilisierung der kubischen  $Ia3d$ -Phase mit zunehmender Substituentengröße ( $\mathbf{Z} = \text{H} < \text{F} < \text{I}$ ). Außerdem weisen Elektronenakzeptoren ( $\text{NO}_2$ ,  $\text{CN}$ ) gegenüber Elektronendonatoren ( $\text{CH}_3$ ,  $\text{OCH}_3$ ) eine deutlich höhere Stabilität der kubischen Phasen auf. Die Beobachtung erklärt sich aufgrund der verringerten Elektronendichte des substituierten aromatischen Kerns, wodurch sich die Kern-Kern-Wechselwirkung deutlich verstärken. <sup>[66,67]</sup> Dagegen tendieren Mesogene mit großen tetraedrischen ( $\text{OCF}_3$ ) oder linearen Substituenten ( $\text{OC}_{10}\text{H}_{21}$ ) zur Ausbildung der kubischen  $I23$ -Phase (Abb. 3.2).



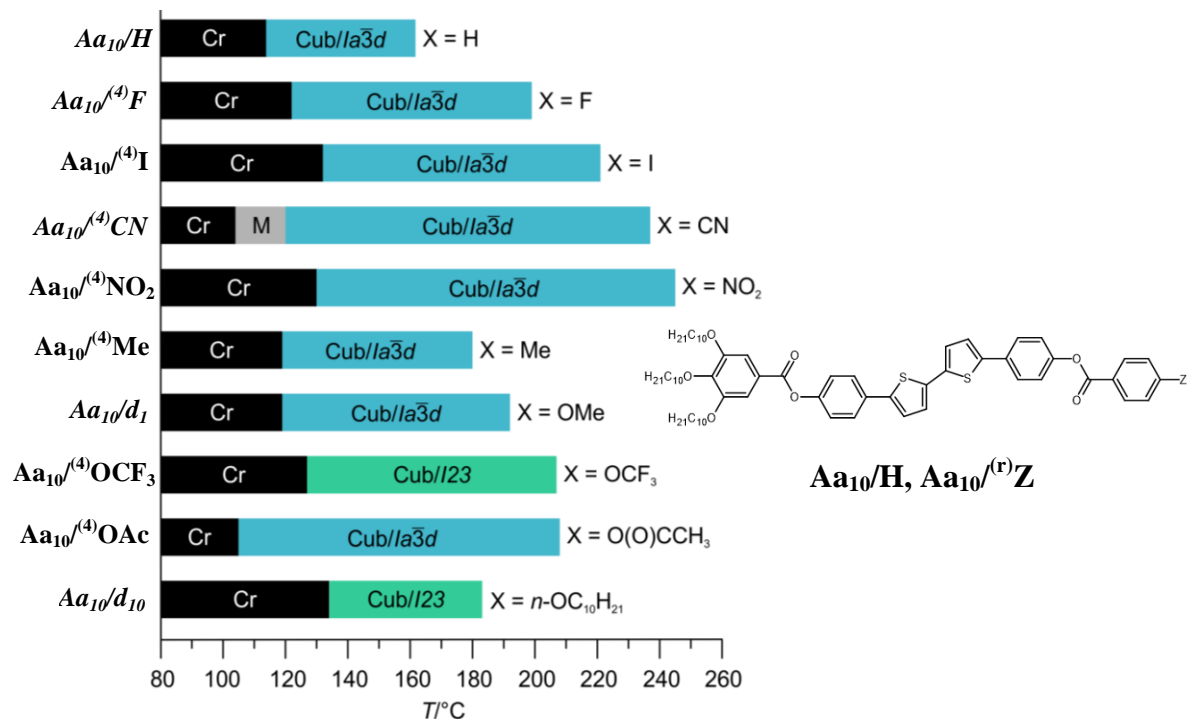
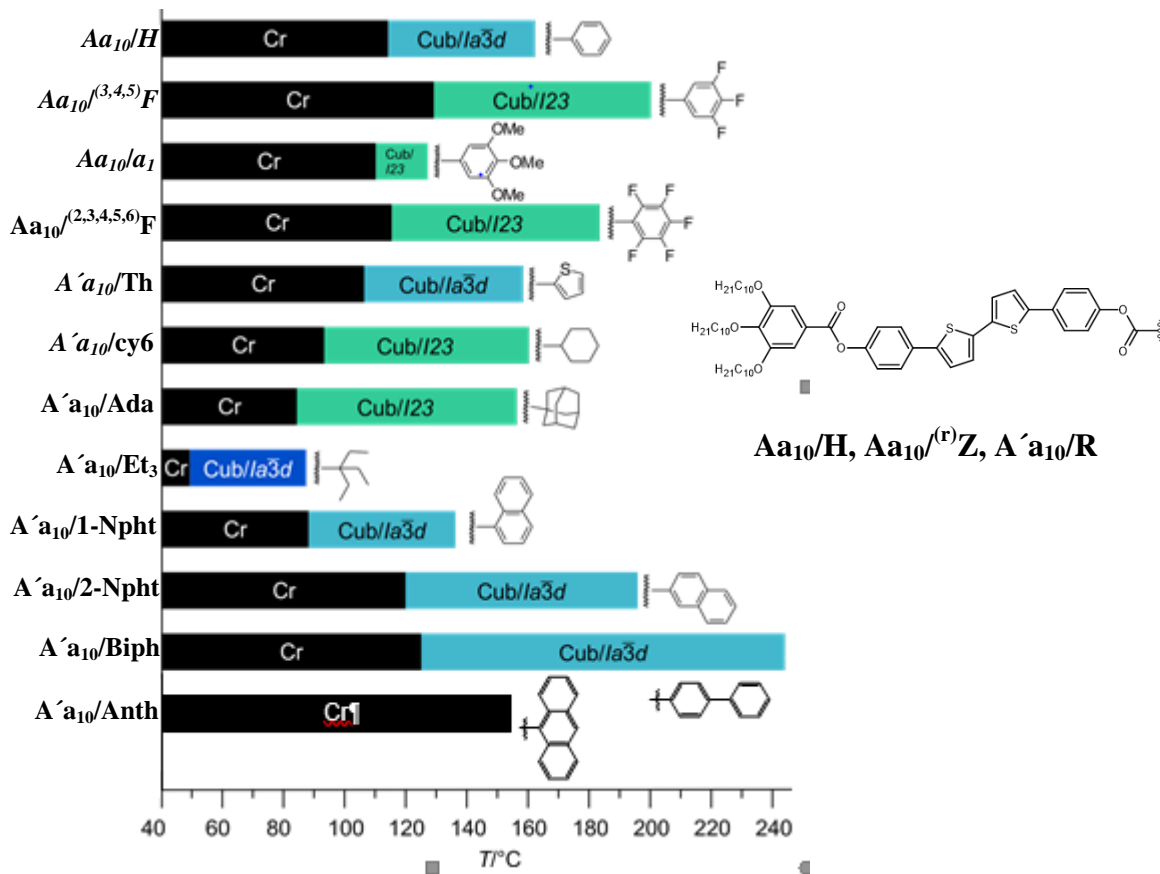


Abbildung 3.2 Mesophasen der para-substituierten polycatenaren Bithiophene  $Aa_{10}^{(4)Z}$  im Heizzyklus. <sup>[65]</sup>

Durch Substituenten in der meta-Stellung des Aromaten ( $Aa_{10}^{(3)Z}$ ) verringert sich der Cub–Iso Übergang deutlich, trotzdem bleiben die kubischen Phasen erhalten (Publ. A). Auch hier stabilisieren die polaren Elektronenakzeptoren ( $Z = F, Br, CN$ ) die kubische Phase gegenüber der unsubstituierten Verbindung ( $Z = H$ ), allerdings deutlich geringer als es in der para-Stellung der Fall ist. Dafür verantwortlich ist die größere sterische Hinderung beim Packen der Moleküle. Darüber hinaus ist ein Übergang von der achiralen  $Ia\bar{3}d$  über eine Koexistenz von  $Ia\bar{3}d$  und  $I23$  zu der chiralen  $I23$ -Phase mit zunehmender Substituentengröße zu beobachten (Abb. 4 a in Publ. A). Wird ein zusätzlicher Substituent in 5-Position ( $Aa_{10}^{(3,5)Z}$ ) hinzugefügt, verstärkt sich der sterische Effekt weiter und die kubische  $Ia\bar{3}d$  wird vollkommen durch die chirale  $I23$ -Phase ersetzt (Abb. 4 b in Publ. A). Nur die Bithiophene mit ortho-Substitution ( $Aa_{10}^{(2)Z}$ ) zeigen eine Destabilisierung der kubischen Phase mit zunehmenden Volumen der Substituenten ( $Z = H < F < I < NO_2$ ) bis hin zum völligen Verlust der kubischen Phase bei  $Z = OMe$  (Abb. 6 b in Publ. A). Bemerkenswert ist allerdings, dass die  $Ia\bar{3}d$ -Phase dennoch erhalten bleibt, trotz des immensen sterischen Effekts. Erst durch eine Zweitsubstitution in der 6-Position ( $Aa_{10}^{(2,6)F}$ ) wird die kubische Phase durch eine synklone  $SmC_5$ -Phase ersetzt. Bemerkenswerterweise hat diese  $SmC$ -Phase eine hohe Tendenz zur Ausbildung chiraler Domänen in homeotropen Zellen (Abb. 6 d-f in Publ. A). Wird die endständige Phenylgruppe durch andere aromatische Ringe und Ringsysteme wie Thiophen, Naphthalin und Biphenyl ( $A'a_{10}/R$ ) ersetzt, bleibt die  $Ia\bar{3}d$ -Phase erhalten. Erst durch Drei- oder Fünfachsubstitution des Benzolrings oder dessen Austausch mit sperrigeren cycloaliphatischen Gruppen wie Cyclohexan (Abb. 3.3) und Adamantan wird ein Übergang zur chiralen kubischen  $I23$ -Phase beobachtet. Besonders hervorzuheben ist die Verbindung mit dem Triethylacetat-Substituenten ( $A'a_{10}/Et_3$ ), die zum Wiedereintritt der  $Ia\bar{3}d$ -Phase mit einem kleinen Gitterparameter führt, obwohl diese Gruppe aufgrund ihrer konformativen Beweglichkeit effektiv größer als die der Adamantylgruppe ist. Damit konnte gezeigt werden, dass es zwei verschiedene  $Ia\bar{3}d$ -Phasen gibt, solche mit relativ langer helikaler Ganghöhe und

großem Gitterparameter ( $Ia3d_{(L)}$ ) und jene jenseits der  $I23$ -Phase mit kurzer Ganghöhe und kleinem Gitterparameter ( $Ia3d_{(S)}$ ). Dies wurde in der Publikation **A** mit Röntgenuntersuchungen und durch Kontaktpräparation verifiziert. In den Kontaktpräparationen findet man die Induktion einer chiralen Konglomeratstruktur der  $I23$ -Phase zwischen den  $Ia3d_{(L)}$  und  $Ia3d_{(S)}$ -Phasen, wohingegen im Kontaktbereich zwischen identischen  $Ia3d$ -Phasen keine  $I23$ -Phase induziert wird (Abb. 3 in Publ. **B** und Abbildung 3.7).<sup>[68]</sup>



**Abbildung 3.3** Mesophasen der polycatenaren Bithiophene  $Aa_{10}^{(r)Z}$  und  $A'a_{10}/R$  mit verschiedenen cyclischen Substituenten im Heizzyklus.<sup>[65]</sup>

Insgesamt ist zu erkennen, dass der Cub-Iso Übergang mit zunehmender Elektronenakzeptorfähigkeit der terminalen Substituenten erhöht wird und die Raumgruppe der gebildeten kubischen Phase stark von der Größe und der Position der Substituenten abhängt (Abb. 3.4). Das heißt, mit zunehmenden Volumen der Substituenten erfolgt eine stärkere helikale Verdrillung der Moleküle entlang des Netzwerks ( $\Phi$ ), welche zur Verkürzung der helikalen Ganghöhe und somit zur Phasensequenz  $Ia3d_{(L)}-I23-Ia3d_{(S)}$  führt. Bemerkenswert ist die Resilienz der kubischen Phasen bezüglich der sterischen Effekte. Während  $Cub_{bi}$ -Phasen normalerweise nur in schmalen Temperaturbereichen bei wenigen Vertretern homologer Reihen auftreten<sup>[30-36,69]</sup> ist hier eine bemerkenswert breite Variation der Molekülstrukturen unter Erhalt der  $Cub_{bi}$ -Phasen möglich. Lediglich  $A'a_{10}/Anth$  mit einer seitlich fixierten Anthraceneinheit weist keine  $Cub_{bi}$ -Phase auf (Abb. 3.3).

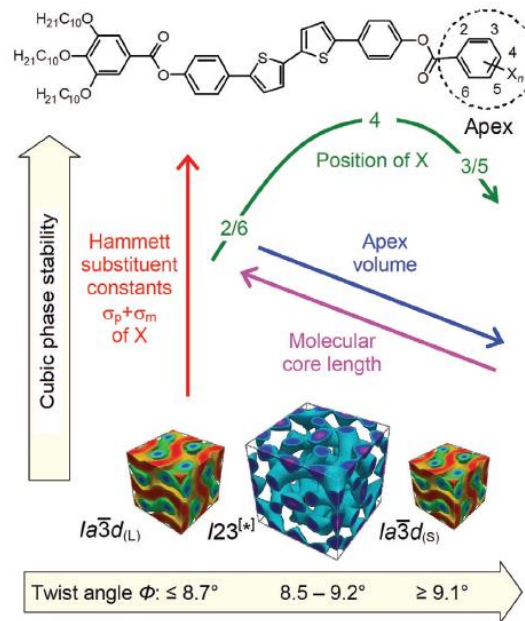


**Abbildung 3.4** Darstellung der Stabilität kubischer Phasen in Abhängigkeit von der Position der Substitution der Bithiophene  $\mathbf{Aa}_{10}^{(r)}\mathbf{Z}$ .<sup>[65]</sup>

Des Weiteren wird in Publikation **A** gezeigt, dass die chirale isotrope Flüssigkeit ( $\text{Iso}_1^{[*]}$ ) nur sehr selten in dieser Serie gefunden wird, und wenn, dann nur als monotrope Phase im Kühlen. Es tritt keine  $\text{Iso}_1^{[*]}$ -Phase bei Substanzen mit polaren Gruppen (Halogene, CN,  $\text{NO}_2$ ,  $\text{OCF}_3$ ) auf, die einzigen Ausnahmen sind Verbindungen mit weniger polaren Methyl- und Methoxygruppen. Der Grund dafür könnte in einer veränderten Packung der Moleküle zu suchen sein. Während Moleküle mit unpolaren Substituenten bevorzugt antiparallel nebeneinander angeordnet sind, wird durch polare Substituenten eine antiparallele End-zu-End Anordnung begünstigt (Abb. 3.5).

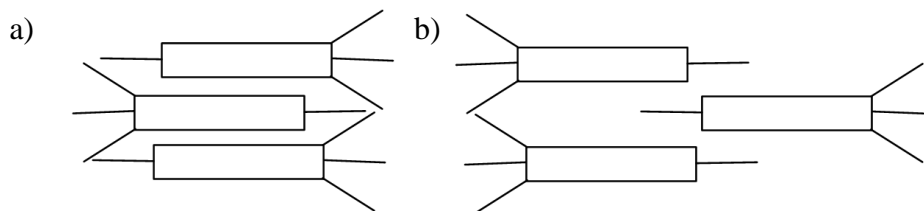


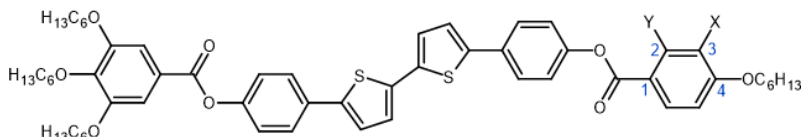
**Abbildung 3.5** Interkallationsmodelle polycatenarer stäbchenförmiger Moleküle. (a) Antiparallele Anordnung bei Verbindungen mit unpolaren Substituenten und (b) antiparallele End-zu-End Anordnung bei Verbindungen mit polaren Substituenten am weniger substituierten Ende.

Die Änderung der Interkallation der Mesogene hat einen signifikanten Einfluss auf die sterischen Gegebenheiten und die Krümmung der Grenzflächen zwischen unpolaren aliphatischen und polaren aromatischen nanosegregierten Bereichen.

### 3.3 Ergänzungen zu Publikation A: Einfluss von Fluorsubstituenten am aromatischen Ring

Die Effekte des Austauschs einer oder zweier H-Atome an der einfachsubstituierten peripheren Benzoateinheit der tetracatenaren Verbindung durch Fluor wurde anhand der Verbindung  $\mathbf{Aa}_6/\mathbf{d}_6$  <sup>[64]</sup> mit vier Hexyloxyketten untersucht. In der Tabelle 3.1 sind die Phasensequenzen der Mesogene ( $\mathbf{Aa}_6/^{(r)}\mathbf{Fd}_6$ ) bei unterschiedlicher Fluorsubstitution zusammengestellt.

**Tabelle 3.1** Mesophasen, Phasenumwandlungstemperaturen und Gitterparameter der Verbindungen  $\mathbf{Aa}_6/^{(r)}\mathbf{Fd}_6$ .<sup>a</sup>



Verb.	X	Y	$T/^\circ\text{C}$ [ $\Delta H/\text{kJ}\cdot\text{mol}^{-1}$ ]	$a/\text{nm}$ ( $T/^\circ\text{C}$ )
$\mathbf{Aa}_6/\mathbf{d}_6$ <sup>[64]</sup>	H	H	H: Cr 139 [55.2] M 171 <sup>b</sup> [-] $\text{Cub}_{\text{bi}}/\text{Ia}3d$ 205 [1.2] $\text{Iso}_1^{[*]}$ 213 [0.2] Iso K: Iso 212 [1.0] $\text{Iso}_1^{[*]}$ 177 [0.3] $\text{Cub}_{\text{bi}}/\text{Ia}3d$ 58 [19.4] Cr	10.3 (180)
$\mathbf{Aa}_6/^{(2)}\mathbf{Fd}_6$	H	F	H: Cr 116 [46.4] $\text{SmC}_s$ 176 [0.6] ( $\text{SmC}_a$ 200 N 200 [0.5] <sup>c</sup> ) Iso K: Iso (198 [0.5] <sup>c</sup> N 198 $\text{SmC}_a$ ) 174 [0.6] $\text{SmC}_s$ 51 [11.5] Cr	–
$\mathbf{Aa}_6/^{(3)}\mathbf{Fd}_6$	F	H	H: Cr 135 [51.9] $\text{Cub}_{\text{bi}}/\text{Ia}3d$ 202 [2.5] Iso K: Iso 199 [0.2] $\text{Iso}_1^{[*]}$ 172 [0.5] $\text{Cub}_{\text{bi}}/\text{Ia}3d < \text{Cr}$	10.1 (180)
$\mathbf{Aa}_6/^{(2,3)}\mathbf{Fd}_6$	F	F	H: Cr 137 [54.6] $\text{Cub}_{\text{bi}}/\text{Ia}3d$ 206 [2.2] Iso K: Iso 205 [0.1] $\text{Iso}_1^{[*]}$ 180 [0.6] $\text{Cub}_{\text{bi}}/\text{Ia}3d < \text{Cr}$	10.0 (180)

<sup>a</sup> Die angegebenen Umwandlungstemperaturen entsprechen den ermittelten Peaktemperaturen des zweiten Heiz (H)- und Kühlgraphen (K) der DSC-Messungen. Die Heiz- und Kühlrate beträgt 10 K/min. <sup>b</sup> Bestimmung der Übergangstemperatur erfolgte an dem Polarisationsmikroskop. <sup>c</sup> Enthalpie beider Übergänge.

Die Substitution in 2-Position zur Carboxylgruppe der Verbindung  $\mathbf{Aa}_6/^{(2)}\mathbf{Fd}_6$  hat den größten Einfluss. Diese Substitution führt zur Destabilisierung der kubischen  $\text{Ia}3d$ -Phase und der chiralen isotropen Flüssigkeit ( $\text{Iso}_1^{[*]}$ ), welche durch synklone ( $\text{SmC}_s$ ) und antikline ( $\text{SmC}_a$ ) smektische C-Phase und eine nematische Phase ersetzt werden. Die Verringerung der Stabilität der kubischen Phase ist aufgrund des erhöhten Raumbedarfs und der damit verbundenen Verringerung der Grenzflächenkrümmung zurückzuführen. Bemerkenswert ist das Auftreten der antiklinen  $\text{SmC}_a$ -Phase als Hochtemperaturphase über der synklinen  $\text{SmC}_s$ -Phase. Normalerweise wird die entgegengesetzte Phasensequenz beobachtet <sup>[71]</sup>.

Dagegen zeigen die Verbindungen  $\mathbf{Aa}_6/^{(3)}\mathbf{Fd}_6$  und  $\mathbf{Aa}_6/^{(2,3)}\mathbf{Fd}_6$  nur eine geringfügige Änderung zu der Referenzsubstanz  $\mathbf{Aa}_6/\mathbf{d}_6$ . Beide weisen die  $\text{Cub}_{\text{bi}}/\text{Ia}3d$ - und die  $\text{Iso}_1^{[*]}$ -Phase auf. Die Stabilität der kubischen Phase ist bei allen drei Substanzen  $\mathbf{Aa}_6/\mathbf{d}_6$ ,  $\mathbf{Aa}_6/^{(3)}\mathbf{Fd}_6$  und  $\mathbf{Aa}_6/^{(2,3)}\mathbf{Fd}_6$  vergleichbar. Lediglich die chirale isotrop flüssige Phase ( $\text{Iso}_1^{[*]}$ ) tritt nach Fluorierung nur noch monotrop auf. Die 3-Fluorierung hat also keinen wesentlichen Einfluss auf die Selbstassemblierung in den LC-Phasen und der Effekt der 2-Fluorierung kann durch zusätzliche 3-Fluorierung zurückgedrängt werden.

### 3.4 Polycatenare Bithiophene mit cycloaliphatischen Endgruppen (Publikation B)

In der Publikation **B** <sup>[68]</sup> wurde der  $Ia3d_{(L)}$ - $I23$ - $Ia3d_{(S)}$  Übergang systematisch untersucht. Dazu wurden Moleküle ( $A'a_{10}/cym$ ) mit einer cycloaliphatischen Endgruppe und einer Anzahl von  $m = 4-12$  Kettengliedern synthetisiert. Es konnte ein kontinuierlicher Übergang der kubischen Phasen von der achiralen  $Ia3d_{(L)}$ -Phase ( $m = 4-5$ ), über die chirale  $I23$ - ( $m = 6-8$ ) zur  $Ia3d_{(S)}$ -Phase ( $m = 12$ ) beobachtet (Tab. 1 in Publ. **B**, Tab. 3.2) und gezeigt werden, dass diese mit den ermittelten helikalen Verdrillungswinkel  $\Phi$  korrelieren (Abb. 3.6).

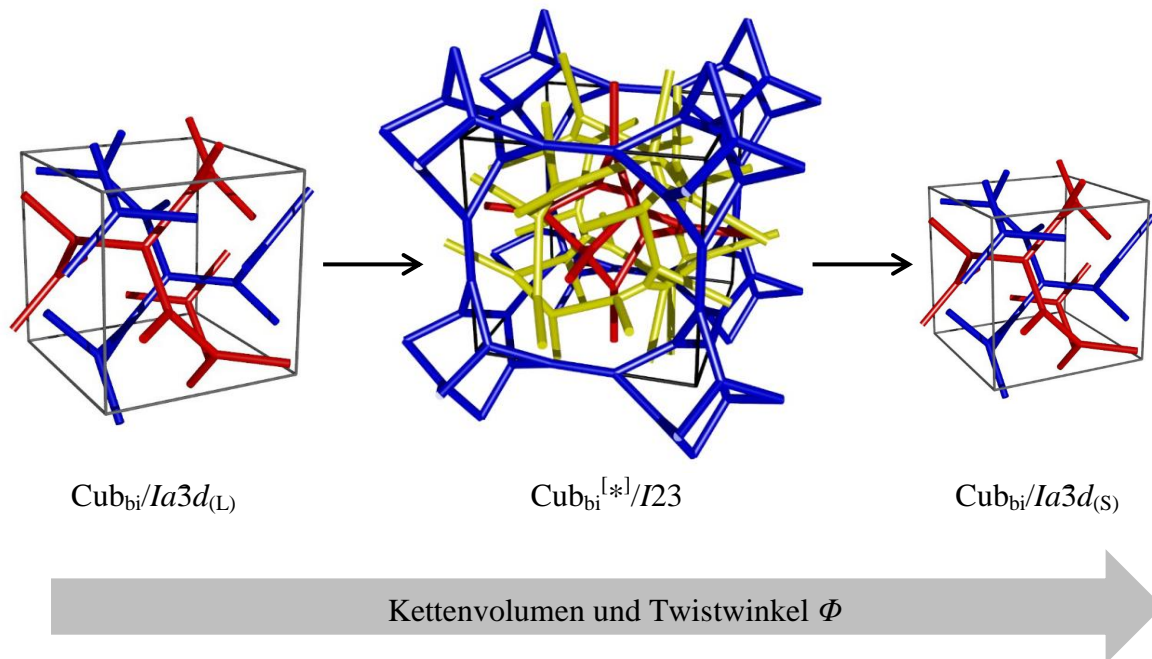


**Abbildung 3.6** Schematische Darstellung der Netzwerke und der Größenverhältnisse der kubischen Elementarzellen in der Phasensequenz  $Ia3d_{(L)}$ - $I23$ - $Ia3d_{(S)}$  bei ansteigenden Kettenvolumen und dem einhergehenden ansteigenden Twistwinkel  $\Phi$  der Moleküle entlang dieser Netzwerke. <sup>[65]</sup>

Darüber hinaus ist es möglich die chirale  $I23$ -Phase im Kontaktbereich zwischen zwei Verbindungen mit  $Ia3d_{(L)}$  ( $m = 4$ ) und  $Ia3d_{(S)}$  ( $m = 12$ ) zu induzieren (Abb. 3 in Publ. **B** und Abb. 3.7).

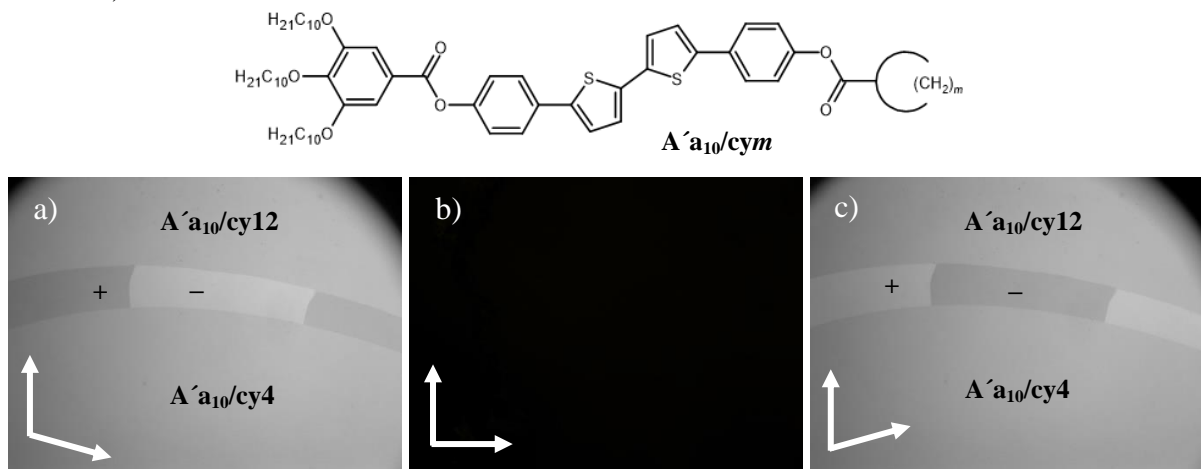


**Abbildung 3.7** Polarisationsmikroskopische Aufnahme des Kontaktpräparats zwischen  $A'a_{10}/cy4$  ( $Ia3d_{(L)}$ ) und  $A'a_{10}/cy12$  ( $Ia3d_{(S)}$ ) bei entkreuzten Polarisatoren (a) mit dem Uhrzeigersinn, (c) entgegen dem Uhrzeigersinn bei einer Temperatur von 129 °C. Im Kontaktbereich ist die induzierte chirale bikontinuierliche kubische  $Cub_{bi}^{[*]}/I23$  anhand der Konglomeratbildung erkennbar.

### 3.5 Ergänzungen zu Publikation B

Es ist anzumerken, dass zum Zeitpunkt der Veröffentlichung der Publikation **B** die *I23*-Phase noch nicht aufgeklärt war und noch als „*Im3m*“ bezeichnet wurde. Das verbesserte Modell der Phasenstruktur wurde von ZENG und UNGAR in der Referenz [60] vorgestellt. Entsprechend diesem Modell vollführen die Helices auf der Distanz zwischen zwei Knotenpunkten in der *I23*-Phase eine Drehung um  $90^\circ$  und in der *Ia3d*-Phase um  $70.5^\circ$ , daraus ergeben sich folgende Formeln <sup>[60]</sup>:

$$(1) \quad \Phi(Ia3d) = 70.5^\circ / [0.354a_{\text{cub}}/0.45\text{nm}],$$

$$(2) \quad \Phi(I23) = 90^\circ / [0.290a_{\text{cub}}/0.45\text{nm}].$$

Damit ist es möglich, die fehlenden Werte des Verdrillungswinkels  $\Phi$  für die kubische *I23*-Phase zu berechnen. Die vervollständigten Werte der Tabelle 1 in Publikation **B** sind in der nachfolgenden Tabelle 3.2 zusammengefasst.

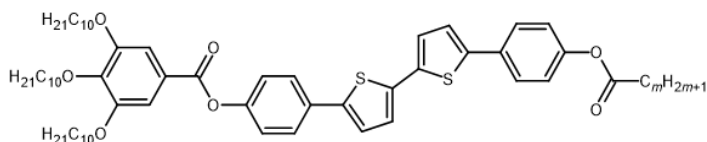
**Tabelle 3.2** Mesophasen, Phasenumwandlungstemperaturen, Gitterparameter und helikale Verdillungswinkel  $\Phi$  der polycatenaren Bithiophene. <sup>a</sup>[68]

Verbg.	$T/^\circ\text{C}$ [ $\Delta H/\text{kJ}\cdot\text{mol}^{-1}$ ]	$a/\text{nm}$ ( $T/^\circ\text{C}$ )	$\Phi/^\circ$
<b><i>Aa</i><sub>10</sub>/<i>H</i></b> <sup>[63]</sup>	H: Cr 114 [39.7] <i>Cub</i> <sub>bi</sub> / <i>Ia3d</i> <sub>(L)</sub> 162 [2.3] Iso K: Iso 156 [1.7] <i>Cub</i> <sub>bi</sub> / <i>Ia3d</i> <sub>(L)</sub> 69 [3.8] Cr	11.0 (116)	8.2
<b><i>A'</i><sub>a10</sub>/<i>cy4</i></b>	H: Cr 92 [17.7] <i>Cub</i> <sub>bi</sub> / <i>Ia3d</i> <sub>(L)</sub> 148 [3.3] Iso K: Iso 141 [2.6] <i>Cub</i> <sub>bi</sub> / <i>Ia3d</i> <sub>(L)</sub> < 0 Cr	10.4 (130)	8.6
<b><i>A'</i><sub>a10</sub>/<i>cy5</i></b>	H: Cr 88 [16.3] <i>Cub</i> <sub>bi</sub> / <i>Ia3d</i> <sub>(L)</sub> 150 [3.0] Iso K: Iso 143 [2.5] <i>Cub</i> <sub>bi</sub> / <i>Ia3d</i> <sub>(L)</sub> < 0 Cr	10.5 (135)	8.5
<b><i>A'</i><sub>a10</sub>/<i>cy6</i></b> <sup>[63]</sup>	H: Cr 93 [33.9] <i>Cub</i> <sub>bi</sub> <sup>[*]</sup> / <i>I23</i> 160 [4.3] Iso K: Iso 152 [3.0] <i>Cub</i> <sub>bi</sub> <sup>[*]</sup> / <i>I23</i> < 0 Cr	15.6 (125)	9.0
<b><i>A'</i><sub>a10</sub>/<i>cy8</i></b>	H: Cr 59 [33.1] <i>Cub</i> <sub>bi</sub> <sup>[*]</sup> / <i>I23</i> 148 [4.5] Iso K: Iso 139 [2.9] <i>Cub</i> <sub>bi</sub> <sup>[*]</sup> / <i>I23</i> < 0 Cr	15.4 (100)	9.1
<b><i>A'</i><sub>a10</sub>/<i>cy12</i></b>	H: Cr 103 [36.6] <i>Cub</i> <sub>bi</sub> / <i>Ia3d</i> <sub>(S)</sub> 113 [2.9] Iso K: Iso 99 [1.5] <i>Cub</i> <sub>bi</sub> / <i>Ia3d</i> <sub>(S)</sub> < 0 Cr	9.4 (108)	9.5
<b><i>A'</i><sub>a10</sub>/<i>br5</i></b>	H: Cr 75 [29.8] <i>Cub</i> <sub>bi</sub> <sup>[*]</sup> / <i>I23</i> 109 [3.4] Iso K: Iso 101 [2.6] <i>Cub</i> <sub>bi</sub> <sup>[*]</sup> / <i>I23</i> < 0 Cr	14.8 (90)	9.4
<b><i>A'</i><sub>a10</sub>/<i>br8</i></b>	H: Cr 57 [43.7] Iso K: Iso 4 [13.9] Cr	–	–
<b><i>A'</i><sub>a10</sub>/<i>lin8</i></b>	H: Cr 90 [5.7] <i>Cub</i> <sub>bi</sub> <sup>[*]</sup> / <i>I23</i> 122 [1.9] Iso K: Iso 113 [1.6] <i>Cub</i> <sub>bi</sub> <sup>[*]</sup> / <i>I23</i> < 0 Cr	16.0 (110)	8.7
<b><i>A'</i><sub>a10</sub>/<i>Et</i><sub>3</sub></b>	H: Cr 49 [8.9] <i>Cub</i> <sub>bi</sub> / <i>Ia3d</i> <sub>(S)</sub> 87 [2.7] Iso K: Iso 74 [1.7] <i>Cub</i> <sub>bi</sub> / <i>Ia3d</i> <sub>(S)</sub> < 0 Cr	8.85 (70)	10.1
<b><i>A'</i><sub>a10</sub>/<i>Ada</i></b>	H: Cr 84 [11.2] <i>Cub</i> <sub>bi</sub> <sup>[*]</sup> / <i>I23</i> 156 [3.6] Iso K: Iso 147 [2.7] <i>Cub</i> <sub>bi</sub> <sup>[*]</sup> / <i>I23</i> < 0 Cr	15.1 (120)	9.25

<sup>a</sup> Die angegebenen Umwandlungstemperaturen entsprechen den ermittelten Peaktemperaturen des zweiten Heiz (H)- und Kühlgraphen (K) der DSC-Messungen. Die Heiz- und Kühlrate beträgt 10 K/min.

Für den Vergleich zwischen linearen und cyclischen Gruppen wurden ergänzend zu den Substanzen mit Alicyclen zwei weitere Verbindungen mit linearen Alkylketten synthetisiert um deren Einfluss der Cyclisierung auf die flüssigkristallinen Eigenschaften zu untersuchen. Diese sind in der Tabelle 3.3 zusammengefasst.

**Tabelle 3.3.** Mesophasen, Phasenumwandlungstemperaturen und Gitterparameter der Verbindungen  $A'a_{10}/linm$ .<sup>a</sup>



Verb.	$m$	$T/^\circ\text{C}$ [ $\Delta H/\text{kJ}\cdot\text{mol}^{-1}$ ]	$a/\text{nm}$ ( $T/^\circ\text{C}$ )	$\Delta T/\text{K}$
$A'a_{10}/lin6$	6	H: Cr 78 [10.9] $\text{Cub}_{bi}/Ia3d$ 109 [-] $\text{Cub}_{bi}^{l*}/I23$ 130 [2.3] Iso K: Iso 121 [1.4] $\text{Cub}_{bi}^{l*}/I23 < \text{Cr}$	10.8, 15.8 (90), (120)	-30
$A'a_{10}/lin8$ [68]	8	H: Cr 90 [5.7] $\text{Cub}_{bi}^{l*}/I23$ 122 [1.9] Iso K: Iso 113 [1.6] $\text{Cub}_{bi}^{l*}/I23 < \text{Cr}$	16.0 (110)	-26
$A'a_{10}/lin12$	12	H: Cr 87 [57.7] $\text{Cub}_{bi}^{l*}/I23$ 120 [2.2] Iso K: Iso 110 [1.6] $\text{Cub}_{bi}^{l*}/I23$ 49 [8.5] $\text{Cr}'$	16.0 (110)	+7

<sup>a</sup> Die angegebenen Umwandlungstemperaturen entsprechen den ermittelten Peaktemperaturen des zweiten Heiz- (H) und Kühlgraphen (K) der DSC-Messungen.  $\Delta T$  gibt die Temperaturdifferenz von  $T_{\text{Cub-Iso}}(\text{lin}) - T_{\text{Cub-Iso}}(\text{cy})$  an.

Aus der Tabelle 3.3 ist ersichtlich, dass eine Vergrößerung der Kohlenstoffzahl bei den linearen Ketten einen geringeren Effekt auf die Mesophasenstabilität hervorruft als bei den cyclischen Einheiten. Daraus resultiert eine Mesophasenstabilisierung durch Cyclisierung bei kurzen Ketten, wohingegen bei langen Ketten eine Destabilisierung zu beobachten ist. Auch auf die Phasensequenz ist der Einfluss der Kohlenstoffzahl bei linearen Ketten geringer als bei den Cyclen. So wird für die Verbindung mit linearen Ketten  $m = 6$  eine monotrope  $Ia3d_{(L)}$ -Phase neben der  $I23$ -Phase gefunden, aber die  $Ia3d_{(S)}$ -Phase wird selbst für  $m = 12$  nicht erreicht.

Eine Gegenüberstellung von Verbindungen mit linearen, verzweigten, cyclischen und polycyclischen aliphatischen Gruppen ungefähr gleichen Volumens ist in Abbildung 3.8 dargestellt. Es wird ersichtlich, dass die Vergrößerung des lateralen Querschnitts der Substituenten zur Vergrößerung des Twistwinkels  $\Phi$  von  $8.7^\circ$  auf  $10.1^\circ$  führt und sich in der Sequenz  $I23-Ia3d_{(S)}$  widerspiegelt (Abb. 3.8).

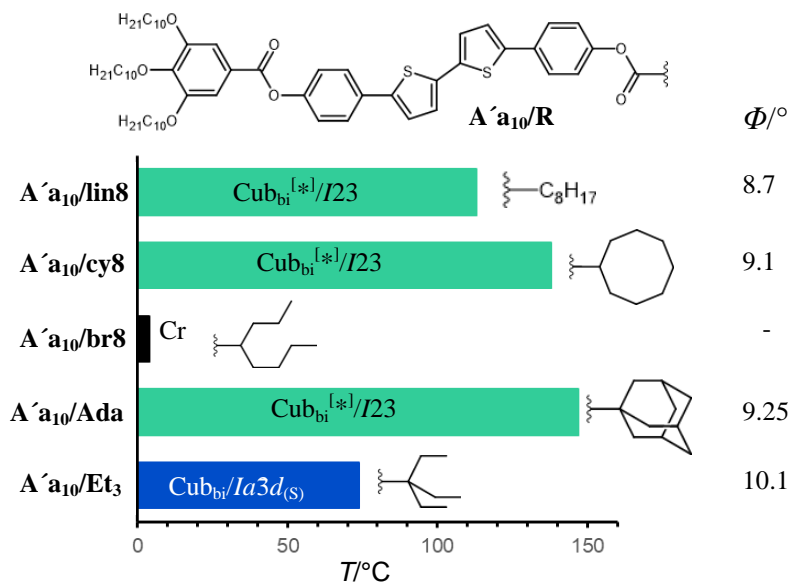


**Abbildung 3.8:** Mesophasen und Verdrillung der Moleküllängsachsen entlang der Netzwerke ( $\Phi$ ) der polycatenaren Bithiophene  $A'a_{10}/R$  im Kühlzyklus in Abhängigkeit von der Struktur des terminalen Substituenten.

### 3.6 Untersuchung der tricatenaeren Bithiophene mit einem 3,5-substituierten Ende (Publikation C)

Der Übergang von den lamellaren Phasen (Sm, Hex) zu den 3D-Strukturen ( $\text{Cub}_{\text{bi}}$ ) ist Gegenstand der Publikation C <sup>[27]</sup>. Wie der Abbildung 3.1 zu entnehmen ist, neigen die unsymmetrischen tetracatenaren Verbindungen ( $Aa_{10}/d_m$ ) <sup>[63]</sup> zu der Ausbildung von kubischen Phasen. Dagegen zeigten die unsymmetrischen tricatenaeren Mesogene sowohl lamellare als auch kubische Phasen. Von diesem Standpunkt aus wurde eine homologe Reihe von unsymmetrischen tricatenaeren Bithiophenen ( $Ab_{10}/d_m$ ) mit 3,5-Substitution an einem Ende und einer linearen Alkyloxyketten am anderen synthetisiert.



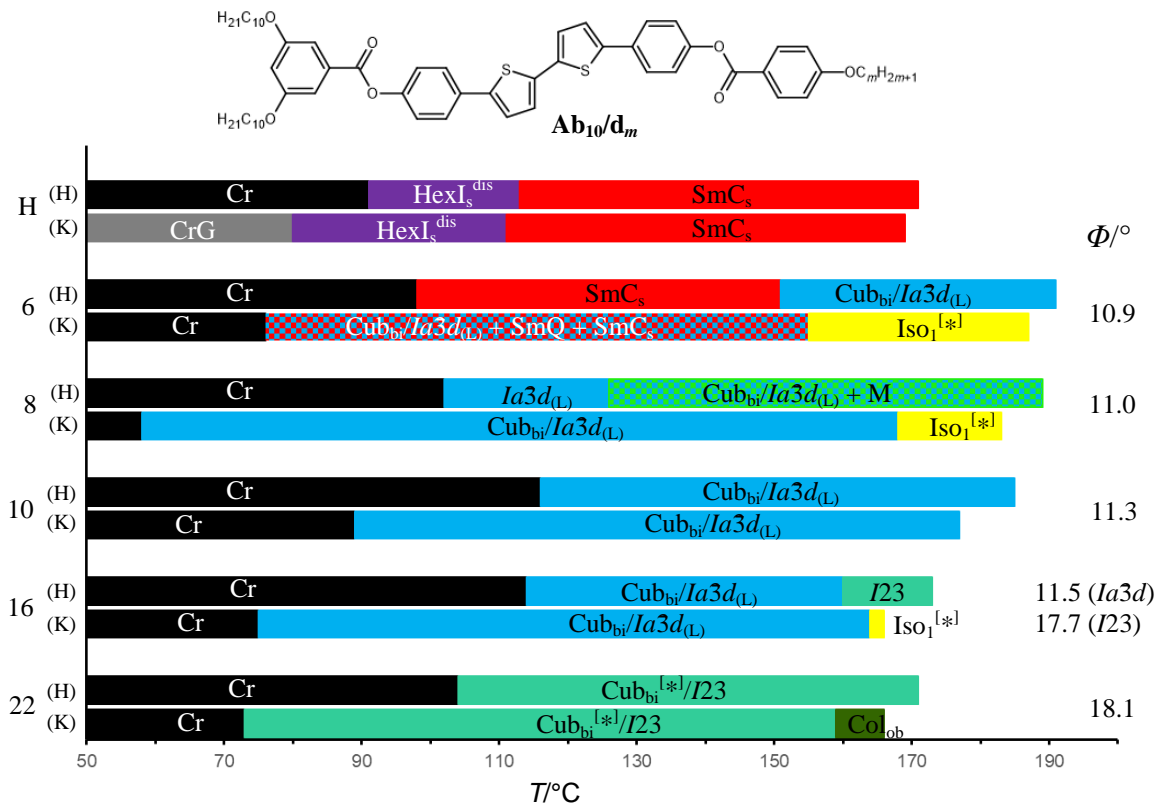


**Abbildung 3.9** Mesophasen der polycatenaren homologen Reihe der Bithiophene  $Ab_{10}/d_m$  im Heiz- und Kühlzyklus und die Twistwinkel  $\Phi$  in den kubischen Phasen.

Das Mesogen mit dem unsubstituierten Phenylring ( $Ab_{10}/H$ ) zeigt enantiotropes Verhalten. Dabei tritt neben der hexatischen I Tieftemperaturphase ( $HexI_s^{dis}$ ) eine synklinale  $SmC_s$ -Hochtemperaturphase ( $SmC_s$ ) auf. Die  $SmC_s$ -Phase bleibt bis zu einer Kettenlänge von  $m = 6$  erhalten und wird anschließend von der kubischen Phase mit  $Ia3d$ -Raumgruppe verdrängt. In dem Übergangsbereich von den lamellaren Strukturen zu den Netzwerkstrukturen treten bei einer Kettenlänge von  $m = 6-8$  verschiedene doppelbrechende und hochviskose Phasen auf, zu denen unter anderem die schwach doppelbrechende  $SmQ$ -Phase (Abb. 3.10 b) und eine stark doppelbrechende unbekannte Phase (M) gehört. Bei einer Kettenlänge von  $m = 8$  beginnend bis zu  $m = 22$  werden ausschließlich kubische Phasen ( $Cub_{bi}/Ia3d_{(L)}$ ,  $Cub_{bi}^{[*]}/I23$ ) gebildet, wobei zwischen  $m = 16$  und  $m = 22$  ein Wechsel von der achiralen  $Ia3d$ - zur chiralen  $I23$ -Phase stattfindet. Die langkettige Verbindung  $Ab_{10}/d_{22}$  bildet zusätzlich eine monotrop auftretende kolumnare Phase neben der  $Cub_{bi}^{[*]}/I23$ -Phase aus.

Die Ausbildung der chiralen isotropen Flüssigkeit ( $Iso_1^{[*]}$ ) kann ausschließlich als monotrope Phase im Kühlen beobachtet werden. Sie findet sich sowohl bei kurzkettingen Verbindungen mit  $m = 6, 8$  als auch bei langen Ketten  $m = 16$  neben der kubischen  $Ia3d$ -Phase, wohingegen sie bei mittleren Kettenlängen und neben der chiralen  $I23$ -Phase nicht gefunden wurde. Die  $Iso_1^{[*]}$ -Phase wird bei weiterer Kettenverkürzung durch die  $SmC_s$ -Hochtemperaturphase und bei Kettenverlängerung durch eine kolumnare Phase substituiert.

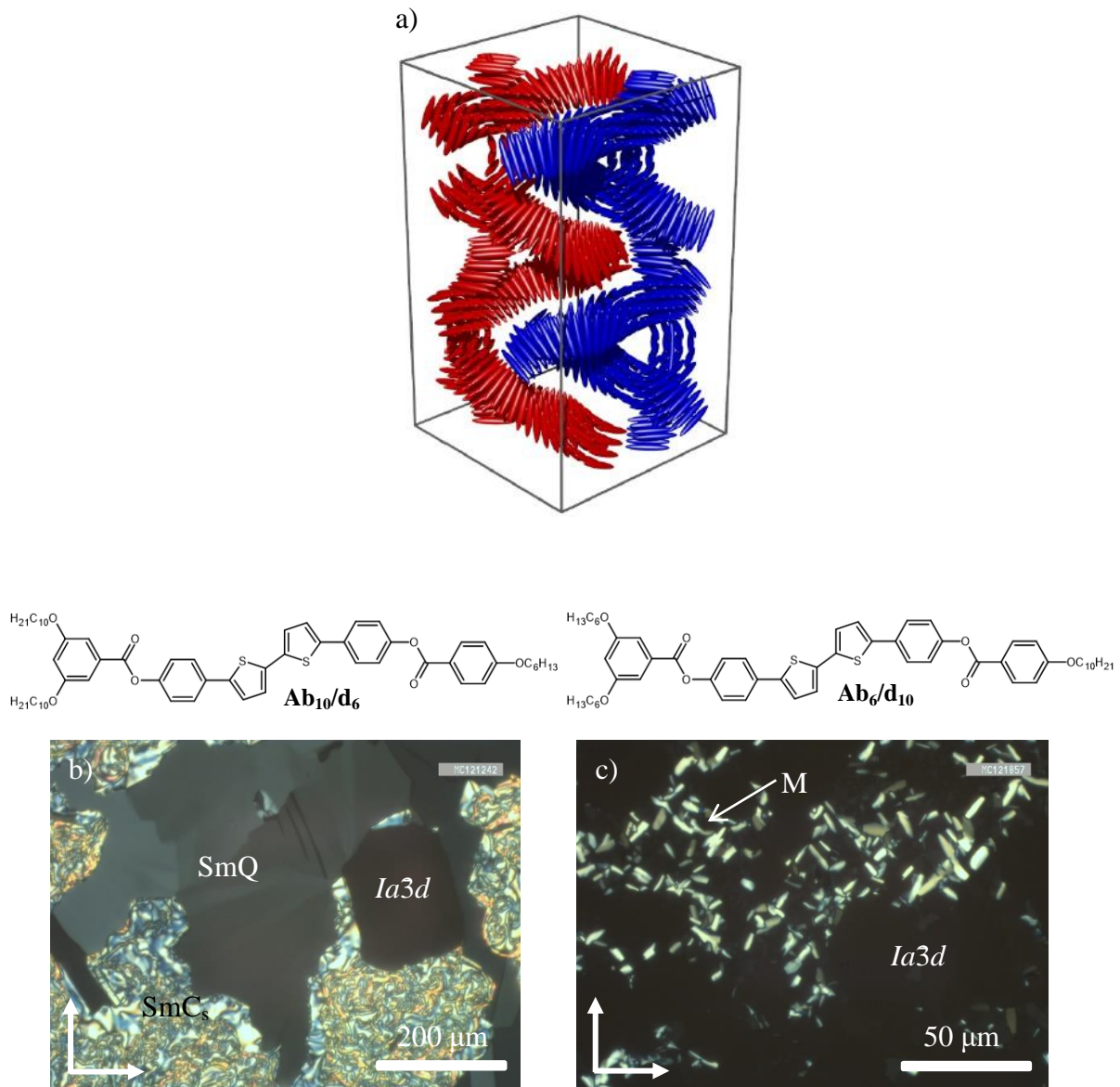


**Abbildung 3.10** Nichtkubische Netzwerkstrukturen in Koexistenz mit kubischen und SmC-Phasen: (a) Modell der Netzwerkstruktur der SmQ-Phase ( $I4,22$ ). Aus Referenz [83], Copyright 2018 Wiley-VCH. (b, c) Optische Texturen der Koexistenzbereiche. (b) Koexistenz der SmQ-,  $Ia3d$ - und SmC<sub>s</sub>-Phase der Substanz  $\mathbf{Ab}_{10}/\mathbf{d}_6$  während des Kühlens bei  $T = 153$  °C. (c) Übergang einer unbekanntenen 3D-Phase (M) in eine kubische  $Ia3d$ -Phase der Verbindung  $\mathbf{Ab}_6/\mathbf{d}_{10}$  während des Heizens bei  $T = 156$  °C.

Durch den Austausch der in 3,5-Position befindlichen Decyloxyketten ( $\mathbf{Ab}_{10}/\mathbf{d}_m$ ) durch kürzere Hexyloxyketten ( $\mathbf{Ab}_6/\mathbf{d}_m$ ) zeigt sich, dass bis zu einer Kettenlänge  $m = 10$  hauptsächlich geneigte smektische Phasen (SmC) gebildet werden. Der Unterschied zu der zuvor diskutierten Reihe ist, dass es sich hierbei um antikline smektische Phasen (SmC<sub>a</sub>) handelt. Zudem wurden Verbindungen mit einer um eine Benzoateinheit verkürzten Struktur synthetisiert und untersucht ( $\mathbf{A}^{\sim}\mathbf{b}_6/m$ ). Bei diesen tritt zusätzlich eine hexatische B Phase auf. Diese Reihen sind in Abbildung 3.11 zusammengefasst und in Publikation C ausführlich diskutiert.

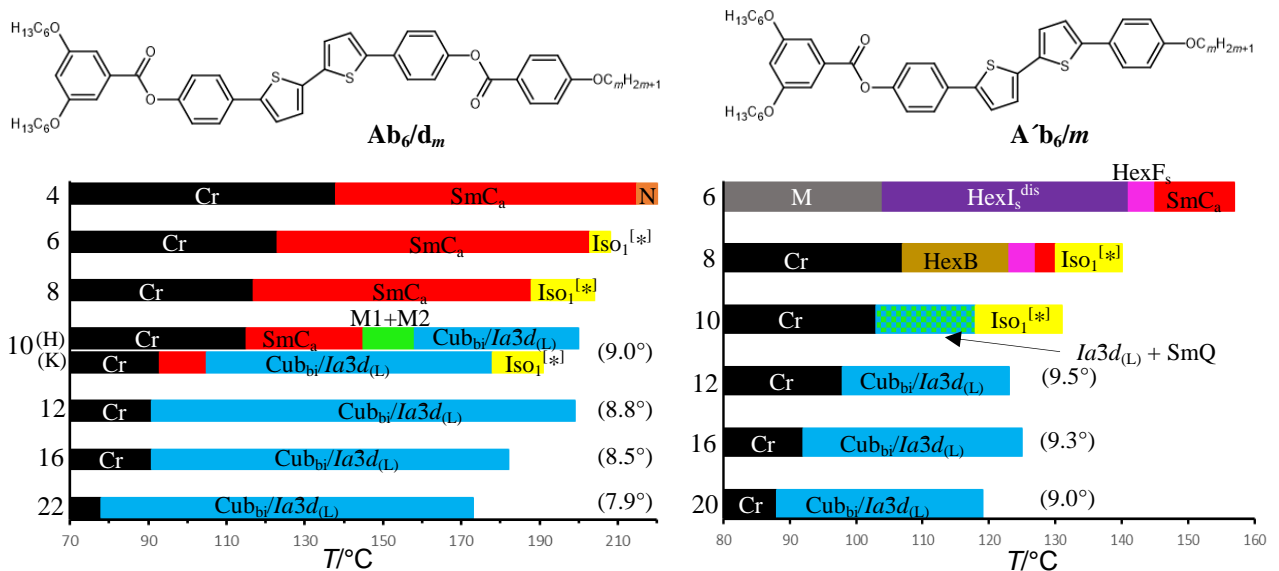


**Abbildung 3.11** Phasensequenzen der homologen Reihen der polycatenaren Bithiophene  $\text{Ab}_{10}/\text{d}_m$  und  $\text{A}^{\text{b}}_6/m$  im Kühlen. Die Werte des Verdrehungswinkels  $\Phi$  der kubischen Phasen sind für die jeweiligen Substanzen in Klammern angegeben. Abkürzung:  $\text{HexI}_s^{\text{dis}}$  = synklone hexatische I-Phase mit  $\text{HexI}_s$  Ordnung der Alkylketten und  $\text{SmC}_s$  Ordnung der aromatischen Kerne

Hierbei ist hervorzuheben, dass für alle besprochenen tricatenaeren Bithiophene die aus dem Gitterparametern der  $\text{Cub}_{\text{bi}}$ -Phasen berechneten Twistwinkel  $\Phi$  mit steigenden Kettenvolumen/-länge kleiner werden (Abb. 3.11). Diese Beobachtung stimmt mit den bisherigen homologen Reihen nicht überein. Sie gilt aber nicht ausschließlich für die homologen Reihen der Bithiophene  $\text{Ab}_{10}/\text{d}_m$ ,  $\text{Ab}_6/\text{d}_m$  und  $\text{A}^{\text{b}}_6/m$ , neue Untersuchungen an polycatenaren [1]-benzothieno-[3,2-*b*]-benzothiophenen<sup>[39]</sup> zeigten ebenfalls eine Verringerung des Twistwinkels  $\Phi$  mit ansteigenden Kettenvolumen/-länge.

Dies kann unter der Annahme erklärt werden, dass für den Twistwinkel  $\Phi$  zwei gegenteilige Effekte entscheidend sind. Die Kettenverlängerung führt einerseits zur Erhöhung des Kettenvolumens, was eine Erhöhung des Twists bewirkt ( $V_{\text{RH}}$ ). Andererseits hat die Verlängerung der Ketten auch einen Einfluss auf die Moleküllänge, aufgrund des Beitrags der linearen in all-*trans* Konformation vorliegenden Segmente der Ketten. Dies führt vor allem bei langkettigen Verbindungen mit hohem all-*trans* Anteil zur Reduzierung des Twistwinkels mit zunehmender Kettenlänge ( $L_{\text{mol}}$ , Abb. 3.12).

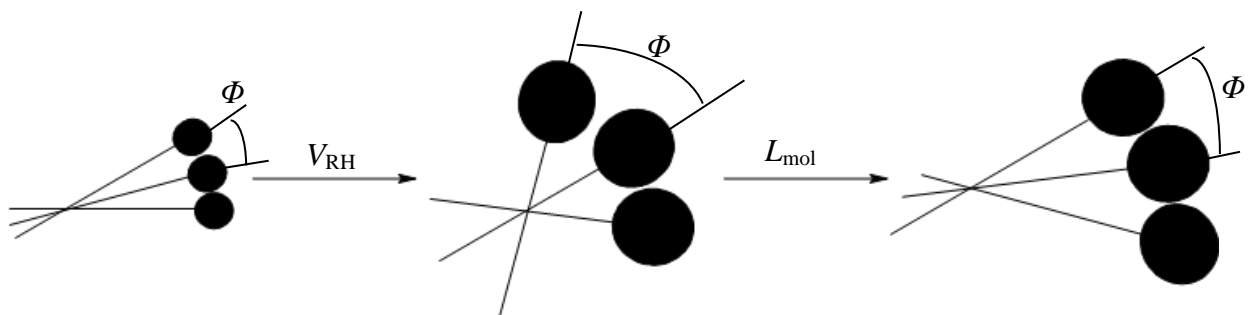


**Abbildung 3.12** Schematische Darstellung der Entwicklung des helikalen Twistwinkels  $\Phi$  in Abhängigkeit des Kettenvolumens ( $V_{\text{RH}}$ ) und der Gesamtmoleküllänge ( $L_{\text{mol}}$ ).

Ergänzend zu den Publikationen wurde der Typ der  $Ia3d$ -Phasen der Verbindungen  $\mathbf{Ab}_n/\mathbf{d}_m$  und  $\mathbf{A}^*\mathbf{b}_6/m$  mittels Kontaktpräparationen zusätzlich bestätigt. In allen untersuchten Fällen konnte eine chirale  $I23$ -Phase im Kontaktbereich mit der  $Ia3d_{(S)}$ -Phase der Verbindung  $\mathbf{Aa}_{10}/\mathbf{Et}_3$  induziert werden, das heißt alle gehören zu den  $Ia3d_{(L)}$ -Phasen.

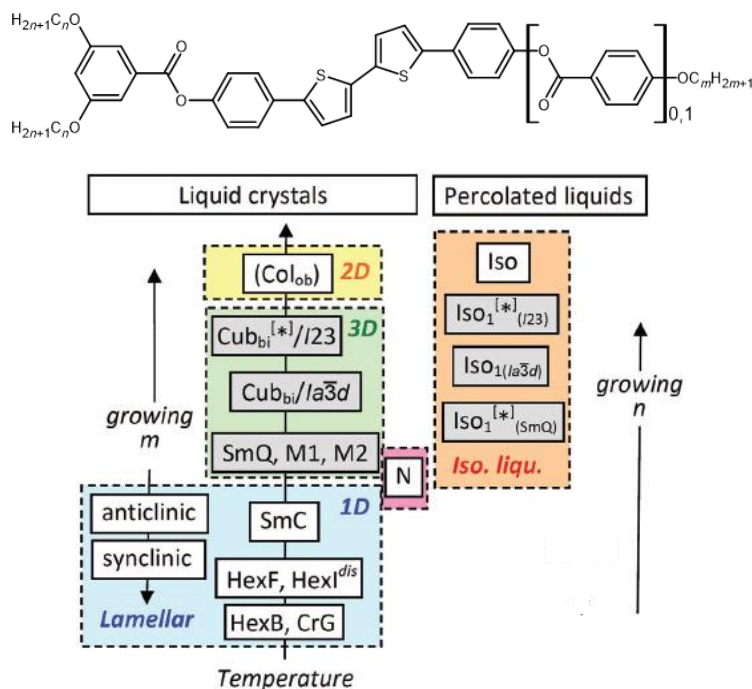


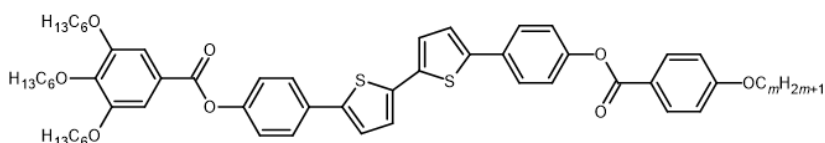
**Abbildung 3.13** Übersicht der Abhängigkeit der Stabilität der auftretenden Mesophasen von Temperatur, Ketten- und Kernlänge der tricatenaeren Bithiophene  $\mathbf{Ab}_{10}/\mathbf{d}_m$ ,  $\mathbf{Ab}_6/\mathbf{d}_m$  und  $\mathbf{A}^*\mathbf{b}_6/m$ .<sup>[27]</sup>

Wie in der Abbildung 3.13 dargestellt erfolgt in all diesen Reihen mit Kettenverlängerung oder Temperaturerhöhung ein Übergang von hexatischen über synklin und antiklin geneigten smektischen Phasen zunächst zu 3D-Netzwerkstrukturen mit kubischer und nichtkubischer Symmetrie und gelegentlich zu kolumnaren Phasen. Am Übergang zur isotropen Flüssigkeit treten zusätzlich chirale ( $ISO_1^{[*]}$ ) oder achirale ( $ISO_1$ ) flüssige Phasen mit lokaler Netzwerkstruktur auf. Die Verlängerung der aromatischen Kernstruktur führt wie erwartet zu einer deutlichen Stabilisierung der Mesophasen.

### 3.7 Ergänzungen zu Publikation C: Vergleich mit tetracatenaren Bithiophenen mit einem 3,4,5-trisubstituierten Ende

Zu Vergleichszwecken wurden neben den tricatenaeren Verbindungen  $\mathbf{Ab}_6/\mathbf{d}_m$  analoge tetracatenare Verbindungen mit 3,4,5-Substitution am Ende synthetisiert und untersucht ( $\mathbf{Aa}_6/\mathbf{d}_m$ ). Die Homologen mit  $m = 2-18$  sind bereits in der Referenz [64] beschrieben, die langkettigen Verbindungen mit  $m = 20-26$  sind neu synthetisiert (Tab. 3.4). Auch in dieser Reihe findet ein Übergang von nematischen und smektischen Phasen zu den 3D-Strukturen mit wachsenden Kettenvolumen statt. Dabei tritt zusätzlich der Übergang von der achiralen kubischen  $Ia3d$ - zu der chiralen  $I23$ -Phase bereits bei  $m > 14$  auf.

**Tabelle 3.4** Mesophasensequenz, Phasenumwandlungstemperaturen und Gitterparameter der Verbindungen **Aa<sub>6</sub>/d<sub>m</sub>**.<sup>a</sup>



Verb.	<i>m</i>	<i>T</i> /°C [ $\Delta H$ /kJ·mol <sup>-1</sup> ]	<i>a</i> /nm ( <i>T</i> /°C)	$\Phi$ /°
<b>Aa<sub>6</sub>/d<sub>4</sub></b> <sup>[64]</sup>	4	H: Cr 134 [30.0] SmC 212 [0.3] N 221 [0.4] Iso K: Iso 215 [0.3] N 204 [0.2] SmC 91 [21.1] Cr	–	–
<b>Aa<sub>6</sub>/d<sub>6</sub></b> <sup>[64]</sup>	6	H: Cr 139 [55.2] M 171 <sup>b</sup> [–] Cub <sub>bi</sub> / <i>Ia3d</i> <sub>(L)</sub> 205 [1.2] Iso <sub>1</sub> <sup>[*]</sup> 213 [0.3] Iso K: Iso 212 [1.0] Iso <sub>1</sub> <sup>[*]</sup> 177 [0.3] Cub <sub>bi</sub> / <i>Ia3d</i> <sub>(L)</sub> 58 [19.4] Cr	10.3 (180)	8.7
<b>Aa<sub>6</sub>/d<sub>14</sub></b> <sup>[64]</sup>	14	H: Cr 120 [46.7] Cub <sub>bi</sub> <sup>[*]</sup> / <i>I23</i> 185 [2.2] Iso K: Iso 182 [0.2] Iso <sub>1</sub> <sup>[*]</sup> 174 [0.9] Cub <sub>bi</sub> <sup>[*]</sup> / <i>I23</i> 96 [1.8] M 81 [24.0] Cr	16.1 (170)	8.7
<b>Aa<sub>6</sub>/d<sub>20</sub></b>	20	H: Cr 117 [46.0] Cub <sub>bi</sub> <sup>[*]</sup> / <i>I23</i> 187 [3.2] Iso K: Iso 178 [2.3] Cub <sub>bi</sub> <sup>[*]</sup> / <i>I23</i> 76 [19.9] Cr	16.9 (160)	8.3
<b>Aa<sub>6</sub>/d<sub>22</sub></b>	22	H: Cr 110 [41.6] Cub <sub>bi</sub> <sup>[*]</sup> / <i>I23</i> 184 [3.2] Iso K: Iso 175 [2.4] Cub <sub>bi</sub> <sup>[*]</sup> / <i>I23</i> [24.4] 69 Cr	17.2 (170)	8.1
<b>Aa<sub>6</sub>/d<sub>26</sub></b>	26	H: Cr 104 [64.8] Cub <sub>bi</sub> <sup>[*]</sup> / <i>I23</i> 176 [2.2] Iso K: Iso 167 [0.6] M 164 [0.2] Cub <sub>bi</sub> <sup>[*]</sup> / <i>I23</i> 70 [39.2] Cr	17.9 (140)	7.8

<sup>a</sup> Die angegebenen Umwandlungstemperaturen entsprechen den ermittelten Peaktemperaturen des zweiten Heiz- (H) und Kühlgraphen (K) der DSC-Messungen. Die Heiz- und Kühlrate beträgt 10 K/min. <sup>b</sup> Bestimmung der Übergangstemperatur erfolgte an dem Polarisationsmikroskop.

Die synthetisierten Verbindungen bilden alle eine chirale Cub<sub>bi</sub>-Phase aus. Zusätzlich zeigt Verbindung **Aa<sub>6</sub>/d<sub>26</sub>** beim Kühlen zunächst eine unbekannte hochviskose und stark doppelbrechende sphärolitische Textur (M), die sofort von der kubischen Phase verdrängt wird (Abb. 3.14 b). Die röntgenographischen Untersuchungen bestätigen, dass es sich bei der kubischen Phase um die chirale Cub<sub>bi</sub>/*I23*-Phase handelt. Es werden für diesen Phasentypen, neben der diffusen Weitwinkelstreuung, auch die typischen (321), (400) und (420) Reflexe des *I23* Gitters im Kleinwinkelbereich gefunden. Die unbekannte doppelbrechende Mesophasen von **Aa<sub>6</sub>/d<sub>26</sub>** konnte nicht untersucht werden, da diese nur in einem schmalen Temperaturbereich von 3 K vorliegt und die Bildung der kubischen Phase zu schnell erfolgt (Abb. 3.14 a). Die Tabelle 3.3 zeigt, dass in der Reihe **Aa<sub>6</sub>/d<sub>m</sub>** die smektischen Phasen zurückgedrängt und bikontinuierliche Phasen (Cub<sub>bi</sub>) begünstigt werden. Die chirale *I23*-Phase wird bei allen Verbindungen mit *m* = 14–26 ausgebildet und der Wiedereintritt einer kubischen *Ia3d*<sub>(S)</sub>-Phase konnte nicht beobachtet werden. Die komplette Phasensequenz *Ia3d*<sub>(L)</sub>–*I23*–*Ia3d*<sub>(S)</sub> konnte bisher nur bei den homologen Reihen ANBC-*n*<sup>[30-33]</sup>, BABH-*n*<sup>[33-35]</sup>, der Reihe der Bithiophene mit cycloaliphatischen Gruppen (Publ. **B**) und der Reihe **A3<sup>n</sup>/1<sup>m</sup>** von DRESSEL<sup>[63]</sup> gefunden werden.

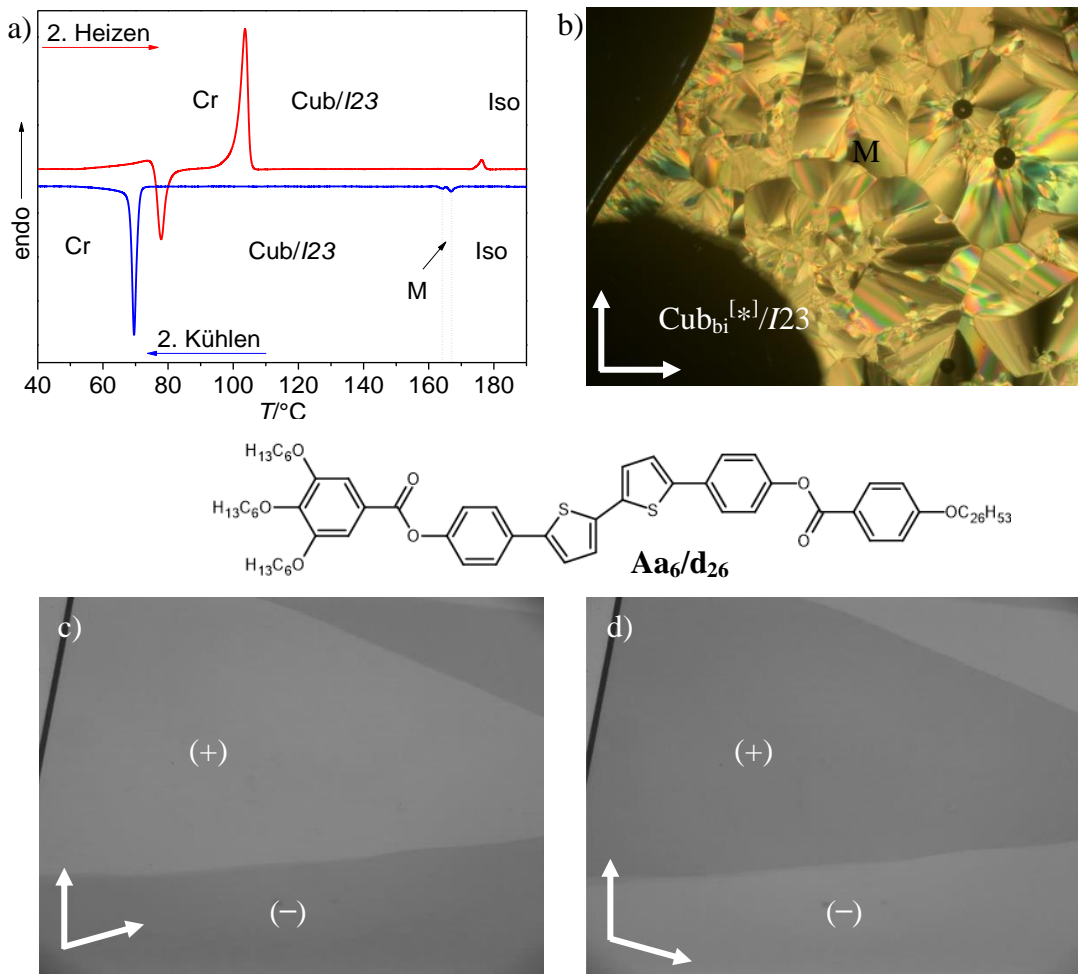


**Abbildung 3.14** Charakterisierung der Verbindung **Aa<sub>6</sub>/d<sub>26</sub>**. (a) DSC Heiz- und Kühlgraphen. (b) Textur der unbekannteten Mesophase M und der Übergang zur kubischen Phase  $\text{Cub}_{\text{bi}}^{[*]/I23}$  während des Abkühlens bei  $T = 164 \text{ }^\circ\text{C}$ . (c-d) Aufnahme der chiralen kubischen  $\text{Cub}_{\text{bi}}^{[*]/I23}$ -Phase (Kühlen bei  $T = 160 \text{ }^\circ\text{C}$ ) zwischen zwei Polarisatoren mit einem Winkel zwischen der Polarisatoren von  $< 90^\circ$  bzw.  $> 90^\circ$ .

## 4. Thermotrope Selbstorganisation der polycatenaren Benzile (Publikation D und E)

4,4'-Diphenyl-1,2-ethandion (Benzil) ist eines der bekanntesten achiralen Moleküle, das in energetisch tiefliegenden chiralen Konformeren vorliegt (eingeschränkte Rotation um die Bindung zwischen den beiden C=O-Gruppen, Abb. 4.1) und daher chirale Kristallstrukturen bildet. [62,88-90]

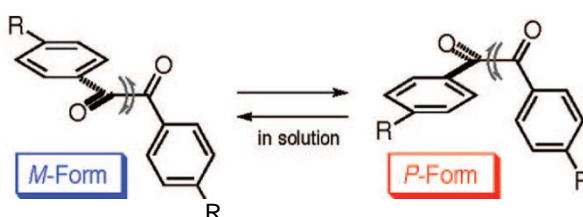


Abbildung 4.1 Schematische Darstellung der vorübergehenden Konformationschiralität des Benzils. [62]

Aus diesem Grund stellte der Benzilgrundkörper eine vielversprechende Einheit dar, um das bestehende Konzept der achiralen Bithiophene zur Ausbildung chiraler bikontinuierlich kubischer und isotrop flüssiger Phasen auf diese neue Struktureinheit zu übertragen. Die Ergebnisse der Untersuchungen sind in den beiden Publikationen **D** [62] und **E** [72] veröffentlicht.

### 4.1 Einfluss der Kernlänge sowie Anzahl und Länge der Alkoxyketten

Es wurden zwei Gruppen von Benzilderivaten synthetisiert und untersucht, zum einen die Benzoate **B'** mit fünf Benzenringen in der rigiden Kerneinheit und die Bisbenzoate **B** mit sechs Ringen. Die fünfkernigen Verbindungen **B'** zeigen in der Regel keine LC-Phasen. Lediglich drei Substanzen mit  $m = 14-18$  (**B'a<sub>10</sub>/14**, **B'a<sub>10</sub>/16**, **B'a<sub>10</sub>/18**, Abb. 4.2) bilden eine monotrope *Ia3d*-Phase aus (Publ. **E**).

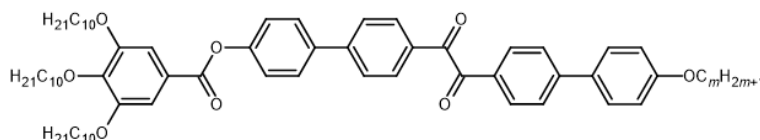


Abbildung 4.2 Struktur der fünfkernigen Benzile **B'a<sub>10</sub>/m**.

Ebenfalls führte der Austausch der Benzoateinheit durch alicyclische (**B'a<sub>10</sub>/cy4**, **B'a<sub>10</sub>/cy12**) oder polycyclische (**B'a<sub>10</sub>/Ada**) Substituenten nicht zu LC-Phasen (Publ. **E**). Die Benzile benötigen also für die Ausbildung stabiler flüssigkristalliner Phasen zwei terminale Benzoateinheiten, das heißt mindestens sechs Benzenringe. Dies ist auf die nichtlineare verdrillte Struktur der zentralen Benzileinheit zurückzuführen. Die Arbeiten konzentrierten sich daher auf die sechskernigen Benzilderivate. In Publikation **D** werden verschiedene alkoxy-substituierte sechskernige Verbindungen beschrieben, während in Publikation **E** der



Fokus auf analogen Verbindungen mit polaren Substituenten anstelle oder neben den Alkoxyketten liegt.

In Publikation **D** wird zunächst wie bei den Bithiophenen im Abschnitt 3.1 (Publ. **C**), die Mesophasensequenz der Benzile mit *n*-Decyloxyketten (**Bx<sub>10</sub>/y<sub>10</sub>**) in Abhängigkeit des Substitutionsmusters untersucht (Abb. 4.3). Es zeigte sich ein Übergang von einer smektischen Phase (SmC, **Bd<sub>10</sub>/d<sub>10</sub>**) über die beiden kubischen Phasen (*Ia3d*, *I23*) zu hexagonal kolumnaren Phasen (Col<sub>hex</sub>, **Ba<sub>10</sub>/c<sub>10</sub>**) mit zunehmender Kettenzahl. Ausschließlich die Verbindung mit sechs *n*-Decyloxyketten (**Ba<sub>10</sub>/a<sub>10</sub>**) ist nicht flüssigkristallin. [62]

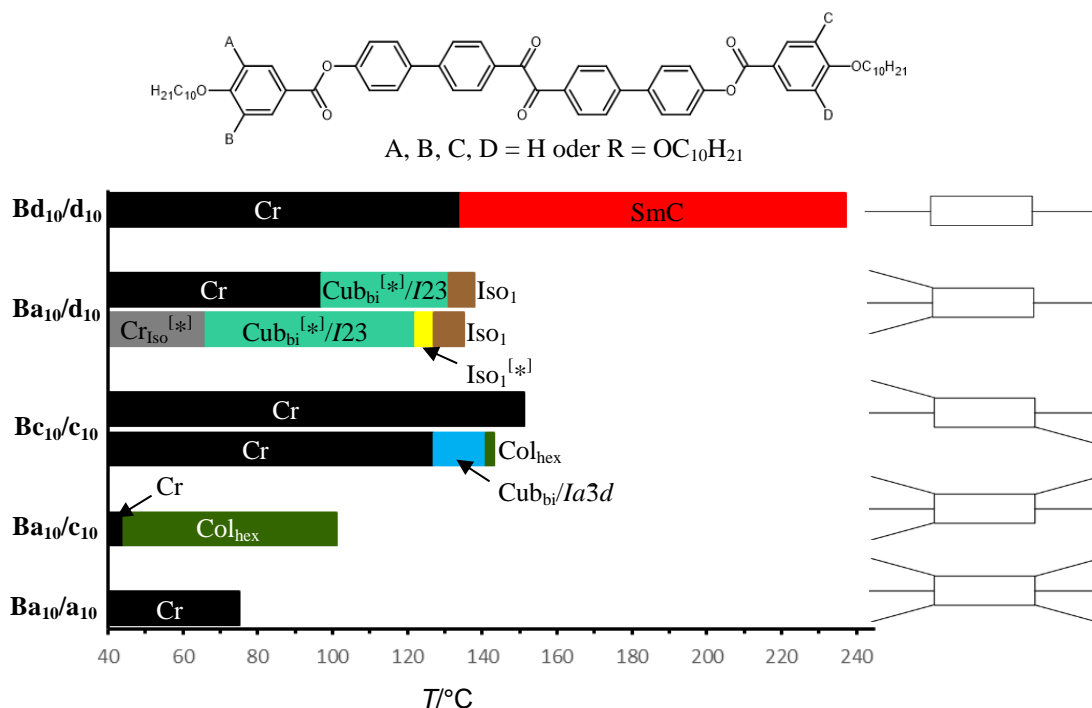


**Abbildung 4.3** Mesophasen der polycatenaren Benzile **Bx<sub>10</sub>/y<sub>10</sub>** in Abhängigkeit von der Kettenanzahl und – position während des Kühlens.

Im Folgenden wird in Publikation **D** eine homologe Reihe bestehend aus unsymmetrischen tetracatenaren Verbindungen (**Ba<sub>10</sub>/d<sub>m</sub>**) im Hinblick auf den steigenden Einfluss des *n*-Alkoxykettenvolumens am weniger substituierten Ende analysiert (Abb. 4.4). Die Substanzen ohne Substituenten (**Ba<sub>10</sub>/H**) und mit einer Methoxygruppe (**Ba<sub>10</sub>/d<sub>1</sub>**) weisen zunächst keine flüssigkristallinen Phasen auf. Erst ab einer Kettenlänge von *m* = 2 treten flüssigkristalline Phasen auf. Es wird ein kontinuierlicher Phasenübergang von *Ia3d*<sub>(L)</sub> (*m* = 2) über *I23* (*m* = 2–10) zu *Ia3d*<sub>(S)</sub> (*m* = 12–16) beobachtet. Dies wird auf die Zunahme des Verdrillungswinkels zwischen den Molekülen zurückgeführt, aufgrund des ansteigenden Volumens der Alkoxyketten. Wie bereits in anderen homologen Reihen gezeigt [63,64], ist auch diese Substanzklasse in der Lage eine chirale isotrope Flüssigkeit (Iso<sub>1</sub><sup>[\*]</sup>) auszubilden. Diese ist jedoch nur metastabil, ist aber über einen breiten Bereich der Kettenlänge (*m* = 2–12) sichtbar und wird bei weiter zunehmenden Kettenvolumen (*m* = 14–16) durch eine hexagonale kolumnare Phase (Col<sub>hex</sub>) ersetzt.



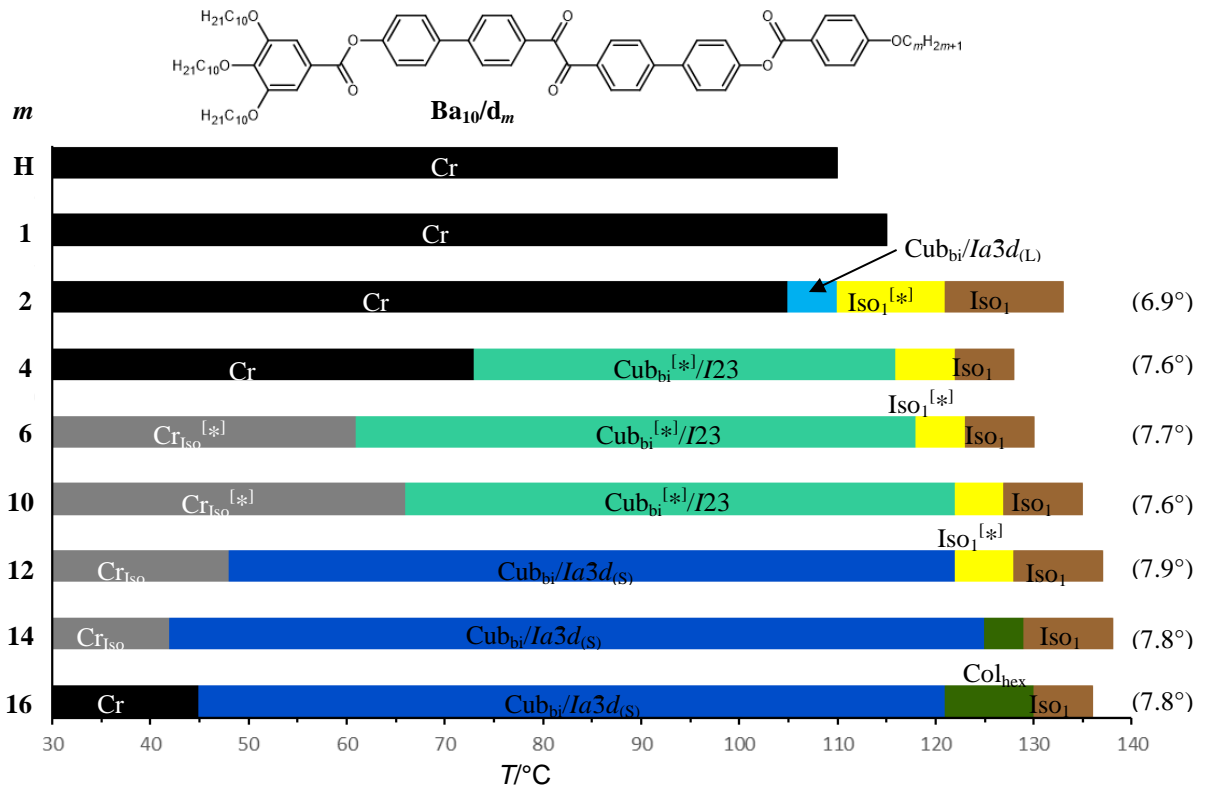


**Abbildung 4.4** Mesophasensequenz der homologen Reihe der polycatenaren Benzile  $\text{Ba}_{10}/\mathbf{d}_m$  in Abhängigkeit von der Kettenlänge während des Kühlens. Die Werte des Verdrillungswinkels  $\Phi$  der kubischen Phasen sind für die jeweiligen Substanzen in Klammern angegeben.

Besonders hervorzuheben ist das Auftreten einer zusätzlichen achiralen isotropen Flüssigkeit (Iso<sub>1</sub>) bei allen flüssigkristallinen Verbindungen der homologen Reihe entweder anstelle oder oberhalb der Iso<sub>1</sub><sup>[\*]</sup>-Phase. Diese lässt sich im DSC durch ein breites und diffuses Signal erkennen (Abb. 4.5 a). In diesem Temperaturbereich findet bei Temperaturniedrigung eine kontinuierliche Verringerung der Signalbreite der diffusen Kleinwinkelstreuung statt. Dies wird als ein nahezu kontinuierlicher Übergang zu einer cybotaktischen Flüssigkeit (Iso<sub>1</sub>) mit fluktuierenden Netzwerken interpretiert (Abb. 4.5 b). Der Übergang Iso<sub>1</sub>-Iso<sub>1</sub><sup>[\*]</sup> ist durch einen etwas schärferen DSC-Peak gekennzeichnet (Abb. 4.5 a), somit erfolgt bereits in der Iso-Phase und besonders in der Iso<sub>1</sub>-Phase ein kontinuierliches Wachstum von helikalen Netzwerken. Bei einer bestimmten Grenzkonnektivität dieser lokalen Netze setzt die Synchronisation des Helixsinns ein und es erfolgt der Übergang zur Iso<sub>1</sub><sup>[\*]</sup>-Phase unter Bruch der Spiegelsymmetrie und Ausbildung eines Konglomerats chiraler Domänen (Abb. 4.5). Dieses Phänomen wird in Publikation **D** für die Reihe der alkoxy-substituierten Verbindungen  $\text{Ba}_{10}/\mathbf{d}_m$  und in Publikation **E** für die zusätzlich kernfluorierten Verbindungen beschrieben.

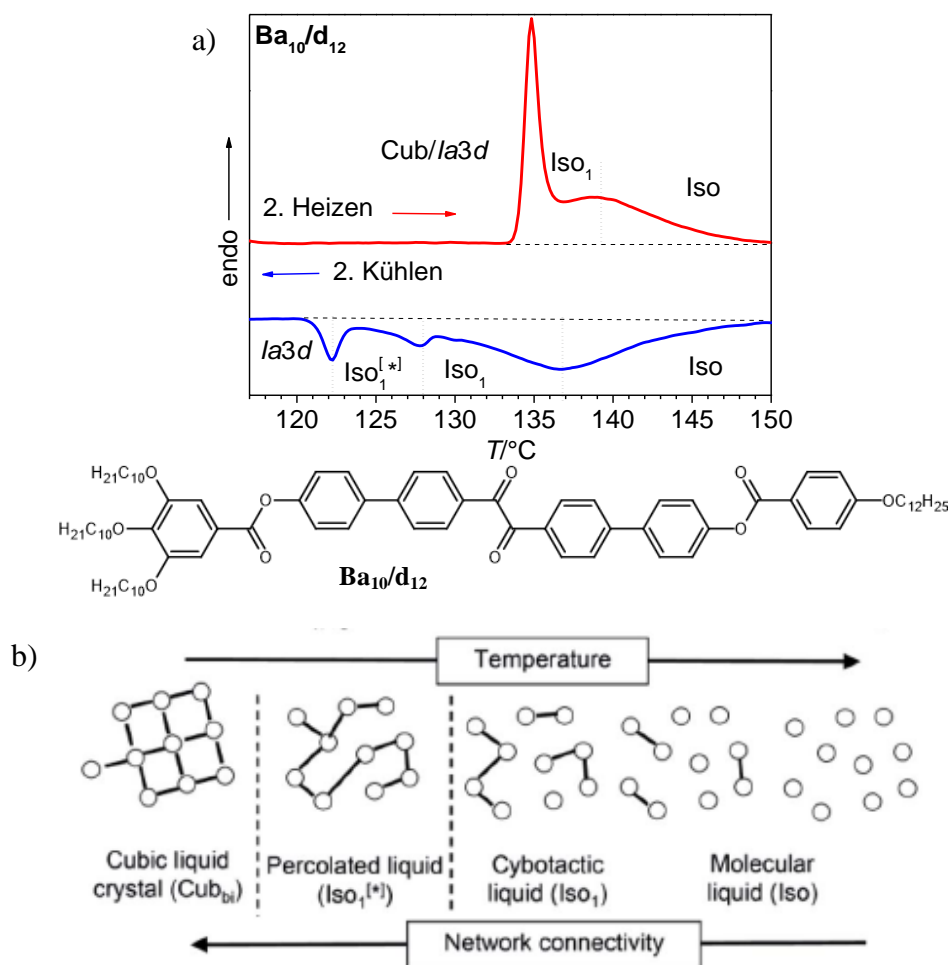


**Abbildung 4.5** Iso-Iso<sub>1</sub>-Iso<sub>1</sub>^{[\*]} Übergang des polycatenaren Benzderivates  $Ba_{10}/d_{12}$ . (a) DSC Heiz- und Kühlkurve. (b) Schematische Darstellung der helikalen Netzwerkkonnektivität in Abhängigkeit der Temperatur während des Iso-Iso<sub>1</sub>-Iso<sub>1</sub>^{[\*]} Übergangs. <sup>[62]</sup>

Ein weiteres besonders hervorzuhebendes Merkmal der Reihe  $Ba_{10}/d_m$  ist das Auftreten von optisch isotropen kristallinen Phasen ( $Cr_{Iso}$ ,  $Cr_{Iso}^{[*]}$ ). Die Verbindungen mit  $m = 6-10$  zeigen nach Kristallisation ein Konglomerat von chiralen Domänen ( $Cr_{Iso}^{[*]}$ ) beim Entkreuzen des Polarisators, welches aus der zuvor gebildeten kubischen  $I23$ -Phase erhalten bleibt. Dagegen zeigen die optisch isotropen kristallinen Phasen der Verbindungen  $m = 12-14$ , welche beim Abkühlen aus der achiralen  $Ia3d$ -Phase erhalten werden, keine optische Aktivität ( $Cr_{Iso}$ , Abb. 4.4). Die polarisationsmikroskopischen Aufnahmen und weitere Details sind in der Veröffentlichung **D** zu finden. <sup>[62]</sup>

Wie in den homologen Reihen der tetracatenaren Bithiophene <sup>[63]</sup>, in den homologen Reihen ANBC- $n$  <sup>[30-33]</sup> und BABH- $n$  <sup>[33-35]</sup> nimmt auch bei den hier beschriebenen polycatenaren Benzolderivaten der Twistwinkel  $\Phi$  zwischen benachbarten Molekülen im Netzwerk mit zunehmenden Kettenvolumen zu und führt zur Phasensequenz  $Ia3d_{(L)}-I23-Ia3d_{(S)}$ .

## 4.2 Einführung polarer Substituenten (Publikation E)

In der Publikation **E** <sup>[72]</sup> wurde auch der Einfluss des Austauschs der linearen *n*-Alkoxykette an der 4-Position der Benzoateinheit (**Ba<sub>10</sub>/d<sub>m</sub>**) durch polare elektronenziehende Gruppen (**Ba<sub>10</sub><sup>(4)</sup>Z**) untersucht (Abb. 4.6). Abgesehen von der Monofluorierung in Verbindung **Ba<sub>10</sub><sup>(4)</sup>F**, führt der Austausch der Alkoxygruppen durch polare Gruppen (CN, NO<sub>2</sub>, OCF<sub>3</sub>) zur Stabilisierung der bikontinuierlichen kubischen *Ia3d*<sub>(L)</sub>-Phase im Vergleich zu den Verbindungen **Ba<sub>10</sub>/d<sub>m</sub>**. Dies ist vermutlich darauf zurückzuführen, dass sich die Elektronendichte im  $\pi$ -System des Aromaten verringert und diese die attraktiven *Kern-Kern* Wechselwirkungen verstärken. Die Stabilität der Phase nimmt in der Reihenfolge F < OCF<sub>3</sub> < CN < NO<sub>2</sub> zu. Dagegen führt die Polyfluorierung (**Ba<sub>10</sub><sup>(3,4,5)</sup>F**, **Ba<sub>10</sub><sup>(2,3,4,5,6)</sup>F**) unter Erhalt der *Ia3d*<sub>(L)</sub>-Phase zu einer Mesophasendestabilisierung, wahrscheinlich infolge des sterischen Effekts der Fluorierung. Wie es bei den Bithiophenen zu beobachten war, wird ebenfalls bei den Benzilen mit polaren Substituenten keine chirale Iso<sub>1</sub><sup>[\*]</sup>-Phase gefunden. Dagegen wird die achirale cybotaktische Iso<sub>1</sub>-Phase gefunden, die bei den Verbindungen **Ba<sub>10</sub><sup>(4)</sup>NO<sub>2</sub>** und **Ba<sub>10</sub><sup>(4)</sup>CN** neben einer lamellaren Phase (SmA) auftritt. Allerdings ist diese SmA-Phase einer *Ia3d*-Phase unmittelbar benachbart (Abb. 4.6), so dass in der Iso<sub>1</sub>-Phase ein Wiedereintritt einer Netzwerkstruktur prinzipiell möglich ist.

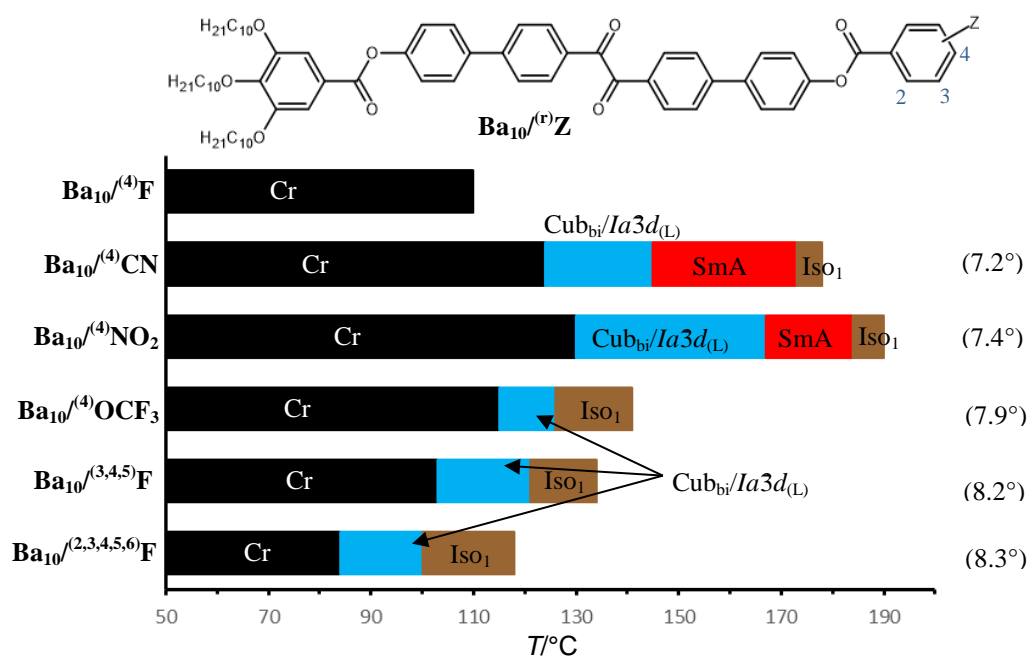


**Abbildung 4.6** Mesophasensequenz der polaren Benzilderivate **Ba<sub>10</sub><sup>(r)</sup>Z** während des Kühlens. Die in Klammern angegebenen Werte entsprechen den helikalen Twistwinkel ( $\Phi$ ) der kubischen *Ia3d*-Phasen.

Weiterführend diente das tetracatenare Benzil **Ba<sub>10</sub>/d<sub>6</sub>** (Abb. 4.4) als Referenz für die Untersuchung des Einflusses von Halogensubstituenten (F, Cl, Br) am weniger substituierten Ende neben der 4-Alkoxykette (Abb. 4.7).

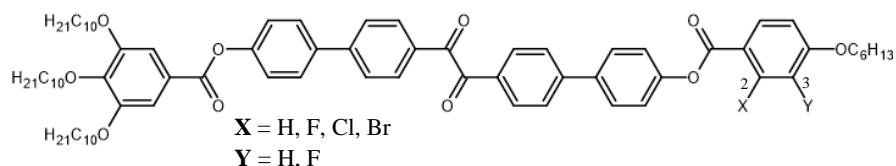


**Abbildung 4.7** Struktur der halogensubstituierten Benzilderivate  $\mathbf{Ba}_{10}^{(r)}\mathbf{Zd}_6$  mit einer Hexyloxykette in 4-Position.

Es zeigt sich, dass eine Halogenierung in der 2-Position zur Carboxylgruppe die chirale kubische  $I23$ -Phase entweder völlig verdrängt (Fluorierung in  $\mathbf{Ba}_{10}^{(2)}\mathbf{Fd}_6$ ) oder diese durch eine monotrope achirale  $Ia\bar{3}d_{(S)}$ -Phase (Cl, Br-Substitution in  $\mathbf{Ba}_{10}^{(2)}\mathbf{Cl}_6$ ,  $\mathbf{Ba}_{10}^{(2)}\mathbf{Br}_6$ ) ersetzt wird. Die chirale  $Iso_1^{[*]}$ -Phase dagegen bleibt der Verbindung  $\mathbf{Ba}_{10}^{(2)}\mathbf{Fd}_6$  erhalten und wird erst bei den größeren Substituenten (Cl, Br) vollständig verdrängt. Wie bei der unsubstituierten Verbindung  $\mathbf{Ba}_{10}/\mathbf{d}_6$  treten auch hier optisch isotrope kristalline Phasen auf, die sich in Abhängigkeit von der zuvor ausgebildeten kubischen Phase unterscheiden ( $Cr_{iso}^{[*]}$  neben  $I23$  und  $Cr_{iso}$  neben  $Ia\bar{3}d$ ). Im Unterschied dazu führt eine Fluorierung in der Position 3 ( $\mathbf{Ba}_{10}^{(3)}\mathbf{Fd}_6$ ) und 2,3 ( $\mathbf{Ba}_{10}^{(2,3)}\mathbf{Fd}_6$ ) zu einer doppelbrechenden kristallinen Phase (Cr). Die Abbildung 4.8 fasst wesentliche Aspekte der erläuterten Phasensequenzen der polycatenaren Benzile  $\mathbf{Ba}_{10}^{(r)}\mathbf{Z}$  und der halogenierten Benzile  $\mathbf{Ba}_{10}^{(r)}\mathbf{Zd}_6$  in Abhängigkeit der molekularen Struktur und der Stabilität der auftretenden kubischen und isotropen Phasen zusammen. Weitere Details sind in der Publikation **E** zu finden. <sup>[72]</sup>

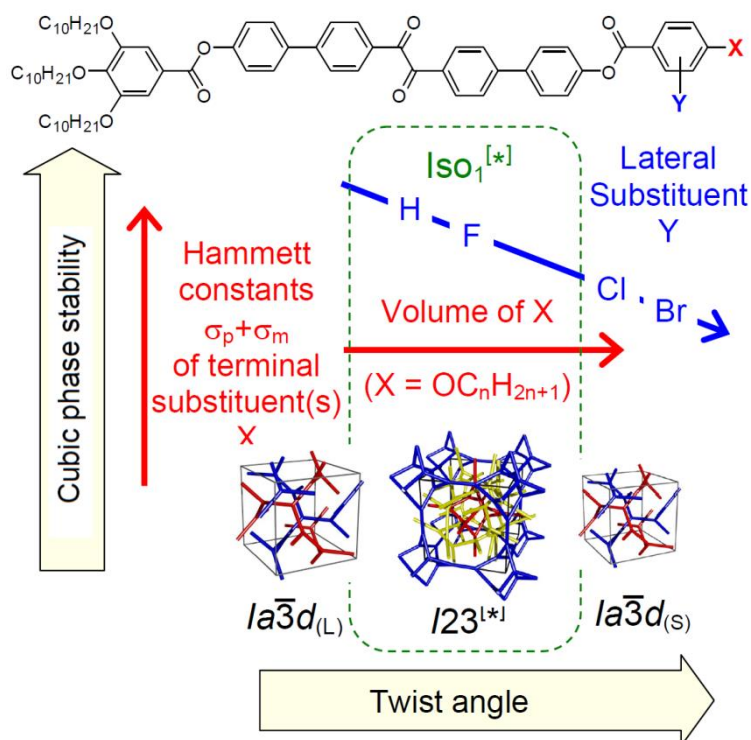


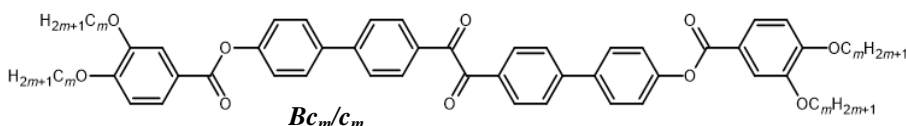
**Abbildung 4.8** Struktur-Eigenschaftsbeziehung der sechskernigen polycatenaren Benzile  $\mathbf{Ba}_{10}^{(r)}\mathbf{Z}$  und  $\mathbf{Ba}_{10}^{(r)}\mathbf{Zd}_6$ . <sup>[72]</sup>

### 4.3 Ergänzungen zu Publikationen D und E

#### 4.3.1 Homologe Reihe symmetrischer tetracatenarer Verbindungen

Ausgehend von der symmetrischen tetracatenaren Substanz **Bc<sub>10</sub>/c<sub>10</sub>** (Publ. **D**, Abb. 4.3) mit *n*-Decyloxyketten in der 3,4-Position an den terminalen Benzoateinheiten wurde der Einfluss der Kettenlänge im Hinblick auf die Stabilität der LC-Phasen untersucht. Die Phasenfolge der Homologen **Bc<sub>m</sub>/c<sub>m</sub>** ist in der Tabelle 4.1 zusammengefasst.

**Tabelle 4.1** Mesophasen, Phasenumwandlungstemperaturen und Gitterparameter der Verbindungen **Bc<sub>m</sub>/c<sub>m</sub>**.<sup>a</sup>



Verb.	<i>m</i>	<i>T</i> /°C [ $\Delta H$ /kJ·mol <sup>-1</sup> ]
<b>Bc<sub>6</sub>/c<sub>6</sub></b>	6	H: Cr 168 [56.0] Iso K: Iso 153 [57.0] Cr
<b>Bc<sub>8</sub>/c<sub>8</sub></b>	8	H: Cr 151 [68.3] Iso K: Iso 144 [60.4] Cr
<b>Bc<sub>10</sub>/c<sub>10</sub></b> <sup>[62]</sup>	10	H: Cr 151 [69.5] Iso K: Iso 143 [12.4] (Col <sub>hex</sub> 141 Cub <sub>bi</sub> /Ia3d) <sup>b</sup> 127 [71.2] Cr
<b>Bc<sub>12</sub>/c<sub>12</sub></b>	12	H: Cr <sub>1</sub> 134 [45.8] Cr <sub>2</sub> 138 [52.6] LC 152 [16.4] Iso K: Iso 150 [16.2] LC 115 [100.7] Cr
<b>Bc<sub>14</sub>/c<sub>14</sub></b>	14	H: Cr 129 [64.4] LC 153 [17.1] Iso K: Iso 150 [16.6] LC 111 [42.1] Cr
<b>Bc<sub>18</sub>/c<sub>18</sub></b>	18	H: Cr 125 [110.6] LC 151 [18.0] Iso K: Iso 149 [17.5] LC 111 [111.8] Cr
<b>Bc<sub>22</sub>/c<sub>22</sub></b>	22	H: Cr 125 [147] LC 147 [18.0] Iso K: Iso 144 [16.9] LC 111 [160.4] Cr

<sup>a</sup> Die angegebenen Umwandlungstemperaturen entsprechen den ermittelten Peaktemperaturen des zweiten Heiz- (H) und Kühlgraphen (K) der DSC-Messungen. Die Heiz- und Kühlrate beträgt 10 K/min. <sup>b</sup> Die gemessene Enthalpie entspricht beiden Übergängen. LC: unbekannte doppelbrechende Mesophase.

Der Tabelle 4.1 ist zu entnehmen, dass eine Verkürzung der Kettenlänge auf *m* = 8 (**Bc<sub>8</sub>/c<sub>8</sub>**) bereits zum völligen Verlust der flüssigkristallinen Phasen führt. Dagegen zeigt eine Kettenverlängerung den Übergang zu einer hochviskosen und doppelbrechenden Mesophase, welche bis zu einer Kettenlänge von *m* = 22 erhalten bleibt. Die Textur ist fächerartig mit isotropen Bereichen, welche durch Rotation des Heiztischs in der Ebene doppelbrechend werden (Abb. 4.9 a). Die röntgenographischen Untersuchungen haben bis zum jetzigen Zeitpunkt keine Aussage über die Struktur der Phase ergeben. Aufgrund ihres Auftretens bei Kettenverlängerung neben einer Cub<sub>bi</sub>-Phase sollte es sich um eine Mesophase aus kolumnaren Aggregaten handeln, welche wahrscheinlich einen nichtzirkularen Querschnitt aufweisen. Die hohe Viskosität lässt auf eine 3D-Ordnung schließen, was auf eine Korrelation zwischen den Säulen hindeutet.

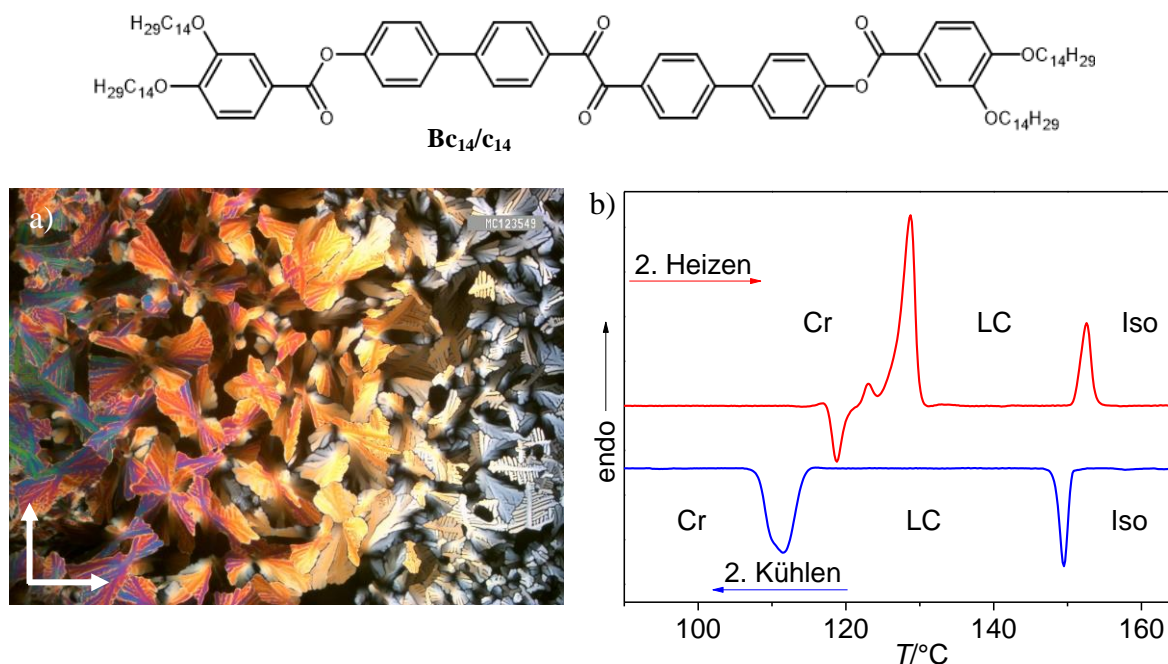
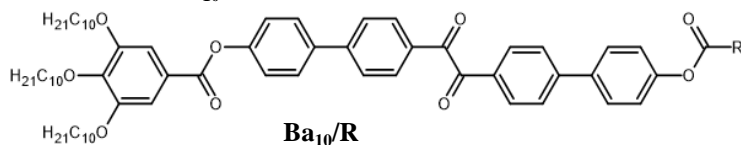


**Abbildung 4.9** Charakterisierung der Verbindung **Bc<sub>14</sub>/c<sub>14</sub>**. (a) Polarisationsmikroskopische Aufnahme der hochviskosen und doppelbrechenden unbekanntem LC-Phase. (b) DSC Heiz- und Kühlgraphen.

#### 4.3.2 Benzilbasierte Polycatenare mit einer verzweigten Endgruppe

**Tabelle 4.2.** Mesophasen, Phasenumwandlungstemperaturen und Gitterparameter der racemischen Benzilderivate **Ba<sub>10</sub>/R**.<sup>a</sup>



Verb.	R	T/°C [ $\Delta H/\text{kJ}\cdot\text{mol}^{-1}$ ]	a/nm (T/°C)
<b>(rac)-Ba<sub>10</sub>/1</b>		H: Cr 64 [15.9] Cub <sub>bi</sub> /Ia3d 94 [3.0] Iso K: Iso 82 [1.7] Cub <sub>bi</sub> /Ia3d < Cr	9.9 (80)
<b>(rac)-B'a<sub>10</sub>/MB</b>		H: Cr 73 [40.0] Iso K: Iso 31 [9.9] Cr	–
<b>(rac)-Ba<sub>10</sub>/Mo</b>		H: Cr 73 [40.2] Iso K: Iso < Cr	–

<sup>a</sup> Die angegebenen Umwandlungstemperaturen entsprechen den ermittelten Peaktemperaturen des zweiten Heiz- (H) und Kühlgraphen (K) der DSC-Messungen. Die Heiz- und Kühlrate beträgt 10 K/min.

In orientierenden Untersuchungen wurden ausgewählte Benzilderivate mit einer verzweigten Einheit am weniger substituierten Ende synthetisiert und untersucht. Aus der Tabelle 4.2 geht hervor, dass das fünfkernige Benzile mit einer kurzen einfach-verzweigten Alkylkette (**(rac)-B'a<sub>10</sub>/MB**) und das sechskernige Benzile mit einer racemischen Mosher-Säure (**(rac)-B'a<sub>10</sub>/Mo**) nicht zur Ausbildung flüssigkristallinen Phasen neigen. Lediglich die sechskernige Verbindung mit einer längeren einfach verzweigten Alkylkette (**(rac)-Ba<sub>10</sub>/1**) zeigt eine Cub<sub>bi</sub>/Ia3d in einem Temperaturbereich von 30 K. Bei den drei synthetisierten Verbindungen handelt es sich um racemische Gemische. Da keine Mesophasen bzw. nur eine achirale Ia3d-

Phase beobachtet wird, wurde auf die Synthese der enantiomerenreinen Verbindungen und die Synthese weiterer Verbindungen verzichtet.





## 5. Zusammenfassung der Ergebnisse

Kürzlich wurde gefunden, dass bikontinuierlich kubische Phasen polycatenarer Moleküle eine helikale Überstruktur aufweisen.<sup>[52,60,61,80]</sup> In der kubischen Phase mit *I23*-Gitter liegen drei verwobene Netzwerke mit einheitlicher Heliciät vor<sup>[60]</sup> und es wird ein spontaner Symmetriebruch unter Ausbildung von Konglomeraten beobachtet. Im Gegensatz dazu sind in der *Ia3d*-Phase zwei enantiomorphe Netzwerke mit entgegengesetzter Helicität kombiniert und diese Phase ist achiral. In Nachbarschaft zu diesen kubischen Phasen wurde des Weiteren der spontane Symmetriebruch in Flüssigkeiten ( $\text{Iso}_1^{[*]}$ ) gefunden.<sup>[61]</sup>

Das Ziel der vorliegenden Arbeit war eine Vertiefung des Verständnisses der Selbstassemblierung polycatenarer Moleküle, insbesondere in Bezug auf die Ausbildung achiraler und chiraler bikontinuierlich kubischer Phasen ( $\text{Cub}_{\text{bi}}/Ia3d$ ,  $\text{Cub}_{\text{bi}}^{[*]}/I23$ ) als auch die chirale isotrope Flüssigkeiten ( $\text{Iso}_1^{[*]}$ ). Dazu wurden einerseits neue 5,5'-Diphenyl-2,2'-bithiophene und andererseits Benzilderivate (Abb. 5.1) synthetisiert und bezüglich ihrer Selbstassemblierung charakterisiert.

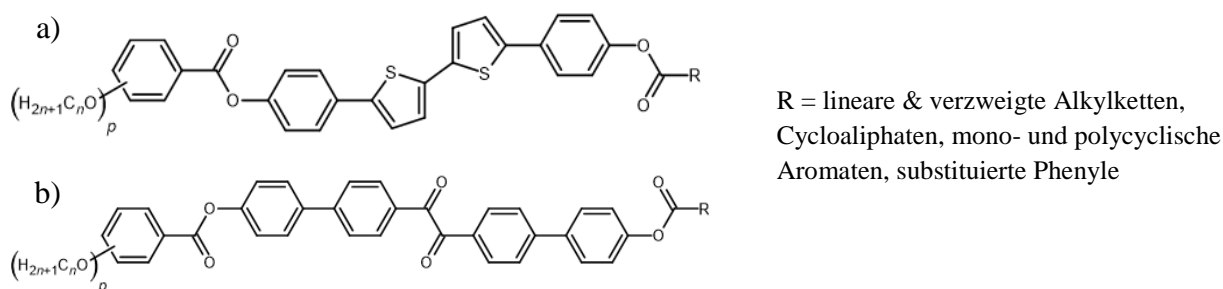


**Abbildung 5.1** Allgemeine Strukturformel der polycatenaren (a) Bithiophene und (b) Benzile.

In der Publikation **A** wird der Einfluss unterschiedlichster Substituenten am endständigen Benzolring tricatenerer Bithiophene auf den Typ und die Stabilität der bikontinuierlichen Phase ( $\text{Cub}_{\text{bi}}$ ) untersucht. Elektronenakzeptoren stabilisieren die  $\text{Cub}_{\text{bi}}$ -Phasen deutlich gegenüber -donatoren. Des Weiteren ist ein Übergang von der achiralen kubischen *Ia3d*- zu der chiralen kubischen *I23*-Phase über eine Koexistenz beider mit steigenden Substituentenvolumen zu erkennen. Erstaunlicherweise zeigen selbst Mesogene mit ortho-Substitutionen trotz der großen sterischen Hinderung breite Bereiche der  $\text{Cub}_{\text{bi}}$ -Phasen. Damit konnte ein robustes Strukturkonzept für das Design bikontinuierlich kubischer Phasen erarbeitet werden. Entscheidend ist dabei die Kettenverteilung, denn nur Moleküle mit unsymmetrischer Kettenverteilung<sup>[27]</sup> bevorzugen die bikontinuierlichen kubischen Phasen ( $\text{Cub}_{\text{bi}}/Ia3d$ ,  $\text{Cub}_{\text{bi}}^{[*]}/I23$ ), wogegen eine symmetrische Kettenverteilung an der linearen Kernstruktur zur Bildung von geeigneten smektischen und kolumnaren Phasen führt.

In den Publikationen **A** und **B** wurde auch der Einfluss verschiedenster alicyclischer Substituenten, kondensierter Aromaten, Heterocyclen und Polycyclen untersucht (Naph, Biph, Ada). Selbst große aromatische Substituenten (Naph, Biph) bilden entweder die achirale *Ia3d*<sub>(L)</sub>-Phase oder die chirale *I23*-Phase (Ada) aus. In der Publikation **B** wurde mit zunehmender Größe eines endständigen alicyclischen Rings die Phasensequenz *Ia3d*<sub>(L)</sub>-*I23*-*Ia3d*<sub>(S)</sub> gefunden. Dabei ist *Ia3d*<sub>(L)</sub> eine Gyroidstruktur mit helikaler Verdrillung

der Moleküle entlang der beiden enantiomorphen Netzwerke, wobei der helikale Verdrillungswinkel  $\Phi$  relativ klein ist und ein langer Pitch resultiert, welcher zu einem großen kubischen Gitterparameter führt. Dementsprechend findet man für  $Ia3d_{(S)}$  eine stärkere Verdrillung, einen kürzeren Pitch und kleineren Gitterparameter. Bemerkenswerterweise wird im Kontaktbereich zwischen diesen beiden achiralen  $Ia3d$ -Phasen eine chirale  $I23$ -Phase induziert.

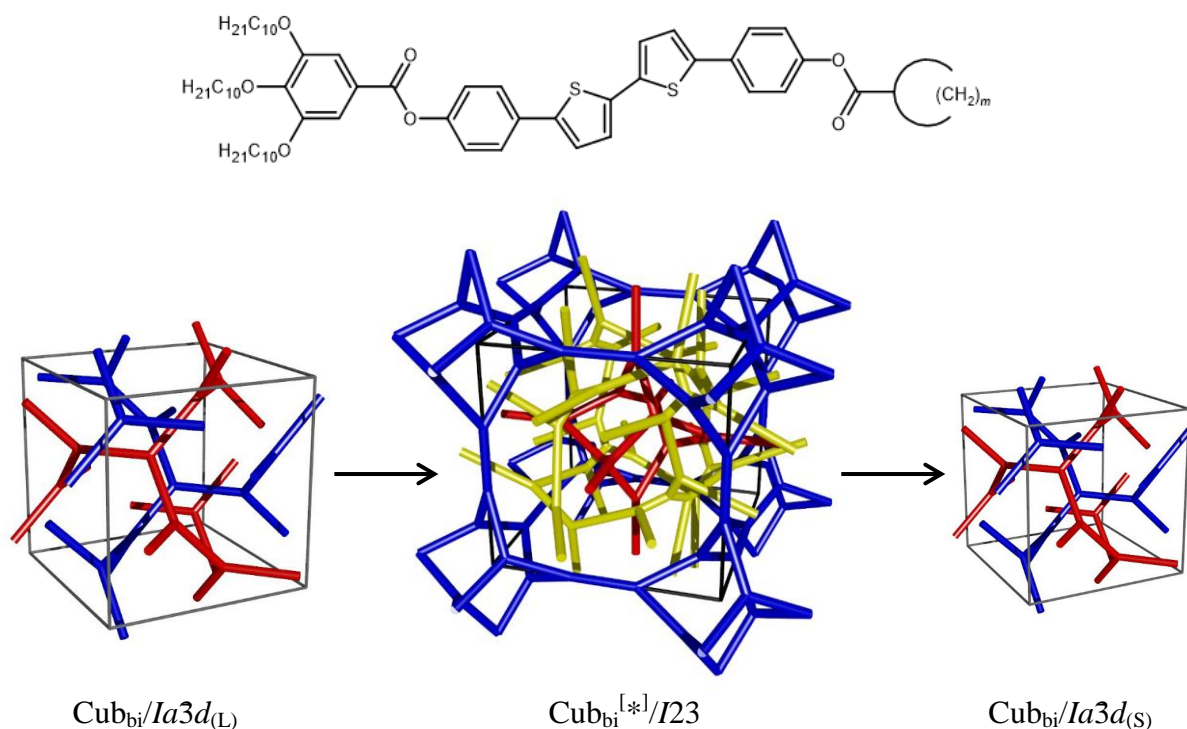


**Abbildung 5.2** Struktur der polycatenaren Mesogene  $A'a_{10}/cym$  mit einem endständigen cyclophatischen Rest ( $m = 4-12$ ). Schematische Darstellung der gefundenen Phasensequenz  $Ia3d_{(L)}-I23-Ia3d_{(S)}$ .

In der Publikation **C** wurde der Übergang von den lamellaren zu den dreidimensionalen Strukturen am Beispiel homologer Reihen tricatenerer Bithiophene untersucht. Mit zunehmender Temperatur und Kettenlänge findet ein Übergang von smektischen und hexatischen lamellaren Strukturen (Sm, Hex) zu den beiden bikontinuierlich kubischen Phasen ( $Ia3d$ ,  $I23$ ) statt. Auffallend für die kubischen Phasen der tricateneren Bithiophene ist, dass im Gegensatz zu den oben genannten tetracatenaren Verbindungen mit steigenden Kettenvolumen ein kleiner werdender Twistwinkel  $\Phi$  gefunden wurde. Dies wurde mit dem Einfluss der Kettenverlängerung auf die effektive Moleküllänge erklärt.

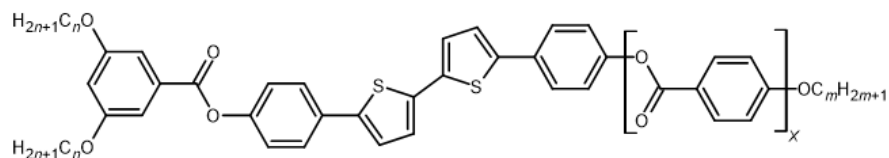


**Abbildung 5.3** Struktur der tricateneren Bithiophene  $Ab_{10}/d_m$  ( $X=1$ ),  $Ab_6/d_m$  ( $X=1$ ) und  $A'b_6/m$  ( $X=0$ ).

Erste homologe Reihen polycatenarer flüssigkristalliner Benzilderivate wurden in den Publikationen **D** und **E** vorgestellt. Auch bei den Benzilverbindungen konnte ein Übergang von den lamellaren (Sm) über die beiden bikontinuierlich kubischen ( $\text{Cub}_{\text{bi}}/Ia3d$ ,  $\text{Cub}_{\text{bi}}^{[*]}/I23$ ) zu den kolumnaren ( $\text{Col}_{\text{hex}}$ ) Phasen beobachtet werden, wenn die Kernstruktur aus mindestens sechs Benzenringe aufgebaut ist.

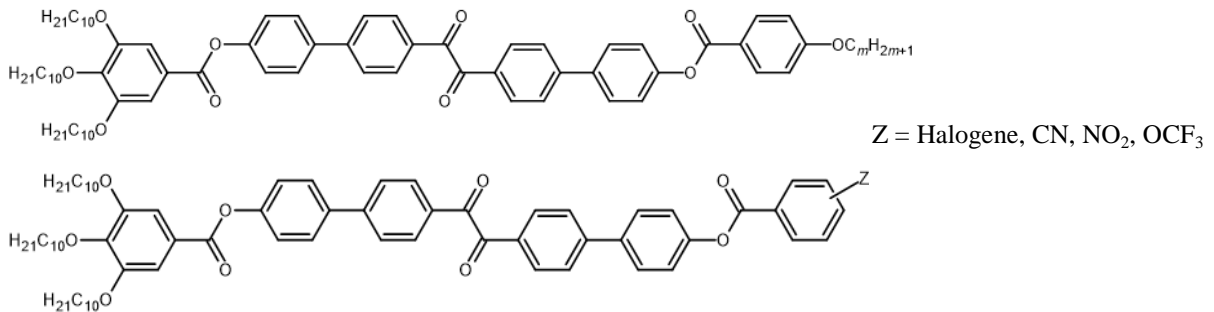


**Abbildung 5.4** Strukturen der polycatenaren Benzilderivate  $\text{Ba}_{10}/\text{d}_m$  und  $\text{Ba}_{10}/\text{Z}^{(r)}$ .

Für die kubischen Phasen ist auch hier die Phasensequenz  $Ia3d_{(L)}-I23-Ia3d_{(S)}$  zu beobachten. Neben der chiralen isotropen Phase ( $\text{Iso}_1^{[*]}$ ) konnte für alle flüssigkristallinen Substanzen auch eine achirale isotrope Flüssigkeit ( $\text{Iso}_1$ ) nachgewiesen werden, welche anstelle der chiralen  $\text{Iso}_1^{[*]}$  oder oberhalb dieser auftreten. Der  $\text{Iso}-\text{Iso}_1-\text{Iso}_1^{[*]}$  Übergang ist bei Temperaturenniedrigung durch ein kontinuierliches Wachstum von helikalen Netzwerken gekennzeichnet bis zum Erreichen eines kritischen Wertes bei dem die Synchronisation des Helixsinns unter Spiegelsymmetriebruch und Ausbildung einer Konglomeratstruktur eintritt (Abb. 5.5 a).

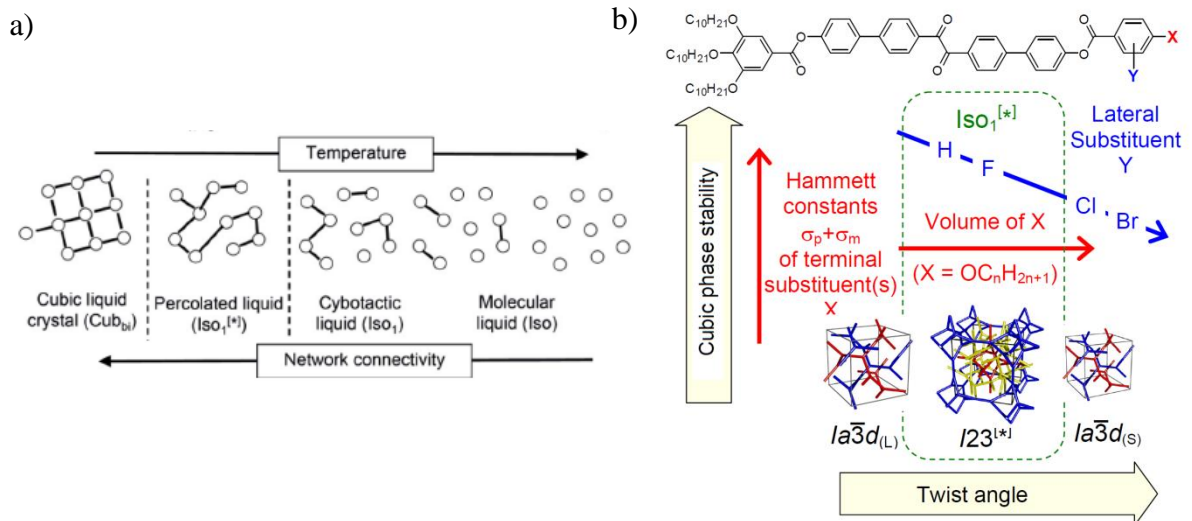


**Abbildung 5.5** (a) Abhängigkeit der Netzwerkkonktivität des  $\text{Iso}-\text{Iso}_1-\text{Iso}_1^{[*]}$  Übergangs während Temperaturänderungen. <sup>[62]</sup> (b) Darstellung der Stabilität kubischer und isotroper Phasen in Abhängigkeit der Position der lateralen Substitution der polycatenaren Benzile  $\text{Ba}_{10}/\text{Z}^{(r)}$  und  $\text{Ba}_{10}/\text{Zd}_6$ . <sup>[72]</sup>

Ein weiteres hervorstechendes Merkmal dieser Reihe ist das Auftreten von zwei optisch isotropen kristallinen Phasen ( $\text{Cr}_{\text{iso}}$ ,  $\text{Cr}_{\text{iso}}^{[*]}$ ), die entweder optisch inaktiv oder aktiv sind, in Abhängigkeit der zuvor gebildeten kubischen Phase ( $Ia3d$ ,  $I23$ ).

Ersetzt man die Alkylketten am weniger substituierten Ende des Benzils durch polare

Substituenten ( $\text{NO}_2$ ,  $\text{CN}$ ,  $\text{OCF}_3$ ), stellt man eine deutliche Stabilisierung der LC-Phasen gegenüber Elektronendonatoren ( $\text{Ba}_{10}/\mathbf{d}_m$ ) aufgrund erhöhter Kern-Kern Interaktionen zwischen elektronenreichen und -armen Kernen fest. Zudem treten hier smektische A-Phasen (SmA) vor dem Übergang in die cybotaktische  $\text{Iso}_1$ -Phase auf.

Die in dieser Arbeit vorgestellten polycatenaren Bithiophen- und Benzilderivate führen zu einem breiten Spektrum an Mesogenen, die befähigt sind die beiden bikontinuierlichen kubischen Phasen ( $\text{Cub}_{\text{bi}}/Ia3d$ ,  $\text{Cub}_{\text{bi}}^{[*]}/I23$ ) über weite Temperaturbereiche auszubilden. In Verbindung mit früheren Arbeiten <sup>[63,64]</sup> konnte so ein umfassender Überblick zum Designkonzept polycatenarer Substanzen erhalten werden. Dabei kristallisiert sich heraus, dass die Chiralität ein zentraler Bestandteil für das Verständnis der Strukturen ist. Dies gilt nicht nur im Hinblick auf die Ausbildung kubischer Phasen, auch für das Verständnis der Ausbildung verschiedenster isotrop flüssiger Phasen ( $\text{Iso}_1^{[*]}$ ,  $\text{Iso}_1$ ) spielt die helikale Anordnung der Moleküle eine immense Rolle. Diese spontane Bildung von helikalen Überstrukturen der achiralen Moleküle in fluiden Systemen hat eine Vielzahl potentieller Anwendungsmöglichkeiten, wie zum Beispiel für Materialien mit nichtlinearen optischen Eigenschaften, photonischen Strukturen und Materialien mit zirkular polarisierten Emissionen<sup>[84,85]</sup> und eventuell auch für die enantioselektive Katalyse <sup>[10,11,86]</sup> nachdem die Konglomeratstruktur durch chirale Dotierstoffe oder chirale physikalische Felder gebrochen und eine einheitliche Chiralität erzeugt wurde.

Ein Ansatzpunkt für weiterführende Arbeiten betrifft den komplexen Übergang von den lamellaren zu den dreidimensionalen Strukturen und die Effekte der helikalen Organisation auf die Phasenstrukturen nichtkubischer Mesophasen mit 3D-Gitter, welche noch aufgeklärt werden müssen.

## 6. Experimenteller Teil

In dem experimentellen Abschnitt wird auf die allgemeinen Methoden der Charakterisierung der Zielverbindungen eingegangen. Des Weiteren folgen die Details der synthetischen Daten der Zwischenstufen und der Substanzen, welche bisher nicht publiziert worden sind. Die analytischen Daten der publizierten Verbindungen sind in den jeweiligen „Supporting information“ der Literaturstellen nachzulesen (Publ. A–E, siehe Anhang A.1).

### 6.1 Charakterisierungsmethoden

Die Untersuchung der mesomorphen Eigenschaften aller synthetisierten Zielverbindungen erfolgte nach standardisierten Methoden zu denen die Polarisationsmikroskopie (POM), die dynamische Differentialkalorimetrie (DSC) und die röntgenographische Untersuchung (XRD) angehören. Zusätzlich wurden Berechnungen zu den phasenspezifischen Parametern durchgeführt, deren Formeln an den jeweiligen Stellen angegeben sind.

#### 6.1.1 Polarisationsmikroskopie (POM)

Die optischen Untersuchungen der Mesogene wurden an dem Polarisationsmikroskop DMRXP der Firma LEICA MICROSYSTEMS in Verbindung mit dem Heiztisch FP 82-HAT der Firma METTLER als Heizquelle und Probenhalter durchgeführt. Die Aufnahme der Texturfotos erfolgte mit der LEICA MC120 HD. Die Untersuchung der Proben erfolgte auf unterschiedliche Weisen. Die Präparation der Proben mit kubischen Phasen wurde in Keilzellen durchgeführt, um eine möglichst große Probenstärke ( $\sim 15 \mu\text{m}$ ) zu erzielen für eine bessere Visualisierung möglicher chiraler Bereiche. Die Untersuchung lamellarer Strukturen wurde in dünnen Proben durchgeführt. Dazu wurde die Probe in den isotropen Bereich erhitzt und zwischen Deckglas und Objektträger aufgenommen.

Die Durchführung von Kontaktpräparaten erfolgte ebenfalls in Keilzellen um eine geeignete Probenstärke für den Kontaktbereich zu erhalten. Auch hier wurden die jeweiligen Substanzen in den isotropen Bereich erhitzt und in der Keilzelle aufgenommen.

#### 6.1.2 Dynamische Differentialkalorimetrie (DSC)

Für die exakte Bestimmung der Übergangstemperaturen und der Übergangsenthalpien wurden die Proben in den Geräten DSC-7 und DSC-8000 vermessen mit einer Heiz- und Kühlrate von 10 K/min. Die entnommenen Werte, falls nicht anders angegeben, entsprechen der zweiten Heiz- und Kühlkurve. Für die Aufnahme der DSC-Messkurve wurde die Substanz in eine Aluminiumkapsel eingewogen und in das Gerät eingeschleust. Als Referenz diente eine mit Luft gefüllte Kapsel.

### 6.1.3 Röntgenbeugungsuntersuchung (XRD)

Die röntgenographische Untersuchung der Proben wurde an dem hausinternen Gerät Kristalloflex 760H der Firma SIEMENS/BRUKER mit monochromatischer Röntgenstrahlung (Cu-K $\alpha$ -Linie;  $\lambda = 1.54 \text{ \AA}$ ) durchgeführt. Die zu untersuchende Substanz wurde entweder nach dem Aufschmelzen in eine Glaskapillare (HILGENBERG) präpariert oder direkt auf einem Objekträger aufgetragen und bestrahlt. Die Diffraktogramme wurden mit dem Flächendetektor Vantec 500 der Firma BRUKER detektiert.

Hochauflösende Kleinwinkel-Pulverdiffraktogramme wurden von Prof. Dr. F. LIU (Universität Xi'an) an der Beamline BL16B1 in Shanghai mit Synchrotronstrahlung aufgenommen. Mehr Details der Untersuchungsmethode sind in dem SI der Publikation **D** <sup>[62]</sup> zu finden.

## 6.2 Synthetischer Teil

### 6.2.1 Allgemeine Betrachtung

Die verwendeten Lösungsmittel wurden nach den Standardverfahren gereinigt und getrocknet. <sup>[73]</sup> Absolutes Tetrahydrofuran, 2-Butanon, Dichlormethan, Pyridin und Methanol wurden von SIGMA ALDRICH bezogen und ohne weitere Reinigung verwendet. Für die analytische Dünnschichtchromatographie (DC) wurden kieselgelbeschichtete Aluminiumfolien (Kieselgel 60 F<sub>254</sub>, MERCK) und für die säulenchromatographische Reinigung der Verbindungen MACHEREY-NAGEL Kieselgel 60 (0.04 – 0.063 mm) verwendet. Die Detektion erfolgte mittels UV-Licht mit den Wellenlängen 254 bzw. 366 nm. Die Angaben der Ausbeuten beziehen sich auf die reine, nach Destillation oder Umkristallisation erhaltene Substanzmenge und sind nicht optimiert.

Die Identifizierung der Substanzen erfolgte über <sup>1</sup>H-, <sup>13</sup>C- und <sup>19</sup>F-NMR Spektroskopie. Die verwendeten Geräte sind VARIAN Gemini 2000 und UNITY Inova 500. Die Messungen wurden bei Standardbedingungen ( $T = 27 \text{ °C}$ , TMS als Standard) durchgeführt und die Auswertung der Spektren wurde mit Hilfe des Programms MESTRENOVA 6.0.2 angefertigt. Die elementare Zusammensetzung der Substanzen wurde mit den Geräten Erba-CHNO-Analyzer 1102 (CARLO ERBA) oder CHNS-932-Analyzer (LECO Co.) durchgeführt. Des Weiteren wurden hochauflösende Massenspektren an dem HR-ESI-TOF (BRUKER) angefertigt. Die Ermittlung der Schmelzpunkte der Vorstufen erfolgte am BOETIUS-Heiztischmikroskop und ist nicht angepasst.

## 6.2.2 Chemikalien

Folgende Chemikalien wurden kommerziell erworben und ohne weitere Reinigung eingesetzt:

(±)-2-Methoxy-2-trifluormethyl-2-phenyllessigsäure ( <i>Sigma-Aldrich</i> )	Triphenylphosphin ( <i>Sigma-Aldrich</i> )
4-Hydroxybenzoesäureethylester ( <i>Sigma-Aldrich</i> )	1-Bromeicosan ( <i>Sigma-Aldrich</i> )
3,4-Dihydroxybenzoesäureethylester ( <i>Sigma-Aldrich</i> )	<i>N, N'</i> -Dicyclohexylcarbodiimid ( <i>Merck</i> )
4-Hydroxybenzaldehyd ( <i>Sigma-Aldrich</i> )	4-(Dimethylamino)pyridin ( <i>Acros</i> )
<i>n</i> -Heptansäure ( <i>Fluka</i> )	Resorcin ( <i>Sigma-Aldrich</i> )
<i>n</i> -Tridecansäure ( <i>Fluka</i> )	Natriumchlorit ( <i>Sigma-Aldrich</i> )
(±)-2-Octanol ( <i>Sigma-Aldrich</i> )	Thionylchlorid ( <i>Sigma-Aldrich</i> )
2-(6-Bromhexyloxy)tetrahydro-2 <i>H</i> -pyran ( <i>Sigma-Aldrich</i> )	Tetrabutylammoniumiodid
	4,4-Dibrombenzil ( <i>Sigma-Aldrich</i> )
	2-Bromthiophen ( <i>Sigma-Aldrich</i> )

Folgende Chemikalien waren bereits in der Arbeitsgruppe vorhanden:

4- <i>n</i> -Methoxybenzoesäure	4- <i>n</i> -Hexadecyloxybenzoesäure
4- <i>n</i> -Ethoxybenzoesäure	4- <i>n</i> -Octadecyloxybenzoesäure
4- <i>n</i> -Butyloxybenzoesäure	3,4-Di- <i>n</i> -hexyloxybenzoesäure
4- <i>n</i> -Hexyloxybenzoesäure	3,4-Di- <i>n</i> -octyloxybenzoesäure
4- <i>n</i> -Octyloxybenzoesäure	3,4-Di- <i>n</i> -decyloxybenzoesäure
4- <i>n</i> -Decyloxybenzoesäure	3,4-Di- <i>n</i> -dodecyloxybenzoesäure
4- <i>n</i> -Dodecyloxybenzoesäure	3,4-Di- <i>n</i> -octadecyloxybenzoesäure
4- <i>n</i> -Tetradecyloxybenzoesäure	Tetrakis(triphenylphosphin)palladium(0)





## 6.3 Allgemeine Arbeitsvorschriften

### 6.3.1 WILLIAMSON Ethersynthese (AAV-1) <sup>[74]</sup>

Das Phenolderivat (1.0 eq), das Alkylbromid oder -tosylat (1.1 eq je OH-Funktion), Kaliumcarbonat (5.0 eq je OH-Funktion) und katalytische Mengen an Tetrabutylammoniumiodid (TBAI) werden in einem geeigneten Lösungsmittel (2-Butanon, DMF) suspendiert. Die Suspension wird im Rückfluss erhitzt und der Reaktionsverlauf dünnschichtchromatographisch verfolgt. Nach beendeter Reaktion wird das auf Raumtemperatur abgekühlte Gemisch mit Wasser versetzt und anschließend mit Chloroform extrahiert. Die vereinigten organischen Phasen werden über Natriumsulfat getrocknet und das Lösungsmittel unter verminderten Druck entfernt. Der Rückstand wird chromatographisch und/oder durch Umkristallisation gereinigt.

### 6.3.2 Veresterung über das Säurechlorid (AAV-2)

Unter einer Argonschutzatmosphäre wird die entsprechende Benzoesäure (1.25 eq) mit Thionylchlorid versetzt und im Rückfluss erhitzt bis sich eine klare Flüssigkeit gebildet hat. Nach dem Abkühlen auf Raumtemperatur wird überschüssiges Thionylchlorid mit Hilfe einer Kühlfalle entfernt. Anschließend wird der Rückstand mit Pyridin, DMAP, dem Phenol (1.0 eq) und Dichlormethan versetzt und bei Raumtemperatur gerührt. Nach beendeter Reaktion wird das Lösungsmittelgemisch unter verminderten Druck entfernt und das Rohprodukt säulenchromatographisch gereinigt.

### 6.3.3 Veresterung nach STEGLICH (AAV-3) <sup>[76]</sup>

Es werden die Carbonsäure (1.0 eq), der Alkohol (1.1 eq), DCC (1.2 eq) und DMAP (katalytische Menge) in Dichlormethan vorgelegt und bei Raumtemperatur gerührt. Die Reaktion wird dünnschichtchromatographisch verfolgt und nach Reaktionsende wird das entstandene Harnstoffderivat abfiltriert und das Lösungsmittel unter verminderten Druck entfernt. Der Rückstand wird säulenchromatographisch und/oder durch Umkristallisation gereinigt.

### 6.3.4 Oxidation von Aldehyden nach PINNICK (AAV-4) <sup>[77,78]</sup>

Der zu oxidierende Aldehyd (1.0 eq) wird zusammen mit Resorcin (1.3 eq) in *t*-Butanol (10 ml/mmol Aldehyd) gelöst, anschließend mit einer Lösung bestehend aus Natriumchlorit (5.8 eq, 80% ig) und Natriumdihydrogenphosphat (3.0 eq) in Wasser (1 ml/mmol NaClO<sub>2</sub>) versetzt und bei Raumtemperatur gerührt. Nach dem Reaktionsende wird das Gemisch unter verminderten Druck eingeeengt und mit weiterem Wasser aufgenommen. Es wird mit konzentrierter Salzsäure pH = 2 eingestellt, das ausgefallene Produkt abfiltriert und mit Wasser und *n*-Hexan gewaschen. Das Produkt wird gegebenenfalls umkristallisiert.

### **6.3.5 Alkalische Esterhydrolyse (AAV-5)**

Der betreffende Ester (1.0 eq) wird in einem geeigneten polaren Lösungsmittel vorgelegt, mit Natriumhydroxid (min. 5.0 eq) versetzt und anschließend im Rückfluss erhitzt bis kein Edukt mehr dünnschichtchromatographisch nachweisbar ist. Nach dem Abkühlen auf Raumtemperatur wird unter Eiskühlung vorsichtig konzentrierte Salzsäure bis  $\text{pH} = 1$  zugegeben. Das ausgefallene Produkt wird abgesaugt, mit Wasser neutral gewaschen und gegebenenfalls umkristallisiert. Flüssigkeiten werden mit Diethylether extrahiert und anschließend das Lösungsmittel unter verminderten Druck entfernt und destillativ gereinigt.

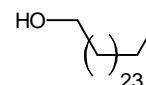
## 6.4 Synthese und analytische Daten

Die Synthesen und analytischen Daten der in den Publikationen **A–E** beschriebenen Verbindungen und deren Zwischenstufen sind in den Supporting Information der jeweiligen Publikationen zu finden. In den Folgenden Abschnitten werden die analytischen Daten der unpublizierten Zwischenstufen und der Substanzen beschrieben.

### 6.4.1 Zwischenstufen

Die analytischen Daten der publizierten Phenole der Bithiophene **1a-d/OH** und Benzile **2a-b/OH** sowie deren Zwischenstufen sind in den Supporting Information (SI) der Publikationen **C, D** und in den Referenzen [63] und [64] zu finden.

1-*n*-Hexacosanol **1** <sup>[79]</sup>

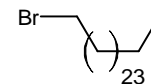


**Vorschrift** Unter einer Inertgasatmosphäre wird Magnesiumspäne (0.7 g, 0.029 mol) in THF (60 ml) vorgelegt und durch die Zugabe von 2-(6-Bromhexyloxy)tetrahydro-2*H*-pyran (5.0 g, 0.019 mol) wird die Reaktion initialisiert. Nach erfolgter Zugabe wird die Lösung für 3 Stunden bei 55 °C erhitzt. Nach dem Abkühlen auf Raumtemperatur wird das GRIGNARD-Reagenz vom überschüssigen Magnesium separiert und auf -5 °C gekühlt. Es erfolgt die Zugabe von 1-Bromeicosan (6.9 g, 0.019 mol) und anschließend das Abkühlen der Lösung auf -50 °C. Im nächsten Schritt wird das in THF gelöste Dilithiumtetrachlorocuprat(II) (4ml) zugegeben, das Gemisch wird zunächst für 2 Stunden bei -50 °C und letztlich 12 Stunden bei Raumtemperatur gerührt. Das Quenchen der Reaktion erfolgt durch Zugabe von gesättigter Ammoniumchlorid-Lösung. Es werden die Phasen getrennt, die wässrige mehrmals mit Chloroform extrahiert und die vereinigten organischen Phasen über Natriumsulfat getrocknet und das Lösungsmittel unter verminderten Druck entfernt. Der Rückstand wird in einem THF/MeOH-Gemisch (1:1) aufgenommen, mit einer katalytischen Menge an Pyridinium-*p*-toluolsulfonat versetzt und für 30 Minuten im Rückfluss erhitzt. Anschließend wird das Lösungsmittelgemisch unter verminderten Druck entfernt und der Rückstand säulenchromatographisch (Eluent: CHCl<sub>3</sub>) gereinigt.

**Ausbeute** 1.5 g (3.92 mmol, 21%), farbloser Feststoff

**Analytik** C<sub>26</sub>H<sub>54</sub>O; *M* = 382.71 g/mol; Smp 82 °C

<sup>1</sup>H NMR (400 MHz, CDCl<sub>3</sub>) δ 3.64 (t, <sup>3</sup>*J* = 6.6 Hz, 2H, OCH<sub>2</sub>CH<sub>2</sub>), 1.60–1.51 (m, 2H, OCH<sub>2</sub>CH<sub>2</sub>), 1.37–1.21 (m, 46H, CH<sub>2</sub>), 0.88 (t, <sup>3</sup>*J* = 6.8 Hz, 3H, CH<sub>3</sub>).

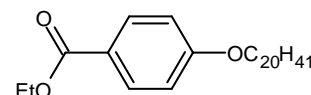
1-*n*-Bromhexacosan **2**

**Vorschrift** In einer Inertgasatmosphäre werden Brom (940 mg, 5.88 mmol) und Triphenylphosphin (1.5 g, 5.88 mmol) in Dichlormethan (60 ml) vorgelegt. Anschließend erfolgt die Zugabe von **1** (1.5 g, 3.92 mmol) gelöst in 20 ml Dichlormethan. Das Gemisch wird für 2 Stunden bei Raumtemperatur gerührt. Die Reaktion wird mittels Natriumthiosulfat-Lösung gequenchet und die Phasen separiert. Die wässrige Phase wird mehrmals mit Chloroform extrahiert, die vereinigten organischen Phasen über Natriumsulfat getrocknet und das Lösungsmittel unter verminderten Druck entfernt. Der Rückstand wird säulenchromatographisch (Eluent:  $\text{CHCl}_3$ ) und durch Umkristallisation aus Essigester gereinigt.

**Ausbeute** 1.1 g (2.47 mmol, 63%), farbloser Feststoff

**Analytik**  $\text{C}_{26}\text{H}_{53}\text{Br}$ ;  $M = 445.60$  g/mol; Smp 53 °C

$^1\text{H}$  NMR (400 MHz,  $\text{CDCl}_3$ )  $\delta$  3.40 (t,  $^3J = 6.9$  Hz, 2H,  $\text{Br-CH}_2\text{CH}_2$ ), 1.89–1.80 (m, 2H,  $\text{Br-CH}_2\text{CH}_2$ ), 1.46–1.37 (m, 2H,  $\text{CH}_2$ ), 1.34–1.21 (m, 44H,  $\text{CH}_2$ ), 0.88 (t,  $^3J = 6.7$  Hz, 3H,  $\text{CH}_3$ ).

4-*n*-Eicosyloxybenzoesäureethylester **3**

**Vorschrift** AAV-1

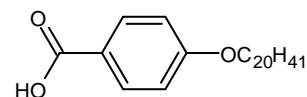
<b>Ansatz</b>	4-Hydroxybenzoesäureethylester	2.0 g (0.012 mol)
	1-Bromeicosan	4.7 g (0.013 mol)
	Kaliumcarbonat	8.3 g (0.060 mol)
	TBAI	kat. Menge
	MEK	120 ml

**Reinigung** Säulenchromatographie (Eluent: *n*-Hexan, anschließend  $\text{CHCl}_3$ )

**Ausbeute** 4.3 g (9.63 mmol, 80%), weißer Feststoff

**Analytik**  $\text{C}_{29}\text{H}_{50}\text{O}_3$ ;  $M = 446.71$  g/mol; Smp 52 °C

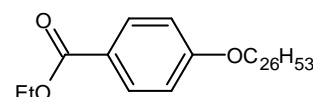
$^1\text{H}$  NMR (400 MHz,  $\text{CDCl}_3$ )  $\delta$  7.98 (d,  $^3J = 9.0$  Hz, 2H, Ar-H), 6.89 (d,  $^3J = 9.0$  Hz, 2H, Ar-H), 4.34 (q,  $^3J = 7.1$  Hz, 2H,  $(\text{O})\text{CCH}_2\text{CH}_3$ ), 4.00 (t,  $^3J = 6.6$  Hz, 2H,  $\text{OCH}_2\text{CH}_2$ ), 1.83–1.74 (m, 2H,  $\text{OCH}_2\text{CH}_2$ ), 1.52–1.40 (m, 2H,  $\text{CH}_2$ ), 1.38 (t,  $^3J = 7.1$  Hz, 3H,  $(\text{O})\text{CCH}_2\text{CH}_3$ ), 1.38–1.21 (m, 32H,  $\text{CH}_2$ ), 0.88 (t,  $^3J = 6.9$  Hz, 3H,  $\text{CH}_3$ ).

4-*n*-Eicosyloxybenzoesäure **4****Vorschrift** AAV-5

**Ansatz** **3** 4.3 g (9.63 mmol)  
 Natriumhydroxid 3.8 g (0.096 mol)  
 Ethanol 120 ml

**Ausbeute** 3.2 g (7.64 mmol, 79%), farbloser Feststoff**Analytik** C<sub>27</sub>H<sub>46</sub>O<sub>3</sub>; *M* = 418.65 g/mol;

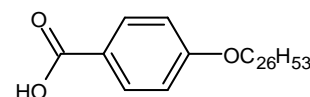
<sup>1</sup>H NMR (400 MHz, CDCl<sub>3</sub>) δ 8.03 (d, <sup>3</sup>*J* = 8.8 Hz, 2H, Ar-H), 6.92 (d, <sup>3</sup>*J* = 8.9 Hz, 2H, Ar-H), 4.02 (t, <sup>3</sup>*J* = 6.5 Hz, 2H, OCH<sub>2</sub>CH<sub>2</sub>), 1.85–1.76 (m, 2H, OCH<sub>2</sub>CH<sub>2</sub>), 1.51–1.41 (m, 2H, CH<sub>2</sub>), 1.38–1.18 (m, 32H, CH<sub>2</sub>), 0.88 (t, <sup>3</sup>*J* = 6.8 Hz, 3H, CH<sub>3</sub>).

4-*n*-Hexacosyloxybenzoesäureethylester **5****Vorschrift** AAV-1

**Ansatz** 4-Hydroxybenzoesäureethylester 200 mg (1.20 mmol)  
**2** 536 mg (1.20 mmol)  
 Caesiumcarbonat 2.0 g (6.00 mmol)  
 TBAI kat. Menge  
 MEK 60 ml

**Reinigung** Umkristallisation aus Essigester/CHCl<sub>3</sub>**Ausbeute** 120 mg (0.23 mmol, 19%), farbloser Feststoff**Analytik** C<sub>35</sub>H<sub>62</sub>O<sub>3</sub>; *M* = 530.86 g/mol; Smp 72 °C

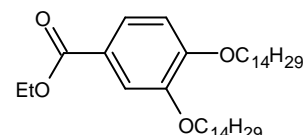
<sup>1</sup>H NMR (400 MHz, CDCl<sub>3</sub>) δ 7.98 (d, <sup>3</sup>*J* = 9.0 Hz, 2H, Ar-H), 6.89 (d, <sup>3</sup>*J* = 9.0 Hz, 2H, Ar-H), 4.34 (q, <sup>3</sup>*J* = 7.1 Hz, 2H, CH<sub>2</sub>CH<sub>3</sub>), 4.00 (t, <sup>3</sup>*J* = 6.6 Hz, 2H, OCH<sub>2</sub>CH<sub>2</sub>), 1.84–1.75 (m, 2H, OCH<sub>2</sub>CH<sub>2</sub>), 1.50–1.41 (m, 2H, CH<sub>2</sub>), 1.38 (t, <sup>3</sup>*J* = 7.1 Hz, 3H, CH<sub>2</sub>CH<sub>3</sub>), 1.41–1.20 (m, 44H, CH<sub>2</sub>), 0.88 (t, <sup>3</sup>*J* = 6.9 Hz, 3H, CH<sub>3</sub>).

4-*n*-Hexacosyloxybenzoesäure **6****Vorschrift** AAV-5

**Ansatz** **5** 120 mg (0.23 mmol)  
 Natriumhydroxid 90 mg (2.23 mmol)  
 Ethanol 30 ml

**Ausbeute** 70 mg (0.14 mmol, 61%), farbloser Feststoff**Analytik** C<sub>33</sub>H<sub>58</sub>O<sub>3</sub>; *M* = 502.81 g/mol;

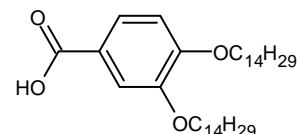
<sup>1</sup>H NMR (400 MHz, CDCl<sub>3</sub>) δ 8.02 (d, <sup>3</sup>*J* = 9.0 Hz, 2H, Ar-H), 6.92 (d, <sup>3</sup>*J* = 8.7 Hz, 2H, Ar-H), 4.02 (t, <sup>3</sup>*J* = 6.6 Hz, 2H, OCH<sub>2</sub>CH<sub>2</sub>), 1.84–1.76 (m, 2H, OCH<sub>2</sub>CH<sub>2</sub>), 1.50–1.42 (m, 2H, CH<sub>2</sub>), 1.40–1.19 (m, 44H, CH<sub>2</sub>), 0.88 (t, <sup>3</sup>*J* = 6.6 Hz, 3H, CH<sub>3</sub>).

3,4-Di-*n*-tetradecyloxybenzoesäureethylester **7****Vorschrift** AAV-1

<b>Ansatz</b>	3,4-Dihydroxybenzoesäureethylester	5.0 g (0.027 mol)
	1-Bromtetradecan	16.7 g (0.060 mol)
	Kaliumcarbonat	37.9 g (0.274 mol)
	TBAI	kat. Menge
	MEK	150 ml

**Reinigung** Säulenchromatographie (Eluent: *n*-Hexan, anschließend CHCl<sub>3</sub>)**Ausbeute** 11.5 g (0.020 mol, 74%), farbloses Öl**Analytik** C<sub>37</sub>H<sub>66</sub>O<sub>4</sub>; *M* = 574.92 g/mol;

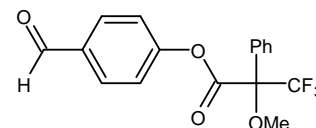
<sup>1</sup>H NMR (400 MHz, CDCl<sub>3</sub>) δ 7.64 (dd, <sup>3</sup>*J* = 8.4 Hz, <sup>4</sup>*J* = 2.0 Hz, 1H, Ar-H), 7.54 (d, <sup>4</sup>*J* = 2.0 Hz, 1H, Ar-H), 6.86 (d, <sup>3</sup>*J* = 8.5 Hz, 1H, Ar-H), 4.34 (q, <sup>3</sup>*J* = 7.1 Hz, 2H, CH<sub>2</sub>CH<sub>3</sub>), 4.04 (t, <sup>3</sup>*J* = 6.7 Hz, 2H, OCH<sub>2</sub>CH<sub>2</sub>), 4.04 (t, <sup>3</sup>*J* = 6.6 Hz, 2H, OCH<sub>2</sub>CH<sub>2</sub>), 1.88–1.78 (m, 4H, OCH<sub>2</sub>CH<sub>2</sub>), 1.52–1.42 (m, 4H, CH<sub>2</sub>), 1.38 (t, <sup>3</sup>*J* = 7.1 Hz, 3H, CH<sub>2</sub>CH<sub>3</sub>), 1.41–1.20 (m, 40H, CH<sub>2</sub>), 0.88 (t, <sup>3</sup>*J* = 6.9 Hz, 6H, CH<sub>3</sub>).

3,4-Di-*n*-tetradecyloxybenzoesäure **8****Vorschrift** AAV-5

<b>Ansatz</b>	<b>8</b>	11.4 g (0.020 mol)
	Natriumhydroxid	8.0 g (0.199 mol)
	Ethanol	100 ml
	dest. Wasser	50 ml

**Ausbeute** 10.4 g (0.019 mol, 96%), farbloser Feststoff**Analytik** C<sub>35</sub>H<sub>62</sub>O<sub>4</sub>; *M* = 546.86 g/mol; Smp 122 °C

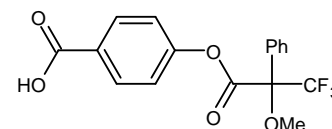
<sup>1</sup>H NMR (400 MHz, CDCl<sub>3</sub>) δ 7.69 (dd, <sup>3</sup>*J* = 8.4 Hz, <sup>4</sup>*J* = 1.9 Hz, 1H, Ar-H), 7.57 (d, <sup>4</sup>*J* = 1.9 Hz, 1H, Ar-H), 6.88 (d, <sup>3</sup>*J* = 8.5 Hz, 1H, Ar-H), 4.08–4.01 (m, 4H, OCH<sub>2</sub>CH<sub>2</sub>), 1.89–1.78 (m, 4H, OCH<sub>2</sub>CH<sub>2</sub>), 1.52–1.42 (m, 4H, CH<sub>2</sub>), 1.39–1.19 (m, 40H, CH<sub>2</sub>), 0.88 (t, <sup>3</sup>*J* = 6.8 Hz, 6H, CH<sub>3</sub>).

4-(2-Methoxy-2-trifluormethylphenylacetyloxy)benzaldehyd **9****Vorschrift** AAV-3

<b>Ansatz</b>	4-Hydroxybenzaldehyd	0.5 g (4.09 mmol)
	2-Methoxy-2-trifluormethyl-2-phenylacessigsäure	1.0 g (4.09 mmol)
	DCC	1.0 g (4.50 mmol)
	DMAP	kat. Menge
	THF	50 ml

**Reinigung** Säulenchromatographie (Eluent: CHCl<sub>3</sub>)**Ausbeute** 1.3 g (3.84 mol, 94%), farbloses Öl**Analytik** C<sub>17</sub>H<sub>13</sub>F<sub>3</sub>O<sub>4</sub>; *M* = 338.28 g/mol;

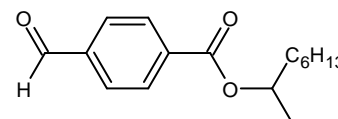
<sup>1</sup>H NMR (500 MHz, CDCl<sub>3</sub>) δ 10.02 (s, 1H, CHO), 7.96 (d, <sup>3</sup>*J* = 8.6 Hz, 2H, Ar-H), 7.66–7.62 (m, 2H, Ar-H), 7.51–7.46 (m, 3H, Ar-H), 7.32 (d, <sup>3</sup>*J* = 8.7 Hz, 2H, Ar-H), 3.69 (s, 3H, OCH<sub>3</sub>); <sup>19</sup>F NMR (470 MHz, CDCl<sub>3</sub>) δ –71.46 (s, CF<sub>3</sub>, 3F).

4-(2-Methoxy-2-trifluormethylphenylacetyloxy)benzoesäure **10****Vorschrift** AAV-4

<b>Ansatz</b>	<b>9</b>	1.3 g (3.84 mmol)
	Natriumchlorit (80%ig)	2.5 g (0.028 mol)
	Resorcin	0.6 g (5.00 mol)
	Natriumdihydrogenphosphat	1.4 g (0.012 mol)
	<i>t</i> -Butanol	40 ml
	dest. Wasser	27 ml

**Ausbeute** 600 mg (1.69 mmol, 44%), farbloser Feststoff**Analytik** C<sub>17</sub>H<sub>13</sub>F<sub>3</sub>O<sub>5</sub>; *M* = 354.28 g/mol; Smp 124 °C

<sup>1</sup>H NMR (500 MHz, CDCl<sub>3</sub>) δ 8.18 (d, <sup>3</sup>*J* = 8.9 Hz, 2H, Ar-H), 7.66–7.62 (m, 2H, Ar-H), 7.50–7.46 (m, 3H, Ar-H), 7.25 (d, <sup>3</sup>*J* = 8.0 Hz, 2H, Ar-H), 3.70 (s, 3H, OCH<sub>3</sub>); <sup>19</sup>F NMR (470 MHz, CDCl<sub>3</sub>) δ –71.48 (s, CF<sub>3</sub>, 3F).

1-(2-Methylheptyl)-4-formylbenzoat **11****Vorschrift** AAV-3

<b>Ansatz</b>	4-Formylbenzoesäure	2.0 g (0.013 mol)
	2-Octanol	2.2 g (0.017 mol)
	DCC	3.3 g (0.016 mol)
	DMAP	kat. Menge
	THF	80 ml

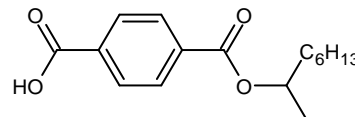
**Reinigung** Säulenchromatographie (Eluent:  $\text{CHCl}_3$ )

**Ausbeute** 3.2 g (0.012 mol, 92%), farbloses Öl

**Analytik**  $\text{C}_{16}\text{H}_{22}\text{O}_3$ ;  $M = 262.34$  g/mol;

$^1\text{H NMR}$  (400 MHz,  $\text{CDCl}_3$ )  $\delta$  10.10 (s, 1H, CHO), 8.19 (d,  $^3J = 8.4$  Hz, 2H, Ar-H), 7.94 (d,  $^3J = 8.1$  Hz, 2H, Ar-H), 5.22–5.13 (m, 1H,  $\text{CHCH}_3$ ), 1.79–1.70 (m, 1H,  $\text{CHCH}_a\text{H}_b$ ), 1.68–1.58 (m, 1H,  $\text{CHCH}_a\text{H}_b$ ), 1.36 (d,  $^3J = 6.3$  Hz, 3H,  $\text{CHCH}_3$ ), 1.43–1.22 (m, 8H,  $\text{CH}_2$ ), 0.87 (t,  $^3J = 6.8$  Hz, 3H,  $\text{CH}_3$ ).

#### 4-(2-methylheptyl)terephthalat **12**



**Vorschrift** AAV-4

<b>Ansatz</b>	<b>11</b>	3.2 g (0.012 mol)
	Natriumchlorit (80% ig)	8.0 g (0.088 mol)
	Resorcin	1.7 g (0.016 mol)
	Natriumdihydrogenphosphat	4.4 g (0.036 mol)
	<i>t</i> -Butanol	120 ml
	dest. Wasser	90 ml

**Ausbeute** 2.5 g (8.98 mmol, 73%), farbloser Feststoff

**Analytik**  $\text{C}_{16}\text{H}_{22}\text{O}_4$ ;  $M = 278.34$  g/mol; Smp 87 °C

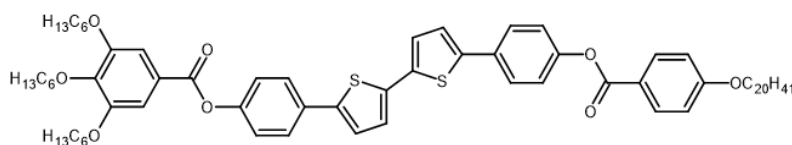
$^1\text{H NMR}$  (400 MHz,  $\text{CDCl}_3$ )  $\delta$  8.18 (d,  $^3J = 8.6$  Hz, 2H, Ar-H), 8.13 (d,  $^3J = 8.6$  Hz, 2H, Ar-H), 5.22–5.14 (m, 1H,  $\text{CHCH}_3$ ), 1.81–1.70 (m, 1H,  $\text{CHCH}_a\text{H}_b$ ), 1.69–1.57 (m, 1H,  $\text{CHCH}_a\text{H}_b$ ), 1.36 (d,  $^3J = 6.3$  Hz, 3H,  $\text{CHCH}_3$ ), 1.45–1.22 (m, 8H,  $\text{CH}_2$ ), 0.88 (t,  $^3J = 6.9$  Hz, 3H,  $\text{CH}_3$ ).



### 6.4.2 Verbindungen mit einem Bithiophen-Grundgerüst

In diesem Abschnitt werden lediglich die zusätzlichen synthetisierten Verbindungen aufgeführt, die in den Publikation A–C nicht beschrieben sind. Die Beschreibungen der dazugehörigen Zwischenstufen sind im Abschnitt 6.4.1 zu finden.

5-[4-(3,4,5-Tri-*n*-hexyloxybenzoyloxy)phenyl]-5'-[4-(4-*n*-eicosyloxybenzoyloxy)phenyl]-2,2'-bithiophen **Aa<sub>6</sub>/d<sub>20</sub>**



**Vorschrift** AAV-2

**Ansatz** 1b/OH 98 mg (0.130 mmol)

**4** 68 mg (0.162 mmol)

Thionylchlorid 2 ml

Pyridin 2 ml

Dichlormethan 4 ml

DMAP kat. Menge

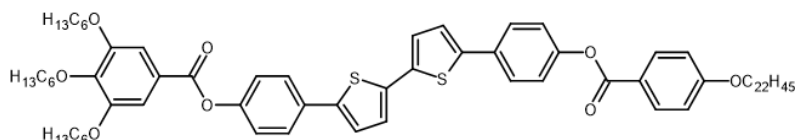
**Reinigung** Säulenchromatographie (Eluent: CHCl<sub>3</sub>), Umkristallisation aus THF/EtOH

**Ausbeute** 138 mg (0.119 mmol, 92%), gelber Feststoff

**Analytik** C<sub>72</sub>H<sub>98</sub>O<sub>8</sub>S<sub>2</sub>; *M* = 1155.67 g/mol;

<sup>1</sup>H NMR (500 MHz, CDCl<sub>3</sub>) δ 8.15 (d, <sup>3</sup>*J* = 9.0 Hz, 2H, Ar-H), 7.66 (d, <sup>3</sup>*J* = 8.8 Hz, 2H, Ar-H), 7.65 (d, <sup>3</sup>*J* = 8.7 Hz, 2H, Ar-H), 7.42 (s, 2H, Ar-H), 7.25–7.22 (m, 6H, Ar-H + Th-H), 7.18 (d, <sup>3</sup>*J* = 3.8 Hz, 2H, Th-H), 6.98 (d, <sup>3</sup>*J* = 9.0 Hz, 2H, Ar-H), 4.09–4.03 (m, 8H, OCH<sub>2</sub>CH<sub>2</sub>), 1.87–1.80 (m, 6H, OCH<sub>2</sub>CH<sub>2</sub>), 1.80–1.74 (m, 2H, OCH<sub>2</sub>CH<sub>2</sub>), 1.52–1.45 (m, 8H, CH<sub>2</sub>), 1.40–1.23 (m, 44H, CH<sub>2</sub>), 0.94–0.86 (m, 12H, CH<sub>3</sub>); <sup>13</sup>C NMR (100 MHz, CDCl<sub>3</sub>) δ 164.9, 164.8 (C=O), 163.6, 153.0, 150.6, 150.5, 143.1, 142.4, 142.2, 136.7, 132.3, 131.8, 131.7, 126.7, 124.6, 124.6, 124.0, 124.0, 123.7, 122.3, 122.3, 121.4, 114.3, 108.6 (Ar-C + Th-C), 73.6, 69.3, 68.3 (OCH<sub>2</sub>), 31.9, 31.7, 31.5, 30.3, 29.7, 29.6, 29.6, 29.5, 29.3, 29.3, 29.1, 26.0, 25.7, 25.7, 22.7, 22.7, 22.6 (CH<sub>2</sub>), 14.1, 14.1, 14.0 (CH<sub>3</sub>); EA: ber.: C 74.83%, H 8.55%; gef.: C 74.78%, H 8.53%.

5-[4-(3,4,5-Tri-*n*-hexyloxybenzoyloxy)phenyl]-5'-[4-(4-*n*-docosyloxybenzoyloxy)phenyl]-2,2'-bithiophen **Aa<sub>6</sub>/d<sub>22</sub>**



**Vorschrift** AAV-2

<b>Ansatz</b>	1b/OH	99 mg (0.131 mmol)
	4- <i>n</i> -Docosyloxybenzoesäure	73 mg (0.164 mmol)
	Thionylchlorid	2 ml
	Pyridin	2 ml
	Dichlormethan	4 ml
	DMAP	kat. Menge

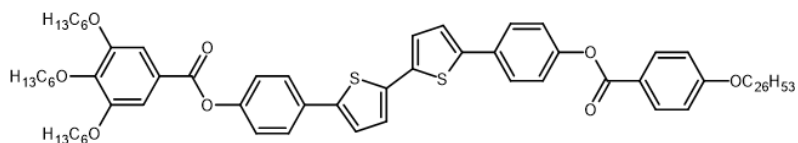
**Reinigung** Säulenchromatographie (Eluent: CHCl<sub>3</sub>/*n*-Hexan 4:1, v/v),  
Umkristallisation aus THF/EtOH

**Ausbeute** 119 mg (0.101 mmol, 77%), gelber Feststoff

**Analytik** C<sub>74</sub>H<sub>102</sub>O<sub>8</sub>S<sub>2</sub>; *M* = 1183.73 g/mol;

<sup>1</sup>H NMR (400 MHz, CDCl<sub>3</sub>) δ 8.15 (d, <sup>3</sup>*J* = 8.9 Hz, 2H, Ar-H), 7.66 (d, <sup>3</sup>*J* = 8.8 Hz, 2H, Ar-H), 7.65 (d, <sup>3</sup>*J* = 8.8 Hz, 2H, Ar-H), 7.42 (s, 2H, Ar-H), 7.25–7.21 (m, 6H, Ar-H + Th-H), 7.18 (d, <sup>3</sup>*J* = 3.8 Hz, 2H, Th-H), 6.98 (d, <sup>3</sup>*J* = 9.0 Hz, 2H, Ar-H), 4.09–4.02 (m, 8H, OCH<sub>2</sub>CH<sub>2</sub>), 1.88–1.80 (m, 6H, OCH<sub>2</sub>CH<sub>2</sub>), 1.80–1.73 (m, 2H, OCH<sub>2</sub>CH<sub>2</sub>), 1.52–1.45 (m, 8H, CH<sub>2</sub>), 1.41–1.23 (m, 48H, CH<sub>2</sub>), 0.95–0.85 (m, 12H, CH<sub>3</sub>); <sup>13</sup>C NMR (100 MHz, CDCl<sub>3</sub>) δ 164.9, 164.8 (C=O), 163.6, 153.0, 150.6, 150.5, 143.1, 142.4, 142.2, 136.8, 136.7, 132.3, 131.8, 131.7, 126.7, 124.6, 124.6, 124.0, 124.0, 123.7, 122.3, 122.31, 121.4, 114.3, 108.6 (Ar-H + Th-H), 73.6, 69.3, 68.3 (OCH<sub>2</sub>), 31.9, 31.7, 31.5, 30.3, 29.7, 29.6, 29.6, 29.5, 29.3, 29.3, 29.1, 26.0, 25.7, 25.7, 22.7, 22.7, 22.6 (CH<sub>2</sub>), 14.1, 14.1, 14.0 (CH<sub>3</sub>); HR-ESI: ber.: 1189.7172 (M<sup>-</sup> + Li), gef.: 1189.7224 (M<sup>-</sup> + Li).

5-[4-(3,4,5-Tri-*n*-hexyloxybenzoyloxy)phenyl]-5'-[4-(4-*n*-hexacosyloxybenzoyloxy)phenyl]-2,2'-bithiophen **Aa<sub>6</sub>/d<sub>26</sub>**



**Vorschrift** AAV-2

<b>Ansatz</b>	1b/OH	80 mg (0.106 mmol)
	<b>6</b>	67 mg (0.132 mmol)
	Thionylchlorid	2 ml
	Pyridin	2 ml
	Dichlormethan	4 ml
	DMAP	kat. Menge

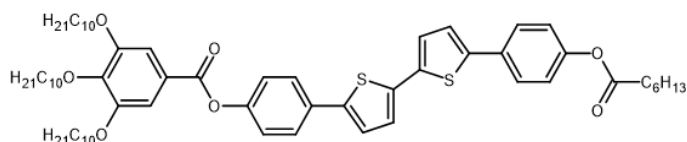
**Reinigung** Säulenchromatographie (Eluent: CHCl<sub>3</sub>/*n*-Hexan 5:1, v/v),  
Umkristallisation aus THF/MeOH

**Ausbeute** 119 mg (0.096 mmol, 91%), gelber Feststoff

**Analytik**  $C_{78}H_{110}O_8S_2$ ;  $M = 1239.83$  g/mol;

$^1H$  NMR (400 MHz,  $CDCl_3$ )  $\delta$  8.15 (d,  $^3J = 8.9$  Hz, 2H, Ar-H), 7.66 (d,  $^3J = 8.7$  Hz, 2H, Ar-H), 7.65 (d,  $^3J = 8.7$  Hz, 2H, Ar-H), 7.42 (s, 2H, Ar-H), 7.25–7.21 (m, 6H, Ar-H + Th-H) 7.18 (d,  $^3J = 3.7$  Hz, 2H, Th-H), 6.98 (d,  $^3J = 8.9$  Hz, 2H, Ar-H), 4.10–4.02 (m, 8H,  $OCH_2CH_2$ ), 1.88–1.73 (m, 8H,  $OCH_2CH_2$ ), 1.52–1.43 (m, 8H,  $CH_2$ ), 1.41–1.21 (m, 56H,  $CH_2$ ), 0.95–0.85 (m, 12H,  $CH_3$ );  $^{13}C$  NMR (100 MHz,  $CDCl_3$ )  $\delta$  164.9, 164.8 (C=O), 163.6, 153.0, 150.6, 150.5, 143.1, 142.4, 142.2, 136.8, 136.7, 132.3, 131.8, 131.7, 126.7, 124.6, 124.6, 124.0, 124.0, 123.7, 122.3, 122.3, 121.4, 114.3, 108.6 (Ar-C + Th-C), 73.6, 69.3, 68.3 ( $OCH_2$ ), 31.9, 31.7, 31.5, 30.3, 29.7, 29.6, 29.6, 29.5, 29.3, 29.3, 29.1, 26.0, 25.7, 25.7, 22.7, 22.7, 22.6 ( $CH_2$ ), 14.1, 14.1, 14.0 ( $CH_3$ ); EA: ber.: C 75.56%, H 8.94%; gef.: C 75.59%, H 8.92%.

5-[4-(3,4,5-Tri-*n*-decyloxybenzoyloxy)phenyl]-5'-(4-*n*-heptanoyloxyphenyl)-2,2'-bithiophen  
A'a<sub>10</sub>/lin6



**Vorschrift** AAV-3

<b>Ansatz</b>	1a/OH	74 mg (0.080 mmol)
	<i>n</i> -Heptansäure	13 mg (0.100 mmol)
	DCC	21 mg (0.100 mmol)
	Dichlormethan	25 ml
	DMAP	kat. Menge

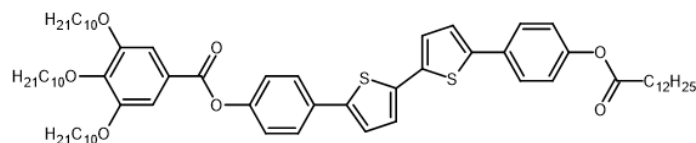
**Reinigung** Säulenchromatographie (Eluent:  $CHCl_3/n$ -Hexan 3:1, v/v),  
Umkristallisation aus THF/MeOH

**Ausbeute** 65 mg (0.063 mmol, 78%), gelber Feststoff

**Analytik**  $C_{64}H_{90}O_7S_2$ ;  $M = 1035.53$  g/mol;

$^1H$  NMR (400 MHz,  $CDCl_3$ )  $\delta$  7.65 (d,  $^3J = 8.6$  Hz, 2H, Ar-H), 7.60 (d,  $^3J = 8.6$  Hz, 2H, Ar-H), 7.42 (s, 2H, Ar-H), 7.25–7.21 (m, 3H, Ar-H + Th-H), 7.20 (d,  $^3J = 3.8$  Hz, 1H, Th-H), 7.19–7.16 (m, 2H, Th-H), 7.12 (d,  $^3J = 8.7$  Hz, 2H, Ar-H), 4.10–4.02 (m, 6H,  $OCH_2CH_2$ ), 2.57 (t,  $^3J = 7.5$  Hz, 2H, (O)CCH<sub>2</sub>), 1.89–1.72 (m, 8H,  $OCH_2CH_2$ ), 1.54–1.21 (m, 48H,  $CH_2$ ), 0.95–0.85 (m, 12H,  $CH_3$ );  $^{13}C$  NMR (100 MHz,  $CDCl_3$ )  $\delta$  172.2, 164.9 (C=O), 153.0, 150.5, 150.2, 143.1, 142.3, 142.3, 136.8, 136.7, 131.8, 131.7, 126.7, 126.6, 124.6, 124.0, 124.0, 123.7, 122.3, 122.1, 108.6 (Ar-C + Th-C), 73.6, 69.3 ( $OCH_2$ ), 34.4 ((O)CCH<sub>2</sub>), 31.9, 31.9, 31.4, 30.3, 29.7, 29.7, 29.6, 29.6, 29.6, 29.4, 29.3, 29.3, 28.8, 26.1, 26.0, 24.9, 22.7, 22.7, 22.5 ( $CH_2$ ), 14.1, 14.0 ( $CH_3$ ); EA: ber.: C 74.23%, H 8.76%, S 6.19%; gef.: C 74.42%, H 8.39%, S 6.78%.

5-[4-(3,4,5-Tri-*n*-decyloxybenzoyloxy)phenyl]-5'-[4-*n*-tridecanoyloxyphenyl]-2,2'-bithiophen **A'a<sub>10</sub>/lin12**



**Vorschrift** AAV-2

<b>Ansatz</b>	1a/OH	72 mg (0.078 mmol)
	<i>n</i> -Tridecansäure	21 mg (0.097 mmol)
	Thionylchlorid	2 ml
	Pyridin	2 ml
	Dichlormethan	4 ml
	DMAP	kat. Menge

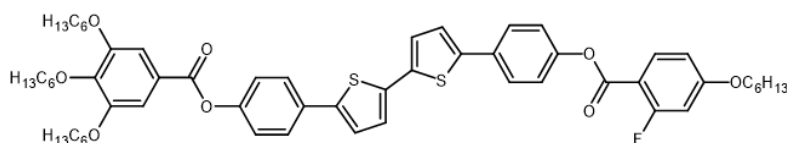
**Reinigung** Säulenchromatographie (Eluent: CHCl<sub>3</sub>/*n*-Hexan 4:1, v/v),  
Umkristallisation aus THF/MeOH

**Ausbeute** 49 mg (0.044 mmol, 56%), gelber Feststoff

**Analytik** C<sub>70</sub>H<sub>102</sub>O<sub>7</sub>S<sub>2</sub>; *M* = 1119.68 g/mol;

<sup>1</sup>H NMR (400 MHz, CDCl<sub>3</sub>) δ 7.65 (d, <sup>3</sup>*J* = 8.7 Hz, 2H, Ar-H), 7.60 (d, <sup>3</sup>*J* = 8.8 Hz, 2H, Ar-H), 7.42 (s, 2H, Ar-H), 7.25–7.21 (m, 3H, Ar-H + Th-H), 7.20 (d, <sup>3</sup>*J* = 3.8 Hz, 1H, Th-H), 7.19–7.16 (m, 2H, Th-H), 7.12 (d, <sup>3</sup>*J* = 8.7 Hz, 2H, Ar-H), 4.09–4.03 (m, 6H, OCH<sub>2</sub>CH<sub>2</sub>), 2.57 (t, <sup>3</sup>*J* = 7.5 Hz, 2H, (O)CCH<sub>2</sub>), 1.88–1.72 (m, 8H, OCH<sub>2</sub>CH<sub>2</sub>), 1.53–1.22 (m, 60H, CH<sub>2</sub>), 0.93–0.85 (m, 12H, CH<sub>3</sub>); <sup>13</sup>C NMR (100 MHz, CDCl<sub>3</sub>) δ 172.2, 164.9 (C=O), 153.0, 150.5, 150.2, 143.1, 142.3, 136.8, 136.7, 131.8, 131.7, 126.7, 126.6, 124.6, 124.0, 124.0, 123.7, 122.3, 122.1, 108.6 (Ar-C + Th-C), 73.6, 69.3 (OCH<sub>2</sub>), 34.4 ((O)CCH<sub>2</sub>), 31.9, 31.9, 30.3, 29.7, 29.7, 29.6, 29.6, 29.4, 29.4, 29.3, 29.3, 29.2, 29.1, 26.1, 26.0, 24.9, 22.7 (CH<sub>2</sub>), 14.1 (CH<sub>3</sub>); EA: ber.: C 75.09%, H 9.18%, S 5.73%; gef.: C 75.03%, H 8.77%, S 6.78%.

5-[4-(3,4,5-Tri-*n*-hexyloxybenzoyloxy)phenyl]-5'-[4-(2-fluor-4-*n*-hexyloxybenzoyloxy)phenyl]-2,2'-bithiophen **Aa<sub>6</sub>/(<sup>2</sup>)Fd<sub>6</sub>**



**Vorschrift** AAV-2

<b>Ansatz</b>	1b/OH	94 mg (0.124 mmol)
	2-Fluor-4- <i>n</i> -hexyloxybenzoesäure <sup>[74]</sup>	37 mg (0.156 mmol)
	Thionylchlorid	2 ml
	Pyridin	2 ml
	Dichlormethan	4 ml
	DMAP	kat. Menge

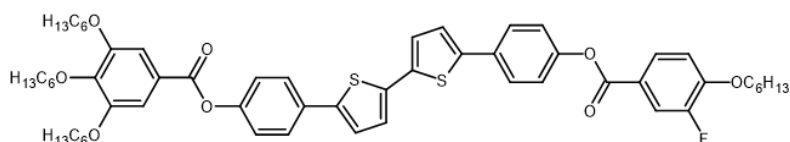
**Reinigung** Säulenchromatographie (Eluent: CHCl<sub>3</sub>/*n*-Hexan 4:1, v/v),  
Umkristallisation aus THF/EtOH

**Ausbeute** 71 mg (0.073 mmol, 59%), gelber Feststoff

**Analytik**  $C_{58}H_{69}FO_8S_2$ ;  $M = 977.29$  g/mol;

$^1H$  NMR (400 MHz,  $CDCl_3$ )  $\delta$  8.05 ("t",  $^3J = 8.7$  Hz, 1H, Ar-H), 7.65 (d,  $^3J_{H,H} = 8.6$  Hz, 2H, Ar-H), 7.65 (d,  $^3J_{H,H} = 8.6$  Hz, 2H, Ar-H), 7.42 (s, 2H, Ar-H), 7.27–7.21 (m, 6H, Ar-H + Th-H), 7.18 (d,  $^3J_{H,H} = 3.8$  Hz, 2H, Th-H), 6.78 (dd,  $^3J_{H,F} = 8.8$  Hz,  $^4J_{H,H} = 2.4$  Hz, 1H, Ar-H), 6.69 (dd,  $^3J_{H,F} = 12.7$  Hz,  $^4J_{H,H} = 2.3$  Hz, 1H, Ar-H), 4.10–4.00 (m, 8H,  $OCH_2CH_2$ ), 1.88–1.80 (m, 6H,  $OCH_2CH_2$ ), 1.79–1.73 (m, 2H,  $OCH_2CH_2$ ), 1.53–1.44 (m, 8H,  $CH_2$ ), 1.41–1.30 (m, 16H,  $CH_2$ ), 0.95–0.87 (m, 12H,  $CH_3$ );  $^{19}F$  NMR (376 MHz,  $CDCl_3$ )  $\delta$  –104.57 (dd,  $^3J_{F,H} = 12.6$  Hz,  $^4J_{F,H} = 8.5$  Hz);  $^{13}C$  NMR (100 MHz,  $CDCl_3$ )  $\delta$  165.0 (d,  $^3J_{C,F} = 11.7$  Hz) 164.9 (C=O), 164.2 (d,  $^1J_{C,F} = 261.3$  Hz) 162.5, 162.4, 153.0, 150.5, 150.2, 143.1, 142.3, 142.2, 136.8, 136.7, 133.8 (d,  $^4J_{C,F} = 2.2$  Hz), 131.8, 131.8, 126.7, 126.6, 124.6, 124.0, 123.7, 122.3, 110.9 (d,  $^3J_{C,F} = 2.8$  Hz), 109.7 (d,  $^2J_{C,F} = 9.6$  Hz), 108.6, 102.9 (d,  $^2J_{C,F} = 25.6$  Hz) (Ar-C + Th-C), 73.6, 69.3, 68.8 ( $OCH_2$ ), 31.7, 31.5, 31.5, 30.3, 29.3, 28.9, 25.7, 25.7, 25.6, 25.6, 22.7, 22.6, 22.5 ( $CH_2$ ), 14.1, 14.0, 14.0 ( $CH_3$ ); EA: ber.: C 71.28%, H 7.12%; gef.: C 71.29%, H 7.01%.

5-[4-(3,4,5-Tri-*n*-hexyloxybenzoyloxy)phenyl]-5'-[4-(3-fluor-4-*n*-hexyloxybenzoyloxy)-phenyl]-2,2'-bithiophen **Aa<sub>6</sub>**/ $^{(3)}$ **Fd<sub>6</sub>**



**Vorschrift** AAV-2

<b>Ansatz</b>	1b/OH	96 mg (0.127 mmol)
	3-Fluor-4- <i>n</i> -hexyloxybenzoesäure <sup>[74]</sup>	38 mg (0.159 mmol)
	Thionylchlorid	2 ml
	Pyridin	2 ml
	Dichlormethan	4 ml
	DMAP	kat. Menge

**Reinigung** Säulenchromatographie (Eluent:  $CHCl_3/n$ -Hexan 4:1, v/v),  
Umkristallisation aus THF/EtOH

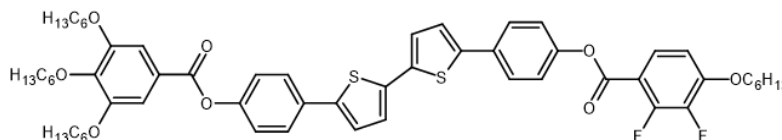
**Ausbeute** 91 mg (0.093 mmol, 73%), gelber Feststoff

**Analytik**  $C_{58}H_{69}FO_8S_2$ ;  $M = 977.29$  g/mol;

$^1H$  NMR (500 MHz,  $CDCl_3$ )  $\delta$  7.98–7.95 (m, 1H, Ar-H), 7.90 (dd,  $^3J_{H,H} = 11.4$  Hz,  $^4J_{H,H} = 2.1$  Hz, 1H, Ar-H), 7.65 (d,  $^3J_{H,H} = 8.6$  Hz, 2H, Ar-H), 7.65 (d,  $^3J_{H,H} = 8.7$  Hz, 2H, Ar-H), 7.41 (s, 2H, Ar-H), 7.25–7.20 (m, 6H, Ar-H + Th-H), 7.18 (d,  $^3J_{H,H} = 3.8$  Hz, 2H, Th-H), 7.03 ("t",  $^3J_{H,H} = 8.4$  Hz, 1H, Ar-H), 4.12 (t,  $^3J_{H,H} = 6.6$  Hz, 2H,  $OCH_2CH_2$ ), 4.09–4.03 (m, 6H,  $OCH_2CH_2$ ), 1.90–1.80 (m, 6H,  $OCH_2CH_2$ ), 1.80–1.73 (m, 2H,  $OCH_2CH_2$ ), 1.52–1.45 (m, 8H,  $CH_2$ ), 1.40–1.30 (m, 16H,  $CH_2$ ), 0.95–0.87 (m, 12H,  $CH_3$ );  $^{19}F$  NMR (470 MHz,  $CDCl_3$ )  $\delta$  –133.61 (m, 1F);  $^{13}C$  NMR (125 MHz,  $CDCl_3$ )  $\delta$  164.9, 164.0 (d,  $^4J_{C,F} = 2.6$  Hz, C=O), 153.0, 152.1, 152.0, 151.9 (d,  $^1J_{C,F} = 247.4$  Hz, Ar-C), 150.4 (d,  $^2J_{C,F} = 22.3$  Hz, Ar-C), 143.1, 142.3, 142.2, 136.8, 136.8, 131.9, 131.8, 127.4 (d,  $^4J_{C,F} = 3.4$  Hz, Ar-C) 126.7, 126.7, 124.6, 124.0, 124.0, 123.7, 122.3, 122.2, 121.7 (d,  $^3J_{C,F} = 6.3$  Hz) 117.8 (d,  $^2J_{C,F} = 20.1$  Hz, Ar-C), 113.4, 108.6 (Ar-C + Th-C), 73.6, 69.5, 69.3 ( $OCH_2$ ), 31.7, 31.5, 31.5, 30.3, 29.2, 28.9, 25.7, 25.7,

25.5, 22.7, 22.6, 22.5 (CH<sub>2</sub>), 14.0, 14.0, 14.0 (CH<sub>3</sub>); EA: ber.: C 71.28%, H 7.12%; gef.: C 71.30%, H 7.13%.

5-[4-(3,4,5-Tri-*n*-hexyloxybenzoyloxy)phenyl]-5'-[4-(2,3-difluor-4-*n*-hexyloxybenzoyloxy)-phenyl]-2,2'-bithiophen **Aa<sub>6</sub>**/(<sup>2,3</sup>)**Fd<sub>6</sub>**



**Vorschrift** AAV-2

<b>Ansatz</b>	1b/OH	100 mg (0.132 mmol)
	2,3-Difluor-4- <i>n</i> -hexyloxybenzoesäure <sup>[74]</sup>	43 mg (0.165 mmol)
	Thionylchlorid	2 ml
	Pyridin	2 ml
	Dichlormethan	4 ml
	DMAP	kat. Menge

**Reinigung** Säulenchromatographie (Eluent: CHCl<sub>3</sub>/*n*-Hexan 5:1, v/v),  
Umkristallisation aus THF/MeOH

**Ausbeute** 104 mg (0.104 mmol, 78%), gelber Feststoff

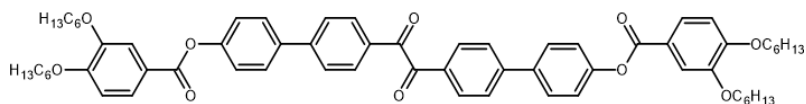
**Analytik** C<sub>58</sub>H<sub>68</sub>F<sub>2</sub>O<sub>8</sub>S<sub>2</sub>; *M* = 995.28 g/mol;

<sup>1</sup>H NMR (400 MHz, CDCl<sub>3</sub>) δ 7.85 (ddd, <sup>3</sup>*J*<sub>H,H</sub> = 9.7 Hz, <sup>4</sup>*J*<sub>H,F</sub> = 7.7 Hz, <sup>5</sup>*J*<sub>H,F</sub> = 2.3 Hz, 1H, Ar-H), 7.66 (d, <sup>3</sup>*J* = 8.6 Hz, 2H, Ar-H), 7.65 (d, <sup>3</sup>*J* = 8.6 Hz, 2H, Ar-H), 7.42 (s, 2H, Ar-H), 7.28–7.21 (m, 6H, Ar-H + Th-H), 7.18 (d, <sup>3</sup>*J* = 3.7 Hz, 2H, Th-H), 6.83 (ddd, <sup>3</sup>*J*<sub>H,H</sub> = 9.0 Hz, <sup>4</sup>*J*<sub>H,F</sub> = 7.2 Hz, <sup>5</sup>*J*<sub>H,F</sub> = 1.8 Hz, 1H, Ar-H), 4.14 (t, <sup>3</sup>*J* = 6.6 Hz, 2H, OCH<sub>2</sub>CH<sub>2</sub>), 4.07 (t, <sup>3</sup>*J* = 6.5 Hz, 2H, OCH<sub>2</sub>CH<sub>2</sub>), 4.06 (t, <sup>3</sup>*J* = 6.5 Hz, 4H, OCH<sub>2</sub>CH<sub>2</sub>), 1.91–1.80 (m, 6H, OCH<sub>2</sub>CH<sub>2</sub>), 1.80–1.73 (m, 2H, OCH<sub>2</sub>CH<sub>2</sub>), 1.53–1.45 (m, 8H, CH<sub>2</sub>), 1.41–1.30 (m, 16H, CH<sub>2</sub>), 0.96–0.87 (m, 12H, CH<sub>3</sub>); <sup>19</sup>F NMR (376 MHz, CDCl<sub>3</sub>) δ –132.11 (ddd, <sup>3</sup>*J*<sub>F,F</sub> = 19.7 Hz, <sup>4</sup>*J*<sub>F,H</sub> = 7.5 Hz, <sup>5</sup>*J*<sub>F,H</sub> = 1.7 Hz, 1F), –157.96 (ddd, <sup>3</sup>*J*<sub>F,F</sub> = 19.7 Hz, <sup>4</sup>*J*<sub>F,H</sub> = 7.1 Hz, <sup>5</sup>*J*<sub>F,H</sub> = 2.1 Hz, 1F); <sup>13</sup>C NMR (125 MHz, CDCl<sub>3</sub>) δ 164.9, 162.0–161.9 (m, C=O), 153.2 (dd, <sup>2</sup>*J*<sub>C,F</sub> = 8.0 Hz, <sup>3</sup>*J*<sub>C,F</sub> = 3.8 Hz), 153.0, 151.83 (dd, <sup>1</sup>*J*<sub>C,F</sub> = 262.6 Hz, <sup>2</sup>*J*<sub>C,F</sub> = 11.5 Hz), 150.5, 150.0, 143.1, 142.3, 142.2, 141.5 (dd, <sup>1</sup>*J*<sub>C,F</sub> = 248.7, <sup>2</sup>*J*<sub>C,F</sub> = 14.2 Hz), 136.8, 136.8, 132.0, 131.8, 127.0 (d, <sup>3</sup>*J*<sub>C,F</sub> = 4.3 Hz) 126.6, 124.6, 124.6, 124.1, 124.0, 123.7, 122.3, 122.2, 111.2 (d, <sup>2</sup>*J*<sub>C,F</sub> = 7.2 Hz) 108.6, 108.4 (d, <sup>3</sup>*J*<sub>C,F</sub> = 2.4 Hz). (Ar-C + Th-C), 73.6, 70.0, 69.3 (OCH<sub>2</sub>), 31.7, 31.5, 31.4, 30.3, 29.3, 28.9, 25.7, 25.7, 25.5, 22.7, 22.6, 22.5 (CH<sub>2</sub>), 14.1, 14.0, 14.0 (CH<sub>3</sub>); EA: ber.: C 69.99%, H 6.89%; gef.: C 69.92%, H 6.68%.

### 6.4.3 Verbindungen mit einem Benzil-Grundgerüst

In diesem Abschnitt werden lediglich die zusätzlichen synthetisierten Verbindungen aufgeführt, die in den Publikation **D–E** nicht beschrieben sind. Die Beschreibungen der dazugehörigen Zwischenstufen sind im Abschnitt 6.4.1 zu finden.

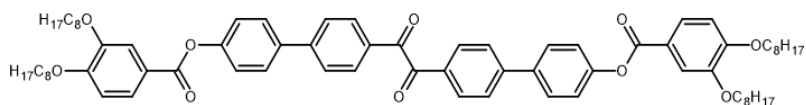
#### 1,2-Bis-[4'-(3,4-di-*n*-hexyloxybenzoyloxy)-1,1'-biphenyl-4-yl]-1,2-ethandion **Bc<sub>6</sub>/c<sub>6</sub>**



**Vorschrift** AAV-2  
**Ansatz** 2b/OH 54 mg (0.137 mmol)  
 3,4-Di-*n*-hexyloxybenzoesäure 110 mg (0.342 mmol)  
 Thionylchlorid 2 ml  
 Pyridin 2 ml  
 Dichlormethan 4 ml  
 DMAP kat. Menge

**Reinigung** Säulenchromatographie (Eluent: CHCl<sub>3</sub>), Umkristallisation aus THF/EtOH  
**Ausbeute** 68 mg (0.068 mmol, 49%), gelblicher Feststoff  
**Analytik** C<sub>64</sub>H<sub>74</sub>O<sub>10</sub>; *M* = 1003.27 g/mol;  
<sup>1</sup>H NMR (400 MHz, CDCl<sub>3</sub>) δ 8.09 (d, <sup>3</sup>*J* = 8.5 Hz, 4H, Ar-H), 7.84 (dd, <sup>3</sup>*J* = 8.5 Hz, <sup>4</sup>*J* = 2.0 Hz, 2H, Ar-H), 7.75 (d, <sup>3</sup>*J* = 8.5 Hz, 4H, Ar-H), 7.71–7.66 (m, 6H, Ar-H), 7.33 (d, <sup>3</sup>*J* = 8.7 Hz, 4H, Ar-H), 6.94 (d, <sup>3</sup>*J* = 8.6 Hz, 2H, Ar-H), 4.13–4.05 (m, 8H, OCH<sub>2</sub>CH<sub>2</sub>), 1.91–1.81 (m, 8H, OCH<sub>2</sub>CH<sub>2</sub>), 1.53–1.45 (m, 8H, CH<sub>2</sub>), 1.42–1.31 (m, 16H, CH<sub>2</sub>), 0.95–0.88 (m, 12H, CH<sub>3</sub>); <sup>13</sup>C NMR (100 MHz, CDCl<sub>3</sub>) δ 194.0 (O=C-C=O), 164.9 (C=O), 154.0, 151.6, 148.7, 146.8, 137.0, 131.8, 130.6, 128.5, 127.6, 124.5, 122.5, 121.3, 114.7, 112.0 (Ar-C), 69.4, 69.1 (OCH<sub>2</sub>), 31.6, 31.5, 29.1, 29.0, 25.7, 25.6, 22.6, 22.6 (CH<sub>2</sub>), 14.0 (CH<sub>3</sub>); EA: ber.: C 76.62%, H 7.43%; gef.: C 76.37%, H 7.18%.

#### 1,2-Bis-[4'-(3,4-di-*n*-octyloxybenzoyloxy)-1,1'-biphenyl-4-yl]-1,2-ethandion **Bc<sub>8</sub>/c<sub>8</sub>**



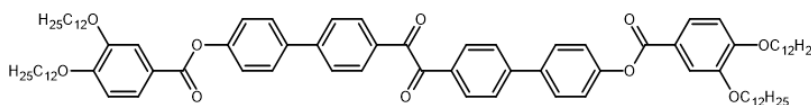
**Vorschrift** AAV-2  
**Ansatz** 2b/OH 51 mg (0.129 mmol)  
 3,4-Di-*n*-octyloxybenzoesäure 122 mg (0.323 mmol)  
 Thionylchlorid 2 ml  
 Pyridin 2 ml  
 Dichlormethan 4 ml  
 DMAP kat. Menge

**Reinigung** Säulenchromatographie (Eluent: CHCl<sub>3</sub>), Umkristallisation aus THF/EtOH  
**Ausbeute** 68 mg (0.061 mmol, 47%), gelblicher Feststoff

**Analytik**  $C_{72}H_{90}O_{10}$ ;  $M = 1115.48$  g/mol;

$^1H$  NMR (400 MHz,  $CDCl_3$ )  $\delta$  8.09 (d,  $^3J = 8.4$  Hz, 4H, Ar-H), 7.84 (dd,  $^3J = 8.5$  Hz,  $^4J = 2.0$  Hz, 2H, Ar-H), 7.75 (d,  $^3J = 8.4$  Hz, 4H, Ar-H), 7.71–7.67 (m, 6H, Ar-H), 7.33 (d,  $^3J = 8.6$  Hz, 4H, Ar-H), 6.94 (d,  $^3J = 8.6$  Hz, 2H, Ar-H), 4.12–4.05 (m, 8H,  $OCH_2CH_2$ ), 1.91–1.81 (m, 8H,  $OCH_2CH_2$ ), 1.52–1.45 (m, 8H,  $CH_2$ ), 1.42–1.24 (m, 32H,  $CH_2$ ), 0.92–0.85 (m, 12H,  $CH_3$ );  $^{13}C$  NMR (125 MHz,  $CDCl_3$ )  $\delta$  194.0 ( $O=C-C=O$ ), 164.9 ( $C=O$ ), 154.0, 151.7, 148.7, 146.8, 137.0, 131.8, 130.6, 128.5, 127.6, 124.5, 122.5, 121.3, 114.7, 112.0 (Ar-C), 69.4, 69.1 ( $OCH_2$ ), 31.8, 31.8, 29.4, 29.3, 29.3, 29.3, 29.3, 29.3, 29.3, 29.3, 29.2, 29.2, 29.1, 26.0, 26.0, 22.7 ( $CH_2$ ), 14.1 ( $CH_3$ ); EA: ber.: C 77.52%, H 8.13%; gef.: C 76.52%, H 7.89%.

1,2-Bis-[4'-(3,4-di-*n*-dodecyloxybenzoyloxy)-1,1'-biphenyl-4-yl]-1,2-ethandion **Bc<sub>12</sub>/c<sub>12</sub>**



**Vorschrift** AAV-2

<b>Ansatz</b>	2b/OH	53 mg (0.134 mmol)
	3,4- <i>n</i> -Dioctyloxybenzoesäure	165 mg (0.336 mmol)
	Thionylchlorid	2 ml
	Pyridin	2 ml
	Dichlormethan	4 ml
	DMAP	kat. Menge

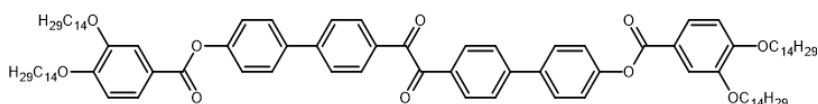
**Reinigung** Säulenchromatographie (Eluent:  $CHCl_3$ ), Umkristallisation aus THF/EtOH

**Ausbeute** 121 mg (0.090 mmol, 67%), gelblicher Feststoff

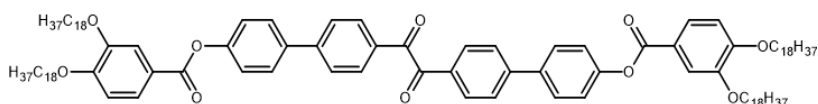
**Analytik**  $C_{88}H_{122}O_{10}$ ;  $M = 1339.90$  g/mol;

$^1H$  NMR (400 MHz,  $CDCl_3$ )  $\delta$  8.09 (d,  $^3J = 8.4$  Hz, 4H, Ar-H), 7.83 (dd,  $^3J = 8.4$  Hz,  $^4J = 2.0$  Hz, 2H, Ar-H), 7.75 (d,  $^3J = 8.4$  Hz, 4H, Ar-H), 7.71–7.66 (m, 6H, Ar-H), 7.33 (d,  $^3J = 8.6$  Hz, 4H, Ar-H), 6.94 (d,  $^3J = 8.6$  Hz, 2H, Ar-H), 4.12–4.05 (m, 8H,  $OCH_2CH_2$ ), 1.91–1.81 (m, 8H,  $OCH_2CH_2$ ), 1.52–1.45 (m, 8H,  $CH_2$ ), 1.42–1.21 (m, 64H,  $CH_2$ ), 0.92–0.85 (m, 12H,  $CH_3$ );  $^{13}C$  NMR (100 MHz,  $CDCl_3$ )  $\delta$  194.0 ( $O=C-C=O$ ), 164.9 ( $C=O$ ), 154.0, 151.6, 148.7, 146.8, 137.0, 131.8, 130.6, 128.5, 127.6, 124.5, 122.5, 121.3, 114.7, 112.0 (Ar-C), 69.4, 69.1 ( $OCH_2$ ), 31.9, 29.7, 29.6, 29.6, 29.6, 29.4, 29.4, 29.3, 29.2, 29.0, 26.0, 26.0, 22.7 ( $CH_2$ ), 14.1 ( $CH_3$ ); EA: ber.: C 78.88%, H 9.18%; gef.: C 78.86%, H 9.14%.



1,2-Bis-[4'-(3,4-di-*n*-tetradecyloxybenzoyloxy)-1,1'-biphenyl-4-yl]-1,2-ethandion **Bc<sub>14</sub>/c<sub>14</sub>**

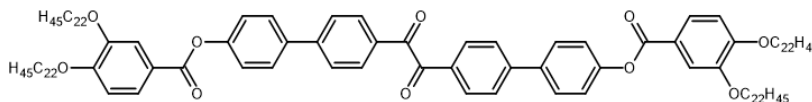
<b>Vorschrift</b>	AAV-2	
<b>Ansatz</b>	2b/OH	54 mg (0.137 mmol)
	<b>8</b>	187 mg (0.342 mmol)
	Thionylchlorid	2 ml
	Pyridin	2 ml
	Dichlormethan	4 ml
	DMAP	kat. Menge
<b>Reinigung</b>	Säulenchromatographie (Eluent: CHCl <sub>3</sub> ), Umkristallisation aus THF/EtOH	
<b>Ausbeute</b>	130 mg (0.090 mmol, 65%), gelblicher Feststoff	
<b>Analytik</b>	C <sub>96</sub> H <sub>138</sub> O <sub>10</sub> ; <i>M</i> = 1452.12 g/mol;	
	<sup>1</sup> H NMR (400 MHz, CDCl <sub>3</sub> ) δ 8.09 (d, <sup>3</sup> <i>J</i> = 8.4 Hz, 4H, Ar-H), 7.83 (dd, <sup>3</sup> <i>J</i> = 8.5 Hz, <sup>4</sup> <i>J</i> = 2.0 Hz, 2H, Ar-H), 7.75 (d, <sup>3</sup> <i>J</i> = 8.5 Hz, 4H, Ar-H), 7.71–7.66 (m, 6H, Ar-H), 7.33 (d, <sup>3</sup> <i>J</i> = 8.7 Hz, 4H, Ar-H), 6.94 (d, <sup>3</sup> <i>J</i> = 8.6 Hz, 2H, Ar-H), 4.12–4.05 (m, 8H, OCH <sub>2</sub> CH <sub>2</sub> ), 1.91–1.81 (m, 8H, OCH <sub>2</sub> CH <sub>2</sub> ), 1.52–1.45 (m, 8H, CH <sub>2</sub> ), 1.41–1.22 (m, 80H, CH <sub>2</sub> ), 0.91–0.85 (m, 12H, CH <sub>3</sub> ); <sup>13</sup> C NMR (125 MHz, CDCl <sub>3</sub> ) δ 194.0 (O=C-C=O), 164.9 (C=O), 154.0, 151.6, 148.7, 146.8, 137.0, 131.8, 130.6, 128.5, 127.6, 124.5, 122.5, 121.3, 114.7, 112.0 (Ar-C), 69.4, 69.1 (OCH <sub>2</sub> ), 31.9, 29.7, 29.7, 29.6, 29.6, 29.4, 29.4, 29.4, 29.2, 29.1, 26.0, 26.0, 22.7 (CH <sub>2</sub> ), 14.1 (CH <sub>3</sub> ); EA: ber.: C 79.40%, H 9.58%; gef.: C 79.12%, H 9.59%.	

1,2-Bis-[4'-(3,4-di-*n*-octadecyloxybenzoyloxy)-1,1'-biphenyl-4-yl]-1,2-ethandion **Bc<sub>18</sub>/c<sub>18</sub>**

<b>Vorschrift</b>	AAV-2	
<b>Ansatz</b>	2b/OH	50 mg (0.127 mmol)
	3,4-Di- <i>n</i> -octadecyloxybenzoesäure	244 mg (0.317 mmol)
	Thionylchlorid	2 ml
	Pyridin	2 ml
	Dichlormethan	4 ml
	DMAP	kat. Menge
<b>Reinigung</b>	Säulenchromatographie (Eluent: CHCl <sub>3</sub> ), Umkristallisation aus THF/EtOH	
<b>Ausbeute</b>	14 mg (0.008 mmol, 7%), gelblicher Feststoff	
<b>Analytik</b>	C <sub>112</sub> H <sub>170</sub> O <sub>10</sub> ; <i>M</i> = 1676.54 g/mol;	
	<sup>1</sup> H NMR (500 MHz, CDCl <sub>3</sub> ) δ 8.09 (d, <sup>3</sup> <i>J</i> = 8.5 Hz, 4H, Ar-H), 7.83 (dd, <sup>3</sup> <i>J</i> = 8.4 Hz, <sup>4</sup> <i>J</i> = 2.0 Hz, 2H, Ar-H), 7.75 (d, <sup>3</sup> <i>J</i> = 8.5 Hz, 4H, Ar-H), 7.71–7.66 (m, 6H, Ar-H), 7.33 (d, <sup>3</sup> <i>J</i> = 8.6 Hz, 4H, Ar-H), 6.94 (d, <sup>3</sup> <i>J</i> = 8.6 Hz, 2H, Ar-H), 4.12–4.05 (m, 8H, OCH <sub>2</sub> CH <sub>2</sub> ), 1.91–1.81 (m, 8H, OCH <sub>2</sub> CH <sub>2</sub> ), 1.54–1.46 (m, 8H, CH <sub>2</sub> ), 1.41–1.22 (m, 80H, CH <sub>2</sub> ), 0.93–0.86 (m, 12H, CH <sub>3</sub> ); <sup>13</sup> C NMR (125 MHz, CDCl <sub>3</sub> ) δ 194.0 (O=C-C=O), 164.9 (C=O), 154.0, 151.6, 148.7, 146.8, 137.0, 131.8, 130.6, 128.5, 127.6, 124.5, 122.5, 121.3, 114.7, 112.0 (Ar-C), 69.4, 69.1	

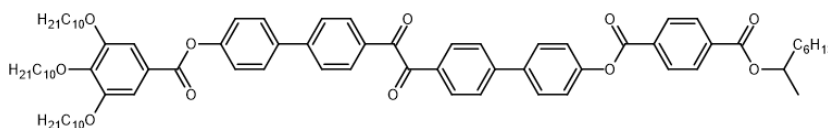
(OCH<sub>2</sub>), 31.9, 29.7, 29.7, 29.6, 29.6, 29.4, 29.4, 29.4, 29.2, 29.1, 26.0, 26.0, 22.7 (CH<sub>2</sub>), 14.1 (CH<sub>3</sub>); EA: ber.: C 80.24%, H 10.22%; gef.: C 80.05%, H 10.19%.

1,2-Bis-[4'-(3,4-di-*n*-docosyloxybenzoyloxy)-1,1'-biphenyl-4-yl]-1,2-ethandion **Bc<sub>22</sub>/c<sub>22</sub>**



**Vorschrift** AAV-2  
**Ansatz** 2b/OH 54 mg (0.137 mmol)  
 3,4-Di-*n*-docosyloxybenzoesäure 187 mg (0.342 mmol)  
 Thionylchlorid 2 ml  
 Pyridin 2 ml  
 Dichlormethan 4 ml  
 DMAP kat. Menge  
**Reinigung** Säulenchromatographie (Eluent: CHCl<sub>3</sub>), Umkristallisation aus THF/EtOH  
**Ausbeute** 141 mg (0.074 mmol, 54%), gelblicher Feststoff  
**Analytik** C<sub>128</sub>H<sub>202</sub>O<sub>10</sub>; *M* = 1900.97 g/mol;  
<sup>1</sup>H NMR (400 MHz, CDCl<sub>3</sub>) δ 8.08 (d, <sup>3</sup>*J* = 8.4 Hz, 4H, Ar-H), 7.83 (dd, <sup>3</sup>*J* = 8.5 Hz, <sup>4</sup>*J* = 2.0 Hz, 2H, Ar-H), 7.75 (d, <sup>3</sup>*J* = 8.5 Hz, 4H, Ar-H), 7.71–7.66 (m, 6H, Ar-H), 7.33 (d, <sup>3</sup>*J* = 8.7 Hz, 4H, Ar-H), 6.94 (d, <sup>3</sup>*J* = 8.6 Hz, 2H, Ar-H), 4.13–4.06 (m, 8H, OCH<sub>2</sub>CH<sub>2</sub>), 1.92–1.80 (m, 8H, OCH<sub>2</sub>CH<sub>2</sub>), 1.52–1.45 (m, 8H, CH<sub>2</sub>), 1.41–1.22 (m, 80H, CH<sub>2</sub>), 0.91–0.85 (m, 12H, CH<sub>3</sub>); <sup>13</sup>C NMR (125 MHz, CDCl<sub>3</sub>) δ 194.0 (O=C-C=O), 164.9 (C=O), 154.0, 151.6, 148.7, 146.8, 137.0, 131.8, 130.6, 128.5, 127.6, 124.5, 122.5, 121.3, 114.7, 112.0 (Ar-C), 69.4, 69.1 (OCH<sub>2</sub>), 31.9, 29.7, 29.7, 29.6, 29.6, 29.4, 29.4, 29.4, 29.2, 29.1, 26.0, 26.0, 22.7 (CH<sub>2</sub>), 14.1 (CH<sub>3</sub>); EA: ber.: C 80.87%, H 10.71%; gef.: C 80.69%, H 10.64%.

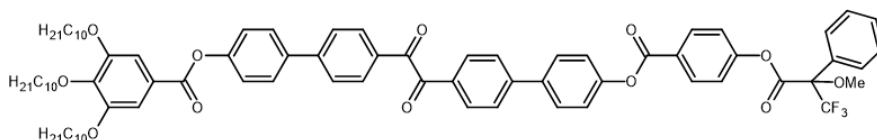
1-[4'-(3,4,5-Tri-*n*-decyloxybenzoyloxy)-(1,1'-biphenyl)-4-yl]-2-{4'-[4-(2-methylheptyloxy-carbonyl)benzoyloxy]-(1,1'-biphenyl)-4-yl}-1,2-ethandion (**rac**)-**Ba<sub>10</sub>/1**



**Vorschrift** AAV-2  
**Ansatz** 2a/OH 89 mg (0.092 mmol)  
**12** 32 mg (0.115 mmol)  
 Thionylchlorid 2 ml  
 Pyridin 2 ml  
 Dichlormethan 4 ml  
 DMAP kat. Menge  
**Reinigung** Säulenchromatographie (Eluent: CHCl<sub>3</sub>), Umkristallisation aus THF/MeOH  
**Ausbeute** 69 mg (0.056 mmol, 61%), gelblicher Feststoff  
**Analytik** C<sub>79</sub>H<sub>102</sub>O<sub>11</sub>; *M* = 1227.65 g/mol;  
<sup>1</sup>H NMR (400 MHz, CDCl<sub>3</sub>) δ 8.26 (d, <sup>3</sup>*J* = 8.6 Hz, 2H, Ar-H), 8.16 (d, <sup>3</sup>*J* = 8.6 Hz, 2H, Ar-H), 8.08 (d, <sup>3</sup>*J* = 8.5 Hz, 2H, Ar-H), 8.08 (d, <sup>3</sup>*J* = 8.5 Hz, 2H, Ar-H), 7.74 (d, <sup>3</sup>*J* = 8.3 Hz, 4H,

Ar-H), 7.69 (d,  $^3J = 8.7$  Hz, 2H, Ar-H), 7.68 (d,  $^3J = 8.7$  Hz, 2H, Ar-H), 7.41 (s, 2H, Ar-H), 7.35 (d,  $^3J = 8.7$  Hz, 2H, Ar-H), 7.31 (d,  $^3J = 8.7$  Hz, 2H, Ar-H), 5.23–5.14 (m, 1H, CHCH<sub>3</sub>), 4.09–4.00 (m, 6H, OCH<sub>2</sub>CH<sub>2</sub>), 1.87–1.71 (m, 7H, OCH<sub>2</sub>CH<sub>2</sub> + CHCH<sub>a</sub>H<sub>b</sub>), 1.68–1.58 (m, 1H, CHCH<sub>a</sub>H<sub>b</sub>), 1.52–1.43 (m, 6H, CH<sub>2</sub>), 1.42–1.18 (m, 47H, CH<sub>2</sub> + CHCH<sub>3</sub>), 0.90–0.83 (m, 12H, CH<sub>3</sub>); <sup>13</sup>C NMR (125 MHz, CDCl<sub>3</sub>) δ 193.9 (O=C-C=O), 165.2, 164.9, 164.3 (C=O), 153.0, 151.5, 151.2, 146.7, 146.6, 143.2, 137.5, 137.1, 135.5, 132.8, 131.9, 131.8, 130.6, 130.1, 129.7, 128.6, 128.5, 127.6, 127.6, 123.6, 122.5, 122.3, 108.7 (Ar-C), 73.6, 72.6, 69.3 (OCH<sub>2</sub> + CHCH<sub>3</sub>), 36.0, 31.9, 31.9, 31.7, 30.3, 29.7, 29.7, 29.6, 29.6, 29.5, 29.4, 29.3, 29.3, 29.1, 26.1, 26.0, 25.4, 22.7, 22.7, 22.6 (CH<sub>2</sub>), 20.0, 14.1, 14.0 (CH<sub>3</sub>); EA: ber.: C 77.29%, H 8.37%; gef.: C 77.12%, H 7.90%.

1-[4'-(3,4,5-Tri-*n*-decyloxybenzoyloxy)-(1,1'-biphenyl)-4-yl]-2-{4'-[4-(2-methoxy-2-trifluoromethylphenylacetoxyl)benzoyloxy]-(1,1'-biphenyl)-4-yl]-1,2-ethandion (**rac**)-**Ba<sub>10</sub>Mo**



<b>Vorschrift</b>	AAV-2	
<b>Ansatz</b>	2a/OH	106 mg (0.110 mmol)
	<b>10</b>	49 mg (0.137 mmol)
	Thionylchlorid	2 ml
	Pyridin	2 ml
	Dichlormethan	4 ml
	DMAP	kat. Menge

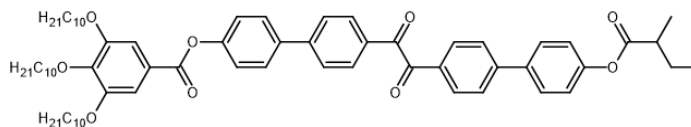
**Reinigung** Säulenchromatographie (Eluent: CHCl<sub>3</sub>/*n*-Hexan 4:1, v/v),  
Umkristallisation aus THF/MeOH

**Ausbeute** 65 mg (0.050 mmol, 45%), gelblicher Feststoff

**Analytik** C<sub>80</sub>H<sub>93</sub>F<sub>3</sub>O<sub>12</sub>; *M* = 1303.58 g/mol;

<sup>1</sup>H NMR (400 MHz, CDCl<sub>3</sub>) δ 8.29 (d,  $^3J = 8.9$  Hz, 2H, Ar-H), 8.12–8.07 (m, 4H, Ar-H), 7.76 (d,  $^3J = 8.3$  Hz, 4H, Ar-H), 7.70 (d,  $^3J = 8.7$  Hz, 2H, Ar-H), 7.69 (d,  $^3J = 8.7$  Hz, 2H, Ar-H), 7.68–7.63 (m, 2H, Ar-H), 7.52–7.47 (m, 3H, Ar-H), 7.42 (s, 2H, Ar-H), 7.34 (d,  $^3J = 8.8$  Hz, 2H, Ar-H), 7.32 (d,  $^3J = 8.8$  Hz, 2H, Ar-H), 7.30 (d,  $^3J = 8.9$  Hz, 2H, Ar-H), 4.10–4.02 (m, 6H, OCH<sub>2</sub>CH<sub>2</sub>), 3.71 (s, 3H, OCH<sub>3</sub>), 1.88–1.79 (m, 4H, OCH<sub>2</sub>CH<sub>2</sub>), 1.79–1.72 (m, 2H, OCH<sub>2</sub>CH<sub>2</sub>), 1.52–1.44 (m, 6H, CH<sub>2</sub>), 1.41–1.21 (m, 36H, CH<sub>2</sub>), 0.91–0.85 (m, 9H, CH<sub>3</sub>); <sup>19</sup>F NMR (376 MHz, CDCl<sub>3</sub>) δ –71.44 (s, 3F); <sup>13</sup>C NMR (125 MHz, CDCl<sub>3</sub>) δ 193.92, 164.91, 164.75, 163.99, 154.06, 152.99, 151.55, 151.21, 146.72, 146.60, 137.44, 137.14, 132.05, 131.86, 131.79, 131.60, 130.58, 130.02, 128.74, 128.56, 128.48, 127.74, 127.63, 127.61, 127.20, 124.28, 123.59, 122.45, 122.30, 121.47, 108.68, 77.23, 76.97, 76.72, 73.60, 69.32, 55.75, 31.91, 31.88, 30.33, 29.70, 29.64, 29.60, 29.56, 29.37, 29.32, 29.29, 26.06, 26.03, 22.67, 22.65, 14.07(CH<sub>3</sub>); EA: ber.: C 73.71%, H 7.19%; gef.: C 73.43%, H 7.19%.

1-[4'-(3,4,5-Tri-*n*-decyloxybenzoyloxy)-1,1'-biphenyl-4-yl]-2-[4'-(2-methylbutanoyloxy)-1,1'-biphenyl-4-yl]-1,2-ethandion (**rac**)-**B'a<sub>10</sub>/MB**



<b>Vorschrift</b>	AAV-3	
<b>Ansatz</b>	2a/OH	124 mg (0.128 mmol)
	2-Methylbutansäure	16 mg (0.160 mmol)
	DCC	32 mg (0.154 mmol)
	Dichlormethan	20 ml
	DMAP	kat. Menge

**Reinigung** Säulenchromatographie (Eluent: CHCl<sub>3</sub>/*n*-Hexan 3:1, v/v),  
Umkristallisation aus THF/MeOH

**Ausbeute** 94 mg (0.089 mmol, 70%), gelblicher Feststoff

**Analytik** C<sub>68</sub>H<sub>90</sub>O<sub>9</sub>; *M* = 1051.44 g/mol;

<sup>1</sup>H NMR (400 MHz, CDCl<sub>3</sub>) δ 8.09 (d, <sup>3</sup>*J* = 8.5 Hz, 2H, Ar-H), 8.08 (d, <sup>3</sup>*J* = 8.5 Hz, 2H, Ar-H), 7.77–7.70 (m, 4H, Ar-H), 7.69 (d, <sup>3</sup>*J* = 8.7 Hz, 2H, Ar-H), 7.64 (d, <sup>3</sup>*J* = 8.7 Hz, 2H, Ar-H), 7.42 (s, 2H, Ar-H), 7.32 (d, <sup>3</sup>*J* = 8.7 Hz, 2H, Ar-H), 7.20 (d, <sup>3</sup>*J* = 8.7 Hz, 2H, Ar-H), 4.09–4.03 (m, 6H, OCH<sub>2</sub>CH<sub>2</sub>), 2.71–2.61 (m, 1H, CHCH<sub>3</sub>), 1.92–1.79 (m, 5H, OCH<sub>2</sub>CH<sub>2</sub> + CHCH<sub>a</sub>H<sub>b</sub>), 1.79–1.72 (m, 2H, OCH<sub>2</sub>CH<sub>2</sub>), 1.71–1.59 (m, 1H, CHCH<sub>a</sub>H<sub>b</sub>), 1.52–1.44 (m, 6H, CH<sub>2</sub>), 1.41–1.20 (m, 21H, CH<sub>2</sub> + CHCH<sub>3</sub>), 1.04 (t, <sup>3</sup>*J* = 7.4 Hz, 3H, CH<sub>3</sub>), 0.92–0.84 (m, 9H, CH<sub>3</sub>); <sup>13</sup>C NMR (100 MHz, CDCl<sub>3</sub>) δ 194.0 (O=C-C=O), 175.1, 164.9 (C=O), 153.0, 151.5, 151.3, 146.7, 146.7, 143.2, 137.2, 137.0, 131.8, 130.6, 128.5, 128.4, 127.6, 123.6, 122.4, 122.2, 108.7 (Ar-C), 73.6, 69.3 (OCH<sub>2</sub>), 41.2 (CHCH<sub>3</sub>), 31.9, 31.9, 30.3, 29.7, 29.7, 29.6, 29.6, 29.4, 29.3, 29.3, 26.8, 26.1, 26.0, 22.7, 22.7 (CH<sub>2</sub>), 16.5, 14.1, 11.6 (CH<sub>3</sub>); EA: ber.: C 77.68%, H 8.63%; gef.: C 77.63%, H 8.62%.

## Literaturverzeichnis

- [1] L. Schmidt-Mende, A. Fechtenkotter, K. Mullen, E. Moons, R. Friend and J. MacKenzie, *Science* **2001**, 293, 1119.
- [2] T. Yasuda, H. Ooi, J. Morita, Y. Akama, K. Minoura, M. Funahashi, T. Shimomura, T. Kato, *Adv. Funct. Mater.* **2009**, 19, 411.
- [3] H. M. G. Barriga, M. N. Holme, M. M. Stevens, *Angew. Chem., Int. Ed.* **2019**, 58, 2958.
- [4] Y. Chen, P. Ma, S. Gui, *BioMed. Res. Int.* **2014**, 2014, 1.
- [5] C.J. Drummond, *Curr. Opin. Colloid Interface Sci.* **2000**, 4, 449.
- [6] C. E. Conn, C. J. Drummond, *Soft Matter* **2013**, 9, 3449.
- [7] M. L. Lynch, P. T. Spicer, *Bicontinuous Liquid Crystals*, CRC Press, Taylor & Francis, **2005**.
- [8] T. Kato, J. Uchida, T. Ichikawa, T. Sakamoto, *Angew. Chem., Int. Ed.* **2018**, 57, 4355.
- [9] M. Antonietti, *Philos. Trans. R. Soc. A* **2006**, 364, 2817.
- [10] N. Uemura, K. Sano, A. Matsumoto, Y. Yoshida, T. Mino, M. Sakamoto, *Chem. Asian J.* **2019**, 14, 4150.
- [11] A. Yoshizawa, M. Kurata, *New J. Chem.* **2019**, 43, 8865.
- [12] J. Steed, D. R. Turner, K. J. Wallace, *Core Concepts in Supramolecular Chemistry and Nanostructures*, Weinheim, Wiley-VCH, **2007**, 1–97
- [13] P. J. Collings, M. Hird, *Introduction to Liquid Crystals - Chemistry and Physics*, Taylor & Francis, London, **1997**.
- [14] C. Tschierske, T. Bellini, *Liquid crystals: Materials design and self-assembly*, Springer, Berlin **2012**.
- [15] D. Demus, *Mol. Cryst. Liq. Cryst.* **1988**, 165, 45.
- [16] A. Ramamoorthy, *Thermotropic Liquid Crystals: Recent Advances*, Springer Dordrecht, **2007**.
- [17] C. Tschierske, *Liquid Crystals: Materials Design and Self Assembly*, Springer Berlin Heidelberg, **2012**.
- [18] L. Mathelitsch, R. Repnik, Z. Bradac, M. Vilfan, S. Kralj, *Phys. Unserer Zeit* **2003**, 3, 134.
- [19] A. Skoulios, D. Guillon, *Mol. Cryst. Liq. Cryst.* **1988**, 165, 317.
- [20] C. Tschierske, *J. Mater. Chem.* **1998**, 8, 1485.
- [21] H.-T. Nguyen, C. Destrade, J. Malthête, *Adv. Mater.* **1997**, 9, 375.
- [22] Y. Fang, A. M. Levelut, C. Destrade, *Liq. Cryst.* **1990**, 7, 265.
- [23] K. Borisch, S. Diele, P. Göring, H. Müller, C. Tschierske, *Liq. Cryst.* **1997**, 22, 427
- [24] M. Wohlgemuth, N. Yufa, J. Hoffman, E. L. Thomas, *Macromolecules* **2001**, 17, 6083.
- [25] H. Tanaka, *Eur. Phys. J. E* **2012**, 35, 113.
- [26] P. J. Steinhardt, D. R. Nelson, M. Ronchetti, *Phys. Rev. B* **1983**, 28, 784.
- [27] T. Reppe, C. Dressel, S. Poppe, A. Eremin, C. Tschierske, *Adv. Optical Mater.* **2020**, 9, 2001572.

- [28] J. M. Seddon, R. H. Templer, *Structure and Dynamics of Membranes - From Cells to Vesicles*, Vol. 1, Elsevier **1995**.
- [29] D. Lombardo, M. A. Kiselev, S. Magazu, P. Calandra, *Adv. Condens. Matter Phys.* **2015**.
- [30] G.W. Gray, B. Jones, F. Marson, *J. Chem. Soc.* **1957**, 393.
- [31] D. Demus, G. Kunicke, J. Neelsen, H. Sackmann, *Z. Naturforsch. A* **1968**, 23, 84.
- [32] S. Kutsumizu, M. Yamada, S. Yano, *Liq. Cryst.* **1994**, 16, 1109.
- [33] S. Kutsumizu, *Isr. J. Chem.* **2012**, 52, 844.
- [34] D. Demus, A. Gloza, H. Hartung, A. Hauser, I. Raphtel, A. Wiegeleben, *Cryst. Res. Technol.* **1981**, 16, 1445.
- [35] S. Kutsumizu, H. Mori, M. Fukatami, S. Naito, K. Sakajiri, K. Saito, *Chem. Mater.* **2008**, 20, 3675.
- [36] M. A. Alam, J. Motoyanagi, Y. Yamamoto, T. Fukushima, J. Kim, K. Kato, M. Takata, A. Saeki, S. Seki, S. Tagawa, T. Aida, *J. Am. Chem. Soc.* **2009**, 131, 17722.
- [37] K. Borisch, S. Diele, P. Göring, C. Tschierske, *Chem. Commun.* **1996**, 237.
- [38] M. Poppe, *Dissertation*, Martin-Luther-Universität Halle-Wittenberg, **2018**.
- [39] O. Kwon, *Dissertation*, Martin-Luther-Universität Halle-Wittenberg, **2021**.
- [40] V. Luzzati, A. Tardieu, T. Gulik-Krzywicki, E. Rivas, F. Reiss-Husson, *Nature* **1968**, 220, 485.
- [41] M. A. Shcherbina, A. V. Bakirova, A. N. Yakunin, V. Percec, U. Beginn, M. Möller, S. N. Chvalun, *Crystallogr. Rep.* **2012**, 57, 151.
- [42] P. Mariani, V. Luzzati, H. Delacroix, *J. Mol. Biol.* **1988**, 204, 165.
- [43] I. W. Hamley, *The physics of block copolymers*, Oxford Univ. Press, Oxford **2003**.
- [44] S. Kutsumizu, *Curr. Opin. Solid. St. M.* **2002**, 6, 537.
- [45] J. F. Sadoc, J. Charvolin, *Acta Cryst.* **1989**, A45, 10.
- [46] G. Ungar, F. Liu, X. Zeng, *Handbook of Liquid Crystals*, Vol. 5, 2nd ed. (Eds: J. W. Goodby, P. J. Collings, T. Kato, C. Tschierske, H. F. Gleeson, P. Raynes), Wiley-VCH, Weinheim **2014**, 363.
- [47] J. M. Seddon, R. H. Templer, *Handbook of Biological Physics*, Vol. 1 (Eds: R. Lipowsky, E. Sackmann), Elsevier, Amsterdam **1995**, 97.
- [48] L. Han, S. Che, *Adv. Mater.* **2018**, 30, 1705708.
- [49] L. van 't Hag, S. L. Gras, E. Conn, C. J. Drummond, *Chem. Soc. Rev.* **2017**, 46, 2705.
- [50] H. Mukai, M. Yokokawa, M. Ichihara, K. Hatsusaka, K. Ohta, *J. Porphyr. Phthalocyanines* **2010**, 14, 188–197.
- [51] X. Zeng, M. Prehm, G. Ungar, C. Tschierske, F. Liu, *Angew. Chem. Int. Ed.* **2016**, 55, 8324.
- [52] C. Dressel, F. Liu, M. Prehm, X. Zeng, G. Ungar, C. Tschierske, *Angew. Chem. Int. Ed.* **2014**, 53, 13115.
- [53] M. M. Safont-Sempere, G. Fernández, F. Würthner, *Chem. Rev.* **2011**, 111, 5784.
- [54] L. Pasteur, *Ann. Chim. Phys.* **1848**, 24, 442.
- [55] S. Toxveard, *Int. J. Mol. Sci.* **2009**, 10, 1290.
- [56] S. Toxvaerd, *Phys. Rev. Lett.* **2000**, 85, 4747.
- [57] A.-M. Levelut, M. Clerc, *Liq. Cryst.* **1998**, 24, 105.
- [58] S. Kutsumizu, K. Morita, S. Yano, S. Nojima, *Liq. Cryst.* **2002**, 29, 1459.
- [59] K. Saito, M. Sorai, *Chem. Phys. Lett.* **2002**, 366, 56.

- [60] X. B. Zeng, G. Ungar, *J. Mater. Chem. C* **2020**, *8*, 5389.
- [61] C. Dressel, T. Reppe, M. Prehm, M. Brautzsch, C. Tschierske, *Nat. Chem.* **2014**, *6*, 971.
- [62] T. Reppe, S. Poppe, X. Cai, Y. Cao, F. Liu, C. Tschierske, *Chem. Sci.* **2020**, *11*, 5902.
- [63] C. Dressel, *Dissertation*, Martin-Luther-Universität Halle-Wittenberg, **2015**.
- [64] T. Reppe, *Masterarbeit*, Martin-Luther-Universität Halle-Wittenberg, **2015**.
- [65] C. Dressel, T. Reppe, S. Poppe, M. Prehm, H. Lu, X. Zeng, G. Ungar, C. Tschierske, *Adv. Funct. Mater.* **2020**, *30*, 2004353.
- [66] K. Kishikawa, *Isr. J. Chem.* **2012**, *52*, 800.
- [67] C. R. Martinez, B. L. Iverson, *Chem. Sci.* **2012**, *3*, 2191.
- [68] T. Reppe, C. Dressel, S. Poppe, C. Tschierske, *Chem. Commun.* **2020**, *56*, 711.
- [69] K. Borisch, S. Diele, P. Göring, H. Kresse, C. Tschierske, *J. Mat. Chem.* **1998**, *8*, 529.
- [70] F. Liu, M. Prehm, X. Zeng, C. Tschierske, G. Ungar, *J. Am. Chem. Soc.* **2014**, *136*, 6846.
- [71] M. Alaasar, S. Poppe, Y. Cao, C. Chen, F. Liu, C. Zhu, C. Tschierske, *J. Mater. Chem. C* **2020**, *8*, 12902.
- [72] T. Reppe, S. Poppe, C. Tschierske, *Chem. Eur. J.* **2020**, *26*, 16066.
- [73] H. G. O. Becker, *Organikum*, Wiley-VCH, Weinheim, **2001**.
- [74] A. Willimason, *Lond. Edinb. Dublin philos. mag. j. sci.*, *37*, 350
- [75] R. Wu, J. S. Schumm, D. L. Pearson, J. M. Tour, *J. Org. Chem.* **1996**, *61*, 6906.
- [76] B. Neises, W. Steglich, *Angew. Chem. Int. Ed. Engl.* **1978**, *17*, 522.
- [77] B. S. Bal, W. E. Childers, H. W. Pinnick, *Tetrahedron* **1981**, *37* 2091.
- [78] B. O. Lindgren, T. Nilsson, *Acta Chem. Scand.* **1973**, *27*, 880.
- [79] L. Holman, C. G. Jørgensen, J. Nielsen, P. d'Ettore, *Proc. R. Soc. B* **2010**, *277*, 3793.
- [80] E. H. Kim, O. N. Kadkin, S. Y. Kim, M.-G. Choi, *Eur. J. Inorg. Chem.* **2011**, 2933.
- [81] M. Imperor-Clerc, *Curr. Opin. Colloid Interface Sci.* **2005**, *9*, 370.
- [82] T. Kajitani, S. Kohmoto, M. Yamamoto, K. Kishikawa, *Chem. Mater.* **2018**, *11*, 2885.
- [83] H. Lu, X. Zeng, G. Ungar, C. Dressel, C. Tschierske, *Angew. Chem. Int. Ed.* **2018**, *11*, 2835.
- [84] Z. J. Zheng, Y. Q. Lu, Q. Li, *Adv. Mater.* **2020**, *32*, 1905318.
- [85] Y. Sang, D. Yang, Z. Shen, P. Duan, M. Liu, *J. Phys. Chem. C* **2020**, *124*, 17274.
- [86] C. Tschierske, C. Dressel, *Symmetry* **2020**, *12*, 1098.
- [87] N. Miyaura, A. Suzuki, *J. Chem. Soc. Chem. Commun.* **1979**, 866
- [88] C. J. Brown, R. Sadanaga, *Acta Crystallogr.* **1965**, *18*, 158
- [89] Q. Shen, K. Hagen, *J. Phys. Chem.* **1987**, *91*, 1357.
- [90] Z. Pawelka, A. Koll, T. Zeegers-Huyskens, *J. Mol. Struct.* **2001**, *597*, 57.





# Anhang

## Inhaltsverzeichnis Anhang

A.1 Auflistung der Publikationen	A-2
Publikationen A	A-4
Publikationen B	A-37
Publikationen C	A-48
Publikationen D	A-95
Publikationen E	A-122



## A.1 Auflistung der Publikationen

Die aufgelisteten Publikationen A–E bilden den Kern dieser Arbeit und sind bereits in den angegebenen wissenschaftlichen Zeitschriften erschienen. Die zusätzlichen Daten der Supporting Information (SI) sind hinter den jeweiligen Artikeln angehängt. Die vollständigen SI mit Synthesen und analytischen Daten der Verbindungen finden sich unter den angegebenen Websites.

- 1.) C. Dressel, T. Reppe, S. Poppe, M. Prehm, H. Lu, X. Zeng, G. Ungar, C. Tschierske, „*Helical networks of  $\pi$ -conjugated rods - A robust design concept for bicontinuous cubic liquid crystalline phases with achiral  $Ia3d$  and chiral  $I23$  lattice*”, *Adv. Funct. Mater.* **2020**, *30*, 2004353. DOI: 10.1002/adfm.202004353. **(Publikation A)**  
SI abrufbar unter: <https://onlinelibrary.wiley.com/doi/full/10.1002/adfm.202004353>
- 2.) T. Reppe, C. Dressel, S. Poppe, C. Tschierske, „*Controlling spontaneous mirror symmetry breaking in cubic liquid crystalline phases by the cycloaliphatic ring size*”, *Chem. Commun.* **2020**, *56*, 711–714. DOI: 10.1039/c9cc09206d. **(Publikation B)**  
SI abrufbar unter: <https://pubs.rsc.org/en/content/articlelanding/2020/cc/c9cc09206d>
- 3.) T. Reppe, C. Dressel, S. Poppe, A. Eremin, C. Tschierske, „*Swallow-Tailed Polycatenars: Controlling Complex Liquid Crystal Self-Assembly and Mirror Symmetry Breaking at the Lamellae-Network Cross-Over*“, *Adv. Optical Mater.* **2021**, *9*, 2001572.  
DOI: 10.1002/adom.202001572. **(Publikation C)**  
SI abrufbar unter: <https://onlinelibrary.wiley.com/doi/full/10.1002/adom.202001572>
- 4.) T. Reppe, S. Poppe, X. Cai, F. Liu, C. Tschierske, „*Spontaneous mirror symmetry breaking in benzil-based soft crystalline, cubic liquid crystalline and isotropic liquid phases*”, *Chem. Sci.* **2020**, *11*, 5902–5908. DOI: 10.1039/d0sc01396j. **(Publikation D)**  
SI abrufbar unter: <https://pubs.rsc.org/en/content/articlelanding/2020/sc/d0sc01396j>
- 5.) T. Reppe, S. Poppe, C. Tschierske, „*Controlling mirror symmetry breaking and network formation in liquid crystalline cubic, isotropic liquid and crystalline phases of benzil-based polycatenars*”, *Chem. Eur. J.*, **2020**, *26*, 16066–16079.  
DOI: 10.1002/chem.202002869. **(Publikation E)**  
SI abrufbar unter: <https://chemistry-europe.onlinelibrary.wiley.com/doi/10.1002/chem.202002869>



## **Publikation A**

### **Helical Networks of $\pi$ -Conjugated Rods – A Robust Design Concept for Bicontinuous Cubic Liquid Crystalline Phases with Achiral $Ia3d$ and Chiral $I23$ Lattice**

Christian Dressel,<sup>[a,+]</sup> Tino Reppe,<sup>[a,+]</sup> Silvio Poppe,<sup>[a]</sup> Marko Prehm,<sup>[a]</sup> Huanjun Lu,<sup>[b]</sup> Xiangbing Zeng,<sup>[b]</sup> Goran Ungar,<sup>[b]</sup> Carsten Tschierske<sup>[a]</sup>

[a] Institute of Chemistry, Martin Luther University Halle-Wittenberg, Kurt-Mothes-Straße 2, 06120 Halle, Germany.

[b] State Key Laboratory for Mechanical Behaviour of Materials, Shaanxi International Research Center for Soft Matter, Xi'an Jiaotong University, Xi'an 710049, P. R. China.

[+] These authors contributed equally to this work.

#### **Abstract**

Bicontinuous cubic liquid crystalline phases of  $\pi$ -conjugated molecules, representing self-assembled networks with cubic symmetry are receiving growing attention due their capacity for charge transport in all three spatial directions and their inherent spontaneous helicity. So far, these phases have been found only in a few compounds with strictly defined molecular structures within a narrow temperature interval and their formation is not predictable. Herein, a robust general design concept of bicontinuous cubic phase is reported. It is based on a nonsymmetric-substituted  $\pi$ -conjugated 5,5'-diphenyl-2,2'-bithiophene platform with one end containing three out-fanning flexible chains and with a range of substituents at the other end (the apex). The cubic phases are stable over broad temperature ranges, often down to ambient temperature, and tolerate a wide range of apex substitution patterns, allowing structural diversity and tailoring of the cubic phase type and of the application relevant properties. With increasing number and size of the apex substituents, a sequence of three different modes of cubic self-assembly is observed, which is explained by an increasing helical twist. Thus, a long pitch and a short pitch achiral double network  $Ia3d$  phase range can be distinguished, with the chiral triple network  $I23$  cubic phase in the intermediate pitch range. This provides new perspectives for the directed design of cubic phase, forming functional materials based on spontaneously formed helical network liquid crystals with tunable application specific properties.

#### **Referenz**

C. Dressel, T. Reppe, S. Poppe, M. Prehm, H. Lu, X. Zeng, G. Ungar, C. Tschierske, *Adv. Funct. Mater.* **2020**, *30*, 2004353. DOI: 10.1002/adfm.202004353.

# Helical Networks of $\pi$ -Conjugated Rods – A Robust Design Concept for Bicontinuous Cubic Liquid Crystalline Phases with Achiral $Ia\bar{3}d$ and Chiral $I23$ Lattice

Christian Dressel, Tino Reppe, Silvio Poppe, Marko Prehm, Huanjun Lu, Xiangbing Zeng, Goran Ungar,\* and Carsten Tschierske\*

Bicontinuous cubic liquid crystalline phases of  $\pi$ -conjugated molecules, representing self-assembled 3D-ordered interpenetrating networks with cubic symmetry, are receiving increasing attention due to their capacity for charge transport in all three dimensions and their inherent spontaneous helicity. Herein, a robust general design concept for creating bicontinuous cubic phases is reported. It is based on a nonsymmetric-substituted  $\pi$ -conjugated 5,5'-diphenyl-2,2'-bithiophene platform with one end containing three out-fanning flexible chains and with a range of substituents at the other end (the apex). The cubic phases are stable over broad temperature ranges, often down to ambient temperature, and tolerate a wide range of apex substitution patterns, allowing structural diversity and tailoring of the cubic phase type and application-relevant properties. With an increasing number and size of apex substituents, a sequence of three different modes of cubic self-assembly is observed, following an increasing helical twist. Thus, two ranges of the achiral double network  $Ia\bar{3}d$  phase range can be distinguished, a long pitch and a short pitch, with the chiral triple network  $I23$  cubic phase in the intermediate pitch range. The findings provide a new prospect for the directed design of cubic phase-forming functional materials based on spontaneously formed helical network liquid crystals with tunable application specific properties.

represent self-assembled supramolecular networks of branched columns which occur in soft matter systems at the transition from lamellar to columnar self-assembly.<sup>[4,5]</sup> They are known for amphiphilic<sup>[6–8]</sup> and dendritic<sup>[9]</sup> molecules and for macromolecules<sup>[10]</sup> in the liquid crystalline (LC) phases of the bulk materials<sup>[11–21]</sup> and the corresponding lyotropic systems with appropriate solvents (in lyotropics abbreviated as  $Cub_V$  phases).<sup>[7,22]</sup> They find applications for encapsulation of biological and bioactive molecules in drug delivery (cubosomes<sup>[23]</sup>), gene transfection, and protein crystallization,<sup>[24]</sup> as templates for the preparation of inorganic porous materials,<sup>[25]</sup> as selective membranes,<sup>[26]</sup> photonic and optical bandgap materials,<sup>[27,28]</sup> and many other.<sup>[5,29]</sup> Presently, they are receiving increasing interest as electron and ion conducting materials<sup>[30–37]</sup> with the unique feature of having conduction pathways in all three spatial directions.<sup>[38–45]</sup>  $Cub_{bi}$  phases of molecules involving  $\pi$ -conjugated rods and organized

## 1. Introduction

Networks are indispensable for information technology, intelligence, and open-end development of complex systems,<sup>[1,2]</sup> and covalently connected molecular networks form the basis of reticular chemistry.<sup>[3]</sup> Bicontinuous cubic phases ( $Cub_{bi}$ )

in helical networks might also become of potential interest for circularly-polarized aggregation-induced emission for applications in a wide range of technologically important fields.<sup>[46–48]</sup>

In the  $Cub_{bi}$  phases there are one, two, or three continuous networks in a continuum between them, i.e., “bicontinuous” stands for (continuous) networks + continuum, irrespective of

Dr. C. Dressel, T. Reppe, Dr. S. Poppe, Dr. M. Prehm, Prof. C. Tschierske  
Institute of Chemistry  
Martin Luther University Halle-Wittenberg  
Kurt-Mothes-Strasse 2, Halle/Saale D-06120, Germany  
E-mail: carsten.tschierske@chemie.uni-halle.de

 The ORCID identification number(s) for the author(s) of this article can be found under <https://doi.org/10.1002/adfm.202004353>.

© 2020 The Authors. Published by Wiley-VCH GmbH. This is an open access article under the terms of the Creative Commons Attribution License, which permits use, distribution and reproduction in any medium, provided the original work is properly cited.

<sup>[†]</sup>Present address: Jiangsu Key Laboratory of Advanced Functional Polymer Design and Application, Soochow University, Suzhou 215123, P. R. China

Dr. H. Lu,<sup>[†]</sup> Dr. X. Zeng, Prof. G. Ungar  
Department of Materials Science and Engineering  
University of Sheffield  
Sheffield S1 3JD, UK  
E-mail: g.ungar@sheffield.ac.uk

Prof. G. Ungar  
State Key Laboratory for Mechanical Behavior of Materials  
Shaanxi International Research Center for Soft Materials  
Xi'an Jiaotong University  
Xi'an 710049, China

DOI: 10.1002/adfm.202004353

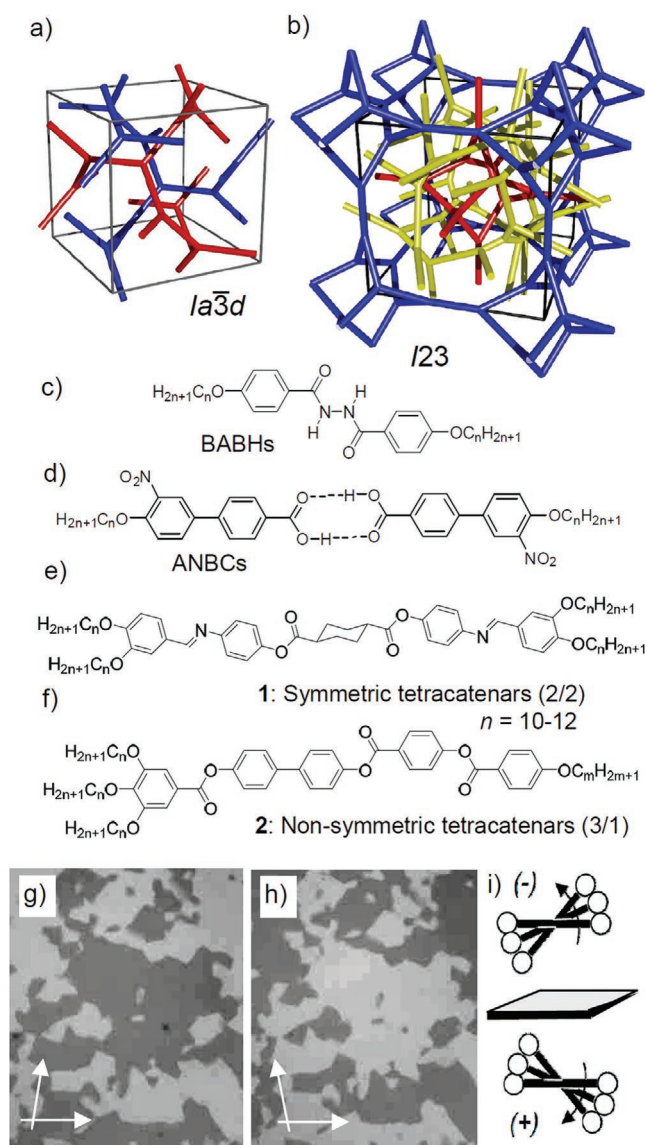


**Figure 1.** The  $Cub_{bi}$  phases formed by rod-like compounds; a) the double gyroid ( $Ia\bar{3}d$ ) involving two networks and b) the  $I23$  phase formed by three networks;<sup>[87,99]</sup> c–f) representative examples for the major classes of rod-like compounds forming these two types of  $Cub_{bi}$  phases; g, h) chiral conglomerate of the  $I23$  phase of  $3/351_2$  as observed upon cooling at  $T = 125$  °C between slightly uncrossed polarizers (contrast enhanced); the width of both images is 0.5 mm; i) the helical twist developing along the networks due to the clashing of the bulky end groups between the molecules organized in the networks shown in (a, b).

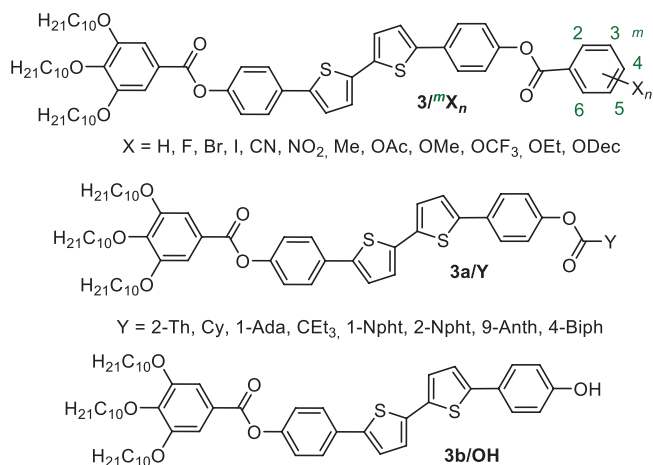
how many networks there are.<sup>[49]</sup> In the most common case, two interwoven networks with three way junctions are organized in a  $Ia\bar{3}d$  lattice (the double gyroid, **Figure 1a**), which is the most frequently observed type of  $Cub_{bi}$  phase.<sup>[7,14,17]</sup> However, as soon as rod-like segments are included in the molecular structure (Figure 1c–f), new cubic and also noncubic network phases can be observed.<sup>[50–65]</sup> In most cases, these rods are organized in the networks and on average lie perpendicular to the network segments.<sup>[14–17,66]</sup> For these  $Cub_{bi}$  phases, beside the  $Ia\bar{3}d$  phase, a second more complex type of cubic phase with a larger

lattice parameter was found.<sup>[13,14,16,67–80]</sup> In early works, it was assigned to the  $Im\bar{3}m$  space group and models involving three minimal surfaces,<sup>[52,81]</sup> three networks,<sup>[82,83]</sup> or combining two networks with additional spherical aggregates<sup>[84,85]</sup> were proposed. Recently, the observation of spontaneous mirror symmetry breaking and formation of chiral conglomerates in this “ $Im\bar{3}m$ ” phase, and occasionally also in the adjacent isotropic liquid phase (Iso<sub>1</sub><sup>[x]</sup>)<sup>[86]</sup> provoked significant interest in this kind of cubic phase and provided a breakthrough in the understanding of its self-assembly. It was shown that in all cases, the “ $Im\bar{3}m$ ” phase is intrinsically chiral, whereas the double gyroid ( $Ia\bar{3}d$ ) is always achiral.<sup>[87–94]</sup> This was explained by a helical organization of the molecules in the networks of these cubic phases. The helix formation is the result of steric repulsion between the end chains of the almost parallel aligned rod-like molecules, requiring a slight twist between the molecules along the network segments (see Figure 1i).<sup>[95,96]</sup> In the  $Ia\bar{3}d$  phase, there are two networks in which the helical sense is opposite (Figure 1a),<sup>[87,97,98]</sup> and therefore it is optically inactive. By contrast, the “ $Im\bar{3}m$ ” phase is composed of three networks (Figure 1b), where the chirality cannot cancel out, leading to a unichiral structure with macroscopic chirality expressed by conglomerate formation (see, for example, Figure 1g, h).<sup>[87]</sup> Due to the proven chirality, the space group of this triple network phase cannot be  $Im\bar{3}m$ ,<sup>[52,82,83]</sup> and recently a model with chiral  $I23$  space group was proposed, where all three nets have three-fold junction as known for the double gyroid (Figure 1b).<sup>[99]</sup>

However, the formation of  $Cub_{bi}$  phases is in general extremely sensitive to slight modifications of the molecular structure, easily leading to transition to the adjacent lamellar or columnar phases.<sup>[11–16]</sup> Therefore,  $Cub_{bi}$  phases are usually not predictable and appear only in narrow temperature ranges for few well designed compounds (Figure 1c–f). The most prominent are rod-like hydrogen bonded dimers of 4'-*n*-alkoxy-3'-nitrobiphenyl-4-carboxylic acids (ANBCs),<sup>[100–104]</sup> the dibenzoyldiazines (BABHs)<sup>[105–111]</sup> (Figure 1c, d),<sup>[16,17,108,110]</sup> and tetracatenar molecules, which can have either a symmetric or a nonsymmetric distribution of the alkyl chains (Figure 1e, f).<sup>[112–124]</sup> Nevertheless, even these compounds are very sensitive to minor molecular structural variations. For example, only the  $NO_2$ - and CN-substituted biphenyl carboxylic acids (Figure 1d) form  $Cub_{bi}$  phases, whereas the nonsubstituted or related halogenated compounds do not.<sup>[125]</sup> Likewise, symmetric tetracatenars with any substituent (e.g.,  $CH_3$ , F, CN) replacing only one H-atom at the core unit do not form any  $Cub_{bi}$  phase.<sup>[116]</sup> Therefore, it is presently not possible to efficiently tailor the phase type and application relevant properties (e.g., band gap) of these compounds by molecular design.

Herein, we introduce the concept of taper-shaped tetracatenars (3/0 tetracatenars;  $m/n$  gives the number of alkyl chains at each end of the rod) as a general design concept for robust  $Cub_{bi}$  phase-forming materials which can be modified by a wide range of substituents at the apex (**Scheme 1**). This makes it possible to tailor the cubic phase type and the electronic properties of the  $\pi$ -conjugated molecules in question. It is also shown that this can be used to steer the helical networks involved in the  $Cub_{bi}$  phase to either a chiral ( $I23$ ) or an achiral  $Cub_{bi}$  phase ( $Ia\bar{3}d$ ).

To this end, the taper-shaped tetracatenar compounds  $3/mX_n$  and  $3a/Y$  were synthesized (Scheme 1). These compounds involve a  $\pi$ -conjugated 5,5'-diphenyl-2,2'-bithiophene rod



**Scheme 1.** Chemical structures of the polycatenar bithiophene derivatives  $3^mX_n$  and  $3a/Y$  under consideration.

providing potential application relevant functional properties.<sup>[126–128]</sup> They are terminated at one end by a 3,4,5-tridecyloxybenzoyloxy group and at the opposite end, referred to as apex, by a series of systematically varied substituents to adjust their capability to self-assemble in network structures with cubic symmetry. In the series of compounds  $3^mX_n$ , the apex is a benzoate unit and the position of the substituent(s) at this unit is indicated by superscripts ( $m$ ) before  $X$  and the number of substituents is added as a subscript ( $n$ ) after  $X$ , e.g.,  $3^{35}I_2$  means two iodines in positions 3 and 5. In compounds  $3a/Y$ , the benzene ring at the apex is replaced by other aromatic, heteroaromatic, alicyclic, or branched units  $Y$ .

## 2. Experimental Section

### 2.1. Synthesis

The synthesis of the tricatener phenol **3b/OH** (Scheme 1) was conducted by Suzuki type boronate cross-coupling reactions, as reported previously.<sup>[86]</sup> Acylation of **3b/OH** with appropriate benzoyl chlorides led to the compounds  $3^mX_n$  and  $3a/Y$ , as described in the Supporting Information.

### 2.2. Investigation Methods

Investigation of the obtained materials was conducted by polarizing optical microscopy (POM) (Optiphot 2, Nikon microscope with a Mettler FP82HT heating stage), differential scanning calorimetry (DSC-7 and DSC-8000 Perkin Elmer, 10 K min<sup>-1</sup> peak temperatures quoted in Table S1 in the Supporting Information), and X-ray diffraction (XRD). In-house XRD was carried out using Cu<sub>Kα</sub> radiation and a Vantec 500 area detector. High-resolution small-angle X-ray scattering patterns were recorded at beamline I22 of Diamond Light Source with a Pilatus 2M detector and at XmaS beamline B28 of the European Synchrotron Radiation Facility (ESRF). Powder samples in capillaries were temperature controlled with a Linkam hot stage.

## 3. Results and Discussion

### 3.1. Characterization of the Cubic Phases

The cubic phases appear uniformly dark between fully (90°) crossed polarizers as they are optically isotropic. The transition from the isotropic liquid (Iso) to the cubic phases was identified by the sudden increase of viscosity associated with a DSC peak with  $\Delta H = 2\text{--}5$  kJ mol<sup>-1</sup>. Usually, there is a 5–12 K supercooling of the Iso–Cub transition relative to the Cub–Iso transition temperature on heating (Tables S1 and S2 in the Supporting Information for numerical data and Figures S1 and S14a in the Supporting Information for representative DSC traces). Polarizing microscopy allows an easy preliminary discrimination between the two cubic phase types formed by rod-like molecules, the  $Ia\bar{3}d$  and  $I23$  phases. The achiral  $Ia\bar{3}d$  phase remains uniformly dark also after rotating one of the polarizers by a small angle out of the fully crossed orientation. By contrast, the mirror symmetry broken  $I23$  phase shows a conglomerate of dark and bright domains after slight rotation of one polarizer by 1°–10° either clockwise or counterclockwise (Figure 1g,h).

For further confirmation, the cubic phases were investigated by XRD. The powder diffraction pattern of the  $Ia\bar{3}d$  phase is characterized by the well resolved (211) and (220) reflections, whereas for  $I23$  a characteristic pattern of the dominating (321) with a shoulder for the (400) reflection and a small (420) reflection is observed (Figure S9 and Tables S3 and S4, Supporting Information). Representative examples were investigated using a synchrotron source (Figures S10–S12 and Tables S5–S9, Supporting Information). The high resolution XRD pattern of the cubic  $Ia\bar{3}d$  and  $I23$  phases of compound  $3^3F$  and  $3^{35}F_2$ , respectively, are shown in Figure 2a,c. The electron density (ED) maps of these two cubic phases, reconstructed on the basis of the diffraction intensities (Figure 2b,d) show the double gyroid structure of the  $Ia\bar{3}d$  phase and the complex triple network structure of the  $I23$  phase. Details of the reconstruction are described in the Supporting Information, and for details of the ED reconstruction in the case of the non-centrosymmetric  $I23$  phase, see also ref. [99].

### 3.2. Tailoring of the Cubic Phases of the Tricatener $3^mX_n$ by Apex Substituents

#### 3.2.1. 4-Substituted Compounds

Figure 3a shows the effect of increasing the size of apex substitution in the terminal 4-position with respect to the COO group (compounds  $3^4X$ ). As shown, even for large substituents, like iodine and OCF<sub>3</sub>, the Cub<sub>bi</sub> phase is retained over a wide temperature range. It should be noted that the transition temperatures in Figure 3a and all following bar diagrams were measured on heating and the observed LC phases represent thermodynamically stable (enantiotropic) phases, whereas on cooling, much broader metastable cubic ranges, often down to ambient temperature, were observed (see Table S1 in the Supporting Information).

Interestingly, the stability and the phase range of the Cub<sub>bi</sub> phase is enlarged by increasing the size of the substituent



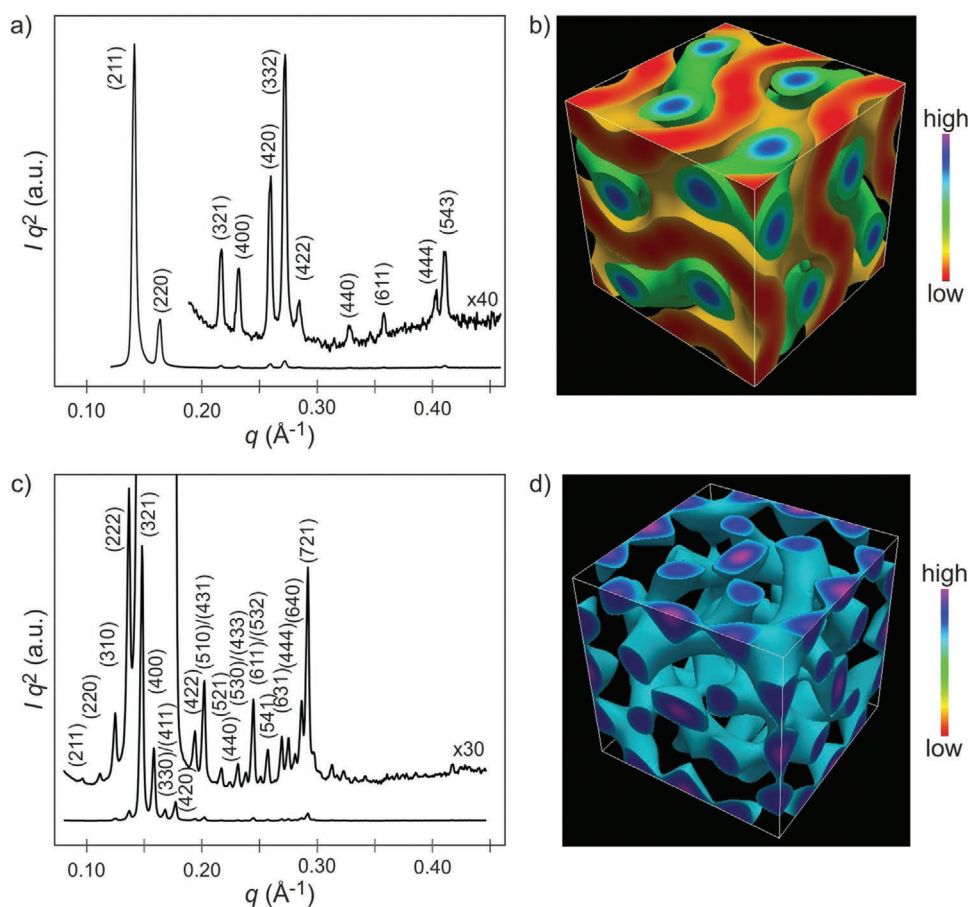


**Figure 2.** a) XRD pattern (recorded at 125 °C) and b) the reconstructed electron density map of the  $Ia\bar{3}d$  cubic phase formed by compound  $3/3^3F$ . In the electron density map, the green isoelectron surface encloses the highest 25% of the total volume, while the orange isoelectron surface encloses the lowest 50% of the unit cell volume. c) XRD pattern recorded at 125 °C and d) the electron density map of the  $I23$  cubic phase formed by compound  $3/3^3F_2$ . The light blue isoelectron surface encloses the higher 25% of the unit cell volume, showing the triple network structure. Vertically expanded diffractograms were added in (a) and (c) to show weaker diffraction peaks; labeled by their Miller indices.

( $H < F < I$ ), whereby electron acceptors (halogens,  $OCF_3$ ,  $CN$ ,  $NO_2$ ), reducing the electron density of the polyaromatic core, have a larger stabilizing effect than donors ( $CH_3$ ,  $OCH_3$ ) with approximately the same volume. This becomes especially evident if  $3/4^3CN$  and  $3/4^3Me$ , both having the same volume of the substituent, but very different Hammett substituent constants (as measures for the electronic substituent effects)<sup>[129]</sup> are compared (Table 1). Table 1 also summarizes the volumes of the different substituents as estimated using crystal volume increments ( $V_c$ )<sup>[130]</sup> and their Hammett constants ( $\sigma_m$ ,  $\sigma_p$ )<sup>[129]</sup>. In most cases, the  $Cub_{bi}$  phase of the 4-substituted compounds is  $Ia\bar{3}d$ , only for the  $OCF_3$  group, the phase type changes to  $I23$ .<sup>[131]</sup> The cubic lattice parameter  $a_{cub}$  of the  $Ia\bar{3}d$  phase of all 3/0 type tricatener compounds  $3/4^3X$  is in the same range between 10.8 and 11.5 nm (Table 1 and Table S1 (Supporting Information)) and only slightly increasing with the volume of the substituent X, whereas that of the  $I23$  phase of  $3/4^3OCF_3$  is about one half larger ( $a_{cub} = 16.2$  nm), in line with the triple network structure. Compound  $3/4^3ODec$ , also forming the  $I23$  phase but belonging to the 3/1-tetracatenar compounds, will be discussed further below.

### 3.2.2. 3-Substituted Compounds

Shifting the substituent X to the lateral 3-position (Figure 4a) provides reduced  $Cub$ – $Iso$  transition temperatures compared to the 4-substituted compounds; only the polar electron acceptor substituents F, Br and especially CN can still stabilize the cubic phase compared to  $X = H$ . This cubic phase stabilizing effect of polar substituents is smaller than for the 4-substituted series, due to the competing effect of the stronger steric distortion of molecular packing by the lateral position of the substituents. The cubic phase stabilizing effect of the polar CN group is again outstanding if compared with Br, having a similar volume. The  $Cub_{bi}$  phase type changes already for  $X = Br$  from  $Ia\bar{3}d$  to  $I23$ , indicating the stronger steric effect of the substituents in the lateral 3-position on the phase type (Figure 4a and Table 2). Only for compound  $3/3^3OEt$ , the  $I23$  phase is observed under all conditions, whereas for compounds  $3/3^3OMe$ ,  $3/3^3Br$ , and  $3/3^3I$ , both  $Cub_{bi}$  phase types,  $Ia\bar{3}d$  and  $I23$ , can be found depending on temperature and other conditions such as cooling rate and thermal history (for a more detailed discussion, see Section S1.4 in the Supporting Information). Overall, with increasing

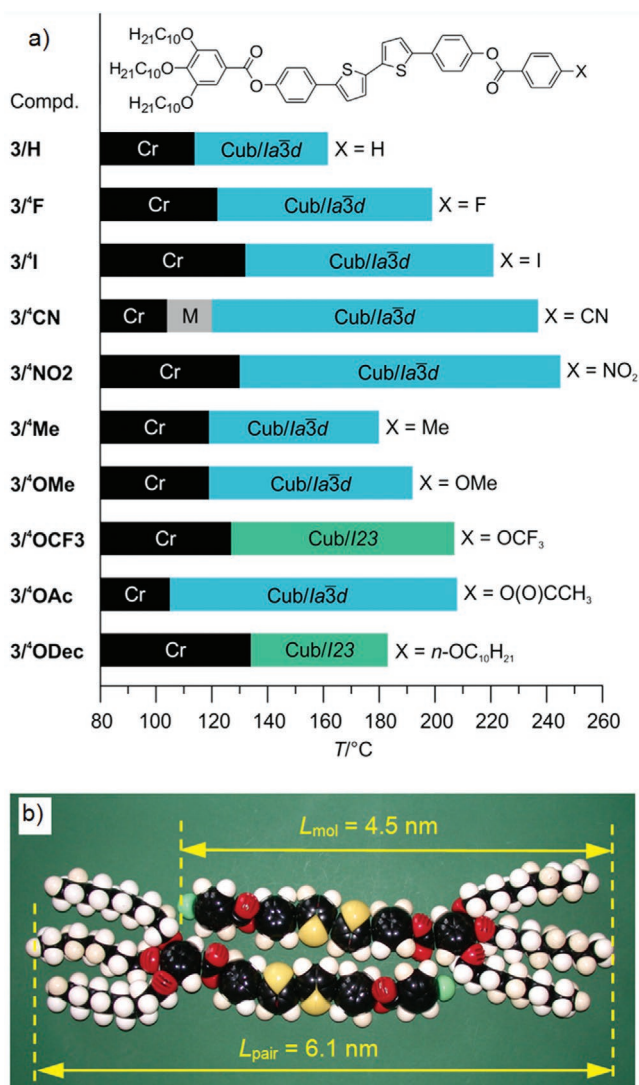


**Figure 3.** a) Mesophases and transition temperatures of compounds  $3^i/X$  as observed on heating; for the numerical data of the transitions on heating and cooling, including transition enthalpy values of  $3^i/H$  and  $3^i/ODec$ , added for comparison, see ref. [87]; for all other compounds, see Table S1 in the Supporting Information; abbreviations: Cr = crystalline solid  $Cub/la\bar{3}d = Cub_{bi}$  phase with  $la\bar{3}d$  lattice; all  $la\bar{3}d$  phases represent long pitch  $la\bar{3}d_{(L)}$  phases;  $Cub/I23 = Cub_{bi}$  phase with  $I23$  lattice, M = unknown mesophase, the isotropic liquid state (Iso) is at the right side of the columns; b) space filling molecular models (CPK models) of the proposed organizations of the molecules of compound  $3^i/F$  in the  $Cub_{bi}$  phase.

volume of X there is a transition from  $la\bar{3}d$  ( $X = H, F$ ) via an  $I23-la\bar{3}d$  dimorphism ( $X = Br, I, OMe$ ) to  $I23$  ( $X = OC_2H_5$ ). In the sequence  $OCH_3-OC_2H_5-OC_{10}H_{21}$ , i.e., by elongation of the alkyloxy chain (Figure 4a), the  $la\bar{3}d$  phase is at first completely removed and replaced by the  $I23$  phase for  $OC_2H_5$  and then the  $la\bar{3}d$  phase re-emerges for  $OC_{10}H_{21}$ . Thus, there appear to be two  $la\bar{3}d$  phase ranges, one favored at small apex size and the second one requiring a significantly larger substituent at the apex; the two are separated by the  $I23$  phase for medium effective volume of the substituent X. The transition from  $3^i/3^iOMe$  to  $3^i/3^iODec$  (and from  $3^i/3^iOMe$  to  $3^i/3^iODec$ , see Figure 3a) can

**Table 1.** Dependence of lattice parameter  $a_{cub}$  and other structural parameters on the volume of the substituent X ( $V_{CX}$ ) in the compounds  $3^i/X$ .

Compounds <sup>a)</sup>	$V_{CX}$ [nm <sup>3</sup> ]	$\sigma_m$	$\sigma_p$	$Cub_{bi}$	$a_{cub}$ [nm]	$n_{raft}$	$\Phi$ [°]
$3^i/H$	6.9	–	–	$la\bar{3}d_{(L)}$	10.8	3.9	8.3
$3^i/F$	12.8	0.34	0.06	$la\bar{3}d_{(L)}$	11.1	4.0	8.1
$3^i/I$	25.6	0.71	0.78	$la\bar{3}d_{(L)}$	11.1	4.0	8.1
$3^i/CN$	31.3	0.56	0.66	$la\bar{3}d_{(L)}$	11.2	4.0	8.0
$3^i/Me$	31.7	–0.07	–0.17	$la\bar{3}d_{(L)}$	11.4	4.2	7.9
$3^i/I$	45.0	0.35	0.18	$la\bar{3}d_{(L)}$	11.3	4.1	7.9
$3^i/OMe$	46.3	0.12	–0.27	$la\bar{3}d_{(L)}$	11.4	4.2	7.9
$3^i/OAc$	58.6	0.39	0.31	$la\bar{3}d_{(L)}$	11.5	4.1	7.8
$3^i/OCF_3$	58.6	0.38	0.35	$I23$	16.2	3.4	8.6

<sup>a)</sup>  $V_{CX}$  = crystal volume of the substituent X, estimated with the crystal volume increments ( $V_c$ ) reported by Immirzi and Perini;<sup>[130]</sup>  $\sigma_m$  and  $\sigma_p$  are Hammett constants (Table S11, Supporting Information);<sup>[129]</sup>  $\sigma_m$  is a measure of the strength of electron withdrawing (+) and electron donating (–) effects via the  $\sigma$  bonds (inductive effect) and  $\sigma_p$  is an analogous measure for the delocalization of the  $\pi$ -electrons (resonance effect); large positive values of  $\sigma_m$  and  $\sigma_p$  indicate electron acceptors, whereas small positive and negative values are typically found for electron donating substituents;  $n_{raft}$  = number of molecules organized in each 0.45 nm thick raft of the networks, calculated as described in Table S10 (Supporting Information);  $\Phi$  = helical twist between adjacent 0.45 nm thick rafts of molecules along the networks, calculated according to:  $\Phi(la\bar{3}d) = 70.5^\circ/[0.354a_{cub}/0.45 \text{ nm}]^{[87]}$  and  $\Phi(I23) = 90^\circ/[0.290a_{cub}/0.45 \text{ nm}]^{[99]}$  abbreviations:  $la\bar{3}d_{(L)}$  = long pitch  $la\bar{3}d$  phase;  $I23 = Cub_{bi}/I23$  phase.

be considered as a transition between two types of polycatenars, the taper-shaped 3/0 tricatensars and the nonsymmetric 3/1 tetracatenars.<sup>[132]</sup>

As shown in Figure 5a,b, this phase sequence is also observed by POM in the contact region between the achiral  $la\bar{3}d$  phases of  $3^i/H$  and  $3^i/3^iODec$  where a ribbon of the chiral  $I23$  phase is induced. Thus, tailoring of the cubic phase structure and mirror symmetry breaking is not only achievable by the design of individual compounds, but also by mixing compounds with different sizes of the substituents.<sup>[111,117]</sup>

### 3.2.3. 3,5-Disubstituted Compounds

The 3,5-disubstitution pattern (Figure 4b) provides an even stronger steric effect than only one 3-substituent, and therefore in all cases, even for  $X = F$ , the  $la\bar{3}d$  phase of  $3^i/H$  is replaced by the  $I23$  phase. Outstanding is again the effect of the polar electron accepting  $NO_2$  group, leading to the highest  $Cub_{bi}$ -Iso transition temperature and the widest cubic range despite its significant size. We attribute this phase stabilization to two main effects. First, the increased dipole moment strengthens the electrostatic intermolecular interactions. Especially, the stronger core–core interaction between the electron-deficient apex and the trialkoxy-substituted electron donor ends in an antiparallel side-by-side packing of the polyaromatic rods (Figure 3b) leads to a denser packing, stabilizing the networks. Second, the polar groups increase the incompatibility of the polyaromatic core units with the nonpolar aliphatic chains,

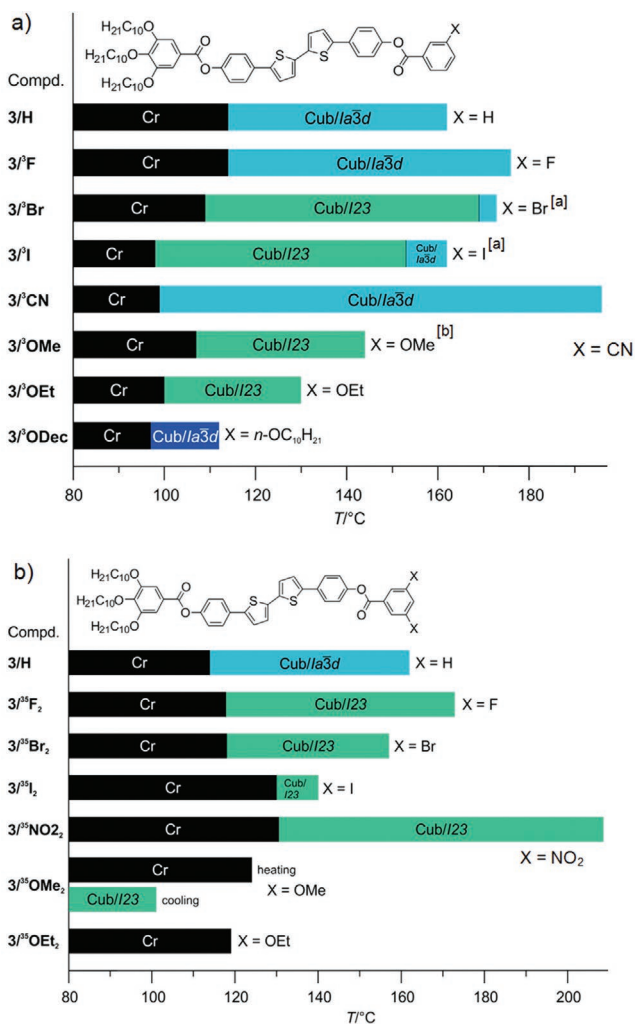


**Figure 4.** Mesophases and transition temperatures a) of compounds  $3/3^mX$  and b) of compounds  $3/3^{35}X_2$ , recorded on heating; for compound  $3/3^mODec$ , a  $Col_{hex}$  phase is formed on cooling from Iso which is rapidly replaced by the  $Ia\bar{3}d$  phase (see Figure S2 in the Supporting Information); the  $Ia\bar{3}d$  phase of  $3/3^mODec$ , indicated by a darker blue, represents a short pitch  $Ia\bar{3}d_{(S)}$  phase, whereas all others, shown in light blue belong to the long pitch  $Ia\bar{3}d_{(L)}$  type. <sup>[a]</sup> For  $3/3^mBr$  and  $3/3^mI$  only, the  $Ia\bar{3}d$  phase is observed on cooling; <sup>[b]</sup> for  $3/3^mOMe$  on cooling,  $Ia\bar{3}d$  and  $I23$  phases were observed, depending on the condition, see Section S1.4 in the Supporting Information; the numerical data are collated in Table S1 in the Supporting Information and for  $3/H$  and  $3/OEt$ , see ref. [87].

additionally contributing to mesophase stability by strengthened segregation.<sup>[15,16,133]</sup> In both series  $3/3^mX$  and  $3/3^{35}X_2$ , there is no significant effect of the volume of the apex on the lattice parameter, it being 15.6–16.4 nm for the  $I23$  phase and 10.4–10.9 nm for the  $Ia\bar{3}d$  phase (Table 2). Only the  $Ia\bar{3}d$  lattice of  $3/3^mODec$  has a significantly smaller size ( $a_{cub} = 9.8$  nm) despite the fact that this compound has the largest and the longest substituent. In the fully intercalated antiparallel organization, the additional long alkyl chain is organized between the other alkyl chains. In this arrangement, the length of the pairs is not changed, but the number of alkyl chains in the periphery grows and this reduces the number of molecules in the network cross-section, which then reduces  $a_{cub}$ .

**Table 2.** Dependence of lattice parameter  $a_{cub}$  and other packing parameters on the volume of the apex ( $V_{apex}$ ) of compounds  $3/3^mX_n$  and  $3a/Y$ .

Compounds <sup>a)</sup>	$V_{apex}$ [nm <sup>3</sup> ]	Cub	$a_{cub}$ [nm]	$n_{raft}$	$\Phi$ [°]
$3/H$	0.11	$Ia\bar{3}d_{(L)}$	10.8	3.9	8.3
$3/3^mF$	0.12	$Ia\bar{3}d_{(L)}$	10.9	3.9	8.2
$3/3^{35}F_2$	0.12	$I23$	15.8	3.3	8.8
$3/3^mCN$	0.13	$Ia\bar{3}d_{(L)}$	10.8	3.7	8.3
$3/3^mBr$	0.14	$Ia\bar{3}d_{(L)}$	10.4	3.5	8.6
		$I23$	16.4	3.5	8.5
$3/3^{35}NO_2$	0.15	$I23$	15.8	3.3	8.8
$3/3^mI$	0.15	$Ia\bar{3}d_{(L)}$	n.d.	–	–
		$I23$	16.2	3.4	8.6
$3/3^mOMe$	0.15	$Ia\bar{3}d_{(L)}$	10.8	3.7	8.3
		$I23$	16.1	3.4	8.7
$3/3^{35}Br_2$	0.15	$I23$	16.1	3.3	8.7
$3/3^mOEt$	0.18	$I23$	15.7	3.2	8.9
$3/3^{35}I_2$	0.19	$I23$	15.6	3.1	9.0
$3/3^mODec$	0.37	$Ia\bar{3}d_{(S)}$	9.8	2.7	9.1
$3/3^{345}F_3$	0.13	$I23$	15.6	3.2	9.0
$3/3^{23456}F_5$	0.14	$I23$	15.6	3.2	9.0
$3/3^{345}OMe$	0.21	$I23$	15.4	2.9	9.1
$3a/Cy$	0.14	$I23$	15.6	3.2	9.0
$3a/Ad$	0.22	$I23$	15.1	2.8	9.2
$3a/CEt_3$	0.18	$Ia\bar{3}d_{(S)}$	8.9	2.4	10.1
$3a/1-Npht$	0.20	$Ia\bar{3}d_{(L)}$	10.6	3.5	8.5
$3a/2-Npht$	0.20	$Ia\bar{3}d_{(L)}$	11.6	4.2	7.7
$3a/Biph$	0.21	$Ia\bar{3}d_{(L)}$	12.0	4.4	7.5

<sup>a)</sup> Abbreviations:  $Ia\bar{3}d_{(S)}$  = short pitch  $Ia\bar{3}d$  phase; for the other abbreviations, see Figure 1 and Table 1;  $V_{apex}$  includes the benzene ring with attached substituents X ( $3/3^mX_n$ ) or the group Y ( $3a/Y$ ); for calculations, see Table S10 in the Supporting Information.

The total length of the networks in each unit cell ( $L_{net}$ ) can be calculated according to  $L_{net} = 8.485a_{Ia\bar{3}d}$  for the  $Ia\bar{3}d$  phase<sup>87</sup> and according to  $L_{net} = 20.68a_{I23}$  for the  $I23$  phase,<sup>[99]</sup> and the number of molecules arranged along this distance is determined by  $L_{net}/n_{cell}$ , where  $n_{cell}$  is the number of molecules per unit cell. Assuming a constant distance between the molecules of 0.45 nm, it is calculated according to  $n_{raft} = n_{cell}/(L_{net}/0.45)$  that about four ( $n_{raft} = 3.9$ ) molecules are organized in the rafts forming the networks of  $3/H$  and only about three ( $n_{raft} = 2.7$ ) for  $3/3^mODec$  (see Table 2). This means that peripheral space filling reduces the diameter of the network segment, which additionally affects the inter-raft twist. In the  $Ia\bar{3}d$  phase, the twist between the molecules in neighboring rafts can be calculated according to  $\Phi(Ia\bar{3}d) = 70.5^\circ/[0.354a_{cub}/0.45 \text{ nm}]^{[87]}$  and in the  $I23$  phase as  $\Phi(I23) = 90^\circ/[0.290a_{cub}/0.45 \text{ nm}]^{[99]}$  Table 2 collates the lattice parameters  $a_{cub}$  and the twist angles  $\Phi$  of compounds  $3/3^mX$  and  $3/3^{35}X_2$  depending on the total volume of the substituted benzene ring at the apex ( $V_{apex}$ ). Interestingly, the calculated twist angle  $\Phi$  continuously rises with expanding apex volume across the  $Ia\bar{3}d \rightarrow I23 \rightarrow Ia\bar{3}d$  transitions from  $8.2^\circ$  to  $8.6^\circ$  in  $Ia\bar{3}d$  via  $8.5^\circ$ – $9.0^\circ$  in  $I23$  to  $9.1^\circ$  for the  $Ia\bar{3}d$  phase of  $3/3^mODec$ . This means that with increasing size of the



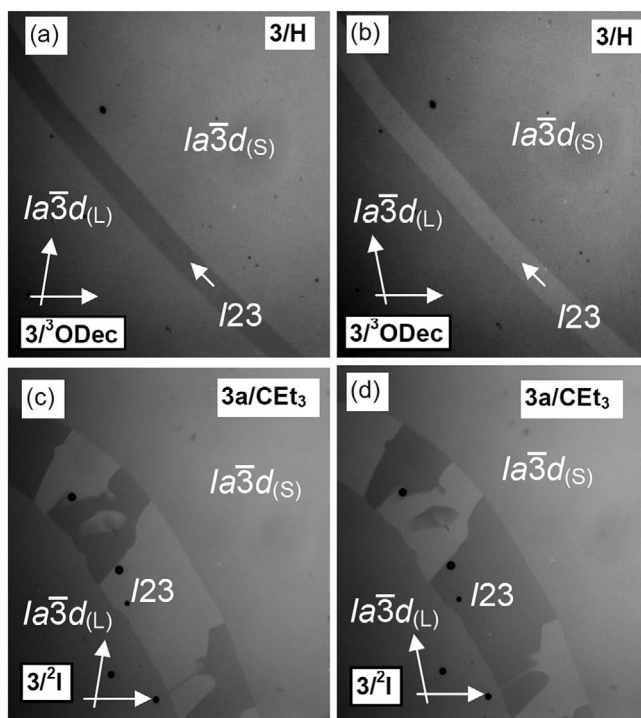


**Figure 5.** Ribbon of the chiral  $I23$  phase developing in the contact region between the achiral  $Ia\bar{3}d$  phases of a,b)  $3/H$  (top/right) and  $3/{}^3\text{ODec}$  (bottom/left) as observed at  $T = 104^\circ\text{C}$  (on cooling, the  $I23$  phase is formed below  $124^\circ\text{C}$  and on heating, it disappears at  $141^\circ\text{C}$ ) and c,d)  $3a/\text{CEt}_3$  (top/right) and  $3/{}^1\text{I}$  (bottom/left) as observed at  $T = 115^\circ\text{C}$  (on cooling, the  $I23$  phase is formed below  $117^\circ\text{C}$  and on heating, it disappears at  $132^\circ\text{C}$ ) after uncrossing the polarizer and analyzer in opposite directions; contrast enhanced, the width of the images is  $0.5\text{ mm}$ .

apex, the helical twist becomes larger and the pitch becomes shorter and therefore a frustration between pitch length and the distance between the junctions arises in the  $Ia\bar{3}d$  phase. At a certain degree of frustration, the  $Ia\bar{3}d$  phase is replaced by the triple network structure with  $I23$  lattice, allowing a larger twist angle  $\Phi$ . However, this advantage of the  $I23$  lattice obviously exists only for a certain range of the helical pitch and upon further increasing the volume of the apex, a mismatch arises also in  $I23$ . The  $I23$  phase appears to be even more sensitive to any mismatch between junction distance and pitch length and after reaching this limit, the  $Ia\bar{3}d$  lattice becomes the thermodynamically more stable mode of self-assembly again. This means that there is a long pitch ( $Ia\bar{3}d_{(L)}$ ) and a short pitch ( $Ia\bar{3}d_{(S)}$ ) phase which are separated by the  $I23$  phase.

### 3.2.4. 3,4-Disubstituted Compounds

In contrast to the 3,5-disubstitution pattern (Figure 4b), 3,4-disubstitution (Figure 6a) stabilizes the cubic phases by 30–40 K compared to the 3-monosubstituted, whereas the effect on the cubic phase type is weaker than for the 3,5 disubstitution pattern. For example, the  $I23$  phase of  $3/{}^3\text{OMe}$  is removed and the  $Ia\bar{3}d$  phase becomes dominant again for the 3,4-dimethoxy-substituted compound  $3/{}^{34}\text{OMe}_2$ . Because no induced  $I23$  phase could be found in the contact region between the  $Ia\bar{3}d_{(L)}$  phase of compound

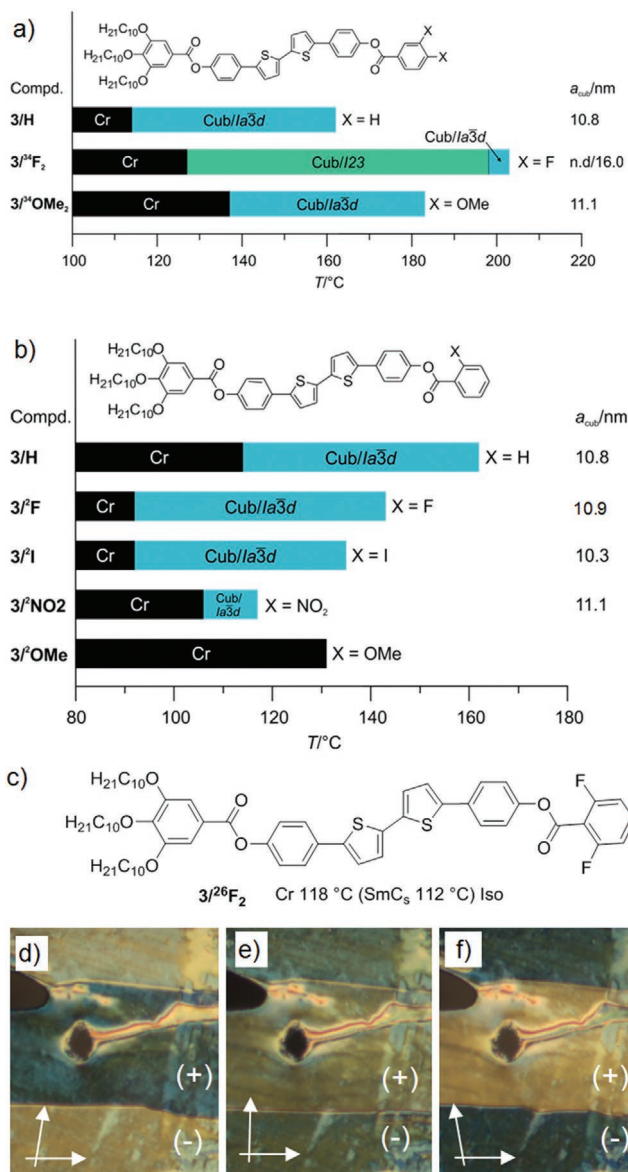


**Figure 6.** Mesophases, transition temperatures, and lattice parameters of a) compounds  $3/{}^{34}\text{X}_2$  and b) of compounds  $3/{}^2\text{X}$ , recorded on heating; in all cases, the  $Ia\bar{3}d$  phase represents a long pitch  $Ia\bar{3}d_{(L)}$  phase (for numerical data of  $3/H$  and  $3/{}^{34}\text{OMe}_2$ , see ref. [87], for all other compounds, see Table S1 in the Supporting Information). c) Molecular structure and transition temperatures ( $T/^\circ\text{C}$ ) of compound  $3/{}^{26}\text{F}_2$  and d–f) chiral domains as observed by POM of the SmC<sub>s</sub> phase of  $3/{}^{26}\text{F}_2$  in a homotropic cell, the view is parallel to the helix axis developing between the two substrate surfaces; for textures observed by rotating the sample between the polarizers, see Figure S4 in the Supporting Information and for a planar texture, see Figure S3 in the Supporting Information.

$3/H$  and the  $Ia\bar{3}d$  phase of  $3/{}^{34}\text{OMe}_2$  (see Figure S5 in the Supporting Information), it is confirmed to belong to the long pitch  $Ia\bar{3}d_{(L)}$  type. This indicates that 4-substitution provides a smaller twisting power and can reduce the stronger effect of the lateral substituents. This reduced twist is also evident from the comparison of the 4- and 3-decyloxy-substituted compounds  $3/{}^4\text{ODec}$  and  $3/{}^3\text{ODec}$  (Figures 3a and 4a) where only the 3-substituted forms the short pitch  $Ia\bar{3}d_{(S)}$  phase and the 4-substituted is still  $I23$ .

### 3.2.5. 2-Substituted and 2,6-Disubstituted Compounds

As expected, the cubic phases are destabilized by the 2-substituents at the apex, due to their especially strong distorting steric effect on the molecular packing in this position (Figure 6b). The cubic phase stability is even for the fluorinated compound  $3/{}^2\text{F}$  and the 2-nitro-substituted compound  $3/{}^2\text{NO}_2$  reduced compared to  $3/\text{H}$ , and the 2-OMe-substituted compound  $3/{}^2\text{OMe}$  does not show any LC phase (melting point: 131 °C). The very different effect of 2-substitution by the  $\text{NO}_2$  group compared to 3-substitution becomes obvious by comparing Figures 4b and 6b. It appears that in 2-position, the mesophase stabilizing effect of this electron acceptor group is switched off and only the destabilizing steric effect remains. This might be due to a twist introduced around the COO group which hinders the electrostatic interaction with the sterically demanding trialkoxy-substituted donor ring in the antiparallel packing. That even in this case the  $\text{Cub}_{\text{bi}}$  phase is retained demonstrates clearly the robustness of the design concept of  $3/0$  tritatenars. While the 2-substitution strongly reduces the stability of the cubic phase, there is no change in the cubic phase type; even  $3/{}^2\text{I}$  forms exclusively the long pitch  $Ia\bar{3}d_{(\text{L})}$  phase, as confirmed by the induction of a chiral  $I23$  phase in the contact region with the  $Ia\bar{3}d_{(\text{S})}$  phase of  $3\text{a}/\text{CEt}_3$  (Figure 5c,d). By contrast, for the isomeric laterally 3-substituted compound  $3/{}^3\text{I}$ , the  $I23$  phase dominates (Figure 4a).

Compound  $3/{}^{26}\text{F}_2$  having two *ortho*-fluorines in the 2- and 6-positions does not form any cubic phase. This compound melts at 118 °C and shows only a monotropic and synclitic tilted  $\text{SmC}_s$  phase on cooling below 112 °C (Figure 6c). A special feature of the  $\text{SmC}_s$  phase of  $3/{}^{26}\text{F}_2$  is the formation of chiral domains in thin homeotropically aligning cells, indicated by an optical texture showing a conglomerate of dark and bright domains inverting their brightness upon inverting the twist sense of the analyzer (Figure 6d–f) and remaining unchanged by rotation of the sample between crossed polarizers (Figure S4, Supporting Information).<sup>[134,135]</sup> In the case of compound  $3/{}^{26}\text{F}_2$ , the steric effects of the two *ortho*-fluorines can obviously stabilize helical conformers around the COO group,<sup>[136]</sup> thus supporting chirality synchronization by helix formation between the substrate surfaces.<sup>[137]</sup> Overall, substitution in the 2-position has a strong destabilizing effect on the  $\text{Cub}_{\text{bi}}$  phase without significantly affecting the cubic space group.

### 3.2.6. 3,4,5-Trisubstituted and 2,3,4,5,6-Pentasubstituted Compounds

The effect of 3,4,5-trisubstitution is shown in Figure 7 for F and OMe substituents as examples. Only the  $I23$  type  $\text{Cub}_{\text{bi}}$  phase is observed for both compounds. Again, the additional additional fluorine in the 4-position of the trisubstituted compound  $3/{}^{345}\text{F}_3$  enhances the cubic phase stability compared to the 3,5-disubstituted compound  $3/{}^{35}\text{F}_2$  by 25 K (Figure 4b). A similar stabilization is observed by comparing the methoxy-substituted compounds  $3/{}^{35}\text{OMe}_2$  (Figure 4b) and  $3/{}^{345}\text{OMe}_3$  (Figure 7). Even the pentafluorobenzoate  $3/{}^{23456}\text{F}_5$  shows exclusively a broad  $\text{Cub}_{\text{bi}}$  phase over a range exceeding that of the nonfluorinated compound  $3/\text{H}$  with a smaller apex. This is mainly attributed to

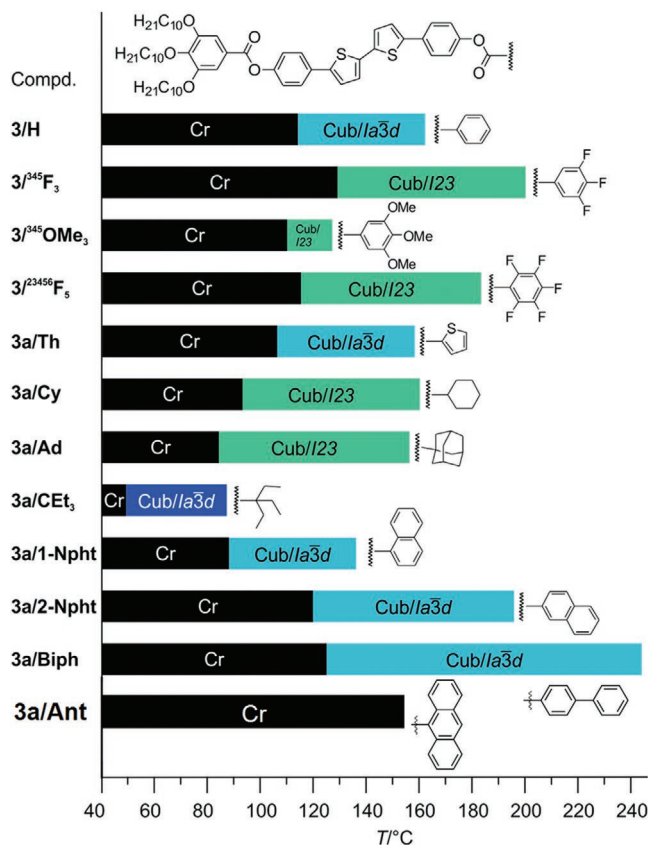


**Figure 7.** Mesophases and transition temperatures of compounds with different types of apex groups on heating; the  $Ia\bar{3}d$  phase of  $3\text{a}/\text{CEt}_3$ , indicated by a darker blue represents a short pitch  $Ia\bar{3}d_{(\text{S})}$  phase, whereas all others, shown in light blue belong to the long pitch  $Ia\bar{3}d_{(\text{L})}$ ; for numerical data of  $3/\text{H}$  and  $3/{}^{345}\text{OMe}_3$ , see ref. [87], for compounds  $3\text{a}/\text{Cy}$ ,  $3\text{a}/\text{Ad}$  and  $3\text{a}/\text{CEt}_3$ , see ref. [117], for all other data, see Tables S1 and S2 in the Supporting Information).

the electron withdrawing effect of the fluorines, increasing the polar core–core interactions. That the steric effect of fluorination is moderate is indicated by the fact that only the  $I23$  phase, but not the short pitch  $Ia\bar{3}d_{(\text{S})}$  phase is observed for the polyfluorinated compounds. Thus, the taper-shaped tritatenars tolerate multiple substitutions at the apex, allowing easy access to  $\pi$ -systems with distinct electronic properties, while retaining their organization in a well-defined 3D network with cubic symmetry. The major general trends provided by the different apex structures and their substitution patterns are summarized in Figure 8.

## 3.3. Tailoring the Cubic Phases by Heterocyclic, Polycyclic Aromatic, and Alicyclic Units at the Apex (Compounds $3\text{a}/\text{Y}$ )

### 3.3.1. Heterocycles and Alicycles at the Apex

Whereas no effect of replacement of benzene at the apex by thiophene is observed, replacing benzene by cyclohexane changes the cubic phase type from  $Ia\bar{3}d$  to  $I23$ , indicating that the aliphatic ring acts as a larger substituent, especially

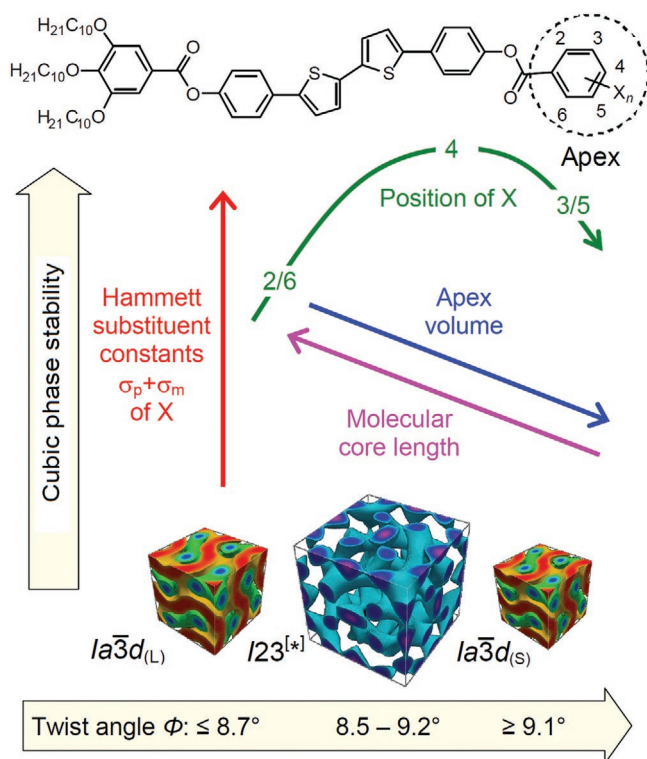


**Figure 8.** Summary of the relations between molecular structure, helical twist, cubic phase type, and cubic phase stability of compounds  $3^m/Y_n$  and  $3a/Y$ ; the slight overlap of the helical twist angles results from uncertainties in the determination of the molecular volumes by the used increments<sup>[130]</sup> and possible effects of electrostatic core–core interactions, additionally contributing to the self-assembly.

due to the additional axial H-atoms which change the flat aromatic ring into a bulky substituent expanded in all three spatial dimensions (Figure 7 and Table 2). It is remarkable that even for the large polycyclic adamantyl group ( $3a/Ad$ ), the  $I23$  phase is retained with almost the same  $Cub_{bi}$ -Iso transition temperature as for the cyclohexyl-substituted compound  $3a/Cy$ .<sup>[117]</sup> Even the triethylacetate  $3a/CET_3$ , which can be considered as a noncyclic ring-opened relative of the adamantane compound  $3a/Ad$ , forms a cubic phase, though with reduced stability.<sup>[117]</sup> That these large substituents at the apex cannot remove the cubic phase confirms once more the robustness of this molecular design concept. In contrast to  $3a/Ad$  with an  $I23$  phase, the cubic phase of  $3a/CET_3$  has an  $Ia\bar{3}d$  space group. The small cubic lattice parameter of  $3a/CET_3$  ( $a_{cub} = 8.85$  nm) and the large twist ( $\Phi = 10.1^\circ$ ) are in line with a short pitch  $Ia\bar{3}d_{(S)}$  phase, which is confirmed by the induction of a chiral  $I23$  phase in the contact region with the  $Ia\bar{3}d_{(L)}$  phase of  $3/H$  (see Figure S6 in the Supporting Information). It shows that the triethylacetate group of  $3a/CET_3$  acts as an even larger substituent than adamantane. The larger effective size should be the result of the increased conformational flexibility compared to adamantane, allowing more bulky conformations to be involved in the equilibrium. The change of the cubic phase type upon increasing the cycloaliphatic ring size from cyclobutyl to cyclododecyl is described in more detail in a previous communication.<sup>[117]</sup> Overall, these bulky aliphatic apex structures have

a strong steric effect on mesophase stability, as well as a strong effect on network helicity.

### 3.3.2. Condensed Aromatics and Biphenyl at the Apex

Broad regions of the  $Ia\bar{3}d_{(L)}$  phase were found for the two naphthalene derivatives, where the higher transition temperatures were observed for the 2-naphthoic acid derivative with the naphthyl group arranged colinear with the rod-like core (Figure 7). By contrast, the side-on attached 1-substituted naphthalene leads to a reduction of the cubic phase stability and the anthracene-9-carboxylate  $3a/Anth$  with two laterally annulated benzene rings does not show any LC phase (Figure 7). Based on the calculated twist angles  $\Phi$  (Table 2) and in line with the results of the optical investigation of the contact regions with the  $Ia\bar{3}d_{(L)}$  and  $Ia\bar{3}d_{(S)}$  phases of related compounds (see Figures S7 and S8 and the additional discussions in Section S14.3 in the Supporting Information), the cubic phase of compounds  $3a/1-Npht$ ,  $3a/2-Npht$ , and  $3a/Biph$  is of the same long pitch  $Ia\bar{3}d_{(L)}$  type. Elongation of the rod-like core by the coaxial 2-naphthyl unit, or by replacing the single benzene ring by a linear biphenyl unit stabilizes the cubic phase (Figure 7), increases the lattice parameter, and reduces the twist angle between adjacent molecules along the networks segment if compared to  $3/H$  (Table 2). Overall, there is a very different behavior of aromatic and cycloaliphatic<sup>[117]</sup> end groups. The flat and rigid aromatics contribute to the length and volume of the core unit and thus reduce the twist angle between the cores, retaining the  $Ia\bar{3}d_{(L)}$  phase. By contrast, aliphatic and cycloaliphatic units tend to segregate from the core and contribute to the space filling in the aliphatic periphery, thus increasing the twist, disfavoring the  $Ia\bar{3}d_{(L)}$  and tending toward  $I23$  and ultimately to  $Ia\bar{3}d_{(S)}$ .

## 3.4. Discussion of Cubic Self-Assembly and Mirror Symmetry Breaking in Relation to the Molecular Structure

### 3.4.1. Helical Twist and Cubic Phase Formation

The lateral distance between the two networks in the  $Ia\bar{3}d$  phase, corresponding to the distance between the minimal surfaces, and calculated as  $d_{net} = \sqrt{3}a_{cub}/4 = 4.7\text{--}4.8$  nm, is only a little bit larger than  $L_{mol}$  (4.4–4.6 nm for most compounds). The antiparallel organization of the molecules with full intercalation of the rod-like cores (Figure 3b) would lead to a length of these pairs of around 6.1 nm. The difference to  $d_{net}$  is considered to be due to partial alkyl chain intercalation and chain folding to efficiently fill the space around the networks. The interfacial curvature provided by the 2:3 ratio of core to alkyl chain cross-sectional areas at the interfaces in this organization of the 3/0 tricaténars (Figure 9b,c) appears to be just right for the formation of  $Cub_{bi}$  phases. A larger 2:4 ratio is obtained for the tetracatenars (Figure 9d,e). Though the 3/1 tetracatenars (Figure 9d) form predominately  $Cub_{bi}$  phases too, the symmetric 2/2 tetracatenars (Figure 9e) are much more sensitive to structural modifications and have, if any, only small  $Cub_{bi}$  ranges beside the dominant lamellar and columnar phases.<sup>[69,116,120–124]</sup> One may argue that, on average, rafts of antiparallel 3/1 tetracatenars are equivalent to those of 2/2



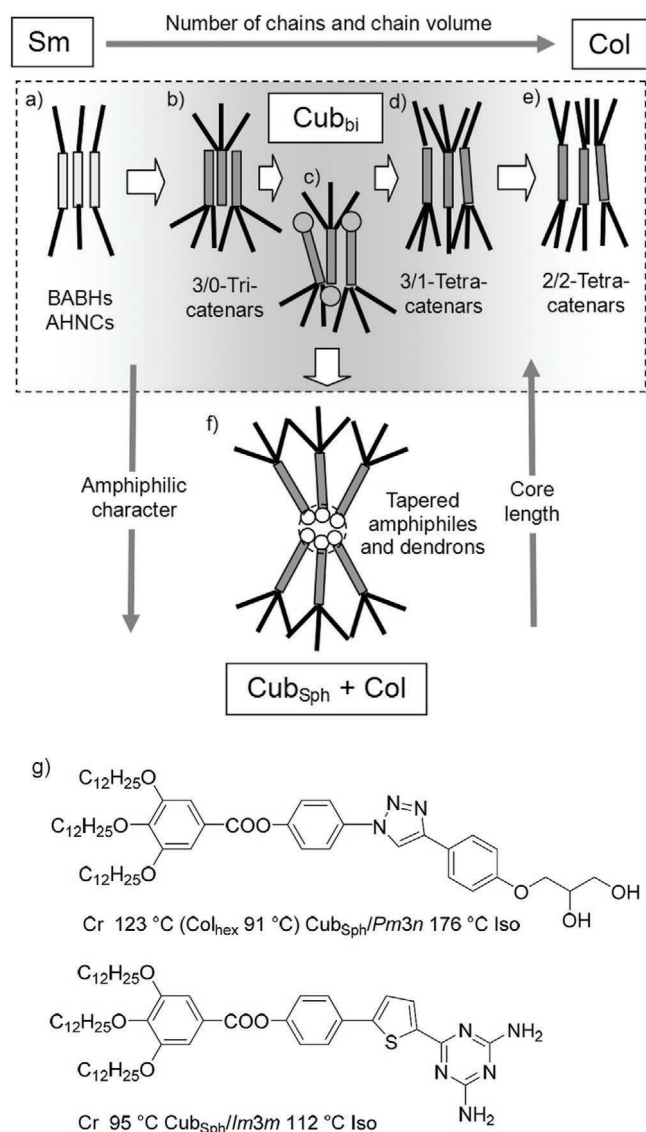


**Figure 9.** a–e) Sketches of self-assembly of cubogenic rod-like molecules depending on the molecular structure (cross-sections of the ribbon-like or columnar segments of the networks). The compounds reported herein belong to types (b–d); f) shows the organization of amphiphilic tapered molecules and g) examples of taper-shaped tricatennars forming micellar (spheroidal) cubic phases ( $Cub_{Sph}$ ).

tetracatenars. However, as the ribbon winds its way through the surrounding of other twisted ribbons, its immediate environment changes and while at one point a symmetric arrangement may be ideal, at other points, more chains may be needed on one side of the ribbon than on the other to plug a local void. Symmetric polycatenars cannot adjust to such local steric requirements. However, it is surprising that such a huge variety of different types of apex substitution, even involving extremely bulky groups as adamantane (**3a/Ad**), pentafluorobenzene (**3/**<sup>23456</sup>**F**<sub>5</sub>), naphthalene (**3a/1-Npht**), and highly branched alkyl chains (**3a/CEt**<sub>3</sub>) can lead to such broad temperature ranges of  $Cub_{bi}$  network phases (Figure 7). It appears that these bulky end groups, favoring the helical twist, allow a denser molecular packing due to an at least

partial synchronization of the overall helical molecular conformers.<sup>[86,95,96,138]</sup> This seems to provide an additional advantage compared to competing lamellar phases, disfavoring the twist, and the columnar phases, having only short range helix correlation.<sup>[95,96,139,140]</sup> If the enthalpic gain of uniform helix packing, provided by the long range transmission of helicity by network formation, exceeds the entropic penalty of chirality synchronization, then the  $Cub_{bi}$  networks can be additionally stabilized over the competing lamellar and columnar modes of self-assembly. It appears that this  $Cub_{bi}$  phase stabilizing effect of polyaromatic cores is more general. For example, robust bicontinuous cubic phases were even found for polyaromatic rods with only two alkyl chains (Figure 9a, e.g., BABHs<sup>[107,108]</sup> and the hydrogen-bonded dimers of the ANBCs, see Figure 1c,d).<sup>[16,101,103,104]</sup> In these cases, alkyl chain intercalation or replacing the alkyl chains by perfluorinated chains<sup>[141,142]</sup> or by adding bulky silyl groups<sup>[74,108]</sup> provides the required interfacial curvature for  $Cub_{bi}$  phase formation. Permanent molecular chirality can further support the helical twist, leading to a series of chirality frustrated LC phases.<sup>[53–55,143]</sup> This contribution of helical packing to  $Cub_{bi}$  phase stabilization is absent for flexible amphiphilic molecules<sup>[7]</sup> and their dendritic<sup>[18,144]</sup> and polymeric analogs (block copolymers)<sup>[10]</sup> which limits their capability of  $Cub_{bi}$  phase formation to narrower ranges and this explains the unexpected  $Cub_{bi}$  phase stability of properly designed rod-like compounds.

Polar substituents like CN and NO<sub>2</sub> with the highest polarity and electron acceptor properties (large  $\sigma_m$  and  $\sigma_p$  Hammett constants, see Table 1 and Table S11 in the Supporting Information) show an especially strong stabilizing effect on the cubic phases due to dipolar interactions and the strengthening of the electrostatic interactions between the electron-rich trialkoxylated and the electron-poor CN-/NO<sub>2</sub>-substituted ends. It appears that polar 3- and 4-substitutions favor a dense packing and increase the intermolecular twist, whereas 2-substitution predominately favors intramolecular twist and reduces the core packing density for steric reasons, thus favoring a transition to lamellar phases (Figure 8). However, only the double *ortho*-substitution of the apex in **3/**<sup>26</sup>**F**<sub>2</sub> and the lateral annulation by two benzene rings in compound **3a/Anth** can remove the cubic phases completely.

Further increasing the polarity of the apex substituents, as for example, by introduction of ionic groups or hydrogen bonding groups has the opposite effect and leads, as shown previously, to hexagonal columnar and micellar cubic phases ( $Cub_{Sph}$ ), even for compounds with a long rigid core (Figure 9g).<sup>[145–152]</sup> In all these cases, the segregation of the polar apex from the aromatic cores sets in, which inhibits the antiparallel side-by-side packing of the aromatic cores (Figure 9f). This changes the ratio of aromatic to aliphatic cross-section areas from 2:3 to 1:3, leading to a much stronger interfacial curvature, favoring columnar and micellar self-assembly. Similarly, reducing the rod length and thus increasing the taper angle supports higher interfacial curvature, too.<sup>[18–21,75,144,145,153]</sup>

#### 3.4.2. Helical Twist and the $1a\bar{3}d_{(L)}-123-1a\bar{3}d_{(S)}$ – Cubic Phase Sequence

For the tapered 3/0 tricatennars reported herein, there is a strong dependence of the space group on the size and position of the

substituent(s) at the apex, leading to the sequence  $Ia\bar{3}d_{(L)} \rightarrow I23 \rightarrow Ia\bar{3}d_{(S)}$  with apex size expansion (Figure 8).<sup>[132]</sup> In line with the double network structure of the  $Ia\bar{3}d$  phase and a triple network structure of the  $I23$  phase, the lattice parameter increases by about  $50 \pm 10\%$  at the  $Ia\bar{3}d_{(L)}$ -to- $I23$  transitions. However, within the  $Ia\bar{3}d$  and the  $I23$  phases, the cubic lattice parameter is almost independent of the size of the apex substituent. There is obviously a compensation of the increasing molecular volume, tending to increase  $a_{\text{cub}}$ , opposed by the increasing twist angle between successive rafts and decreasing the number of molecules in a raft, both contributing to a reduction in  $a_{\text{cub}}$  (Tables 1 and 2 and Table S10 in the Supporting Information). Because the molecules in the twisted ribbons must arrive almost perpendicular to the plane of the network junction, a frustration arises between optimal helical pitch and the junction distance. At the same time, the twist angle  $\Phi$  between successive rafts is a compromise between  $\Phi$ -increasing tendency of the clashing end groups and the  $\Phi$ -reducing tendency of the rod-like cores, which prefer to lie parallel and maximize their  $\pi$ - $\pi$  interaction. Another contribution comes from the diastereomeric relation and coupling between supra-molecular helical twist and transient molecular helicity. All these affect the choice of the cubic phase type.<sup>[87,95]</sup> Each structure in the sequence  $Ia\bar{3}d_{(L)}$ - $I23$ - $Ia\bar{3}d_{(S)}$  represents the solution best suited to accommodate a certain range of the twist angle  $\Phi$ . With increasing apex size, the increasing  $\Phi$  reaches up to about  $8.7^\circ$  for the long pitch  $Ia\bar{3}d_{(L)}$  phase,  $8.5^\circ$ - $9.2^\circ$  for the  $I23$  phase, and  $\geq 9.1^\circ$  for the short pitch  $Ia\bar{3}d_{(S)}$  phase (see Figure 8, Tables 1 and 2, and Table S10 in the Supporting Information). These values refer to molecules involving the bisbenzoylated 5,5'-diphenyl-2,2'-bithiophene core unit. They can deviate from these values, for example, if the alkyl chain at the apex is especially long ( $X = \text{OC}_{10}\text{H}_{21}$ ), or as the length and shape of the core is changed, though the fundamental phase sequence remains the same.<sup>[117]</sup> Depending on the contribution of the substituent to the volume effect and the twist, the lattice parameter can increase, as observed for the BABHs and ANBCs,<sup>[101,103,104,107,108]</sup> remain almost constant, as reported here for compounds  $3^m\text{X}_n$  and  $3a/Y$ , or even decreases with increasing volume of the substituents, as recently reported for benzil-based polycatenars.<sup>[154]</sup> However, in all cases, the twist angle increases with the apex volume, leading to the sequence  $Ia\bar{3}d_{(L)}$ - $I23$ - $Ia\bar{3}d_{(S)}$ . While the cubic phase destabilizing steric effect of apex substitution increases from the 4- via the 3- to the 2-position, the effect on the  $\text{Cub}_{\text{bi}}$  phase structure is the largest for the sidewise-directed lateral 3-position and is smaller for the inward-directed lateral 2- and the terminal 4-position (Figure 8).

## 4. Summary and Conclusions

Overall, the concept of taper-shaped 3/0 tricenars, involving an extended rod-like unit, represents a new robust platform for the design of LC network structures with cubic symmetry. In most cases, the  $\text{Cub}_{\text{bi}}$  phases ( $Ia\bar{3}d$  and  $I23$ ), representing interwoven networks with 3-way junctions, are the only observed LC phases in wide temperature ranges and for a wide variety of groups attached to the apex, including perfluorinated aromatics, heteroaromatics, alicyclic and polycyclic rings, and even for highly

branched chains (Figures 3, 4, 6–8). Often, these network phases are stable down to ambient temperature (Tables S1 and S2, Supporting Information). An organization with locally adjustable antiparallel side-by-side packing of the rod-like cores, leading to a 2:3 average ratio of core-to-chain width (Figures 3b and 9b,c), is proposed to be responsible for the robustness of the  $\text{Cub}_{\text{bi}}$  phases and their strongly preferred formation over lamellar and columnar modes of organization. The chirality-synchronized helical packing in the networks is thought to additionally stabilize the cubic phases by allowing a denser molecular packing. The observed insensitivity of cubic network formation to apex substitution by a large diversity of functional groups allows tuning of the electronic properties (HOMO–LUMO bandgap) of the  $\pi$ -conjugated rod-like cores organized in the helical networks. This potential for application as functional materials is augmented by the possibility of switching between an achiral ( $Ia\bar{3}d$ ) and chiral ( $I23$ ) state. With increasing size of the apex the sequence  $Ia\bar{3}d_{(L)}$ - $I23$ - $Ia\bar{3}d_{(S)}$  is observed which appears to be universal and is explained by an increasing helical twist along the networks (see Figure 8, Tables 1 and 2, and Table S10 in the Supporting Information). The long pitch and short pitch  $Ia\bar{3}d$  phases are considered as distinct ranges of the same macroscopically achiral gyroid double network phase, which is interrupted for a certain twist angle range by the homochiral triple network  $I23$  phase (Figure 8). The helical twist angle can be adjusted by design of the individual molecules or, alternatively, by mixing short and long pitch  $Ia\bar{3}d$  phases (Figure 5).

Overall, this work provides a general understanding of supra-molecular self-assembly in  $\text{Cub}_{\text{bi}}$  network phases depending on details of the molecular structure and thus paves the way to the directed design of cubogenic and spontaneously chiral functional materials with tunable application-relevant properties. More generally, it provides insights into the process of spontaneous mirror symmetry breaking in soft matter,<sup>[95,96,136,155]</sup> and it shows the importance of network formation for this process. Spontaneous emergence of chirality during self-assembly is also of paramount interest for circularly-polarized emission<sup>[46–48]</sup> and photonic applications,<sup>[27,28]</sup> and for new dynamic routes to absolute enantioselective synthesis.<sup>[156–158]</sup>

## Supporting Information

Supporting Information is available from the Wiley Online Library or from the author.

## Acknowledgements

C.D. and T.R. contributed equally to this work. For support with synchrotron experiments, the authors are grateful to Dr. O. Shebanova and Prof. N. Terill at station I22, Diamond Light Source, and Dr. O. Bikondoa and Dr. P. Thompson at the EPSRC-funded XMaS beam line at ESRF. Financial support is acknowledged from the 111 Project 2.0 of China (Grant No. BP2018008) and from the EPSRC (Grant Nos. EP-P002250, EP-T003294).

## Conflict of Interest

The authors declare no conflict of interest.



## Keywords

bicontinuous cubic phases, chirality, helical superstructures, liquid crystals, mirror symmetry breaking, self-assembly, supramolecular networks

Received: May 20, 2020

Revised: July 6, 2020

Published online:

- [1] S. Otto, *Acc. Chem. Res.* **2012**, *45*, 2200.
- [2] B. A. Grzybowski, K. Fitzner, J. Paczesny, S. Granick, *Chem. Soc. Rev.* **2017**, *46*, 5647.
- [3] M. O'Keeffe, O. M. Yaghi, *Chem. Rev.* **2012**, *112*, 675.
- [4] S. Hyde, S. Andersson, K. Larsson, Z. Blum, T. Landh, S. Lidin, B. W. Ninham, *The Language of Shape: The Role of Curvature in Condensed Matter: Physics, Chemistry and Biology*, Elsevier, Amsterdam **1997**.
- [5] M. L. Lynch, P. T. Spicer, *Bicontinuous Liquid Crystals*, Surfactant Science Series, Vol. 127, CRC Press – Taylor & Francis Group, Boca Raton, FL, USA **2005**.
- [6] V. Luzzati, R. Vargas, P. Mariani, A. Gulik, H. Delacroix, *J. Mol. Biol.* **1993**, *229*, 540.
- [7] J. M. Seddon, R. H. Templer, in *Handbook of Biological Physics*, Vol. 1 (Eds: R. Lipowsky, E. Sackmann), Elsevier, Amsterdam **1995**, pp. 97–160.
- [8] G. L. Jackson, D. V. Perroni, M. K. Mahanthappa, *J. Phys. Chem. B* **2017**, *121*, 9429.
- [9] M. A. Shcherbina, A. V. Bakirova, A. N. Yakunin, V. Percec, U. Beginn, M. Möller, S. N. Chvalun, *Crystallogr. Rep.* **2012**, *57*, 151.
- [10] A. J. Meuler, M. A. Hillmyer, F. S. Bates, *Macromolecules* **2009**, *42*, 7221.
- [11] S. Diele, P. Göring, in *Handbook of Liquid Crystals*, Vol. 2B (Eds: D. Demus, J. Goodby, G. W. Gray, H.-W. Spiess, V. Vill), Wiley-VCH, Weinheim, Germany **1998**, pp. 887–900.
- [12] S. Diele, *Curr. Opin. Colloid Interface Sci.* **2002**, *7*, 333.
- [13] M. Imperor-Clerc, *Curr. Opin. Colloid Interface Sci.* **2005**, *9*, 370.
- [14] G. Ungar, F. Liu, X. Zeng, in *Handbook of Liquid Crystals*, Vol. 5, 2nd ed. (Eds: J. W. Goodby, P. J. Collings, T. Kato, C. Tschierske, H. F. Gleeson, P. Raynes), Wiley-VCH, Weinheim **2014**, pp. 363–436.
- [15] C. Tschierske, *Angew. Chem., Int. Ed.* **2013**, *52*, 8828.
- [16] C. Tschierske, *J. Mater. Chem.* **2001**, *11*, 2647.
- [17] S. Kutsumizu, *Isr. J. Chem.* **2012**, *52*, 844.
- [18] S. N. Chvalun, M. A. Shcherbina, A. N. Yakunin, J. Blackwell, V. Percec, *Polym. Sci., Ser. A* **2007**, *49*, 158.
- [19] K. Borisch, S. Diele, P. Göring, C. Tschierske, *Chem. Commun.* **1996**, 237.
- [20] K. Borisch, S. Diele, P. Göring, H. Kresse, C. Tschierske, *J. Mater. Chem.* **1998**, *8*, 529.
- [21] K. Borisch, C. Tschierske, P. Göring, S. Diele, *Chem. Commun.* **1998**, 2711.
- [22] L. van 't Hag, S. L. Gras, C. E. Conn, C. J. Drummond, *Chem. Soc. Rev.* **2017**, *46*, 2705.
- [23] H. M. G. Barriga, M. N. Holme, M. M. Stevens, *Angew. Chem., Int. Ed.* **2019**, *58*, 2958.
- [24] C. E. Conn, C. J. Drummond, *Soft Matter* **2013**, *9*, 3449.
- [25] M. Antonietti, *Philos. Trans. R. Soc., A* **2006**, *364*, 2817.
- [26] N. Marets, D. Kuo, J. R. Torrey, T. Sakamoto, M. Henmi, H. Katayama, T. Kato, *Adv. Healthcare Mater.* **2017**, *6*, 1700252.
- [27] K. Bisoyi, T. J. Bunning, Q. Li, *Adv. Mater.* **2018**, *30*, 1706512.
- [28] H.-Y. Hsueh, Y.-C. Ling, H.-F. Wang, L.-Y. C. Chien, Y.-C. Hung, E. L. Thomas, R.-M. Ho, *Adv. Mater.* **2014**, *26*, 3225.
- [29] L. Han, S. Che, *Adv. Mater.* **2018**, *30*, 1705708.
- [30] W. Pisula, M. Zorn, J. Y. Chang, K. Müllen, R. Zentel, *Macromol. Rapid Commun.* **2009**, *30*, 1179.
- [31] M. Funahashi, *J. Mater. Chem. C* **2014**, *2*, 7451.
- [32] Y. Shimizu, K. Oikawa, K.-i. Nakayama, D. Guillon, *J. Mater. Chem.* **2007**, *17*, 4223.
- [33] M. Funahashi, H. Shimura, M. Yoshio, T. Kato, *Struct. Bonding* **2008**, *128*, 151.
- [34] J. Hanna, A. Ohno, H. Iino, *Thin Solid Films* **2014**, *554*, 58.
- [35] M. Kumar, S. Kumar, *Polym. J.* **2017**, *49*, 85.
- [36] S. Sergeyev, W. Pisula, Y. H. Geerts, *Chem. Soc. Rev.* **2007**, *36*, 1902.
- [37] T. Kobayashi, Y.-X. Li, A. Ono, X.-B. Zeng, T. Ichikawa, *Chem. Sci.* **2019**, *10*, 6245.
- [38] T. Kobayashi, T. Ichikawa, T. Kato, H. Ohno, *Adv. Mater.* **2017**, *29*, 1604429.
- [39] H. Zhang, L. Li, M. Möller, X. Zhu, J. J. Hernandez Rueda, M. Rosenthal, D. A. Ivanov, *Adv. Mater.* **2013**, *25*, 3543.
- [40] T. Kato, M. Yoshio, T. Ichikawa, B. Soberats, H. Ohno, M. Funahashi, *Nat. Rev. Mater.* **2017**, *2*, 17001.
- [41] T. Kato, J. Uchida, T. Ichikawa, T. Sakamoto, *Angew. Chem., Int. Ed.* **2018**, *57*, 4355.
- [42] T. Ichikawa, M. Yoshio, A. Hamasaki, S. Taguchi, F. Liu, X. B. Zeng, G. Ungar, H. Ohno, T. Kato, *J. Am. Chem. Soc.* **2012**, *134*, 2634.
- [43] E. J. W. Crossland, M. Kamperman, M. Nedelcu, C. Ducati, U. Wiesner, D.-M. Smilgies, G. E. S. Toombes, M. A. Hillmyer, S. Ludwigs, U. Steiner, H. J. Snaith, *Nano Lett.* **2009**, *9*, 2807.
- [44] J.-M. Suisse, H. Mori, H. Monobe, S. Kutsumizu, Y. Shimizu, *Soft Matter* **2011**, *7*, 11086.
- [45] G. Park, K. Goossens, T. J. Shin, C. W. Bielawski, *Chem. - Eur. J.* **2018**, *24*, 6399.
- [46] F. Song, Z. Zhao, Z. Liu, J. W. Y. Lam, B. Z. Tang, *J. Mater. Chem. C* **2020**, *8*, 3284.
- [47] Y. Sang, J. Han, T. Zhao, P. Duan, M. Liu, *Adv. Mater.* **2019**, 1900110.
- [48] Anuradha, D. D. La, M. Al Kobaisi, A. Gupta, S. V. Bhosale, *Chem. Eur. J.* **2017**, *23*, 3950.
- [49] Only recently single network Cub LC phases have been predicted and first examples have been experimentally observed.<sup>[57,58]</sup>
- [50] Besides the rod-like segments, also bent and disk-like units can lead to Cub phases in few cases.
- [51] A.-M. Levelut, C. Germain, P. Keller, L. Liebert, J. Billard, *J. Phys.* **1983**, *44*, 623.
- [52] A.-M. Levelut, M. Clerc, *Liq. Cryst.* **1998**, *24*, 105.
- [53] M. Yoneya, *Chem. Rec.* **2011**, *11*, 66.
- [54] T. Yamamoto, I. Nishiyama, M. Yoneya, H. Yokoyama, *J. Phys. Chem. B* **2009**, *113*, 11564.
- [55] I. Nishiyama, *Chem. Rec.* **2009**, *9*, 340.
- [56] H. Lu, X. Zeng, G. Ungar, C. Dressel, C. Tschierske, *Angew. Chem., Int. Ed.* **2018**, *57*, 2835.
- [57] X. Zeng, S. Poppe, A. Lehmann, M. Prehm, C. Chen, F. Liu, H. Lu, G. Ungar, C. Tschierske, *Angew. Chem.* **2019**, *131*, 7453.
- [58] S. Poppe, X. Cheng, C. Chen, X. Zeng, R.-B. Zhang, F. Liu, G. Ungar, C. Tschierske, *J. Am. Chem. Soc.* **2020**, *142*, 3296.
- [59] A. J. Mukhtyar, F. A. Escobedo, *Macromolecules* **2018**, *51*, 9781.
- [60] F. Liu, M. Prehm, X. B. Zeng, C. Tschierske, G. Ungar, *J. Am. Chem. Soc.* **2014**, *136*, 6846.
- [61] S. Poppe, C. Chen, F. Liu, C. Tschierske, *Chem. Commun.* **2018**, *54*, 11196.
- [62] X. B. Zeng, M. Prehm, G. Ungar, C. Tschierske, F. Liu, *Angew. Chem., Int. Ed.* **2016**, *55*, 8324.
- [63] M. Poppe, C. Chen, F. Liu, S. Poppe, C. Tschierske, *Chem. - Eur. J.* **2017**, *23*, 7196.
- [64] M. Poppe, C. Chen, H. Ebert, S. Poppe, M. Prehm, C. Kerzig, F. Liu, C. Tschierske, *Soft Matter* **2017**, *13*, 4381.
- [65] C. Chen, R. Kieffer, H. Ebert, M. Prehm, R.-B. Zhang, X. Zeng, F. Liu, G. Ungar, C. Tschierske, *Angew. Chem., Int. Ed.* **2020**, *59*, 2725.

- [66] Cub phases with the molecules organized on the minimal surfaces in the middle of the continuum between the networks are rare; there are also rod-like molecules having laterally alkyl-substituted rods, forming  $Cub_{bi}$  phases with the rods aligned parallel to the networks<sup>[57,58,60–62]</sup> or parallel to the minimal surfaces.<sup>[65]</sup>
- [67] B.-K. Cho, A. Jain, S. M. Gruner, U. Wiesner, *Science* **2004**, 305, 1598.
- [68] I. Bury, B. Heinrich, C. Bourgogne, D. Guillon, B. Donnio, *Chem. - Eur. J.* **2006**, 12, 8396.
- [69] D. W. Bruce, *Acc. Chem. Res.* **2000**, 33, 831.
- [70] K. Hatsusaka, K. Ohta, I. Yamamoto, H. Shirai, *J. Mater. Chem.* **2001**, 11, 423.
- [71] M.d. A. Alam, J. Motoyanagi, Y. Yamamoto, T. Fukushima, J. Kim, K. Kato, M. Takata, A. Saeki, S. Seki, S. Tagawa, T. Aida, *J. Am. Chem. Soc.* **2009**, 131, 17722.
- [72] K. Hatsusaka, M. Kimura, K. Ohta, *Bull. Chem. Soc. Jpn.* **2003**, 76, 781.
- [73] P. Massiot, M. Imperor-Clerc, M. Veber, R. Deschenaux, *Chem. Mater.* **2005**, 17, 1946.
- [74] E. Nishikawa, E. T. Samulski, *Liq. Cryst.* **2000**, 27, 1463.
- [75] X. Cheng, M. K. Das, S. Diele, C. Tschierske, *Langmuir* **2002**, 18, 6521.
- [76] R. A. Reddy, U. Baumeister, C. Keith, H. Hahn, H. Lang, C. Tschierske, *Soft Matter* **2007**, 3, 558.
- [77] S. Kang, M. Harada, X. Li, M. Tokita, J. Watanabe, *Soft Matter* **2012**, 8, 1916.
- [78] J. Matraszek, J. Zapala, J. Mieczkowski, D. Pocięcha, E. Gorecka, *Chem. Commun.* **2015**, 51, 5048.
- [79] M. Lee, B.-K. Cho, H. Kim, J.-Y. Yoon, W.-C. Zin, *J. Am. Chem. Soc.* **1998**, 120, 9168.
- [80] M. Lee, Y.-S. Yoo, *J. Mater. Chem.* **2002**, 12, 2161.
- [81] W. T. Gozdz, R. Holyst, *Phys. Rev. E* **1996**, 54, 5012.
- [82] X. Zeng, G. Ungar, M. Imperor-Clerc, *Nat. Mater.* **2005**, 4, 562.
- [83] X. Zeng, L. Cseh, G. H. Mehl, G. Ungar, *J. Mater. Chem.* **2008**, 18, 2953.
- [84] K. Ozawa, Y. Yamamura, S. Yasuzuka, H. Mori, S. Kutsumizu, K. Saito, *J. Phys. Chem. B* **2008**, 112, 12179.
- [85] K. Saito, Y. Yamamura, Y. Miwa, S. Kutsumizu, *Phys. Chem. Chem. Phys.* **2016**, 18, 3280.
- [86] C. Dressel, T. Reppe, M. Prehm, M. Brautzsch, C. Tschierske, *Nat. Chem.* **2014**, 6, 971.
- [87] C. Dressel, F. Liu, M. Prehm, X. B. Zeng, G. Ungar, C. Tschierske, *Angew. Chem., Int. Ed.* **2014**, 53, 13115.
- [88] C. Dressel, W. Weissflog, C. Tschierske, *Chem. Commun.* **2015**, 51, 15850.
- [89] M. Alaasar, M. Prehm, Y. Cao, F. Liu, C. Tschierske, *Angew. Chem., Int. Ed.* **2016**, 55, 312.
- [90] M. Alaasar, S. Poppe, Q. Dong, F. Liu, C. Tschierske, *Chem. Commun.* **2016**, 52, 13869.
- [91] M. Alaasar, S. Poppe, Q. Dong, F. Liu, C. Tschierske, *Angew. Chem., Int. Ed.* **2017**, 56, 10801.
- [92] The first report on mirror symmetry breaking in cubic phases came from Kishikawa and co-workers,<sup>[93]</sup> though the structure of the cubic phase and the origin of chirality were unclear at that time.
- [93] T. Kajitani, S. Kohmoto, M. Yamamoto, K. Kishikawa, *Chem. Mater.* **2005**, 17, 3812.
- [94] H. R. Brand, H. Pleiner, *Eur. Phys. J. E: Soft Matter Biol. Phys.* **2019**, 42, 142.
- [95] C. Tschierske, G. Ungar, *ChemPhysChem* **2016**, 17, 9.
- [96] C. Tschierske, *Liq. Cryst.* **2018**, 45, 2221.
- [97] A twist in the organization of the  $la\bar{3}d$  phase was first discussed by Kutsumizu and co-workers.<sup>[98]</sup>
- [98] Y. Nakazawa, Y. Yamamura, S. Kutsumizu, K. Saito, *J. Phys. Soc. Jpn.* **2012**, 81, 094601.
- [99] X. B. Zeng, G. Ungar, *J. Mater. Chem. C* **2020**, 8, 5389.
- [100] G. W. Gray, B. Jones, F. Marson, *J. Chem. Soc.* **1957**, 393.
- [101] D. Demus, G. Kunicke, J. Neelsen, H. Z. Sackmann, *Z. Naturforsch., A: Phys. Sci.* **1968**, 23, 84.
- [102] S. Kutsumizu, T. Ichikawa, M. Yamada, S. Nojima, S. Yano, *J. Phys. Chem. B* **2000**, 104, 10196.
- [103] S. Kutsumizu, K. Morita, T. Ichikawa, S. Yano, S. Nojima, T. Yamaguchi, *Liq. Cryst.* **2002**, 29, 1447.
- [104] S. Kutsumizu, K. Morita, S. Yano, S. Nojima, *Liq. Cryst.* **2002**, 29, 1459.
- [105] H. Schubert, J. Hauschild, D. Demus, S. Hoffmann, *Z. Chem.* **1978**, 18, 256.
- [106] D. Demus, A. Gloza, H. Hartung, A. Hauser, I. Rapthel, A. Wiegeleben, *Cryst. Res. Technol.* **1981**, 16, 1445.
- [107] S. Kutsumizu, H. Mori, M. Fukatami, S. Naito, K. Sakajiri, K. Saito, *Chem. Mater.* **2008**, 20, 3675.
- [108] S. Kutsumizu, Y. Yamada, T. Sugimoto, N. Yamada, T. Udagawa, Y. Miwa, *Phys. Chem. Chem. Phys.* **2018**, 20, 7953.
- [109] S. Kutsumizu, I. Tokiwa, A. Kawafuchi, Y. Miwa, Y. Yamamura, K. Saito, *Phys. Chem. Chem. Phys.* **2016**, 18, 9013.
- [110] P. Göring, S. Diele, S. Fischer, A. Wiegeleben, G. Pelzl, H. Stegemeyer, W. Thyen, *Liq. Cryst.* **1998**, 25, 467.
- [111] S. Kutsumizu, S. Miisako, Y. Miwa, M. Kitagawa, Y. Yamamura, K. Saito, *Phys. Chem. Chem. Phys.* **2016**, 18, 17341.
- [112] M. Vogrin, N. Vaupotic, M. M. Wojcik, J. Mieczkowski, K. Madrak, D. Pocięcha, E. Gorecka, *Phys. Chem. Chem. Phys.* **2014**, 16, 16067.
- [113] B. Pansu, Y. Nastishin, M. Imperor-Clerc, M. Veber, H. T. Nguyen, *Eur. Phys. J. E: Soft Matter Biol. Phys.* **2004**, 15, 225.
- [114] J. M. Wolska, J. Wilk, D. Pocięcha, J. Mieczkowski, E. Gorecka, *Chem. - Eur. J.* **2017**, 23, 6853.
- [115] J. M. Wolska, D. Pocięcha, J. Mieczkowski, E. Gorecka, *Liq. Cryst.* **2016**, 43, 235.
- [116] A. I. Smirnova, B. Heinrich, B. Donnio, D. W. Bruce, *RSC Adv.* **2015**, 5, 75149.
- [117] T. Reppe, C. Dressel, S. Poppe, C. Tschierske, *Chem. Commun.* **2020**, 56, 711.
- [118] a) H. T. Nguyen, C. Destrade, A.-M. Levelut, J. Malthete, *J. Phys.* **1986**, 47, 553; b) A.-M. Levelut, Y. Fang, *Colloq. Phys.* **1990**, 51, C7-229.
- [119] J. Malthete, H. T. Nguyen, C. Destrade, *Liq. Cryst.* **1993**, 13, 171.
- [120] H. T. Nguyen, C. Destrade, J. Malthete, *Adv. Mater.* **1997**, 9, 375.
- [121] H. T. Nguyen, C. Destrade, J. Malthete, in *Handbook of Liquid Crystals*, Vol. 2B (Eds: D. Demus, J. Goodby, G. W. Gray, H.-W. Spiess, V. Vill), Wiley-VCH, Weinheim **1998**, pp. 865–885.
- [122] W. Weissflog, in *Handbook of Liquid Crystals*, Vol. 5, 2nd ed. (Eds: J. W. Goodby, J. P. Collings, T. Kato, C. Tschierske, H. F. Gleeson, P. Raynes), Wiley-VCH, Weinheim **2014**, pp. 89–174.
- [123] D. W. Bruce, S. A. Hudson, *J. Mater. Chem.* **1994**, 4, 479.
- [124] K. E. Rowe, D. W. Bruce, *J. Mater. Chem.* **1998**, 8, 331.
- [125] G. W. Gray, B. M. Warrall, *J. Chem. Soc.* **1959**, 1545.
- [126] A. Mishra, C.-Q. Ma, P. Bäuerle, *Chem. Rev.* **2009**, 109, 1141.
- [127] C. Wang, H. Dong, W. Hu, Y. Liu, C. Zhu, *Chem. Rev.* **2012**, 112, 2208.
- [128] F. C. Spano, *Acc. Chem. Res.* **2010**, 43, 429.
- [129] C. Hansch, A. Leo, R. W. Taft, *Chem. Rev.* **1997**, 97, 2995.
- [130] A. Immirzi, B. Perini, *Acta Crystallogr., Sect. A: Found. Adv.* **1977**, 33, 216.
- [131] Also compound **3/ODec** (Figure 3a) forms the  $I23$  lattice, but this compound is considered as  $3/1$  tetracatenar as the substituent at the apex provides an additional long alkyl chain.
- [132] The phase sequence  $la\bar{3}d-I23-la\bar{3}d$  is the same as previously observed for the ANBCs and BABHs<sup>[17]</sup> and for tricaténars with alicyclic apex upon ring expansion.<sup>[117]</sup>
- [133] A. Pegenau, T. Hegmann, C. Tschierske, S. Diele, *Chem. - Eur. J.* **1999**, 5, 1643.

- [134] This behavior is very similar to that observed for the SmCPR<sup>[6]</sup> phase of bent-core molecules, where the emerging polarization leads to geometrical layer chirality, supporting the twisted organization.<sup>[135]</sup>
- [135] M. Alaasar, M. Prehm, M. Nagaraj, J. K. Vij, C. Tschierske, *Adv. Mater.* **2013**, *25*, 2186.
- [136] H. Takezoe, *Top. Curr. Chem.* **2012**, *318*, 303.
- [137] P. S. Salter, P. W. Benzie, R. A. Reddy, C. Tschierske, S. J. Elston, E. P. Raynes, *Phys. Rev. E* **2009**, *80*, 031701.
- [138] R. P. Lemieux, *Acc. Chem. Res.* **2001**, *34*, 845.
- [139] L. Tauchi, T. Nakagaki, M. Shimizu, E. Itoh, M. Yasutake, K. Ohta, *J. Porphyrins Phthalocyanines* **2013**, *17*, 1080.
- [140] M. Lehmann, M. Hugel, *Angew. Chem., Int. Ed.* **2015**, *54*, 4110.
- [141] E. Nishikawa, J. Yamamoto, H. Yokoyama, *J. Mater. Chem.* **2003**, *13*, 1887.
- [142] A. Yoshizawa, *Polym. J.* **2012**, *44*, 490.
- [143] A.-M. Levelut, E. Hallouin, D. Bennemann, G. Heppke, D. Lotzsch, *J. Phys. II* **1997**, *7*, 981.
- [144] B. M. Rosen, C. J. Wilson, D. A. Wilson, M. Peterca, M. R. Imam, V. Percec, *Chem. Rev.* **2009**, *109*, 6275.
- [145] B. M. Rosen, M. Peterca, C. Huang, X. Zeng, G. Ungar, V. Percec, *Angew. Chem., Int. Ed.* **2010**, *49*, 7002.
- [146] S. Lecommandoux, H.-A. Klok, M. Sayar, S. I. Stupp, *J. Polym. Sci., Part A: Polym. Chem.* **2003**, *41*, 3501.
- [147] X. H. Cheng, X. Q. Bai, S. Jing, H. Ebert, M. Prehm, C. Tschierske, *Chem. - Eur. J.* **2010**, *16*, 4588.
- [148] X. H. Cheng, F. W. Su, R. Huang, H. F. Gao, M. Prehm, C. Tschierske, *Soft Matter* **2012**, *8*, 2274.
- [149] H. Dai, X. Yang, X. Tan, F. Su, X. Cheng, F. Liu, C. Tschierske, *Chem. Commun.* **2013**, *49*, 10617.
- [150] X. Tan, L. Kong, H. Dai, X. Cheng, F. Liu, C. Tschierske, *Chem. - Eur. J.* **2013**, *19*, 16303.
- [151] M.-H. Yen, J. Chairapa, X. B. Zeng, Y. Liu, L. Cseh, G. H. Mehl, G. Ungar, *J. Am. Chem. Soc.* **2016**, *138*, 5757.
- [152] X. H. Yao, L. Cseh, X. B. Zeng, M. Xue, Y. S. Liu, G. Ungar, *Nanoscale Horiz.* **2017**, *2*, 43.
- [153] V. Percec, M. Glodde, T. K. Bera, Y. Miura, I. Shiyonovskaya, K. D. Singer, V. S. K. Balagurusamy, P. A. Heiney, I. Schnell, A. Rapp, H.-W. Spiess, S. D. Hudsonk, H. Duank, *Nature* **2002**, *419*, 384.
- [154] T. Reppe, S. Poppe, X. Cai, Y. Cao, F. Liu, C. Tschierske, *Chem. Sci.* **2020**, *11*, 5902.
- [155] D. M. Walba, in *Materials-Chirality, Topics in Stereochemistry*, Vol. 24 (Eds: M. M. Green, R. J. M. Nolte, E. W. Meijer), Wiley, Hoboken, NJ **2003**, pp. 457–518.
- [156] A. Yoshizawa, M. Kurata, *New J. Chem.* **2019**, *43*, 8865.
- [157] N. Uemura, K. Sano, A. Matsumoto, Y. Yoshida, T. Mino, M. Sakamoto, *Chem. - Asian J.* **2019**, *14*, 4150.
- [158] Y. Nagata, R. Takeda, M. Sugimoto, *ACS Cent. Sci.* **2019**, *5*, 1235.

# ADVANCED FUNCTIONAL MATERIALS

## Supporting Information

for *Adv. Funct. Mater.*, DOI: 10.1002/adfm.202004353

Helical Networks of  $\pi$ -Conjugated Rods – A Robust Design  
Concept for Bicontinuous Cubic Liquid Crystalline Phases  
with Achiral  $Ia3-d$  and Chiral  $I23$  Lattice

*Christian Dressel, Tino Reppe, Silvio Poppe, Marko Prehm,  
Huanjun Lu, Xiangbing Zeng, Goran Ungar,\* and Carsten  
Tschierske\**

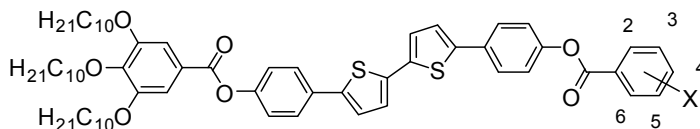
## Supporting Information

### **Helical networks of $\pi$ -conjugated rods - A robust design concept for bicontinuous cubic liquid crystalline phases with achiral $Ia\bar{3}d$ and chiral $I23$ lattice**

*Christian Dressel, Tino Reppe, Silvio Poppe, Marko Prehm, Huanjun Lu, Xiangbing Zeng, Goran Ungar,\* Carsten Tschierske\**

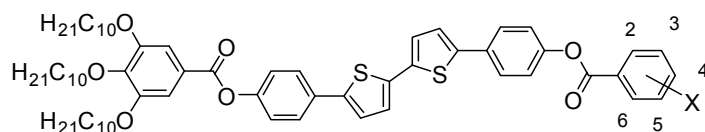
## S1. Additional Data

## S1.1 Transition temperatures and enthalpy values

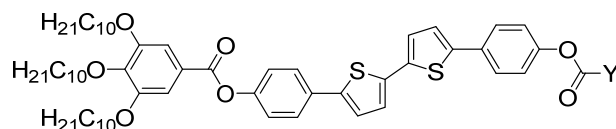
**Table S1.** Phase transitions, transition temperatures ( $T/^\circ\text{C}$ ) and transition enthalpy values of the investigated compounds **3/X**.<sup>a</sup>

Verb.	X	Pos.	$T/^\circ\text{C}$ [ $\Delta H/\text{kJ}\cdot\text{mol}^{-1}$ ]	$a_{\text{cub}}/\text{nm}$
<b>3<sup>4</sup>F</b>	F	4	H2: Cr 122 [22.4] Cub/ <i>Ia</i> $\bar{3}d$ 199 [2.2] Iso K1: Iso 190 [-1.9] Cub/ <i>Ia</i> $\bar{3}d$ 83 [-27.1] Cr	11.1
<b>3<sup>4</sup>I</b>	I	4	H1: Cr 132 [39.3] Cub/ <i>Ia</i> $\bar{3}d$ 221 [2.6] Iso K1: Iso 210 [-2.0] Cub/ <i>Ia</i> $\bar{3}d$	11.3
<b>3<sup>4</sup>CN</b>	CN	4	H1:Cr 104 [46.1] Cub/ <i>Ia</i> $\bar{3}d$ 237 [2.5] Iso K1: Iso 224 [-2.1] Cub/ <i>Ia</i> $\bar{3}d$ 87 [-0.3] M <sub>x</sub>	11.2
<b>3<sup>4</sup>Me</b>	CH <sub>3</sub>	4	H1: Cr 118 [40.1] Cub/ <i>Ia</i> $\bar{3}d$ 180 [1.6] Iso K2: Iso 175 [-0.1] Iso <sub>1</sub> <sup>[*]</sup> 155 [-0.5] Cub/ <i>Ia</i> $\bar{3}d$	11.4
<b>3<sup>4</sup>CF<sub>3</sub></b>	OCF <sub>3</sub>	4	H2: Cr 127 [30.1] Cub <sup>[*]</sup> / <i>I23</i> 206 [2.0] Iso K2: Iso 194 [-2.1] Cub <sup>[*]</sup> / <i>I23</i>	16.2
<b>3<sup>4</sup>NO<sub>2</sub></b>	NO <sub>2</sub>	4	H2: Cr 128 [39.3] Cub/ <i>Ia</i> $\bar{3}d$ 244 [2.1] Iso K1: Iso 233 [-1.8] Cub/ <i>Ia</i> $\bar{3}d$	11.1
<b>3<sup>4</sup>OAc</b>	OOCCH <sub>3</sub>	4	H1: Cr 105 [20.2] Cub/ <i>Ia</i> $\bar{3}d$ [1.7] Iso K1: Iso 189 [-0.9] Cub/ <i>Ia</i> $\bar{3}d$	11.5
<b>3<sup>3</sup>F</b>	F	3	H2: Cr 114 [26.1] Cub/ <i>Ia</i> $\bar{3}d$ 176 [2.6] Iso K1: Iso 167 [-2.0] Cub/ <i>Ia</i> $\bar{3}d$ 87 [-0.3] Cr'	10.9
<b>3<sup>3</sup>Br</b>	Br	3	H2: Cr 109 [19.7] Cub <sup>[*]</sup> / <i>I23</i> 169 [0.3] Cub/ <i>Ia</i> $\bar{3}d$ 173 [2.6] Iso K1: Iso 165 [-2.1] Cub/ <i>Ia</i> $\bar{3}d$	10.4 <sub><i>Ia</i><math>\bar{3}d</math></sub> 16.4 <sub><i>I23</i></sub>
<b>3<sup>3</sup>I</b>	I	3	H1: Cr 99 [22.5] Cub <sup>[*]</sup> / <i>I23</i> 154 [-] Cub/ <i>Ia</i> $\bar{3}d$ 163 [2.3] Iso K1: Iso 155 [-1.6] Cub/ <i>Ia</i> $\bar{3}d$	16.2 <sub><i>I23</i></sub>
<b>3<sup>3</sup>OMe</b>	OMe	3	H1:Cr 107 [57.2] Cub <sup>[*]</sup> / <i>I23</i> 144 [2.8] Iso K1: Iso 140 [-2.0] Cub <sup>[*]</sup> / <i>I23</i> + Cub/ <i>Ia</i> $\bar{3}d$ < 0 Cr	10.8 <sub><i>Ia</i><math>\bar{3}d</math></sub> 16.0 <sub><i>I23</i></sub>
<b>3<sup>3</sup>ODec</b>	OC <sub>10</sub> H <sub>21</sub>	3	H2: Cr 97 [37.2] Cub/ <i>Ia</i> $\bar{3}d$ [3.4] 112 Iso K1: Iso 105 [-2.5] Col <sub>hex</sub> → Cub/ <i>Ia</i> $\bar{3}d$ 87 [-0.3] Cr'	9.8
<b>3<sup>3</sup>CN</b>	CN	3	H1: Cr 99 [49.6] Cub/ <i>Ia</i> $\bar{3}d$ 196 [2.8] Iso K1: Iso 186 [-1.9] Cub/ <i>Ia</i> $\bar{3}d$	10.8
<b>3<sup>2</sup>F</b>	F	2	H1: Cr 92 [34.9] Cub/ <i>Ia</i> $\bar{3}d$ 143 [2.1] Iso K2: Iso 137 [-0.1] Iso <sub>1</sub> <sup>[*]</sup> 133 [-1.4] Cub/ <i>Ia</i> $\bar{3}d$	10.9
<b>3<sup>2</sup>NO<sub>2</sub></b>	NO <sub>2</sub>	2	H2: Cr 106 [21.8] Cub/ <i>Ia</i> $\bar{3}d$ 117 [1.0] Iso K2: Iso 100 [-0.8] M1 87 [-21.3] Cr	11.1
<b>3<sup>2</sup>I</b>	I	2	H2: Cr 89 [35.5] Cub/ <i>Ia</i> $\bar{3}d$ 135 [2.2] Iso K2: Iso 125 [-1.7] Cub/ <i>Ia</i> $\bar{3}d$	10.3
<b>3<sup>2</sup>OMe</b>	OMe	2	H1: Cr 131 [64.2] Iso K1: Iso 82 [-37.3] Cr	-

<sup>a</sup> Peak temperatures of the first (H1) or second DSC-heating (H2) or cooling scans (K1, K2) at 10 K/min; Abbreviations: Iso<sub>1</sub><sup>[\*]</sup> = spontaneously mirror symmetry broken isotropic liquid phase; M1 = non cubic 3D phase (distorted *Ia* $\bar{3}d$  phase) M<sub>x</sub> = unknown mesophases or crystalline phase; for the other abbreviations, see main text; <sup>b</sup>determined by polarizing microscopy; <sup>c</sup> the Col<sub>hex</sub> phase is formed on cooling from Iso which is immediately replaced by the *Ia* $\bar{3}d$  phase.

**Table S1** (continued). Phase transitions, transition temperatures ( $T/^\circ\text{C}$ ) and transition enthalpy values of the investigated compounds **3/X**.<sup>a</sup>

Verb.	X	Pos.	$T/^\circ\text{C}$ [ $\Delta H/\text{kJ}\cdot\text{mol}^{-1}$ ]	$a_{\text{cub}}/\text{nm}$
<b>3/3<sup>4</sup>F<sub>2</sub></b>	F	3,4	H2: Cr 126 [27.6] Cub <sup>[*]</sup> /I23 198 [0.3] Cub/ <i>Ia</i> $\bar{3}d$ 203 [2.4] Iso K2: Iso 192 [-1.9] Cub/ <i>Ia</i> $\bar{3}d$	16.0
<b>3/3<sup>5</sup>F<sub>2</sub></b>	F	3,5	H2: Cr 118 [27.9] Cub <sup>[*]</sup> /I23 173 [2.9] Iso K1: Iso 162 [-2.1] Cub <sup>[*]</sup> /I23	15.8
<b>3/3<sup>5</sup>Br<sub>2</sub></b>	Br	3,5	H1: Cr 118 [35.4] Cub <sup>[*]</sup> /I23 157 [3.3] Iso K1: Iso 145 [-2.2] Cub <sup>[*]</sup> /I23 < 0 Cr	16.1
<b>3/3<sup>5</sup>NO<sub>2</sub></b>	NO <sub>2</sub>	3,5	H1: Cr 131 [28.0] Cub <sup>[*]</sup> /I23 209 [2.9] Iso K1: Iso 195 [-2.3] Cub <sup>[*]</sup> /I23	15.8
<b>3/3<sup>5</sup>I<sub>2</sub></b>	I	3,5	H2: Cr 130 [41.1] Cub <sup>[*]</sup> /I23 140 [2.0] Iso K2: Iso 127 [-1.7] Cub <sup>[*]</sup> /I23	15.6
<b>3/3<sup>5</sup>OMe<sub>2</sub></b>	OMe	3,5	H2: Cr 124 [52.8] Iso K1: Iso 101 [-1.8] Cub <sup>[*]</sup> /I23 69 [2.6] Cr	-
<b>3/3<sup>5</sup>OEt<sub>2</sub></b>	OEt	3,5	H2: Cr 119 [63.3] Iso K2: Iso 61 [-15.5] Cr	-
<b>3/3<sup>45</sup>F<sub>3</sub></b>	F	3,4,5	H2: Cr 129 [28.8] Cub <sup>[*]</sup> /I23 200 [3.2] Iso K1: Iso 188 [-2.5] Cub <sup>[*]</sup> /I23	15.6
<b>3/2<sup>3456</sup>F<sub>5</sub></b>	F	2,3,4,5,6	H1: Cr 115 <sup>b</sup> Cub <sup>[*]</sup> /I23 184 [3.0] Iso K1: Iso 171 [-2.1] Cub <sup>[*]</sup> /I23	15.6
<b>3/2<sup>6</sup>F<sub>2</sub></b>	F	2,6	H2: Cr 118 Iso K2: Iso 112 SmC <sub>s</sub> 53 Cr	-

**Table S2**. Phase transitions, transition temperatures ( $T/^\circ\text{C}$ ) and transition enthalpy values of compounds **3a/Y**.<sup>a</sup>

Verb.	Y	$T/^\circ\text{C}$ [ $\Delta H/\text{kJ}\cdot\text{mol}^{-1}$ ]	$a_{\text{cub}}/\text{nm}$
<b>3a/Th</b>	2-thienyl	H1: Cr 106 [34.0] Cub/ <i>Ia</i> $\bar{3}d$ 158 [2.2] Iso K2: Iso 153 [-2.0] Cub/ <i>Ia</i> $\bar{3}d$	10.8
<b>3a/1-Npht</b>	1-naphthyl	H2: Cr 88 [19.5] Cub/ <i>Ia</i> $\bar{3}d$ 136 [1.7] Iso K2: Iso 123 [-1.3] Cub/ <i>Ia</i> $\bar{3}d$ <20 Cr	10.6
<b>3a/2-Npht</b>	2-naphthyl	H2: Cr 120 [38.6] Cub/ <i>Ia</i> $\bar{3}d$ 196 [2.0] Iso K2: Iso 187 [-0.1] Iso <sub>1</sub> <sup>[*]</sup> 182 [-1.1] Cub/ <i>Ia</i> $\bar{3}d$ 40 [-2.8] Cr <sup>*</sup>	11.6
<b>3a/Biph</b>	4-biphenyl	H1: Cr 125 [43.9] Cub/ <i>Ia</i> $\bar{3}d$ 244 [2.2] Iso K1: Iso 233 [-1.6] Cub/ <i>Ia</i> $\bar{3}d$ 83 [-18.8] Cr	12.0
<b>3a/Anth</b>	9-anthranlyl	H1: Cr 156 [47.7] Iso K1: Iso 123 [-43.1] Cr	-



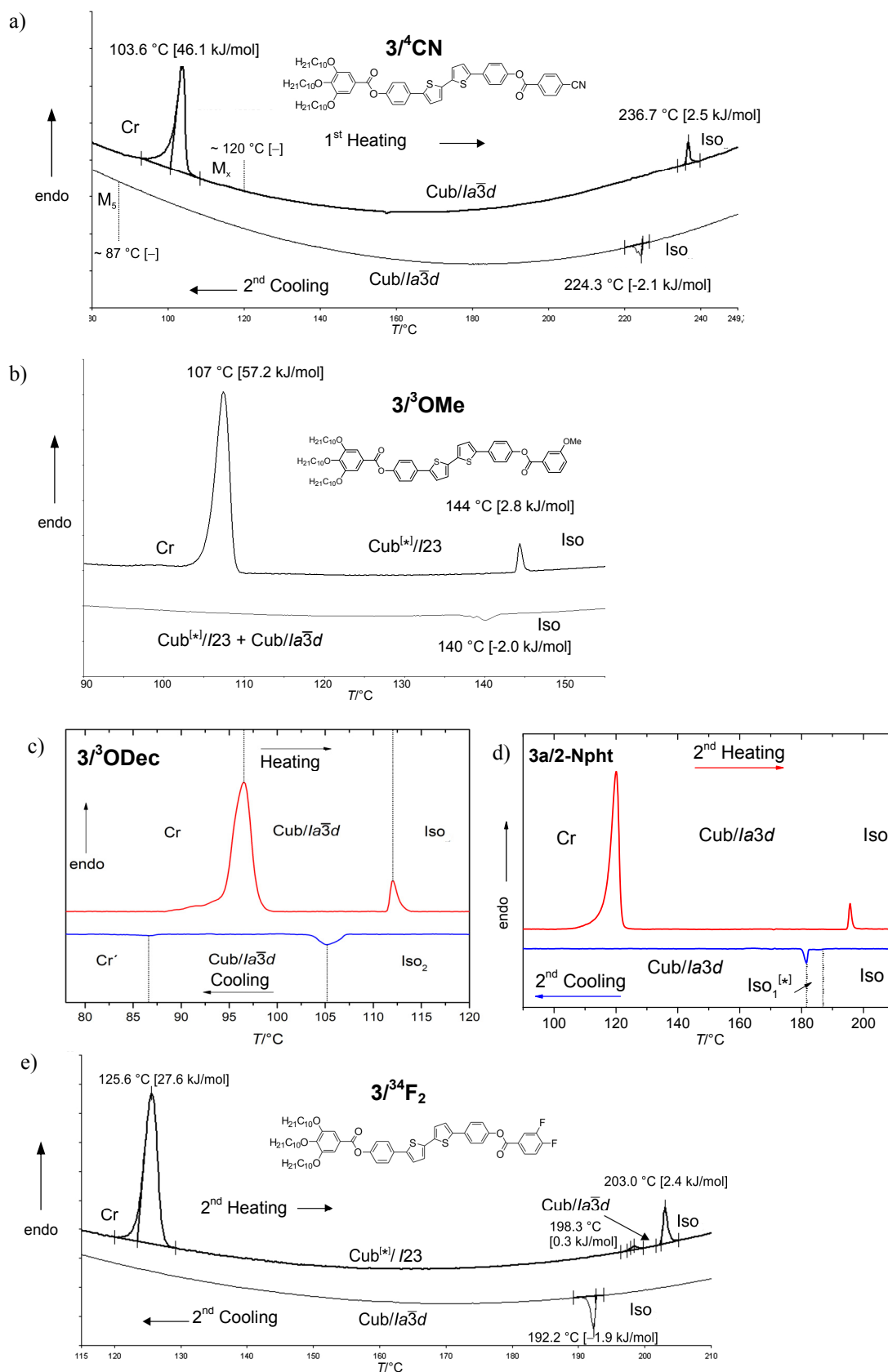


**Figure S1.** Representative DSC traces ( $10 \text{ K min}^{-1}$ ) of compounds a) **3<sup>4</sup>CN** b) **3<sup>3</sup>OMe**, c) **3<sup>3</sup>ODec**, d) **3a/2-Npht** and e) **3<sup>3</sup>F<sub>2</sub>**.



## S1.2 Additional textures

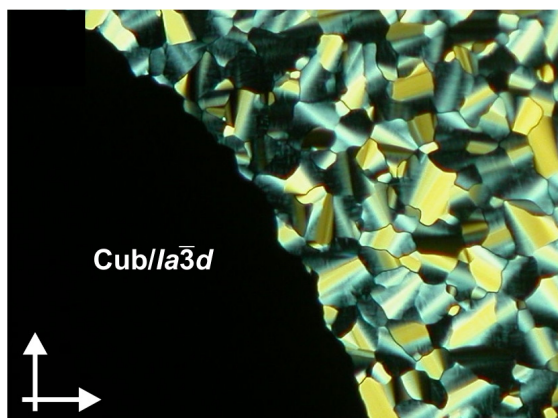


**Figure S2.** Textures of the mesophases of compound  $3/3\text{ODec}$ . Growth of the  $\text{Cub}_{\text{bi}}/\text{Ia}\bar{3}d_{\text{(S)}}$  phase (black, left) from the birefringent  $\text{Col}_{\text{hex}}$  phase (right) first formed immediately upon cooling from Iso at  $T = 105\text{ }^\circ\text{C}$ ; the width of the image is 1 mm.

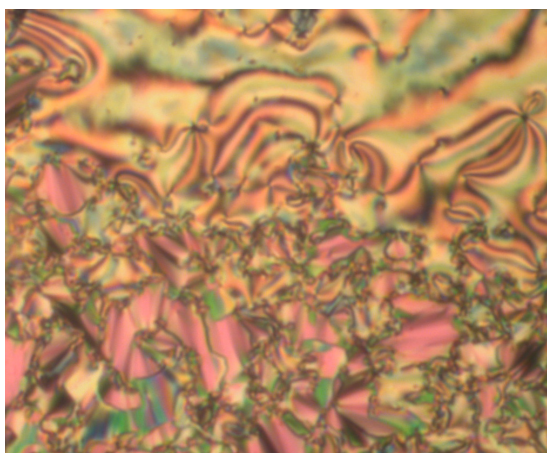


**Figure S3.** Texture of the  $\text{SmC}_s$  phase as observed on cooling of compound  $3/26\text{F}_2$  at  $T = 110\text{ }^\circ\text{C}$ , showing the fan texture with extinctions inclined with the directions of the polarizers (bottom) and the Schlieren texture (top); the width of the image is 1 mm.

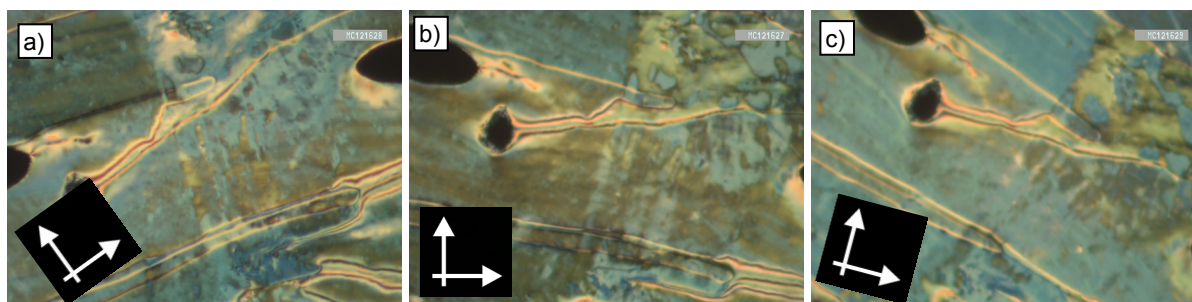


**Figure S4.**  $\text{SmC}_s$  phase as observed on cooling compound  $3/26\text{F}_2$  in a homeotropic cell at  $T = 110\text{ }^\circ\text{C}$ , observed between crossed polarizers; the brightness of the domains does not change by rotating the sample between the polarizers, excluding a tilt alignment as origin of the change of domain brightness by rotating the polarizer (see Fig. 1g-h); the width of the images is 0.8 mm.

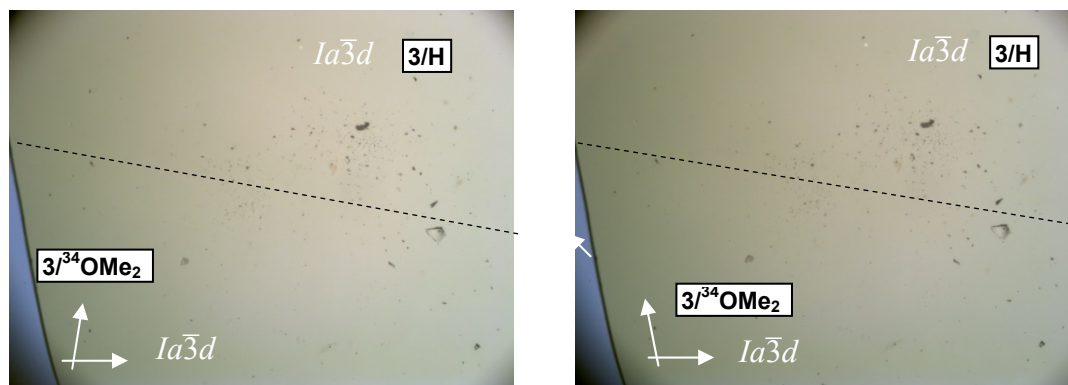


**Figure S5.** Contact region between the  $Ia\bar{3}d$  phases of compounds **3/H** and **3/<sup>34</sup>OMe<sub>2</sub>** at  $T = 125$  °C as observed between slightly uncrossed polarizers; the absence of an induced conglomerate texture of the  $I23$  phase indicates that both  $Ia\bar{3}d$  phases represent long pitch  $Ia\bar{3}d_{(L)}$  type phases; the dashed line indicates approximate position of the phase boundary.

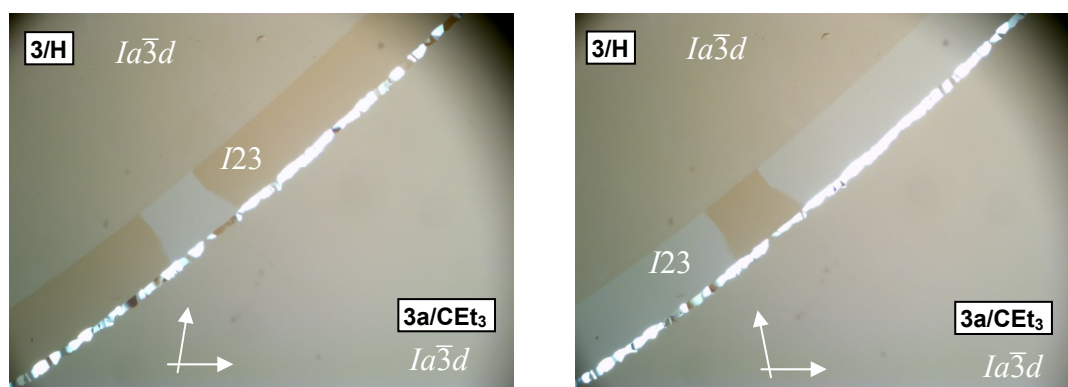


**Figure S6.** Contact region between the  $Ia\bar{3}d$  phases of compounds **3/H** and **3a/CET<sub>3</sub>** at  $T = 73$  °C as observed between slightly uncrossed polarizers; the induced conglomerate texture of the  $I23$  phase indicates that the  $Ia\bar{3}d$  phase of **3a/CET<sub>3</sub>** represent short pitch type phase  $Ia\bar{3}d_{(S)}$ ; in this case an additional birefringent, most probably columnar phase is induced besides the  $I23$  phase.

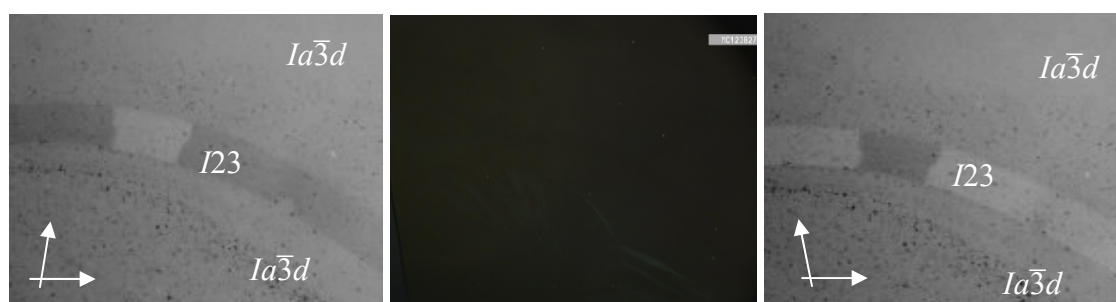


**Figure S7.** Contact region between the  $Ia\bar{3}d$  phases of compounds **3a/CET<sub>3</sub>** (top) and **2-Npht** (bottom) at  $T = 125$  °C as observed between slightly uncrossed polarizers (left, right) and crossed polarizers (middle); the induced conglomerate texture of the  $I23$  phase (on cooling formed below  $126$  °C and on heating it disappears at  $141$  °C) indicates that the  $Ia\bar{3}d$  phase of **2-Npht** represent long pitch type phase  $Ia\bar{3}d_{(L)}$ ; contrast enhanced.

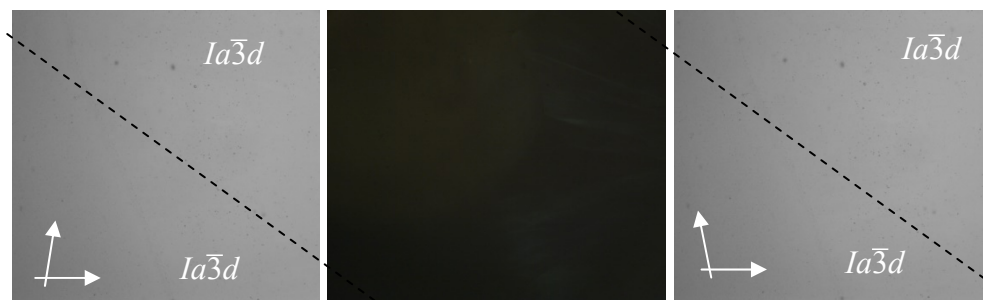


**Figure S8.** Contact region between the  $Ia\bar{3}d$  phases of compounds **1-Npht** (top) and **2-Npht** (bottom) at  $T = 130\text{ }^{\circ}\text{C}$  as observed between slightly uncrossed polarizers (left, right) and crossed polarizers (middle); the absence of an induced conglomerate texture of the  $I23$  phase indicates that both  $Ia\bar{3}d$  phases represent long pitch  $Ia\bar{3}d_{(L)}$  type phases; the dashed line indicates approximate position of the phase boundary.

### S1.3 Additional XRD data

**Table S3.** Crystallographic data of compounds **3/X**.

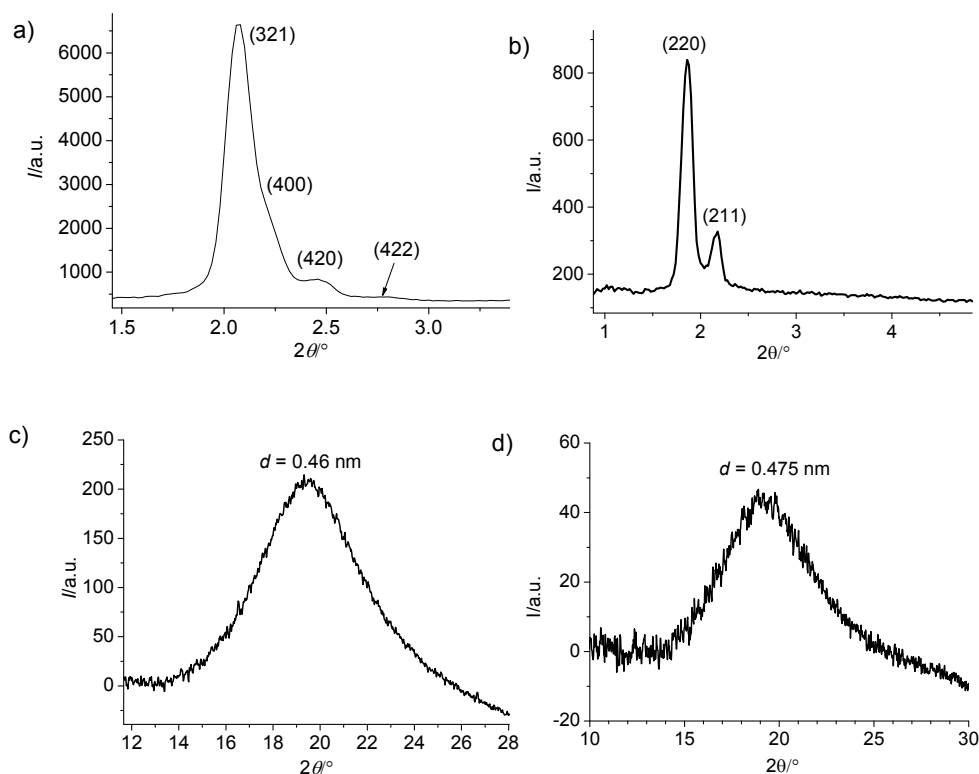
Comp.	$T/^{\circ}\text{C}$	$2\theta/^{\circ}$	$d/\text{nm}$	$hkl$	$d_{\text{calc}}/\text{nm}$	$\Delta$	$a_{\text{cub}}/\text{nm}$
<b>3<sup>A</sup>F</b>	130	1.952	4.526	211	4.526	0.00	$Ia\bar{3}d$ : 11.09
		2.305	3.832	220	3.920	0.09	
		3.878	2.278	422	2.263	0.02	
<b>3<sup>A</sup>I</b>	140	1.921	4.599	211	4.599	0.00	$Ia\bar{3}d$ : 11.26
		2.205	4.006	220	3.983	0.02	
		3.659	2.415	332	2.402	0.01	
<b>3<sup>A</sup>Me</b>	140	1.896	4.659	211	4.659	0.00	$Ia\bar{3}d$ : 11.41
		2.179	4.054	220	4.035	0.02	
<b>3<sup>A</sup>OCF<sub>3</sub></b>	150	2.040	4.330	321	4.330	0.00	$I23$ : 16.20
		2.195	4.025	400	4.050	0.03	
		2.407	3.670	420	3.623	0.05	
<b>3<sup>A</sup>NO<sub>2</sub></b>	150	1.950	4.530	211	4.530	0.00	$Ia\bar{3}d$ : 11.10
		2.247	3.932	220	3.923	0.01	
<b>3<sup>A</sup>OAc</b>	140	1.884	4.690	211	4.690	0.00	$Ia\bar{3}d$ : 11.49
		2.127	4.154	220	4.062	0.09	
<b>3<sup>B</sup>Br</b>	140	2.083	4.242	211	4.242	0.00	$Ia\bar{3}d$ : 10.39
		2.402	3.679	220	3.674	0.01	
	171	2.014	4.386	321	4.386	0.00	$I23$ : 16.41
		2.135	4.138	400	4.103	0.03	
		2.247	3.932	411	3.868	0.06	
2.501	3.533	332	3.499	0.02			
<b>3<sup>B</sup>I</b>	130	2.038	4.335	321	4.335	0.00	$I23$ : 16.22
		2.188	4.038	400	4.055	0.02	
		2.397	3.685	420	3.627	0.06	
<b>3<sup>B</sup>CN</b>	140	2.001	4.415	211	4.415	0.00	$Ia\bar{3}d$ : 10.81
		2.303	3.836	220	3.823	0.01	

Table S3 (continued). Crystallographic data of compounds **3/X**.

Comp.	$T/^\circ\text{C}$	$2\theta/^\circ$	$d/\text{nm}$	$hkl$	$d_{\text{calc}}/\text{nm}$	$\Delta$	$a_{\text{cub}}/\text{nm}$
<b>3/<sup>3</sup>ODec</b>	105	2.203	4.009	211	4.009	0.00	$Ia\bar{3}d$ : 9.82
		2.525	3.499	220	3.472	0.02	
<b>3/<sup>2</sup>F</b>	120	1,992	4,436	211	4.436	0.00	$Ia\bar{3}d$ : 10.87
		2,291	3,856	220	3.842	0.02	
<b>3/<sup>2</sup>I</b>	110	2.091	4.225	211	4.225	0.00	$Ia\bar{3}d$ : 10.34
		2.380	3.712	220	3.659	0.05	
<b>3/<sup>2</sup>NO<sub>2</sub></b>	115	1.96	4.52	211	4.52	0.00	$Ia\bar{3}d$ : 11.07
		2.25	3.92	220	3.91	0.01	
<b>3/<sup>34</sup>F<sub>2</sub></b>	135	2068	4.271	321	4.271	0.00	$I23$ : 15.98
		2.216	3.987	400	3.995	0.01	
		2.442	3.617	420	3.573	0.04	
		2.771	3.188	422	3.262	0.07	
<b>3/<sup>35</sup>I<sub>2</sub></b>	135	2.121	4.165	321	4.165	0.00	$I23$ : 15.58
		2.267	3.897	400	3.896	0.03	
<b>3/<sup>35</sup>NO<sub>2</sub></b>	180	2.10	4.21	321	4.21	0.00	$I23$ : 15.76
		2.23	3.97	400	3.94	0.03	
<b>3/<sup>345</sup>F<sub>3</sub></b>	150	2.121	4.165	321	4.165	0.00	$I23$ : 15.58
		2282	3.872	400	3.896	0.02	
		2.483	3.558	420	3.485	0.07	
<b>3/<sup>23456</sup>F<sub>5</sub></b>	140	2.116	4.175	321	4.175	0.00	$I23$ : 15.62
		2.286	3.864	400	3.905	0.04	
		2.495	3.541	420	3.493	0.05	

Table S4. Crystallographic data of compounds **3a/Y**.

Comp.	$T/^\circ\text{C}$	$2\theta/^\circ$	$d/\text{nm}$	$hkl$	$d_{\text{calc}}/\text{nm}$	$\Delta$	$a_{\text{cub}}/\text{nm}$
<b>3a/Th</b>	125	1.99	4.43	211	4.43	0.00	$Ia\bar{3}d$ : 10.85
		2.29	3.85	220	3.84	0.01	
		2.37	3.73	332	3.66	0.07	
<b>3a/1-Nph</b>	120	2.033	4.35	211	4.35	0.00	$Ia\bar{3}d$ : 10.64
		2.34	3.78	220	3.76	0.02	
<b>3a/2-Nph</b>	180	1.86	4.75	211	4.75	0.00	$Ia\bar{3}d$ : 11.63
		2.16	4.09	220	4.11	0.02	
<b>3a/Biph</b>	180	1.81	4.88	211	4.88	0.00	$Ia\bar{3}d$ : 11.95
		2.08	4.25	220	4.22	0.03	



**Figure S9.** Representative  $2\theta$  scan of the diffraction patterns a) of the  $I23$  phase of  $3/^{34}\text{F}_2$  at  $T = 135\text{ }^\circ\text{C}$  and b) of the  $Ia\bar{3}d$  phase of  $3a/2\text{-Naph}$  at  $T = 180\text{ }^\circ\text{C}$ .

**Table S5.** Diffraction data of the  $Ia\bar{3}d$  phase of compound  $3/^{34}\text{F}$ , measured at  $125\text{ }^\circ\text{C}$ , including Miller indices, measured ( $d$ ) and best-fit ( $d_{\text{calc}}$ )  $d$ -spacings of diffraction peaks, diffraction peak intensities (corrected by powder geometry and multiplicity), peak multiplicity and phases used in reconstruction of electron density maps. The best-fit lattice parameter  $a$  is  $10.89\text{ nm}$ .

Indices ( $hkl$ )	$d$ (nm)	$d_{\text{calc}}$ (nm)	Intensity	Multiplicity	Phase
(211)	4.44	4.48	100	24	$\pi$
(220)	3.85	3.86	28.9	12	$\pi$
(321)	2.91	2.91	0.3	48	$\pi$
(400)	2.72	2.72	2.0	6	$\pi$
(420)	2.43	2.43	1.2	24	$\pi$
(332)	2.32	2.31	2.1	24	0
(422)	2.22	2.21	0.3	24	0
(440)	1.92	1.91	0.3	12	0
(611)	1.77	1.76	-	24	-
(444)	1.57	1.56	-	8	-
(543)	1.54	1.53	-	48	-

**Table S6.** Diffraction data of the *I23* phase of compound  $3/^{35}\text{F}_2$ , measured at 125 °C, including Miller indices, measured (*d*-exp.) and best-fit (*d*-calc.) *d*-spacings of diffraction peaks, diffraction peak intensities (corrected by powder geometry and multiplicity), peak multiplicity and phases used in reconstruction of electron density maps. The best-fit lattice parameter  $a_{\text{cub}}$  is 15.79 nm.

Indices ( <i>hkl</i> )	<i>d</i> -exp. (nm)	<i>d</i> -calc. (nm)	Intensity	Multiplicity	Phase
(211)	6.44	6.45	-	24	–
(220)	5.58	5.58	-	12	–
(301)	5.00	4.99	1.4	12	0
(310)*			-	12	
(222)	4.56	4.56	8.0	8	$-0.21\pi$
(321)	4.22	4.22	58.3	24	$-0.93\pi$
(312)*			70.0	24	$-0.59\pi$
(400)	3.95	3.95	100	6	0
(411)	3.72	3.72	0.3	12	$-0.80\pi$
(330)	3.72	3.72	0.3	12 12	0
(420)	3.53	3.53	-	-	-
(422)	3.22	3.22	-	-	-
(431)/(510)	3.10	3.10	-	-	-
(521)	2.88	2.88	-	-	-
(440)	2.78	2.79	-	-	-
(433)/(530)	2.70	2.71	-	-	-
(442)	2.63	2.63	-	-	-
(532)/(611)	2.56	2.56	-	-	-
(620)	25.0	25.0	-	-	-
(541)	2.43	2.44	-	-	-
(631)	2.33	2.33	-	-	-
(444)	2.28	2.28	-	-	-
(550)	2.23	2.23	-	-	-
(640)	2.19	2.19	-	-	-
(721)	2.15	2.15	-	-	-
(642)	2.11	2.11	-	-	-

\* For *I23* space groups a general reflection (*hkl*) where  $h \neq k \neq l$  is inequivalent to (*hlk*), even though they overlap in the powder diffraction pattern, they could have different intensities and different structure factor  $F(hkl)$  phases. The intensity ratio between the two diffraction peaks is taken from the simulated diffraction pattern.



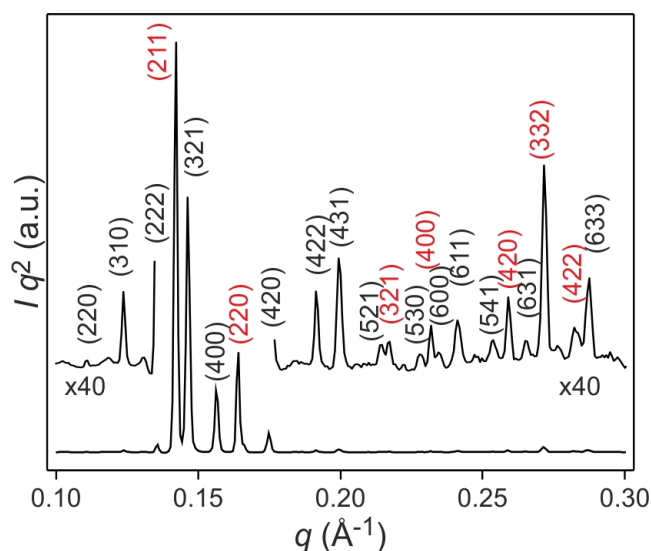


**Figure S10.** XRD pattern of compound  $3^3\text{OMe}$  at  $116\text{ }^\circ\text{C}$  showing a mixture of  $I23$  (peaks labelled in black) and  $Ia\bar{3}d$  (peaks labelled in red) phases.

**Table S7.** Experimental and calculated  $d$ -spacings of XRD reflections of the  $Ia\bar{3}d$  and  $I23$  phases in  $3^3\text{OMe}$  at  $116\text{ }^\circ\text{C}$ .

$Ia\bar{3}d$ :

$(hkl)$	$d$ (nm)	$d_{\text{calc.}}$ (nm)
(211)	4.42	4.43
(220)	3.83	3.84
(321)	2.89	2.90
(400)	2.71	2.71
(420)	2.43	2.42
(332)	2.32	2.31
(422)	2.23	2.21
$a = 10.85\text{ nm}$		

$I23$ :

$(hkl)$	$d$ (nm)	$d_{\text{calc.}}$ (nm)
(310)	5.06	5.08
(222)	4.65	4.64
(321)	4.30	4.30
(400)	4.03	4.02
(420)	3.59	3.60
(422)	3.27	3.29
(431)	3.16	3.15
(521)	2.93	2.93
(530)	2.75	2.75
(600)	2.68	2.68
(611)	2.61	2.61
(541)	2.47	2.48
(631)	2.37	2.37
(550)	2.28	2.27
(633)	2.19	2.19
$a = 16.08\text{ nm}$		

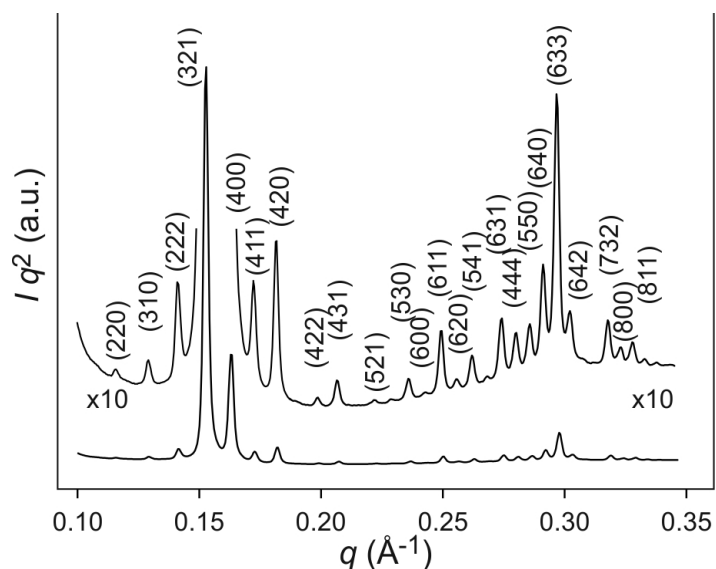


**Figure S11.** XRD pattern of the  $I23$  phase of compound  $3/^{35}\text{Br}_2$  at  $125^\circ\text{C}$ .

**Table S8.** Experimental and calculated  $d$ -spacings of XRD reflections of the  $Ia\bar{3}d$  and  $I23$  phases in  $3/^{35}\text{Br}_2$  at  $125^\circ\text{C}$ .

$(hkl)$	$d$ (nm)	$d_{\text{calc}}$ (nm)
(220)	5.52	5.52
(310)	4.93	4.94
(222)	4.51	4.51
(321)	4.17	4.17
(400)	3.90	3.90
(411)/(330)	3.68	3.68
(420)	3.49	3.49
(422)	3.19	3.19
(431)/(510)	3.06	3.06
(521)	2.85	2.85
(440)	2.76	2.76
(530)	2.68	2.68
(611)	2.53	2.53
(620)	2.47	2.47
(541)	2.41	2.41
(622)	2.35	2.35
(631)	2.30	2.30
(444)	2.25	2.25
(550)	2.21	2.21
(640)	2.17	2.16
(633)	2.12	2.12
(642)	2.09	2.09
(732)	1.98	1.98
(800)	1.95	1.95
(811)	1.92	1.92
(820)	1.89	1.89
$a = 16.08$ nm		



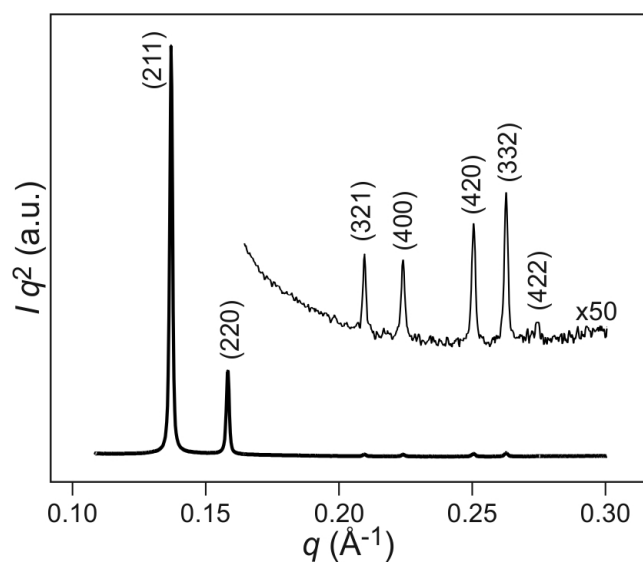


**Figure S12.** XRD pattern of the  $Ia\bar{3}d$  phase of compound  $3^4CN$  at 200°C.

**Table S9.** Experimental and calculated  $d$ -spacings of XRD reflections of the  $Ia\bar{3}d$  phase of  $3^4CN$  at 200 °C. Best-fit lattice parameter  $a = 11.21$  nm.

$(hkl)$	$d$ (nm)	$d_{\text{calc.}}$ (nm)
(211)	4.58	4.58
(220)	3.97	3.96
(321)	3.00	3.00
(400)	2.80	2.80
(420)	2.51	2.51
(332)	2.39	2.39
(422)	2.29	2.29

Table S10. Structural data of the investigated cubic phases ( $a_{\text{cub}}$ ).<sup>a</sup>

Compd.	Ref.	Phase	$a_{\text{cub}}/\text{nm}$	$V_{\text{cell}}/\text{nm}^3$	$V_{\text{mol}}/\text{nm}^3$	$n_{\text{cell}}$	$L_{\text{net}}/\text{nm}$	$n_{\text{raft}}$	$\Phi/^\circ$
<b>3<sup>H</sup></b>	S4	Cub/ $Ia\bar{3}d_{(L)}$	10.8	1260	1.46	771	91.6	3.79	8.3
<b>3<sup>A</sup>F</b>	-	Cub/ $Ia\bar{3}d_{(L)}$	11.1	1368	1.46	837	94.2	4.00	8.1
<b>3<sup>A</sup>I</b>	-	Cub/ $Ia\bar{3}d_{(L)}$	11.3	1443	1.49	865	95.9	4.06	7.9
<b>3<sup>A</sup>Me</b>	-	Cub/ $Ia\bar{3}d_{(L)}$	11.4	1482	1.48	894	96.7	4.16	7.9
<b>3<sup>A</sup>OMe</b>	S4	Cub/ $Ia\bar{3}d_{(L)}$	11.4	1482	1.49	888	96.4	4.15	7.9
<b>3<sup>A</sup>ODec</b>	S4	Cub/ $I23$	17.9	5753	1.71	3004	370.2	3.65	<b>7.8</b>
<b>3<sup>A</sup>OCF<sub>3</sub></b>	-	Cub/ $I23$	16.2	4252	1.51	2515	335.0	3.38	<b>8.6</b>
<b>3<sup>A</sup>CN</b>	-	Cub/ $Ia\bar{3}d_{(L)}$	11.2	1405	1.48	848	95.0	4.02	8.0
<b>3<sup>A</sup>NO<sub>2</sub></b>	-	Cub/ $Ia\bar{3}d_{(L)}$	11.1	1368	1.47	831	94.2	3.97	8.1
<b>3<sup>A</sup>OAc</b>	-	Cub/ $Ia\bar{3}d_{(L)}$	11.5	1517	1.52	891	97.6	4.11	7.8
<b>3<sup>3</sup>F</b>	-	Cub/ $Ia\bar{3}d_{(L)}$	10.9	1295	1.46	792	92.5	3.85	8.2
<b>3<sup>3</sup>Br</b>	-	Cub/ $Ia\bar{3}d_{(L)}$	10.4	1125	1.48	679	88.2	3.46	8.6
		Cub/ $I23$	16.4	4411	1.48	2662	339.2	3.53	<b>8.5</b>
<b>3<sup>3</sup>I</b>	-	Cub/ $I23$	16.2	4252	1.49	2548	335.0	3.42	<b>8.6</b>
<b>3<sup>3</sup>CN</b>	-	Cub/ $Ia\bar{3}d_{(L)}$	10.8	1260	1.48	760	91.6	3.73	8.3
<b>3<sup>3</sup>OMe</b>	-	Cub/ $Ia\bar{3}d_{(L)}$	10.85	1277	1.49	765	92.1	3.74	8.3
		Cub/ $I23$	16.1	4173	1.49	2501	332.9	3.38	<b>8.7</b>
<b>3<sup>3</sup>OEt</b>	S4	Cub/ $I23$	15.7	3840	1.51	2271	324.7	3.15	<b>8.9</b>
<b>3<sup>3</sup>ODec</b>	-	Cub/ $Ia\bar{3}d_{(S)}$	9.8	941	1.71	491	83.2	2.66	<b>9.1</b>
<b>3<sup>34</sup>F<sub>2</sub></b>	-	Cub/ $I23$	16.0	4096	1.47	2488	330.9	3.38	<b>8.7</b>
<b>3<sup>34</sup>OMe<sub>2</sub></b>	S4	Cub/ $Ia\bar{3}d_{(L)}$	11.1	1368	1.52	804	94.2	3.84	8.1
<b>3<sup>35</sup>F<sub>2</sub></b>		Cub/ $I23$	15.8	3944	1.47	2396	326.7	3.30	<b>8.8</b>
<b>3<sup>35</sup>Br<sub>2</sub></b>		Cub/ $I23$	16.1	4173	1.51	2468	332.9	3.34	<b>8.7</b>
<b>3<sup>35</sup>I<sub>2</sub></b>	-	Cub/ $I23$	15.6	3796	1.53	2216	322.6	3.09	<b>9.0</b>
<b>3<sup>35</sup>NO<sub>2</sub></b>	-	Cub/ $I23$	15.8	3944	1.49	2364	326.7	3.26	<b>8.8</b>
<b>3<sup>2</sup>F</b>	-	Cub/ $Ia\bar{3}d_{(L)}$	10.9	1295	1.46	792	92.5	3.85	8.2
<b>3<sup>2</sup>I</b>	-	Cub/ $Ia\bar{3}d_{(L)}$	10.3	1093	1.49	655	87.4	3.37	8.7
<b>3<sup>2</sup>NO<sub>2</sub></b>	-	Cub/ $Ia\bar{3}d_{(L)}$	11.1	1368	1.47	831	94.2	3.97	8.1
<b>3<sup>345</sup>F<sub>3</sub></b>	-	Cub/ $I23$	15.6	3796	1.47	2306	322.6	3.22	<b>9.0</b>
<b>3<sup>345</sup>OMe<sub>3</sub></b>	S4	Cub/ $I23$	15.4	3624	1.56	2075	318.5	2.93	<b>9.1</b>
<b>3<sup>23456</sup>F<sub>5</sub></b>	-	Cub/ $I23$	15.6	3796	1.48	2290	322.6	3.19	<b>9.0</b>
<b>3a/Th</b>	-	Cub/ $Ia\bar{3}d$	10.9	1277	1.44	792	92.5	3.85	8.3
<b>3a/Cy</b>	S5	Cub/ $I23$	15.6	3796	1.49	2275	322.6	3.17	<b>9.0</b>
<b>3a/Ad</b>	S5	Cub/ $I23$	15.1	3443	1.56	1971	312.3	2.84	<b>9.2</b>
<b>3a/CEt<sub>3</sub></b>	S5	Cub/ $Ia\bar{3}d_{(S)}$	8.9	693	1.53	405	63.8	2.4	<b>10.1</b>
<b>3a/1-Npht</b>	-	Cub/ $Ia\bar{3}d_{(L)}$	10.6	1191	1.53	695	89.9	3.48	8.5
<b>3a/2-Npht</b>	-	Cub/ $Ia\bar{3}d_{(L)}$	11.6	1561	1.53	911	98.4	4.17	7.7
<b>3a/Biph</b>	-	Cub/ $Ia\bar{3}d_{(L)}$	12.0	1728	1.56	989	101.8	4.37	7.5

<sup>a</sup> Abbreviations:  $V_{\text{cell}} = a_{\text{cub}}^3$  = volume of the unit cell;  $V_{\text{mol}}$  = molecular volume as calculated with the crystal volume increments of Immirzi;<sup>S1</sup>  $n_{\text{cell}}$  number of molecules in a unit cell, calculated according to  $0.893 V_{\text{cell}}/V_{\text{mol}}$ , where the factor 0.893 is a correction for the different packing density in the crystalline and the LC state;  $L_{\text{net}}$  = total length of the networks per unit cell ( $L_{\text{net}} = 8.485a_{Ia\bar{3}d}$  and  $L_{\text{net}} = 20.68a_{I23}$ , respectively);  $n_{\text{raft}}$  = number of molecules organized in each 0.45 nm tick raft of the networks, calculated according to  $n_{\text{raft}} = n_{\text{cell}}/(L_{\text{net}}/0.45)$ ;  $\Phi$  = twist angle between adjacent molecules in the networks of the  $Ia\bar{3}d$ - phases;  $\Phi(Ia\bar{3}d) = 70.5^\circ/[0.354a_{\text{cub}}/0.45\text{nm}]$ ,  $\Phi(I23) = 90^\circ/[0.290a_{\text{cub}}/0.45\text{nm}]$ .<sup>S3</sup>

## S1.4. Other Data

Table S11. Selected steric and electronic parameters of the substituents X.

X	$V_{cX}/$ $\times 10^{-3} \text{ nm}^3$	$\sigma_m$	$\sigma_p$
H	6.9	-	-
F	12.8	0.34	0.06
Br	33.0	0.39	0.23
I	45.0	0.35	0.18
CN	31.3	0.56	0.66
NO <sub>2</sub>	25.6	0.71	0.78
CH <sub>3</sub>	31.7	-0.07	-0.17
OCH <sub>3</sub>	46.3	0.12	-0.27
OC <sub>2</sub> H <sub>5</sub>	71.1	0.10	-0.24
OC <sub>10</sub> H <sub>21</sub>	269.5	0.10 <sup>a</sup>	-0.32 <sup>a</sup>
OCF <sub>3</sub>	58.6	0.38	0.35
OCOCH <sub>3</sub>	58.6	0.39	0.31

$V_c$  is the crystal volume of the group estimated with the crystal volume increments reported by Immirzi;<sup>S1</sup>  $\sigma_m$  and  $\sigma_p$  are Hammett constants;<sup>S2</sup>  $\sigma_m$  is a measure of the strength of electron withdrawing (+) and electron donating (-) effects via the  $\sigma$ -bonds (inductive effect) and  $\sigma_p$  is an analogous measure for the delocalization mainly of the  $\pi$ -electrons (resonance effect); large positive values of  $\sigma_m$  and  $\sigma_p$  indicate electron acceptors whereas small positive and negative values are typically found for electron donating substituents. Data were taken from ref.S2; <sup>a</sup> values for OC<sub>4</sub>H<sub>9</sub>.

## S1.4 Additional Discussion

## S1.4.1 Dependence of cubic phase formation on the conditions.

**Compound 3<sup>3</sup>OMe.** - On heating the *I23* phase of 3<sup>3</sup>OMe is stable until the transition to the isotropic liquid. However, upon slow cooling ( $< 1 \text{ K min}^{-1}$ ) from the liquid state the achiral *Ia $\bar{3}d$*  phase is formed, only fast cooling ( $> 10 \text{ K min}^{-1}$ ) leads to the *I23* phase. Cooling with an intermediate rate provides a mixture of both cubic phases, where chiral dark and bright domains (*I23*) coexist with achiral areas having an intermediate brightness (*Ia $\bar{3}d$* , see Fig. S13a). That indeed *Ia $\bar{3}d$*  and *I23* coexist was confirmed by XRD where reflections of both phases coexist (Fig. S10 and Table S7). The ratio *Ia $\bar{3}d$* /*I23* does not change on further cooling, as the transformation becomes slow at lower temperature. However, as shown in Fig. S13b,c, annealing the sample with coexisting *Ia $\bar{3}d$*  and *I23* phases close to the Cub-Iso transition temperature slowly transforms *Ia $\bar{3}d$*  into *I23*. This means that the chiral *I23* phase is the thermodynamically stable cubic phase, whereas the achiral *Ia $\bar{3}d$*  phase is formed upon slow cooling from the achiral Iso phase. However, upon fast cooling, leading to a stronger delay of the Iso-Cub transition (super-cooling) the formation of the chiral *I23* phase takes place exclusively. It is postulated that at reduced temperature local symmetry breaking in the liquid phase (leading to a Iso<sub>1</sub><sup>[\*]</sup>-like local structure) becomes more important and favours the formation of the chiral *I23* phase, though no separate Iso<sub>1</sub><sup>[\*]</sup> range can be observed in this case.

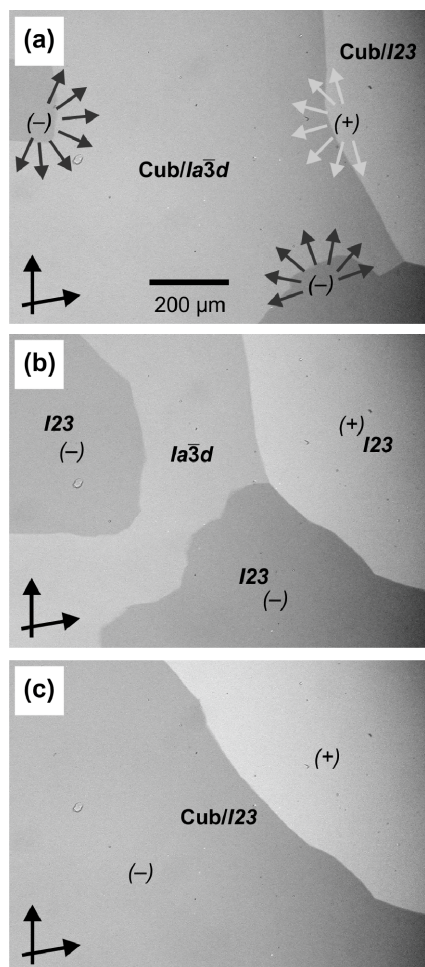


**Figure S13.** Cubic phases of 3<sup>3</sup>OMe as observed by POM with polarizers being slightly uncrossed after cooling from the isotropic liquid at 130 °C; a) coexisting *I23* and *Ia3d* phases as observed immediately after cooling; b) growing *I23* which in c) after 10 min has replaced the *Ia3d* phase completely; contrast enhanced, the width of the images is 1 mm.

**3<sup>3</sup>Br and 3<sup>3</sup>I.** - For 3<sup>3</sup>Br and 3<sup>3</sup>I there is an *I23* → *Ia3d* transition on heating (see Fig. S14), whereas on cooling from the isotropic liquid only the *Ia3d* phase is formed (see Table S1), independent on the cooling rate. Also in these cases the formation of the achiral *Ia3d* phase on cooling from the achiral Iso phase is favoured, but the transition to *I23* cannot be observed. Hence, for these two compounds the formation of the mirror symmetry broken *I23* phase appears to be a bit less favoured compared to 3<sup>3</sup>OMe (see Fig. S14 and Table S1).

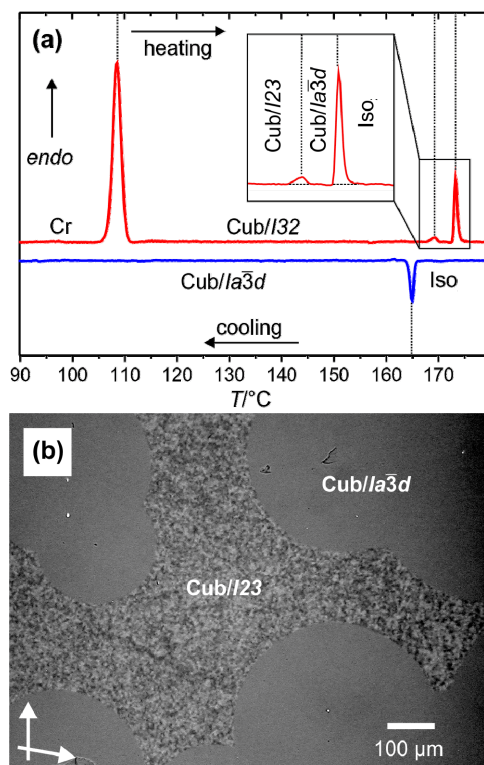


**Figure S14.** a) DSC traces of compound  $3^3\text{Br}$  and b)  $I23-Ia\bar{3}d$  transition on heating at  $T = 169^\circ\text{C}$  as observed between slightly uncrossed polarizers.

$3^2\text{NO}_2$ . – The  $\text{Cub}_{\text{bi}}/Ia\bar{3}d$  phase of this compound is observed only on heating, whereas on cooling a non-cubic 3D phase with highly birefringent mosaic texture (M1) is formed, which is stable on further cooling (Table S1) and represents a distorted version of the  $Ia\bar{3}d$  lattice.

#### S1.4.2 Birefringence in the cubic phase range.

In some cases birefringence can appear on cooling the  $\text{Cub}_{\text{bi}}$  phases. If the development of birefringence is associated with a change of the XRD pattern, these represent non-cubic LC phases with 3D lattice, denoted here as M (e.g.  $3^4\text{CN}$ ), which will be discussed in separate future contributions. In other cases development of a weak birefringence is not associated with any DSC peak or any change in the XRD pattern. This is shown in Fig. S15 for compound  $3^3\text{H}$  as a representative example. We attribute this to a developing strain caused by thermal shrinkage, which slightly deforms the cubic domains.

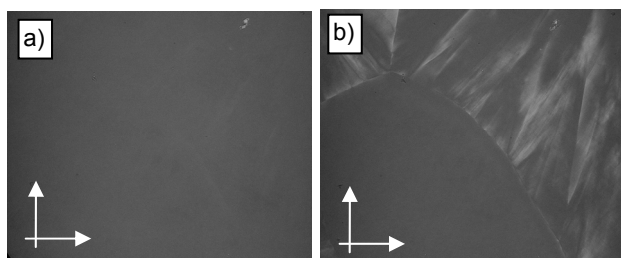


**Figure S15.** a, b) Developing strain-induced birefringence in the  $Ia\bar{3}d$  phase of compound  $3^3\text{H}$  as observed between crossed polarizers; a) completely isotropic appearance at  $T = 155^\circ\text{C}$  and b) weakly birefringent texture as observed on cooling to  $T = 80^\circ\text{C}$ .



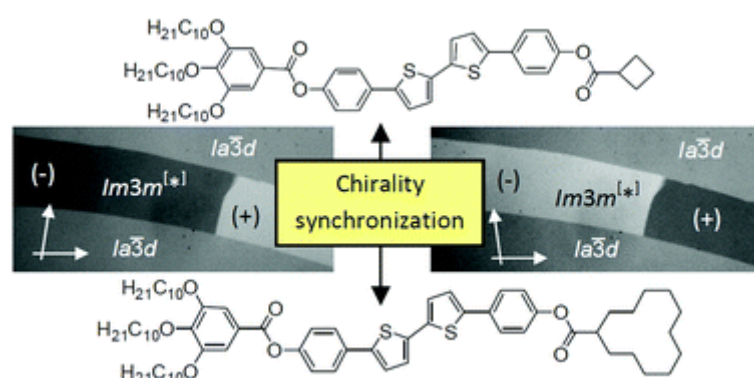
## Publikation B

Reproduktion mit der Genehmigung der Royal Society of Chemistry. Copyright 2020 Royal Society of Chemistry.

### Controlling spontaneous mirror symmetry breaking in cubic liquid crystalline phases by the cycloaliphatic ring size

Tino Reppe,<sup>[a]</sup> Christian Dressel,<sup>[a]</sup> Silvio Poppe,<sup>[a]</sup> Carsten Tschierske<sup>[a]</sup>

[a] Institute of Chemistry, Martin Luther University Halle-Wittenberg, Kurt-Mothes-Straße 2, 06120 Halle, Germany.



#### Abstract

Rod-like molecules combining a fork-like triple chain end and a cycloaliphatic apex are introduced as a new design concept for materials with broad ranges of bicontinuous cubic ( $Cub_{bi}$ ) phases. By ring expansion from  $n = 4$  to 12 a sequence of three  $Cub_{bi}$  phases is observed; the achiral double gyroid  $Ia\bar{3}d$  phase, a chiral “ $Im\bar{3}m$ ” phase and an achiral reentrant  $Ia\bar{3}d$  phase. The chiral “ $Im\bar{3}m$ ” phase is formed if the helical twist between the molecules along the networks is in the range of  $8.6^\circ$ – $9.5^\circ$ , either for the individual compounds or their mixtures.

#### Referenz

T. Reppe, C. Dressel, S. Poppe, C. Tschierske, *Chem. Comm.* **2020**, 56, 711–714.  
DOI: 10.1039/c9cc09206d.




 Cite this: *Chem. Commun.*, 2020, 56, 711

 Received 26th November 2019,  
Accepted 9th December 2019

DOI: 10.1039/c9cc09206d

rsc.li/chemcomm

# Controlling spontaneous mirror symmetry breaking in cubic liquid crystalline phases by the cycloaliphatic ring size†

 Tino Reppe, Christian Dressel, Silvio Poppe and Carsten Tschierske \*

Rod-like molecules combining a fork-like triple chain end and a cycloaliphatic apex are introduced as a new design concept for materials with broad ranges of bicontinuous cubic ( $\text{Cub}_{\text{bi}}$ ) phases. By ring expansion from  $n = 4$  to 12 a sequence of three  $\text{Cub}_{\text{bi}}$  phases is observed; the achiral double gyroid  $la\bar{3}d$  phase, a chiral " $Im\bar{3}m$ " phase and an achiral re-entrant  $la\bar{3}d$  phase. The chiral " $Im\bar{3}m$ " phase is formed if the helical twist between the molecules along the networks is in the range of  $8.6^\circ$ – $9.5^\circ$ , either for the individual compounds or their mixtures.

Mirror symmetry breaking and chirality synchronisation of achiral soft and liquid crystalline (LC) materials provides a new non-ex-chiral-pool route to chiral functional materials.<sup>1</sup> It has been observed in nematic, smectic and columnar LC phases,<sup>2,3</sup> but recently it was also found in bicontinuous cubic ( $\text{Cub}_{\text{bi}}$ ) LCs<sup>4,5</sup> and even in isotropic liquids ( $\text{Iso}_1$ <sup>[\*]</sup>).<sup>6</sup> The  $\text{Cub}_{\text{bi}}$  phases have attracted much attention by virtue of their ubiquitous presence in nature and their significant interest for conducting and photonic materials, as matrices for protein crystallization and templates for sol-gel syntheses.<sup>7,8</sup>  $\text{Cub}_{\text{bi}}$  phases are formed by different types of amphiphilic compounds either in aqueous systems (lyotropic phases)<sup>8</sup> or as pure compounds (thermotropic phases).<sup>9</sup> Amphiphilicity can be due to a polar-apolar molecular structure or a combination of rod-like polyaromatic cores with flexible chains, both leading to nano-segregation of the incompatible units.<sup>10</sup> Among the rod-like molecules forming  $\text{Cub}_{\text{bi}}$  phases the 4'-*n*-alkyloxy-3'-nitrophenyl-4-carboxylic acids (ANBCs),<sup>11</sup> the 1,2-bis(4'-*n*-alkanoyloxybenzoyl hydrazines) (BABHs)<sup>12</sup> and the so-called polycatenar compounds, having more than only two terminal chains at their ends<sup>13</sup> are the most common. In the  $\text{Cub}_{\text{bi}}$  phases the polyaromatic cores form the networks and the end chains fill the continuum around them. In these networks the rods are aligned (anti)parallel to each other

and on average perpendicular to the networks. The most preferred  $\text{Cub}_{\text{bi}}$  phase is the double gyroid phase (space group  $la\bar{3}d$ ) involving two networks with three-way junctions (see Fig. 1a).<sup>8,9</sup> There is a second common, but more complex type of  $\text{Cub}_{\text{bi}}$  phases with a different space group and a significantly larger lattice parameter,<sup>14</sup> whose precise structure is still under discussion. Its X-ray diffraction pattern was indexed to the space group  $Im\bar{3}m$  and a triple network structure (Fig. 1b)<sup>15</sup> or a double network involving additional spherical aggregates were suggested.<sup>16</sup>

This  $\text{Cub}_{\text{bi}}$  phase was recently found to be inherently chiral<sup>4,5</sup> and the discovery of this supramolecular chirality provided an improved general understanding of the cubic phases formed by rod-like compounds.<sup>2,4a</sup> Accordingly, the clashing of the bulky molecular peripheries leads to a helical twist (Fig. 1c) which is transmitted to the macroscopic scale by the network structure of the  $\text{Cub}_{\text{bi}}$  phases. The  $la\bar{3}d$  phase involves two enantiomorphic networks with opposite handedness (red, blue) and therefore it is achiral (Fig. 1a). However, in the  $Im\bar{3}m$  phase this degeneracy is broken either by a third network (Fig. 1b), that chirality cannot

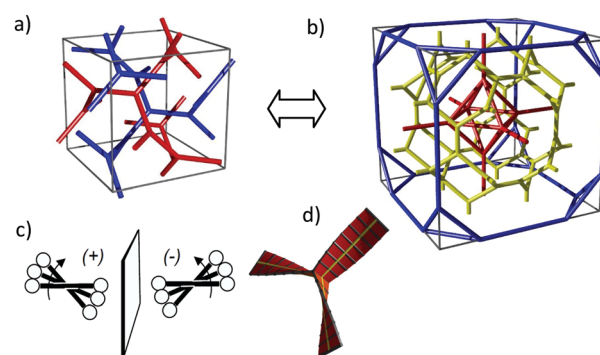
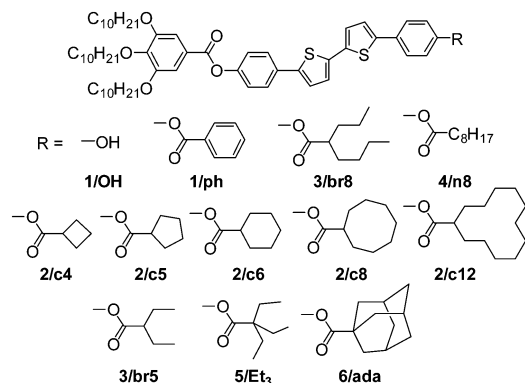


Fig. 1 Schematics showing (a) the achiral  $la\bar{3}d$  (double gyroid) and (b) the chiral  $Im\bar{3}m$ <sup>[\*]</sup> triple network structure of the  $\text{Cub}_{\text{bi}}$  phases formed by polycatenar mesogens and (c) clashing of the molecular peripheries leads to helical twist; (d) shows the continuous transmission of helicity across the junctions of the gyroid; (a) and (b) were reproduced with permission from ref. 4a, copyright, 2014, Wiley-VCH.

Institute of Chemistry, Martin Luther University Halle-Wittenberg, Kurt-Mothes-Straße 2, 06120 Halle, Germany. E-mail: carsten.tschierske@chemie.uni-halle.de

† Electronic supplementary information (ESI) available: Methods, syntheses, analytical data, additional XRD and structural data. See DOI: 10.1039/c9cc09206d





Scheme 1 Chemical structures of the compounds **1–6** under investigation.

be extinguished, or by the synchronization of the helix sense between the networks (as shown for the SmQ phase<sup>17</sup>). The highest symmetry chiral space group derived from the achiral  $Im\bar{3}m$  space group would be  $I432$ .<sup>4</sup> However, it is not sure if indeed the highest symmetry lattice is chosen and, in addition, it is questionable if the proposed structures, either involving some 5-way junctions (see red net in Fig. 1b)<sup>15</sup> or spherical aggregates,<sup>16</sup> could be stable for these rod-like molecules, and probably an alternative model has to be developed. Though, " $Im\bar{3}m^{[*]}$ " is still used to indicate this type of spontaneously chiral  $Cub_{bi}$  phase, it is in this case not considered as a crystallographic space group.

The availability of materials with  $Cub_{bi}$  phases is limited, and it is usually observed for only few compounds with specific alkyl chain lengths in narrow temperature ranges.<sup>8,9</sup> There are only few systems which are known to be less sensitive and show  $Cub_{bi}$  phases over wider ranges, namely the ANBCs and BABHs.<sup>9,11,12</sup> Therefore, the design of new materials forming  $Cub_{bi}$  phases over wide temperature ranges is still a challenging demand.

Herein such a new class of  $Cub_{bi}$  phase forming compounds is provided and the focus is on the elucidation of the molecular structural parameters which favour  $Cub_{bi}$  phase formation and determine the specific type of cubic phase, either  $la\bar{3}d$  or  $Im\bar{3}m^{[*]}$ . To this end compounds **2/cn** (Scheme 1) having a cycloaliphatic unit attached to the apex of a three-forked 2,5'-diphenyl-2,2'-dithiophene core were synthesized and compared with related non-cyclic (**3–5**) and a polycyclic adamantane substituted compound (**6/ada**).

The compounds of series **2–6** were synthesized from the previously reported phenol **1/OH**<sup>4a,6a</sup> by acylation using standard procedures, see ESI.† Though the isotropic liquid and the cubic phases both appear completely dark between crossed polarizers, the transition to the cubic phases can be detected by a strong increase of the viscosity at the Iso  $\rightarrow$   $Cub_{bi}$  transition which is associated with a DSC peak. There is a hysteresis of this transition, being 6 to 14 K lower on cooling than on heating (see Table S1, ESI.†), which is another typical feature of cubic LC phases. The type of cubic phase is identified by investigation between slightly uncrossed polarizers where only the  $Im\bar{3}m^{[*]}$  phase shows a conglomerate of optically active dark and bright chiral domains (Fig. 2b, c and Fig. S5, ESI.†), whereas the  $la\bar{3}d$  phase is achiral and does not show such domains (Fig. S4, ESI.†).

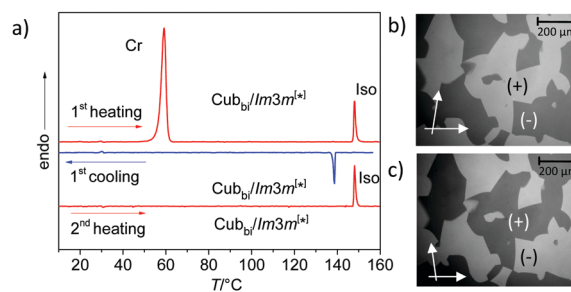


Fig. 2 Investigation of compound **2/c8**. (a) DSC heating and cooling traces ( $10\text{ K min}^{-1}$ ); (b and c) optically active domains in the  $Cub_{bi}/Im\bar{3}m^{[*]}$  phase at  $140\text{ }^{\circ}\text{C}$  as observed between slightly uncrossed polarizers after rotation in (b) clockwise and (c) anticlockwise direction (contrast enhanced).

The lattice type is additionally confirmed by the distinct positions of the small angle X-ray diffraction peaks in these two phase types, with the most intense reflections being either  $\sqrt{6}$  (211) and  $\sqrt{8}$  (220) for  $la\bar{3}d$  or  $\sqrt{14}$  (321),  $\sqrt{16}$  (400) and  $\sqrt{20}$  (422) for  $Im\bar{3}m^{[*]}$  (see Fig. S2a, S3a and Tables S2, S3, ESI.†).<sup>4a</sup> In the  $la\bar{3}d$  phases the lattice parameter  $a_{cub}$  has a ratio of  $\sqrt{3}a_{cub}/4$  to the molecular length, indicating that the distance between the middle of the networks corresponds to approximately one (0.86–1.09) molecular length (Table S5, ESI.†). The deviation from being exactly one could be due to a changing degree of intercalation of rods and apices (Fig. S7, ESI.†).<sup>12b</sup> The LC character of the cubic phases is obvious from the diffuse wide angle scattering with maxima at 0.45–0.46 nm (see Fig. S2b and S3b, ESI.†) confirming the absence of any fixed positions for the individual molecules.

Compound **1/ph** with a benzene ring at the apex forms an enantiotropic  $la\bar{3}d$  phase between 114 and  $162\text{ }^{\circ}\text{C}$ .<sup>4a</sup> Replacement of the benzene ring by a cyclohexane ring (**2/c6**) increases the cubic phase range and changes the  $Cub_{bi}$  phase type from  $la\bar{3}d$  to  $Im\bar{3}m^{[*]}$ , while there is no significant change of the  $Cub_{bi}$ –Iso transition temperature (Table 1). The additional axial H-atoms make cyclohexane an effectively bulkier group compared to the relatively flat benzene ring of **1/ph**.

Table 1 Phase transitions, lattice parameters ( $a_{cub}$ ) and twist angles between the molecules in neighbouring rafts ( $\Phi/^\circ$ ) in the  $Cub_{bi}$  phases of compounds **1–6**<sup>a</sup>

Compd	$T^a/^\circ\text{C}$ [ $\Delta H\text{ kJ mol}^{-1}$ ]		$a_{cub}/\text{nm}$ ( $T/^\circ\text{C}$ )	$\Phi/^\circ$
<b>1/ph</b> <sup>4a</sup>	Cr 114 [39.7] $la\bar{3}d$ 162 [2.3] Iso		11.0 (116)	8.2
<b>2/c4</b>	Cr 92 [17.7] $la\bar{3}d$ 148 [3.3] Iso		10.4 (130)	8.6
<b>2/c5</b>	Cr 88 [16.3] $la\bar{3}d$ 150 [3.0] Iso		10.5 (135)	8.5
<b>2/c6</b>	Cr 93 [33.9] $Im\bar{3}m^{[*]}$ 160 [4.3] Iso		15.6 (125)	—
<b>2/c8</b>	Cr 59 [33.1] $Im\bar{3}m^{[*]}$ 148 [4.5] Iso		15.4 (100)	—
<b>2/c12</b>	Cr 103 [36.6] $la\bar{3}d$ 113 [2.9] Iso		9.4 (108)	9.5
<b>3/br5</b>	Cr 75 [29.8] $Im\bar{3}m^{[*]}$ 109 [3.4] Iso		14.8 (90)	—
<b>3/br8</b>	Cr 57 [43.7] Iso		—	—
<b>4/lin8</b>	Cr 90 [5.7] $Im\bar{3}m^{[*]}$ 122 [1.9] Iso		16.0 (110)	—
<b>5/Et<sub>3</sub></b>	Cr 49 [8.9] $la\bar{3}d$ 87 [2.7] Iso		8.85 (70)	10.1
<b>6/ada</b>	Cr 84 [11.2] $Im\bar{3}m^{[*]}$ 156 [3.6] Iso		15.1 (120)	—

<sup>a</sup> DSC peak temperatures on heating at  $10\text{ K min}^{-1}$ ; for transitions on cooling, see Table S1, ESI; for molecular structures, see Scheme 1; abbreviations: Cr = crystalline solid,  $la\bar{3}d$  = bicontinuous cubic phase with double gyroid structure;  $Im\bar{3}m^{[*]}$  = mirror symmetry broken bicontinuous cubic phase; Iso = isotropic liquid;  $\Phi(la\bar{3}d) = 70.5^\circ/[0.354a_{cub}/0.45]$ ,<sup>4a</sup> for DSCs, see Fig. S1, ESI.

In a next step the effect of the ring size was investigated systematically. All compounds **2/c4**–**2/c12** with cycloaliphatic end groups form cubic phases which do not crystallize on cooling (see DSC in Fig. 2a and Fig. S1, ESI†). Only after storage at 20 °C for several days partial crystallization takes place. The Cub<sub>bi</sub>–Iso transition temperatures first increase with growing ring size from 148 °C for **2/c4** to 160 °C for **2/c6** and then decrease again to 113 °C for **2/c12** (Table 1). In addition, there is a significant effect of the ring size on the cubic phase type. The cyclobutane and cyclopentane carboxylates **2/c4** and **2/c5** show the *la3d* phase, whereas the *Im3m*<sup>[\*]</sup> phase is observed for the compounds **2/c6**–**2/c8** with larger ring sizes, and surprisingly, the largest one, the cyclododecane carboxylate **2/c12** forms a *la3d* phase again. Thus, the sequence *la3d*–*Im3m*<sup>[\*]</sup>–*la3d* with an re-entrance of the *la3d* phase is observed by increasing the ring size.‡ Remarkably, the lattice parameter of the *la3d* phase ( $a_{\text{cub}}$ ) of compound **2/c4** with a smaller cyclobutane is 1 nm longer than that of compound **2/c12** with the larger cyclododecane ring (Table 1), meaning that the number of molecules per unit cell ( $n_{\text{cell}}$ ) decreases by ring expansion. In the *Im3m*<sup>[\*]</sup> phase, occurring between the two *la3d* phases, the lattice parameter is about 50% larger and the number of molecules per unit cell is about three to five times the number in the *la3d* phases (see Table S4, ESI†).

The chiral *Im3m*<sup>[\*]</sup> phase is also found in the contact region between the achiral *la3d* phases of the two compounds **2/c4** and **2/c12**. In the contact area between them a concentration gradient develops and a ribbon composed of dark and bright chiral domains can be observed by optical microscopy between not exactly 90° crossed polarizers (Fig. 3). Rotating the analyzer into the opposite direction with respect to the polarizer reverses the brightness of the domains, whereas rotation of the sample between crossed polarizers does not change the domains. The maximum of the Cub–Iso transition of the induced *Im3m*<sup>[\*]</sup> phase on heating is at 143 °C. This means that mixing the *la3d* phases of two compounds with different ring size causes the same effect as adjusting the ring size by synthesis of discrete single compounds. This is of practical interest as it allows the preparation of eutectic multi-component mixtures forming the chiral *Im3m*<sup>[\*]</sup> phase over broad temperature ranges down to ambient temperature and below. It also shows that simple mixing of two achiral compounds can lead to a spontaneously mirror symmetry broken system.‡<sup>18</sup>

In order to investigate the effect of the aliphatic ring structure on self-assembly two compounds related to **2/c8** were synthesized, the linear *n*-nonanoate **4/n8** and the 2-propylhexanoate **3/br8** with a branched apex, both with the same total number of eight C-atoms

in the aliphatic part ( $n = 8$ ). The branched compound **3/br8** does not form any LC phase, it has a melting point at 57 °C and on cooling it crystallizes at 4 °C (Fig. S1g, ESI†). The linear compound **4/n8** forms an *Im3m*<sup>[\*]</sup> cubic phase, too, just like **2/c8**, but the Cub<sub>bi</sub>–Iso transition is reduced by 26 K. This shows that cyclization is a powerful tool to stabilize cubic LC phases.

The distorting effect of chain branching becomes smaller for compounds **3/br5** with two shorter ethyl branches, but nevertheless, there is still a large stabilizing effect of cyclization, enhancing the cubic phase stability by 40 K and changing the cubic phase type from *Im3m*<sup>[\*]</sup> for **3/br5** to *la3d* for **2/c5**, reflecting the smaller effective size of the cyclic apex.

Increasing the volume of the apex by adding one more ethyl group to the apex of **3/br5** retains the Cub<sub>bi</sub> phase (**5/Et<sub>3</sub>**), but the phase type is changed from *Im3m*<sup>[\*]</sup> to *la3d*. Miscibility experiments with the *la3d* phase of **2/c4** or **2/c5** indicate the induction of a chiral ribbon of the *Im3m*<sup>[\*]</sup> phase between them (see Fig. S6, ESI†), thus confirming that the two *la3d* phases are of a different type, in line with the different size of their apices.

The adamantane-1-carboxylate **6/ada** is related to **5/Et<sub>3</sub>** by having a triply branched aliphatic units at the apex, but in this case incorporated in a polycyclic entity. **6/ada** forms a *Im3m*<sup>[\*]</sup> phase, though the total number of aliphatic C-atoms at the apex is increased from 7 in **5/Et<sub>3</sub>** to 10 in **6/ada** (Table 1). This observation is in line with the smaller effective size of the adamantyl group due to the reduced conformational freedom of the polycyclic hydrocarbon compared to the flexible diethylbutanoate unit of **5/Et<sub>3</sub>**, capable of assuming several bulky conformations.

Thus, the effect of the apex substituent could be traced back to a series of competing volume effects. The first determines the degree of interfacial curvature, *i.e.* if a lamellar, Cub<sub>bi</sub> or a columnar phase is formed.<sup>10</sup> It is a remarkable feature of the investigated compounds that exclusively Cub<sub>bi</sub> phases were observed. This volume effect is only expressed by the change of the Cub<sub>bi</sub> phase type and the Cub<sub>bi</sub>–Iso transition temperature (Table 1).

As shown in Table 1, the lattice parameter  $a_{\text{cub}}$  decreases with growing effective apex size. The number of molecules calculated from  $a_{\text{cub}}$  for each column segment between the junctions in the two gyroid networks of the *la3d* phase is about 29 for **2/c4** and only about 19 for **2/c12**. Simultaneously, the distance between the junctions decreases from 3.7 nm for **2/c4** to 3.3 nm for **2/c12** (see Table S4, ESI†). Hence, the number of molecules organized side-by-side in each stratum (raft) of the columns with an assumed height of 0.45 nm is 3.5 for **2/c4** and only about 2.6 for **2/c12** (see Table S4, ESI†). This means that with growing apex size there is a decreasing number of molecules in each of the rafts and also the number of rafts along the column segments between the junctions decreases.

Most importantly, the apex volume affects the twist between the rods organized along the networks (Fig. 1c). This twist is caused by the clashing of the bulky molecular ends and is transmitted by the network junctions throughout the whole network. The *la3d* phase has trigonal junctions with a fixed dihedral angle of 70.5° between them (Fig. 1a). A continuous twist of the molecules between the junctions by this angle is required for a smooth merging of the rods without defects at the junctions (Fig. 1d). With growing apex volume the distance

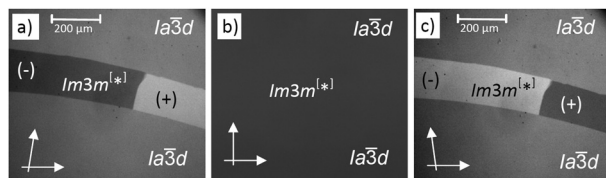


**Fig. 3** Chiral domains of the *Im3m*<sup>[\*]</sup> phase induced between the achiral *la3d* phases of compounds **2/c4** (top) and **2/c12** (bottom) at  $T = 129$  °C (contrast enhanced); on cooling the *Im3m*<sup>[\*]</sup> phase appears at 130 °C and on heating it disappears at 143 °C; for the contact region between **2/c4** and **5/Et<sub>3</sub>**, see Fig. S6, ESI†.

between the junctions decreases (see above) and consequently the twist angle  $\Phi$  between adjacent rod-like cores along the column segments increases (Table 1 and Fig. S4, ESI†). A twist angle between the molecules in adjacent rafts of 8.2–8.6° is found in the  $la\bar{3}d$  phases. If the twist angle exceeds this value the gyroid is replaced by the  $Im3m^{[*]}$  structure. However, the  $la\bar{3}d$  lattice appears again upon further chain volume enlargement, as for example observed in the series of cyclic compounds **2/cn**. The calculated twist angle is 9.5° in the re-entrant  $la\bar{3}d$  phase of **2/c12** and an even larger value of 10.1° is calculated for the  $la\bar{3}d$  phase of **5/Et<sub>3</sub>** (Table 1). Hence, the chiral  $Im3m^{[*]}$  phase becomes the thermodynamically more stable alternative mode of self-assembly replacing the achiral double gyroid if the intermolecular twist exceeds 8.6°. However, this structure appears to be even more sensitive to the twist angle change and becomes the less stable structure as the twist in the competing  $la\bar{3}d$  phase reaches 9.5°. This is a generally observed feature‡ and any new or modified model of the  $Im3m^{[*]}$  phase has to give a convincing explanation of this observation.

Overall, a new design concept of robust thermotropic Cub<sub>bi</sub> phase forming materials, based on tricatena compounds with a cycloaliphatic apex is introduced, providing a tool for stabilizing Cub<sub>bi</sub> phases over broad temperature ranges. In this respect these compounds are advantageous over related compounds with linear or branched alkyl chains at the apex. It also allows the engineering of the cubic phase type ( $la\bar{3}d$  vs.  $Im3m^{[*]}$ ) and hence the control of emergence of supermolecular chirality. The remarkable re-entrance of the  $la\bar{3}d$  phase is not yet fully understood. However, it appears that for a twist angle in the range between 8.6 and 9.5° the chiral  $Im3m^{[*]}$  phase becomes the thermodynamically more stable alternative structure with respect to the achiral double gyroid ( $la\bar{3}d$ ), irrespectively if it is formed by a single compound or in mixtures of compounds with different apex size. This observation is difficult to explain with the presently existing models of the cubic “ $Im3m$ ” phase<sup>15,16</sup> and requires a further refinement of these models.

## Conflicts of interest

There are no conflicts to declare.

## Notes and references

‡ A phase sequence  $la\bar{3}d-Im3m^{[*]}-la\bar{3}d$  with increasing terminal alkyl chains length was observed for the ANBCs<sup>11</sup> and BABHS.<sup>12</sup> For the latter the  $Im3m^{[*]}$  phase was also induced between the  $la\bar{3}d$  phases of different homologues.<sup>18</sup>

- H. K. Bisoyi, T. J. Bunning and Q. Li, *Adv. Mater.*, 2018, **30**, 1706512; B. Chang, X. Li and T. Sun, *Eur. Polym. J.*, 2019, **118**, 365; Y. Sang, J. Han, T. Zhao, P. Duan and M. Liu, *Adv. Mater.*, 2019, 1900110.
- (a) C. Tschierske, *Liq. Cryst.*, 2018, **45**, 2221; (b) C. Tschierske and G. Ungar, *ChemPhysChem*, 2016, **17**, 9.
- K. V. Le, H. Takezoe and F. Araoka, *Adv. Mater.*, 2017, 1602737.
- (a) C. Dressel, F. Liu, M. Prehm, X. B. Zeng, G. Ungar and C. Tschierske, *Angew. Chem., Int. Ed.*, 2014, **53**, 13115; (b) M. Alaasar, S. Poppe, Q. Dong, F. Liu and C. Tschierske, *Chem. Commun.*, 2016, **52**, 13869.
- (a) T. Kajitani, S. Kohmoto, M. Yamamoto and K. Kishikawa, *Chem. Mater.*, 2005, **17**, 3812; J. M. Wolska, J. Wilk, D. Pocięcha, J. Mieczkowski and E. Gorecka, *Chem. – Eur. J.*, 2017, **23**, 6853; (b) H. R. Brand and H. Pleiner, *Eur. Phys. J. E: Soft Matter Biol. Phys.*, 2019, **42**, 142.
- (a) C. Dressel, T. Reppe, M. Prehm, M. Brautzsch and C. Tschierske, *Nat. Chem.*, 2014, **6**, 971; (b) C. Dressel, W. Weissflog and C. Tschierske, *Chem. Commun.*, 2015, **51**, 15850; (c) M. Alaasar, M. Prehm, Y. Cao, F. Liu and C. Tschierske, *Angew. Chem., Int. Ed.*, 2016, **55**, 312; M. Alaasar, S. Poppe, Q. Dong, F. Liu and C. Tschierske, *Angew. Chem., Int. Ed.*, 2017, **56**, 10801.
- T. Kato, J. Uchida, T. Ichikawa and T. Sakamoto, *Angew. Chem., Int. Ed.*, 2018, **57**, 4355.
- Bicontinuous Liquid Crystals*, ed. M. L. Lynch and P. T. Spicer, CRC Press, Taylor & Francis Group, Boca Raton, FL, 2005; L. van't Hag, S. L. Gras, C. E. Conn and C. J. Drummond, *Chem. Soc. Rev.*, 2017, **46**, 2705.
- (a) G. Ungar, F. Liu and X. B. Zeng, in *Handbook of Liquid Crystals*, ed. J. W. Goodby, P. J. Collings, T. Kato, C. Tschierske, H. Gleeson and P. Raynes, Wiley-VCH, 2nd edn, 2014, vol. 5; (b) S. Kutsumizu, *Isr. J. Chem.*, 2012, **52**, 844; (c) M. Yoneya, *Chem. Rec.*, 2011, **11**, 66.
- C. Tschierske, *J. Mater. Chem.*, 2001, **11**, 2647.
- G. W. Gray, B. Jones and F. Marson, *J. Chem. Soc.*, 1957, 393; S. Kutsumizu, K. Morita, T. Ichikawa, S. Yano, S. Nojima and T. Yamaguchi, *Liq. Cryst.*, 2002, **29**, 1447.
- (a) H. Schubert, J. Hauschild, D. Demus and S. Hoffmann, *Z. Chem.*, 1978, **18**, 256; (b) Y. Yamamura, Y. Nakazawa, S. Kutsumizu and K. Saito, *Phys. Chem. Chem. Phys.*, 2019, **21**, 32705.
- H. T. Nguyen, C. Destradre and J. Malthete, *Adv. Mater.*, 1997, **9**, 375; D. W. Bruce, *Acc. Chem. Res.*, 2000, **33**, 831.
- A. M. Levelut and M. Clerc, *Liq. Cryst.*, 1998, **24**, 105.
- X. B. Zeng, G. Ungar and M. Imperor-Clerc, *Nat. Mater.*, 2005, **4**, 562.
- K. Saito, Y. Yamamura, Y. Miwa and S. Kutsumizu, *Phys. Chem. Chem. Phys.*, 2016, **18**, 3280.
- H. J. Lu, X. B. Zeng, G. Ungar, C. Dressel and C. Tschierske, *Angew. Chem., Int. Ed.*, 2018, **57**, 2835.
- S. Kutsumizu, S. Miisako, Y. Miwa, M. Kitagawa, Y. Yamamura and K. Saito, *Phys. Chem. Chem. Phys.*, 2016, **18**, 17341.

## Supporting Information

### Controlling spontaneous mirror symmetry breaking in cubic liquid crystalline phases by the cycloaliphatic ring size

Tino Reppe, Christian Dressel, Silvio Poppe and Carsten Tschierske<sup>a,\*</sup>

<sup>a</sup> Institute of Chemistry, Martin-Luther-University Halle-Wittenberg, Kurt-Mothes-Straße 2,  
06120 Halle

#### 1. Methods

**Optical and calorimetric investigations.** Phase transitions were determined by polarizing microscopy (Leica DMR XP) in conjunction with a heating stage (FP 82 HT, Mettler) and controller (FP 90, Mettler) and by differential scanning calorimetry (DSC-7, Perkin Elmer) at heating/cooling rates of 10 K min<sup>-1</sup> (peak temperatures). If not otherwise noted transition temperatures and –enthalpies were taken from the second heating and cooling curve. Optical investigation was carried out under equilibrium conditions between glass slides which were used without further treatment, sample thickness was ~15 µm. A full wavelength retardation plate was used to determine the sign of birefringence. Optical micrographs were taken using a Leica MC120HD camera.

#### **X-ray diffraction.**

X-ray investigations (Kristalloflex 760H, Siemens) on powder-like samples were carried out using Ni filtered CuK $\alpha$  radiation (15 to 30 min exposure time). The samples were prepared in the isotropic state on a glass plate and cooled (rate: 5 K·min<sup>-1</sup>) to the measuring temperature. The samples were held on a temperature controlled heating stage and the diffraction patterns were recorded with a 2D detector (Vantec 500, Bruker); exposure time was 15-20 min. The sample-detector distance for the samples was 9.00 cm for WAXD and 26.90 cm for SAXD measurements. The diffraction patterns obtained were transform to 1D plots using GADDS over the full Chi range.

## 2. Additional data

### 2.1 DSC traces and transition temperatures

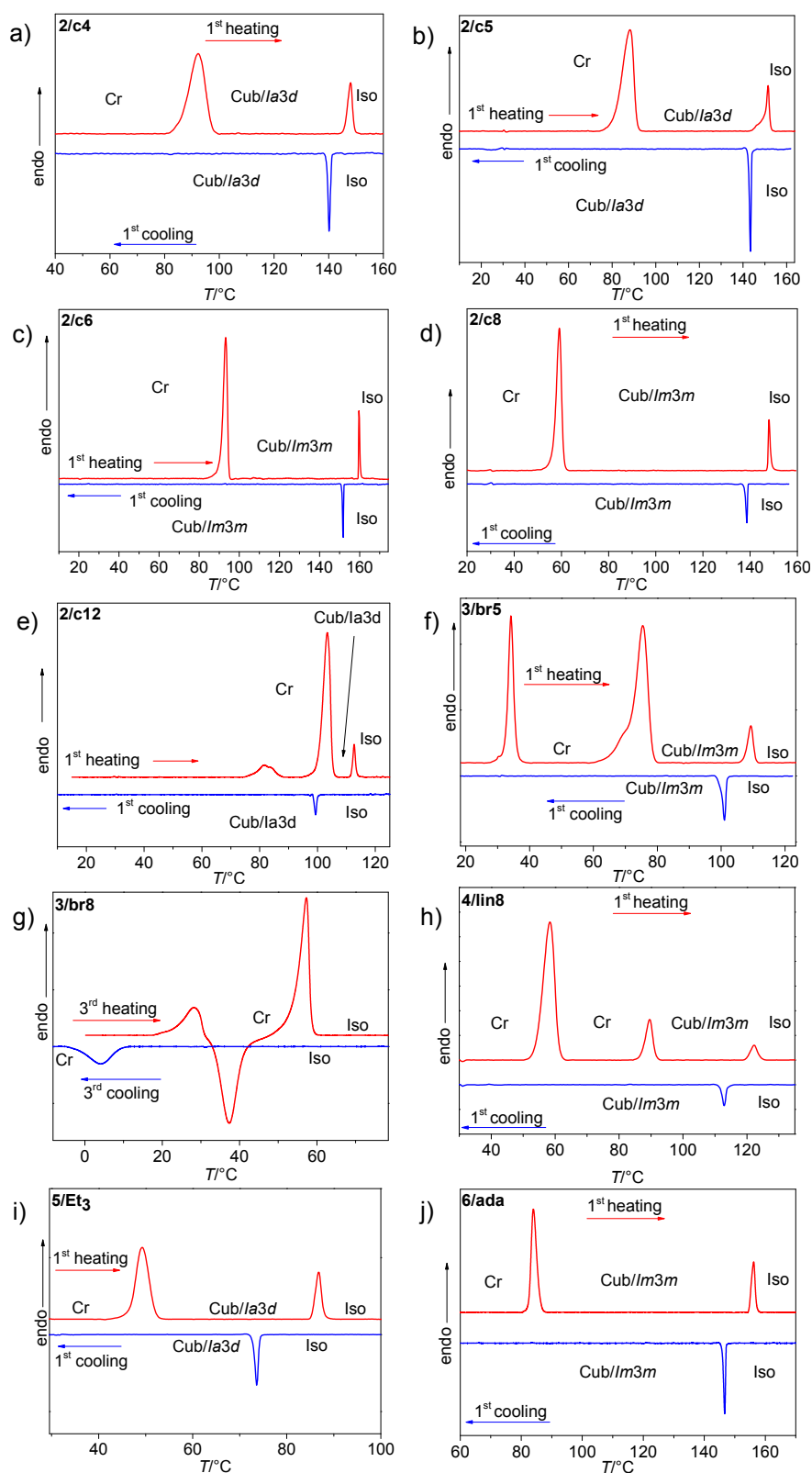
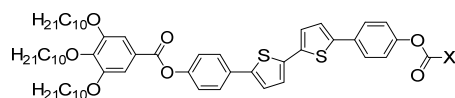


Figure S1. DSC traces (10 K·min<sup>-1</sup>) of compounds 2-6.

**Table S1.** Transition temperatures and –enthalpies of compounds **1-6** on heating (H) and cooling (C).



Compd.	X	$T/^\circ\text{C}$ [ $\Delta H/\text{kJ}\cdot\text{mol}^{-1}$ ]
<b>1/ph<sup>SI</sup></b>	phenyl	H: Cr 114 [39.7] Cub <sub>bi</sub> / <i>Ia</i> $\bar{3}d$ 162 [2.3] Iso C: Iso 156 [-1.7] Cub <sub>bi</sub> / <i>Ia</i> $\bar{3}d$ 69 [-3.8] Cr
<b>2/c4</b>	cyclobutyl	H: Cr 92 [17.7] Cub <sub>bi</sub> / <i>Ia</i> $\bar{3}d$ 148 [3.3] Iso C: Iso 141 [-2.6] Cub <sub>bi</sub> / <i>Ia</i> $\bar{3}d$ < 0 Cr
<b>2/c5</b>	cyclopentyl	H: Cr 88 [16.3] Cub <sub>bi</sub> / <i>Ia</i> $\bar{3}d$ 150 [3.0] Iso C: Iso 143 [-2.5] Cub <sub>bi</sub> / <i>Ia</i> $\bar{3}d$ < 0 Cr
<b>2/c6</b>	cyclohexyl	H1: Cr 93 [33.9] Cub <sub>bi</sub> / <i>Im</i> $\bar{3}m^{[*]}$ 160 [4.3] Iso C1: Iso 152 [-3.0] Cub <sub>bi</sub> / <i>Im</i> $\bar{3}m^{[*]}$ < 0 Cr
<b>2/c8</b>	cyclooctyl	H: Cr 59 [33.1] Cub <sub>bi</sub> / <i>Im</i> $\bar{3}m^{[*]}$ 148 [4.5] Iso C: Iso 139 [-2.9] Cub <sub>bi</sub> / <i>Im</i> $\bar{3}m^{[*]}$ < 0 Cr
<b>2/c12</b>	cyclododecyl	H: Cr 103 [36.6] Cub <sub>bi</sub> / <i>Ia</i> $\bar{3}d$ 113 [2.9] Iso C: Iso 99 [-1.5] Cub <sub>bi</sub> / <i>Ia</i> $\bar{3}d$ < 0 Cr
<b>3/br5</b>	3-pentyl	H: Cr 75 [29.8] Cub <sub>bi</sub> / <i>Im</i> $\bar{3}m^{[*]}$ 109 [3.4] Iso C: Iso 101 [-2.6] Cub <sub>bi</sub> / <i>Im</i> $\bar{3}m^{[*]}$ < 0 Cr
<b>3/br8</b>	4-octyl	H: Cr 57 [43.7] Iso C: Iso 4 [-13.9] Cr
<b>4/lin8</b>	-octyl	H: Cr 90 [5.7] Cub <sub>bi</sub> / <i>Im</i> $\bar{3}m^{[*]}$ 122 [1.9] Iso C: Iso 113 [-1.6] Cub <sub>bi</sub> / <i>Im</i> $\bar{3}m^{[*]}$ < 0 Cr
<b>5/Et<sub>3</sub></b>	2,2-(diethyl)propyl	H: Cr 49 [8.9] Cub <sub>bi</sub> / <i>Ia</i> $\bar{3}d$ 87 [2.7] Iso C: Iso 74 [-1.7] Cub <sub>bi</sub> / <i>Ia</i> $\bar{3}d$ < 0 Cr
<b>6/ada</b>	1-adamantyl	H1: Cr 84 [11.2] Cub <sub>bi</sub> / <i>Im</i> $\bar{3}m^{[*]}$ 156 [3.6] Iso C1: Iso 147 [-2.7] Cub <sub>bi</sub> / <i>Im</i> $\bar{3}m^{[*]}$ < 0 Cr

## 2.2 XRD data

**Table S2.** SAXS data of Cub<sub>bi</sub>/*Ia* $\bar{3}d$  phases of compounds **2/c4**, **2/c5**, **2/c12**, **5/Et<sub>3</sub>**.

Compd.	( <i>hkl</i> )	$d_{\text{obs}}$ – spacing/nm	$d_{\text{calc}}$ – spacing/nm	$d_{\text{obs}} - d_{\text{calc}}$	$a_{\text{cub}}$ /nm ( $T/^\circ\text{C}$ )
<b>2/c4</b>	(211)	4.23	4.23	0.00	10.35
	(220)	3.73	3.66	0.07	(130)
<b>2/c5</b>	(211)	4.28	4.28	0.00	10.49
	(220)	3.73	3.71	0.02	(135)
<b>2/c12</b>	(211)	3.84	3.84	0.00	9.40
	(220)	3.34	3.33	0.01	(108)
<b>5/Et<sub>3</sub></b>	(211)	3.61	3.61	0.00	8.85
	(220)	3.15	3.13	0.02	(70)



**Table S3.** SAXS data of  $\text{Cub}_{\text{bi}}/\text{Im}3m^{[*]}$  phases of compounds **2/c6**, **2/c8**, **3/br5**, **4/lin8** and **6/ada**.

Compd.	(hkl)	$d_{\text{obs}} - \text{spacing/nm}$	$d_{\text{calc}} - \text{spacing/nm}$	$d_{\text{obs}} - d_{\text{calc}}$	$a_{\text{cub}}/\text{nm} (T/^{\circ}\text{C})$
<b>2/c6</b>	(321)	4.18	4.18	0.00	15.64 (125)
	(400)	3.87	3.91	0.04	
	(420)	3.53	3.50	0.04	
	(422)	3.14	3.19	0.05	
<b>2/c8</b>	(321)	4.11	4.11	0.00	15.38 (100)
	(400)	3.83	3.85	0.02	
	(420)	3.44	3.44	0.00	
<b>2/c8</b>	(321)	4.07	4.07	0.00	15.24 (140)
	(400)	3.80	3.81	0.01	
	(420)	3.45	3.41	0.04	
<b>3/br5</b>	(321)	3.96	3.96	0.00	14.81 (90)
	(400)	3.67	3.70	0.03	
	(420)	3.36	3.31	0.05	
<b>4/lin8</b>	(321)	4.28	4.28	0.00	16.01 (110)
	(400)	4.03	4.00	0.03	
	(420)	3.57	3.58	0.01	
<b>6/ada</b>	(321)	4.04	4.04	0.00	15.13 (120)
	(400)	3.76	3.78	0.03	
	(420)	3.41	3.38	0.03	

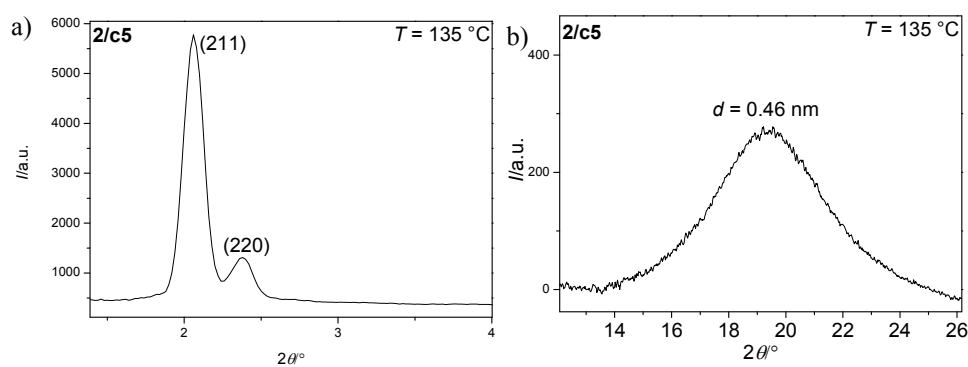


**Figure S2.** XRD data of the  $\text{Cub}_{\text{bi}}/\text{Ia}3d$  phase of compound **2/c5**, a)  $2\theta$  scan of the small angle area, as inset powder-like diffraction pattern with indexed reflexes, b)  $2\theta$  scan of the wide angle area.

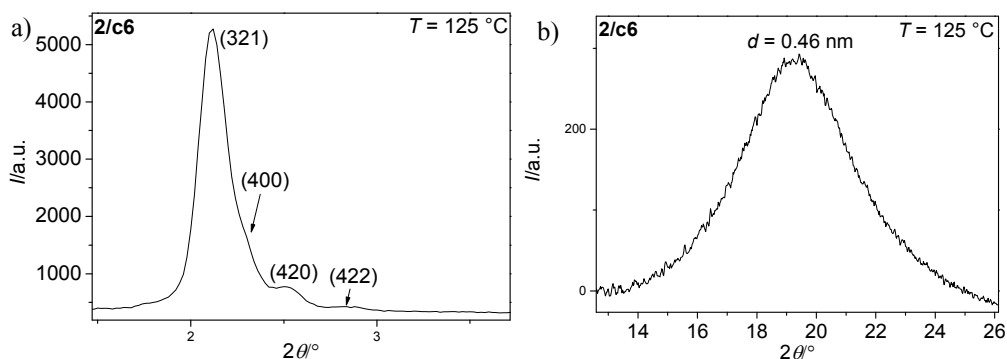


**Figure S3.** XRD data of the  $\text{Cub}_{\text{bi}}/\text{Im}3m^{[*]}$  phase of compound **2/c6**, a)  $2\theta$  scan of the small angle area, as inset powder-like diffraction pattern with indexed reflexes, b)  $2\theta$  scan of the wide angle area.

**Table S4.** Structural data of the investigated cubic phases.<sup>a</sup>

Compd.	Phase	$a_{\text{cub}}/\text{nm}$	$V_{\text{cell}}/\text{nm}^3$	$V_{\text{mol}}/\text{nm}^3$	$n_{\text{cell}}^b$	$n_{\text{rod}}^c$	$d_{\text{node}}/\text{nm}$	$n_{\text{strat}}^d$	$\Phi/^\circ$
<b>1/ph</b>	$\text{Cub}/\text{Ia}\bar{3}d$	11.0	1331	1.46	814	34	3.89	3.9	8.2
<b>2/c4</b>	$\text{Cub}/\text{Ia}\bar{3}d$	10.4	1125	1.44	698	29	3.68	3.5	8.6
<b>2/c5</b>	$\text{Cub}/\text{Ia}\bar{3}d$	10.5	1158	1.46	708	30	3.71	3.6	8.5
<b>2/c6</b>	$\text{Cub}_{\text{bi}}/\text{Im}3m^{[*]}$	15.6	3796	1.49	2275	-	-	-	-
<b>2/c8</b>	$\text{Cub}_{\text{bi}}/\text{Im}3m^{[*]}$	15.4	3652	1.54	1991	-	-	-	-
<b>2/c12</b>	$\text{Cub}/\text{Ia}\bar{3}d$	9.4	831	1.64	452	19	3.32	2.6	9.5
<b>3/br5</b>	$\text{Cub}_{\text{bi}}/\text{Im}3m^{[*]}$	14.8	3242	1.48	1956	-	-	-	-
<b>4/lin8</b>	$\text{Cub}_{\text{bi}}/\text{Im}3m^{[*]}$	16.0	4096	1.55	2360	-	-	-	-
<b>5/Et<sub>3</sub></b>	$\text{Cub}/\text{Ia}\bar{3}d$	8.9	693	1.53	405	17	3.13	2.4	10.1
<b>6/ada</b>	$\text{Cub}_{\text{bi}}/\text{Im}3m^{[*]}$	15.1	3443	1.56	1971	-	-	-	-

<sup>a</sup> Abbreviations:  $n_{\text{cell}}$  number of molecules in a unit cell;  $V_{\text{cell}} = a_{\text{cub}}^3$  = volume of the unit cell;  $V_{\text{mol}}$  = molecular volume as calculated with the crystal volume increments of Immirzi<sup>S2</sup>,  $\Phi$  = twist angle between adjacent molecules in the networks of the  $\text{Ia}\bar{3}d$ -phases; <sup>b</sup> calculated according to  $0.893 V_{\text{cell}}/V_{\text{mol}}$ , where the factor 0.893 is a correction for the different packing density in the crystalline and the LC state;  $\Phi(\text{Ia}\bar{3}d) = 70.5^\circ/[0.354a_{\text{cub}}/0.45\text{nm}]$ ; <sup>c</sup>  $n_{\text{rod}} = n_{\text{cell}}/24$  = number of molecules in each column segment between two junctions; <sup>d</sup>  $n_{\text{strat}} =$  number of molecules organized side by side in each 0.45 nm high stratum of the column segments, calculated from the distance between the junctions  $d_{\text{node}} = a_{\text{cub}}/(2\sqrt{2})$  and an assumed height of each stratum of  $h = 0.45$  nm, according to:  $n_{\text{strat}} = n_{\text{rod}}/(d_{\text{node}}/h)$

**Table S5.** Structural data of the investigated  $\text{Cub}_{\text{bi}}/\text{Ia}\bar{3}d$  phases.<sup>a</sup>

Compd.	Phase	$a_{\text{cub}}/\text{nm}$	$d/\text{nm}$	$L_{\text{mol}}/\text{nm}$	$d/L_{\text{mol}}$
<b>1/ph</b>	$\text{Cub}/\text{Ia}\bar{3}d$	11.0	4.8	4.4	1.09
<b>2/c4</b>	$\text{Cub}/\text{Ia}\bar{3}d$	10.4	4.5	4.3	1.05
<b>2/c5</b>	$\text{Cub}/\text{Ia}\bar{3}d$	10.5	4.5	4.4	1.02
<b>2/c12</b>	$\text{Cub}/\text{Ia}\bar{3}d$	9.4	4.1	4.7	0.87
<b>5/Et<sub>3</sub></b>	$\text{Cub}/\text{Ia}\bar{3}d$	8.9	3.8	4.4	0.86

<sup>a</sup>  $d =$  "layer spacing" along the body diagonal of the unit cell:  $d = \sqrt{3}a_{\text{cub}}/4$ , see ref.<sup>S3</sup>;  $L_{\text{mol}}$  was determined with space filling CPK models assuming the most stretched molecular conformation.



## 2.3 Additional textures

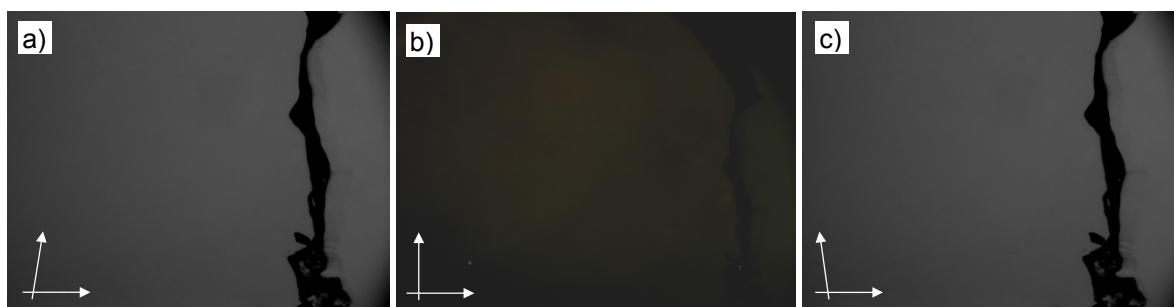


**Figure S4.**  $Ia\bar{3}d$  phase of  $5/Et_3$  at  $52\text{ }^\circ\text{C}$  as observed between b) crossed polarizers polarizers and being slightly uncrossed either in a) anticlockwise or c) clockwise direction; at the right there is a phase boundary to air.



**Figure S5.**  $Im3m^{[*]}$  phase of  $3/br5$  at  $100\text{ }^\circ\text{C}$  as observed between b) crossed polarizers polarizers and being slightly uncrossed either in a) anticlockwise or c) clockwise direction.

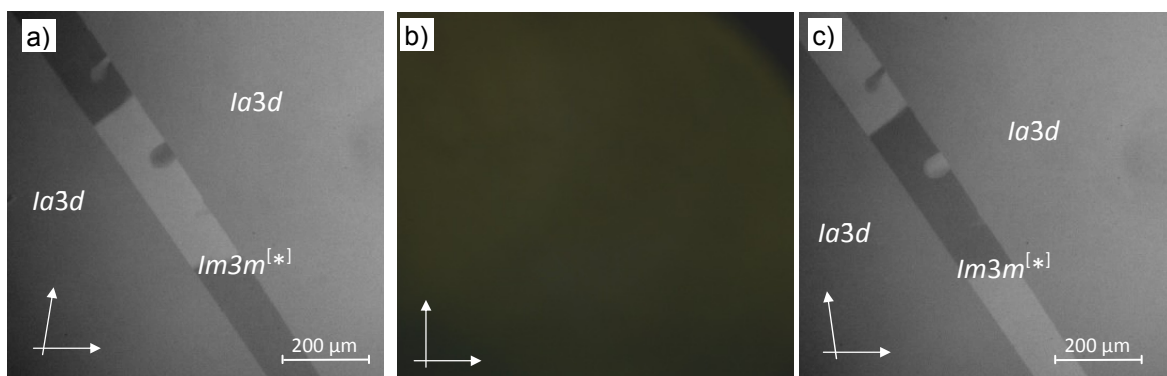


**Figure S6.** Chiral domains of the  $Im3m^{[*]}$  phase, induced between the achiral  $Ia\bar{3}d$  phases of compounds  $2/c4$  (top/right) and  $5/Et_3$  (bottom/left) at  $T = 124\text{ }^\circ\text{C}$ ; the  $Im3m^{[*]}$  phase appears at  $125\text{ }^\circ\text{C}$  on cooling and disappears at  $T = 141\text{ }^\circ\text{C}$  on heating.

## 2.4 Structural models

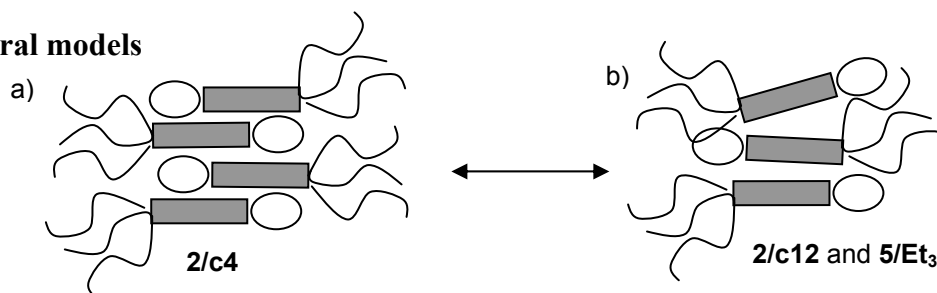


**Figure S7.** Transition between a) the intercalated structure where the apices are mixed with the polyaromatic cores and b) the fully segregated structure of aromatic cores with apices



## **Publikation C**

### **Swallow-Tailed Polycatenars: Controlling Complex Liquid Crystal Self-Assembly and Mirror Symmetry Breaking at the Lamellae-Network Cross-Over**

Tino Reppe,<sup>[a]</sup> Christian Dressel,<sup>[a]</sup> Silvio Poppe,<sup>[a]</sup> Alexey Eremin,<sup>[b]</sup> Carsten Tschierske<sup>[a]</sup>

[a] Institute of Chemistry, Martin Luther University Halle-Wittenberg, Kurt-Mothes-Straße 2, 06120 Halle, Germany.

[b] Institute of Physics, Otto von Guericke University Magdeburg, Universitätsplatz 2, 39106 Magdeburg, Germany.

#### **Abstract**

Controlling the spatial organization of  $\pi$ -conjugated molecules in soft systems is of importance for the design of new materials with application relevant optimized properties. Here, soft self-assembly of functional multi-chained  $\pi$ -conjugated 5,5'-diphenyl-2,2'-bithiophenes is investigated. Focus is on molecules with a 3,5-disubstitution pattern at one end and no or only a single chain at the other end. By elongation of the single terminal chain, a transition from lamellar phases to helical networks is observed. With lowering the temperature, the lamellar phase types change from smectic via hexatic to crystalline. In some cases, different kinds of orders are combined in a single uniform lamellar structure. Moreover, a transition from uniform (synclitic) to alternating (anticlinal) tilt in adjacent layers is observed with decreasing chain length or rising temperature, due to a change of the molecular conformation from tuning fork like to Y-shaped. For compounds terminated with a long chain, helical self-assembly of the  $\pi$ -conjugated rods in networks takes place, leading either to a racemic ( $Ia3d$ , gyroid) or a spontaneous mirror symmetry broken ( $I23$ ) bicontinuous cubic phase and a chiral isotropic liquid phase ( $Iso_1^{[*]}$ ) as well. This work establishes rules for controlling the self-assembly of functional  $\pi$ -conjugated rods in soft matter and fluids.

#### **Referenz**

T. Reppe, C. Dressel, S. Poppe, A. Eremin, C. Tschierske, *Adv. Optical Mater.* **2021**, 9, 2001572. DOI: 10.1002/adom.202001572.

# Swallow-Tailed Polycatenars: Controlling Complex Liquid Crystal Self-Assembly and Mirror Symmetry Breaking at the Lamellae-Network Cross-Over

Tino Reppe, Christian Dressel, Silvio Poppe, Alexey Eremin, and Carsten Tschierske\*

Controlling the spatial organization of  $\pi$ -conjugated molecules in soft systems is of importance for the design of new materials with application relevant optimized properties. Here, soft self-assembly of functional multi-chained  $\pi$ -conjugated 5,5'-diphenyl-2,2'-bithiophenes is investigated. Focus is on molecules with a 3,5-disubstitution pattern at one end and no or only a single chain at the other end. By elongation of the single terminal chain, a transition from lamellar phases to helical networks is observed. With lowering the temperature, the lamellar phase types change from smectic via hexatic to crystalline. In some cases, different kinds of orders are combined in a single uniform lamellar structure. Moreover, a transition from uniform (synclinic) to alternating (anticlinic) tilt in adjacent layers is observed with decreasing chain length or rising temperature, due to a change of the molecular conformation from tuning fork like to Y-shaped. For compounds terminated with a long chain, helical self-assembly of the  $\pi$ -conjugated rods in networks takes place, leading either to a racemic ( $Ia\bar{3}d$ , gyroid) or a spontaneous mirror symmetry broken ( $I23$ ) bicontinuous cubic phase and a chiral isotropic liquid phase ( $Iso_1^{[3]}$ ) as well. This work establishes rules for controlling the self-assembly of functional  $\pi$ -conjugated rods in soft matter and fluids.

## 1. Introduction


Using sunlight as a sustainable energy source is of vital interest for the survival of the continuously growing mankind. As known from nature, efficient light-harvesting requires the aggregation and defined organization of arrays of  $\pi$ -conjugated

molecules in soft self-organized supramolecular systems.<sup>[1,2]</sup> Extended  $\pi$ -conjugated systems are also of significant interest for application as charge carrier in organic semiconductors,<sup>[3]</sup> luminescent materials (e.g., AIEgens),<sup>[4]</sup> and for circular polarized emission in helical assemblies.<sup>[5]</sup> Therefore, tuning the organization of these  $\pi$ -conjugated rods in soft matter systems is fundamental and requires the understanding of their general design rules. Liquid crystals (LCs) are of great interest as stimuli-responsive and switchable optical materials in displays, photonics<sup>[6]</sup> and in sensor applications.<sup>[7,8]</sup> Rod-like  $\pi$ -conjugated molecules with multiple end-chains, the so-called polycatenar molecules, have received significant interests as they provide a huge variety of different LC phases ranging from lamellar (smectic, Sm) via bicontinuous cubic ( $Cub_{bi}$ ) to columnar (Col)<sup>[9–11]</sup> and even micellar cubic phases.<sup>[3]</sup> This observation has contributed to the recognition of the importance of

nano-segregation for LC phase formation and demonstrated the similarity of the fundamental self-assembly principles in lyotropic systems formed by amphiphiles, in LC phases and in the solid state morphologies of block copolymers.<sup>[12,13]</sup> Among the self-assembled structures of polycatenar molecules, the  $Cub_{bi}$  phases<sup>[14,15]</sup> received special attention because of their potential for applications, as for example in 3D conducting<sup>[16]</sup> and photonic materials,<sup>[17]</sup> being the result of their interwoven network structure (see Section 3.6).<sup>[14,18]</sup> Generally the  $Cub_{bi}$  phases are found at the transition between lamellar and columnar modes of self-assembly as a result of the developing interface curvature.<sup>[12,19–21]</sup> The most common  $Cub_{bi}$  phase is the double gyroid with space group  $Ia\bar{3}d$  and three way junctions forming two interwoven networks,<sup>[21,22]</sup> but also double diamond phases ( $Pn\bar{3}m$ ) with four-way junctions and primitive networks with six-way junctions ( $Im\bar{3}m$ ) are known.<sup>[14,19]</sup> Only recently the related single network cubic phases were found in thermotropic LCs.<sup>[23]</sup> There is also a  $Cub_{bi}$  phase with more complex triple network structure (previously designated as  $Im\bar{3}m$ ) which is only formed in systems involving rod-like units, the polycatenars being the most prominent, and different models are under discussion, as will be described in Section 3.6.<sup>[24–26]</sup> The recent discovery of helix formation, spontaneous mirror symmetry breaking, optical activity and enormous chirality

T. Reppe, Dr. C. Dressel, Dr. S. Poppe, Prof. C. Tschierske  
Institute of Chemistry  
Martin Luther University Halle-Wittenberg  
Kurt-Mothes-Str. 2, D-06120 Halle (Saale), Germany  
E-mail: carsten.tschierske@chemie.uni-halle.de

Prof. A. Eremin  
Department of Nonlinear Phenomena  
Institute of Physics  
Otto von Guericke University Magdeburg  
D-39106 Magdeburg, Germany

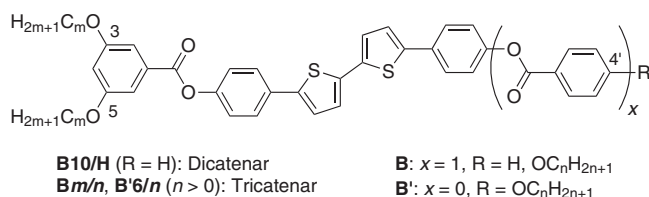
 The ORCID identification number(s) for the author(s) of this article can be found under <https://doi.org/10.1002/adom.202001572>.

© 2020 The Authors. Advanced Optical Materials published by Wiley-VCH GmbH. This is an open access article under the terms of the Creative Commons Attribution-NonCommercial License, which permits use, distribution and reproduction in any medium, provided the original work is properly cited and is not used for commercial purposes.

DOI: 10.1002/adom.202001572

amplification effects, observed in some of the  $Cub_{bi}$  phases,<sup>[27–32]</sup> in the adjacent non-cubic tetragonal<sup>[33]</sup> and the isotropic liquid phases ( $Iso_{1}^{[*]}$ ) of these achiral polycatenar compounds<sup>[34–36]</sup> has renewed the interest in this class of compounds.<sup>[37–39]</sup> Such spontaneously chiral soft matter systems are of potential technological interest and might also be of importance for the understanding of the mechanism of emergence of uniform chirality.<sup>[40–42]</sup>

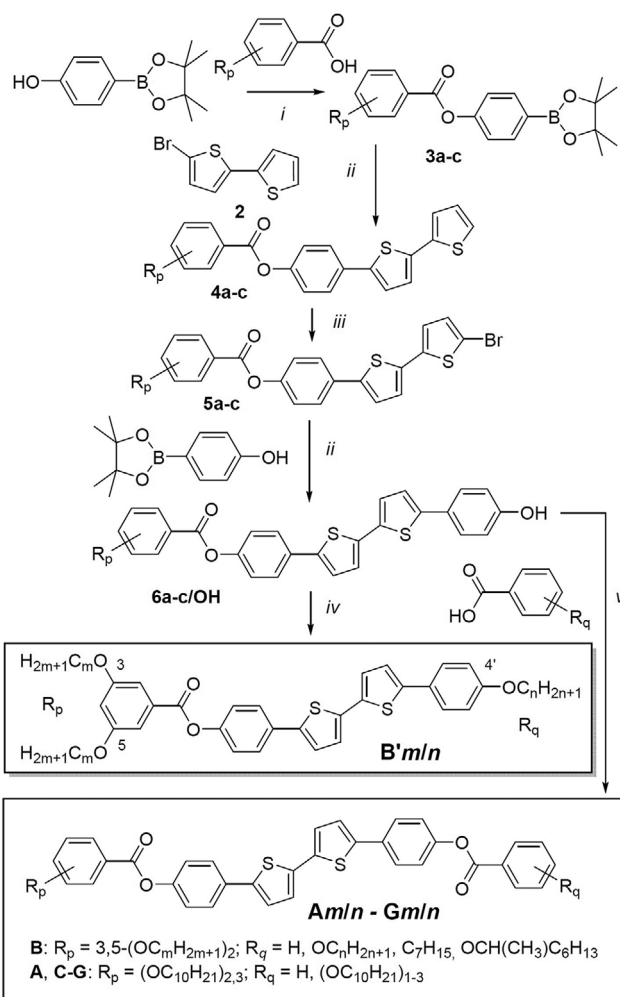
In this work we explore structural modification of 5,5'-diphenyl-2,2'-bithiophene-based polycatenar compounds<sup>[27a,28,29,33,34a]</sup> and we establish the fundamental understanding of these effect on the mesogenic self-assembly at the crossover from lamellar phases to helical networks. The study focuses on new series of compounds with an 3,5-disubstitution pattern at one end and being either non-terminated (**Bm/H**) or terminated with only a single alkyl chain at the other end (**Bm/n** and **B'G/n**). Although the 3,5-disubstitution pattern was used in few cases for the design of columnar LCs,<sup>[43–48]</sup>  $Cub_{bi}$  phases,<sup>[9,24,36,49–52]</sup> and functional liquids,<sup>[53]</sup> it is much less common compared to the huge number of examples of materials with 3,4-disubstitution and the 3,4,5-trisubstitution patterns.<sup>[9]</sup>



It is shown that these new swallow-tailed<sup>[54,55]</sup> compounds provide access to unique materials combining a rich diversity of different modes of self-assembly. Firstly, they offer a new access to the anticlinic-tilted smectic phases ( $SmC_a$ ). Secondly, several higher ordered hexatic ( $Hex$ ) and crystalline lamellar mesophases, including those combining smectic and hexatic self-assembly in a single uniform structure, are observed. Thirdly, chiral and achiral  $Cub_{bi}$  phases, birefringent 3D mesophases and a mirror symmetry broken isotropic liquid ( $Iso_{1}^{[*]}$ ) involving helically organized bithiophene units are obtained by only tiny changes of the molecular structure. An understanding of this exceptionally wide diversity of self-assembled soft matter structures is based on transitions between tuning fork like and Y-like conformations leading to distinct degrees of intercalation, and thus, to the transition between lamellar organizations and helical self-assembly in networks.

## 2. Methods

The synthesis of the compounds was performed as described in **Scheme 1**, for details see the Supporting Information.<sup>[56]</sup> The compounds were investigated by optical microscopy between crossed or slightly uncrossed polarizers (polarizing microscopy = POM) in films between glass plates and in freely suspended thin films, by differential scanning calorimetry (DSC) and by X-ray scattering, small-angle scattering (SAXS) and wide-angle scattering (WAXS), of powder-like samples and aligned samples. The used instrumentation and other details are described in the Supporting Information.



**Scheme 1.** Synthesis of compounds under investigation. Reagents and conditions: i) DCC, DMAP, DCM, RT; ii)  $[Pd(PPh_3)_4]$ , THF/sat.  $NaHCO_3$ -solution, reflux; iii) NBS, THF, RT, absence of light; iv)  $C_nH_{2n+1}Br$ ,  $K_2CO_3$ ,  $Bu_4NI$ , MEK, reflux; v): 1) benzoic acid +  $SOCl_2$ , 2) **6a-c/OH**, pyridine, DMAP, DCM, RT.

## 3. Results and Discussion

### 3.1. Effects of Alkyl Chain Number and Chain Distribution

For compounds with decyl chains, as example, the effect of the number and position of the chains was investigated (**Figure 1** and Table S6, Supporting Information). As shown in **Figure 1**, there is a transition from a synclinic tilted lamellar phase ( $SmC_s$ ) via  $Cub_{bi}$  to  $Col_{hex}$  upon increasing the number of alkyl chains from three via four to five. Compounds with two chains (e.g., **B10/H**) form only lamellar phases, those with five and more chains exclusively columnar phases ( $Col_{hex}$ , **G10/10**) and those with three and four chains can form lamellar,  $Cub_{bi}$ , as well as columnar phases, depending on structural details. For example, a non-symmetric chain distribution (**A10/10**,<sup>[27a]</sup> **A10/H**,<sup>[27a]</sup> and **B10/10**) is favorable for  $Cub_{bi}$  phase formation, whereas the more symmetric analogs **C10/10** and **D10/10** form only a smectic phase ( $SmC_s$ ).

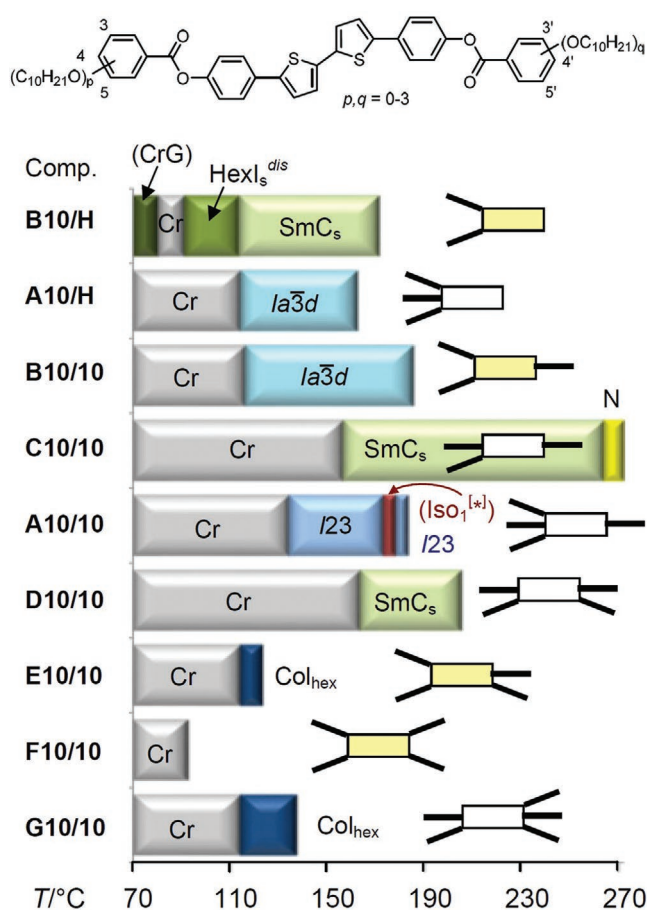


**Figure 1.** Phase transitions of the polycatenar compounds **A–G** as observed on heating and depending on the number and position of the alkyl chains, indicated with pictograms (special focus is on those indicated in yellow); monotropic phases, only observed on cooling, are shown in brackets; Cr, crystalline solid;  $Iso_1^{[*]}$ , mirror symmetry broken isotropic liquid composed of a conglomerate of chiral domains with opposite optical rotation; N, nematic LC phase;  $SmC_s$ , synclinc tilted lamellar LC phase;  $HexI_s^{dis}$ , synclinc tilted hexatic I-phase with  $HexI_s$ -like order of the alkyl chains and  $SmC_s$ -like order of the aromatic cores; CrG, crystalline lamellar G phase;  $Ia\bar{3}d$ , achiral  $Cub_{bi}$  phase with  $Ia\bar{3}d$  space group ( $Cub_{bi}/Ia\bar{3}d$ );  $I23$ ,  $Cub_{bi}$  phase with  $I23$  space group ( $Cub_{bi}^{[sk]}/I23$ ), this cubic phase forms a conglomerate of chiral domains with opposite optical rotation (Figure 7e);  $Col_{hex}$ , hexagonal columnar LC phase; for numerical data on heating and cooling, see Table 1 and Table S6, Supporting Information.

Moreover, the 3,4-disubstitution pattern of the three chain compound **C10/10** favors smectic phases whereas the isomeric compound **B10/10** with 3,5-disubstitution pattern forms a  $Cub_{bi}$  phase, indicating the importance of the molecular shape, being tuning fork like for the smectogenic 3,4-disubstituted compound **C10/10** and Y-like for the cubogenic 3,5-disubstituted compound **B10/10**. Interestingly, the  $Cub_{bi}$  phase is achiral with  $Ia\bar{3}d$  space group for the taper shaped tricatener compounds **A10/H** and **B10/10** which have the alkyl chains at only one end and becomes chiral with  $I23$  space group for the tetracatenars compound **A10/10** with an additional chain at the opposite end. This indicates the importance of chain number (and chain volume) for the selection of the  $Cub_{bi}$  phase type and emergence of mirror symmetry breaking in the soft matter phases

of these achiral molecules. Generally, the 3,5-disubstitution pattern lowers all transition temperatures compared to the related 3,4- and the 3,4,5-substituted compounds, which shifts the LC ranges toward ambient temperature (Figure 1). Only for compound **F10/10** having the 3,5-disubstitution at both ends soft self-assembly is completely lost due to this effect.

### 3.2. Self-Assembly of Compound B10/H with Two Chains at the Same End

Compound **B10/H** has only two chains which are both attached at the same 3,5-substituted end of a rod-like core. It shows three reproducible phase transitions in the DSC traces (Figure 2d and Table 1). On cooling the first transition from the isotropic liquid to a synclinc  $SmC_s$  phase takes place at 169 °C ( $3.0\text{--}2.8\text{ kJ mol}^{-1}$ ). As shown in Figure 2a, the optical extinction brushes in POM are inclined with the direction of the analyzer by an angle of  $\approx 40^\circ$ . This corroborates with a uniform tilt direction of the molecules in adjacent layers (synclinc tilt =  $SmC_s$ ).

The diffuse WAXS with a maximum at  $d = 0.45\text{ nm}$  confirms the liquid-like order in the layers (Figure 2e) and the sharp small angle scattering at  $d = 4.21\text{ to }4.26\text{ nm}$  (Figure 2f, Figure S22c, Supporting Information) corresponds to the molecular length  $L_{mol} = 4.2\text{ nm}$  (Figure 3a). In the 2D scattering patterns of aligned samples the wide angle scattering maximum is inclined to the layer reflection with a tilt angle of  $\beta = 37^\circ$  (Figure 2e and Figure S22a,b, Supporting Information). In a smectic phase with this  $d$ -value and a tilt of  $37^\circ$  the required molecular length would be  $L = d/\cos\beta = 5.3\text{ nm}$ . This is significantly longer than  $L_{mol}$  and therefore excludes the fully intercalated and non-segregated packing shown in Figure 3a. In contrast, the full segregation of the aromatic and aliphatic units in the antiparallel packing with intercalation of only the aromatic cores leads to a layer thickness of  $5.5\text{ nm}$  (Figure 3b) which is close to  $5.3\text{ nm}$ . This mode of packing is not only supported by the segregation of the flexible aliphatic chains from the rigid polyaromatic units, but also allows a side-by-side packing of an equal number of chains and aromatic cores (2/2) in the respective layers, which minimizes the interfacial curvature, and thus supports the lamellar organization.

Upon cooling, at the phase transition at 111 °C, the homeotropic texture becomes smoother and no change is visible in the planar regions, and there is no visible change at the next phase transition at 80 °C, either (Figure 2b,c). The birefringence as well as the inclination of the extinctions in planar alignment is retained in all three phases, meaning that the tilt correlation and the tilt angle do not change markedly (Figure 2a–c). Also the SAXS pattern remains almost the same in all three mesophases, that is, all of them represent synclinc tilted lamellar phases (Figure S22c,e,f, Supporting Information). Clear changes can be observed for the wide-angle scattering, which has a diffuse character in the  $SmC_s$  range and becomes narrower and asymmetric at 111 °C (Figure 2e). The angular scattering profile can be deconvoluted into a sharper peak at  $d = 0.46\text{ nm}$  and a diffuse one with a maximum at  $d = 0.42\text{ nm}$  (Figure 2e, Figure S22g, Supporting Information). This scattering pattern is similar to that reported by Heppke et al. for the so-called  $SmM^*/SmM$  phases of chiral rod-like compounds and their racemates.<sup>[57,58]</sup> Based on the powder X-ray scattering data in



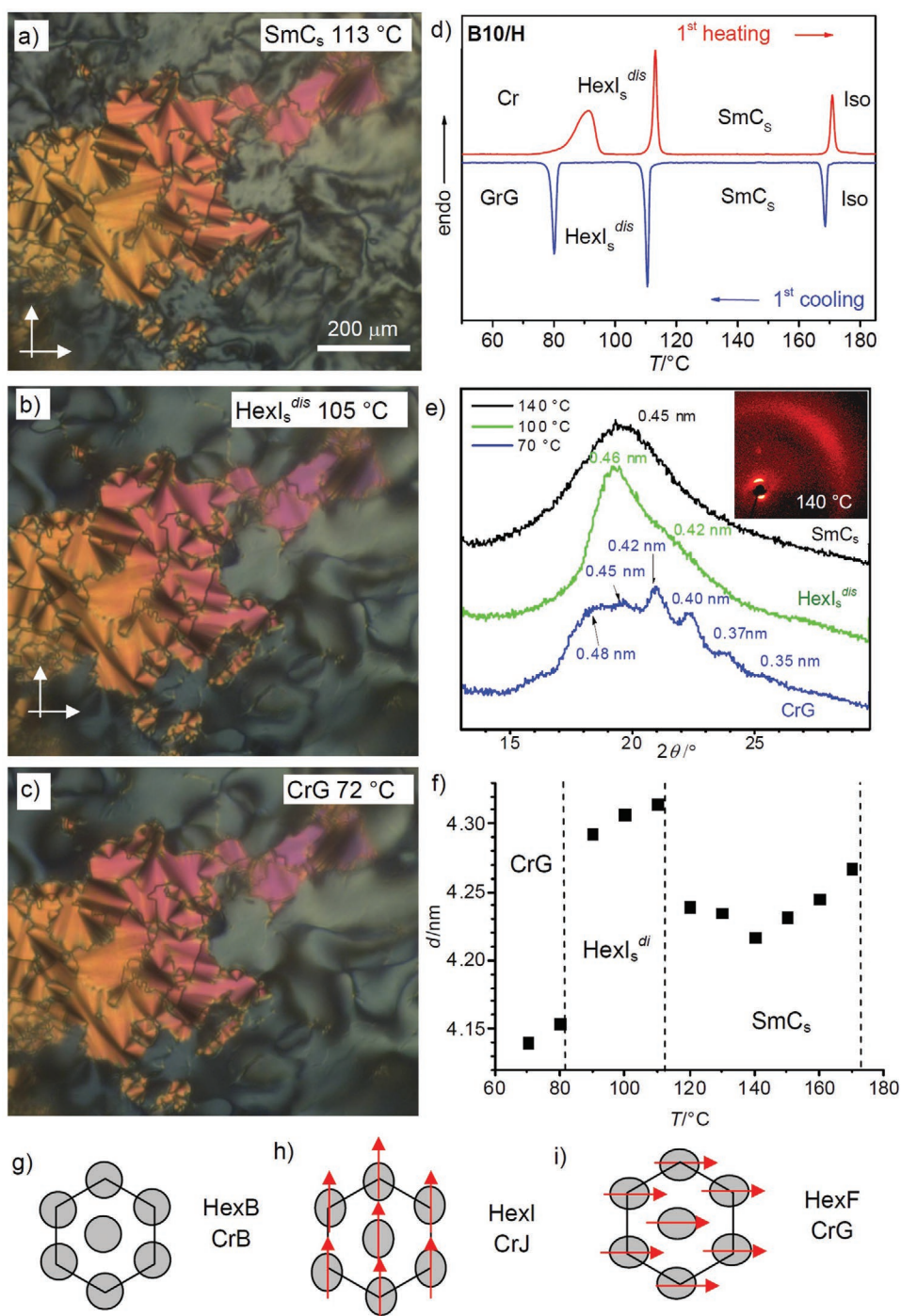
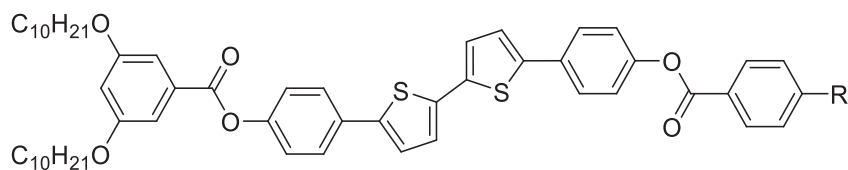


**Figure 2.** Investigation of B10/H. a–c) Textures in the distinct mesophases at the given temperatures as observed between crossed polarizers in planar (red/yellow; view is parallel to the layers) and homeotropic aligned regions (gray; view is along the layer normal); for additional textures, see Figure S8, Supporting Information; d) DSC traces (10 K min<sup>-1</sup>); e) WAXS patterns in the distinct mesophases and f) the dependence of the *d*-value of the layer reflection on temperature (see also Figure S22, Supporting Information). In g–i), the structures of the hexatic and corresponding crystalline phases are shown schematically; the grey circles and ellipses represent the cross sections of the molecules, the arrows show the tilt direction of the molecules with respect to the 2D lattice, the view is along the layer normal, showing the organization of the molecules in the layers.

Figure 2e,f, we propose a model where aliphatic and aromatic segments are fully segregated (Figure 3b). The synclonic SmC<sub>s</sub> layers of the aromatic cores, providing the diffuse scattering with a maximum at *d* = 0.42 nm, alternate with higher ordered

and also synclonic tilted HexI<sub>s</sub>-like (Figure 2h) alkyl chain layers,<sup>[59–61]</sup> giving rise to the sharper scattering at *d* = 0.46 nm. Similar segregated structures with different order in the distinct sublayers have been found for swallow-tailed molecules with

**Table 1.** Phase transitions and lattice parameters of the di- and tricatenerans **B10/n** depending on the 4'-alkyl chain length (*n*).



Comp. <sup>a)</sup>	<i>n</i>	Phase transitions <i>T</i> [°C] [ $\Delta H/k$ ] mol <sup>-1</sup> ]	<i>d</i> /nm ( <i>T</i> [°C])	<i>a</i> <sub>cub</sub> /nm ( <i>T</i> [°C])
<b>B10/H</b>	H	H: Cr 91 [10.9] HexI <sub>s</sub> <sup>dis</sup> 113 [5.9] SmC <sub>s</sub> 171 [3.0] Iso C: Iso 169 [-2.8] SmC <sub>s</sub> 111 [-5.9] HexI <sub>s</sub> <sup>dis</sup> 80 [-5.3] CrG <20 Cr	–	4.26 (140) 4.33 (100)
<b>B10/6</b>	OC <sub>6</sub> H <sub>13</sub>	H: Cr 98 [24.9] SmC <sub>s</sub> 151 [0.4] Cub <sub>bi</sub> / <i>la</i> $\bar{3}$ <i>d</i> 191 [1.8] Iso C: Iso 187 [-0.1] Iso <sup>[sk]</sup> 155 [-] Cub <sub>bi</sub> / <i>la</i> $\bar{3}$ <i>d</i> + SmQ + SmC <sub>s</sub> <sup>b)</sup> 76 [-21.7] Cr	4.5 (120)	10.9 (170)
<b>B10/8</b>	OC <sub>8</sub> H <sub>17</sub>	H: Cr 102 [30.5] Cub <sub>bi</sub> / <i>la</i> $\bar{3}$ <i>d</i> 126 [-] M1 138 [-] 189 [2.1] Iso C: Iso 183 [-0.1] Iso <sup>[sk]</sup> 168 [-0.6] Cub <sub>bi</sub> / <i>la</i> $\bar{3}$ <i>d</i> 58 [-19.3] Cr	–	11.0 (180)
<b>B10/10</b>	OC <sub>10</sub> H <sub>21</sub>	H: Cr 116 [53.4] Cub <sub>bi</sub> / <i>la</i> $\bar{3}$ <i>d</i> 185 [2.3] Iso C: Iso 177 [-1.3] Cub <sub>bi</sub> / <i>la</i> $\bar{3}$ <i>d</i> 89 [-33.5] Cr	–	11.3 (150)
<b>B10/16</b>	OC <sub>16</sub> H <sub>33</sub>	H: Cr 114 [74.3] Cub <sub>bi</sub> / <i>la</i> $\bar{3}$ <i>d</i> [-] 160 Cub <sub>bi</sub> <sup>[sk]</sup> /I23 173 [2.0] Iso C: Iso 166 [-0.1] Iso <sup>[sk]</sup> 164 [-0.7] Cub <sub>bi</sub> / <i>la</i> $\bar{3}$ <i>d</i> 75 [-17.1] Cr	–	11.5 (130) 17.7 (165)
<b>B10/22</b>	OC <sub>22</sub> H <sub>45</sub>	H: Cr 104 [34.8] Cub <sub>bi</sub> <sup>[sk]</sup> /I23 171 [2.8] Iso C: Iso 166 [-1.7] Col <sub>ob</sub> 159 [-0.7] Cub <sub>bi</sub> <sup>[sk]</sup> /I23 73 [-43.4] Cr	–	18.1 (140)

<sup>a)</sup>Peak temperatures as obtained by DSC at a scanning rate of 10 K min<sup>-1</sup> on heating (H) or cooling (C); Iso, isotropic liquid; SmQ, low birefringent mesophases with mosaic-like texture, presumably representing a tetragonal 3D phase composed of helical networks with 90° four-way junctions (see Figure 7c),<sup>[33]</sup> M1, low birefringent mesophase with non-specific texture (see Figure S10a, Supporting Information), only observed on heating; Col<sub>ob</sub>, oblique columnar phase (Figures S11 and S21c, Supporting Information); for the other abbreviations, see Figure 1; for DSC traces, see Figure 2a and Figure S2, Supporting Information; for X-ray data, see Tables S1 and S2, Supporting Information; <sup>b)</sup>All three phases can coexist in different ratios depending on the precise conditions; due to slow transitions no DSC peaks can be observed.

perfluorinated alkyl chains<sup>[62]</sup> and could possibly play a role in hexatic phases of LC polymers.<sup>[63]</sup> Due to the combination of the hexatic chain order and SmC<sub>s</sub>-like core order this phase is designated here as HexI<sub>s</sub><sup>dis</sup>. The mesophase at the lowest temperature shows the typical pattern of a tilted crystalline smectic phase, which can satisfactorily be indexed to either G or J (Figure 2e,i and Figure S22h, Supporting Information and Tables S3 and S4, Supporting Information).<sup>[59,60,64]</sup> As the unit cell of the G phase contains a number of molecules closer to the theoretical value of two (Tables S3 and S4, Supporting Information), we prefer this assignment. It appears that this phase results from the simultaneous crystallization of the aromatic and aliphatic layers.

### 3.3. Synclinc Tilted Lamellar Phases of Compounds **B10/n**

The synclinc SmC<sub>s</sub> phase, observed for the two-chain compound **B10/H** is retained for the 4'-hexyloxy substituted tricatener compound **B10/6** where it is stable up to 151 °C; above this temperature it is replaced by an optically isotropic Cub<sub>bi</sub> phase (Table 1). This is in line with the growing interfacial curvature caused by the space required by the additional alkyl chain at the apex, which becomes even more important at higher temperature due to thermal expansion. The layer spacing in the SmC<sub>s</sub> phase is *d* = 4.5 nm which, despite of the expanded molecular length of *L*<sub>mol</sub> = 5.1 nm, is only slightly larger than for **B10/H** without the additional apex-chain. This means that the organization should be dominated by an antiparallel packing of themolecules with fully segregated aromatic and alkyl chain layers, as shown in Figure 3d. This retains the layer spacing of the smectic phase despite of the elongation of the molecule, and is likely to provide an increased tendency

to assume interfacial curvature (2 rods vs 3 chains side-by-side), leading to a transition from lamellar to Cub<sub>bi</sub> phases. The longer homologues show exclusively cubic phases and therefore will be discussed further below.

### 3.4. Anticlinic Smectic Phases of the Swallow-Tailed Compounds **B6/n** with Short 3,5-Chains

In the series of compounds **B6/n** with two shorter hexyloxy chains at the 3,5-substituted end the transition temperatures are much higher and smectic phases can be found up to a longer apex chain length of *n* = 10, for which a Cub<sub>bi</sub> phase coexists with a smectic phase and for the next homologue **B6/12** exclusively the Cub<sub>bi</sub> phase is observed (Table 2). However, as shown below, the smectic phases of all compounds **B6/n** have anticlinic tilt (SmC<sub>a</sub>) and there are no additional hexatic or crystalline low temperature phases, irrespectively if the 4'-chain is odd- or even-numbered (**B6/6** vs **B6/5**, see Table 2), or if it is an alkyl (**B6/6a**) or alkoxy chain.<sup>[65]</sup>

The optical textures of planar samples of the smectic phase show dark extinction brushes parallel to the polarizer and analyzer (Figure 4b,c), thus indicating that the optical axis is parallel to the layer normal. Homeotropic samples show birefringent schlieren textures with dominating two brush disclinations, but also few 4-brush disclinations can be found (Figure 4a). This texture is in line with an anticlinic tilted SmC<sub>a</sub> phase.<sup>[66–70]</sup> In the synclinc tilted SmC<sub>s</sub> phases there would be only 4-brush disclinations, whereas in a non-tilted SmA<sub>b</sub> phase<sup>[71,72]</sup> exclusively two brush disclinations would be expected.<sup>[73]</sup> Thus, the textures in planar as



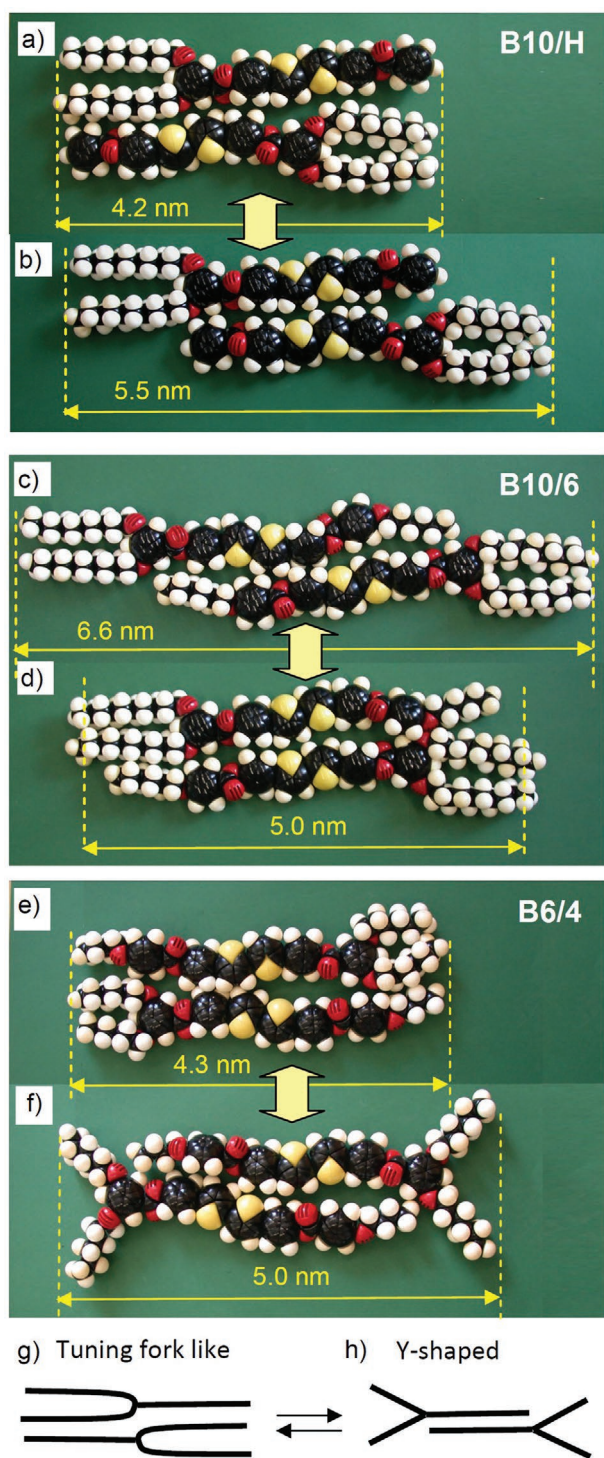


**Figure 3.** Space filling CPK models of pairs of a,b) compound **B10/H** in a) the non-segregated fully intercalated organization ( $L = L_{mol}$ ) and b) segregated organization with intercalation of the aromatic cores only; c,d) compound **B10/6** in c) a non-segregated organization with intercalation of the single 4'-alkyl chains and aromatic cores and d) fully segregated and intercalated pair; e,f) compound **B6/4** in e) shown the fully intercalated organization with a tuning fork like conformation and in f) in a partly intercalated packing with Y-shaped conformations. In (d)  $L$  considers the different ratio of short and long chains. g,h) Schematics of the distinct molecular conformations and their preferred packing modes.

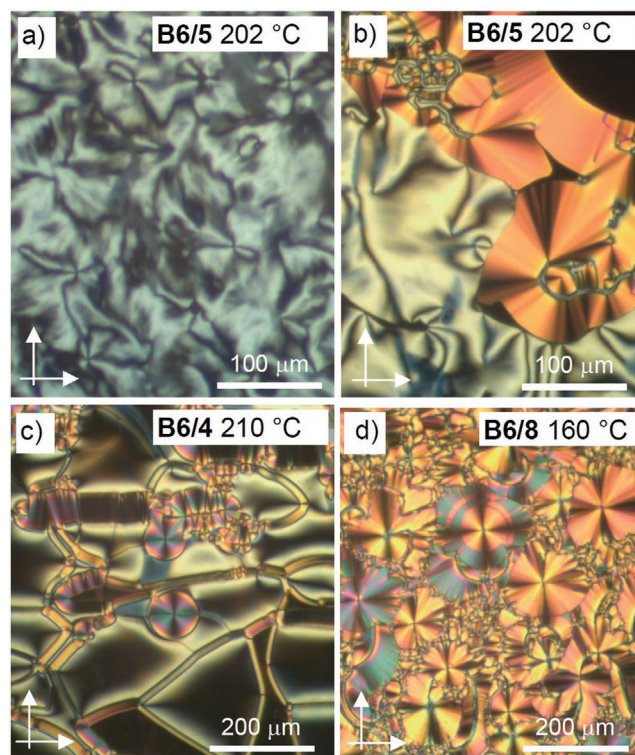


**Figure 4.** a–d) Typical textures of the  $SmC_a$  phases of compounds **B6/n** as observed between crossed polarizers (white arrows) for the indicated compounds at the given temperatures; for additional textures, see Figures S12 and S13, Supporting Information.

well as in homeotropic alignment indicate the formation of an anticlinic  $SmC_a$  phase for the compounds **B6/n** (see also Figure S13, Supporting Information). The anticlinic tilt is corroborated by investigation of freely suspended (FS) films of compound **B6/5** (Figure S16a,b, Supporting Information), where the Schlieren texture, involving half-integer and rare integer defects, remains the same at oblique incidence, independent on the tilt direction of the film with respect to the beam direction.

For compounds **B6/4–B6/10** the layer spacing is around  $d = 4.2$  nm and almost independent on the alkyl chain length (Table 2 and Figure S19a–c, Supporting Information). Only for **B6/10** a slight increase of the layer spacing to  $d = 4.4$  nm is observed. The completely intercalated and fully segregated organization of **B6/4**, shown in Figure 3e, would lead only to a value of  $L = 4.3$  nm for the molecular pairs which would not allow the development of a reasonable tilt and therefore appears less likely. Only mixing of the 4'-alkyl chains with the aromatic rods in the partly intercalated structure in Figure 3f leads to pairs with a length of 5.0 nm allowing a significant tilt. Moreover, in this arrangement the molecules can easily assume a Y-shape, where the 3,5-chains tend to be aligned almost parallel to the layer planes (Figure 3f,h). This reduces the out-of-plane inter-layer fluctuations and favors the anticlinic character of tilt.<sup>[66,74]</sup> Simultaneously, in this Y-conformation the chains are less ordered and therefore no hexatic phase can be observed in the series of compound **B6/n**. This

Y-conformation becomes difficult for longer 3,5-chains (compounds **B10/n**) which favor a parallel alignment of the alkyl chains (Figure 3c) to maximize the dispersion interactions and to minimize the excluded volume.<sup>[75]</sup> The resulting tuning fork like conformation (Figure 3g) supports the synclinal tilt correlation by allowing more interlayer fluctuations.<sup>[74]</sup>

For compounds **6/n** with a longer 4'-alkyl chain ( $n > 10$ ) the intercalation of the incompatible aromatics and alkyl chains becomes unfavorable and these chains are forced to be located in common layers with the 3,5-chains (as shown for **B10/6** and **B6/4** in Figure 3d,e). This enlarges the effective cross-sectional area of the alkyl chains, thus increasing the interface curvature and driving the system from smectic toward  $Cub_{bi}$  phases, as indeed observed upon chain elongation (see Table 2).

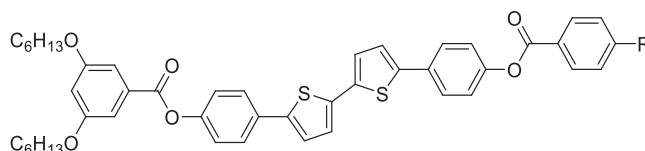
### 3.5. Lamellar Phases in the Series **B'6/n** with Short Cores: Transitions from Anticlinic Smectic to Synclinal Tilted and Non-Tilted Hexatic Phases

The series of compounds **B'6/n** with a shorter five-ring core forms lamellar phases only for the compounds with  $n = 6$  and 8

(Table 3). The X-ray scattering pattern confirms a smectic phase (Figures S23a,b and S24a, Supporting Information) with a diffuse wide angle scattering (Figure 5h) in the high-temperature smectic phase of **B'6/6**. The typical fan-like textures with dark extinctions parallel to the polarizers in planar alignment and a low birefringent schlieren texture with two- and four brush disclinations in homeotropic alignment indicate a  $SmC_a$  phase (Figure 5a,b), which is additionally confirmed by investigation of FS films, as described above for **B6/5** (see Figure S16c, Supporting Information).

The layer spacing of **B'6/6** is with  $d = 4.3$  nm almost the same as for the longer molecule **B6/6** ( $d = 4.2$  nm) and quite a bit longer than the single molecular length of **B'6/6** ( $L_{mol} = 3.9$  nm). This excludes the fully intercalated and completely segregated packing (similar to Figure 3e) and indicates an only partly intercalated packing with the alkyl chain at the apex mixed between the aromatic cores, the same as described for compounds **B6/n** and shown in Figure 3f and Figure S26c, Supporting Information. These pairs have a length  $L = 4.8$  nm allowing a bit smaller tilt of about 20–25°. On cooling **B'6/6** there are additional phase transitions. These transitions are most clearly seen in homeotropic samples, where the schlieren

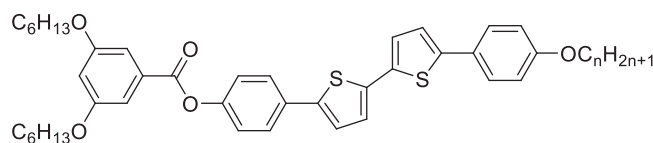
**Table 2.** Phase transitions and lattice parameters of the swallow-tailed tricaténars **B6/n** with different groups at the apex.



Comp. <sup>a)</sup>	R	Phase transitions $T$ [°C] [ $\Delta H$ k] mol <sup>-1</sup>	$d$ /nm ( $T$ [°C])	$a_{cub}$ /nm ( $T$ [°C])
<b>B6/4</b>	OC <sub>4</sub> H <sub>9</sub>	H: Cr 138 [29.0] $SmC_a$ 215 [1.4] N 220 [0.4] Iso C: Iso 217 [-0.5] N 212 [-1.3] $SmC_a$ 104 [-21.5] Cr	4.2 (180)	–
<b>B6/5</b>	OC <sub>5</sub> H <sub>11</sub>	H: Cr 139 [32.2] $SmC_a$ 209 [2.2] Iso C: Iso 207 N 206 [-2.1] <sup>b)</sup> $SmC_a$ 104 [-25.2] Cr	4.1 (180)	–
<b>B6/6</b>	OC <sub>6</sub> H <sub>13</sub>	H: Cr 123 [25.9] $SmC_a$ 203 [1.7] Iso <sup>1[sk]</sup> 208 [0.1] Iso C: Iso 205 [-0.1] Iso <sup>1[sk]</sup> 199 [-1.5] $SmC_a$ 87 [-19.4] Cr	4.1 (160)	–
<b>B6/8</b>	OC <sub>8</sub> H <sub>17</sub>	H: Cr 117 [21.7] $SmC_a$ 184 [0.9] Iso <sup>1[sk]</sup> 200 [0.1] Iso C: Iso 198 [-0.1] Iso <sup>1[sk]</sup> 177 [-0.8] $SmC_a$ 96 [-21.7] Cr	4.2 (150)	–
<b>B6/10</b>	OC <sub>10</sub> H <sub>21</sub>	H: Cr 115 [65.3] $SmC_a$ 145 [-] <sup>c)</sup> M1 150 [-] <sup>c)</sup> M1 + M2 151–156 [-] <sup>c)</sup> $Cub_{bi}/la\bar{3}d$ 198 [2.7] Iso C: Iso 191 [-0.3] Iso <sup>1[sk]</sup> 178 [-] <sup>c)</sup> $Cub_{bi}/la\bar{3}d$ 105 [-] <sup>c)</sup> $SmC_a$ 93 [-61.3] Cr	4.4 (120)	10.0 (170)
<b>B6/12</b>	OC <sub>12</sub> H <sub>25</sub>	H: Cr 111 [55.8] $Cub_{bi}/la\bar{3}d$ 197 [2.9] Iso C: Iso 189 [-2.1] $Cub_{bi}/la\bar{3}d$ 91 [-55.9] Cr	–	10.2 (160)
<b>B6/16</b>	OC <sub>16</sub> H <sub>33</sub>	H: Cr 105 [27.2] $Cub_{bi}/la\bar{3}d$ 191 [3.1] Iso C: Iso 182 [-2.1] $Cub_{bi}/la\bar{3}d$ 91 [-29.4] Cr	–	10.6 (150)
<b>B6/22</b>	OC <sub>22</sub> H <sub>45</sub>	H: Cr 94 [45.7] $Cub_{bi}/la\bar{3}d$ 180 [2.4] Iso C: Iso 173 [-2.1] $Cub_{bi}/la\bar{3}d$ 78 [-44.6] Cr	–	11.3 (140)
<b>B6/6a</b>	C <sub>6</sub> H <sub>13</sub>	H: Cr 124 [28.9] $SmC_a$ 206 [2.0] Iso <sup>1[sk]</sup> 209 [0.2] Iso C: Iso 206 [-0.1] Iso <sup>1[sk]</sup> 203 [-1.9] $SmC_a$ 88 [-23.3] Cr	4.2 (150)	–
<b>B6/7Me</b>	OCH(CH <sub>3</sub> )C <sub>6</sub> H <sub>13</sub>	H: Cr 116 [32.0] $Cub_{bi}/la\bar{3}d$ 130 [1.8] Iso C: Iso 121 [-1.5] $Cub_{bi}/la\bar{3}d < 20$ Cr	–	8.9 (125)

<sup>a)</sup>Peak temperatures as obtained by DSC at a scanning rate of 10 K min<sup>-1</sup> on heating (H) or cooling (C);  $SmC_a$ , anticlinic tilted SmC phase; M2, 3D mesophases with medium birefringence (see Figure 7i); for the other abbreviations, see Figure 1 and Table 1; for DSC traces, see Figure S3a–h, Supporting Information; for X-ray data, see Tables S1 and S5, Supporting Information; <sup>b)</sup>Enthalpy for both transitions Iso-N- $SmC_a$ ; <sup>c)</sup>Enthalpy value cannot be determined because the transition is slow; these transition temperatures were obtained by optical investigations.

**Table 3.** Phase transitions and lattice parameters of the swallow-tailed tricaténars **B'6/n** depending on the length of the 4'-alkyl chain (*n*).



Comp. <sup>a)</sup>	<i>n</i>	Phase transitions <i>T</i> [°C] [ $\Delta H$ kJ mol <sup>-1</sup> ]	<i>a</i> <sub>cub</sub> /nm ( <i>T</i> [°C])
<b>B'6/6</b>	6	H: M 109 [4.3] HexI <sub>s</sub> <sup>dis</sup> 144 [7.3] HexF <sub>s</sub> 147 [0.1] SmC <sub>a</sub> 159 [4.4] Iso C: Iso 156 [-4.3] SmC <sub>a</sub> 145 [-0.1] HexF <sub>s</sub> 141 [-6.5] HexI <sub>s</sub> <sup>dis</sup> 104 [-3.3] M	–
<b>B'6/8</b>	8	H: Cr 114 [10.9] HexB 125 HexF <sub>s</sub> 128 [2.9] <sup>b)</sup> SmC <sub>a</sub> 135 [1.0] Iso <sub>1</sub> <sup>[sk]</sup> 142 [0.2] Iso C: Iso 140 [-0.3] Iso <sub>1</sub> <sup>[sk]</sup> 130 [-1.0] SmC <sub>a</sub> 127 HexF <sub>s</sub> 123 [-2.7] <sup>b)</sup> HexB 107 [-11.2] Cr	–
<b>B'6/10</b>	10	H: Cr 113 [44.8] SmQ + Cub <sub>bi</sub> / <i>la</i> $\bar{3}d$ <sup>c)</sup> 128 [0.2] Iso <sub>1</sub> <sup>[sk]</sup> 137 [2.2] Iso C: Iso 131 [-0.2] Iso <sub>1</sub> <sup>[sk]</sup> 118 [-] SmQ + Cub <sub>bi</sub> / <i>la</i> $\bar{3}d$ <sup>c)</sup> 103 [-26.1] Cr	9.2(115)
<b>B'6/12</b>	12	H: Cr 114 [52.3] Cub <sub>bi</sub> / <i>la</i> $\bar{3}d$ 133 [2.8] Iso C: Iso 123 [-1.1] Cub <sub>bi</sub> / <i>la</i> $\bar{3}d$ 98 [-51.1] Cr	9.4 (125)
<b>B'6/16</b>	16	H: Cr 102 [62.3] Cub <sub>bi</sub> / <i>la</i> $\bar{3}d$ 128 [3.6] Iso C: Iso 125 [-3.0] Cub <sub>bi</sub> / <i>la</i> $\bar{3}d$ 92 [-52.6] Cr	9.6(120)
<b>B'6/20</b>	20	H: Cr 106 [90.9] Cub <sub>bi</sub> / <i>la</i> $\bar{3}d$ 124 [3.9] Iso C: Iso 119 [-3.2] Cub <sub>bi</sub> / <i>la</i> $\bar{3}d$ 88 [-85.2] Cr	10.0 (115)

<sup>a)</sup>Peak temperatures as obtained by DSC at a scanning rate of 10 K min<sup>-1</sup> on heating (H) or cooling (C); HexB, hexatic B phase (molecules are orthogonal to the layer planes); M, unknown low temperature lamellar phase (see Figures S15 and S24b, Supporting Information); for other abbreviations, see Figure 1 and Table 1; for DSC traces, see Figure S4, Supporting Information; for X-ray data, see Tables S1 and S5, Supporting Information; <sup>b)</sup>Transition enthalpy for both transitions CrB-HexF<sub>s</sub>-SmC<sub>a</sub>; <sup>c)</sup>Both phases coexist in different ratio depending on the conditions.

texture becomes mosaic like at the first phase transition at 145 °C (Figure 5d) and further changes with reduction of birefringence at the next transition at 141 °C (Figure 5f). In the planar sample the first transition at 145 °C is associated with a decrease of birefringence and the dark brushes of the fans become birefringent, indicating the onset of a synclitic tilt (Figure 5c). No significant change can be observed at the next phase transition at 141 °C (Figure 5e).

In the SAXS patterns of **B'6/6** the layer reflection is retained and the *d*-value increases on cooling (Figure 5i) mainly attributed to the alkyl chain stretching in the more ordered lamellar phases.<sup>[76]</sup> Moreover, there is a pronounced change of the shape of the WAXS (Figure 5h). The diffuse wide angle scattering in the SmC<sub>a</sub> phase narrows slightly at 145 °C and then splits into two scatterings with very different width at the next transition at 141 °C. Based on the optical textures and the shape of the WAXS we attribute the first transition at 145 °C to a transition to a HexF<sub>s</sub> phase (Figures 5h and 2h).<sup>[77]</sup> The shape of the powder WAXS pattern in the next low temperature phase is characterized by a relative sharp scattering at *d* = 0.46 nm which we attribute to HexI<sub>s</sub>-like packing in the layers of the alkyl chains (Figure 2i) and an additional diffuse scattering due to the SmC<sub>s</sub>-like ordered aromatic cores, similar as observed for the HexI<sub>s</sub><sup>dis</sup> phase of compound **B10/H**.

An additional transition at 104 °C obviously leads to a soft crystalline lamellar phase which is not further specified (M, see Figures S15 and S24, Supporting Information). It appears that reduction of the aromatic core length increases the influence of alkyl chain packing on LC self-assembly, and thus a similar sequence of smectic, hexatic and crystalline lamellar phases, as also found for **B10/H** with longer chains, but reduced chain number, can be observed.

A sequence of different lamellar phases is also observed for the next homologue **B'6/8** (Figure 6), however the phases are distinct from those of **B'6/6**. The high temperature phase is again a SmC<sub>a</sub> phase (Figure 6a). On cooling the birefringence of the schlieren texture decreases, the fans become broken (Figure 6b) and the wide-angle scattering sharpens slightly, in line with a SmC<sub>a</sub>-HexF<sub>s</sub> transition (Figure 6e). Again the layer spacing increases due to the chain stretching (Figure 6f), but this effect is even larger than for **B'6/6**. In powder patterns the wide angle scattering remains symmetric and in aligned samples it has a maximum around the equator, as typical for the HexF phase (Figure 6e and Figure S25, Supporting Information).<sup>[59,60,78]</sup> The stripe patterns across the fans, occurring at the transition to HexF (Figure 6b) indicates the transition to a synclitic tilt (HexF<sub>s</sub>). Finally the homeotropic areas become optically isotropic, the *d*-value of the layer scattering reaches *d* = 5.0 nm indicating a non-tilted organization. This *d*-value is much larger than *L*<sub>mol</sub> = 4.2 nm (Figure 6f), but close to the length of pairs of molecules with non-segregated partly intercalated organization (similar to Figure 3c, *L* = 5.1 nm, see Figure S27b, Supporting Information). All these observations confirm a transition from the anticlinic SmC<sub>a</sub> phase, at first assuming a synclitic tilt upon growing packing density in the HexF<sub>s</sub> phase to a non-tilted organization of the molecules in the HexB phase (Figure 2g). As typical for the transition to hexatic phases, the orientational order parameter (*S*) determined from the  $\chi$ -scan of the WAXS of aligned samples,<sup>[79]</sup> increases significantly at the transition to the hexatic phases (Figure 6e, right inset and Figure S25, Supporting Information). FS film investigations indicate a layer-by-layer SmC<sub>a</sub>-HexF<sub>s</sub> transition and a following continuous decreasing birefringence indicates



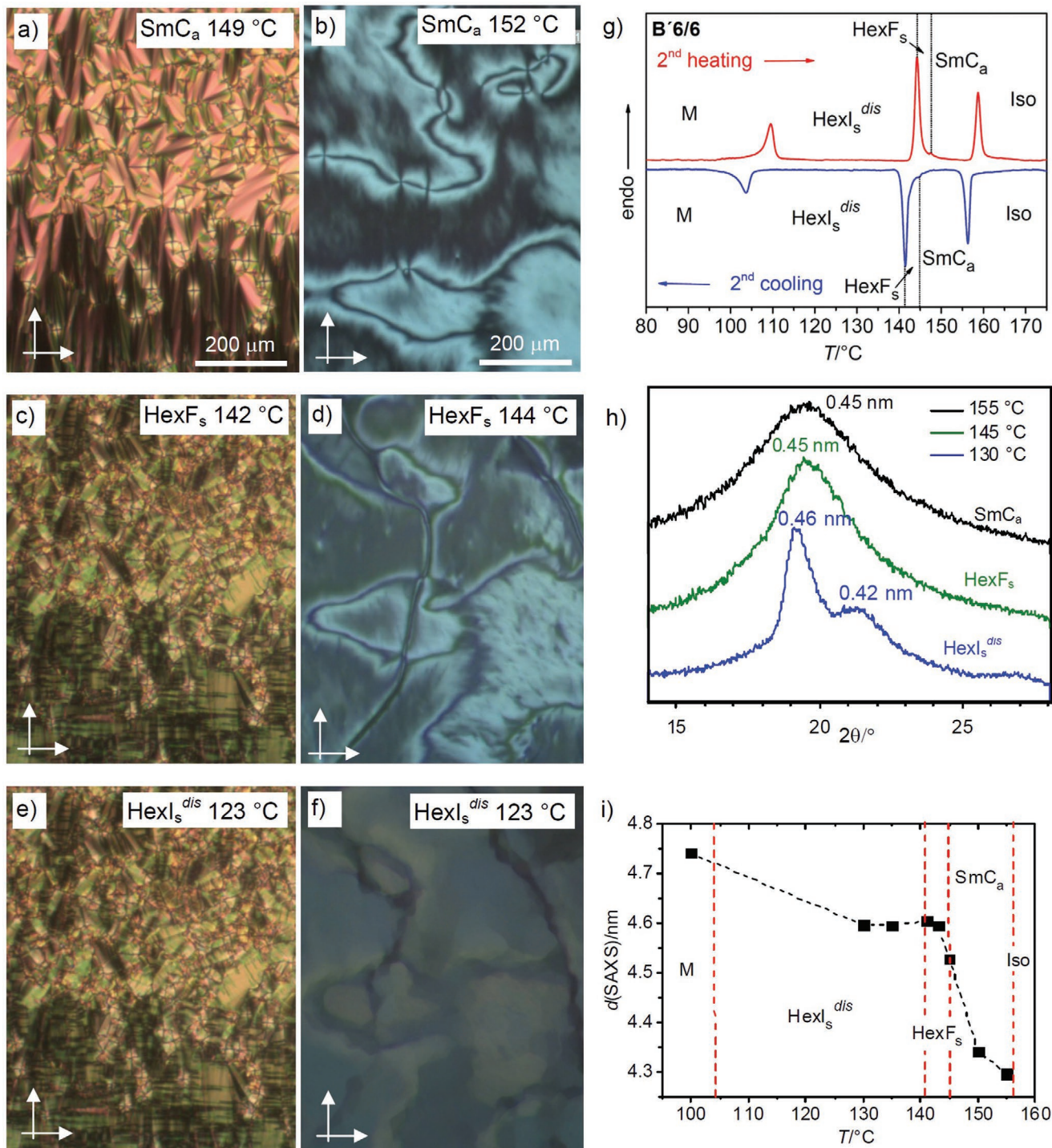


**Figure 5.** Investigation of compound B'6/6. a–f) Optical textures in planar (left) and homeotropic samples (right) as observed between crossed polarizers (white arrows) on cooling at the given temperatures in the indicated phases (for the transition Hexl<sub>s</sub><sup>dis</sup>-M, see Figure S15, Supporting Information); g) DSC heating and cooling traces at 10 K min<sup>-1</sup>; h) shape of the WAXS with *d*-values of the maxima and i) plots of the *d*-values of layer spacing depending on temperature; for more details, see Figures S23 and S24, Supporting Information).

a continuous reduction and removal of the tilt at the transition to HexB (Figure S16c–f, Supporting Information). For the following homologues of the series B'6/*n* the smectic and hexatic phases are removed and replaced by the Cub<sub>bi</sub> phase.

### 3.6. Cub<sub>bi</sub> Phases

The formation of the optically isotropic Cub<sub>bi</sub> phases from the birefringent SmC phases (SmC<sub>s</sub>/SmC<sub>a</sub>) is indicated by the

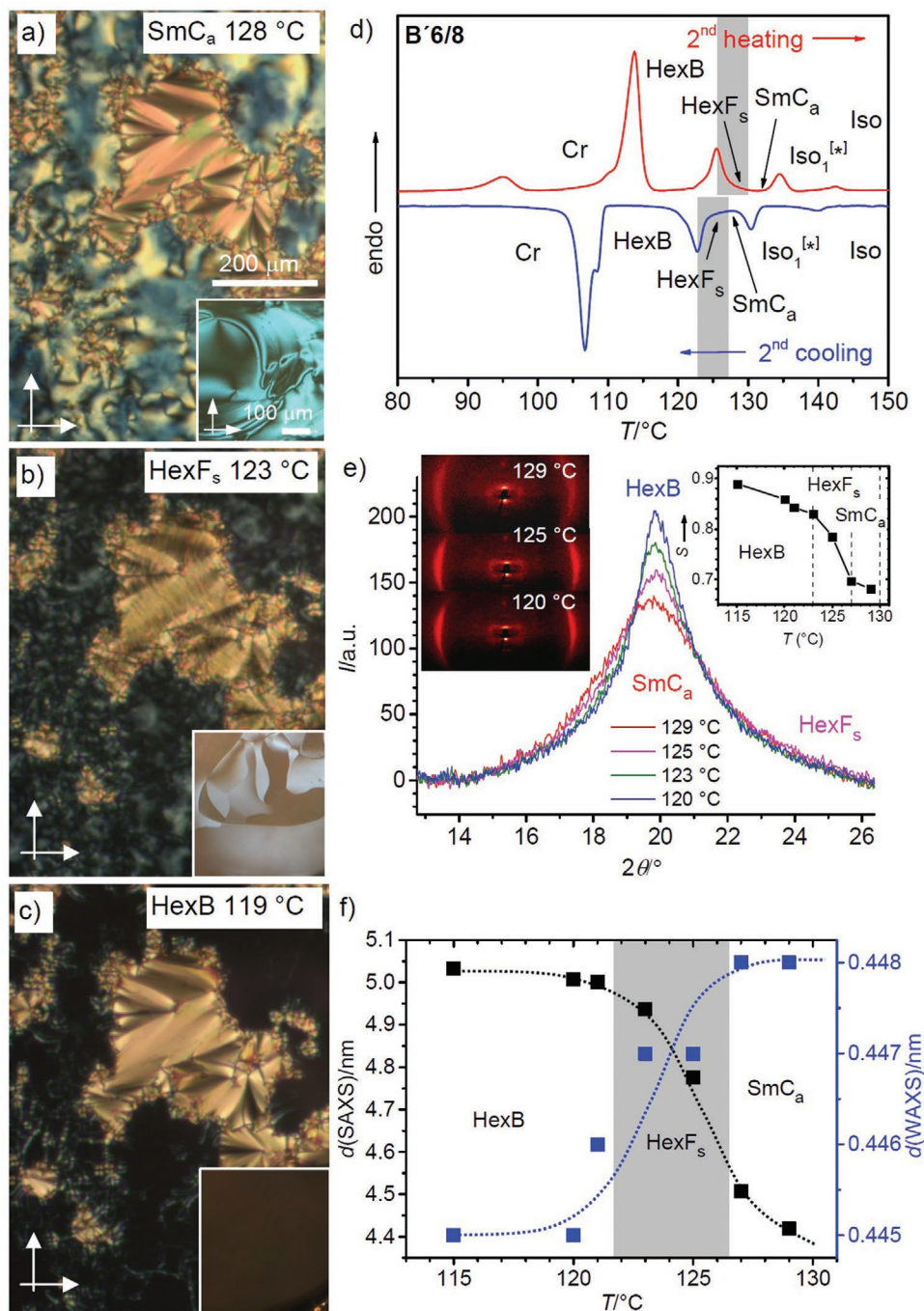


**Figure 6.** Investigation of the lamellar phases of compound **B'6/8**. a–c) Optical textures as observed between crossed polarizers in samples combining regions with planar alignment (fan-textures) with those having homeotropic alignment (gray), on cooling at the given temperatures in the indicated phases; the insets show the corresponding textures of freely suspended films (for details, see Figure S16c–f, Supporting Information); d) DSC heating and cooling traces at  $10 \text{ K min}^{-1}$ ; e) change of the shape of the WAXS (see also Figure S25, Supporting Information), and f) plots of the  $d$ -values of layer spacing and WAXS maximum depending on temperature; in e) the inset on the left shows the 2D scattering pattern of an aligned sample at the indicated temperature and that on the right shows the development of the orientational order parameter ( $S$ ) depending on temperature (see Figure S25, Supporting Information).

appearance of optically isotropic areas (Figure 7g), whereas the transition from the isotropic liquids (Iso, Iso<sub>1</sub><sup>[\*]</sup>) to Cub<sub>bi</sub> is only detected by a significant increase of viscosity. While the liquids flow under gravity, the isotropic Cub<sub>bi</sub> phases represent

viscoelastic solids which occasionally can grow as single crystals.<sup>[80]</sup> In most cases this transition is associated with a small DSC peak, often accompanied by a significant hysteresis of the phase transition on cooling. Moreover, transitions involving



Cub<sub>bi</sub> phases are often slow and then become invisible in the DSC traces. In the X-ray scattering patterns the cubic phases are identified by the presence of several sharp small angle Bragg peaks together with a completely diffuse wide angle scattering, the latter confirming the LC state (Figures S20b and S21b, Supporting Information). The cubic lattice type can be deduced from the relative positions of the most intense small angle scatterings either corresponding to the (211) and (220) indices of the  $Ia\bar{3}d$  lattice (Figure 7a and Figure S20a, Supporting Information) or the (321), (400) and (420) indices of the  $I23$  lattice (Figure 7b and Figure S21a, Supporting Information).<sup>[15,27a,28–31]</sup> The assignment to the distinct lattices is for polycatenar compounds easily confirmed by optical investigations between not fully crossed polarizers, where the  $I23$  phase shows a conglomerate of dark and bright domains which invert their brightness by rotating the analyzer into the opposite direction (Figure 7e).<sup>[27a,28]</sup> This indicates the presence of chiral domains as typical for the triple network  $I23$  structure (Figure 7b).<sup>[27a]</sup> In contrast, for the Cub<sub>bi</sub> phases with double network structure and space group  $Ia\bar{3}d$  (Figure 7a) no such domains can be found (Figure 7f).<sup>[27a,29,81]</sup> In the Cub<sub>bi</sub> phases the rod-like cores are organized in the networks which are separated by the continuum of the alkyl chains (Figure 7a,b). The orientation of the rods is on average perpendicular or slightly tilted to the networks and in this configuration the crowded periphery of the polycatenars inhibits a parallel arrangement of the tightly packed polyaromatic rods. This mismatch leads to a helical twist  $\Phi$  along the networks (Figure 7d)<sup>[27,28,34]</sup> and the network junctions allow a transmission of uniform helix sense over macroscopic distances. The double gyroid with  $Ia\bar{3}d$  space group (Figure 7a)<sup>[14,15,19,82]</sup> involves two interwoven enantiomorphic networks with opposite helicity and connected by three way junctions, leading to an achiral overall structure. This helically twisted organization in the achiral  $Ia\bar{3}d$  phases of rod-like molecules was recently supported by soft resonant X-ray scattering.<sup>[83]</sup> In this structure the twist between two three-fold junctions is 70.5°, which must fit with the total of the twists  $\Phi$  between adjacent molecules located on the way between two junctions.<sup>[27]</sup> If a mismatch arises other alternative structures are formed. The most common is the triple network structure with  $I23$  symmetry (Figure 7b),<sup>[39]</sup> previously known as “ $Im\bar{3}m$ ” phase,<sup>[24,26]</sup> which is chiral, not only because the chirality of the three networks cannot compensate, but also as a result of preferred homochiral helix packing.<sup>[27]</sup> The Cub<sub>bi</sub>/ $Ia\bar{3}d$  phase was found in all three series of compounds **Bm/n** and **B'6/n** after crossing a certain critical length of the 4'-alkyloxychain of  $n \geq 8$  for the series **B10/n** and  $n \geq 10$  for the series **B6/n** and **B'6/n**. The Cub<sub>bi</sub>/ $I23$  phase requires long chains at both ends (**B10/n** with  $n \geq 16$ ).

As obvious from the comparison of compounds **B6/8** and **B6/7Me** with the same number of carbon atoms, but with linear and branched apex chains, respectively, chain branching favors Cub<sub>bi</sub> phase formation over lamellar self-assembly, due to the larger effective cross section of these conformationally more disordered branched chains (Table 2). Increasing alkyl chain dynamics (by increasing temperature or by chain branching) does not only change the interface curvature and shifts the aggregate shape and phase type from lamellar to Cub<sub>bi</sub>, it also distorts the core-core interactions and thus decreases the phase

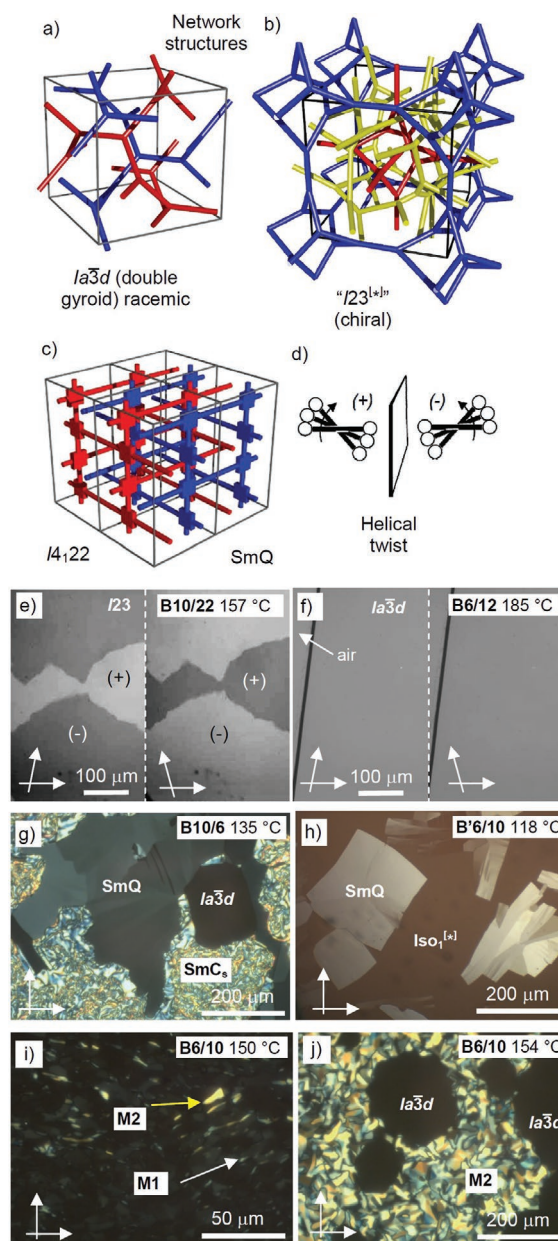


**Figure 7.** a–c) The major helical network structures presently known for polycatenar mesogens;<sup>[33,39]</sup> d) development of the helical twist by clashing of the end groups attached to rod-like cores;<sup>[32b]</sup> the helices propagate along the red, blue, and yellow networks. e, f) Textures of Cub<sub>bi</sub> phases observed under slightly uncrossed polarizers (in e) the contrast is enhanced). g–j) Representative optical textures of birefringent intermediate phases as observed between crossed polarizers; g) coexisting SmC<sub>s</sub>, Cub<sub>bi</sub>/ $Ia\bar{3}d$ , and SmQ phases on cooling **B10/6** from Iso<sub>1</sub><sup>[32]</sup> between non-treated microscopic glass plates (for textures in an ITO cell, see Figure S9, Supporting Information); h) SmQ phase of **B'6/10** as growing from Iso<sub>1</sub><sup>[32]</sup> on slow cooling (for the SmQ-Cub<sub>bi</sub>/ $Ia\bar{3}d$  transition, see Figure S10b, Supporting Information) and i, j) development of the M1 and M2 phases on heating compound **B6/10**, i) low birefringent mosaic texture (white arrow) of the M1 phase (see also Figure S10a, Supporting Information) with bright crystallites of the M2 phase with higher birefringence (yellow arrow) which in j) become dominating and transform into the Cub<sub>bi</sub>/ $Ia\bar{3}d$  phase on further heating. b) Reproduced with permission.<sup>[39]</sup> Copyright 2020, The Royal Chemical Society. c) Reproduced with permission.<sup>[33]</sup> Copyright 2020, Wiley-VCH.

transition temperatures, including the Iso<sub>1</sub><sup>[\*]</sup>-Iso transition, that is, the upper critical temperature of mirror symmetry breaking. Therefore, the transition temperatures of **B6/7Me** are much lower and the Iso<sub>1</sub><sup>[\*]</sup> phase of **B6/8** is suppressed (see also Section 3.8).

The cubic phases in the series **B6/n** and **B'6/n** have exclusively the *Ia3d* space group, whereas in the series of compounds **B10/n** with longer 3,5-chains an additional cubic phase with *I23* space group is observed for  $n \geq 16$ . For **B10/16** the formation of either the chiral Cub<sub>bi</sub><sup>[\*]</sup>/*I23* or the achiral Cub<sub>bi</sub>/*Ia3d* phase depends on the conditions; on heating there is a *Ia3d* – *I23* transition whereas on cooling only the *Ia3d* phase is found (Table 1). For **B10/22** with the longest alkyl chain exclusively the *I23* phase is observed on heating and cooling. This shows that a certain minimum chain length (or chain volume) is required for the formation of the mirror symmetry broken Cub<sub>bi</sub><sup>[\*]</sup>/*I23* phase.<sup>[15b,27–32]</sup> Only in one case, for the compound with the longest total chain length (**B10/22**), a columnar phase (Col<sub>ob</sub>) accompanies the Cub<sub>bi</sub><sup>[\*]</sup>/*I23* phase as a high temperature phase, resulting from the further increased interface curvature provided by this long chain (see Table 1 and Figure S11, Supporting Information). However, the Col<sub>ob</sub> phase is metastable and can only be observed on cooling, whereas on heating a direct Cub<sub>bi</sub><sup>[\*]</sup>/*I23*-Iso transition takes place.

### 3.7. Birefringent Mesophases with 3D Lattice

For compounds with a total chain length of  $m + n = 16$  to 18, being located at the transition from lamellar to Cub<sub>bi</sub>/*Ia3d* organization (compounds **B10/6**, **B10/8**, **B6/10**, and **B'6/10**, see Tables 1–3) Cub<sub>bi</sub> phase formation is accompanied by the formation of other birefringent mesophases with 3D lattice, either representing distorted versions of the Cub<sub>bi</sub>/*Ia3d* phase,<sup>[20]</sup> or arising from alternative helix packings (e.g., SmQ, see Figure 7c<sup>[33]</sup>). The formation of these intermediate phases at the lamellae-to-network transition is strongly dependent on the conditions, including thermal history of the sample, heating and cooling rates, boundary conditions, and modes of alignment. Often their formation is slow and therefore these transitions do not show up in the DSC traces (see Figures S2–S4, Supporting Information). Usually they are metastable and are rapidly replaced by the developing Cub<sub>bi</sub>/*Ia3d* phase, being the more stable phase. Therefore, their investigation, especially by X-ray scattering, is difficult and we can only describe qualitatively some typical observations. One of the intermediate phases is likely to be the SmQ phase which is characterized by a low birefringent mosaic-like texture, typically appearing gray, even in thick samples.<sup>[34]</sup> It is often observed on cooling from the mirror symmetry broken Iso<sub>1</sub><sup>[\*]</sup> phase (see next section) and once formed it rapidly transforms into the Cub<sub>bi</sub>/*Ia3d* phase on further cooling or isothermal with time. This helical network phase with tetragonal *I4<sub>1</sub>22* symmetry and 90° four-way network junctions was recently solved (Figure 7c).<sup>[33]</sup> It is proposed to represent an intermediate state at the transition from the mirror symmetry broken Iso<sub>1</sub><sup>[\*]</sup> phase with uniform helix sense to the racemic *Ia3d* phase, requiring the inversion of the helix sense for half of the networks. We assume that the low birefringent phases occurring at the Iso<sub>1</sub><sup>[\*]</sup>-Cub<sub>bi</sub> transition of

**B10/6** (Figure 7g) and **B'6/10** (Figure 7h) are likely to represent a SmQ phase, too. Also the low birefringent phase designated as M1 (compounds **B10/8**, **B6/10**, Tables 1 and 2) could possibly be the SmQ phase, though a specific texture cannot be observed in these cases (Figure 7i and Figure S10a, Supporting Information) and confirmation by X-ray scattering is not possible due to metastability and coexistence with other phases. Only the M2 phase of **B6/10**, having higher birefringence (Figure 7j), is likely to be different and related to similar birefringent 3D phases with tetragonal,<sup>[11,24,84–87]</sup> orthorhombic<sup>[88]</sup> or rhombohedral symmetry.<sup>[89]</sup>

In summary, formation of birefringent 3D phases is a general phenomenon, associated with the lamellar-Cub<sub>bi</sub>/*Ia3d* cross-over. In each of the investigated series it is observed for only one or two homologues with a certain chain length of  $m + n = 16$  to 18. Upon further chain elongation the non-cubic phases are removed and exclusively the Cub<sub>bi</sub> phases remain with the sequence *Ia3d* → *I23*. Notably, in the investigated series of compounds there are obviously no birefringent 3D phases occurring as intermediate phases at the transition between the *Ia3d* and *I23* phases.

### 3.8. Mirror Symmetry Broken Isotropic Liquid Phase Iso<sub>1</sub><sup>[\*]</sup>

The formation of an isotropic liquid mesophase showing a conglomerate of chiral domains with opposite optical rotation (Iso<sub>1</sub><sup>[\*]</sup>, see Figure 8a,b) is associated with the lamellar-to-Cub<sub>bi</sub> transition upon alkyl chain elongation, too. This chiral liquid formed by achiral molecules is considered as a percolated liquid with a dynamic helical network structure, which provides a long range transmission of uniform chirality in the enantiomeric domains of the conglomerate, but without assuming a long range cubic lattice.<sup>[29,30–32,34a]</sup> The helical self-assembly is supported by transiently chiral helical molecular conformations, as provided by the twisted 5,5'-diphenyl-2,2'-bithiophene core of the reported compounds.<sup>[32,34a]</sup>

Interestingly, FS films can be drawn in the Iso<sub>1</sub><sup>[\*]</sup> range; Figure 8d shows the FS film of the Iso<sub>1</sub><sup>[\*]</sup> phase of **B'6/8**. Those films have non-uniform thickness (Figure S28e, Supporting Information) and appear without any visible texture between crossed polarizers, though the films are metastable and limited in size. Like liquid fibers subjected to the Rayleigh-plateau instability, liquid films exhibit thinning instability and collapse too.<sup>[90]</sup> In smectics, it is the 1D periodic structure which is responsible for stabilization of freely suspended films.<sup>[91]</sup> The unexpected film formation of the Iso<sub>1</sub><sup>[\*]</sup> phase can be attributed to the dynamic network structure,<sup>[30]</sup> which, like in the case of polymers (and some oligomesogens<sup>[92]</sup>), stabilizes the films and leads to a non-Newtonian behavior. Additionally, correlation of the nano clusters can be induced by the free surfaces, similar to some nematic phases forming dynamic metastable films.<sup>[93]</sup> The films are even stable across the Iso<sub>1</sub><sup>[\*]</sup>-Iso transition. Also heating of the FS SmC<sub>a</sub> film to the SmC<sub>a</sub>-Iso<sub>1</sub><sup>[\*]</sup> transition temperature leads to Iso<sub>1</sub><sup>[\*]</sup> films (Figure 8e,f and Figure S27, Supporting Information). Only in sufficiently thick films (>100 μm) mirror symmetry breaking takes place and domains of opposite chirality can be observed, thinner films appear to be achiral. Interestingly, these chiral domains have



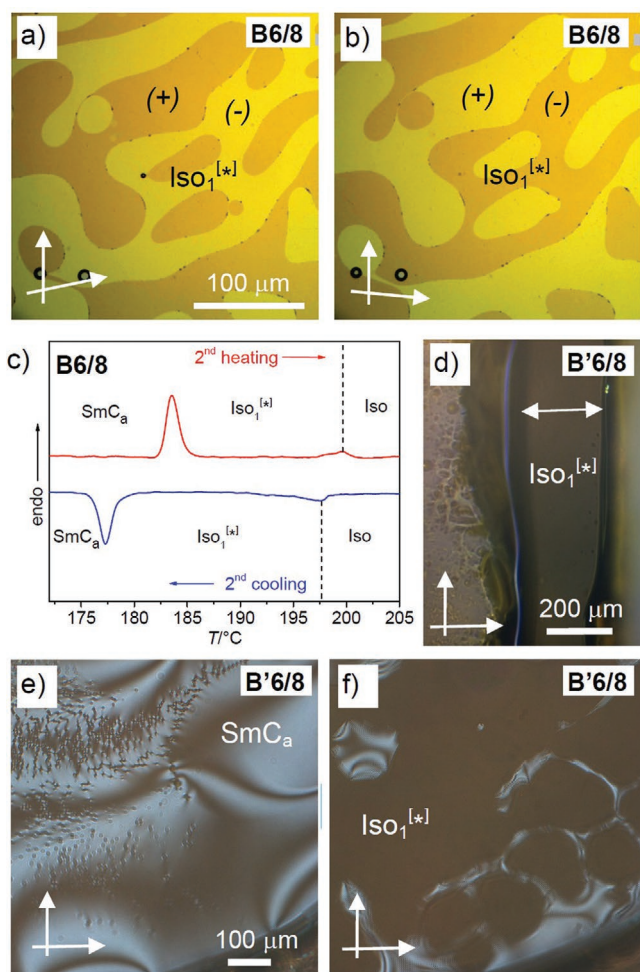


**Figure 8.** a,b) Chiral conglomerate of the mirror symmetry broken  $\text{Iso}_1^{[*]}$  phase of **B6/8** at 185 °C as observed in  $\approx 50 \mu\text{m}$  thick films between two glass plates and between polarizers, being slightly uncrossed in different directions; c) DSC traces showing the  $\text{SmC}_a$ - $\text{Iso}_1^{[*]}$ -Iso transitions on heating and cooling ( $10 \text{ K min}^{-1}$ ). d–f) FS films of **B'6/8** as observed between crossed polarizers (white arrows); d) FS films drawn in the  $\text{Iso}_1^{[*]}$  phase between two supports (right and left) at  $T = 138 \text{ °C}$ ; the film thickness is 200–800 nm; e,f)  $\text{SmC}_a$ - $\text{Iso}_1^{[*]}$  transition as observed on slow heating of a FS film drawn in the  $\text{SmC}_a$  phase (see also Figure S28, Supporting Information). A film without polarizers is shown in Figure S28e, Supporting Information; FS films between twisted polarizers show chiral domains only if the film has sufficient thickness and then the chiral domains rapidly fuse with formation of a homochiral film which also appears uniform.

an unequal distribution with one sign of chirality dominating. Once this imbalance has developed the film becomes rapidly homochiral, due to the huge chirality amplification capability of the  $\text{Iso}_1^{[*]}$  phase. The capability of chirality amplification was previously reported for samples between glass substrates as shown in Figure S4, Supporting Information of ref. [34a]. Due to the ubiquitous presence of tiny chirality sources in the environment, in most cases the FS  $\text{Iso}_1^{[*]}$  films of sufficient thickness appear homogeneously chiral almost from the beginning.

In the series of compounds **Bm/n** and **B'6/n** the formation of the  $\text{Iso}_1^{[*]}$  phase is associated with the  $\text{SmC}$ -to- $\text{Cub}_{\text{bi}}/\text{Ia}\bar{3}d$  transition, irrespectively if the  $\text{SmC}$  phase is synclinal or

anticlinal. It is observed for a medium chain length around  $n = 6$ –10 (**B10/n**:  $n = 6, 8$ , **B6/n**:  $n = 6$ –10 and **B'6/n**:  $n = 8, 10$ , see Tables 1–3). For most compounds it is only observed on cooling as a monotropic phase replacing the  $\text{Ia}\bar{3}d$  phase, but for compounds **B'6/8**, **B6/8** and **B6/6a** it is an enantiotropic phase occurring directly above  $\text{SmC}_a$  (without accompanying  $\text{Cub}_{\text{bi}}$  phase) and having the broadest enantiotropic  $\text{Iso}_1^{[*]}$  range for **B6/8**. As shown in Figure 8c, the Iso- $\text{Iso}_1^{[*]}$  transition is associated with a small enthalpy in the DSC traces which is attributed to the chirality synchronization.<sup>[30,31]</sup> Previous temperature dependent SAXS experiments have indicated a continuously decreasing line width, and hence, growing correlation length of the helical aggregates around the continuous Iso- $\text{Iso}_1^{[*]}$  transition, and a jump to resolution limited Bragg peaks at the discontinuous  $\text{Iso}_1^{[*]}$  to  $\text{Cub}_{\text{bi}}$  transition.<sup>[31,34a]</sup> The Iso- $\text{Iso}_1^{[*]}$  transition was also investigated by optical rotation and circular dichroism.<sup>[27a]</sup> Based on all these investigations the model of a dynamic network structure of the  $\text{Iso}_1^{[*]}$  phase was suggested.<sup>[30–32,34a,42]</sup> Recent results of NMR relaxation and NMR diffusion measurements at the  $\text{Cub}_{\text{bi}}$ -Iso- $\text{Iso}_1^{[*]}$  transitions of other achiral polycatenar molecules support this model of a local  $\text{Cub}_{\text{bi}}$ -like structure of the Iso- $\text{Iso}_1^{[*]}$  transition.<sup>[94a]</sup> and theoretical work supports the importance of network formation for mirror symmetry breaking.<sup>[95]</sup> In the case reported here, the spontaneous chirality evolves by the chirality synchronization in the dynamic helical superstructure of the  $\text{Iso}_1^{[*]}$  phase.<sup>[32]</sup> In fact, there is some similarity with the  $\text{Iso}_1^{[*]}$  phase occurring besides chirality frustrated LC phases of permanently chiral molecules (\*),<sup>[11a,b,96,97]</sup> the most prominent example being the BPIII phase.<sup>[98]</sup> It should be noted, that Iso- $\text{Iso}_1^{[*]}$  transitions have previously been reported to occur besides cubic LC phases,<sup>[15b,97a]</sup> but the helical network structure and the capability of these  $\text{Iso}_1^{[*]}$  phases of mirror symmetry breaking, first reported in ref. [27a], were not recognized at that time. Moreover, liquid state polymorphism is a general feature of complex liquids, which is not yet fully recognized,<sup>[42,99,100]</sup> but of great importance for biosystems, too.<sup>[32,101]</sup>

The  $\text{Iso}_1^{[*]}$  phase and related isotropic mesophases often appear in proximity to the  $\text{SmQ}$  phase, a birefringent 3D phase with tetragonal lattice (Figure 7c)<sup>[33,96]</sup> and therefore, it is likely that the local structure in the dynamic networks of the  $\text{Iso}_1^{[*]}$  phases of the investigated compounds is similar to the helical network structure with  $90^\circ$  four-way junctions as recently proposed for this  $\text{SmQ}$  phase ( $\text{Iso}_1^{[*]}(\text{SmQ})$ ).<sup>[33]</sup> For compounds **B6/6**, **B6/8**, **B'6/8** and **B6/6a** the  $\text{Iso}_1^{[*]}$  phase appears between the achiral isotropic liquid (Iso) and the anticlinal  $\text{SmC}_a$  phase, in these cases without any competing  $\text{SmQ}$  or  $\text{Ia}\bar{3}d$  phase and it is formed on heating as well as on cooling, without the strong hysteresis being typical for the  $\text{Iso}_1^{[*]} \rightarrow \text{Ia}\bar{3}d$  transition (Figure 8c). In these cases the  $\text{SmQ}$ -like local network structure in the  $\text{Iso}_1^{[*]}$  phase transforms directly into an achiral lamellar phase, without requiring a helix inversion. Interestingly, as soon as the  $\text{Ia}\bar{3}d$  phase emerges in the phase sequence, also other 3D phases ( $\text{SmQ}$ , M1, M2) appear, which can be explained by the required helix inversion at the  $\text{Iso}_1^{[*]}-\text{Ia}\bar{3}d$  transition. The transition from the conglomerate of the chiral  $\text{Iso}_1^{[*]}$  phases to the racemic  $\text{Ia}\bar{3}d$  phase requires a helix inversion for half of the networks which is a collective process in the networks and therefore requires a significant activation energy which



makes this inversion slow.<sup>[33]</sup> Therefore, a homogeneous chiral intermediate phase, not requiring helix inversion (e.g., SmQ) is formed first. However, it is metastable and in a second step slowly transforms into the racemic  $Ia\bar{3}d$  phase by partial helix inversion. As the achiral  $Ia\bar{3}d$  phase becomes dominating with growing chain length, the chiral Iso<sub>1</sub><sup>[\*]</sup> phase disappear together with the SmQ phase and the other non-cubic 3D phases. It is likely that with chain elongation the local structure of the Iso/Iso<sub>1</sub> phase becomes  $Ia\bar{3}d$  like, which is achiral.<sup>[102]</sup>

Whereas for the compounds **Bm/n** and **B'6/n** exclusively the chiral Iso<sub>1</sub><sup>[\*]</sup><sub>(SmQ)</sub> and achiral isotropic liquid phases could be observed, in the related series of the tetracatenars compounds **Am/n** with one more chain and significantly larger chain volume (3,4,5-trisubstitution, see compound **A10/10** in Figure 1) the Iso<sub>1</sub><sup>[\*]</sup> phase appears again and occurs in proximity to the mirror symmetry broken Cub<sub>bi</sub><sup>[\*]</sup>/I23 phase.<sup>[27a,29,34]</sup> Therefore, it appears likely that there are two different types of Iso<sub>1</sub><sup>[\*]</sup> phases having different local network structures, being either SmQ-like with 90° four-way junctions (Figure 7c) for those located close to the lamellar–Cub<sub>bi</sub>/Ia $\bar{3}d$  cross-over (Iso<sub>1</sub><sup>[\*]</sup><sub>(SmQ)</sub>), compounds **B** and **B'**) and I23-like with almost 120° three-way junctions for those occurring besides the Cub<sub>bi</sub><sup>[\*]</sup>/I23 phase (Iso<sub>1</sub><sup>[\*]</sup><sub>(I23)</sub>; compounds **A**, see Figure 7b). An achiral Iso<sub>1</sub> phase, presumably with local  $Ia\bar{3}d$  structure was detected for related 3,5-substituted tricaténars with azobenzene cores<sup>[52,103]</sup> and 3,4,5-substituted benzil based tetracatenars<sup>[30,31]</sup> which completes the overall sequence Iso<sub>1</sub><sup>[\*]</sup><sub>(SmQ)</sub>–Iso<sub>1</sub><sub>(Ia $\bar{3}d$ )</sub>–Iso<sub>1</sub><sup>[\*]</sup><sub>(I23)</sub> of the percolated network liquids upon alkyl chain expansion (see Figure 9). This series of percolated liquids is analogous to the sequence SmQ–Cub<sub>bi</sub>/Ia $\bar{3}d$ –Cub<sub>bi</sub><sup>[\*]</sup>/I23 observed for the related LC phases with long range periodic network structure. In contrast to the Iso<sub>1</sub><sup>[\*]</sup> to Ia $\bar{3}d$  transformation, which is accompanied by birefringent 3D phases, no such intermediate phases could be found for the Iso<sub>1</sub><sup>[\*]</sup> to I23 transition,<sup>[29–31]</sup> probably because no helix inversion is required for the transition between these two chiral phases.

#### 4. Summary

This work provides a systematic investigation of the structure-property relations of a new kind of swallow-tailed polycatenar compounds at the transition from lamellar to helical network phases. The compounds involve the functional 5,5'-diphenyl-2,2'-bithiophene core, which is of interest as fluorescent (AIE active) and charge carrying unit for the development of new multifunctional organic electronic materials. As well known, the local organization of these  $\pi$ -conjugated rods determines the application relevant properties and, therefore, the understanding of the fundamental rules of their soft self-assembly is of general interest.

The effect of the alkyl chain number and alkyl chain distribution is shown in Figure 1. The main focus is on swallow-tailed compounds having the rarely used 3,5-disubstitution pattern at one end combined with a non-substituted or 4'-alkyloxysubstituted apex (Scheme 1). Their conformation can change depending on alkyl chain length and temperature between a Y-like and a tuning fork like shape (Figure 3g,h); the main self-assembled structures formed by these compounds and their development depending on the molecular structure are summarized

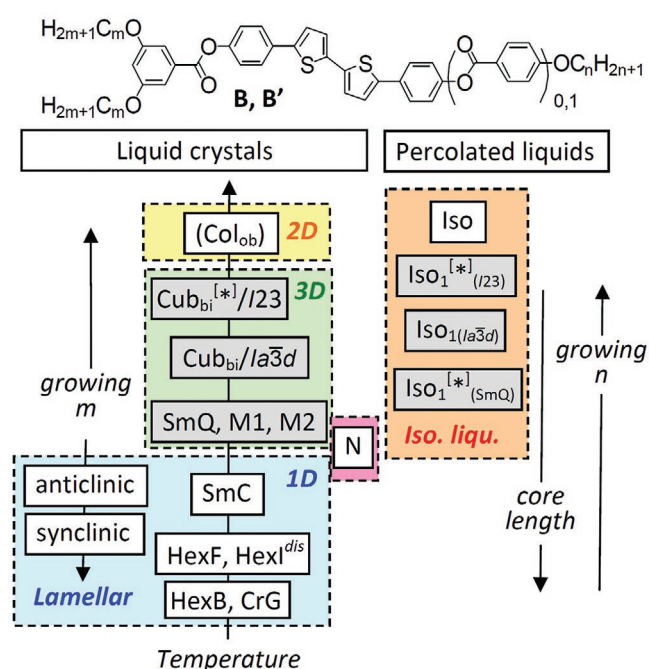


**Figure 9.** Overview over the structure-mesophases relations of the investigated compounds; Iso<sub>1</sub><sub>(Ia $\bar{3}d$ )</sub> and Iso<sub>1</sub><sup>[\*]</sup><sub>(I23)</sub> were not observed for compounds **B** and **B'**, but were added for completeness of the phase sequences; gray background indicates helical network phases.

in Figure 9. By chain elongation a transition from lamellar phases to bicontinuous cubic phases, first with achiral  $Ia\bar{3}d$  space group and upon further chain elongation with the chiral and spontaneous mirror symmetry broken Cub<sub>bi</sub><sup>[\*]</sup>/I23 phase (Figure 7a,b), followed by a columnar phase (Col<sub>ob</sub>), is observed.

The lamellar phases represent tilted smectic phases which are synclinic tilted if the 3,5-chains are sufficiently long, and become anticlinic tilted for shorter chains. Thus, this molecular structure provides a new class of anticlinic SmC<sub>a</sub> materials, being of interest for antiferroelectric and orthoconic LCs for display applications.<sup>[67]</sup> Another specific feature of these compounds is the formation of a series of hexatic low temperature phases. At the transition to the hexatic phases the tilt correlation becomes synclinic (HexF<sub>s</sub>, HexI<sub>s</sub><sup>dis</sup>) or the tilt is removed (HexB, see Figure 2g–i). In addition, new variants of hexatic phases combining hexatic order of the alkyl chains with more disordered aromatic cores (HexI<sub>s</sub><sup>dis</sup>) were observed.

Finally, it is shown that the SmC–Cub<sub>bi</sub>/Ia $\bar{3}d$  transitions are accompanied by the formation of additional modes of self-assembly, among them birefringent 3D mesophases, as the tetragonal SmQ phase (Figure 7c) and a mirror symmetry broken isotropic liquid phase (Iso<sub>1</sub><sup>[\*]</sup>, Figure 8). It is shown that for the latter freely suspended films can be drawn, which can become local mirror symmetry broken and even homogeneously chiral, due to the chirality synchronization in the dynamic helical network with proposed SmQ-like local structure. A sequence of chiral (Iso<sub>1</sub><sup>[\*]</sup>) and achiral (Iso<sub>1</sub>) percolated liquids with local network structures, resembling those of the adjacent cubic and non-cubic LC network phases is proposed to occur depending on the alkyl chain length and thus changing intermolecular twist (Figure 9).

Overall, this work contributes to the general understanding of the soft matter self-assembly at the lamellae-network transition and the mechanism of spontaneous mirror symmetry breaking in fluids, being of technological interest for the development of novel functional materials and devices.

## Supporting Information

Supporting Information is available from the Wiley Online Library or from the author.

## Acknowledgements

This work was supported by the Deutsche Forschungsgemeinschaft (Ts 39/24-2 and ER 467/8-2).

Open access funding enabled and organized by Projekt DEAL.

## Conflict of Interest

The authors declare no conflict of interest.

## Keywords

antclinic smectic phases, bicontinuous cubic phases, bithiophenes, helical networks, hexatic phases, liquid crystals, mirror symmetry breaking, polycatenars

Received: September 13, 2020

Revised: October 23, 2020

Published online:

- [1] Y.-X. Hu, W.-J. Li, P.-P. Jia, X.-Q. Wang, L. Xu, H.-B. Yang, *Adv. Opt. Mater.* **2020**, *8*, 2000265.
- [2] Y. Tsutsui, W. Zhang, S. Ghosh, T. Sakurai, H. Yoshida, M. Ozaki, T. Akutagawa, S. Seki, *Adv. Opt. Mater.* **2020**, *8*, 1902158.
- [3] T. Yasuda, H. Ooi, J. Morita, Y. Akama, K. Minoura, M. Funahashi, T. Shimomura, T. Kato, *Adv. Funct. Mater.* **2009**, *19*, 411.
- [4] a) J. Mei, N. L. C. Leung, R. T. K. Kwok, J. W. Y. Lam, B. Z. Tang, *Chem. Rev.* **2015**, *115*, 11718. b) Y. Li, S. Liu, T. Han, H. Zhang, C. Chuah, R. T. K. Kwok, J. W. Y. Lam, B. Z. Tang, *Mater. Chem. Front.* **2019**, *3*, 2207; c) H.-T. Feng, J. W. Y. Lam, B. Z. Tang, *Coord. Chem. Rev.* **2020**, *406*, 213142.
- [5] F. Song, Z. Zhao, Z. Liu, J. W. Y. Lam, B. Z. Tang, *J. Mater. Chem. C* **2020**, *8*, 3284.
- [6] L. Wang, Q. Li, *Adv. Funct. Mater.* **2016**, *26*, 10.
- [7] W. Goodby, P. J. Collings, T. Kato, C. Tschierske, H. Gleeson, P. Raynes, *Handbook of Liquid Crystals*, 2nd ed., Wiley-VCH, Weinheim, Germany **2014**.
- [8] Q. Li, *Nanoscience with Liquid Crystals. – From Self-Organized Nanostructures to Applications*, Springer, Cham, Switzerland **2014**.
- [9] a) J. Malthete, H. T. Nguyen, C. Destrade, *Liq. Cryst.* **1993**, *13*, 171; b) H. T. Nguyen, C. Destrade, J. Malthete, *Adv. Mater.* **1997**, *9*, 375; c) M. Gharbia, A. Gharbi, H. T. Nguyen, J. Malthete, *Curr. Opin. Colloid Interf. Sci.* **2002**, *7*, 312; d) D. W. Bruce, *Acc. Chem. Res.* **2000**, *33*, 831; e) H. T. Nguyen, C. Destrade, J. Malthete, in *Handbook of Liquid Crystals* (Eds: D. Demus, J. Goodby, G. W. Gray, H.-W. Spiess, V. Vill), Wiley-VCH, Weinheim, Germany **1998**, pp. 865–900; f) W. Weissflog, in *Handbook of Liquid Crystals*, 2nd ed. (Eds: J. W. Goodby, J. P. Collings, T. Kato, C. Tschierske, H. F. Gleeson, P. Raynes), Wiley-VCH, Weinheim, Germany **2014**, pp. 89–174.
- [10] a) J. Malthete, A. M. Levelut, N. H. Tinh, *J. Phys. Lett.* **1985**, *46*, 875; b) N. H. Tinh, J. Malthete, C. Destrade, *Mol. Cryst. Liq. Cryst. Lett.* **1985**, *2*, 133; c) N. H. Tinh, C. Destrade, A. M. Levelut, J. Malthete, *J. Phys.* **1986**, *47*, 553; d) D. Guillon, A. Skoulios, J. Malthete, *Europhys. Lett.* **1987**, *3*, 67; e) C. Destrade, N. H. Tinh, A. Roubineau, A. M. Levelut, *Mol. Cryst. Liq. Cryst.* **1988**, *159*, 163; f) A. M. Levelut, J. Malthete, C. Destrade, N. H. Tinh, *Liq. Cryst.* **1987**, *2*, 877; g) N. T. Nguyen, C. Destrade, J. Malthete, *Liq. Cryst.* **1990**, *8*, 797.
- [11] a) I. Nishiyama, *Chem. Rec.* **2009**, *9*, 340; b) M. Yoneya, *Chem. Rec.* **2011**, *11*, 66; c) E. Nishikawa, J. Yamamoto, H. Yokoyama, *J. Mater. Chem.* **2003**, *13*, 1887; d) E. Nishikawa, E. T. Samulski, *Liq. Cryst.* **2000**, *27*, 1463; e) A. Yoshizawa, *Polym. J.* **2012**, *44*, 490.
- [12] a) C. Tschierske, *J. Mater. Chem.* **2001**, *11*, 2647; b) C. Tschierske, *Annu. Rep. Prog. Chem. Sect. C* **2001**, *97*, 191; c) C. Tschierske, *Isr. J. Chem.* **2012**, *52*, 935; d) C. Tschierske, in *Handbook of Liquid Crystals*, 2nd ed., Vol. 5 (Eds: J. W. Goodby, J. P. Collings, T. Kato, C. Tschierske, H. F. Gleeson, P. Raynes), Wiley-VCH, Weinheim, Germany **2014**, pp. 1–88.
- [13] C. Tschierske, *Angew. Chem., Int. Ed.* **2013**, *52*, 8828.
- [14] L. Han, S. Che, *Adv. Mater.* **2018**, *30*, 1705708.
- [15] a) G. Ungar, F. Liu, X. B. Zeng, in *Handbook of Liquid Crystals* (Eds: W. Goodby, P. J. Collings, T. Kato, C. Tschierske, H. Gleeson, P. Raynes), Wiley-VCH, Weinheim, Germany **2014**; b) S. Kutsumizu, *Isr. J. Chem.* **2012**, *52*, 844.
- [16] T. Kato, J. Uchida, T. Ichikawa, T. Sakamoto, *Angew. Chem., Int. Ed.* **2018**, *57*, 4355.
- [17] M. Maldovan, A. M. Urbas, N. Yufa, W. C. Carter, E. L. Thomas, *Phys. Rev. B* **2002**, *65*, 165123.
- [18] M. L. Lynch, P. T. Spicer, *Bicontinuous Liquid Crystals*, CRC Press, Taylor & Francis Group, Boca Raton, FL **2005**.
- [19] a) J. M. Seddon, R. H. Templer, in *Handbook of Biological Physics* (Eds: R. Lipowsky, E. Sackmann), Elsevier Science B.V., Amsterdam **1995**, pp. 97–160; b) S. T. Hyde, in *Handbook of Applied Surface and Colloid Chemistry* (Ed: K. Holmberg), Wiley-VCH, Weinheim, Germany **2001**, pp. 299–332; c) L. van 't Hag, S. L. Gras, C. E. Conn, C. J. Drummond, *Chem. Soc. Rev.* **2017**, *46*, 2705.
- [20] a) A. J. Meuler, M. A. Hillmyer, F. S. Bates, *Macromolecules* **2009**, *42*, 7221; b) E. L. Thomas, *Sci. Chin. Chem.* **2018**, *61*, 25.
- [21] S. Hyde, S. Andersson, K. Larsson, Z. Blum, T. Landh, S. Lidin, B. W. Ninham, *The Language of Shape: The Role of Curvature in Condensed Matter: Physics, Chemistry and Biology*, Elsevier Science B.V., Amsterdam **1997**.
- [22] A. H. Schoen, *NASA Technical Note TN D-5541* **1970**.
- [23] a) X. Zeng, S. Poppe, A. Lehmann, M. Prehm, C. Chen, F. Liu, H. Lu, G. Ungar, C. Tschierske, *Angew. Chem., Int. Ed.* **2019**, *58*, 7375; b) S. Poppe, X. H. Cheng, C. L. Chen, X. B. Zeng, R. B. Zhang, F. Liu, G. Ungar, C. Tschierske, *J. Am. Chem. Soc.* **2020**, *142*, 3296; c) C. Chen, M. Poppe, S. Poppe, C. Tschierske, F. Liu, *Angew. Chem., Int. Ed.* **2020**, *59*, 20820.
- [24] A. M. Levelut, M. Clerc, *Liqu. Cryst.* **1998**, *24*, 105.
- [25] a) X. B. Zeng, G. Ungar, M. Imperor-Clerc, *Nat. Mater.* **2005**, *4*, 562. b) X. Zeng, L. Cseh, G. H. Mehl, G. Ungar, *J. Mater. Chem.* **2008**, *18*, 2953.
- [26] a) K. Saito, Y. Yamamura, Y. Miwa, S. Kutsumizu, *Phys. Chem. Chem. Phys.* **2016**, *18*, 3280. b) N. Vaupotic, M. Salamonczyk, J. Matraszek, M. Vogrin, D. Pocięcha, E. Gorecka, *Phys. Chem. Chem. Phys.* **2020**, *22*, 12814.
- [27] a) C. Dressel, F. Liu, M. Prehm, X. B. Zeng, G. Ungar, C. Tschierske, *Angew. Chem., Int. Ed.* **2014**, *53*, 1115; b) M. Alaasar, S. Poppe, Q. Dong, F. Liu, C. Tschierske, *Chem. Commun.* **2016**, *52*, 13869.

- [28] T. Reppe, C. Dressel, S. Poppe, C. Tschierske, *Chem. Commun.* **2020**, 56, 711.
- [29] C. Dressel, T. Reppe, S. Poppe, M. Prehm, H. Lu, X. Zeng, G. Ungar, C. Tschierske, *Adv. Funct. Mater.* **2020**, *30*, 2004353.
- [30] T. Reppe, S. Poppe, X. Cai, Y. Cao, F. Liu, C. Tschierske, *Chem. Sci.* **2020**, *11*, 5902.
- [31] T. Reppe, S. Poppe, C. Tschierske, *Chem. - Eur. J.* **2020**, *26*, <https://doi.org/10.1002/chem.202002869>.
- [32] a) C. Tschierske, *Liqu. Cryst.* **2018**, *45*, 2221; b) C. Tschierske, G. Ungar, *ChemPhysChem* **2016**, *17*, 9.
- [33] H. J. Lu, X. B. Zeng, G. Ungar, C. Dressel, C. Tschierske, *Angew. Chem., Int. Ed.* **2018**, *57*, 2835.
- [34] a) C. Dressel, T. Reppe, M. Prehm, M. Brautzsch, C. Tschierske, *Nat. Chem.* **2014**, *6*, 971; b) C. Dressel, W. Weissflog, C. Tschierske, *Chem. Commun.* **2015**, 51, 15850.
- [35] M. Alaasar, M. Prehm, Y. Cao, F. Liu, C. Tschierske, *Angew. Chem., Int. Ed.* **2016**, *55*, 312.
- [36] M. Alaasar, S. Poppe, Q. Dong, F. Liu, C. Tschierske, *Angew. Chem., Int. Ed.* **2017**, *56*, 10801.
- [37] a) J. M. Wolska, J. Wilk, D. Pocięcha, J. Mieczkowski, E. Gorecka, *Chem. - Eur. J.* **2017**, *23*, 6853; b) H. R. Brand, H. Pleiner, *Eur. Phys. J. E* **2019**, *42*, 142.
- [38] S. Kutsumizu, S. Miisako, Y. Miwa, M. Kitagawa, Y. Yamamura, K. Saito, *Phys. Chem. Chem. Phys.* **2016**, *18*, 17341.
- [39] X. B. Zeng, G. Ungar, *J. Mater. Chem. C* **2020**, *8*, 5389.
- [40] A. Guijarro, M. Yus, *The Origin of Chirality in the Molecules of Life*, RSC, Cambridge, UK **2009**.
- [41] J. Buchs, L. Vogel, D. Janietz, M. Prehm, C. Tschierske, *Angew. Chem., Int. Ed.* **2017**, *56*, 280.
- [42] C. Tschierske, C. Dressel, *Symmetry* **2020**, *12*, 1098.
- [43] a) J. Barbera, E. W. Diaz, M. R. Dahrouch, E. Y. Elgueta, M. L. Parra, *Supramol. Chem.* **2014**, *26*, 373; b) Y. Sun, Y.-X. Wang, M. Wu, W. Yuan, Y. Chen, *Chem. Asian J.* **2017**, *12*, 52.
- [44] A. Escande, L. Guénée, E. Terazzi, T. B. Jensen, H. Nozary, C. Piguet, *Eur. J. Inorg. Chem.* **2010**, 2746.
- [45] J. H. Wild, K. Bartle, M. O'Neill, S. M. Kelly, R. P. Tuffin, *Liq. Cryst.* **2006**, *33*, 635.
- [46] G. S. Lim, B. M. Jung, S. J. Lee, H. H. Song, C. Kim, J. Y. Chang, *Chem. Mater.* **2007**, *19*, 460.
- [47] a) A. Kotlewski, W. F. Jager, E. Mendes, S. J. Picken, *Liq. Cryst.* **2010**, *37*, 579; b) A. Sautter, C. Thalacker, F. Würthner, *Angew. Chem., Int. Ed.* **2001**, *40*, 4425.
- [48] U. Beginn, G. Lattermann, *Mol. Cryst. Liq. Cryst.* **1994**, *241*, 215.
- [49] M. Imperor-Clerc, P. Sotta, M. Veber, *Liq. Cryst.* **2000**, *27*, 1001.
- [50] C. Destrade, N. H. Tinh, *Mol. Cryst. Liq. Cryst.* **1988**, *159*, 163.
- [51] X. Wang, C. M. Cho, W. Y. Say, A. Y. X. Tan, C. He, H. S. O. Chan, J. Xu, *J. Mater. Chem.* **2011**, *21*, 5248.
- [52] M. Alaasar, S. Poppe, Y. Cao, C. Chen, F. Liu, C. Zhu, C. Tschierske, *J. Mater. Chem. C* **2020**, *8*, 12902.
- [53] H. Li, S. S. Babu, S. T. Turner, D. Neher, M. J. Hollamby, T. Seki, S. Yagai, Y. Deguchi, H. Möhwal, T. Nakanishi, *J. Mater. Chem. C* **2013**, *1*, 1943.
- [54] The expression “swallow-tailed” was originally coined for rod-like molecules having a branched terminal chain with two branches of (almost) equal length in the terminal chains, examples are the benzylidene malonates reported in ref. [55], with a molecular shape and orientation of the alkyl chains being in some respect similar to that provided by the 3,5-disubstitution pattern at the terminal benzene ring. However, the swallow-tailed 3,5-disubstituted polycatenars have the chains directly attached to the rod-like core.
- [55] W. Weissflog, A. Wiegelegen, S. Diele, D. Demus, *Cryst. Res. Technol.* **1984**, *19*, 583.
- [56] In all cases, with one exception (compound **B6/6a**) all alkyl chain are attached via an ether oxygen to the core unit, that is, the substituents represent alkoxy groups, though for simplicity “alkyl chain” or “chains” is used throughout this manuscript.
- [57] a) G. Heppke, D. Löttsch, D. Demus, S. Diele, K. Jahn, H. Zschke, *Mol. Cryst. Liq. Cryst.* **1991**, *208*, 9; b) G. Heppke, D. Löttsch, N. K. Sharma, D. Demus, S. Diele, K. Jahn, M. Neundorf, *Mol. Cryst. Liq. Cryst.* **1994**, *241*, 275.
- [58] The structure of this SmM\*/SmM phase is not clear, especially as no aligned samples have yet been obtained for this phase.<sup>[57]</sup>
- [59] J. M. Seddon, in *Handbook of Liquid Crystals* (Eds: D. Demus, J. Goodby, G. W. Gray, H.-W. Spies, V. Vill), Wiley VCH, Weinheim, Germany **1998**, pp. 636–679.
- [60] G. W. Gray, J. W. G. Goodby, *Smectic Liquid Crystals – Textures and Structures*, L. Hill, Philadelphia, PA **1984**.
- [61] a) P. A. C. Gane, A. J. Leadbetter, P. G. Wrighton, *Mol. Cryst. Liq. Cryst.* **1981**, *66*, 247; b) J. J. Benattar, F. Moussa, M. Lambert, *J. Phys. Lett.* **1981**, *42*, 67.
- [62] S. Diele, D. Lose, H. Kruth, G. Pelzl, F. Guittard, A. Cambon, *Liq. Cryst.* **1996**, *21*, 603.
- [63] a) B. I. Ostrovskii, S. N. Sulyanov, N. I. Boiko, V. P. Shibaev, *Liq. Cryst.* **1998**, *25*, 153; b) N. Koshimizu, Y. Aizawa, K. Sakajiri, K. Shikinaka, K. Shigehara, S. Kang, M. Tokita, *Macromolecules* **2015**, *48*, 3653.
- [64] a) X.-H. Liu, B. Henrich, I. Manners, D. Guillon, D. W. Bruce, *J. Mater. Chem.* **2000**, *10*, 637; b) S. Gierlotka, J. Przedmojski, B. Pura, *Liq. Cryst.* **1988**, *3*, 1535.
- [65] Compound **B6/4** with the shortest 4'-alkoxy chain shows an additional small range of a nematic (N) phase at highest temperature (Figure S12a,b, Supporting Information). The N phase is also found for **B6/5** over a very short temperature range of <1 K on cooling and is removed for **B6/6**, which has exclusively the SmC<sub>a</sub> phase, in this case occurring below an Iso<sub>1</sub><sup>[61]</sup> phase (see Section 3.8).
- [66] a) J. Lagerwall, F. Giesselmann, *ChemPhysChem* **2006**, *7*, 20; b) H. Takezoe, E. Gorecka, M. Čepič, *Rev. Mod. Phys.* **2010**, *82*, 897; c) A. Fukuda, Y. Takanishi, T. Isozaki, K. Ishikawa, H. Takezoe, *J. Mater. Chem.* **1994**, *4*, 997.
- [67] a) S. Lagerwall, A. Dahlgren, P. Jägemalm, P. Rudquist, K. D'havØ, H. Pauwels, R. Dabrowski, W. Drzewinski, *Adv. Funct. Mater.* **2001**, *11*, 87; b) P. Perkowski, Z. Rasezewski, W. Piecek, J. Kedzierski, J. Rutkowska, J. Zielinski, X. W. Sun, *Opto-Electron. Rev.* **2011**, *19*, 34.
- [68] Y. Takanishi, H. Takezoe, A. Fukuda, H. Komura, J. Watanabe, *J. Mater. Chem.* **1992**, *2*, 71.
- [69] a) I. Nishiyama, J. W. Goodby, *J. Mater. Chem.* **1992**, *2*, 1015; b) Y. Ouchi, Y. Yoshioka, H. Ishii, K. Seki, M. Kitamura, R. Noyori, Y. Takanishi, I. Nishiyama, *J. Mater. Chem.* **1995**, *5*, 2297; c) J. Thisayukta, E. T. Samulski, *J. Mater. Chem.* **2004**, *14*, 1554; d) S.-L. Wu, F.-D. Chen, *Liq. Cryst.* **2004**, *31*, 607; e) W. Drzewiński, R. Dabrowski, K. Czupryński, J. Przedmojski, M. Neubert, *Ferroelectrics* **1998**, *212*, 281; f) K.-T. Kang, S. K. Lee, C. W. Park, S. H. Cho, J. G. Lee, S.-K. Choi, Y. B. Kim, *Bull. Korean Chem. Soc.* **2006**, *27*, 1364.
- [70] a) P. Mach, R. Pindak, A.-M. Levelut, P. Barois, H. T. Nguyen, C. C. Huang, L. Furenid, *Phys. Rev. Lett.* **1998**, *81*, 1015; b) H. F. Gleeson, L. S. Hirst, *ChemPhysChem* **2006**, *7*, 321.
- [71] a) T. Hegmann, J. Kain, S. Diele, G. Pelzl, C. Tschierske, *Angew. Chem., Int. Ed.* **2001**, *40*, 887; b) R. Pratibha, N. V. Madhusudana, B. K. Sadashiva, *Science* **2000**, *288*, 2184; c) V. Yelamaggad, I. S. Shashikala, V. P. Tamilenthir, D. S. S. Rao, G. G. Nair, S. K. Prasad, *J. Mater. Chem.* **2008**, *18*, 2096; d) B. K. Sadashiva, R. A. Reddy, R. Pratibha, N. V. Madhusudana, *Chem. Commun.*

- 2001, 20, 2140; e) K. Kishikawa, T. Inoue, Y. Sasaki, S. Aikyo, M. Takahashi, S. Kohmoto, *Soft Matter* **2011**, 7, 7532.
- [72] R. Pratihba, N. V. Madhusudana, B. K. Sadashiva, *Eur. Phys. Lett.* **2007**, 80, 46001.
- [73] H. R. Brand, P. E. Cladis, H. Pleinert, *Macromolecules* **1992**, 225, 7223.
- [74] M. A. Glaser, N. A. Clark, *Phys. Rev. E* **2002**, 66, 021711.
- [75] J. P. Wagner, P. R. Schreiner, *Angew. Chem., Int. Ed.* **2015**, 54, 12274.
- [76] Associated with the phase transition is the occurrence of weak 2nd and 3rd order layer reflections with the 3rd order being more intense than the 2nd order, representing a typical feature of the increasing sharpness of the layers in the hexatic LC phases (Figures S23 and S25, Supporting Information).
- [77] M. Neundorf, Ph.D. Thesis, Martin Luther University Halle-Wittenberg **1993**, pp. 56–59.
- [78] G. Albertini, S. Melone, G. Poeti, F. Rustichelli, G. Torquati, *Mol. Cryst. Liq. Cryst.* **1984**, 104, 121.
- [79] a) M. Deutsch, *Phys. Rev. A* **1991**, 44, 8264; b) P. Davidson, D. Petermann, A. Levelut, *A. J. Phys. II* **1995**, 5, 113.
- [80] C. Even, M. Imperor-Clerc, P. Pieranski, *Eur. Phys. J. E* **2006**, 20, 89.
- [81] Besides the major optical and X-ray scattering investigation methods used here, cubic phases have in some cases also been characterized by means of soft resonance X-ray scattering<sup>[83]</sup> and imaging methods, like AFM and TEM, especially for the larger structures of polymers, dendrimers and in cubosomes,<sup>[14,15,18–21]</sup> and the dynamics was occasionally studied by NMR experiments;<sup>[94]</sup> investigation of the faceting of cubic single crystals, slowly grown from solutions or melts, allows confirmation of the crystallographic space group.<sup>[80]</sup>
- [82] A. H. Schoen, *Interface Focus* **2012**, 2, 658.
- [83] a) Y. Cao, M. Alaasar, A. Nallapaneni, M. Salamonczyk, P. Marinko, E. Gorecka, C. Tschierske, F. Liu, N. Vaupotic, C. Zhu, *Phys. Rev. Lett.* **2020**, 125, 027801; b) Y. Cao, C. Feng, A. Jakli, C. Zhu, F. Liu, *Giant* **2020**, 2, 100018.
- [84] M. Vogrin, N. Vaupotic, M. Wojcik, J. Mieczkowski, K. Madrak, D. Pocięcha, E. Gorecka, *Phys. Chem. Chem. Phys.* **2014**, 16, 16067.
- [85] a) D. Demus, D. Marzotko, N. K. Sharma, A. Wiegeleben, *Kryst. Tech.* **1980**, 15, 331; b) A.-M. Levelut, B. Donnio, D. W. Bruce, *Liq. Cryst.* **1997**, 22, 753.
- [86] A.-M. Levelut, E. Hallouin, D. Bennemann, G. Heppke, D. Löttsch, *J. Phys. II* **1997**, 7, 981.
- [87] B. Pansu, Y. Nastishin, M. Imperor-Clerc, M. Veber, H. T. Nguyen, *Eur. Phys. J. E* **2004**, 15, 225.
- [88] a) J.-H. Ryu, M. Lee, in *Structure and Bonding*, Vol. 128 (Ed: T. Kato), Springer-Verlag, Berlin Heidelberg **2008**, pp. 63–98; b) L.-Y. Shi, Y. Zhou, X.-H. Fan, Z. Shen, *Macromolecules* **2013**, 46, 5308.
- [89] J. Kain, S. Diele, G. Pelzl, C. Lischka, W. Weissflog, *Liq. Cryst.* **2000**, 27, 11.
- [90] a) L. Rayleigh, *Proc. London Math. Soc.* **1879**, 10, 4; b) A. Eremin, U. Kornek, S. Stern, R. Stannarius, F. Araoka, H. Takezoe, H. Nadasi, W. Weissog, A. Jakli, *Phys. Rev. Lett.* **2012**, 109, 017801.
- [91] M. A. Durán-Olivencia, R. S. Gvalani, S. Kalliadasis, G. A. Pavliotis, *J. Stat. Phys.* **2019**, 174, 579.
- [92] M. K. Srinatha, S. Poppe, G. Shanker, M. Alaasar, C. Tschierske, *J. Mol. Liq.* **2020**, 317, 114244.
- [93] N. Sebastian, M.-G. Tamba, R. Stannarius, M. R. de la Fuente, M. Salamonczyk, G. Cukrov, J. Gleeson, S. Sprunt, A. Jáklí, C. Welch, Z. Ahmed, G. H. Mehl, A. Eremin, *Phys. Chem. Chem. Phys.* **2016**, 18, 19299.
- [94] a) A. Gradišek, M. Cifelli, M. Wojcik, T. Apih, S. V. Dvinskikh, E. Gorecka, V. Domenici, *Crystals* **2019**, 9, 178; b) O. Söderman, U. Henriksson, *Langmuir* **2020**, 36, 5927.
- [95] H. R. Brand, H. Pleiner, *Eur. Phys. J. E* **2017**, 40, 34.
- [96] G. M. Barretto, P. J. Collings, D. Bennemann, D. Löttsch, G. Heppke, *Liq. Cryst.* **2001**, 28, 629.
- [97] a) J. W. Goodby, D. A. Dunmur, P. J. Collings, *Liq. Cryst.* **1995**, 19, 703; b) M. Manai, A. Gharbi, J. P. Marcerou, H. T. Nguyen, J. C. Rouillon, *Physica B* **2005**, 368, 168.
- [98] O. Henrich, K. Stratford, M. E. Cates, D. Marenduzzo, *Phys. Rev. Lett.* **2011**, 106, 107801.
- [99] M. Cifelli, V. Domenici, *Phys. Chem. Chem. Phys.* **2007**, 9, 1202.
- [100] a) R. Kurita, H. Tanaka, *J. Phys. Cond. Mat.* **2005**, 17, L293; b) H. Tanaka, *Eur. Phys. J. E* **2012**, 35, 113; c) F. Sciortino, S. Mossa, E. Zaccarelli, P. Tartaglia, *Phys. Rev. Lett.* **2004**, 93, 055701; d) Y. Zhuang, K. Zhang, P. Charbonneau, *Phys. Rev. Lett.* **2016**, 116, 098301; e) M. A. Anisimov, M. Duska, F. Caupin, L. E. Amrhein, A. Rosenbaum, R. J. Sadus, *Phys. Rev. X* **2018**, 8, 011004.
- [101] A. A. Hyman, C. A. Weber, F. Jülicher, *Annu. Rev. Cell. Dev. Biol.* **2014**, 30, 39.
- [102] It is also interesting to note that upon increasing  $n$  in the series  $B6/n$ , the  $Iso_{[5]}$  phase replaces the nematic phase (Table 2). Hence, it appears that there is a competition between the development of long range orientational order and helical self-assembly as the parallel packing of the molecules becomes distorted and the preferred average molecular conformation changes from rod-like to helical by chain elongation.
- [103] Compared to the related azobenzene based compounds with 3,5-disubstitution pattern at one end,<sup>[52]</sup> the smectic phases of compounds  $Bm/n$  and  $B'6/n$  have larger tilt angles. Due to the larger tilt, the tilt correlation is stronger and no indications of uniaxial smectic phases with or without helical superstructure can be found. Though HexB phases were observed in both series, the  $SmI_s$  phases of the azobenzenes are replaced by  $SmI_s^{dis}$  phases with reduced core order. Because only short hexyl chains were used for the azobenzenes, no  $SmC_s$  and I23 phases and transitions associated with these phases could be observed.



# ADVANCED OPTICAL MATERIALS

## Supporting Information

for *Adv. Optical Mater.*, DOI: 10.1002/adom.202001572

**Swallow-Tailed Polycatenars: Controlling Complex Liquid  
Crystal Self-Assembly and Mirror Symmetry Breaking at the  
Lamellae-Network Cross-Over**

*Tino Reppe, Christian Dressel, Silvio Poppe, Alexey Eremin,  
and Carsten Tschierske\**

## Supporting Information

### **Swallow-tailed mesogen: Controlling complex liquid crystal self-assembly and mirror symmetry breaking at the lamellae-network cross-over**

*Tino Reppe<sup>1</sup>, Christian Dressel<sup>1</sup>, Silvio Poppe<sup>1</sup>, Alexey Eremin<sup>2</sup>, Carsten Tschierske<sup>1</sup>*

<sup>1</sup> Institute of Chemistry, Martin Luther University Halle-Wittenberg, Kurt Mothes Str. 2, D-06120 Halle (Saale), Germany; carsten.tschierske@chemie.uni-halle.de

<sup>2</sup> Department of Nonlinear Phenomena, Institute of Physics, Otto von Guericke University Magdeburg, Magdeburg, Germany

## 1. Additional Data

### 1.1 DSC traces and textures

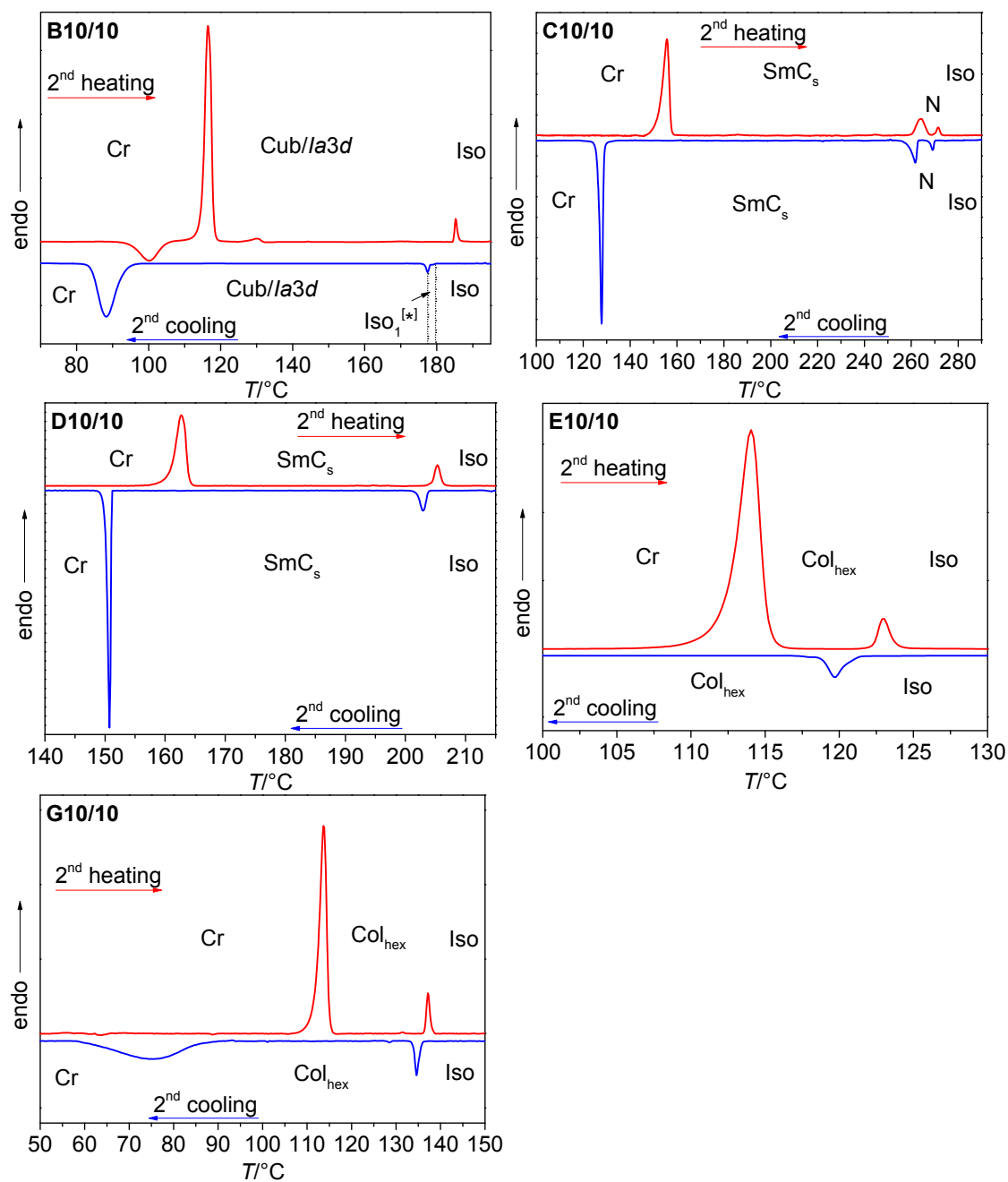


**Figure S1.** DSC heating and cooling traces of compounds A10/10–G10/10 recorded at 10 K min<sup>-1</sup>.



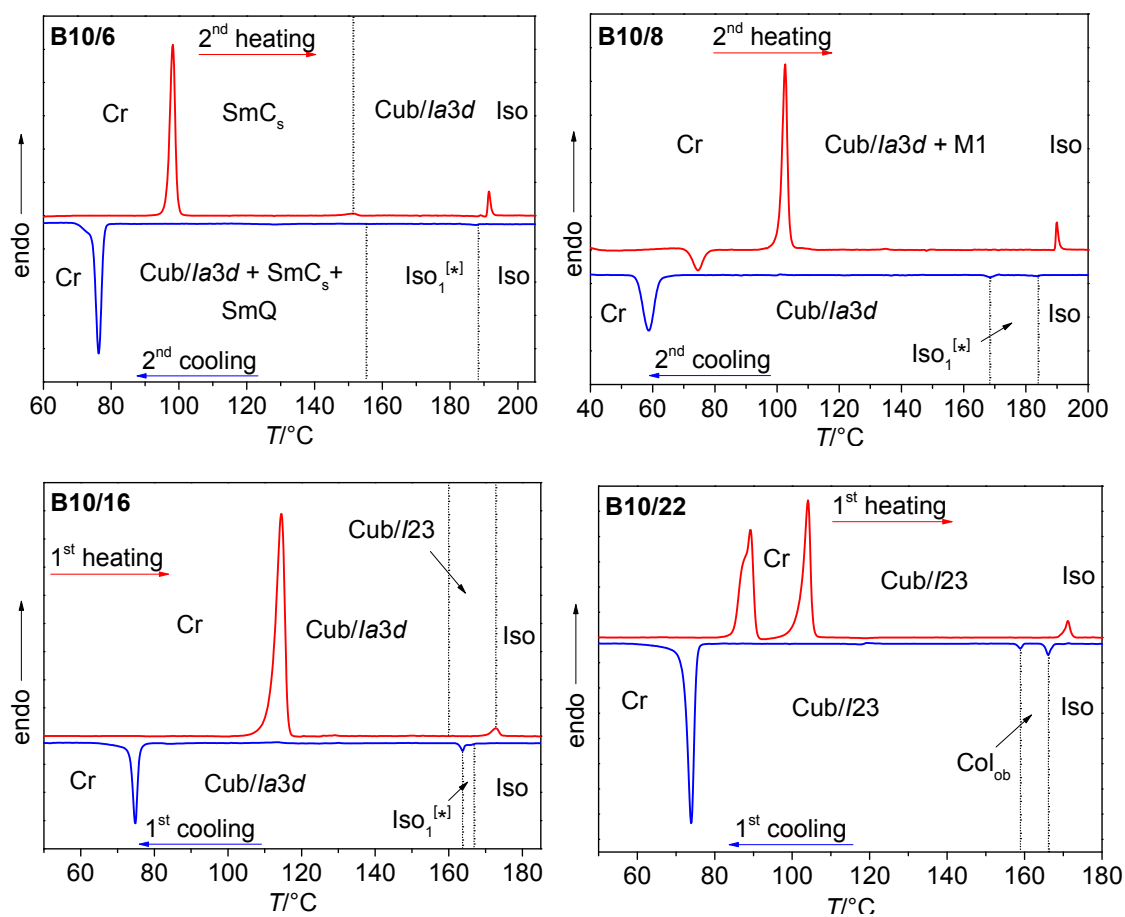
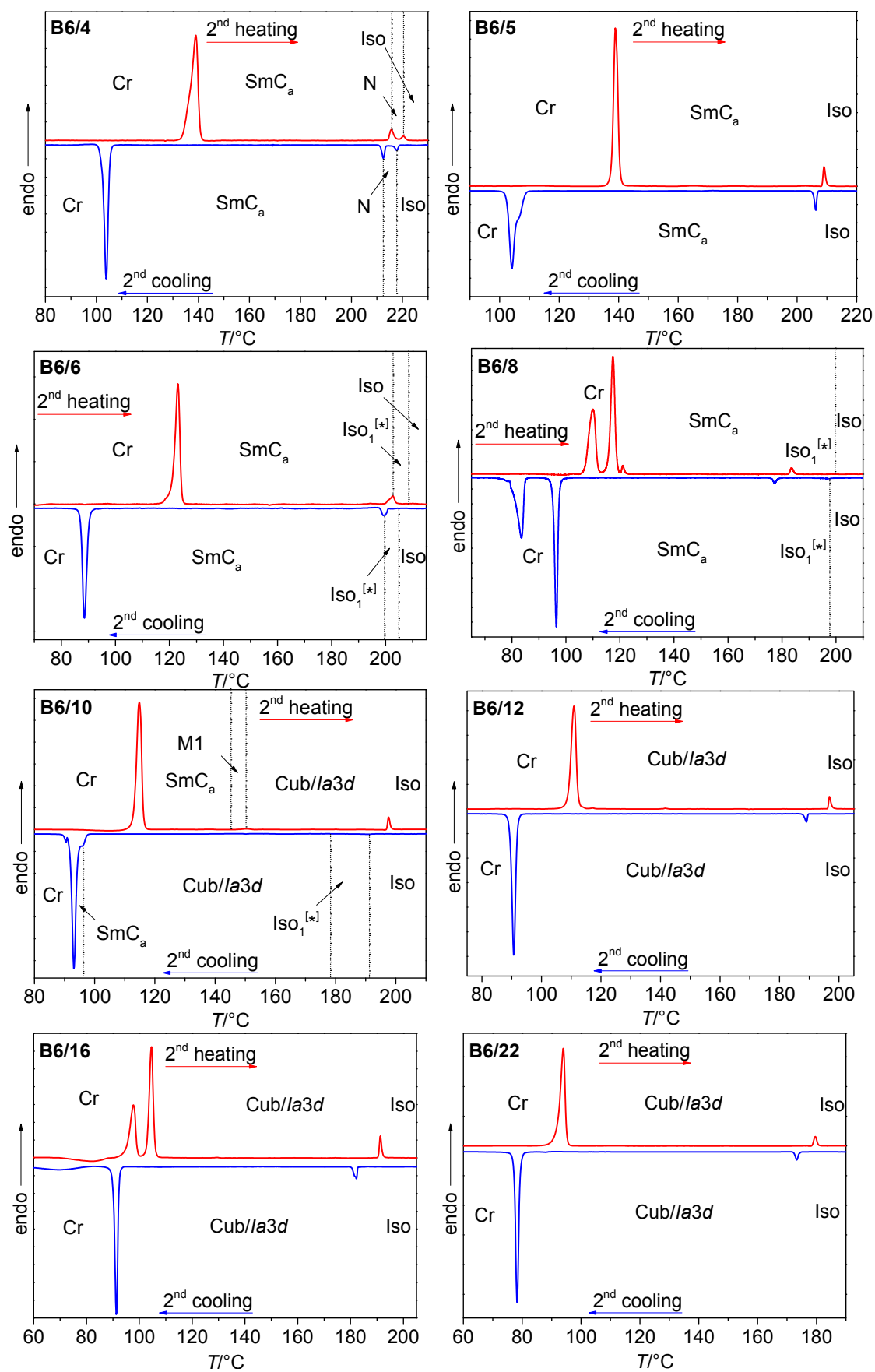
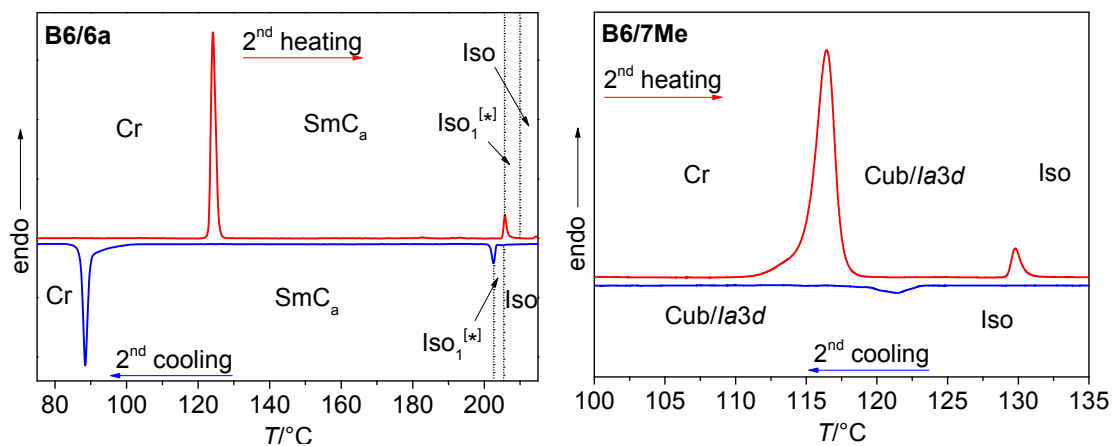


Figure S2. DSC heating and cooling traces of compounds B10/*n* recorded at 10 K min<sup>-1</sup>.



**Figure S3.** DSC heating and cooling traces of compounds **B6/n** recorded at 10 K min<sup>-1</sup>.



**Figure S3** (continued). DSC heating and cooling traces of compounds **B6/*n*** recorded at  $10\text{ K min}^{-1}$ .

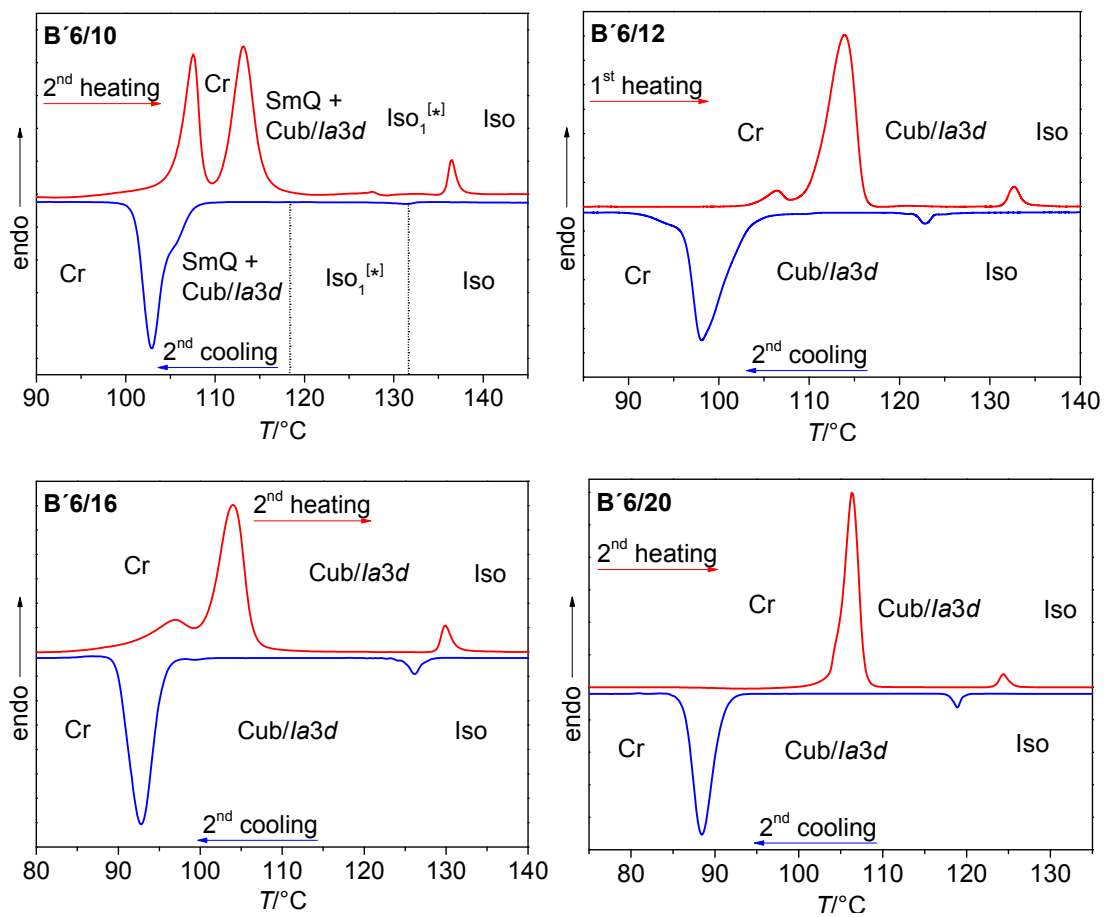


**Figure S4.** DSC heating and cooling traces of compounds **B'6/*n*** recorded at  $10\text{ K min}^{-1}$ .

## 1.2 Additional textures

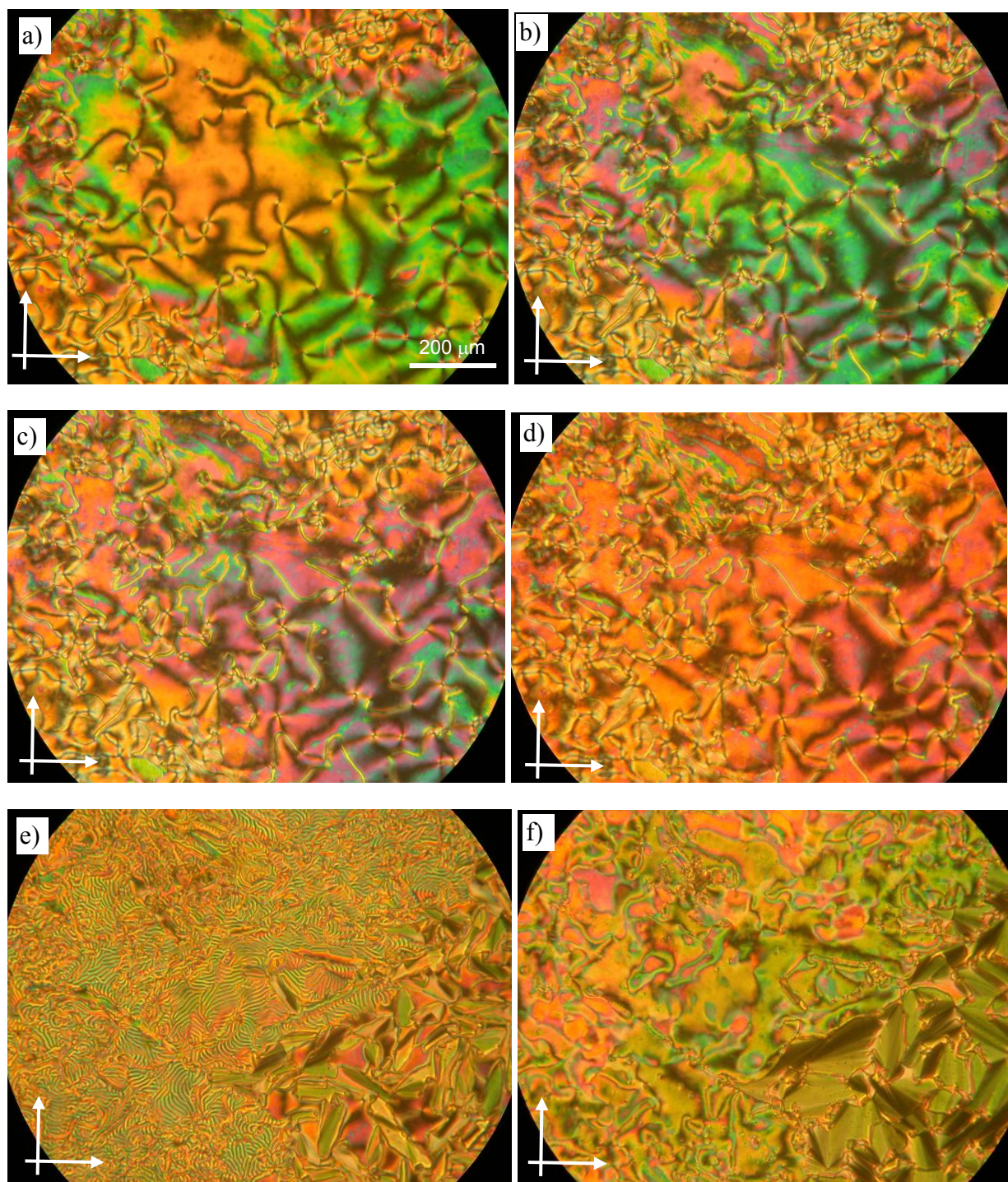


**Figure S5.** Textures of C10/10 as observed on cooling; a-d) nematic phase at 269, 268, 266 and 264 °C, respectively; e) N-SmC<sub>s</sub>-transition at 263 °C and f) SmC<sub>s</sub> phase at 260 °C.



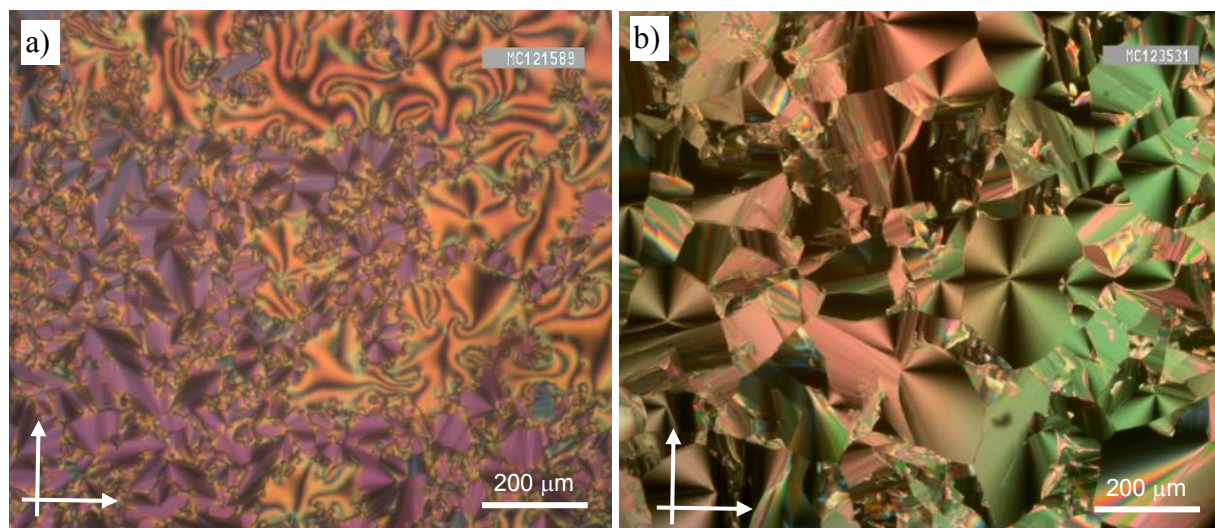


**Figure S6.** Textures of a) the  $\text{SmC}_s$  phase of **D10/10** at 190 °C and c) the  $\text{Col}_{\text{hex}}$  phase of **E10/10** at  $T = 115$  °C, as observed on cooling between crossed polarizers.

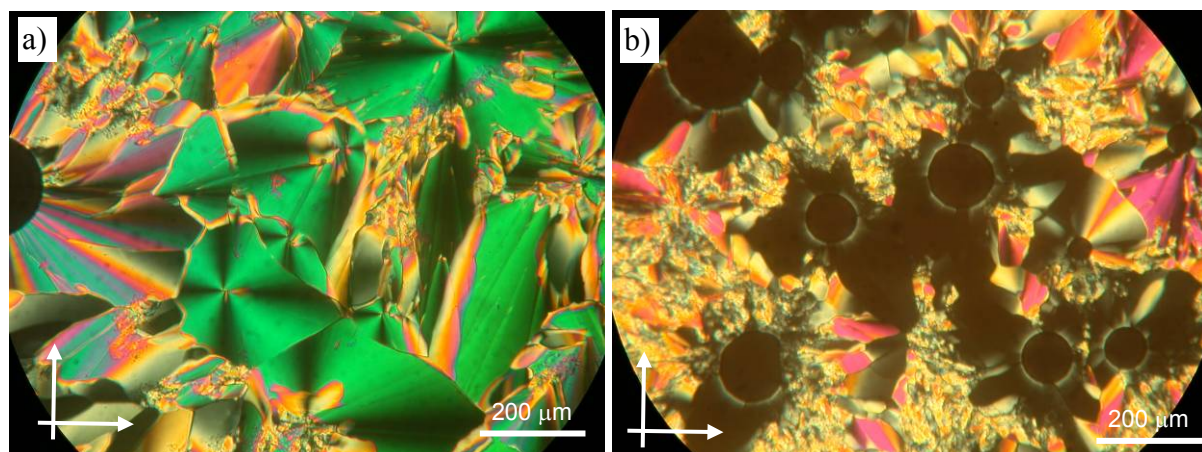


**Figure S7.** Textures of the  $\text{Col}_{\text{hex}}$  phase of **G10/10** at 130 °C in different areas of the sample, as observed on cooling between crossed polarizers.

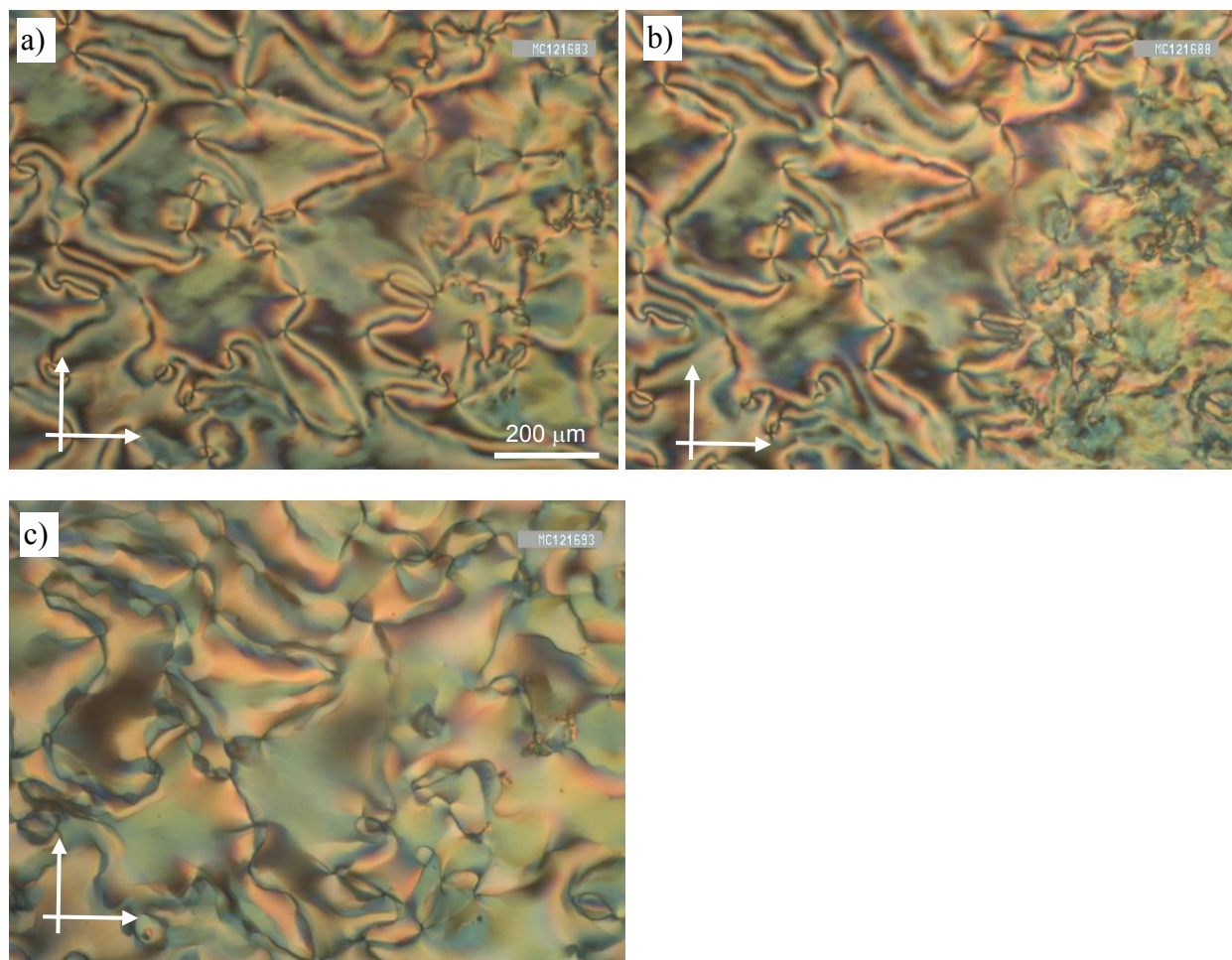


**Figure S8.** Textures of **B10/H** in a homeotropic cell. a)  $\text{SmC}_s$  phase at 116 °C, b)  $\text{SmC}_s$ - $\text{HexI}_s^{\text{dis}}$  transition at 111 °C and c)  $\text{HexI}_s^{\text{dis}}$  phase at 107 °C.

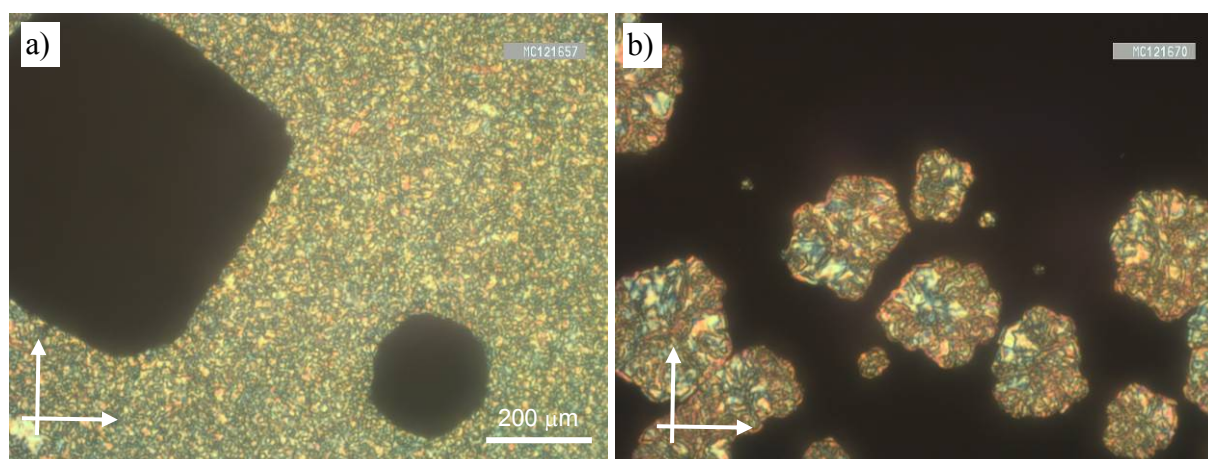


**Figure S9.** Textures of compound **B10/6** in an ITO cell (6  $\mu\text{m}$ ) a) transition  $\text{SmC}$ -to- $\text{Cub}_{b_i}/Ia\bar{3}d$  on cooling at 151 °C and b) transition  $\text{Cub}_{b_i}/Ia\bar{3}d$ -to- $\text{SmC}_s$  on heating at 140 °C.



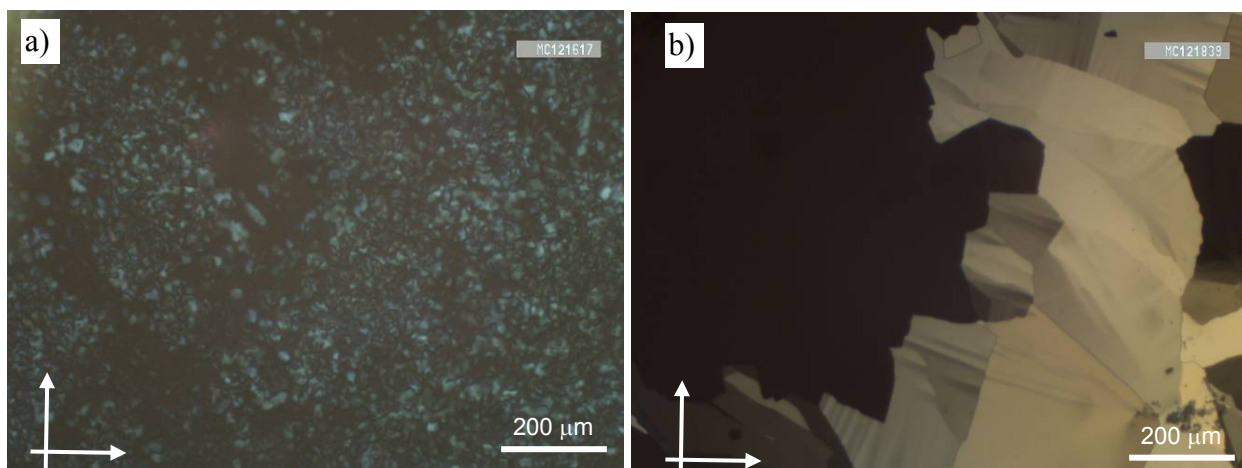


**Figure S10.** a) Texture of the low birefringent non-cubic M1 phase of compound **B10/8** as observed on heating at 130 °C. b) Growth of the  $\text{Cub}_{\text{bi}}/\text{Ia}\bar{3}d$  phase (left) into the SmQ phase (right) on cooling **B'6/10** at 117 °C.

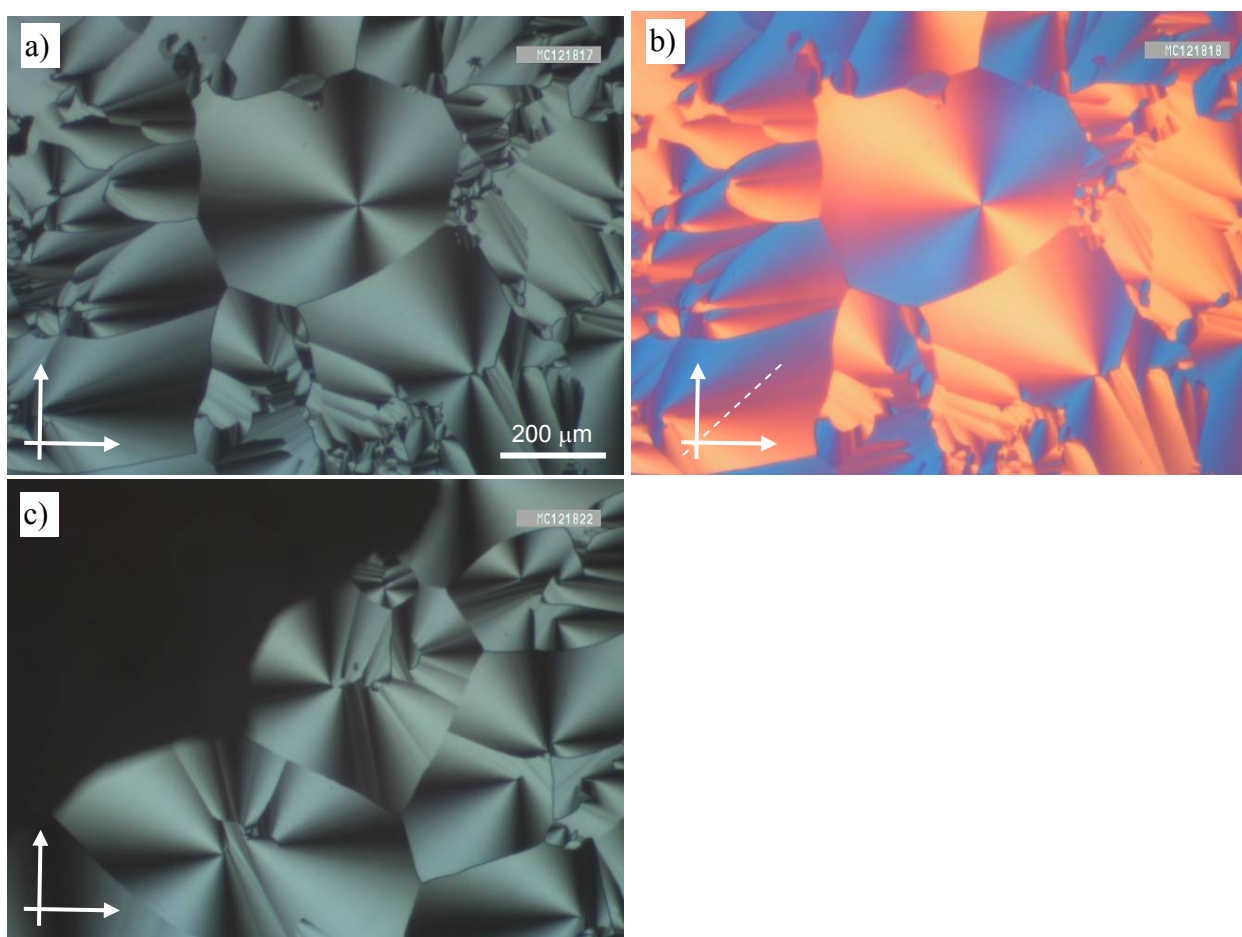


**Figure S11.** Textures of the  $\text{Col}_{\text{ob}}$  phase of **B10/22** as observed on cooling between crossed polarizers a)  $\text{Col}_{\text{ob}}$  phase at 162 °C, b) shows the same area with additional  $\lambda$ -plate indicating negative birefringence, confirming the alignment of the  $\pi$ -conjugated rods on average perpendicular or only slightly tilted to the column long axis; the indicatrix slow axis is indicated by the dashed line; c)  $\text{Col}_{\text{ob}}$ -to- $\text{Cub}_{\text{bi}}/\text{I}23$ -transition at 159 °C.



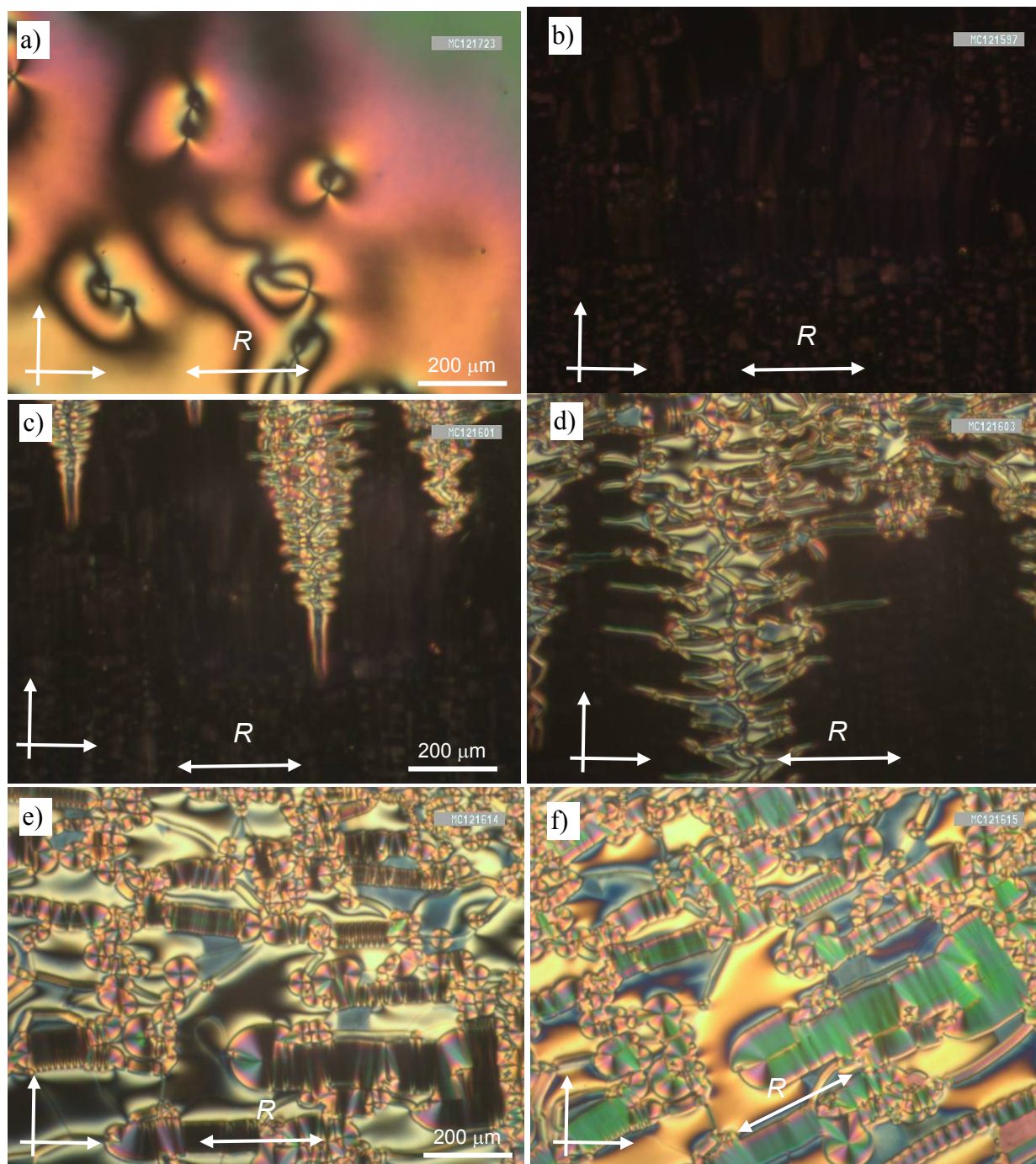


**Figure S12.** Textures of compound **B6/4** as observed between crossed polarizers in a 6 μm ITO cell on cooling from Iso to SmC<sub>a</sub> a) N phase at 217 °C immediately after the transition from Iso; b) N phase after transition to a completely uniformly aligned sample with the director parallel to the rubbing direction (*R*) at 215 °C, c, d) N-SmC<sub>a</sub> transition at 212 °C and e, f) SmC<sub>a</sub> phase at 210 °C; f) is rotated between the crossed polarizers.

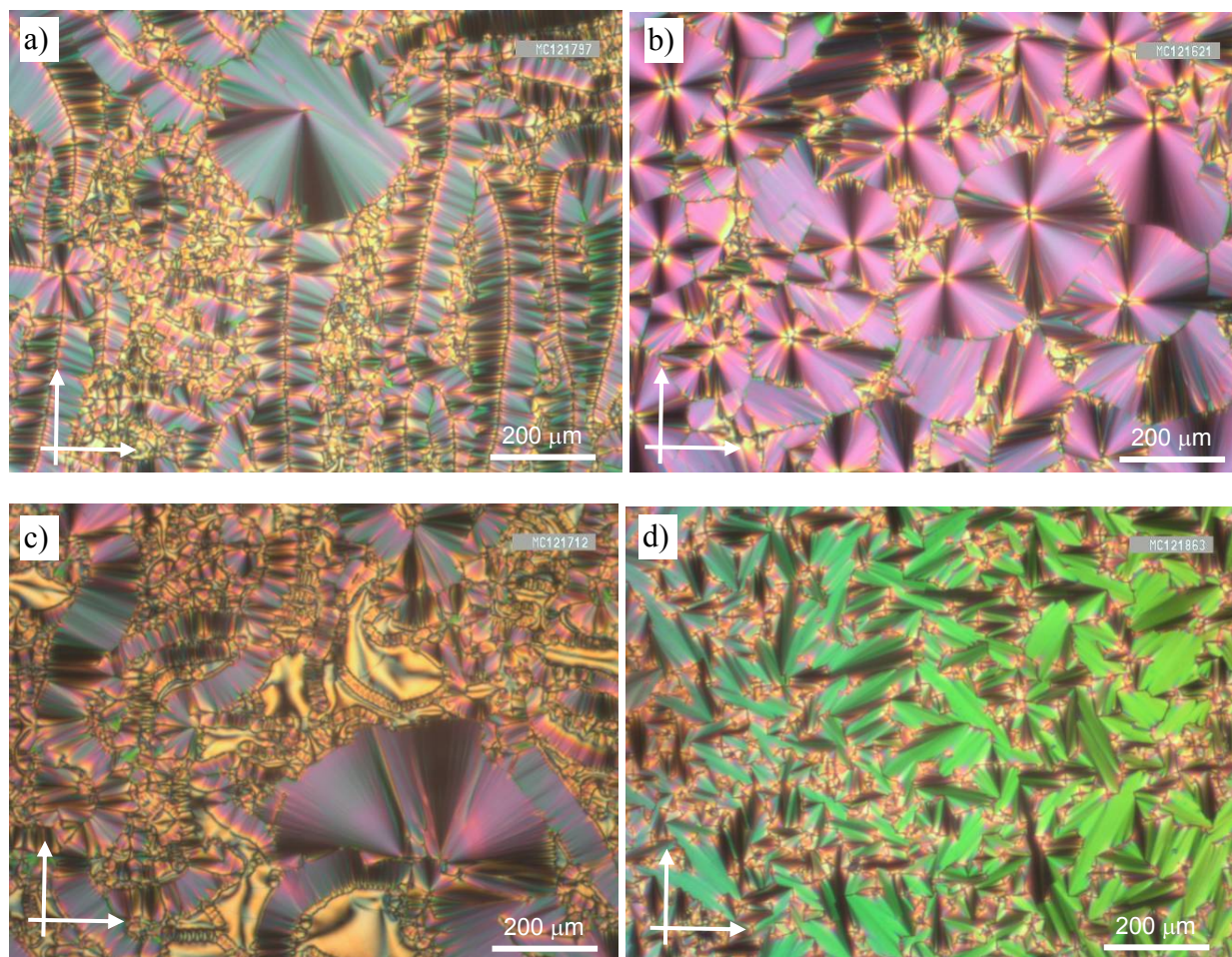


**Figure S13.** Planar textures of the  $\text{SmC}_a$  phase of a) **B6/5** at 200 °C; b) of **B6/6** at 190 °C; c) **B6/6a** at 200 °C and **B'6/8** at 128 °C, as observed on cooling between crossed polarizers.



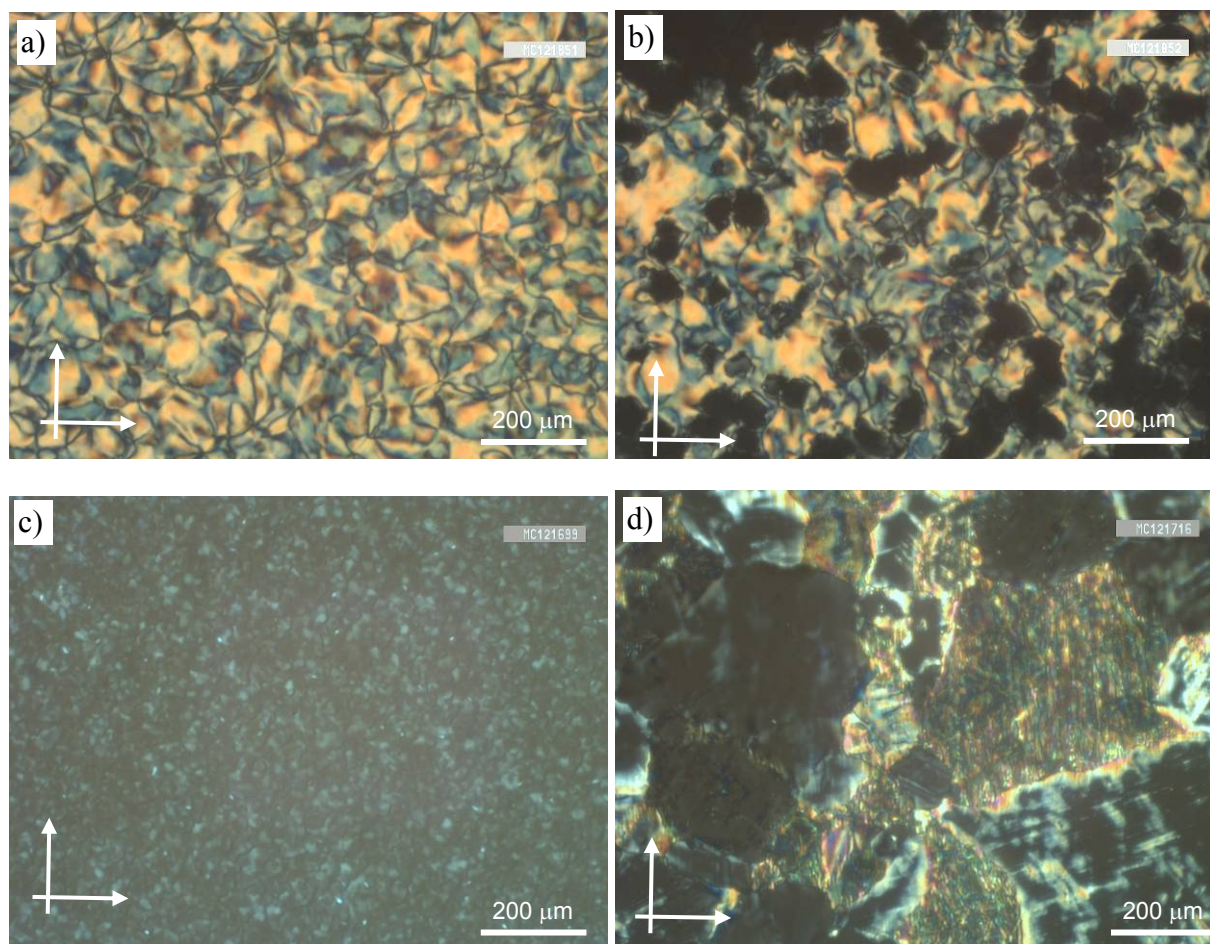


**Figure S14.** Textures of the mesophase of **B6/10** as observed on heating between crossed polarizers. a) highly birefringent Schlieren texture of the  $\text{SmC}_a$  phase at 132 °C; b)  $\text{SmC}_a$ -M1 transition at 145 °C; c) M1 phase at 148 °C (brightness enhanced); d)  $\text{Cub}_{bi}/Ia\bar{3}d$  to  $\text{SmC}_a$  transition on cooling at 105 °C.

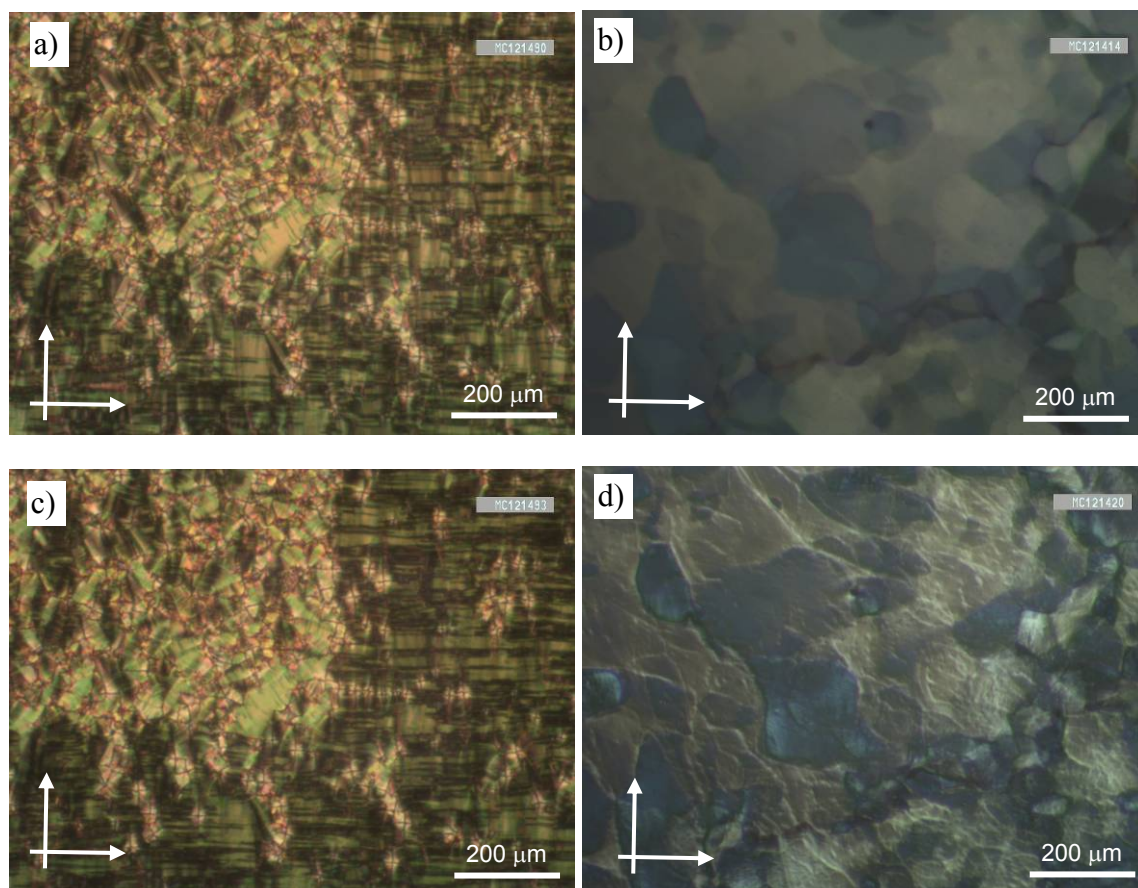


**Figure S15.** Textures of the mesophase of **B'6/6** as observed on cooling between crossed polarizers, a, b) in the  $\text{HexI}_s^{\text{dis}}$  phase at 123 °C and c, d) in the M phase at 96 °C; a, c) in a planar aligning ITO cell and b, d) in a homeotropic cell. For the textures at higher temperature, see Fig. 5.



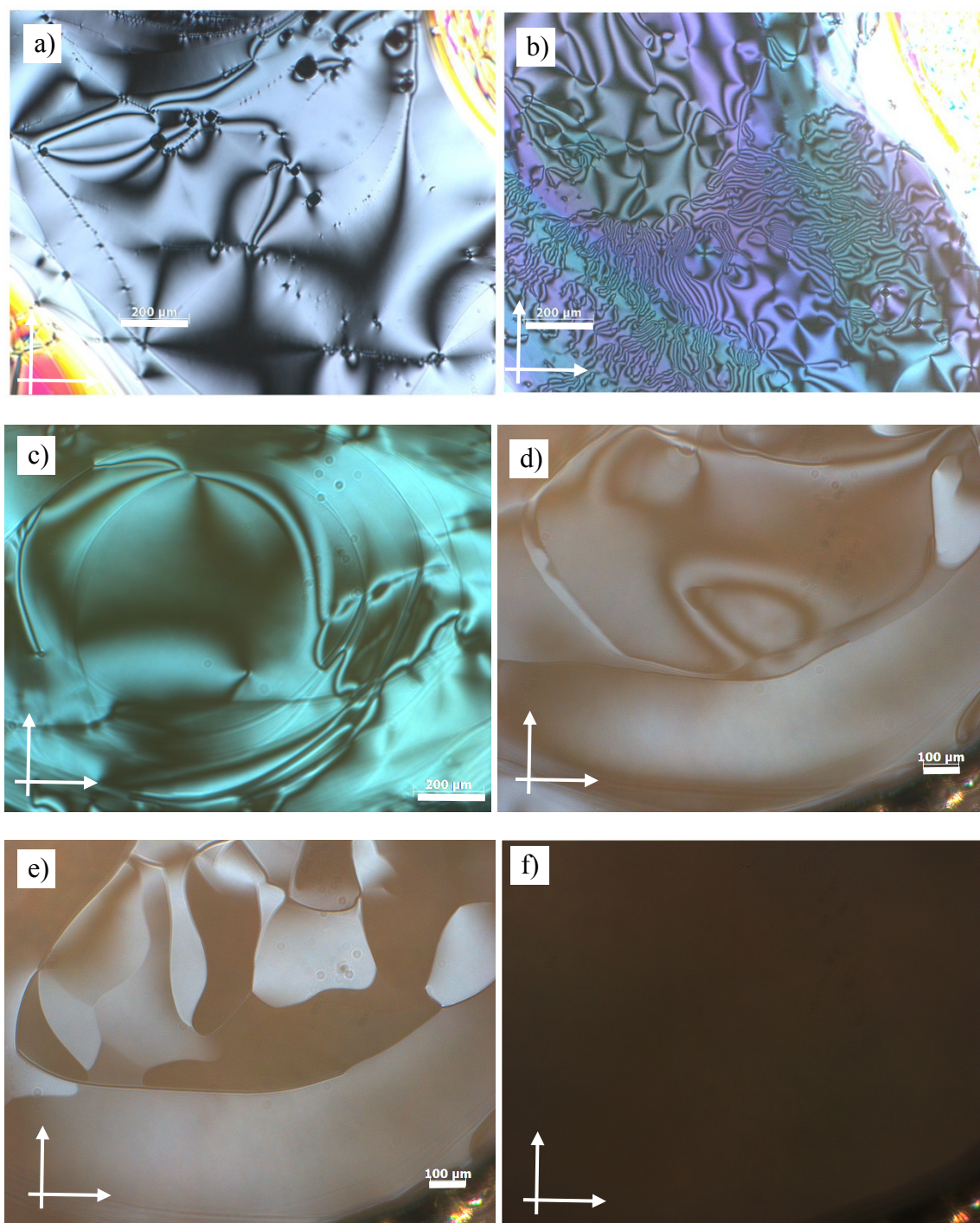


**Figure S16.** Investigation of freely suspended films. a,b)  $\text{SmC}_a$  phase of **B6/5**: a) transmission image at  $T = 180^\circ\text{C}$  (thickness approx. 80 nm) and b) in reflection at  $T = 160^\circ\text{C}$ ; (non-uniform thickness 100 – 500 nm); c-f)  $\text{SmC}_a$ -HexF<sub>s</sub>-HexB transition of compound **B'6/8**: c)  $\text{SmC}_a$  phase at  $129^\circ\text{C}$ . Inclination of the film with respect to the beam does not change the maximum of the optical transmission. This suggests that the structure of the phase is anticlinic. d,e) Images taken during the  $\text{SmC}_a$ -HexF transition, which occurs in a layer-by-layer fashion when cascades of domain walls propagating through the film ( $T = 127^\circ\text{C}$ ); the Schlieren texture transforms into a birefringent mosaic-like texture. f) Fully developed HexB film appearing completely dark between crossed polarisers. The image confirms the uniaxial character of the phase.

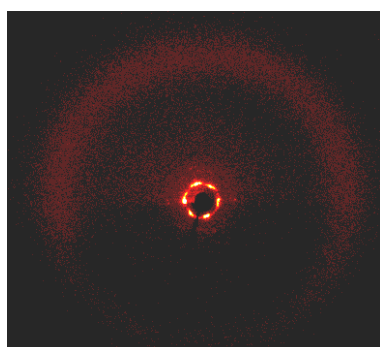
## 1.3 Additional XRD-data

Table S1. SAXS data of the  $\text{Cub}_{\text{bi}}/Ia\bar{3}d$  phases of the investigated compounds.

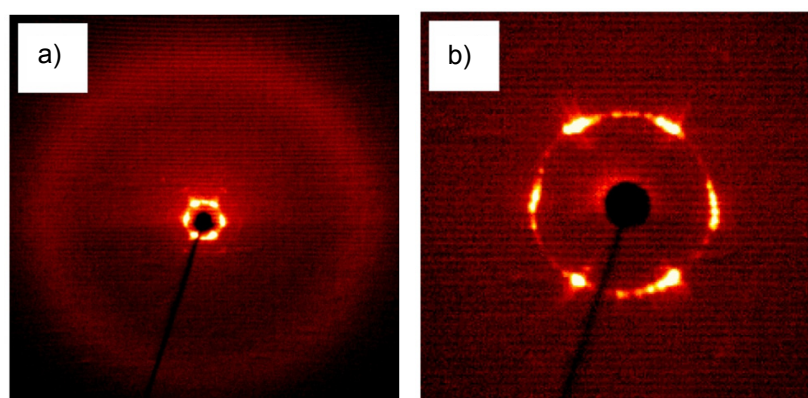
Compd.	(hkl)	$d_{\text{obs}} - \text{spacing/nm}$	$d_{\text{calc}} - \text{spacing/nm}$	$d_{\text{obs}} - d_{\text{calc}}$	$a_{\text{cub}}/\text{nm} (T/^{\circ}\text{C})$
<b>B10/6</b>	(211)	4.45	4.45	0.00	10.90
	(220)	3.89	3.85	0.04	(170)
<b>B10/8</b>	(211)	4.48	4.48	0.00	10.96
	(220)	3.88	3.88	0.00	(180)
<b>B10/10</b>	(211)	4.61	4.61	0.00	11.30
	(220)	4.02	3.99	0.03	(150)
<b>B10/16</b>	(211)	4.69	4.69	0.00	11.50
	(220)	4.12	4.07	0.05	(130)
<b>B6/10</b>	(211)	4.08	4.08	0.00	9.99
	(220)	3.58	3.53	0.05	(170)
<b>B6/12</b>	(211)	4.18	4.18	0.00	10.23
	(220)	3.63	3.62	0.01	(160)
<b>B6/16</b>	(211)	4.31	4.31	0.00	10.56
	(220)	3.75	3.73	0.02	(150)
<b>B6/22</b>	(211)	4.62	4.62	0.00	11.32
	(220)	4.02	4.00	0.02	(140)
<b>B'6/10</b>	(211)	3.75	3.75	0.00	9.19
	(220)	3.28	3.25	0.03	(115)
<b>B'6/12</b>	(211)	3.82	3.82	0.00	9.35
	(220)	3.31	3.30	0.01	(125)
<b>B'6/16</b>	(211)	3.90	3.90	0.00	9.56
	(220)	3.39	3.38	0.01	(120)
<b>B'6/20</b>	(211)	4.07	4.07	0.00	9.97
	(220)	3.54	3.53	0.01	(115)
<b>B6/7Me</b>	(211)	3.65	3.65	0.00	8.94
	(220)	3.17	3.16	0.01	(125)

**Table S2.** SAXS data of  $\text{Cub}_{\text{bi}}/I23^{[*]}$  phases of the investigated compounds.

Compd.	(hkl)	$d_{\text{obs}} - \text{spacing}/\text{nm}$	$d_{\text{calc}} - \text{spacing}/\text{nm}$	$d_{\text{obs}} - d_{\text{calc}}$	$a_{\text{cub}}/\text{nm} (T/^{\circ}\text{C})$
<b>B10/16</b>	(321)	4.74	4.74	0.00	17.73 (165)
	(400)	4.46	4.43	0.03	
	(420)	3.84	3.78	0.06	
<b>B10/22</b>	(321)	4.85	4.85	0.00	18.13 (140)
	(400)	4.47	4.53	0.06	
	(420)	4.04	4.05	0.01	



Compd.	hk	$d_{\text{obs}} - \text{spacing}/\text{nm}$	$d_{\text{calc}} - \text{spacing}/\text{nm}$	$d_{\text{obs}} - d_{\text{calc}}$	$a_{\text{hex}}/\text{nm} (T/^{\circ}\text{C})$
<b>E10/10</b>	10	3.719	3.719	0.00	4.28 (118)
	11	2.192	2.147	-0.05	
	20	1.846	1.860	0.01	

**Figure S17.** XRD pattern of a partly aligned sample of the  $\text{Col}_{\text{hex}}$  phase of compound **E10/10**. at  $T = 120^{\circ}\text{C}$  with numerical XRD data.

Compd.	hk	$d_{\text{obs}} - \text{spacing} / \text{nm}$	$d_{\text{calc}} - \text{spacing}/\text{nm}$	$d_{\text{obs}} - d_{\text{calc}}$	$a_{\text{hex}}/\text{nm} (T/^{\circ}\text{C})$
<b>G10/10</b>	10	3.916	3.914	0.00	4.52 (130)
	11	2.227	2.260	-0.03	
	20	1.976	1.957	0.02	

**Figure S18.** a) WAXS and b) SAXS of an aligned sample of the  $\text{Col}_{\text{hex}}$  phase of compound **G10/10**. at  $T = 130^{\circ}\text{C}$  with numerical XRD data ( $n_{\text{cell}} = a_{\text{hex}}^2 \cdot \sin 60^{\circ} \cdot h \cdot 602.2/M = 3.7$ , calculated with  $M = 1340 \text{ g} \cdot \text{mol}^{-1}$  and  $h = 0.47$  and assuming  $\rho = 1 \text{ g cm}^{-3}$ ).



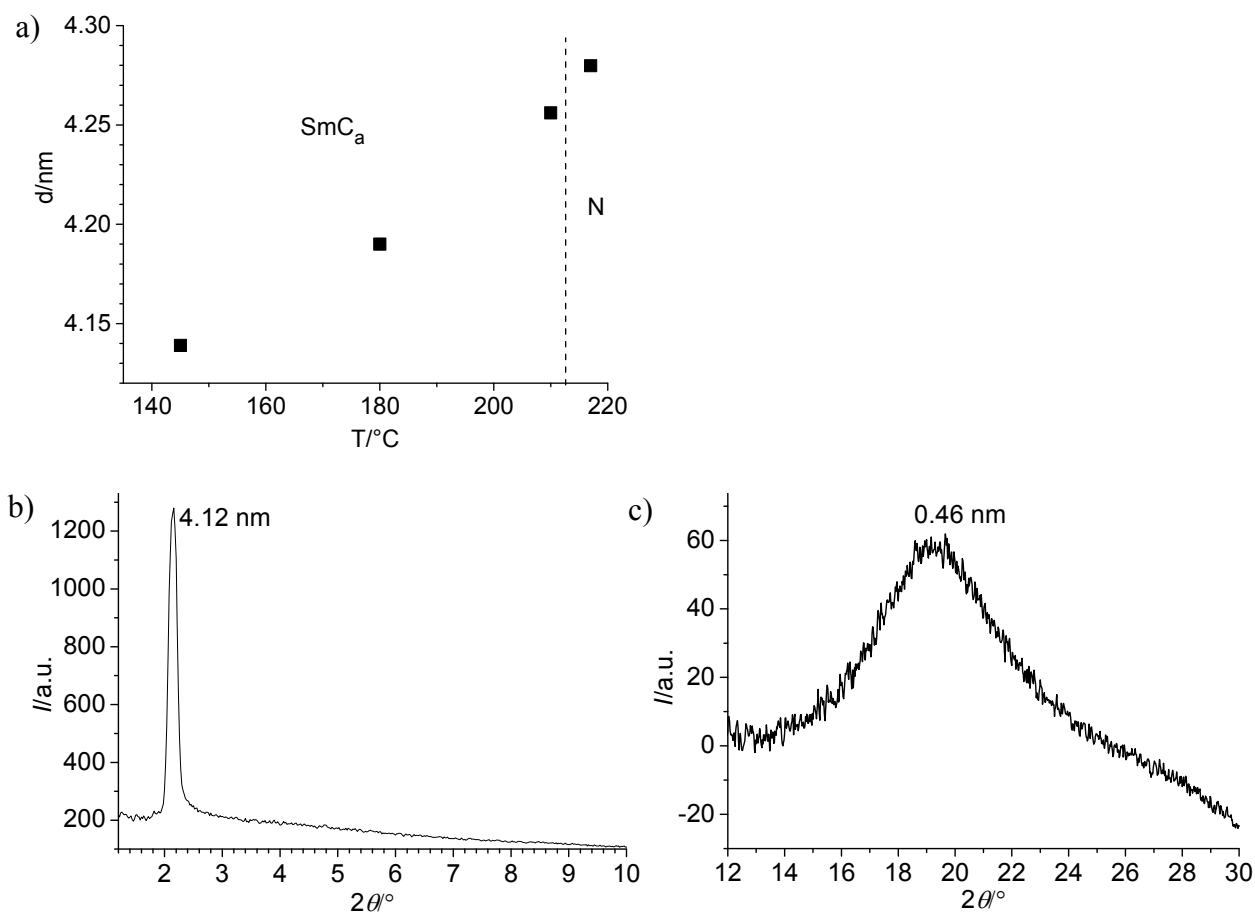


**Figure S19.** XRD patterns of the  $\text{SmC}_a$  phases of compounds **B6/n**. a) Development of the  $d$ -values in the  $\text{SmC}_a$  phase of **B6/4** on cooling; b) SAXS pattern and c) WAXS of the  $\text{SmC}_a$  phase of **B6/5** at 180 °C,

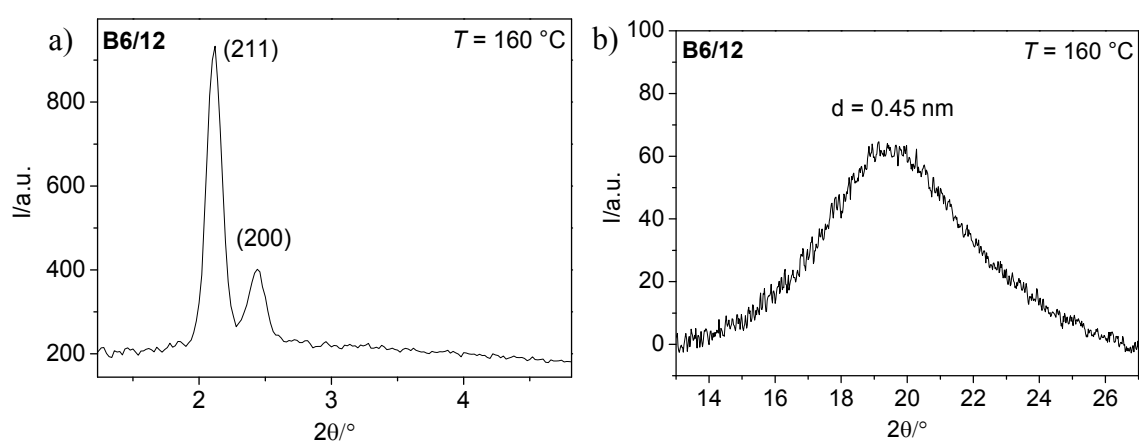
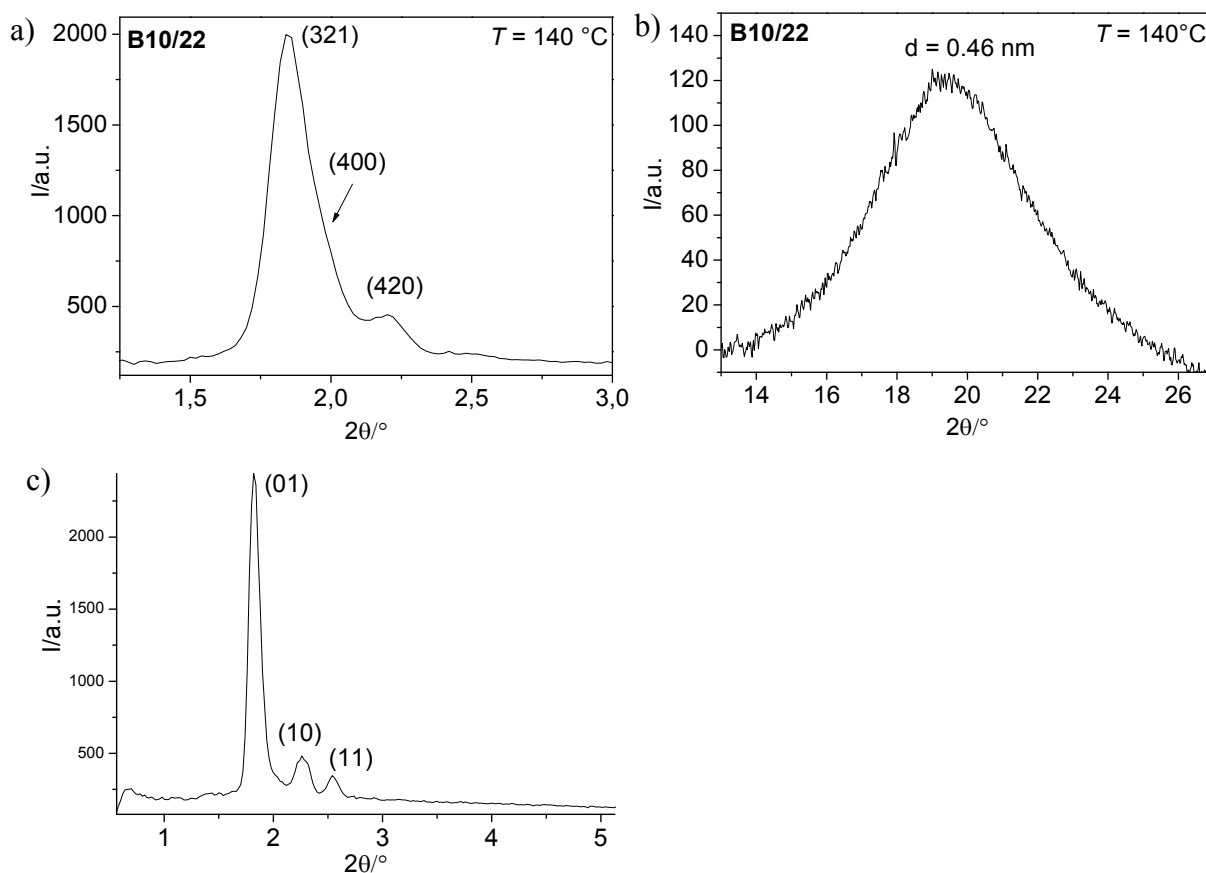


**Figure S20.** a) SAXS and b) WAX patterns of the  $\text{Cub}_{\text{bi}}/\text{Ia}\bar{3}d$  phase of **B6/12**.



Compd.	hkl	$d_{\text{obs}}$ – spacing/nm	$d_{\text{calc}}$ – spacing/nm	$d_{\text{obs}} - d_{\text{calc}}$	$a, b/\text{nm}, \gamma/^\circ$ ( $T/^\circ\text{C}$ )
<b>B10/22</b>	(01)	4.833	4.833	0.00	4.02, 4.98, 76.06 (162)
	(10)	3.905	3.905	0.00	
	(11)	3.474	3.474	0.00	
<b>B10/22</b>	(01)	4.833	4.833	0.00	5.68, 7.03, 43.41 (162)
	(10)	3.905	3.905	0.00	
	(12)	3.474	3.474	0.00	

**Figure S21.** a) SAXS and b) WAX patterns of the  $\text{Cub}_{\text{bi}}^{[*]}/I23$  phase of **B10/22** at 140°C and c) diffraction pattern of the  $\text{Col}_{\text{ob}}$  phase with two possible indexations, that one with  $\text{Col}_{\text{ob}}/p2$ :  $a = 4.02$  nm,  $b = 4.98$  nm,  $\gamma = 76.1^\circ$  being more likely, because it better fits with the molecular dimensions.

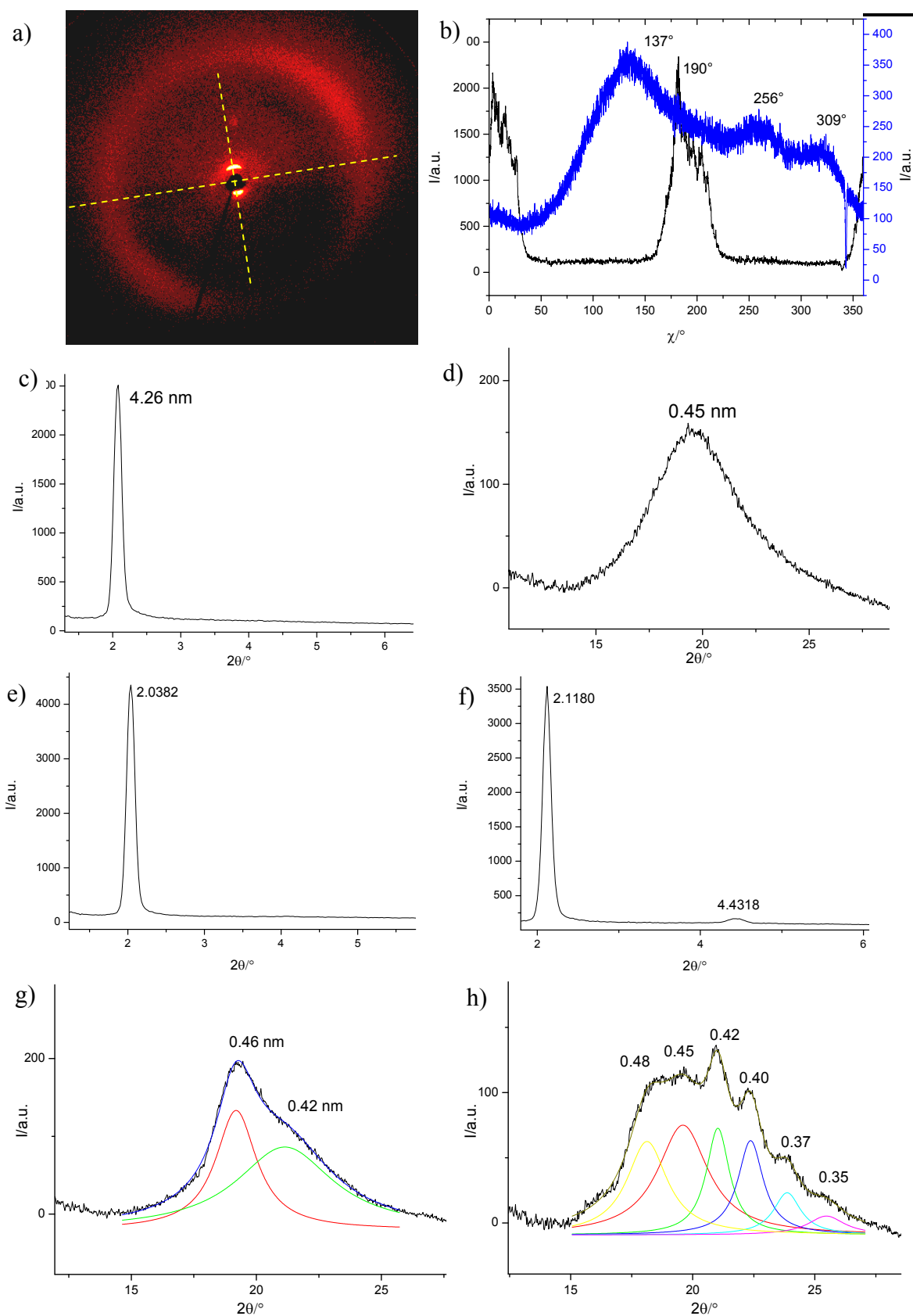


**Figure S22.** XRD patterns of B10/H a) 2D pattern of a surface aligned sample in the  $\text{SmC}_s$  phase with b) the corresponding  $\chi$ -scan, indicating a tilt of  $\sim 37^\circ$  in the  $\text{SmC}_s$  phase at  $140^\circ\text{C}$ ; c, d) show c) the SAXS and d) the WAXS scans in the  $\text{SmC}_s$  phase at  $140^\circ\text{C}$ ; e, f) SAXS scans and g, h) WAXS scans e, g) in the  $\text{HexI}_s^{\text{dis}}$  phase at  $100^\circ\text{C}$  and f, h) in the CrG phase at  $70^\circ\text{C}$ .

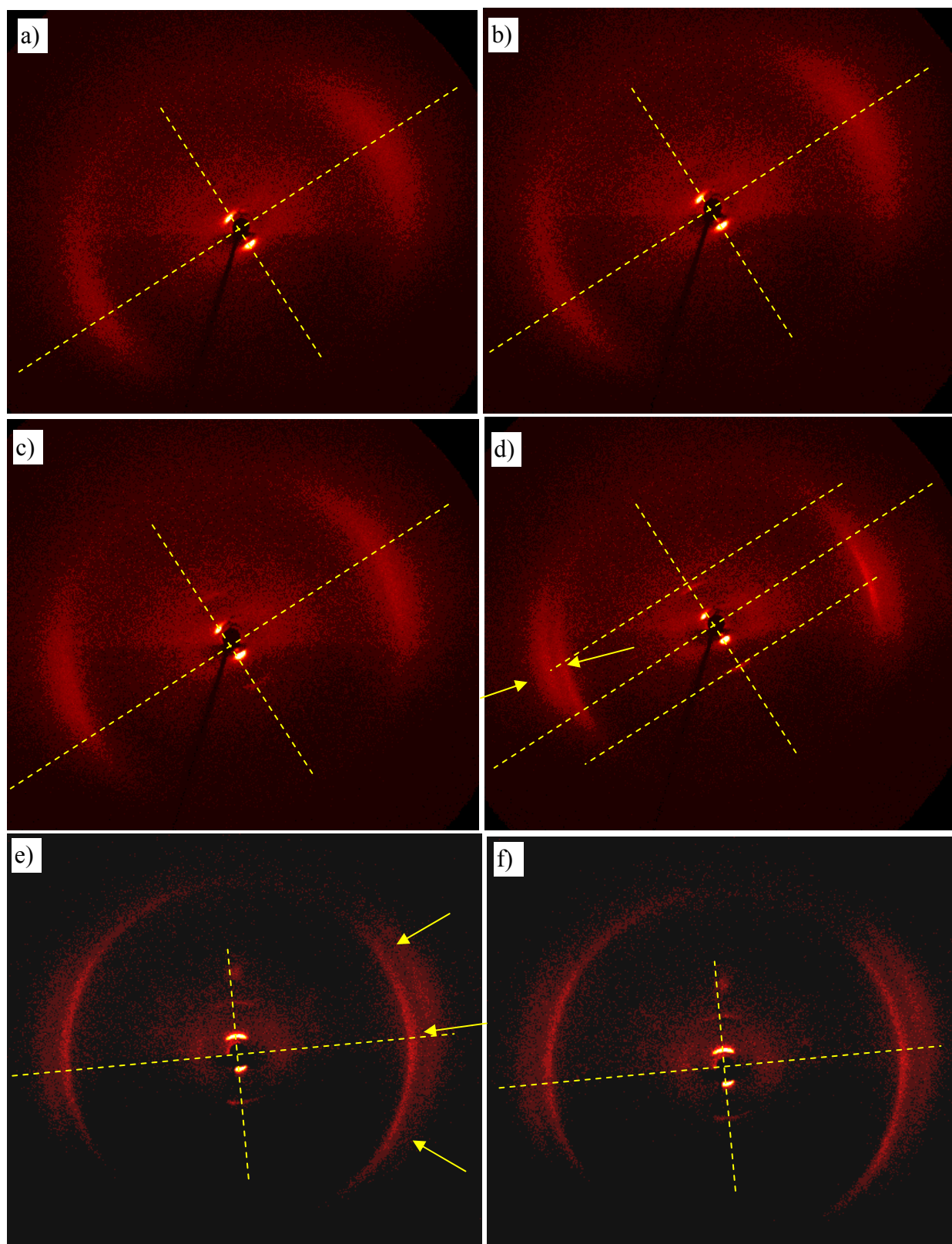


**Figure S23.** 2D-XRD patterns of surface aligned samples of **B'6/6** a,b) in the  $\text{SmC}_a$  phase at 155/150 °C, c,d) in the  $\text{HexF}_s$  phase at 145/143 °C and e,f) in the  $\text{SmI}_s^{dis}$  phase at 135/130 °C (different sample).

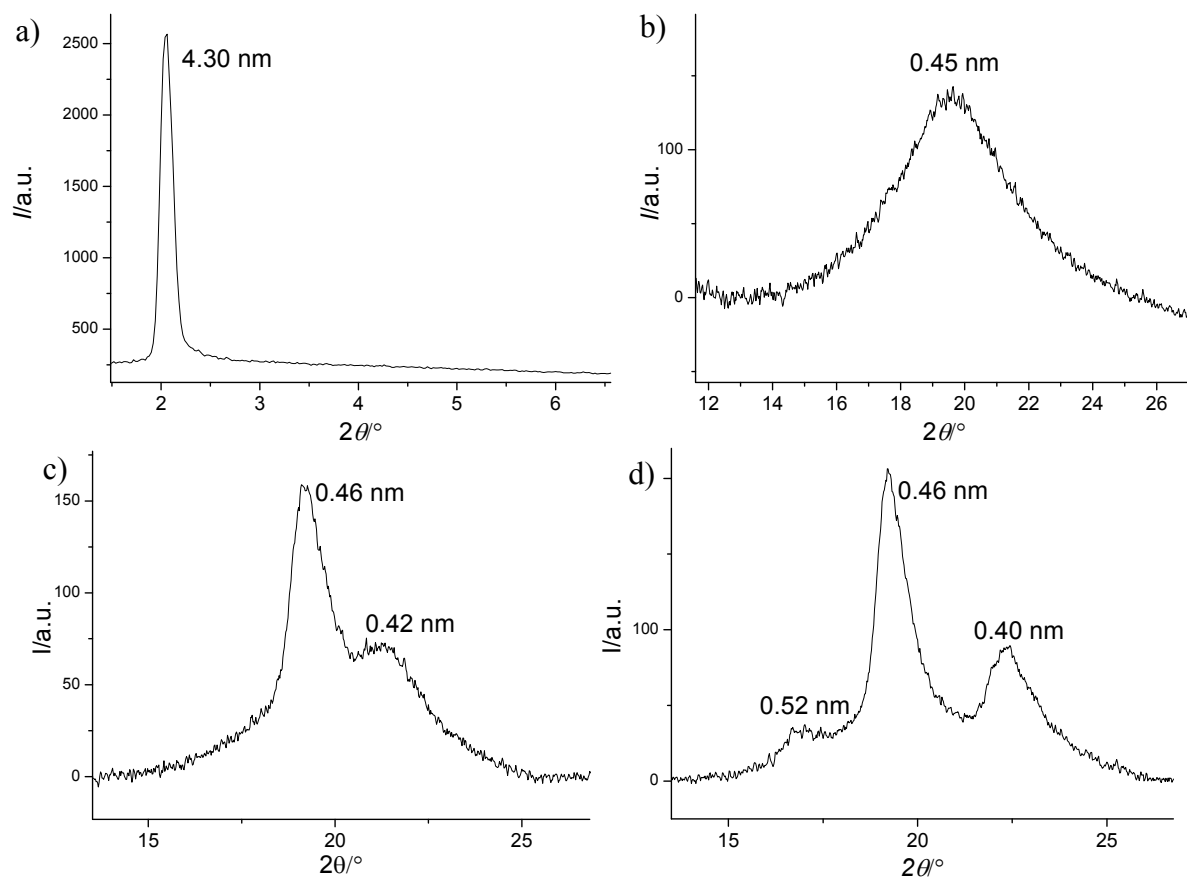


**Figure S24.** Additional powder XRD patterns of **B'6/6** a) powder XRD pattern in the  $\text{SmC}_a$  phase at 155 °C and b) WAXS pattern of the  $\text{SmC}_a$  phase at 150 °C, c) WAXS pattern of the  $\text{SmI}_S^{dis}$  phase at 130 °C and d, e) WAXS pattern of the M phase at 100 °C.

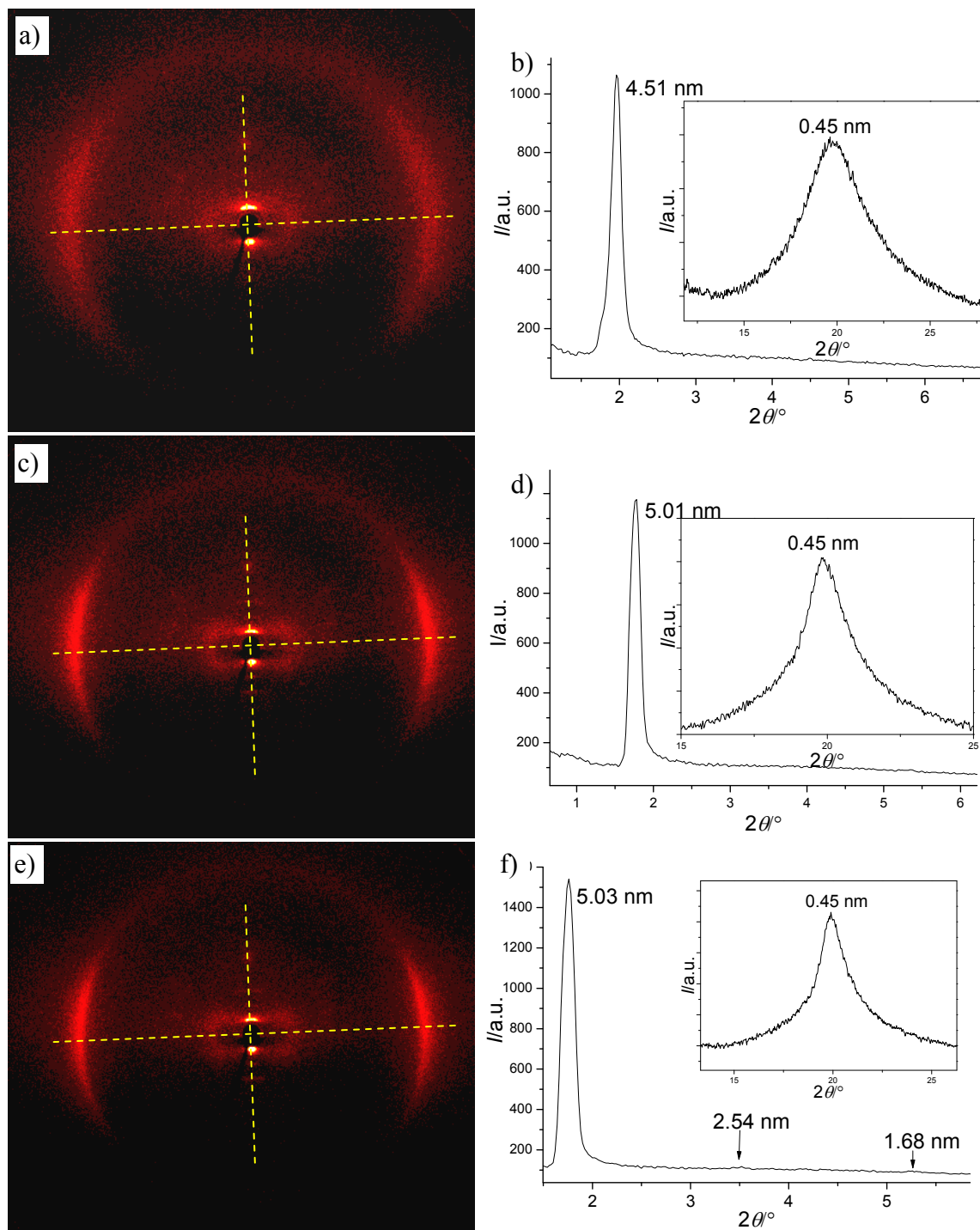


**Figure S25.** 2D-XRD patterns with corresponding SAXS scans (WAXS scans as inset) of surface aligned samples of **B'6/8** a, b) in the weakly tilted  $\text{SmC}_a$  phase at 127 °C, c, d) in the  $\text{HexF}_s$  phase at 120 °C and e, f) in the  $\text{HexB}$  phase at 115 °C; in the Hexatic phases the third order layer reflection is stronger than the second order, as typically observed for hexatic phases.



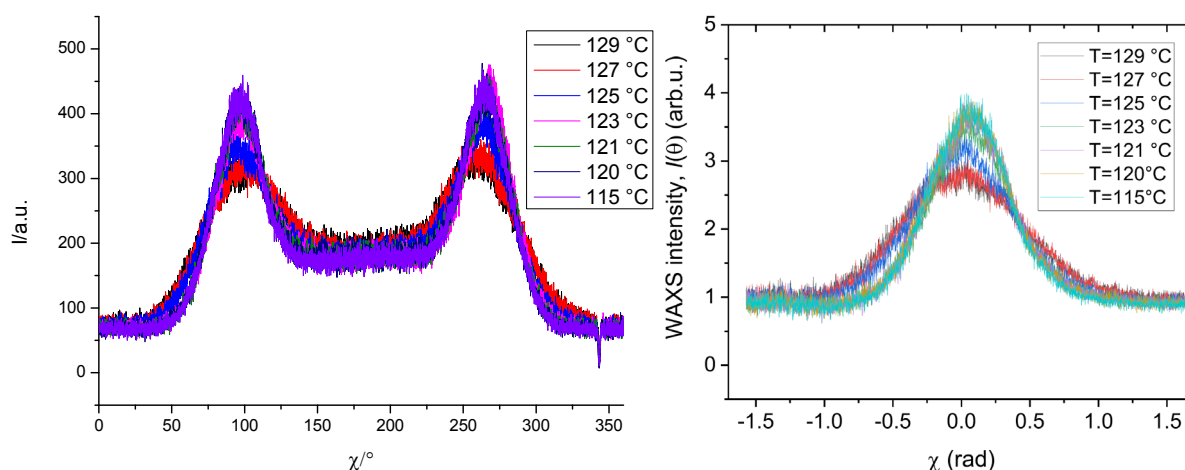


**Figure S26.** a) Original  $\chi$ -scans over the wide angle scattering ( $2\theta=15-20^\circ$ ) of a surface aligned sample of **B'6/8** and b)  $I = f(\chi)$  curves after normalization with a Gauss function, as used for the estimation of the development of the orientational order parameter at the  $\text{SmC}_s$ -HexF<sub>s</sub>-HexB transition according to ref. S4 (right inset in Fig. 6e), the tilt was not considered.

**Table S3.** X-ray data and indexation of the low temperature phase of **B10/H** to a CrG phase with resulting lattice parameters.

Compd.	hkl	$d_{\text{obs}}$ – spacing/nm	$d_{\text{calc}}$ – spacing/nm	$d_{\text{obs}} - d_{\text{calc}}$	$a, b, c/\text{nm}, \beta/^\circ$ ( $T/^\circ\text{C}$ )
<b>B10/H</b>	(001)	4.171	4.171	0.00	1.07, 0.49, 5.25, 52.6 (100) $V_{\text{cell}} = 2.17 \text{ nm}^3$
	(011)	0.482	0.485	0.00	
	(201)	0.450	0.450	0.00	
	(200/110)	0.423	0.424	0.00	
	(20-1)	0.398	0.398	0.00	
	(-113)	0.373	0.374	0.00	
	(213)	0.350	0.349	0.00	

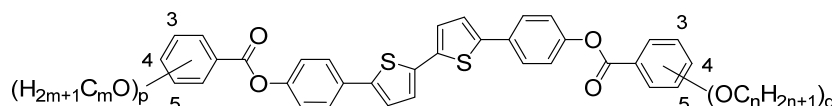
**Table S4.** X-ray data and indexation of the low temperature phase of **B10/H** to a CrJ phase with resulting lattice parameters.

Compd.	hkl	$d_{\text{obs}}$ – spacing/nm	$d_{\text{calc}}$ – spacing/nm	$d_{\text{obs}} - d_{\text{calc}}$	$a, b, c/\text{nm}, \beta/^\circ$ ( $T/^\circ\text{C}$ )
<b>B10/H</b>	(001)	4.17	4.171	0.00	0.69, 0.85, 5.86, 45.4 (110) $V_{\text{cell}} = 2.45 \text{ nm}^3$
	(100)	0.482	0.491	0.01	
	(111)	0.450	0.452	0.00	
	(110/020)	0.423	0.425	0.00	
	(11-1)	0.398	0.398	0.00	
	(-112)	0.373	0.375	0.00	
	(-113)	0.350	0.351	0.00	

**Table S5.** XRD data of the non-cubic phases of the investigated compounds.

Compd.	LC phase	(hkl)	<i>d</i> /nm ( <i>T</i> /°C)
<b>B6/4</b>	SmC <sub>a</sub>	(10)	4.19 (180)
<b>B6/5</b>	SmC <sub>a</sub>	(10)	4.12 (180)
<b>B6/6</b>	SmC <sub>a</sub>	(10)	4.14 (160)
<b>B6/6a</b>	SmC <sub>a</sub>	(10)	4.17 (150)
<b>B'6/6</b>	SmC <sub>a</sub>	(10)	4.30 (155)
	HexF <sub>S</sub>	(10)	4.53 (145)
	HexI <sub>S</sub>	(10)	4.60 (130)
<b>B'6/8</b>	SmC <sub>a</sub>	(10)	4.42 (129)
	HexF <sub>S</sub>	(10)	4.78 (125)
	HexB	(10)	5.01 (120)
<b>B10/H</b>	SmC <sub>S</sub>	(10)	4.26 (140)
	HexI <sub>S</sub>	(10)	4.33 (100)
<b>C10/10</b>	SmC <sub>S</sub>	(10)	3.57 (165)
<b>D1/10</b>	SmC <sub>S</sub>	(10)	3.3 (170)
<b>E10/10</b>	Col <sub>hex</sub>	(10)	4.28 (118)
<b>G10/10</b>	Col <sub>hex</sub>	(10)	4.52 (130)

## 1.3 Additional structural data and molecular models

**Table S6.** Phase transitions and lattice parameters of the polycatenar compounds **A10/n** and **B10/n** (with  $n = 0$  and 10) to **G10/10** depending on the number and position of the alkyl chains and ordered according to increasing total alkyl chain number.<sup>[a]</sup>

$Xm/n$	$p^{(pos)}$	$q^{(pos)}$	$p+q$	$T/^\circ\text{C}$ [ $\Delta H/\text{kJ}\cdot\text{mol}^{-1}$ ]	$a/\text{nm}$ ( $T/^\circ\text{C}$ )	$d/\text{nm}$ ( $T/^\circ\text{C}$ )
<b>B10/H</b>	$2^{(3,5)}$	0	2	H: Cr 91 [10.9] HexI <sub>s</sub> <sup>dis</sup> 113 [5.9] SmC <sub>s</sub> 171 [3.0] Iso C: Iso 169 [-2.8] SmC <sub>s</sub> 111 [-5.9] HexI <sub>s</sub> <sup>dis</sup> 80 [-5.3] CrG <20 Cr		4.26 (140) 4.33 (100)
<b>A10/H</b> <sup>[S5]</sup>	$3^{(3,4,5)}$	0	3	H2: Cr 114 [39.7] Cub <sub>bi</sub> / <i>Ia</i> $\bar{3}$ <i>d</i> 162 [2.3] Iso C: Iso 156 [-1.7] Cub <sub>bi</sub> / <i>Ia</i> $\bar{3}$ <i>d</i> 69 [-3.8] Cr'	10.8 (125)	
<b>B10/10</b>	$2^{(3,5)}$	$1^{(4)}$	3	H: Cr 116 [53.4] Cub <sub>bi</sub> / <i>Ia</i> $\bar{3}$ <i>d</i> 185 [2.3] Iso C: Iso 177 [-1.3] Cub <sub>bi</sub> / <i>Ia</i> $\bar{3}$ <i>d</i> 89 [-33.5] Cr	10.3 (150)	
<b>C10/10</b>	$2^{(3,4)}$	$1^{(4)}$	3	H2: Cr 156 [33.6] SmC <sub>s</sub> 264 [6.3] N 272 [1.2] Iso C: Iso 269 [-1.4] N 263 [-5.9] SmC <sub>s</sub> 128 [-28.7] Cr		3.6 (165)
<b>A10/10</b> <sup>[S5]</sup>	$3^{(3,4,5)}$	$1^{(4)}$	4	H2: Cr 134 [49.9] <b>Cub<sub>bi</sub><sup>[*]</sup>/<i>I23</i></b> 183 [2.2] Iso C: Iso 178 [-0.3] <b>Iso<sub>1</sub><sup>[*]</sup></b> 173 [-1.1] <b>Cub<sub>bi</sub><sup>[*]</sup>/<i>I23</i></b> 109 [-46.0] Cr	17.9 (140)	
<b>D10/10</b>	$2^{(3,4)}$	$2^{(3,4)}$	4	H2: Cr 163 [57.8] SmC <sub>s</sub> 205 [9.5] Iso C: Iso 203 [-9.2] SmC <sub>s</sub> 150 [-57.6] Cr		3.3 (170)
<b>E10/10</b>	$2^{(3,5)}$	$2^{(3,4)}$	4	H: Cr 114 [47.6] Col <sub>hex</sub> 123 [3.3] Iso C: Iso 120 [-3.1] Col <sub>hex</sub> <20 Cr	4.3 (118)	

<sup>a</sup> Peak temperatures as obtained by DSC at a scanning rate of 10 K/min on heating (H, H2 = second heating) or cooling (C);  $d$  = layer spacing in the lamellar phases and  $a_{\text{cub}}$  = cubic lattice parameter; abbreviations: Cr = crystalline solid; Iso = isotropic liquid; Iso<sub>1</sub><sup>[\*]</sup> = mirror symmetry broken isotropic liquid composed of a conglomerate of chiral domains with opposite optical rotation; N = nematic LC phase; SmC<sub>s</sub> = synclinic tilted lamellar LC phase; HexI<sub>s</sub><sup>dis</sup> = synclinic tilted hexatic I-phase with HexI<sub>s</sub>-like order of the alkyl chains and SmC<sub>s</sub>-like order of the aromatic cores; CrG = crystalline lamellar G phase; Cub<sub>bi</sub>/*Ia* $\bar{3}$ *d* = achiral bicontinuous cubic phase with *Ia* $\bar{3}$ *d* space group; Cub<sub>bi</sub><sup>[\*]</sup>/*I23* = bicontinuous cubic phase with *I23* space group, this cubic phase forms a conglomerate of chiral domains with opposite optical rotation (<sup>[\*]</sup>); Col<sub>hex</sub> = columnar LC phase with hexagonal lattice; mirror-symmetry broken phases are shown in bold; for more details, see Fig. S1 (DSCs), Figs. S5-S7 (textures) and Figs. S17,S18 (XRD); for XRD data, see Tables S1 and S5 and for structural data, see Table S6

## Molecular models

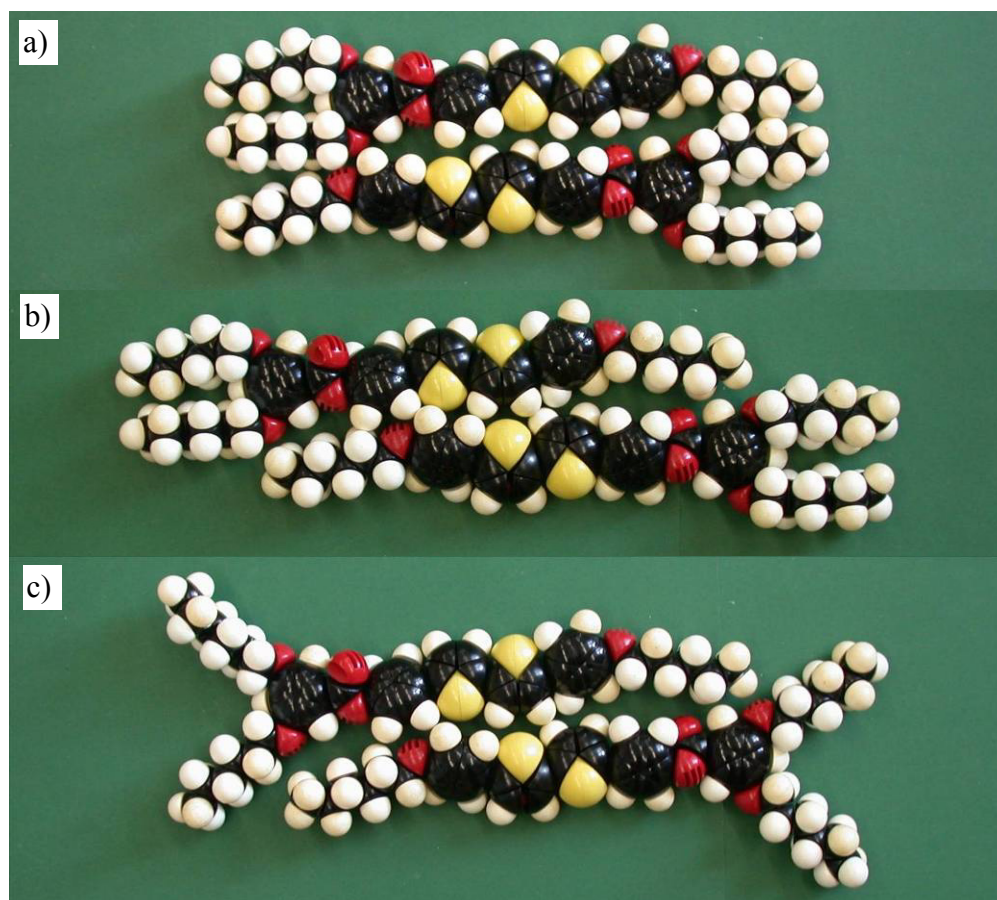


**Figure S27.** Space filling molecular models showing distinct possible modes the organization of **B'6/6**, a) with completely segregated aromatic cores and alkyl chains ( $L = 3.9$  nm), b) with mixed cores and 4'-chains with molecules in the tuning-fork-like conformation with almost parallel 3,5-chains ( $L = 5.1$  nm) and c) same arrangement assuming a Y-shaped conformation ( $L = 4.8$  nm).

## 2.5. FS film experiments with the $\text{Iso}_1^{[*]}$ phase of B'6/8.

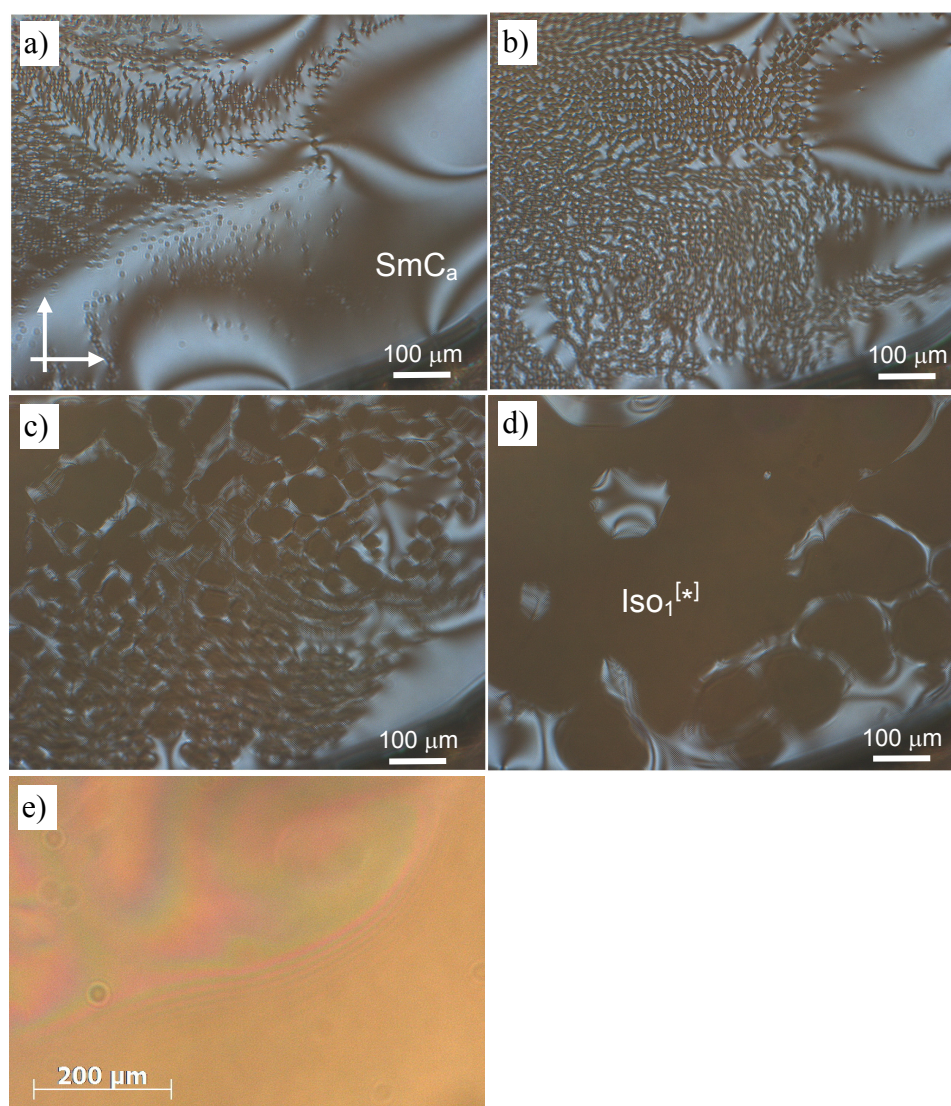


**Figure S28.** a-d)  $\text{SmC}_a$ - $\text{Iso}_1^{[*]}$  transition of **B'6/8** as observed on slow heating of a *freely suspended* film as observed between crossed polarizers (arrows); the chiral domains cannot be observed in this experiment since the thickness is not sufficient enough to provide the necessary optical rotation; e) image of a freely suspended film at  $T = 135\text{ }^\circ\text{C}$  remaining on heating from the  $\text{SmC}_a$  phase, as observed without polarizers. The interference colours indicate variations of the thickness in the film. The colours change continuously and no sharp boundaries or dislocations can be observed. This suggests that the mesophase does not have a well defined smectic-type layer structure.

## 2. Investigation methods

### Optical and calorimetric investigations

Phase transitions were determined by polarizing microscopy (Leica DMR XP) in conjunction with a heating stage (FP 82 HT, Mettler) and controller (FP 90, Mettler) and by differential scanning calorimetry (DSC 8000, Perkin Elmer) at heating/cooling rates of  $10\text{ K min}^{-1}$  (peak temperatures). If not otherwise noted transition temperatures and  $-\Delta H$  were taken from the second heating and cooling curve. Optical investigation was carried out under equilibrium conditions between glass slides which were used without further treatment, sample thickness was



~15  $\mu\text{m}$ . A full wavelength retardation plate was used to determine the sign of birefringence. Optical micrographs were taken using a Leica MC120HD camera.

### **X-ray diffraction.**

X-ray investigations (Kristalloflex 760H, Siemens) on powder-like samples were carried out using Ni filtered  $\text{CuK}\alpha$  radiation (15 to 30 min exposure time). The samples were prepared in the isotropic state on a glass plate and cooled (rate:  $5 \text{ K}\cdot\text{min}^{-1}$ ) to the measuring temperature. Surface-aligned samples were obtained on slow cooling (rate:  $0.5 \text{ K}\cdot\text{min}^{-1}$ ) from the isotropic state. The samples were held on a temperature controlled heating stage and the diffraction patterns were recorded with a 2D detector (Vantec 500, Bruker); exposure time was 15-20 min. The sample-detector distance for the samples was 9.00 cm for WAXD and 26.90 cm for SAXD measurements. The diffraction patterns obtained were transform to 1D plots using GADDS over the full Chi range.

### **Freely suspended films**

Freely suspended films were drawn across a 10 x 3 mm opening in a rectangular glass frame mounted in a heat stage (LINKAM 350). Optical observations were made with a polarising microscope AxioImager Pol (Carl Zeiss GmbH). Both transmission and reflection modes were used. The film thickness was measured using interferometry in reflection. The character of the tilt in the SmC-type phases was determined by observation of the films in transmission at an oblique incidence.





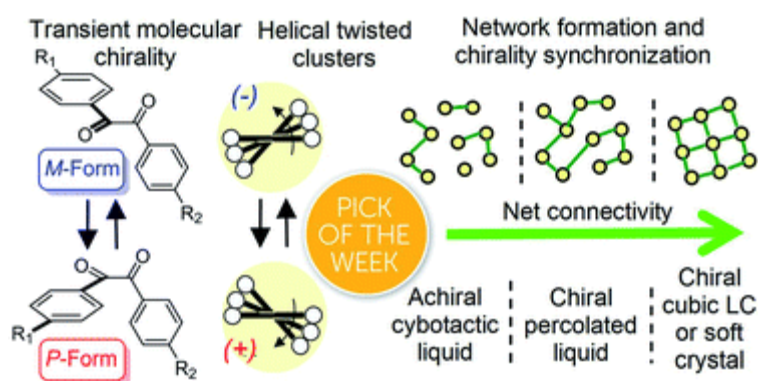
## Publikation D

### Spontaneous mirror symmetry breaking in benzil-based soft crystalline, cubic liquid crystalline and isotropic liquid phases

Tino Reppe <sup>[a]</sup>, Silvio Poppe <sup>[a]</sup> Xiaoqian Cai, <sup>[b]</sup> Yu Cao, <sup>[b]</sup> Feng Liu, <sup>[b]</sup> Carsten Tschierske <sup>[a]</sup>

[a] Institute of Chemistry, Martin Luther University Halle-Wittenberg, Kurt-Mothes-Straße 2, 06120 Halle, Germany.

[b] State Key Laboratory for Mechanical Behaviour of Materials, Shaanxi International Research Center for Soft Matter, Xi'an Jiaotong University, Xi'an 710049, P. R. China.



#### Abstract

Benzil (diphenylethane-1,2-dione), which is a long known example for an achiral molecule crystallizing in a chiral space group, can also show mirror symmetry breaking in the fluid state if it is suitably functionalized. For some of the new benzil derivatives even three different subsequent mirror symmetry broken soft matter states with a chiral conglomerate structure can be observed. One is an isotropic liquid, the second one a cubic liquid crystal with a complex network structure and the third is a soft crystalline solid. Chirality develops by helical self-assembly combined with dynamic network formation, thus allowing macroscopic chirality synchronization. These achiral molecules, combining a transiently chiral bent core with multiple alkyl chains, provide a unique link between the mirror symmetry breaking phenomena observed for polycatenar and bent-core mesogens. The homogeneously chiral networks are of interest for application as chiral materials, and as templates for chiral recognition, separation and enantioselective catalysis.

#### Referenz

T. Reppe, S. Poppe, X. Cai, Y. Cao, F. Liu, C. Tschierske, *Chem. Sci.* **2020**, *11*, 5902–5908.  
DOI: 10.1039/d0sc01396j.

Cite this: *Chem. Sci.*, 2020, **11**, 5902

All publication charges for this article have been paid for by the Royal Society of Chemistry

## Spontaneous mirror symmetry breaking in benzil-based soft crystalline, cubic liquid crystalline and isotropic liquid phases†

Tino Reppe,<sup>a</sup> Silvio Poppe,<sup>a</sup> Xiaoqian Cai,<sup>b</sup> Yu Cao,<sup>b</sup> Feng Liu<sup>ib</sup>\*<sup>b</sup> and Carsten Tschierske<sup>ib</sup>\*<sup>a</sup>

Benzil (diphenylethane-1,2-dione), which is a long known example for an achiral molecule crystallizing in a chiral space group, can also show mirror symmetry breaking in the fluid state if it is suitably functionalized. For some of the new benzil derivatives even three different subsequent mirror symmetry broken soft matter states with a chiral conglomerate structure can be observed. One is an isotropic liquid, the second one a cubic liquid crystal with a complex network structure and the third is a soft crystalline solid. Chirality develops by helical self-assembly combined with dynamic network formation, thus allowing macroscopic chirality synchronization. These achiral molecules, combining a transiently chiral bent core with multiple alkyl chains, provide a unique link between the mirror symmetry breaking phenomena observed for polycatenar and bent-core mesogens. The homogeneously chiral networks are of interest for application as chiral materials, and as templates for chiral recognition, separation and enantioselective catalysis.

Received 8th March 2020

Accepted 29th April 2020

DOI: 10.1039/d0sc01396j

rsc.li/chemical-science

Mirror symmetry breaking and development of uniform chirality is considered essential for the development of life. Understanding and controlling the formation of chirality is crucial across different disciplines. In biosystems the chirality of nucleic acids, sugars and amino acids enables the formation of the helical nanostructures of DNA and proteins.<sup>1</sup> Enantioselective synthesis, catalysis and autocatalysis<sup>2</sup> were successfully developed during recent decades for the synthesis of enantiopure molecules from achiral precursors. This requires expensive chiral reagents or catalysts, synthesized in multistep processes from the chiral pool of nature. However, there is a more economic approach to homochirality, because it can also emerge spontaneously as a result of physical processes such as crystallization,<sup>3</sup> as for example shown for the Viedma ripening,<sup>4</sup> where rapidly enantiomerizing racemic mixtures of chiral molecules, or even achiral molecules crystallizing in a chiral space group spontaneously form uniform chiral crystals with optical activity (OA). The combination of generation of chiral centers with deracemization by dynamic crystallization provides a new absolute asymmetric synthesis methodology.<sup>5</sup>

Likewise, spontaneous chirality can also emerge during the formation of liquid crystalline (LC) phases and even in liquids due to a dynamic process of chirality synchronization,<sup>6</sup> which is the subject of this contribution.

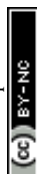
One of the most prominent examples of achiral molecules crystallizing in a chiral space group is benzil (**1**, Fig. 1a), whose OA has been more closely studied than for any other organic crystal.<sup>7,8</sup> In the chiral crystal structure the molecules assume a helical conformation with a torsion angle of the O=C–C=O bond of about  $\alpha = 110^\circ$ .<sup>7</sup> This twisted (skewed) cisoid conformation is also found as a preferred conformation in the gas phase<sup>9</sup> and in solution.<sup>10</sup> However, the energy barrier for the rotation around the O=C–C=O bond is relatively low and in solution or in the melted state it leads to optical inactivity. Thus benzil is a typical transiently chiral molecule capable of mirror symmetry breaking in the crystalline state by Viedma ripening.<sup>11</sup>

Recently, we have observed emergence of OA in bicontinuous cubic (Cub<sub>bi</sub>) LC phases<sup>12</sup> (Fig. 1d) and even in isotropic liquids (Iso<sub>1</sub><sup>[\*]</sup>) by formation of conglomerates of chiral domains.<sup>13</sup> This OA is related to the helical nano-scale organization of the molecules in these Cub<sub>bi</sub> and Iso<sub>1</sub><sup>[\*]</sup> phases.<sup>6</sup> The question arises whether the transient chirality of the benzil unit can support the development of this spontaneous dissymmetry. Moreover, the twisted conformation leads to a non-linear bent shape of the aromatic core, providing some similarity to bent-core molecules, which are also known for their capability of showing mirror symmetry breaking.<sup>14–16</sup> In this case besides helix formation the reduction of the phase symmetry to C<sub>2v</sub>, due

<sup>a</sup>Institute of Chemistry, Martin Luther University Halle-Wittenberg, Kurt-Mothes-Straße 2, 06120 Halle, Germany. E-mail: carsten.tschierske@chemie.uni-halle.de

<sup>b</sup>State Key Laboratory for Mechanical Behaviour of Materials, Shaanxi International Research Center for Soft Matter, Xi'an Jiaotong University, Xi'an 710049, P. R. China. E-mail: feng.liu@xjtu.edu.cn

† Electronic supplementary information (ESI) available. See DOI: 10.1039/d0sc01396j



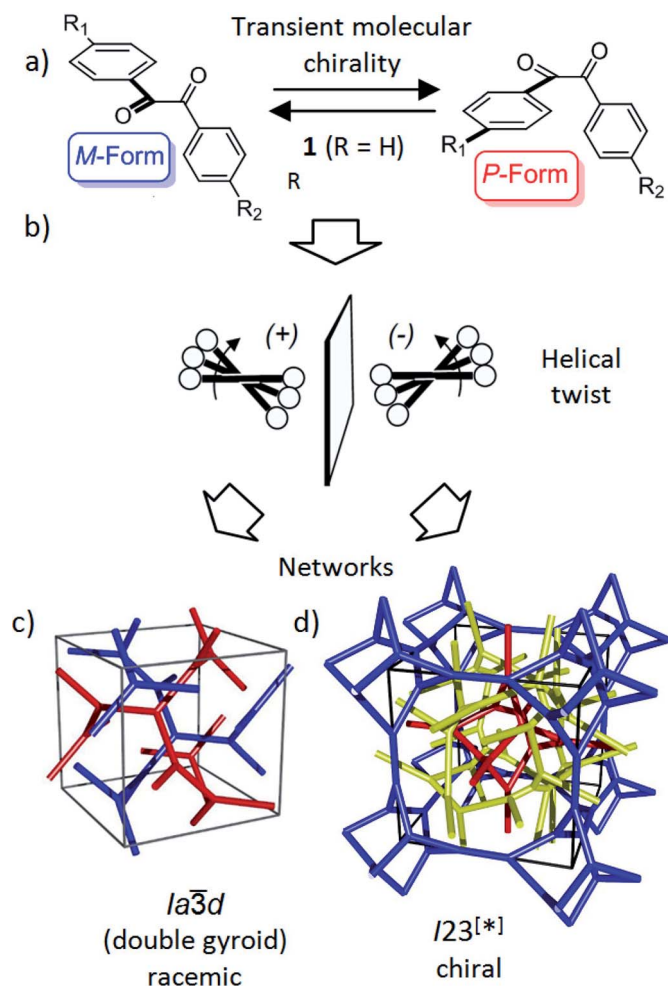


Fig. 1 Schematics showing (a) the transient chirality of benzil derived molecules; and (b) the development of the helical twist by clashing of the bulky end groups attached to the cores and (c and d) the network structure of the  $\text{Cub}_{\text{bi}}$  phases under discussion.<sup>25</sup> The benzil based polyaromatic cores form the helical networks which are embedded in the continuum filled by the terminal chains. (c and d) were reproduced from ref. 25 by permission of The Royal Society of Chemistry.

to the organization of the tilted molecules with their bent direction parallel to the layer planes (see Fig. S16<sup>†</sup>), contributes to symmetry breaking.<sup>14</sup>

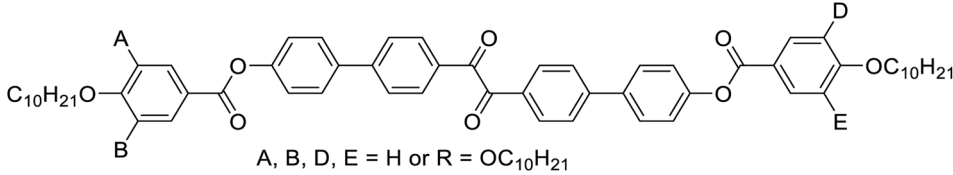
Besides the well-known case of lyotropic LCs,<sup>17</sup>  $\text{Cub}_{\text{bi}}$  phases are also known to be formed in solvent-free (thermotropic) systems by rod-like polyaromatic molecules with two<sup>18,19</sup> or multiple alkyl end-chains (polycatenar compounds),<sup>20</sup> branched chains (swallow tailed compounds)<sup>21</sup> or other bulky end groups.<sup>22</sup> In these  $\text{Cub}_{\text{bi}}$  phases the rods form networks and the alkyl chains fill the space between them (Fig. 1c and d). Within the networks the orientation of the rods is perpendicular or slightly tilted with respect to the local network direction and the mismatch of the cross sectional areas of these cores with the cross sectional area of the terminally attached chains leads to the curvature of the aggregates, and simultaneously, to a helical twist along the networks (Fig. 1b).<sup>6,12a</sup> There are two major types of such thermotropic  $\text{Cub}_{\text{bi}}$  phases, the double gyroid phase

(space group  $Ia\bar{3}d$ ) and the triple network phase designated as  $Im\bar{3}m$  (Fig. 1c and d).<sup>18,23,24</sup> The  $Ia\bar{3}d$  phase involves two helical networks with opposite handedness (red, blue in Fig. 1c) and therefore it is achiral.<sup>12a</sup> However, in the  $Im\bar{3}m$  phase this degeneracy is broken by the presence of three networks<sup>24</sup> and the synchronization of the helix sense between them.<sup>12a</sup> The chiral space group with the highest symmetry, derived from the achiral  $Im\bar{3}m$  space group would be  $I432$ ,<sup>12</sup> but the actual space group was recently identified as  $I23$ .<sup>25</sup> In this new structural model of the “ $Im\bar{3}m$ ” type  $\text{Cub}_{\text{bi}}$  phase there are three networks with all junctions being threefold, but with distances and twist angles between the junctions being slightly different from those in the  $Ia\bar{3}d$  phase (Fig. 1d).

Herein we report the first mirror symmetry broken LC phases formed by a series of suitably designed multi-chain benzil derivatives (Tables 1 and 2). The decyloxy substituted compounds with a different number of chains are labelled as 2–6 according to their order in Table 1. Compounds 3 have three decyloxy chains at one end and either no chain (compound 3/H) or a single *n*-alkyloxy chain with a variable length at the other end (compounds 3/*n*); here the number *n* after the slash indicates the length of this chain (Table 2). The respective compounds were synthesized as described in Scheme S1<sup>†</sup> and the experimental procedures are given in the ESI.<sup>†</sup> Analysis of their self-assembly was performed by polarizing optical microscopy (POM), differential scanning calorimetry (DSC) and X-ray diffraction (XRD). As is obvious from Table 1, with the growing number of *n*-decyl chains a transition from lamellar (SmC, 2) *via* two different types of  $\text{Cub}_{\text{bi}}$  phases ( $Ia\bar{3}d$ ,  $I23$ <sup>[\*]</sup>, 3/10, 4) to hexagonal columnar phases ( $\text{Col}_{\text{hex}}$ , 4, 5) is observed. Only the hexaalkyl substituted compound 6 does not show any LC phase. The SmC and  $\text{Col}_{\text{hex}}$  phases were indicated by their typical birefringent optical textures observed between crossed polarizers (Fig. 2e, h and S2–S5<sup>†</sup>) and were confirmed by XRD for compounds 2 and 5 (Table S6<sup>†</sup>). The transition from the isotropic liquid state (Iso) to the  $\text{Cub}_{\text{bi}}$  phases was indicated by a small exotherm in the DSC scans, accompanied by an increase in the viscosity while the phase remained optically isotropic. The cubic phase types are distinguished by optical investigation between polarizers, rotated by a small angle ( $\sim 5^\circ$ ) out of the  $90^\circ$  crossed orientation, where only the  $I23$  phase shows a conglomerate of optically active (dark and bright) domains ( $I23$ <sup>[\*]</sup> phase), whereas  $Ia\bar{3}d$  is optically inactive (Fig. 2f and g).<sup>12</sup> Interestingly, the  $\text{Cub}_{\text{bi}}$  phase type depends on the chain distribution and the chain length (Tables 1 and 2); for the symmetric compound 4 the achiral  $Ia\bar{3}d$  phase occurs as a monotropic (metastable) phase below  $\text{Col}_{\text{hex}}$ , whereas the non-symmetric compound 3/10 has exclusively a broad range of the mirror symmetry broken  $I23$ <sup>[\*]</sup> phase. To the best of our knowledge, these are the first benzil derivatives forming cubic LC phases, whereas a few benzil based compounds involving amide groups were found to form exclusively columnar LC phases.<sup>26</sup>

Here we focus on the homologous series of the non-symmetric tetracatenars 3/*n* where only 3/H and 3/1 are non-mesomorphic and all the following homologues form  $\text{Cub}_{\text{bi}}$  phases (Table 2). In this series the  $\text{Cub}_{\text{bi}}$  phase type changes



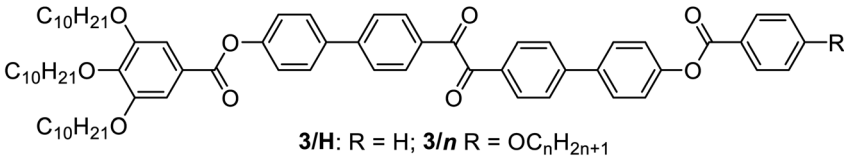
Table 1 Phase transitions of compounds 2–6 on heating<sup>a</sup>


Compd.	A	B	D	E	$T/^\circ\text{C}$ [ $\Delta H$ kJ mol <sup>-1</sup> ]
2	H	H	H	H	Cr 149 [27.0] SmC <sup>b</sup> 243 [12.0] Iso
3/10	R	R	H	H	Cr 97 [63.2] ( <b>Cr<sub>Iso</sub></b> <sup>[*]</sup> 90 [17.6]) <b>Cub<sub>bi</sub>/I23</b> <sup>[*]</sup> 131 [2.2] Iso <sub>1</sub> 138 [5.7] Iso
4	R	H	R	H	Cr 151 [69.5] ( <b>Cub<sub>bi</sub>/Ia3d</b> 141 Col <sub>hex</sub> 143 [12.4] <sup>c</sup> ) Iso
5	R	R	R	H	Cr 92 [14.2] Col <sub>hex</sub> <sup>d</sup> 105 [7.1] Iso
6	R	R	R	R	Cr 84 [33.2] Iso

<sup>a</sup> DSC peak temperatures at 10 K min<sup>-1</sup>; values in round parantheses indicate monotropic phases, only observed on cooling; abbreviations: Cr = crystalline solid, SmC = tilted lamellar phase, Cub<sub>bi</sub>/Ia3d = achiral Cub<sub>bi</sub> phase with the Ia3d space group, Cub<sub>bi</sub>/I23<sup>[\*]</sup> = mirror symmetry broken Cub<sub>bi</sub> phase with the I23 space group; Iso = achiral isotropic liquid; Iso<sub>1</sub><sup>[\*]</sup> = mirror symmetry broken Iso phase; for DSC traces, see Fig. S1, and for textures, see Fig. S2–S5. <sup>b</sup>  $d = 3.66$  nm. <sup>c</sup> Enthalpies of both transitions. <sup>d</sup>  $a_{\text{hex}} = 4.39$  nm.

from Ia3d ( $n = 2$ ) via I23<sup>[\*]</sup> ( $n = 4$ –10) to Ia3d again ( $n = 12$ –16), upon chain elongation. The high resolution diffraction patterns of the I23<sup>[\*]</sup> phase of 3/4 and the Ia3d phase of 3/16, recorded

with a synchrotron source, are shown as representative examples in Fig. 2a and b. Besides the diffuse wide angle scattering (Fig. S7b and c<sup>†</sup>), there are several sharp small angle scatterings,

Table 2 Phase transitions, lattice parameters ( $a_{\text{cub}}$ ), number of molecules in the neighbouring rafts ( $n_{\text{raft}}$ ) and twist angles between the rafts ( $\Phi/^\circ$ ) in the Cub<sub>bi</sub> phases of compounds 3/H and 3/ $n$ <sup>a</sup>


3/ $n$	$T/^\circ\text{C}$ [ $\Delta H$ kJ mol <sup>-1</sup> ]	$a_{\text{cub}}$ /nm	$n_{\text{raft}}$	$\Phi/^\circ$	$L_{\text{mol}}$ /nm
3/H	H: Cr 126 [52.2] Iso C: Iso 110 [27.3] Cr	—	—	—	4.2
3/1	H: Cr 127 [36.3] Iso C: Iso 115 [36.4] Cr	—	—	—	4.3
3/2	H: Cr 120 [37.9] <b>Ia3d<sub>(L)</sub></b> 127 [1.8] Iso <sub>1</sub> 135 [2.8] Iso C: Iso 133 [2.7] Iso <sub>1</sub> 121 [0.2] <b>Iso<sub>1</sub></b> <sup>[*]</sup> 110 [0.3] <b>Ia3d<sub>(L)</sub></b> 105 [31.3] Cr	12.9	5.0	6.9	4.4
3/4	H: Cr 128 [53.5] Iso C: Iso 128 [4.5] Iso <sub>1</sub> 122 [0.4] <b>Iso<sub>1</sub></b> <sup>[*]</sup> 116 [0.7] <b>I23</b> <sup>[*]</sup> 73 [21.2] Cr	18.4	4.0	7.6	4.6
3/6	H: Cr 118 [64.6] ( <b>Cr<sub>Iso</sub></b> <sup>[*]</sup> 82 [17.3]) <b>I23</b> <sup>[*]</sup> 126 [2.2] Iso <sub>1</sub> 134 [5.7] Iso C: Iso 130 [7.1] Iso <sub>1</sub> 123 [0.5] <b>Iso<sub>1</sub></b> <sup>[*]</sup> 118 [1.1] <b>I23</b> <sup>[*]</sup> 61 [15.3] <b>Cr<sub>Iso</sub></b> <sup>[*]</sup>	18.1	3.8	7.7	4.8
3/10	H: Cr 97 [63.2] ( <b>Cr<sub>Iso</sub></b> <sup>[*]</sup> 90 [17.6]) <b>I23</b> <sup>[*]</sup> 131 [2.2] Iso <sub>1</sub> 138 [5.7] Iso C: Iso 135 [5.9] Iso <sub>1</sub> 127 [0.3] <b>Iso<sub>1</sub></b> <sup>[*]</sup> 122 [0.9] <b>I23</b> <sup>[*]</sup> 66 [17.8] <b>Cr<sub>Iso</sub></b> <sup>[*]</sup>	18.4	3.7	7.6	5.2
3/12	H: Cr 114 [47.0] <b>Ia3d<sub>(S)</sub></b> 135 [3.4] Iso <sub>1</sub> 139 [6.2] Iso C: Iso 137 [8.9] Iso <sub>1</sub> 128 [0.3] <b>Iso<sub>1</sub></b> <sup>[*]</sup> 122 [0.7] <b>Ia3d<sub>(S)</sub></b> 48 [17.9] Cr <sub>Iso</sub> < 20 Cr	11.4	3.3	7.9	5.4
3/14	H: Cr 108 [44.1] <b>Ia3d<sub>(S)</sub></b> 135 [2.7] Iso <sub>1</sub> 138 [7.2] Iso C: Iso 136 [9.2] Iso <sub>1</sub> 129 [1.4] Col <sub>hex</sub> 125 [0.5] <b>Ia3d<sub>(S)</sub></b> 42 [16.9] Cr <sub>Iso</sub> < 20 Cr	11.3	3.2	7.8	5.6
3/16	H: Cr 80 [36.4] <b>Ia3d<sub>(S)</sub></b> 133 [3.1] Iso <sub>1</sub> 139 [6.1] Iso C: Iso 136 [6.0] Iso <sub>1</sub> 130 [2.3] Col <sub>hex</sub> 121 [0.5] <b>Ia3d<sub>(S)</sub></b> 45 [25.0] Cr	11.5	3.2	7.8	5.8

<sup>a</sup> DSC peak temperatures on heating/cooling (H/C) at 10 K min<sup>-1</sup>;  $n_{\text{raft}} = n_{\text{cell}}/(L_{\text{net}}/0.45)$  with  $L_{\text{net}} = 20.68a_{I23}$ ; and  $L_{\text{net}} = 8.485a_{Ia3d}$ ;  $\Phi(Ia3d) = 70.5^\circ/[0.354a_{\text{cub}}/0.45 \text{ nm}]$ ;  $\Phi(I23) = 90^\circ/[0.290a_{\text{cub}}/0.45 \text{ nm}]$ ; <sup>b</sup>  $L_{\text{mol}}$  = maximum molecular length as determined with space filling models assuming a molecular bend of 110° and all-*trans* alkyl chains, see Fig. S15; abbreviations: Iso<sub>1</sub> = achiral cybotactic isotropic liquid (see Fig. 3d), Cr = birefringent crystalline solid; Cr<sub>Iso</sub> = optically isotropic crystalline mesophase; Cr<sub>Iso</sub><sup>[\*]</sup> = mirror symmetry broken Cr<sub>Iso</sub> forming a conglomerate of chiral domains; Ia3d<sub>(S)</sub> = short pitch Ia3d phase with a smaller number of molecules in the unit cell/rafts and a larger twist angle  $\Phi$  than in Ia3d<sub>(L)</sub> = long pitch Ia3d phase with a larger number of molecules in the unit cell/rafts and a smaller twist angle  $\Phi$ ; for other abbreviations, see Table 1; chiral phases are shown in bold; because the transitions Iso–Iso<sub>1</sub> are very broad (see Table S1) it is difficult to determine precise enthalpy values; for DSC traces, see Fig. S1 and for XRD data, see Tables S1–S7 and Fig. S7 and S10–S14.





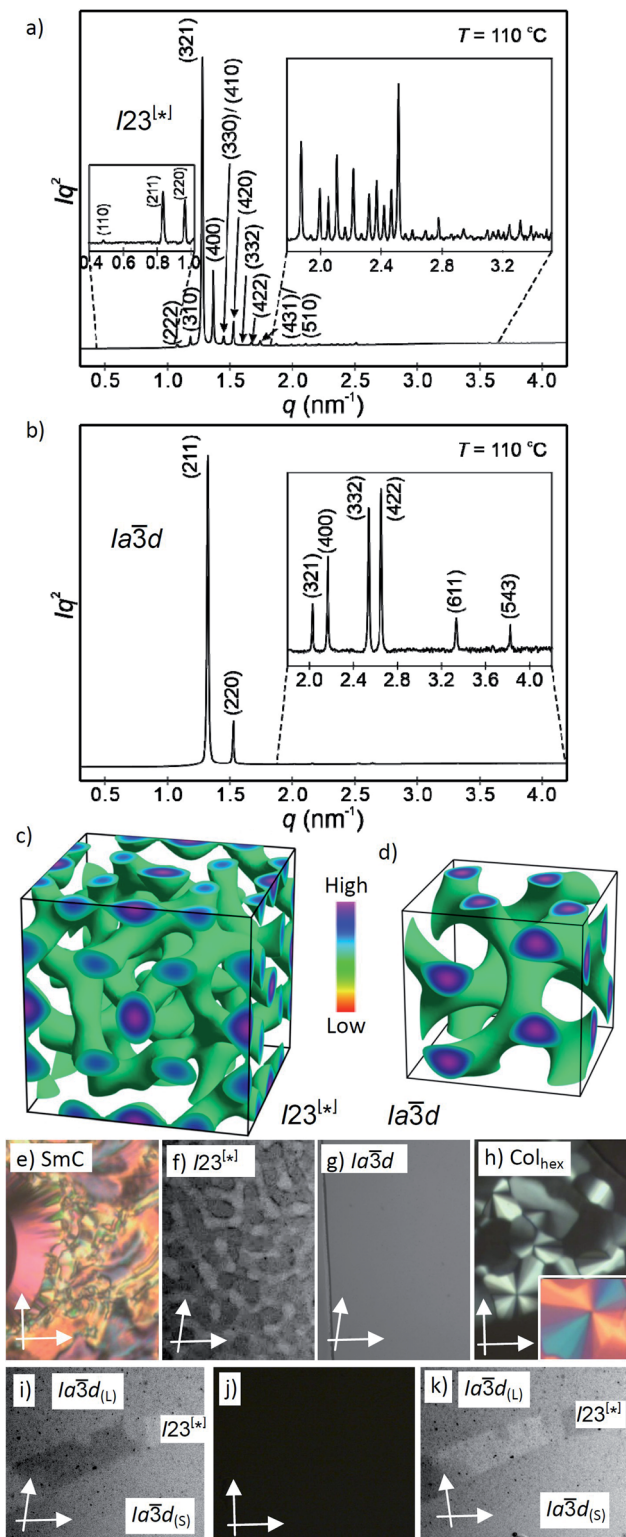


**Fig. 2** (a and b) SAXS diffractograms of the  $I23^{[*]}$  (**3/4**) and the  $Ia\bar{3}d_{(S)}$  (**3/16**) phases (for the synchrotron source and for numerical data, see Tables S4 and S5;† the full indexations of the  $I23^{[*]}$  phase and the WAXS scans are shown in Fig. S7†); (c and d) reconstructed electron density maps of the  $I23^{[*]}$  and  $Ia\bar{3}d_{(S)}$  phase; the aromatic cores are located in the networks formed by the green iso-surfaces, the space between is filled by the alkyl chains; for more details, see the ESI, and Fig. S8† for the individual networks; (e–h) the textures of the (e) SmC phase of **3/10** at 230 °C; (f) the  $Cub_{bi}/I23^{[*]}$  phase of **3/10** at 121 °C and

the strongest being indexed either to (211) and (220) of the  $Ia\bar{3}d$  lattice or (321), (400) and (420) reflections of the  $I23^{[*]}$  lattice. The electron density maps (Fig. 2c, d and S9†) reconstructed from these patterns are in agreement with the proposed phase structures shown schematically in Fig. 1c and d. The method of selecting the correct phase combination is described in previous work.<sup>12,25,27</sup> The cubic lattice parameter is around 11–13 nm for  $Ia\bar{3}d$  and 18 nm for  $I23^{[*]}$ , in line with a double- and triple-network structure, respectively. Remarkably, the  $Ia\bar{3}d$  lattice is the largest for the smallest molecule **3/2** ( $L_{mol} = 4.4$  nm;  $a_{cub} = 12.9$  nm) and becomes smaller for the  $Ia\bar{3}d$  phases of the larger compounds **3/12–3/16** with much longer chains ( $L_{mol} = 5.8–6.3$  nm;  $a_{cub} = 11.3–11.5$  nm).<sup>28</sup> In line with this, in the  $Ia\bar{3}d$  phase of **3/2** about 5 molecules are arranged side-by-side in the cross section of the networks, whereas for **3/12–3/16** there are only 3.2 molecules (Tables 2 and S7†). The twist between the molecules in the adjacent rafts with a height of 0.45 nm ( $\Phi$ ) can be calculated as  $\sim 7^\circ$  in the long pitch  $Ia\bar{3}d_{(L)}$  phase of **3/2** and  $\sim 8^\circ$  for the short pitch  $Ia\bar{3}d_{(S)}$  phase of compounds **3/12–3/16** (Table 2). The intermediate homologues **3/4–3/10** escape from forming the  $Ia\bar{3}d$  phase by assuming the triple network  $I23^{[*]}$  structure instead. The twist in this network is almost constant 7.6–7.7° and between the angles in the  $Ia\bar{3}d_{(L)}$  and  $Ia\bar{3}d_{(S)}$  phases. The  $I23^{[*]}$  phase obviously allows for these twist angles a better fit of the helical pitch length with junction distances and inter-junction twist angles than in the competing  $Ia\bar{3}d$  lattices.<sup>12a,25</sup> This phase sequence was also reported for the  $Cub_{bi}$  phases of other rod-like molecules<sup>18a,19,29</sup> and it is observed in the contact regions between the achiral  $Ia\bar{3}d_{(L)}$  and  $Ia\bar{3}d_{(S)}$  phases of **3/2** and **3/12–3/16**, respectively, where a concentration gradient develops, and in a certain concentration range the chiral conglomerate of the  $I23^{[*]}$  phase is induced (Fig. 2i–k).<sup>29,30</sup>

In addition to the cubic phases, for compounds **3/2–3/12** a mirror symmetry broken isotropic liquid ( $Iso_1^{[*]}$  phase) occurs as a metastable (monotropic) phase on cooling the achiral  $Iso$  phase and replaces a part of the  $Cub_{bi}$  phase range (Table 2). The  $Iso_1^{[*]}$  phase disappears at the transition from  $n = 12$  to 14 right after the transition from  $I23^{[*]}$  to  $Ia\bar{3}d_{(S)}$  occurring from  $n = 10$  to 12. Hence, it can be concluded that the local structure in the  $Iso_1^{[*]}$  phase is likely to be related to that of the chiral  $I23^{[*]}$  triple network (Fig. 1d). Remarkably, for **3/2–3/12** the transition  $Iso-Iso_1^{[*]}$  takes place in two separate steps, as indicated by the DSC trace of **3/12** (Fig. 3a). A very broad feature within the isotropic liquid range (with a maximum around 137 °C on cooling) indicates the transition from an ordinary

(g)  $Cub_{bi}/Ia\bar{3}d_{(S)}$  phase of **3/12** at 120 °C, as observed between slightly uncrossed polarizers; (h)  $Col_{hex}$  phase of **3/10** at 141 °C; the inset shows the texture with an additional  $\lambda$ -plate, indicating that the phase is optically negative, *i.e.* the orientation of the aromatic cores is perpendicular or only slightly tilted to the column long axis; (i–k) show the induced chiral  $I23^{[*]}$  phase in the contact region between the achiral  $Ia\bar{3}d_{(L)}$  phase of **3/2** (top) and the  $Ia\bar{3}d_{(S)}$  phase of **3/16** (bottom); the orientation of the polarizers is shown by white arrows; the width of the POM images in (e–k) is 200  $\mu m$ , and in (f), (i) and (k) the contrast is enhanced; for additional textures, see also Fig. S2–S6.†





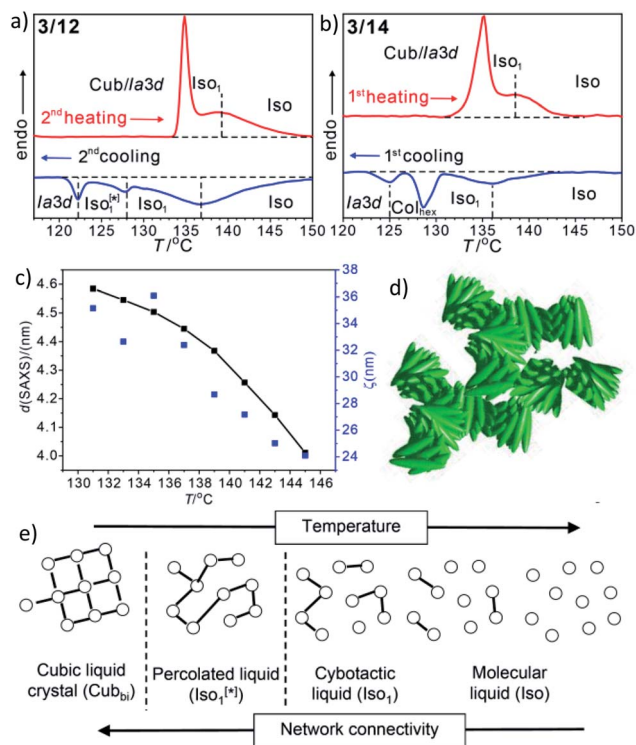


Fig. 3 (a and b) sections of the DSC traces ( $10 \text{ K min}^{-1}$ ) of compounds 3/12 and 3/14 (see Fig. S1† for complete traces); (c) plot of the  $d$ -values (black) and the correlation length ( $\zeta$ , blue) of the small angle scattering of 3/12 in the isotropic liquid phases (see also Fig. S10 and S11†); (d) sketch of the fused helical clusters in the  $\text{Iso}_1^{[*]}$  phase; (e) schematic sketch showing the transition from Iso via a cybotactic and a percolated liquid to  $\text{Cub}_{\text{bi}}$  by increasing the transient network connectivity; the dots represent locally ordered clusters, the lines indicate the connections between them, and the vertical dotted lines indicate phase transitions.

isotropic liquid (Iso) to a kind of cybotactic isotropic liquid with a fluctuating local network structure ( $\text{Iso}_1$ ),<sup>31</sup> which is still achiral (Tables 2 and S1†). With further decrease in the temperature the number of linkages between the clusters increases. Mirror symmetry breaking sets in at the next much sharper transition at  $128^\circ\text{C}$  which we attribute to the transition from the cybotactic to a percolated liquid, after crossing a certain critical density of connectivity between the cybotactic clusters,<sup>6a,32</sup> thus leading to a long range transmission of the helical twist, and hence, chirality ( $\text{Iso}_1^{[*]}$ ). In the  $\text{Iso}_1^{[*]}$  range the connections are transient and at the next transition at  $122^\circ\text{C}$  they become permanent with formation of the  $Ia\bar{3}d$  phase (or  $I23^{[*]}$  for the shorter homologues, Fig. 3e). In the temperature range of the isotropic liquid phases there is an almost continuous increase in the line width of the small angle XRD scattering (Fig. 3c) and there is also no obvious discontinuity in the viscosity, as indicated by optical microscopy, where all three isotropic liquid phases flow under the influence of gravity. Only at the transition to the cubic phase the material suddenly becomes viscoelastic. The enthalpy of the Iso– $\text{Iso}_1$  transition increases with the growing chain length with a distinct jump from  $n = 4$  to 6 (Table 2), in line with improved rod-chain segregation, supporting the cluster formation.

For the longer homologues 3/14 and 3/16 the  $\text{Iso}_1^{[*]}$  phase is replaced by a  $\text{Col}_{\text{hex}}$  phase (Fig. 3b). The growing chain length obviously disfavours the branching, thus leading to predominately linear aggregates which do not form networks, but assume long range order and transform to the achiral  $\text{Col}_{\text{hex}}$  phase.

Another interesting feature of compounds 3/6–3/10 is that on further cooling from the  $\text{Cub}_{\text{bi}}/I23^{[*]}$  phase a transition to an optically isotropic crystalline mesophase is observed, in which, the conglomerate texture is retained ( $\text{Cr}_{\text{Iso}}^{[*]}$  phase, see Fig. 4c–f). Because this transition is associated with a change in the XRD pattern and a sharp transition with a significant transition enthalpy of  $17\text{--}18 \text{ kJ mol}^{-1}$  (Table 2 and Fig. 4g), it cannot be a glass transition. The XRD pattern of the  $\text{Cr}_{\text{Iso}}^{[*]}$  phase is characterized by a relatively broad small angle scattering, with a maximum at  $d = 5.38 \text{ nm}$  for 3/6 (Fig. 4h) and  $5.45 \text{ nm}$  for 3/10, approximately corresponding to the lengths of the respective intercalated anti-parallel molecular pairs ( $5.5 \text{ nm}$ , see Fig. S15†). In the wide angle range, there are three broad scatterings with very low intensity (Fig. 4i, S12 and S13†), which can tentatively be attributed to the mean alkyl chain distance ( $0.44 \text{ nm}$ ) and the edge-to-edge and face-to-face packing distances of the aromatics ( $0.56/0.37 \text{ nm}$ ). This diffraction pattern is similar to those typically recorded for the symmetry broken soft crystalline mesophases of bent-core mesogens, helical nanofilaments (HNFs),<sup>16,33a</sup> helical nano-crystallites (HNCs)<sup>34</sup> and related helical phases,<sup>35</sup> which in some respect can be considered as solvent free gels.<sup>16,36,37</sup> A transition from the LC  $\text{Cub}_{\text{bi}}$  phase to a soft crystalline network structure, where the polyaromatic rods and parts of the aliphatic chains assume a crystalline packing, appears likely. Similar to the bent-core mesogens, the directed packing of the twisted and bent 4,4'-diphenylbenzil units (Fig. S15†) is likely to contribute to the development of the helical packing modes in the liquid, LC and especially in the soft crystalline mesophases of compounds 3/ $n$ . For compounds 3/12 and 3/14, forming the achiral  $Ia\bar{3}d_{\text{(s)}}$  cubic phase instead of  $I23^{[*]}$ , the isotropic crystalline phase appears to be achiral ( $\text{Cr}_{\text{Iso}}$ , see Fig. S6†), though the XRD pattern (Fig. S14†) is almost the same as for 3/6 and 3/10. Whether this phase is intrinsically achiral, or the symmetry breaking at the transition from the achiral  $Ia\bar{3}d_{\text{(s)}}$  to a  $\text{Cr}_{\text{Iso}}^{[*]}$  phase can only develop locally, as the OA domains are too small to be observable by optical investigation, cannot be decided at present.

In summary, first benzil derivatives forming a series of LC phases, ranging from lamellar via two types of  $\text{Cub}_{\text{bi}}$  phases to columnar, have been obtained. Mirror symmetry breaking is observed in three of the soft matter phases, the isotropic liquid, the liquid crystalline  $\text{Cub}_{\text{bi}}/I23^{[*]}$  phase and in the soft crystalline phase ( $\text{Cr}_{\text{Iso}}^{[*]}$ ). This work contributes to the understanding of the development of mirror symmetry breaking in isotropic liquids as a consequence of network formation and increasing network-connectivity (Fig. 3e). In addition, these molecules with a bend around the central  $\text{O}=\text{C}-\text{C}=\text{O}$  bond appear to provide the still missing link between the mirror symmetry broken modes of soft self-assembly observed in polycatenars and in bent-core LC systems,<sup>6,15,16,33,36b,38</sup> bent mesogenic dimers<sup>6,16,36a</sup> and oligomers.<sup>39</sup> Moreover, as the  $\text{Iso}_1^{[*]}$  and  $\text{Cub}_{\text{bi}}/I23^{[*]}$  phases



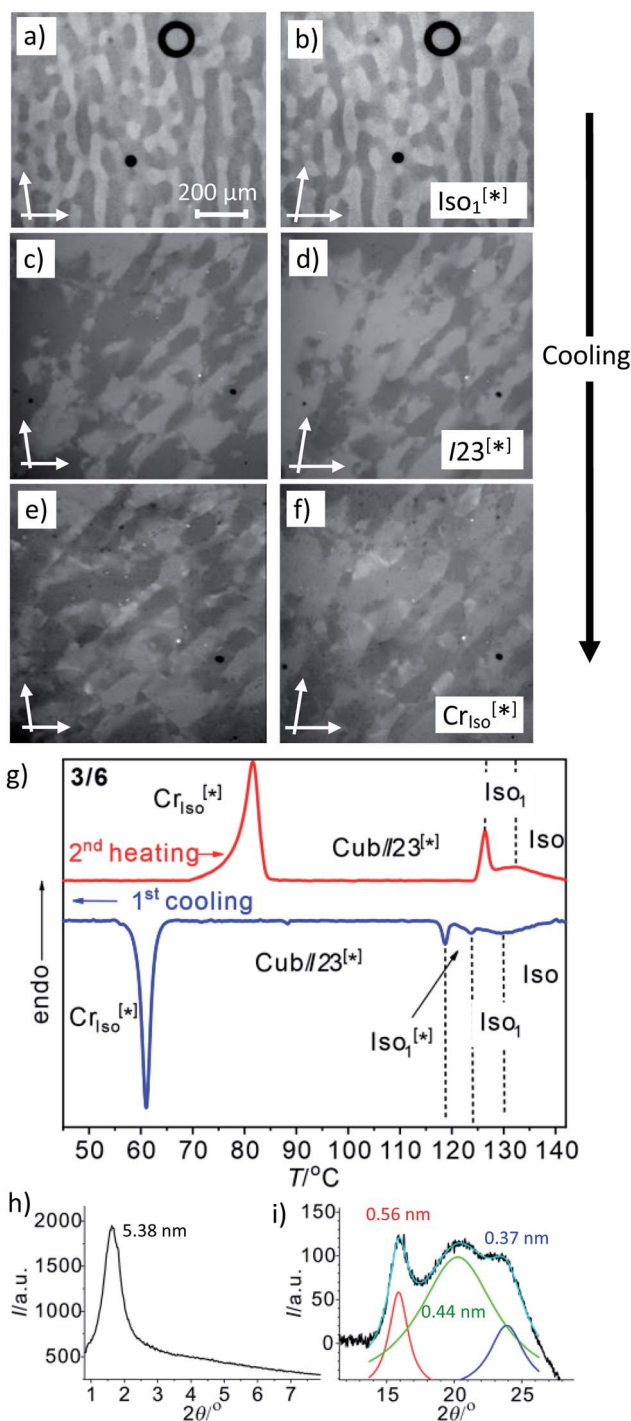


Fig. 4 The mirror symmetry broken mesophases of compound 3/6. (a–f) Conglomerates of optically active domains: (a and b) in the liquid  $\text{Iso}_1^{[*]}$  phase at 120 °C; (c and d) in the LC  $\text{Cub}_{\text{bi}}//23^{[*]}$  phase at 110 °C and (e and f) in the soft crystalline  $\text{Cr}_{\text{Iso}}^{[*]}$  phase at 60 °C, as observed on cooling between slightly uncrossed polarizers rotated by 5°; (a, c and e) in the anticlockwise and (b, d and f) in the clockwise direction (contrast enhanced). (g) DSC heating and cooling traces (10 K  $\text{min}^{-1}$ ); (h) small angle and (i) wide angle XRD pattern in the  $\text{Cr}_{\text{Iso}}^{[*]}$  phase at 50 °C (see also Fig. S12<sup>†</sup> for the complete diffraction pattern and Fig. S13<sup>†</sup> for the diffraction pattern of 3/10).

can provide giant chirality amplification,<sup>6,13</sup> the homogeneously chiral crystalline networks, once developed from these spontaneously mirror symmetry broken soft matter states, could be of interest as chiral templates for chiral recognition and separation, and the emerging field of dynamic enantioselective catalysis.<sup>37,39,40</sup>

## Conflicts of interest

There are no conflicts to declare.

## Acknowledgements

This work was supported by the Deutsche Forschungsgemeinschaft (Ts 39/24-2), the National Natural Science Foundation of China (No. 21761132033, 21774099 and 21374086) and the Science and Technology Agency of Shaanxi Province (2016KW-050 and 2018KWZ-03). The authors are grateful to Beamline BL16B1 at SSRF (Shanghai Synchrotron Radiation Facility, China) for providing the beamtime.

## References

- 1 A. Guijarro and M. Yus, *The Origin of Chirality in the Molecules of Life*, RSC, Publishing, Cambridge, 2009.
- 2 K. Soai, T. Kawasaki and A. Matsumoto, *Chem. Rec.*, 2014, **14**, 70–83.
- 3 D. B. Amabilino and R. M. Kellogg, *Isr. J. Chem.*, 2011, **51**, 1034–1040.
- 4 C. Viedma, *Phys. Rev. Lett.*, 2005, **94**, 065504; P. Cintas and C. Viedma, *Chirality*, 2012, **24**, 894–898; J. E. Hein, B. H. Cao, C. Viedma, R. M. Kellogg and D. G. Blackmond, *J. Am. Chem. Soc.*, 2012, **134**, 12629–12636.
- 5 R. R. E. Steendam, J. M. M. Verkade, T. J. B. van Benthem, H. Meekes, W. J. P. van Enckevort, J. Raap, F. P. J. T. Rutjes and E. Vlieg, *Nat. Commun.*, 2014, **5**, 5543; N. Uemura, K. Sano, A. Matsumoto, Y. Yoshida, T. Mino and M. Sakamoto, *Chem.-Asian J.*, 2019, **14**, 4150–4153.
- 6 (a) C. Tschierske, *Liq. Cryst.*, 2018, **45**, 2221–2252; (b) C. Tschierske and G. Ungar, *ChemPhysChem*, 2016, **17**, 9–26.
- 7 C. J. Brown and R. Sadanaga, *Acta Crystallogr.*, 1965, **18**, 158–164.
- 8 T. Kawasaki, Y. Harada, K. Suzuki, T. Tobita, N. Florini, G. Palyi and K. Soai, *Chem. Lett.*, 2008, **10**, 4085–4088.
- 9 Q. Shen and K. Hagen, *J. Phys. Chem.*, 1987, **91**, 1357–1360.
- 10 Z. Pawelka, A. Koll and T. Zeegers-Huyskens, *J. Mol. Struct.*, 2001, **597**, 57–66.
- 11 D. T. McLaughlin, T. P. Thao Nguyen, L. Mengnjo, C. Bian, Y. H. Leung, E. Goodfellow, P. Ramrup, S. Woo and L. A. Cuccia, *Cryst. Growth Des.*, 2014, **14**, 1067–1076.
- 12 (a) C. Dressel, F. Liu, M. Prehm, X. B. Zeng, G. Ungar and C. Tschierske, *Angew. Chem., Int. Ed.*, 2014, **126**, 13331–13336; (b) M. Alaasar, S. Poppe, Q. Dong, F. Liu and C. Tschierske, *Chem. Commun.*, 2016, **52**, 13869–13872.
- 13 (a) C. Dressel, T. Reppe, M. Prehm, M. Brautzsch and C. Tschierske, *Nat. Chem.*, 2014, **6**, 971–977; (b) C. Dressel, W. Weissfog and C. Tschierske, *Chem. Commun.*, 2015, **51**,



- 15850–15853; (c) M. Alaasar, M. Prehm, Y. Cao, F. Liu and C. Tschierske, *Angew. Chem., Int. Ed.*, 2016, **55**, 312–316; (d) M. Alaasar, S. Poppe, Q. Dong, F. Liu and C. Tschierske, *Angew. Chem., Int. Ed.*, 2017, **56**, 10801–10805.
- 14 D. R. Link, G. Natale, R. Shao, J. E. MacLennan, N. A. Clark, E. Korblova and D. M. Walba, *Science*, 1997, **278**, 1924–1927.
- 15 R. A. Reddy and C. Tschierske, *J. Mater. Chem.*, 2006, **16**, 907–961.
- 16 K. V. Le, H. Takezoe and F. Araoka, *Adv. Mater.*, 2017, 1602737.
- 17 *Bicontinuous Liquid Crystals*, ed. M. L. Lynch and P. T. Spicer, CRC Press, Taylor & Francis Group, Boca Raton, FL, 2005.
- 18 (a) S. Kutsumizu, *Isr. J. Chem.*, 2012, **52**, 844–853; (b) G. Ungar, F. Liu and X. B. Zeng, in *Handbook of Liquid Crystals*, ed. J. W. Goodby, P. J. Collings, T. Kato, C. Tschierske, H. F. Gleeson and P. Raynes, Wiley-VCH, 2nd edn, 2014, vol. 5, pp. 363–436.
- 19 Y. Yamamura, Y. Nakazawa, S. Kuzumizu and K. Saito, *Phys. Chem. Chem. Phys.*, 2019, **21**, 23705–23712.
- 20 H. T. Nguyen, C. Destrade and J. Malthete, *Adv. Mater.*, 1997, **9**, 375–388; D. W. Bruce, *Acc. Chem. Res.*, 2000, **33**, 831–840.
- 21 I. Nishiyama, *Chem. Rec.*, 2009, **9**, 340–355; M. Yoneya, *Chem. Rec.*, 2011, **11**, 66–76.
- 22 E. Nishikawa, J. Yamamoto and H. Yokoyama, *J. Mater. Chem.*, 2003, **13**, 1887–1893; E. Nishikawa and E. T. Samulski, *Liq. Cryst.*, 2000, **27**, 1463–1471; A. Yoshizawa, *Polym. J.*, 2012, **44**, 490–502; S. Kutsumizu, I. Tokiwa, A. Kawafuchi, Y. Miwa, Y. Yamamura and K. Saito, *Phys. Chem. Chem. Phys.*, 2016, **18**, 9013–9020.
- 23 A. M. Levelut and M. Clerc, *Liq. Cryst.*, 1998, **24**, 105–115.
- 24 X. B. Zeng, G. Ungar and M. Imperor-Clerc, *Nat. Mater.*, 2005, **4**, 562–567.
- 25 X. B. Zeng and G. Ungar, *J. Mater. Chem. C*, 2020, **8**, 5389–5398.
- 26 S. Debnath, H. F. Srouf, B. Donnio, M. Fourmigue and F. Camerel, *RSC Adv.*, 2012, **2**, 4453–4462.
- 27 X. B. Zeng, S. Poppe, A. Lehmann, M. Prehm, C. L. Chen, F. Liu, H. J. Lu, G. Ungar and C. Tschierske, *Angew. Chem., Int. Ed.*, 2019, **58**, 7375–7379.
- 28 This is in contrast to a previous series of rod-like molecules with only two terminal chains, forming a similar sequence  $Ia\bar{3}d-I23^{[*]}-Ia\bar{3}d$  with the growing chain length, but with an increasing  $d$ -value.<sup>18a,19</sup>
- 29 T. Reppe, C. Dressel, S. Poppe and C. Tschierske, *Chem. Commun.*, 2020, **56**, 711–713.
- 30 S. Kutsumizu, S. Miisako, Y. Miwa, M. Kitagawa, Y. Yamamura and K. Saito, *Phys. Chem. Chem. Phys.*, 2016, **18**, 17341–17344.
- 31 J. W. Goodby, D. A. Dunmur and P. J. Collings, *Liq. Cryst.*, 1995, **19**, 703–709.
- 32 H. R. Brand and H. Pleiner, *Eur. Phys. J. E*, 2017, **40**, 34.
- 33 (a) L. E. Hough, H. T. Jung, D. Krüerke, M. S. Heberling, M. Nakata, C. D. Jones, D. Chen, D. R. Link, J. Zasadzinski, G. Heppke, J. P. Rabe, W. Stocker, E. Korblova, D. M. Walba, M. A. Glaser and N. A. Clark, *Science*, 2009, **325**, 456–460; (b) L. E. Hough, M. Spannuth, M. Nakata, D. A. Coleman, C. D. Jones, G. Dantlgraber, C. Tschierske, J. Watanabe, E. Korblova, D. M. Walba, J. E. MacLennan, M. A. Glaser and N. A. Clark, *Science*, 2009, **325**, 452–456.
- 34 M. Alaasar, M. Prehm and C. Tschierske, *Chem.–Eur. J.*, 2016, **22**, 6583–6597; M. Alaasar, M. Prehm, M. Brautzsch and C. Tschierske, *J. Mater. Chem. C*, 2014, **2**, 5487–5501; M. Alaasar, M. Prehm, M. Brautzsch and C. Tschierske, *Soft Matter*, 2014, **10**, 7285–7296; M. Alaasar, M. Prehm and C. Tschierske, *Chem.–Eur. J.*, 2016, **22**, 6583–6597.
- 35 S. Shadpour, A. Nemat, N. J. Boyd, L. Li, M. E. Prevot, S. L. Wakerlin, J. P. Vanegas, M. Salamonczyk, E. Hegmann, C. Zhu, M. R. Wilson, A. I. Jakli and T. Hegmann, *Mater. Horiz.*, 2019, **6**, 959–968.
- 36 (a) A. Zep, M. Salamonczyk, N. Vaupotic, D. Pocięcha and E. Gorecka, *Chem. Commun.*, 2013, **49**, 3119–3121; (b) J. Matraszek, N. Topnani, N. Vaupotic, H. Takezoe, J. Mieczkowski, D. Pocięcha and E. Gorecka, *Angew. Chem., Int. Ed.*, 2016, **55**, 3468–3472.
- 37 Z. Shen, Y. Sang, T. Wang, J. Jiang, Y. Meng, Y. Jiang, K. Okuro, T. Aida and M. Liu, *Nat. Commun.*, 2019, **10**, 3976.
- 38 Cubic phases of bent core mesogens: R. A. Reddy, U. Baumeister, C. Keith, H. Hahn, H. Lang and C. Tschierske, *Soft Matter*, 2007, **3**, 558–570; S. Kang, M. Harada, X. Li, M. Tokita and J. Watanabe, *Soft Matter*, 2012, **8**, 1916–1922; J. Matraszek, J. Zapala, J. Mieczkowski, D. Pocięcha and E. Gorecka, *Chem. Commun.*, 2015, **51**, 5048–5051.
- 39 A. Yoshizawa and M. Kurata, *New J. Chem.*, 2019, **43**, 8865–8868.
- 40 Y. Nagata, R. Takeda and M. Sugimoto, *ACS Cent. Sci.*, 2019, **5**, 1235; S. E. Denmark, *ACS Cent. Sci.*, 2019, **5**, 1117–1119.



## Electronic Supporting Information

### **Spontaneous mirror symmetry breaking in benzil-based soft crystalline, liquid crystalline cubic and isotropic liquid phases**

Tino Reppe,<sup>a</sup> Silvio Poppe,<sup>a</sup> Xiaoqian, Cai,<sup>b</sup> Yu, Cao,<sup>b</sup> Feng Liu<sup>b\*</sup> and Carsten Tschierske<sup>a\*</sup>

<sup>a</sup> Institute of Chemistry, Martin Luther University Halle-Wittenberg, Kurt-Mothes-Straße 2, 06120 Halle, Germany. E-mail: carsten.tschierske@chemie.uni-halle.de

<sup>b</sup> State Key Laboratory for Mechanical Behaviour of Materials, Shaanxi International Research Center for Soft Matter, Xi'an Jiaotong University, Xi'an 710049, P.R. China. E-mail: feng.liu@xjtu.edu.cn

# Content

<b>1. Methods</b> .....	S3
<b>2. Additional Data</b> .....	S4
2.1 DSC traces .....	S4
2.2 Additional textures .....	S6
2.3 Additional XRD-data .....	S10
2.4 Structural data .....	S18
<b>3. Additional Figures</b> .....	S19
<b>4. Synthesis and Analytical Data</b> .....	S19
4.1 General .....	S19
4.2 General procedures .....	S20
4.3 Intermediates .....	S20
4.4 Compounds <b>2</b> and <b>4-6/n</b> .....	S21
4.5 Compounds <b>3/H</b> and <b>3/n</b> .....	S21
4.6 Representative NMR spectra .....	S26
<b>5. References</b> .....	S27

## 1. Methods

**Optical and calorimetric investigations.** Phase transitions were determined by polarizing microscopy (Leica DMR XP) in conjunction with a heating stage (FP 82 HT, Mettler) and controller (FP 90, Mettler) and by differential scanning calorimetry (DSC-7, Perkin Elmer) at heating/cooling rates of 10 K min<sup>-1</sup> (peak temperatures). If not otherwise noted transition temperatures and –enthalpies were taken from the second heating and cooling curve. Optical investigation was carried out under equilibrium conditions between glass slides which were used without further treatment, sample thickness was ~15 μm. A full wavelength retardation plate was used to determine the sign of birefringence. Optical micrographs were taken using a Leica MC120HD camera.

### X-ray diffraction.

**In-house measurements.** X-ray investigations (Kristalloflex 760H, Siemens) on powder-like samples were carried out using Ni filtered CuKα radiation (15 to 30 min exposure time). The samples were prepared in the isotropic state on a glass plate and cooled (rate: 5 K·min<sup>-1</sup>) to the measuring temperature. The samples were held on a temperature controlled heating stage and the diffraction patterns were recorded with a 2D detector (Vantec 500, Bruker); exposure time was 15-20 min. The sample-detector distance for the samples was 9.00 cm for WAXD and 26.90 cm for SAXD measurements. The diffraction patterns obtained were transform to 1D plots using GADDS over the full Chi range.

### Synchrotron XRD

**Synchrotron X-ray diffraction and electron density reconstruction.** - High-resolution small-angle powder diffraction experiments were recorded on Beamline BL16B1 at Shanghai Synchrotron Radiation Facility, SSRF. Samples were held in evacuated 1 mm capillaries. A Linkam hot stage with a thermal stability within 0.2 °C was used, with a hole for the capillary drilled through the silver heating block and mica windows attached to it on each side. A MarCCD detector was used. *q* calibration and linearization were verified using several orders of layer reflections from silver behenate and a series of *n*-alkanes. The measurement of the positions and intensities of the diffraction peaks is carried out using Galactic PeakSolve™ program, where experimental diffractograms are fitted using Gaussian shaped peaks. The diffraction peaks are indexed on the basis of their peak positions, and the lattice parameters and the plane/space groups are subsequently determined.

### The reconstructed electron density map of Cubic phases

The electron density  $E(xyz)$  can be generated by structural factor  $F(hkl)$  with Fourier transform

$$E(xyz) = \sum_{hkl} F(hkl) \exp[i2\pi(hx+ky+lz)] \quad (\text{Eqn. 1})$$

Here,  $F(hkl)$  is a complex number with real part  $A(hkl)$  and imaginary part  $B(hkl)$ .  $F(hkl)$  is related with observed scattering intensity  $I$ .

$$F(hkl) = |F(hkl)| \exp[i\phi(hkl)] = \sqrt{I(hkl)} \exp[i\phi(hkl)] \quad (\text{Eqn. 2})$$

Thus, the equation 1 can be rewritten as

$$E(xyz) = \sum_{hkl} \sqrt{I(hkl)} [A(hkl)\cos\phi(hkl) + B(hkl)\sin\phi(hkl)] \quad (\text{Eqn. 3})$$

Where  $\phi(hkl)$  is the phase. For centrosymmetric phase, e.g.  $Ia3d$ ,  $\phi(hkl)$  is either 0 or  $\pi$ , which makes it possible for a trial and error approach. The correct phase combination is determined by the proper physical merit.

However, for non-centrosymmetric phase, such as  $I23$ ,  $\phi(hkl)$  is arbitrary between 0 and  $\pi$ . Taking the model from a relevant work,<sup>S2</sup> we applied similar phases and intensity distributions on the phases we studied in this work.



## 2. Additional Data

### 2.1 DSC traces

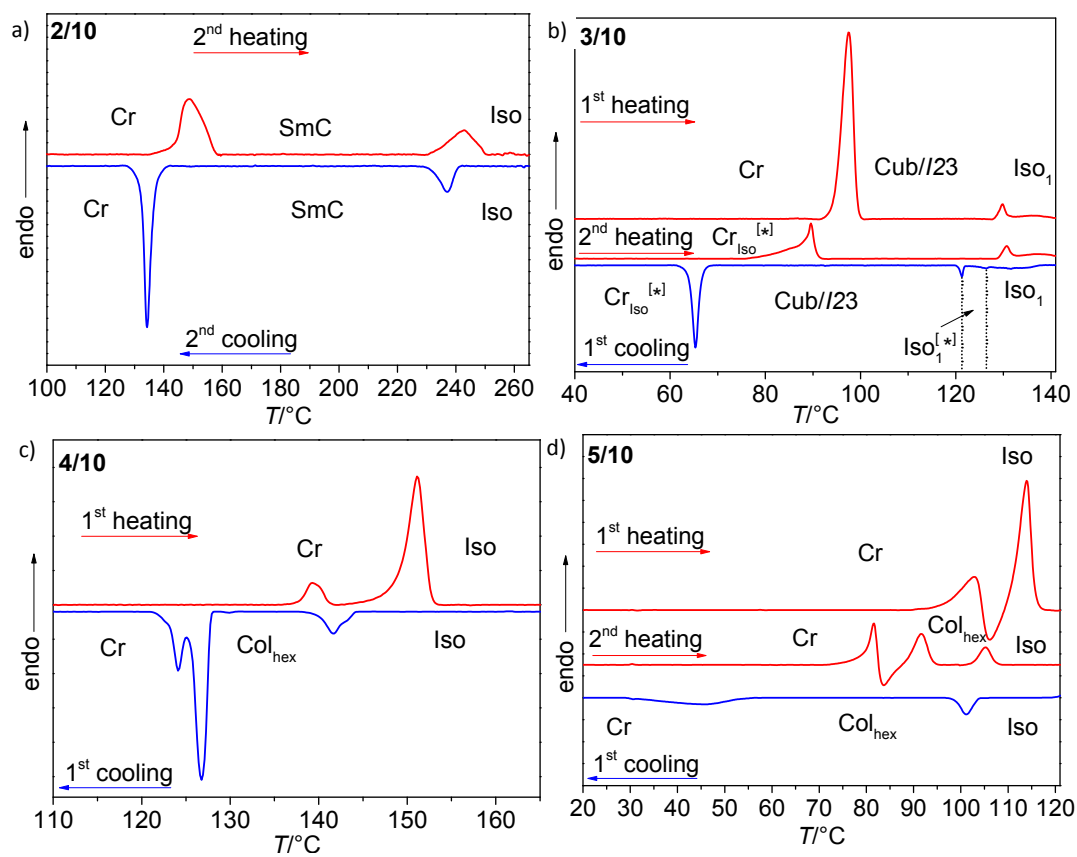


**Figure S1.** DSC heating and cooling traces of compounds **2/10-5/10** recorded at 10 K min<sup>-1</sup>.

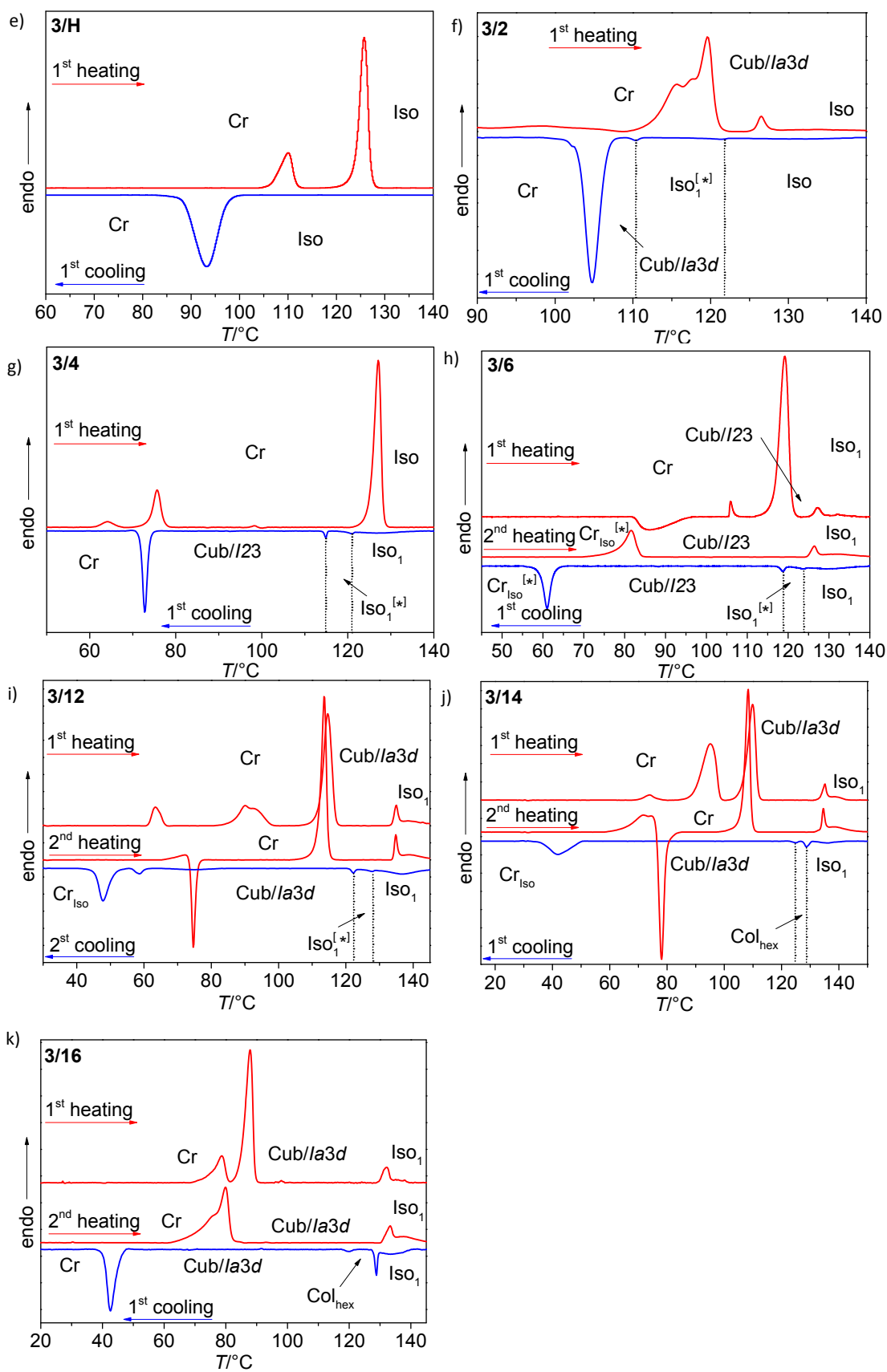


**Figure S1** (continued). DSC heating and cooling traces of compounds **3/n** as recorded at  $10 \text{ K min}^{-1}$ .

**Table S1.** Temperature ranges of the Iso-Iso<sub>1</sub> transitions.

$3/n$	heating $T/^{\circ}\text{C}$ [ $\Delta H$ kJ mol <sup>-1</sup> ]	cooling $T/^{\circ}\text{C}$ [ $\Delta H$ kJ mol <sup>-1</sup> ]
<b>3/2</b>	Iso <sub>1</sub> 129-146 [2.8] Iso	Iso 144-122 [2.7] Iso <sub>1</sub>
<b>3/4</b>	-	Iso 140-123 [4.5] Iso <sub>1</sub>
<b>3/6</b>	Iso <sub>1</sub> 124-152 [5.7] Iso	Iso 149-116 [7.1] Iso <sub>1</sub>
<b>3/10</b>	Iso <sub>1</sub> 128-147 [5.7] Iso	Iso 144-120 [5.9] Iso <sub>1</sub>
<b>3/12</b>	Iso <sub>1</sub> 136-151 [6.2] Iso	Iso 150-129 [8.9] Iso <sub>1</sub>
<b>3/14</b>	Iso <sub>1</sub> 131-152 [7.2] Iso	Iso 153-120 [9.2] Iso <sub>1</sub>
<b>3/16</b>	135-148 [6.1] Iso	Iso 146-131 [6.0] Iso <sub>1</sub>

## 2.2 Additional textures

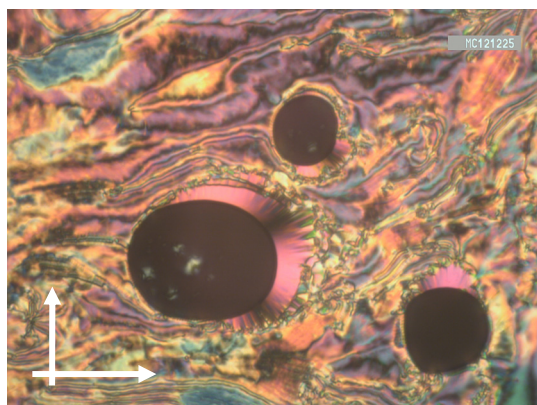


**Figure S2.** Textures of the (synclinic) SmC phase of **2/10** at 230 °C, showing the Schlieren texture and a fan-like texture around the air bubbles (black dots); the direction of the extinctions indicates a synclinic tilt of about 35 °; the arrows indicate the orientation of polarizer and analyzer; the width of the POM image is 0.8 mm.

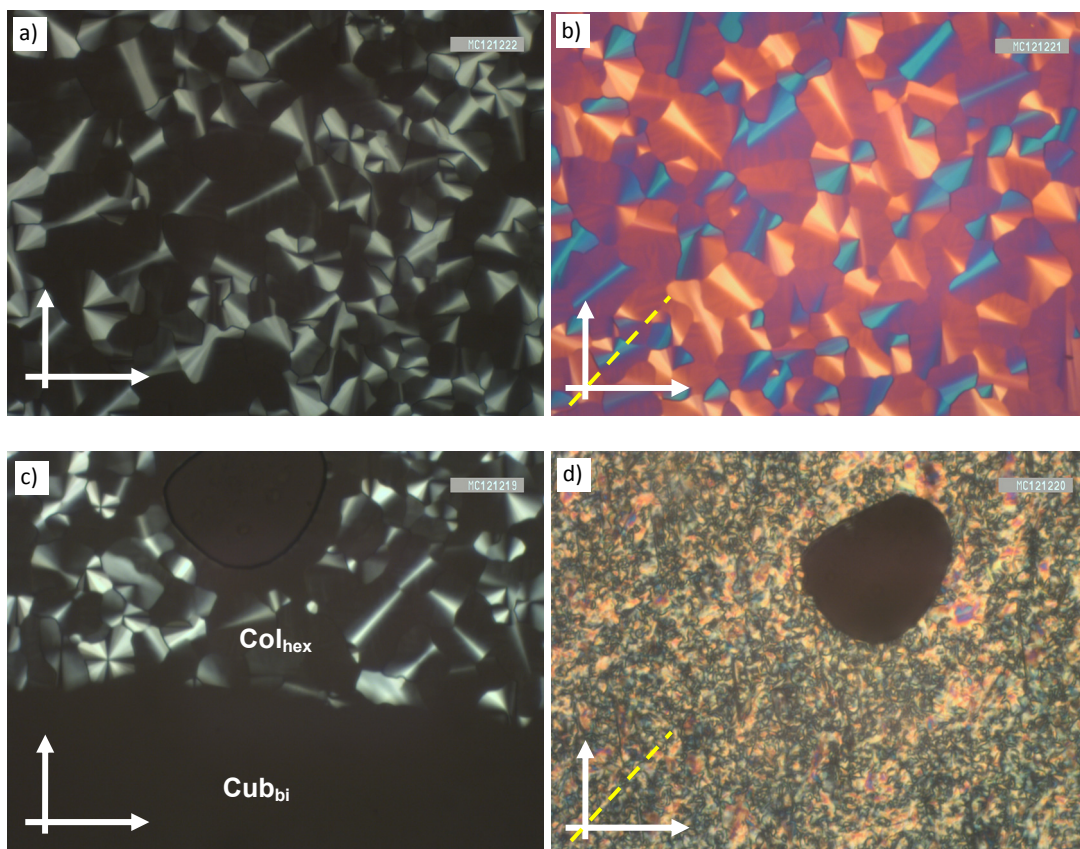


**Figure S3.** Textures of the  $\text{Col}_{\text{hex}}$  phase of **4/10** at 142 °C, a) between crossed polarizers (the dark areas represent homeotropic (optically isotropic) regions where the columns are perpendicular to the substrate surfaces, confirming the uniaxiality of the columnar phase) and b) with additional  $\lambda$ -retarder plate (the indicatrix direction is SW-NE), indicating negative birefringence and confirming an alignment of the  $\pi$ -conjugated aromatic cores with their long axes on average perpendicular to the column long axes; c) shows the transition to the  $\text{Cub}_{\text{bi}}/Ia\bar{3}d$  phase at  $T = 141$  °C, immediately followed by d) crystallization of the sample at the same temperature; the width of the POM images is 0.8 mm.

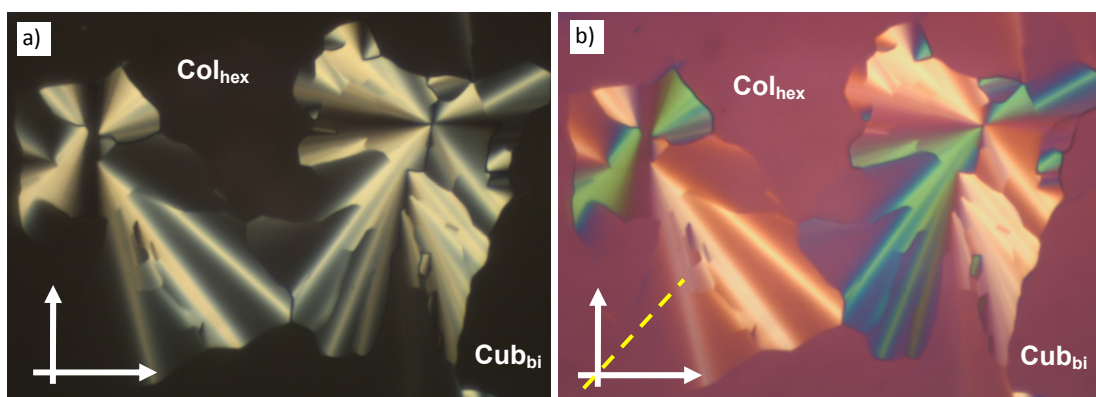


**Figure S4.** Textures of the  $\text{Col}_{\text{hex}}$  and  $\text{Cub}_{\text{bi}}/Ia\bar{3}d$  phases of **3/16** at 123 °C a) between crossed polarizers (the dark at the left areas represent homeotropic (optically isotropic) regions where the columns are perpendicular to the substrate surfaces, confirming the uniaxiality of the columnar phase; the dark area at the right is the growing  $\text{Cub}_{\text{bi}}/Ia\bar{3}d$  phase) and b) with additional  $\lambda$ -retarder plate (the indicatrix direction, shown as yellow dotted line is SW-NE) indicating negative birefringence and confirming an alignment of the  $\pi$ -conjugated aromatic cores with their long axes on average perpendicular to the column long axes; the width of the POM images is 0.8 mm.

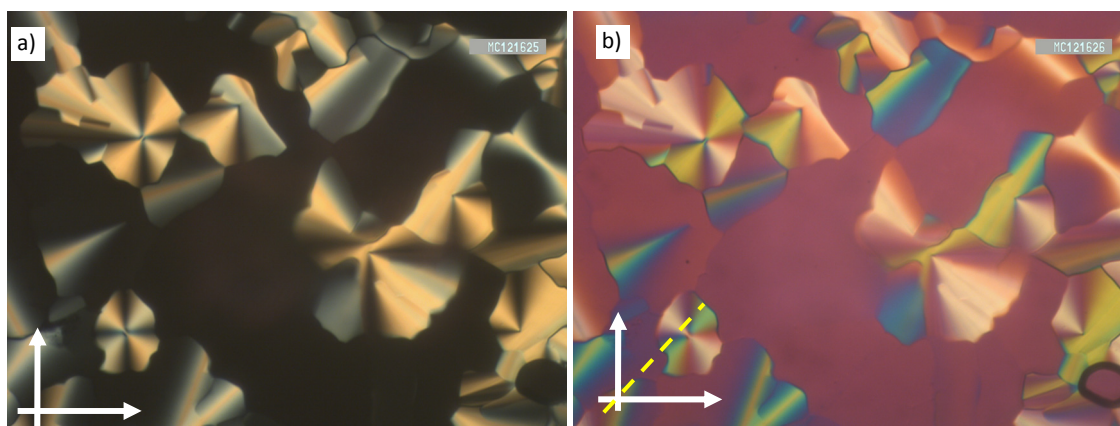


**Figure S5.** Textures of the  $\text{Col}_{\text{hex}}$  phase of **5/10** at 100 °C a) between crossed polarizers (the dark at the left areas represent homeotropic (optically isotropic) regions confirming the uniaxiality of the columnar phase; b) with additional  $\lambda$ -retarder plate indicating negative birefringence. The width of the POM images is 0.8 mm.



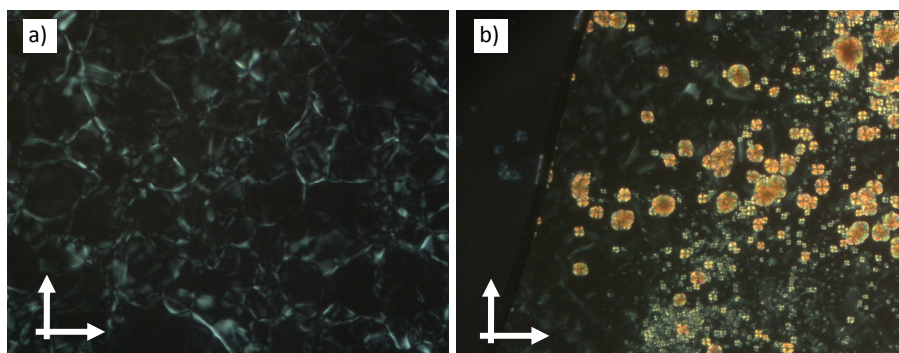


**Figure S6.** a) Achiral  $Cr_{Iso}$  phase of **3/12** at 35 °C; the weak birefringence, occurring already in the  $Cub_{bi}/Ia\bar{3}d$  phase at 80 °C is most likely due to a strain between the cubic domains arising on cooling; b) shows the crystallization of the birefringent Cr phase from the  $Cr_{Iso}$  phase of **3/14**; the width of the POM images is 0.8 mm.



## 2.3 Additional XRD-data

### 2.3.1 Cub<sub>bi</sub> phases

**Table S2.** SAXS data of the Cub<sub>bi</sub>/*Ia* $\bar{3}d$  phases of the investigated compounds.

Compd.	( <i>hkl</i> )	$d_{\text{obs}}$ – spacing/nm	$d_{\text{calc}}$ – spacing/nm	$d_{\text{obs}} - d_{\text{calc}}$	$a_{\text{cub}}$ /nm ( <i>T</i> /°C)
<b>3/2</b>	(211)	5.28	5.28	0.00	12.92 (122)
	(220)	4.60	4.57	0.03	
<b>3/12</b>	(211)	4.65	4.65	0.00	11.38 (125)
	(220)	4.05	4.02	0.03	
<b>3/14</b>	(211)	4.63	4.63	0.00	11.34 (125)
	(220)	4.03	4.01	0.02	
<b>3/16</b>	(211)	4.70	4.70	0.00	11.51 (120)
	(220)	4.10	4.07	0.03	

**Table S3.** SAXS data of Cub<sub>bi</sub>/*I23*<sup>[\*]</sup> phases of the investigated compounds.

Compd.	( <i>hkl</i> )	$d_{\text{obs}}$ – spacing/nm	$d_{\text{calc}}$ – spacing/nm	$d_{\text{obs}} - d_{\text{calc}}$	$a_{\text{cub}}$ /nm ( <i>T</i> /°C)
<b>3/4</b>	(321)	4.92	4.92	0.00	18.39 (110)
	(400)	4.55	4.60	0.05	
	(420)	4.06	4.11	0.05	
<b>3/6</b>	(321)	4.84	4.84	0.00	18.12 (123)
	(400)	4.54	4.53	0.01	
	(420)	4.13	4.05	0.08	
<b>3/10</b>	(321)	4.92	4.92	0.00	18.42 (110)
	(400)	4.57	4.60	0.03	
	(420)	4.16	4.12	0.04	

**Table S4.** Experimental and calculated  $d$ -spacings, relative integrated intensities for the  $\text{Cub}/I23^{[*]}$  phase of  $3/4$  at  $110\text{ }^\circ\text{C}$  from synchrotron-based SAXS. All intensities values are Lorentz and multiplicity corrected. The phases and intensities used in the reconstruction of the electron density map of the  $\text{Cub}_{\text{bi}}/I23$  phase is based on the results from reference S2.

$(hkl)$	$d_{\text{obs.}}$ - spacings (nm)	$d_{\text{cal.}}$ - spacings (nm)	$intensity$	$phase$
(110)	12.88	12.98	0.01	/
(211)	7.48	7.49	0.06	/
(220)	6.48	6.49	0.09	/
(310)	5.80	5.80	0.77	0
(222)	5.30	5.30	9.68	$-0.24\pi$
(321)	4.90	4.90	30.21	$-0.91\pi$
(312)			66.83	$-0.59\pi$
(400)	4.59	4.59	100.00	0
(330)	4.33	4.33	1.81	0
(411)			1.71	$-0.81\pi$
(420)	4.11	4.10	15.54	0
(332)	3.91	3.91	0.06	/
(422)	3.75	3.75	1.05	/
(431)	3.60	3.60	0.38	/
(510)			0.75	/
(432)	3.35	3.41	0.24	/
(440)	3.25	3.24	0.06	/
(433)	3.15	3.15	0.12	/
(530)			0.12	/
(442)	3.06	3.06	0.10	/
(600)			0.41	/
(532)	2.98	2.98	0.10	/
(611)			0.21	/
(620)	2.91	2.90	0.05	/
(541)	2.84	2.83	0.17	/
(622)	2.77	2.77	0.02	/

(631)	2.71	2.71	0.11	/
(444)	2.65	2.65	0.84	/
(543)	2.60	2.60	0.03	/
(550)			0.10	/
(710)			0.05	/
(640)	2.55	2.54	0.23	/
(552)	2.50	2.50	0.24	/
(633)			0.24	/
(721)			0.12	/
(642)	2.46	2.45	0.02	/
(730)	2.41	2.41	0.04	/
(651)	2.33	2.33	0.01	/
(732)			0.01	/
(800)	2.26	2.29	0.39	/
(660)	2.14	2.16	0.09	/
(840)	2.03	2.05	0.05	/
(833)	2.00	2.03	0.02	/
(910)			0.02	/
(842)	1.98	2.00	0.02	/
(655)	1.96	1.98	0.01	/
(761)			0.01	/
(664)	1.94	1.96	0.08	/
(844)	1.86	1.87	0.05	/
(770)	1.84	1.85	0.06	/
(860)	1.82	1.84	0.04	/
(862)	1.79	1.80	0.01	/
$a_{\text{cub}} = 18.35 \text{ nm}$				

**Table S5.** Experimental and calculated  $d$ -spacings, relative integrated intensities, and phases used in the reconstruction of electron densities for the  $Cub/Ia\bar{3}d$  phase of **3/16** at 110°C from synchrotron-based SAXS. All intensities values are Lorentz and multiplicity corrected.

$(hkl)$	$d_{\text{obs.}}$ - spacings (nm)	$d_{\text{cal.}}$ - spacings (nm)	$intensity$	$phase$
(211)	4.74	4.74	100.00	$\pi$
(220)	4.11	4.11	25.94	$\pi$
(321)	3.11	3.11	0.06	0
(400)	2.91	2.91	1.07	$\pi$
(332)	2.48	2.48	0.41	$\pi$
(422)	2.38	2.37	0.46	0
(532)	1.89	1.89	0.03	/
(611)			0.05	/
(543)	1.64	1.64	0.03	/
$a_{\text{cub}} = 11.62 \text{ nm}$				

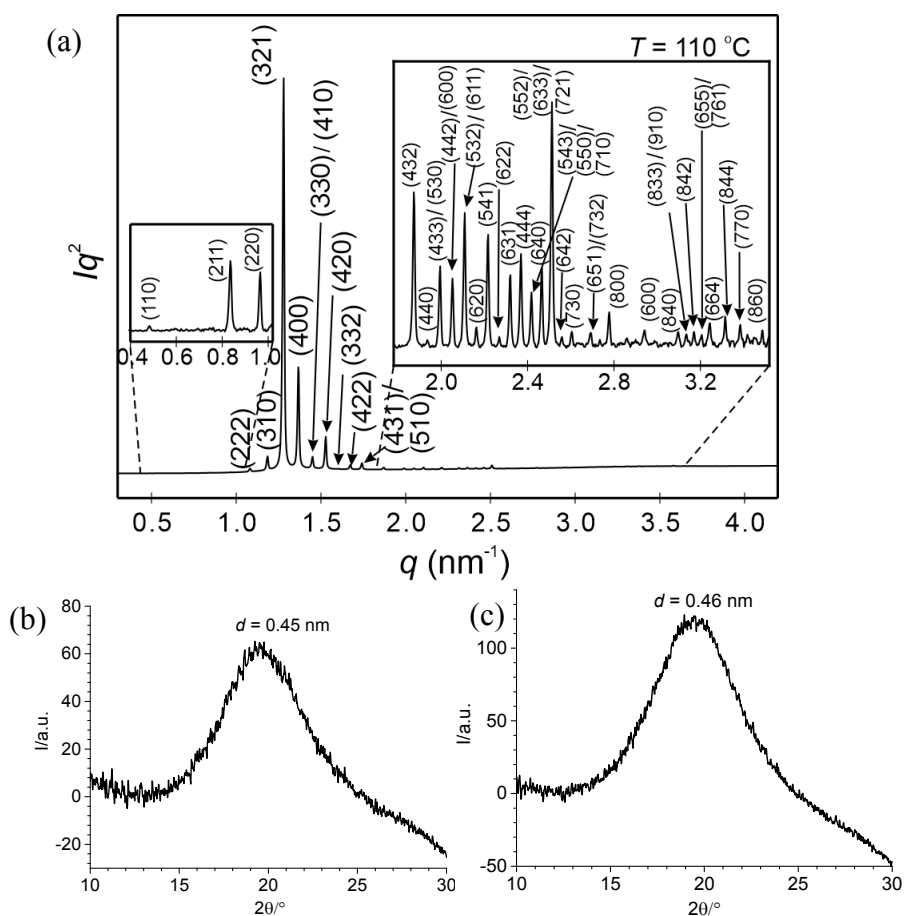


**Figure S7.** a) and b) SAXS/WAXS diffractogram of the  $I23^{[*]}$  phase of **3/4** at 110 °C; c) WAXS diffractogram of the  $Ia\bar{3}d$  phase of **3/16** at 120 °C.

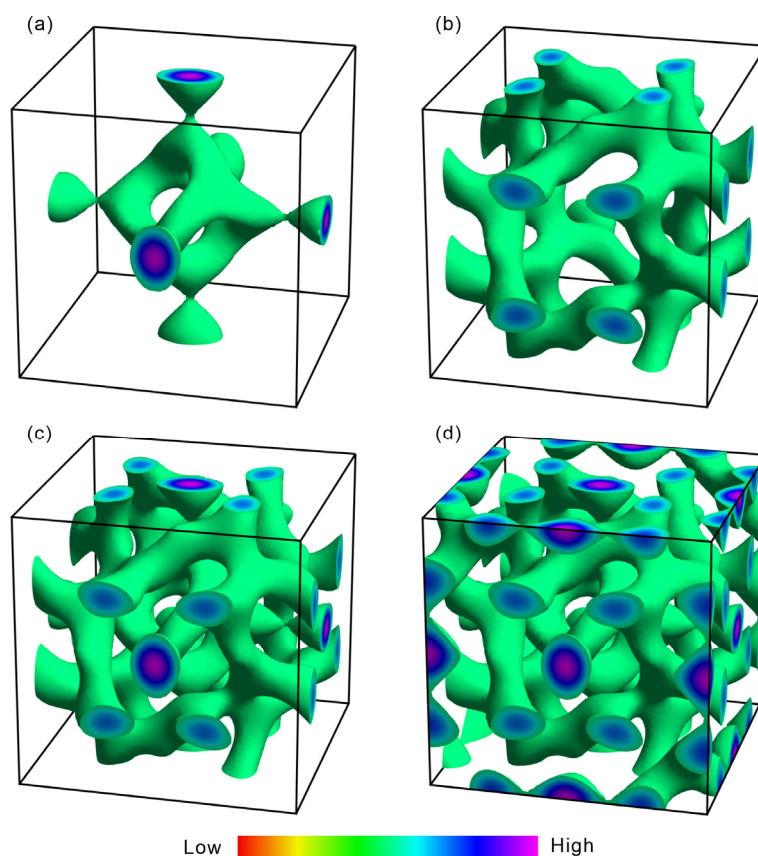


**Figure S8.** Reconstructed electron density maps of the triple network cubic phase with space group symmetry  $I23$ . The green isosurfaces enclose the high electron density (blue/purple, aromatic cores) regions of the 3D electron density map: (a) Inner network; (b) middle network; (c) inner and middle networks; (d) inner, middle and outer networks. The low electron density (red/yellow, alkyl chains) regions are omitted for clarifying the networks.

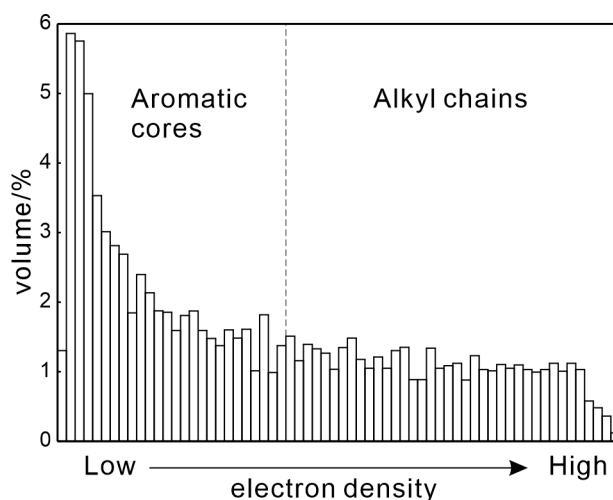


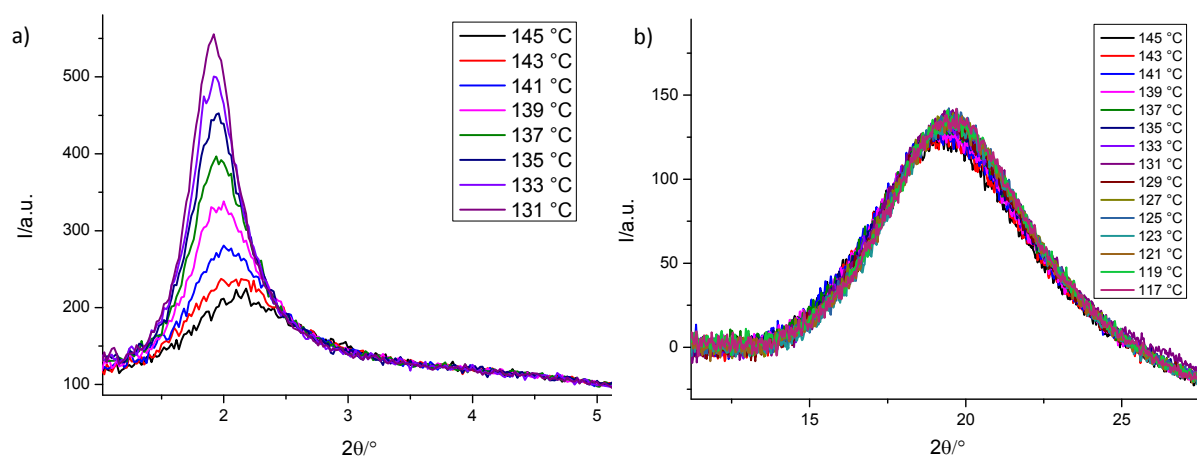
**Figure S9.** The electron density histogram of the  $Ia\bar{3}d$  phase of compound **3/16**, calculated based on the phase combination listed in Table S5. The volume ratio of high and low electron density region is 0.4:0.6 for aromatic cores and alkyl tails, respectively.

### 2.3.2 Smectic and columnar phases

**Table S6.** SAXS data of the smectic and columnar phases.

Compd.	Phase	( <i>hk</i> )	$d_{\text{obs}}$ – spacing/nm	$a/\text{nm}$ ( $T/^\circ\text{C}$ )
<b>2/10</b>	SmC	10	3.66	3.66 (170)
<b>3/14</b>	Col <sub>hex</sub>	10	4.41	5.09 (131)
<b>5/10</b>	Col <sub>hex</sub>	10	4.39	4.39 (95)

### 2.3.3 Isotropic mesophases

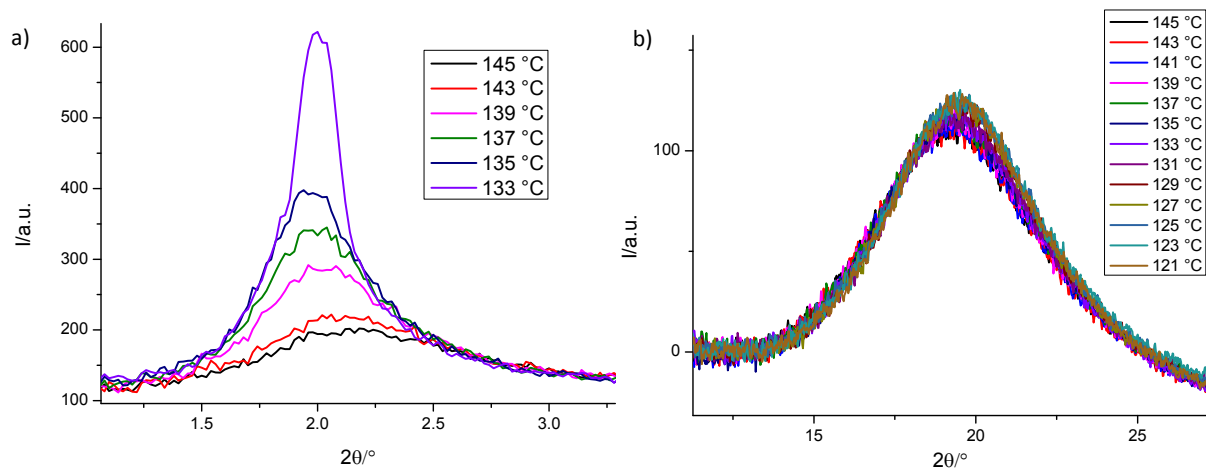


$T/^\circ\text{C}$	$2\theta/^\circ$	$\theta/^\circ$	$\theta/\text{rad}$	$d/\text{nm}$	$\text{FWHM}/^\circ$	$\zeta/\text{nm}$
145	2.203	1.101	0.019	4.011	0.81	24
143	2.132	1.066	0.019	4.143	0.73	25
141	2.075	1.038	0.018	4.257	0.64	27
139	2.023	1.011	0.018	4.368	0.58	29
137	1.987	0.994	0.017	4.445	0.50	32
135	1.962	0.981	0.017	4.504	0.44	36
133	1.943	0.972	0.017	4.546	0.48	33
131	1.927	0.963	0.017	4.585	0.44	35

$\zeta$  – correlation length in nm, determined with the Scherrer-equation

**Figure S10.** a) SAXS patterns in the the isotropic mesophase of **3/12** on cooling from 145 to 131 °C with numerical values in the table; below 131 °C the cubic phase is formed during exposure time; b) WAXS on cooling from 145-117 °C (steps of 2K).





$T/^\circ\text{C}$	$2\theta/^\circ$	$\theta/^\circ$	$\theta/\text{rad}$	$d/\text{nm}$	$\text{FWHM}/^\circ$	$\zeta/\text{nm}$
145	2.232	1.116	0.019	3.958	0.78	26
143	2.175	1.088	0.019	4.061	0.71	27
141	2.139	1.069	0.019	4.131	0.66	28
139	2.070	1.035	0.018	4.268	0.59	29
137	2.023	1.011	0.018	4.367	0.49	34
135	1.997	0.999	0.017	4.424	0.46	35
133	1.995	0.998	0.017	4.428	0.26	63

$\zeta$  – correlation length in nm, determined with the Scherrer-equation

**Figure S11.** a) SAXS patterns in the the isotropic mesophases of **3/14** on cooling from 145 to 133 °C with numerical values in the table; b) WAXS on cooling from 145-121 °C (steps of 2K).

### 2.3.4 Crystalline mesophase

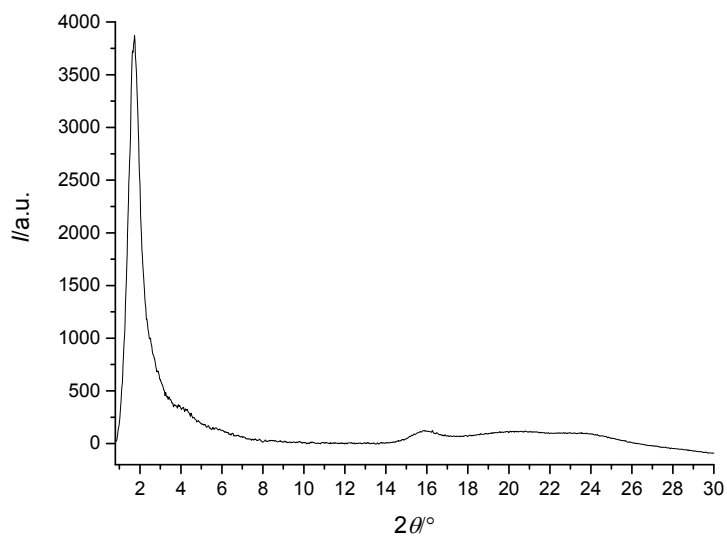


**Figure S12.** Full range XRD pattern of the crystalline isotropic mesophase ( $\text{Cr}_{\text{iso}}^{[*]}$ ) of **3/6** at 50 °C.

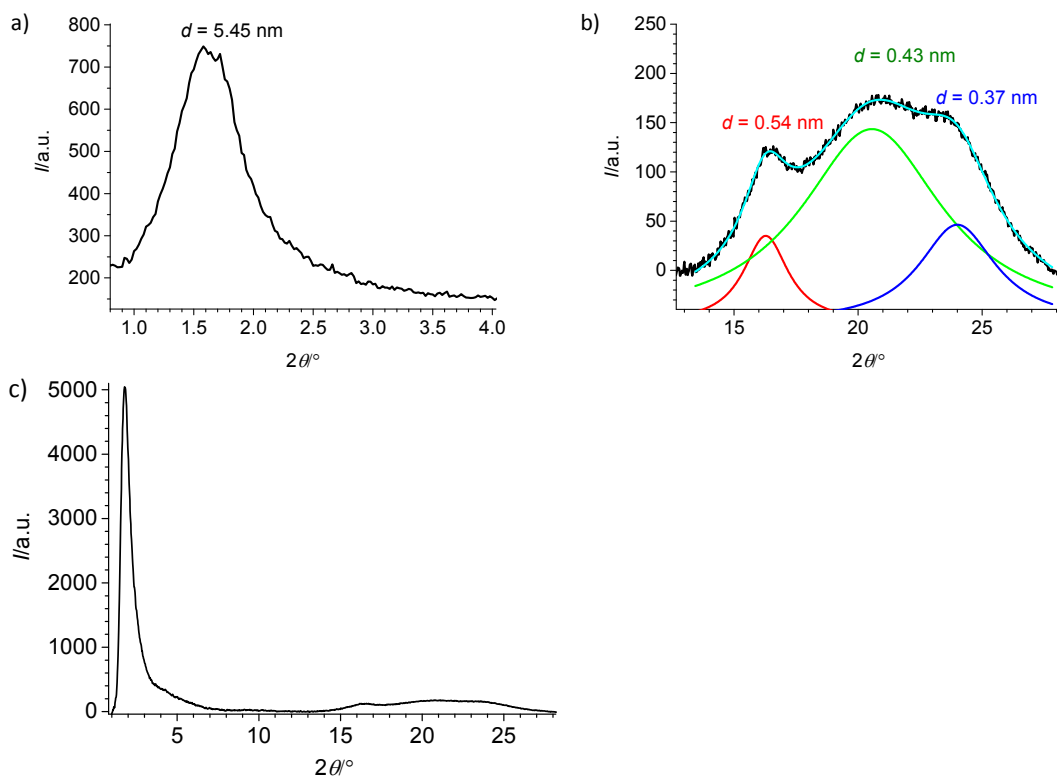


**Figure S13.** a) SAXS and b) WAXS pattern and c) full range XRD pattern of the conglomerate type chiral crystalline isotropic mesophase ( $Cr_{iso}^{[*]}$ ) of **3/10** at 25 °C.

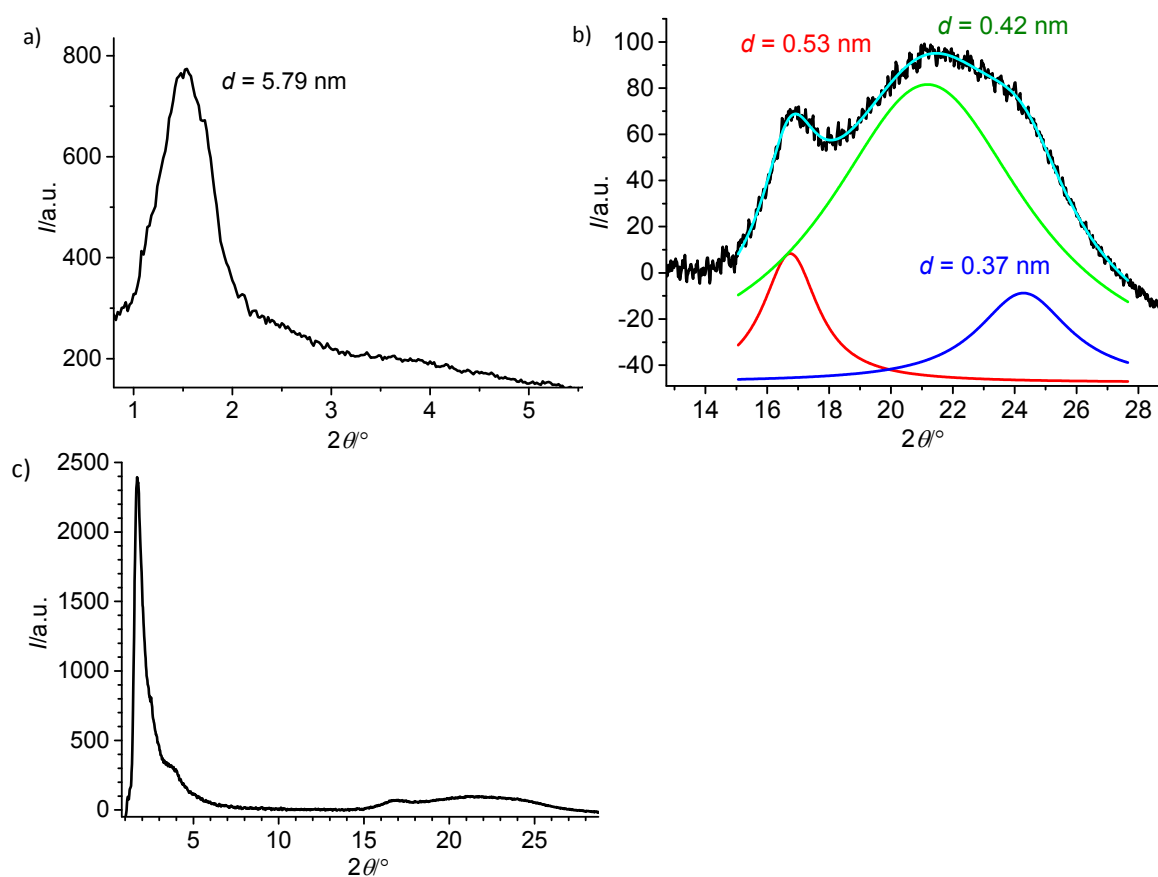


**Figure S14.** a) SAXS and b) WAXS pattern and c) full range XRD pattern of the achiral crystalline isotropic mesophase ( $Cr_{iso}$ ) of **3/12** at 25 °C.

## 2.4 Structural data

**Table S7.** Structural data of the cubic phases of the investigated compounds.<sup>a</sup>

Compd.	Phase	$a_{\text{cub}}/\text{nm}$	$V_{\text{cell}}/\text{nm}^3$	$V_{\text{mol}}/\text{nm}^3$	$n_{\text{cell}}^{\text{b}}$	$L_{\text{net}}^{\text{c}}/\text{nm}$	$n_{\text{strat}}^{\text{d}}$	$\Phi/^\circ$ <sup>e</sup>
<b>3/2</b>	<i>Ia3d</i>	12.9	2147	1.59	1206	109.5	5.0	6.9
<b>3/4</b>	<i>I23</i>	18.4	6230	1.64	3392	380.5	4.0	7.6
<b>3/6</b>	<i>I23</i>	18.1	5930	1.69	3133	374.3	3.8	7.7
<b>3/10</b>	<i>I23</i>	18.4	6230	1.79	3108	380.5	3.7	7.6
<b>3/12</b>	<i>Ia3d</i>	11.4	1482	1.84	719	96.7	3.3	7.9
<b>3/14</b>	<i>Ia3d</i>	11.3	1443	1.89	681	95.9	3.2	7.9
<b>3/16</b>	<i>Ia3d</i>	11.5	1521	1.94	700	97.6	3.2	7.8

<sup>a</sup> Abbreviations:  $n_{\text{cell}}$  number of molecules in a unit cell;  $V_{\text{cell}} = a_{\text{cub}}^3$  = volume of the unit cell;  $V_{\text{mol}}$  = molecular volume as calculated with the crystal volume increments of Immirzi;<sup>S1</sup>;  $L_{\text{net}}$  = total network length per unit cell;  $n_{\text{strat}}$  = number of molecules organized side by side in each 0.45 nm high stratum of the column segments;  $\Phi$  = twist angle between adjacent molecules in the networks of the *Ia3d*- phases; <sup>b</sup> calculated according to  $0.893 V_{\text{cell}}/V_{\text{mol}}$ , where the factor 0.893 is a correction for the different packing density in the crystalline and the LC state; <sup>c</sup>  $L_{\text{net}}$  = total network length, calculated as  $L_{\text{net}} = 20.68 a_{I23}$ ;  $L_{\text{net}} = 8.485 a_{Ia3d}$ ; <sup>S2</sup> <sup>e</sup> calculated according to  $n_{\text{cell}}/(L_{\text{net}}/0.45)$  for an assumed height of each stratum of  $h = 0.45$  nm; <sup>c</sup> calculated according to:  $\Phi(Ia3d) = 70.5^\circ/[0.354a_{\text{cub}}/0.45\text{nm}]$ ;  $\Phi(I23) = 90^\circ/[0.290a_{\text{cub}}/0.45\text{nm}]$ ; though  $\Phi(I23)$  refers to the inner and outer networks, the average twist in the middle network, consisting of shorter and longer segments is less than 1 % smaller.<sup>S2</sup>

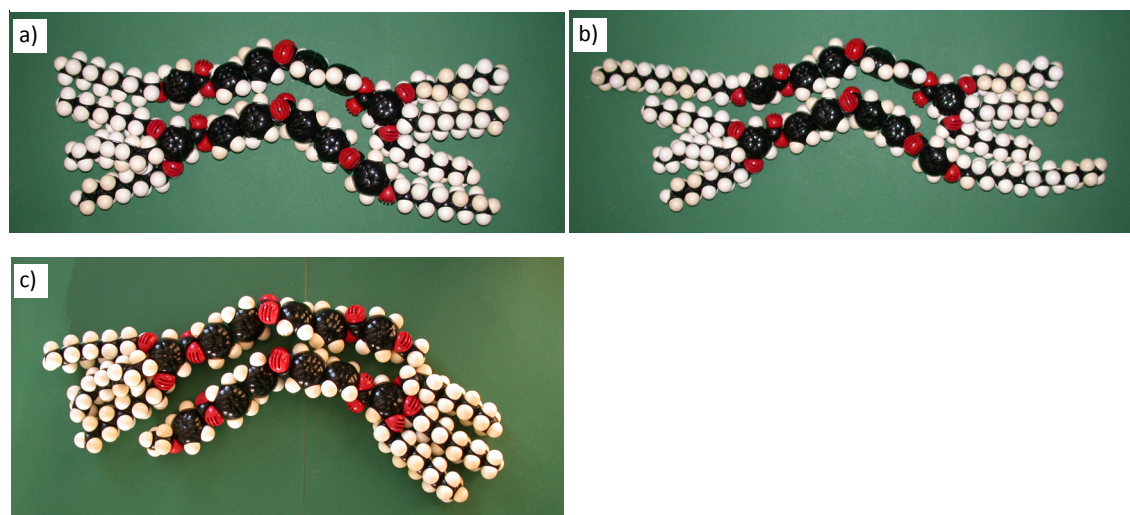


**Figure S15.** Space filling models of antiparallel pairs of compound a) **3/10** ( $L = 5.5$  nm), b) **3/16** ( $L = 5.5 + 1.6$  nm for the overhangs of the longer chains) and c) **3/2** ( $L = 5.5$  nm).

### 3. Additional Figures

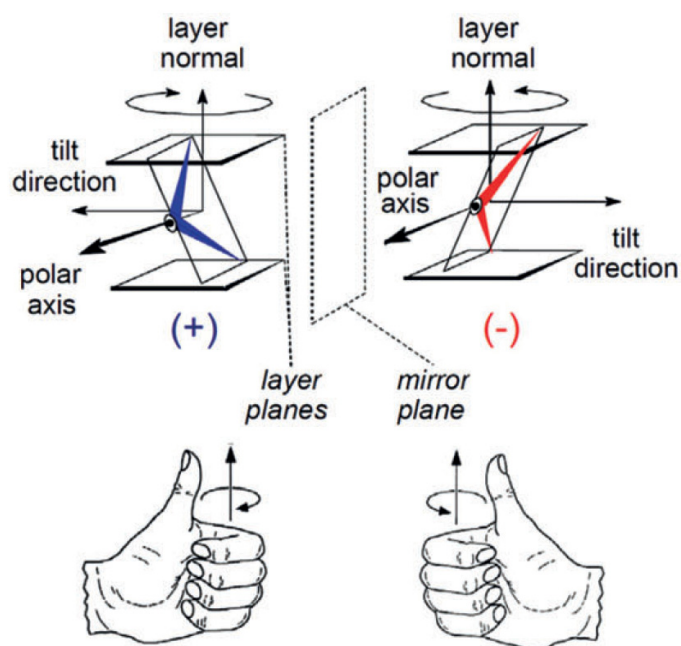


**Figure S16.** Layer chirality in the polar SmC phases of bent-core mesogens. The orthogonal combination of tilt and polar order leads to reduced  $C_{2v}$  symmetry and superstructural chirality of the layers (adapted from ref.<sup>S3</sup>); blue/red color indicates the chirality sense.

## 4. Synthesis and Analytical Data

### 4.1 General

Unless otherwise noted, all starting materials were purchased from commercial sources and were used without further purification. Column chromatography was performed with silica gel 60 (63-200  $\mu\text{m}$ , Fluka). Determination of structures and purity of intermediates and products was obtained by NMR spectroscopy (VARIAN Gemini 2000 and Unity Inova 500, all spectra were recorded at 27  $^{\circ}\text{C}$ ). Microanalyses were performed using a CARLO Erba-CHNO 1102 elemental analyzer. The purity of all products was checked with thin layer chromatography (silicagel 60 F254, Merck).  $\text{CHCl}_3$  and  $\text{CHCl}_3/n$ -hexane mixtures were used as eluents and the spots were detected by UV radiation. 4-Hydroxyphenylboronic acid pinacol ester, 1,2-bis(4-bromophenyl)-1,2-ethanedione and 1,2-bis(4-hydroxyphenyl)-1,2-ethanedione were purchased from Sigma Aldrich and used as received. The 4-alkoxybenzoic acids were available from previous synthesis in our laboratory and have been synthesized by alkylation of ethyl 4-hydroxybenzoate followed by saponification.

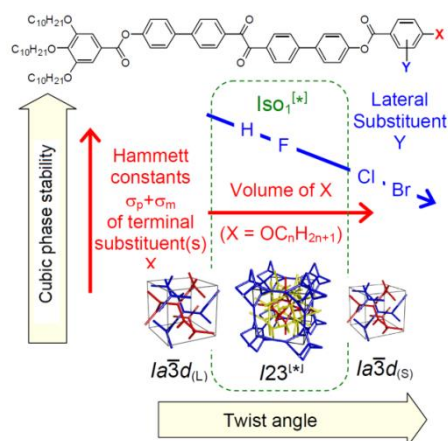


## Publikation E

### Controlling mirror symmetry breaking and network formation in liquid crystalline cubic, isotropic liquid and crystalline phases of benzil-based polycatenars

Tino Reppe,<sup>[a]</sup> Silvio Poppe,<sup>[a]</sup> Carsten Tschierske<sup>[a]</sup>

[a] Institute of Chemistry, Martin Luther University Halle-Wittenberg, Kurt-Mothes-Straße 2, 06120 Halle, Germany.



#### Abstract

Spontaneous development of chirality in systems composed of achiral molecules is important for new routes to asymmetric synthesis, chiral superstructures and materials, as well as for the understanding of the mechanisms of emergence of prebiotic chirality. Herein it is shown that the 4,4'-diphenylbenzil unit is a universal transiently chiral bent building block for the design of multi-chained (polycatenar) rod-like molecules capable of forming a wide variety of helically twisted network structures in the liquid, the liquid crystalline (LC) and the crystalline state. Single polar substituents at the apex of tricatenaar molecules support the formation of the achiral (racemic) cubic double network phase with *Ia*3*d* symmetry and relatively small twist along the networks. The combination of an alkyl chain with fluorine substitution leads to the homogeneously chiral triple network phase with *I*2*3* space group, and in addition, provides a mirror symmetry broken liquid and also a crystalline conglomerate. Replacing F by Cl or Br further increases the twist, leading to a short pitch double gyroid *Ia*3*d* phase which is achiral again. The effects of the structural variations on the network structures, either leading to achiral phases or chiral conglomerates are analyzed.

#### Referenz

T. Reppe, S. Poppe, C. Tschierske, *Chem. Eur. J.*, **2020**, *26*, 16066–16079.  
DOI:10.1002/chem.202002869.



## Chirality | Hot Paper |

# Controlling Mirror Symmetry Breaking and Network Formation in Liquid Crystalline Cubic, Isotropic Liquid and Crystalline Phases of Benzil-Based Polycatenars

Tino Reppe, Silvio Poppe, and Carsten Tschierske\*<sup>[a]</sup>

**Abstract:** Spontaneous development of chirality in systems composed of achiral molecules is important for new routes to asymmetric synthesis, chiral superstructures and materials, as well as for the understanding of the mechanisms of emergence of prebiotic chirality. Herein, it is shown that the 4,4'-diphenylbenzil unit is a universal transiently chiral bent building block for the design of multi-chained (polycatenar) rod-like molecules capable of forming a wide variety of helically twisted network structures in the liquid, the liquid crystalline (LC) and the crystalline state. Single polar substituents at the apex of tricatener molecules support the formation of

the achiral (racemic) cubic double network phase with  $la\bar{3}d$  symmetry and relatively small twist along the networks. The combination of an alkyl chain with fluorine substitution leads to the homogeneously chiral triple network phase with  $I23$  space group, and in addition, provides a mirror symmetry broken liquid. Replacing F by Cl or Br further increases the twist, leading to a short pitch double gyroid  $la\bar{3}d$  phase, which is achiral again. The effects of the structural variations on the network structures, either leading to achiral phases or chiral conglomerates are analyzed.

## Introduction

Dynamic self-assembled networks of any kind represent the fundamental basis of open-end development in complex systems. For example, neural networks are responsible for the development of the brain and consciousness, chemical networks are the basis of metabolism, data networks for information technology and so on.<sup>[1–4]</sup> Bicontinuous cubic ( $Cub_{bi}$ ) liquid crystalline phases can be considered as soft self-assembled networks, which have attracted a lot of interest for conducting and photonic materials, as matrices for protein crystallization and as templates for sol–gel syntheses.<sup>[5,6]</sup> Recently, these fluid networks were recognized to be responsible for transmission and amplification of chirality in fluid systems, and thus could provide a new potential route to prebiotic chirality.<sup>[7,8]</sup>  $Cub_{bi}$  phases are known for different types of small molecular<sup>[9–11]</sup> or polymeric<sup>[12]</sup> amphiphiles, either in aqueous systems (lyotropic phases)<sup>[6,13]</sup> or as pure compounds (thermotropic phases).<sup>[9,10,14]</sup> Amphiphilicity can be based on any intramolecular difference

of intermolecular interactions leading to nano-segregation of incompatible units,<sup>[15]</sup> like polar and nonpolar<sup>[11]</sup> or rod-like polycyclic aromatic cores and flexible chains.<sup>[16–27]</sup>

In the  $Cub_{bi}$  phases of rod-like compounds the double gyroid phase with space group  $la\bar{3}d$  involving two networks with three-way junctions (see Figure 1 a)<sup>[6,9]</sup> and a more complex triple network structure with larger lattice parameters and  $I23$  space group, also involving exclusively three-way junctions, were observed.<sup>[9,22,23]</sup> The networks are separated by the alkyl chains organized around the infinite minimal surfaces located in the middle between them.<sup>[28]</sup> The  $I23^{*k}$ -type  $Cub_{bi}$  phase is exceptional, not only as it is the only presently known  $Cub_{bi}$  phase with triple network structure, it was recently also found to be inherently chiral<sup>[29–31]</sup> and the discovery of this supramolecular chirality provided an improved general understanding of the cubic phases formed by rod-like molecules. The most prominent are the 4'-*n*-alkyloxy-3'-nitrophenyl-4-carboxylic acids (ANBCs)<sup>[32]</sup> and the 1,2-bis(4'-*n*-alkyloxybenzoyl)hydrazines (BABHs),<sup>[33,34]</sup> both involving hydrogen bonding and having only one alkyl chain at each end, and the so-called polycatenar compounds, having more than only two terminal chains (Scheme 1).<sup>[35–37]</sup> In the  $Cub_{bi}$  phases of these compounds the rod-like cores are organized in the networks with the long axes perpendicular or slightly tilted to the local net direction. The clashing of the bulky molecular peripheries leads to a helical twist along the networks (Figure 1 d), which is transmitted by the junctions to the macroscopic scale.<sup>[29a,38]</sup> The  $la\bar{3}d$  phase with only two enantiomorphous networks with opposite handedness is macroscopically achiral (Figure 1 a).<sup>[39]</sup> In the triple network phase this degeneracy is broken by the third network (Figure 1 b) and a synchronization of the helix

[a] T. Reppe, Dr. S. Poppe, Prof. Dr. C. Tschierske  
Institute of Chemistry  
Martin Luther University Halle-Wittenberg  
Kurt-Mothes-Straße 2, 06120 Halle (Germany)  
E-mail: carsten.tschierske@chemie.uni-halle.de

Supporting information and the ORCID identification number(s) for the author(s) of this article can be found under:  
<https://doi.org/10.1002/chem.202002869>.

© 2020 The Authors. Published by Wiley-VCH GmbH. This is an open access article under the terms of Creative Commons Attribution NonCommercial License, which permits use, distribution and reproduction in any medium, provided the original work is properly cited and is not used for commercial purposes.

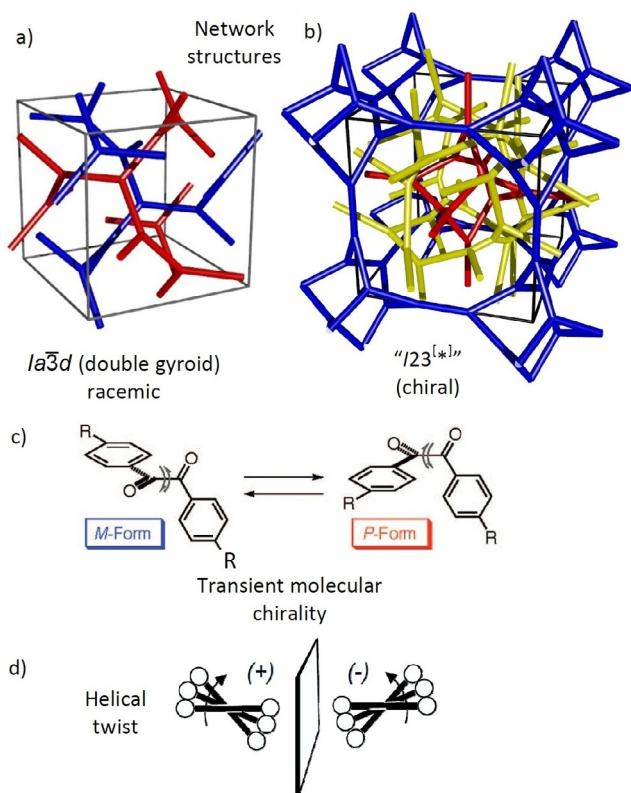
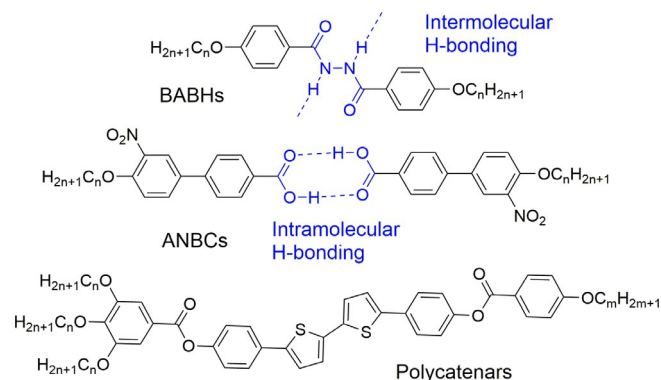


**Figure 1.** Schematics showing the networks of a) the  $Cub_{bi}/Ia\bar{3}d$  phase and b) the triple network  $I23^{[3]}$  phase; c) shows the transient chirality of the benzil unit and d) the development of the helical twist by clashing of bulky end groups attached to the cores.<sup>[44]</sup> The polyaromatic cores are located in the networks and aligned almost perpendicular to the network directions, the continuum between them is filled by the terminal alkyl chains; b) was reproduced from ref. [31] by permission of The Royal Society of Chemistry.



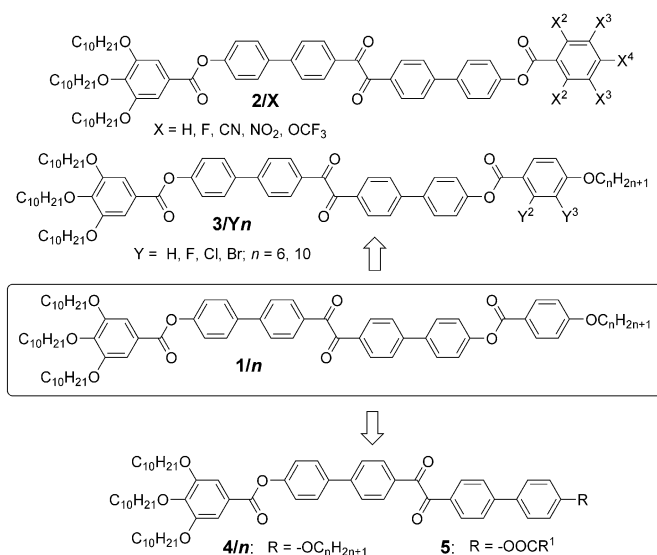
**Scheme 1.** Structures of the BABH and ANBC based rod-like hydrogen bonded molecules and supramolecules, and an example of a polycatenar mesogens forming  $Cub_{bi}$  phases.

sense between the interwoven networks leads to uniform chirality ( $I23^{[3]}$  phase, the spontaneous chirality is indicated by  $^{[3]}$ ).<sup>[40–43]</sup>

Notably, there are two distinct type of  $Ia\bar{3}d$  phases, occurring on either side of the  $I23^{[3]}$  phase, a long pitch (low twist)  $Ia\bar{3}d_{(L)}$  and a short pitch (high twist)  $Ia\bar{3}d_{(S)}$  phase, leading to the phase sequence  $Ia\bar{3}d_{(L)}/I23^{[3]}/Ia\bar{3}d_{(S)}$  with growing twist be-

tween the molecules along the networks.<sup>[44–46]</sup> In previous work we have shown that these rod-like molecules do not only form mirror symmetry broken cubic phases, mirror symmetry breaking is in some cases even observed in the adjacent isotropic liquid phases ( $Iso_1^{[3]}$ ), forming liquid conglomerates.<sup>[45,47]</sup> These  $Iso_1^{[3]}$  phases usually occur besides one of the  $Cub_{bi}$  phases and therefore they are considered as liquid network phases.<sup>[38,44]</sup>

The 4,4'-diphenylbenzil derived polycatenars **1/n** (Scheme 2) with a torsion of the  $O=C-C=O$  bond,<sup>[48]</sup> represent transiently chiral molecules,<sup>[38]</sup> which were recently shown to even form a sequence of three mirror symmetry broken mesophases, thus transferring chirality from the isotropic liquid ( $Iso_1^{[3]}$ ) via the liquid crystalline ( $Cub_{bi}/I23^{[3]}$ ) to the crystalline state ( $Cr_{Iso}^{[3]}$ ).<sup>[44]</sup> Herein we expand this class of compounds by investigating the importance of the core length (compounds **4/n** and **5** in Scheme 2) and the effect of polar substituents in lateral position (compounds **3/Yn**) or at one end (at the apex, compounds **2/X** in Scheme 2) on the self-assembly, network formation and spontaneous mirror symmetry breaking in the liquid state.



**Scheme 2.** Structures of the compounds under investigation, for details of the structures, see Tables 1–4.

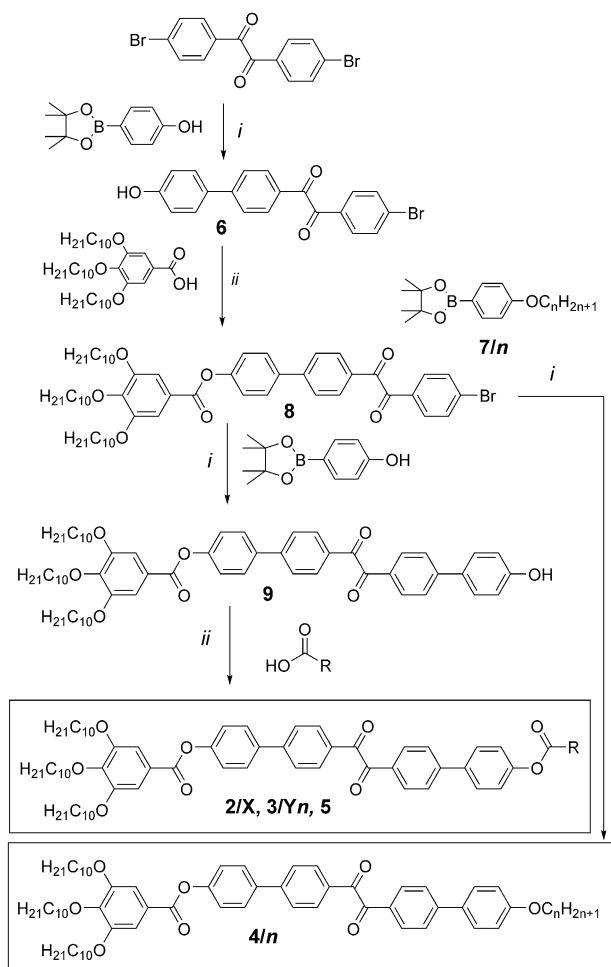
## Experimental Section

### Synthesis

The target compounds were synthesized according to Scheme 3. Compounds **2/X**, and **5** were obtained by acylation of the phenol **9**<sup>[44]</sup> using the experimental procedures given in the Supporting Information (SI). The alkoxy compounds **4/n** were synthesized from the aryl bromide **8** by Suzuki cross-coupling with 4-alkoxyphenylboronic acid pinacol esters **7/n**.

### Investigations

Investigations of the compounds were performed by polarizing optical microscopy between crossed and slightly uncrossed polarizers (POM), differential scanning calorimetry (DSC) and X-ray scattering



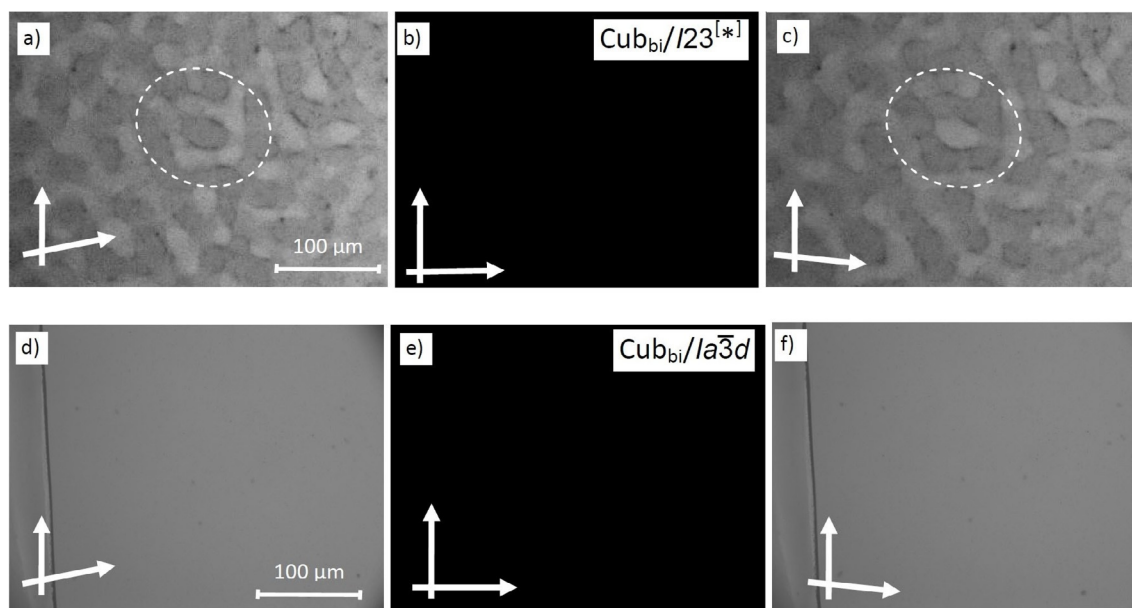
**Scheme 3.** Synthesis of the benzil-based compounds 2–5. Reagents and conditions: (i) THF, sat.  $\text{NaHCO}_3$  solution,  $[\text{Pd}(\text{PPh}_3)_4]$ , reflux; (ii)  $\text{SOCl}_2$ , abs. pyridine, DCM, DMAP,  $25^\circ\text{C}$ .

(small angle X-ray scattering = SAXS and wide angle scattering = WAXS) with the instrumentation described in the Supporting Information. The transition from the isotropic liquid state to the  $\text{Cub}_{\text{bi}}$  phases on cooling was identified by an increase of viscosity associated with a small DSC peak (Figure S1) while the phase remains optically isotropic (Figure 2b,e). In the X-ray scattering patterns of the  $\text{Cub}_{\text{bi}}$  phases there are several small angle scatterings besides the diffuse wide angle scattering. The diffuse character of the wide angle scattering with a maximum around  $d = 0.45$  nm (Figures S3b and S4b) confirms the LC state having no fixed positions of the individual molecules. The small angle scattering positions can be indexed either to (211) and (220) of a  $1a\bar{3}d$  lattice or to (321), (400) and (420) of the  $I23^{[*]}$  lattice (Tables S2 and S3). Figures S3 and S4 show representative SAXS patterns of these two cubic phase types. Additional confirmation of the cubic phase type was gained from optical investigation under a polarizing microscope between polarizers slightly rotated by a few degrees out of the exactly  $90^\circ$  twisted orientation where only the  $I23^{[*]}$  phase shows a conglomerate of chiral (dark and bright) domains which invert their brightness by changing the twist direction of the analyzer (see Figure 2a–c) whereas the  $1a\bar{3}d$  phase does not, and therefore is achiral (Figure 2c–f).<sup>[29a]</sup> In a similar way the achiral isotropic melted state (Iso, Iso) is distinguished from the conglomerates formed by the mirror symmetry broken  $\text{Iso}_1^{[*]}$  phase. The non-cubic LC phases were indicated by their typical birefringent textures as observed by POM between crossed polarizers and confirmed by SAXS investigation (see Section 3.3 and Table S4).

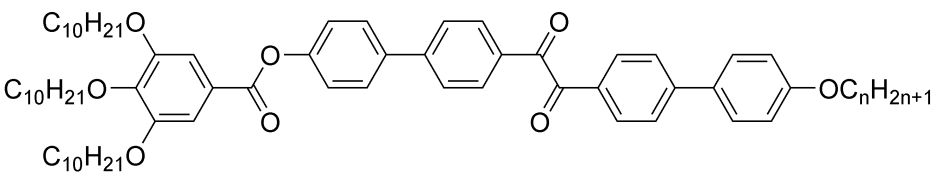
## Results and Discussion

### The series of tetracatenar compounds 4/n

In the series of compounds 4/n with a shorter 5-ring core, incorporating one benzoate unit less than the 6-ring compounds 1/n, the homologues with a chain length between  $n = 14$  and 18 form a monotropic  $\text{Cub}_{\text{bi}}$  phase on cooling, whereas all other homologues have exclusively crystalline phases



**Figure 2.** POM images as observed between crossed (middle) and slightly uncrossed polarizers (left, right) for a–c) the  $I23^{[*]}$  phase of 1/10 at  $105^\circ\text{C}$  as obtained after cooling from the  $\text{Iso}_1^{[*]}$  phase and d–f) the achiral  $1a\bar{3}d$  phase of  $3^2\text{Br}6$  at  $70^\circ\text{C}$  as observed on cooling from Iso.

**Table 1.** Phase transitions of the homologous series of compounds **4/n** measured on heating and cooling (10 K min<sup>-1</sup>).<sup>[a]</sup>


Compound	<i>n</i>	Heating: <i>T</i> [°C] [ $\Delta H$ in kJ mol <sup>-1</sup> ]	Cooling: <i>T</i> [°C] [ $\Delta H$ in kJ mol <sup>-1</sup> ]
<b>4/4</b>	4	Cr 82 [48.0] Iso	Iso 45 [-19.5] Cr
<b>4/6</b>	6	Cr 91 [64.2] Iso	Iso 42 [-21.7] Cr
<b>4/8</b>	8	Cr 96 [51.4] Iso	Iso 63 [-45.2] Cr
<b>4/10</b> <sup>[44]</sup>	10	Cr 102 [54.7] Iso	Iso 81 [-53.3] Cr
<b>4/12</b>	12	Cr 80 [66.5] Iso	Iso 57 [-49.4] Cr
<b>4/14</b>	14	Cr 82 [78.3] Iso	Iso 69 [-6.5] Iso <sub>1</sub> , 49 [-1.3] Cub/ <i>la</i> 3 <i>d</i> 31 [-6.0] Cr <sup>[c]</sup>
<b>4/16</b>	16	Cr 83 [75.3] Iso	Iso 70 [-6.1] Iso <sub>1</sub> , 55 [-1.9] Cub/ <i>la</i> 3 <i>d</i> 31 [-2.5] Cr <sup>[c]</sup>
<b>4/18</b>	18	Cr 84 [92.3] Iso	Iso 66 [-19.9] <sup>[b]</sup> Iso <sub>1</sub> , 56 [-1.3] Cub/ <i>la</i> 3 <i>d</i> 37 [-7.7] Cr <sup>[c]</sup>
<b>4/20</b>	20	Cr 86 [110.0] Iso	Iso 66 [-83.8] Cr

[a] DSC peak temperatures on heating at 10 K min<sup>-1</sup>. Abbreviations: Cr = crystalline solid, Iso = achiral isotropic liquid; Cub/*la*3*d* = achiral bicontinuous cubic phase; though the direct assignment of the *la*3*d* type was not possible, based on the large chain length a *la*3*d*<sub>(s)</sub> type appears more likely; for DSCs of compounds **4/14**–**4/18**, see Figures 3 and S1a–c. [b] Transition is accompanied by partial crystallization. [c] Partial crystallization.

(Table 1). Even for these three compounds, due to rapid crystallization, the phase transitions can only be recorded on cooling by DSC and optical investigations, whereas crystallization takes place during the exposure time of attempted XRD investigations. The assignment of these cubic phases to the *la*3*d* space group is therefore only based on optical investigations, indicating the absence of chiral domains in the isotropic mesophases with high viscosity.

Only for **4/14** and **4/16** the transition from Iso to Cub<sub>bi</sub>/*la*3*d* takes place without partial crystallization on cooling. The most interesting feature of these compound is an additional transition in the isotropic liquid state before the transition to the cubic phase (Table 1, Figures 3 and Figure 1a–c). On cooling compound **4/14**, as example, a broad feature occurs in the DSC traces in the temperature range of the isotropic liquid phase, indicating a liquid state polyamorphism (liquid–liquid

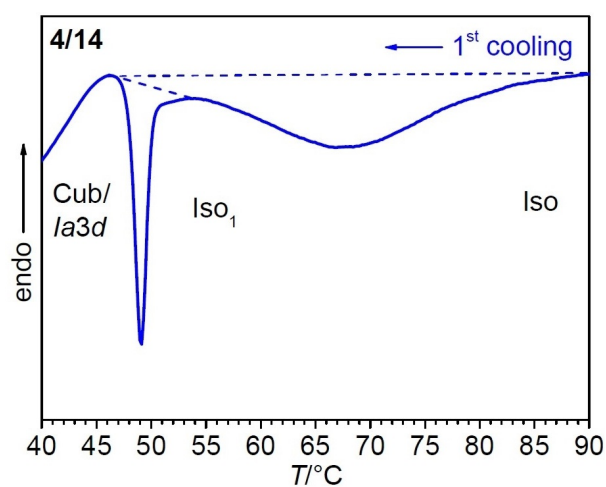


**Figure 3.** DSC of compound **4/14** showing the Iso–Iso<sub>1</sub>–Cub<sub>bi</sub>/*la*3*d* transition ranges; full heating and cooling scans are shown in Figure S1 a, the DSCs of **4/16** and **4/18** are shown in Figure S1 b,c.

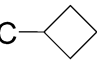
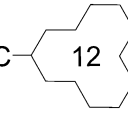
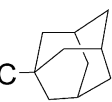
transitions, see Figure 3).<sup>[9b,38,44,46,49a]</sup> The additional sharp peak at the transition to the cubic phase is associated with a sudden change from fluidity to viscoelasticity. The majority of the enthalpy of this Iso–Iso<sub>1</sub>–Cub<sub>bi</sub> transition is involved in this broad feature (6–7 kJ mol<sup>-1</sup>) which is interpreted as a growth of aggregates which fuse to a network structure and continuously increases network connectivity (Iso<sub>1</sub> phase),<sup>[38a,44, 49a]</sup> being in line with recent results of <sup>1</sup>H-NMR diffusion and relaxation studies.<sup>[49b]</sup> At a certain degree of network connectivity, the long range cubic lattice composed of two interwoven gyroid networks with three way junctions is formed. This is indicated by a sharp peak with small enthalpy (1.3–1.9 kJ mol<sup>-1</sup>). There is no indication of any mirror symmetry breaking in the Iso<sub>1</sub> phase range and therefore we assume a similar *la*3*d*-like network with three way junctions, but without long range order for the structure of the achiral Iso<sub>1</sub> phase. As the Iso<sub>1</sub> phase flows under gravity like any other ordinary liquid, the network must be highly dynamic and we consider it as a kind of percolated network liquid.<sup>[44]</sup> The very broad Iso–Iso<sub>1</sub> transition is interpreted as a continuous growth process fusing the cybotactic clusters to dynamic networks.<sup>[38a,44]</sup> Though this broad DSC feature was also observed for compound **4/18**, the Iso–Iso<sub>1</sub> transition is in this case accompanied by a partial crystallization, as indicated by the changed shape and larger enthalpy of this broad transition (Figure S1 c).

#### Tetracatenar compound **5/n** with an acyl chain and tricate-nar compounds **5** with cyclic units at the apex

Attempts to widen the cubic range of compounds **4/n** by using acyloxy chains (**5/12**) or alicyclic and polycyclic units (compounds **5/c4**, **5/c12** and **5/Ad**) instead of alkyloxy chains failed (see Table 2), though in the series of polycatenar dicarboxylates of 5,5'-diphenyl-2,2'-dithiophene (Scheme 1) a significant mesophases stabilizing effect of these cycloaliphatic units was found.<sup>[45]</sup> As shown in Table 2 all these compounds **5** are



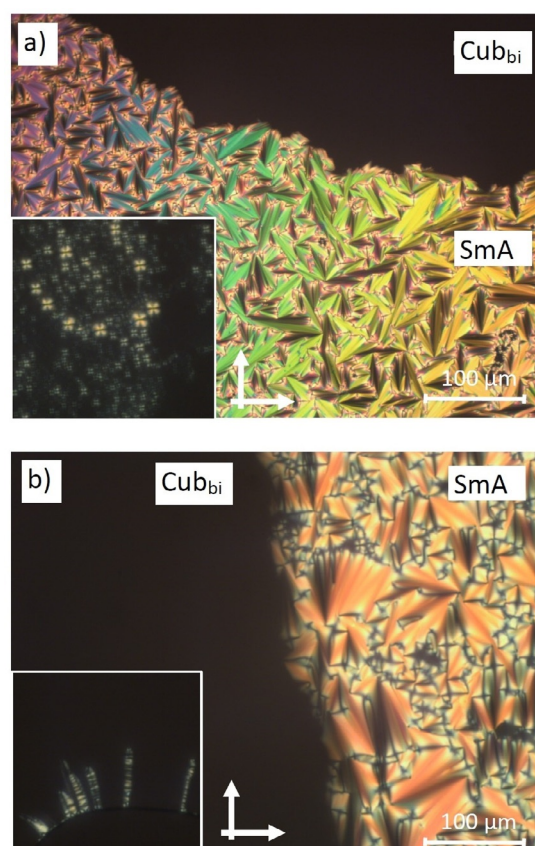
**Table 2.** Phase transitions of compounds **5** on heating and cooling (DSC at 10 Kmin<sup>-1</sup>).

Compound	R	T [°C] [ $\Delta H$ in kJ mol <sup>-1</sup> ]
4/12 <sup>(b)</sup>	OC <sub>12</sub> H <sub>25</sub>	H: Cr 80 [66.5] Iso C: Iso 57 [-49.4] Cr
5/12	OOC <sub>12</sub> H <sub>25</sub>	H: Cr 87 [53.4] Iso C: Iso 65 [-45.4] Cr
5/c4		H: Cr 104 [67.0] Iso C: Iso 45 [-19.8] Cr
5/c12		H: Cr 106 [66.8] Iso C: Iso <20 Cr
5/Ad		H: Cr 79 [35.5] Iso C: Iso <20 Cr

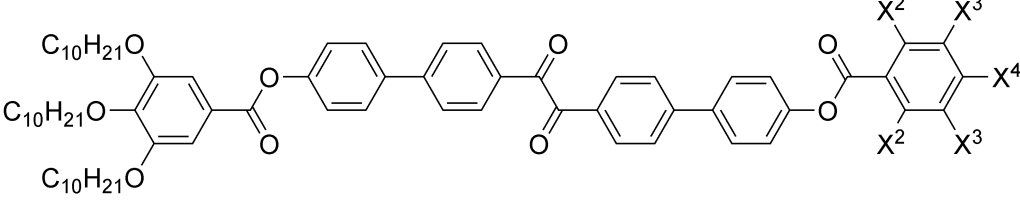
crystalline solids, some of them can be supercooled even down to room temperature without mesophase formation before the onset of crystallization. It appears that the capability of the non-symmetric 5-ring tetracatenars **4** for mesophase formation is limited to only few examples with long aliphatic chains. Therefore, the focus of the following work is on compounds **2** and **3** with a polyaromatic core involving six benzene rings.

#### Tricatenar compounds with polar substituents at the apex

We expanded the structure of the tetracatenar six-ring compounds **1/n** either by introduction of halogens in lateral positions of the apex or by replacing the alkoxy chain at the apex by polar electron withdrawing substituents (tricate-nar compounds **2/X**). As shown in Table 3, electron withdrawing groups, especially CN and NO<sub>2</sub>, lead to compounds with wide ranges of LC phases, most probably due to increasing polar core-core interactions between the electron deficit aromatics as well as by donor-acceptor interactions with the electron-donor-substituted trialkoxylated ends in an antiparallel packing.<sup>[45,50]</sup> **2/CN** and **2/NO<sub>2</sub>** show an enantiotropic phase sequence Iso-Iso<sub>1</sub>-SmA-Cub<sub>bi</sub> on cooling. The SmA phases were confirmed by their typical fan-like textures with extinctions parallel to the directions of analyzer and polarizer (Figure 4a,b), and the optically isotropic appearance of their homeotropic aligned samples (see insets in Figure 4a,b), thus confirming optically uniaxial non-tilted SmA phases. The SAXS patterns show only one sharp scattering with  $d=5.5$  (**2/CN**) or  $d=5.3$  nm (**2/NO<sub>2</sub>**, see Table S4), being a bit larger than the molecular lengths  $L_{\text{mol}}=4.5$  and 4.6 nm, respectively, measured for the most extended conformation of space filling models (Figure 5a). Thus, it can be concluded that an almost fully interca-



**Figure 4.** Textures of a) **2/CN** at  $T=147$  °C and b) **2/NO<sub>2</sub>** at  $T=167$  °C in planar aligned samples showing the growth of the Cub<sub>bi</sub>/*1a3d* phase (dark area) into the fan textures of the birefringent SmA phases on cooling; the insets show the homeotropic textures of the SmA phases at 150 and 170 °C, respectively; the arrows indicate the orientation of polarizer and analyzer.

**Table 3.** Phase transitions, lattice parameters ( $a_{\text{cub}}$ ) and twist angles between the molecules in neighboring rafts ( $\Phi$ ) in the  $\text{Cub}_{\text{bi}}$  phases of compounds **2/X**.<sup>[a]</sup>


Compound	X <sup>4</sup>	X <sup>3</sup>	X <sup>2</sup>	T [°C] [ $\Delta H$ in kJ mol <sup>-1</sup> ]	$n_{\text{raft}}$	$a_{\text{cub}}$ [nm] ( $\Phi$ /°)
<b>1/0</b> <sup>[44]</sup>	H	H	H	H: Cr 126 [52.2] Iso; C: Iso 110 [27.3] Cr	–	–
<b>1/1</b> <sup>[44]</sup>	OMe	H	H	H: Cr 127 [36.3] Iso; C: Iso 115 [36.4] Cr	–	–
<b>1/2</b> <sup>[44]</sup>	OEt	H	H	H: Cr 120 [37.9] $la\bar{3}d_{\text{(L)}}$ 127 [1.8] Iso <sub>1</sub> 135 [1.9] Iso C: Iso 133 [–1.3] Iso <sub>1</sub> 121 [–0.2] Iso <sub>1</sub> <sup>[b]</sup> 110 [–0.3] $la\bar{3}d_{\text{(L)}}$ 105 [–31.3] Cr	4.9	12.9 (6.9)
<b>1/14</b> <sup>[44]</sup>	OC <sub>14</sub> H <sub>29</sub>	H	H	H: Cr 108 [44.1] $la\bar{3}d_{\text{(S)}}$ 135 [2.9] Iso <sub>1</sub> 138 [7.0] Iso C: Iso 136 [–3.1] Iso <sub>1</sub> 129 [–1.2] Col <sub>hex</sub> 125 [–0.4] $la\bar{3}d_{\text{(S)}}$ 42 [–16.9] Cr <sub>Iso</sub> < 20 Cr	3.2	11.3 (7.9)
<b>2/F</b>	F	H	H	H: Cr 126 [26.5] Iso; C: Iso 110 [27.3] Cr	–	–
<b>2/CN</b>	CN	H	H	H: Cr 145 [25.0] $la\bar{3}d_{\text{(L)}}$ 165 [1.2] SmA <sup>[b]</sup> 176 [1.0] Iso <sub>1</sub> 183 Iso C: Iso 178 [–2.9] Iso <sub>1</sub> 173 [–0.8] SmA 145 [–0.9] $la\bar{3}d_{\text{(L)}}$ 124 [–34.4] Cr H: Cr 149 [38.9] $la\bar{3}d_{\text{(L)}}$ 181 [2.0] SmA <sup>[c]</sup> 187 [1.7] Iso <sub>1</sub> 193 [2.5] Iso C: Iso 190 [–3.0] Iso <sub>1</sub> 184 [–1.5] SmA 167 [–1.8] $la\bar{3}d_{\text{(L)}}$ 130 [–41.0] Cr	4.6	12.4 (7.2)
<b>2/NO<sub>2</sub></b>	NO <sub>2</sub>	H	H	H: Cr 123 [24.9] $la\bar{3}d_{\text{(L)}}$ 135 [2.2] Iso <sub>1</sub> 143 [4.0] Iso C: Iso 141 [–2.4] Iso <sub>1</sub> 126 [–1.6] $la\bar{3}d_{\text{(L)}}$ 115 [–25.3] Cr	4.5	12.1 (7.4)
<b>2/OCF<sub>3</sub></b>	OCF <sub>3</sub>	H	H	H: Cr 123 [28.1] $la\bar{3}d_{\text{(L)}}$ 130 [2.9] Iso <sub>1</sub> 138 [3.4] Iso C: Iso 134 [–3.4] Iso <sub>1</sub> 121 [–2.2] $la\bar{3}d_{\text{(L)}}$ 103 [–26.4] Cr	3.8	11.3 (7.9)
<b>2/F<sub>3</sub></b>	F	F	H	H: Cr 103 [39.7] $la\bar{3}d_{\text{(L)}}$ 112 [2.0] Iso <sub>1</sub> 123 [5.2] Iso C: Iso 118 [–7.7] Iso <sub>1</sub> 100 [–1.6] $la\bar{3}d_{\text{(L)}}$ 84 [–43.1] Cr	3.6	10.9 (8.2)
<b>2/F<sub>5</sub></b>	F	F	F	H: Cr 103 [39.7] $la\bar{3}d_{\text{(L)}}$ 112 [2.0] Iso <sub>1</sub> 123 [5.2] Iso C: Iso 118 [–7.7] Iso <sub>1</sub> 100 [–1.6] $la\bar{3}d_{\text{(L)}}$ 84 [–43.1] Cr	3.5	10.8 (8.3)

[a] DSC peak temperatures on heating/cooling (H/C) at 10 K min<sup>-1</sup>;  $n_{\text{raft}}$  = number of molecules in the cross section of the networks, calculated for rafts with a height of 0.45 nm; for details of the calculations see Table S5;  $a_{\text{cub}}$  = cubic lattice parameter;  $\Phi(la\bar{3}d)$  = twist between adjacent molecules (rafts), calculated according to  $\Phi(la\bar{3}d) = 70.5^\circ / (0.354 a_{\text{cub}} / 0.45 \text{ nm})$ ; <sup>[29a]</sup> for DSCs, see Figures 7 and S1 and for X-ray scattering data Tables S2–S5 and Figures S3 and S4; for the Iso–Iso<sub>1</sub> transitions, representing broad features the maxima of the features are given, the complete temperature ranges are listed in Table S1; abbreviations: SmA = non-tilted lamellar (smectic A) phase;  $la\bar{3}d_{\text{(L)}}$  = long pitch (small  $\Phi$ )  $la\bar{3}d$  phase;  $la\bar{3}d_{\text{(S)}}$  = short pitch (large  $\Phi$ )  $la\bar{3}d$  phase; for the other abbreviations, see Table 1; [b]  $d = 5.5$  nm; [c]  $d = 5.3$  nm.

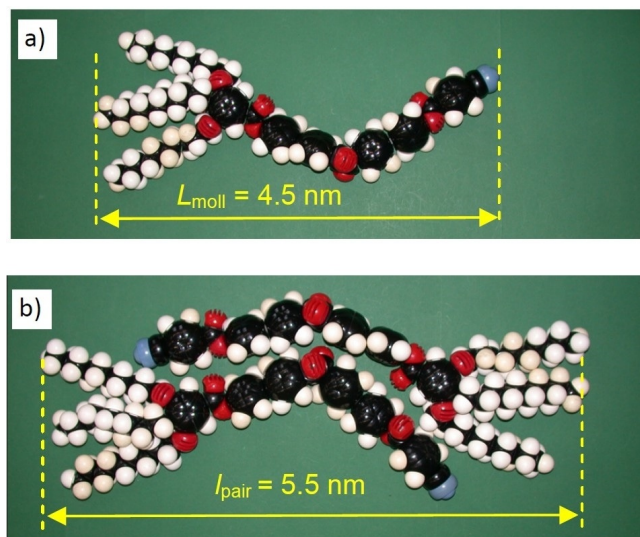


**Figure 5.** a) Space filling models of compound **2/CN** and b) its antiparallel pair with fully intercalated aromatic cores.

lated antiparallel organization of the molecules in the layers, providing a layer distance of 5.5 nm, is present (Figure 5b).

In the cubic phases two main small angle scattering peaks are observed which can be indexed to (211) and (220) of a  $la\bar{3}d$  lattice; the calculated lattice parameters  $a_{\text{cub}}$  are 12.4 nm for **2/CN** (155 °C) and 12.1 nm for **2/NO<sub>2</sub>** (160 °C, see Tables 3, S2 and S4). According to  $d_{\text{rod}} = \sqrt{3} \times a_{\text{cub}} / 4$  the distance between the two networks is  $d_{\text{rod}} = 5.4$  and 5.2 nm, respectively (see Table S5). This distance corresponds to the separation of the minimal surface and is similar to the layer distances measured in the adjacent SmA phases. This is in line with a non-tilted fully intercalated organization of the polyaromatic rods in the networks (Figure 5b). The cubic phase stability (and mesophases stability in general) of the 4-substituted compounds **2/X** grows in the order  $X = \text{F} < \text{OCF}_3 < \text{CN} < \text{NO}_2$  with rising Hammett constants of the substituents ( $\sigma_m + \sigma_p$  for  $\text{F} = 0.4$ ;  $\text{OCF}_3 = 0.7$ ;  $\text{CN} = 1.2$  and  $\text{NO}_2 = 1.5$ ).<sup>[51]</sup>

Increasing degree of fluorination at the apex has a similar effect as CN/NO<sub>2</sub> substitution. Though the monofluorinated compound **2/F** does not show any LC phase, probably due to its rapid crystallization on cooling, taking place already at 110 °C, the further increase of the number of fluorines induces cubic phases. This works for aromatic fluorination<sup>[52]</sup> (**2/F<sub>3</sub>** and **2/F<sub>5</sub>**) as well as for the fluorination of the OCH<sub>3</sub> group (compound **2/OCF<sub>3</sub>**, see Table 3), though there is a competition with the simultaneously growing steric effect of fluorination.



All compounds **2/X** with polar substituents form exclusively the achiral  $la\bar{3}d$  phase and no  $I23^{[*]}$  or  $Iso_1^{[*]}$  phase can be observed, whereas compounds with alkyloxy chains, acting as donor-substituents ( $\sigma_m + \sigma_p = -0.22$  for  $OC_4H_9$ )<sup>[51]</sup> form a sequence  $la\bar{3}d_{(L)}-I23^{[*]}-la\bar{3}d_{(S)}$  upon chain elongation.<sup>[9b,44,45,53]</sup> The number of molecules in the cross-section of the networks ( $n_{rafr}$ , see Tables 3 and S5) is 3.5–3.8 for the fluorinated compounds and 4.5–4.6 for the  $NO_2$  and CN substituted compounds.

Here the question arises which kind the  $la\bar{3}d$  phase – long pitch or short pitch – is actually formed by compounds **2/X**. The twist angles of  $7.9-8.3^\circ$  for the fluorinated and  $7.2-7.4^\circ$  for the CN/ $NO_2$  substituted compounds are intermediate between the values expected for the two cases ( $<7^\circ$  for  $la\bar{3}d_{(S)}$  and  $>9^\circ$  for  $la\bar{3}d_{(L)}$ , respectively).<sup>[31,44,45]</sup> As previously shown, the chiral  $I23^{[*]}$  phase can be induced between different  $la\bar{3}d$  phase types, whereas no such phase is induced between  $la\bar{3}d$

phases belonging to the same type.<sup>[44,45,54-56]</sup> As shown in Figure 6 a stripe of an  $I23^{[*]}$  phase with chiral conglomerate texture is observed in the contact region between the  $Cub_{bi}$  phase of **1/14**,<sup>[44]</sup> known to form the  $la\bar{3}d_{(S)}$  type, and the  $la\bar{3}d$  phases of the compounds **2/CN**, **2/OCF<sub>3</sub>** and **2/F<sub>3</sub>**. This means that the developing concentration gradient leads to the sequence  $la\bar{3}d_{(L)}-I23^{[*]}-la\bar{3}d_{(S)}$  with increasing concentration of compounds **2/X**. Therefore, the  $la\bar{3}d$  phases of all these polar substituted compounds **2/X** must be considered as long pitch (low twist)  $la\bar{3}d_{(L)}$ -type phases.

No mirror symmetry broken  $Iso_1^{[*]}$  phase can be found besides any of the  $la\bar{3}d_{(L)}$  phases of the polar substituted compounds **2/X** (Table 3), though, as shown in Figure 7 for compounds **2/NO<sub>2</sub>** and **2/OCF<sub>3</sub>**, a broad feature occurs in the DSC traces in the temperature range of the isotropic liquid state. This indicates a transition to a percolated  $Iso_1$  phase before the

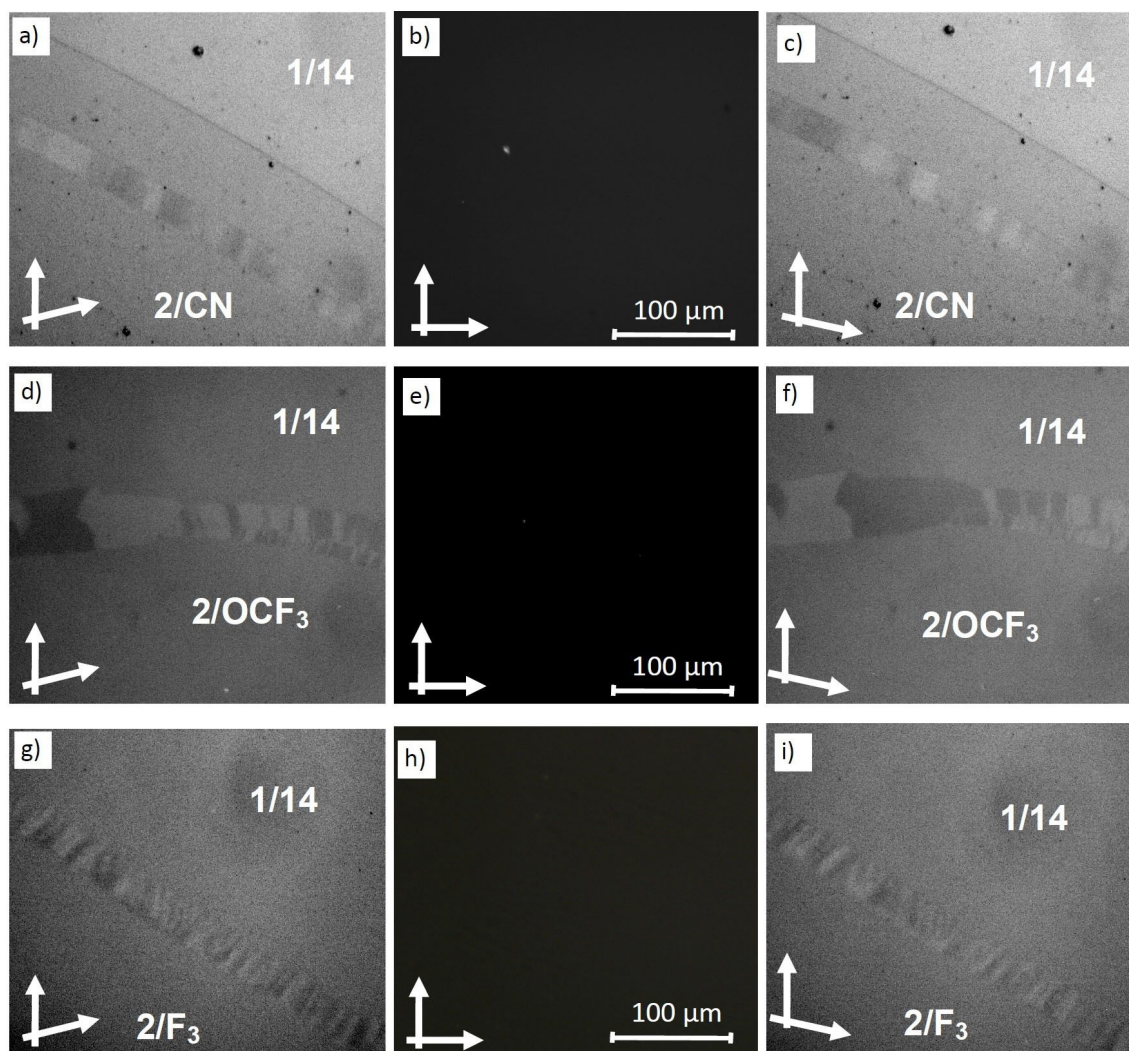


**Figure 6.** Development of chiral conglomerates of the induced  $I23^{[*]}$  phase in the contact regions between the achiral  $la\bar{3}d$  phases of a–c) **1/14** ( $la\bar{3}d_{(S)}$ )<sup>[44]</sup> and **2/CN** at  $149^\circ\text{C}$ , d–f) **1/14** and **2/OCF<sub>3</sub>** at  $121^\circ\text{C}$  and g–i) **1/14** with **2/F<sub>3</sub>** at  $126^\circ\text{C}$ , at the left and right between slightly rotated polarizers and in the middle between crossed polarizers. The induction of a  $I23^{[*]}$  ribbon indicates that both  $la\bar{3}d$  phases should have different structure, that is, that they represent  $la\bar{3}d_{(L)}$  phases for compounds **2/X**. The absence of any birefringence between crossed polarizers indicates the absence of any induced birefringent non-cubic mesophases and the inversion of the brightness by inverting the direction of the analyzer indicates the presence of a chiral conglomerate in the  $I23^{[*]}$  ribbons; the phase boundary in a, c) represents the  $Iso_1-Cub_{bi}$  transition of the **1/14 + 2/CN** mixture.

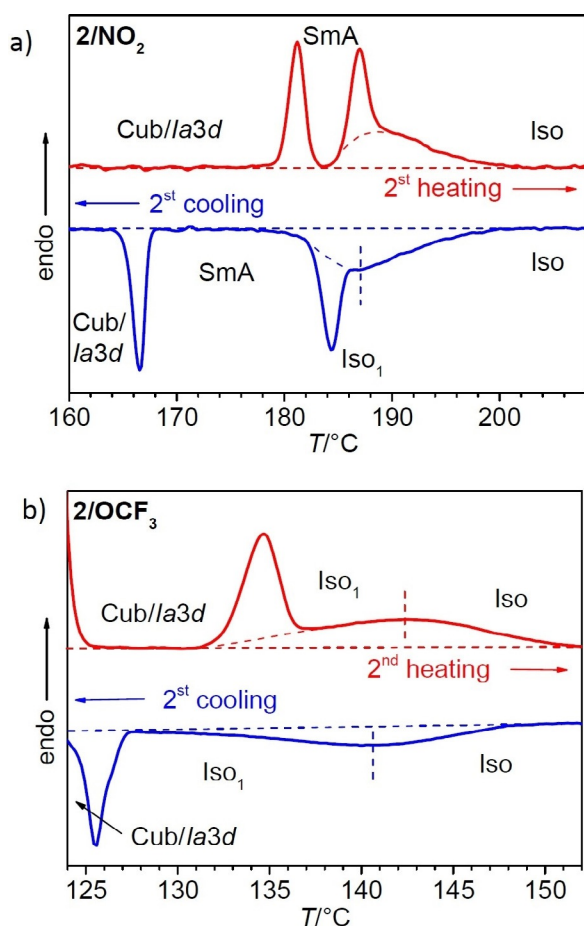


**Figure 7.** Representative DSC heating and cooling traces of compounds **2/X** showing a) the Iso–Iso<sub>1</sub>–SmA–Cub<sub>bi</sub>/la<sub>3d(L)</sub> transition of **2/NO<sub>2</sub>** and b) the Iso–Iso<sub>1</sub>–Cub<sub>bi</sub>/la<sub>3d(L)</sub> transition of **2/OCF<sub>3</sub>**; for full scans and the DSC traces of the other compounds, see Figure S1 d,g.

cubic phase is formed (see also Figure S1), independent if the la<sub>3d(L)</sub> phase is separated from the isotropic liquid phase by an additional SmA range (**2/NO<sub>2</sub>**, **2/CN**, Figure 7a and Figure S1 e) or not (**2/OCF<sub>3</sub>**, **2/F<sub>nr</sub>**, Figure 7b and Figure S1 h–j). This shape of the diffuse DSC feature is similar to that observed for compound **4/14** (Figure 3a) and the ANBCs.<sup>[32b,c]</sup> In contrast, other polycatenar compounds, like the 5,5′-diphenyl-2,2′-dithiophene bisbenzoates (Scheme 1) do not show this kind of Iso–Iso<sub>1</sub> transition.<sup>[29a,45]</sup> Related Iso–Iso<sub>1</sub> transitions were previously reported in the series of the hydrogen bonded dimers of the ANBCs with hydrogen bonding forming the rod-like cores, but not for the BABHs with *intermolecular* hydrogen bonding between the cores (see Scheme 1),<sup>[9b,49a]</sup> providing stronger core–core interactions. The absence of an Iso–Iso<sub>1</sub> transition in some cases could therefore be interpreted by a network structure of the liquid phase, being present in the whole range of the isotropic liquid state. This would mean that the isotropic liquids of the strongly aggregating molecules can be considered as Iso<sub>1</sub> phases, being present in the whole investigated temperature range of the liquid state even at high temperatures, whereas for the weakly aggregating bent benzil derivatives they develop only shortly before the transition to the Cub<sub>bi</sub> phase. Over-

all, the broad Iso–Iso<sub>1</sub> transition appears to occur adjacent to LC network phases if the network develops in a limited pre-transitional temperature range of the liquid phase.<sup>[9b,38,49a]</sup>

Chirality synchronization by transition to the mirror symmetry broken Iso<sub>1</sub><sup>[\*]</sup> phase, takes place after reaching a certain degree of network connectivity, which is independent if there is an observable Iso–Iso<sub>1</sub> transition (Figure 8a,b,d) or not,<sup>[45,47]</sup> meaning that chirality synchronization in the liquid state takes place after the dynamic network with a sufficient degree of connectivity has developed. However, not in all cases of liquid network phases (Iso<sub>1</sub>) mirror symmetry breaking with formation of the Iso<sub>1</sub><sup>[\*]</sup> phase takes place (Figures 7 and 8c,d). The reason could either be an insufficient connectivity of the network achieved in the liquid state or a tendency to develop a racemic la<sub>3d</sub>-like network structure (see further below).

### Non-symmetric tetracatenars with additional fluorine substitution at the less substituted terminal

Compound **1/6**<sup>[44]</sup> was shown in previous work to form a unique sequence of three mirror symmetry broken phases with conglomerate texture (Figure 8a). At the transition from the ordinary isotropic liquid (Iso) on cooling a percolated Iso<sub>1</sub> phase is formed around 130 °C. This is achiral and becomes chiral at the next phase transition at 123 °C which is attributed to a transition to an Iso<sub>1</sub><sup>[\*]</sup> network phase. This turns into the chiral Cub<sub>bi</sub>/I23<sup>[\*]</sup> phase at 118 °C which then on further cooling crystallizes at 61 °C with formation of an optically isotropic crystalline mesophase Cr<sub>iso</sub><sup>[\*]</sup> composed of a chiral conglomerate (Figure 8a and Table 4).<sup>[44]</sup> Fluorination in the peripheral 3-position at the less substituted end (compound **3/2F6**) retains the fundamental phase sequence, though the Iso<sub>1</sub><sup>[\*]</sup> phase is only observable on cooling and the isotropic Cr<sub>iso</sub><sup>[\*]</sup> phase is replaced by a birefringent crystalline phase (Cr), see Table 4 and Figure S1 k,l.

Fluorination at the inside directed 2-position (**3/2F6**) retains the mirror symmetry broken Iso<sub>1</sub><sup>[\*]</sup> and Cr<sub>iso</sub><sup>[\*]</sup> phases, but removes the cubic I23<sup>[\*]</sup> phase of **1/6** completely, that is, there is a direct transition Iso<sub>1</sub><sup>[\*]</sup> to Cr<sub>iso</sub><sup>[\*]</sup> (Table 4, Figure 9 and Figure S1 m). There is no observable change of the conglomerate texture at the transition from Iso<sub>1</sub><sup>[\*]</sup> to Cr<sub>iso</sub><sup>[\*]</sup> (Figure 9a–d), though it is associated with a significant transition enthalpy of 22–24 kJ mol<sup>−1</sup>.<sup>[57]</sup> As also observed for **1/6**,<sup>[44]</sup> the SAXS pattern of the Cr<sub>iso</sub><sup>[\*]</sup> phase of **3/2F6** is characterized by a relatively broad scattering, with a maximum at  $d = 5.35$  nm, being very similar to the length of intercalated molecular pairs (Figure 9 f). The broadening of the small angle scattering indicates a distorted structure with short correlation length of  $\approx 30$  nm (Scherrer equation) corresponding to about 5–6 network distances. The multiple wide-angle scatterings indicate a crystalline phase (Figure 9g) and can be attributed to the mean alkyl chain distance (0.43 nm) and the lateral edge-to-edge and face-to-face packing of the aromatics (0.56/0.37 nm), very similar to the Cr<sub>iso</sub><sup>[\*]</sup> phase reported for **1/6**.<sup>[44]</sup> The unusually low intensity of the wide angle scatterings (see Figure S6)<sup>[58]</sup> and the optical isotropy are in line with a strongly distorted structure with crystallized polyaromatic cores and alkyl chain seg-



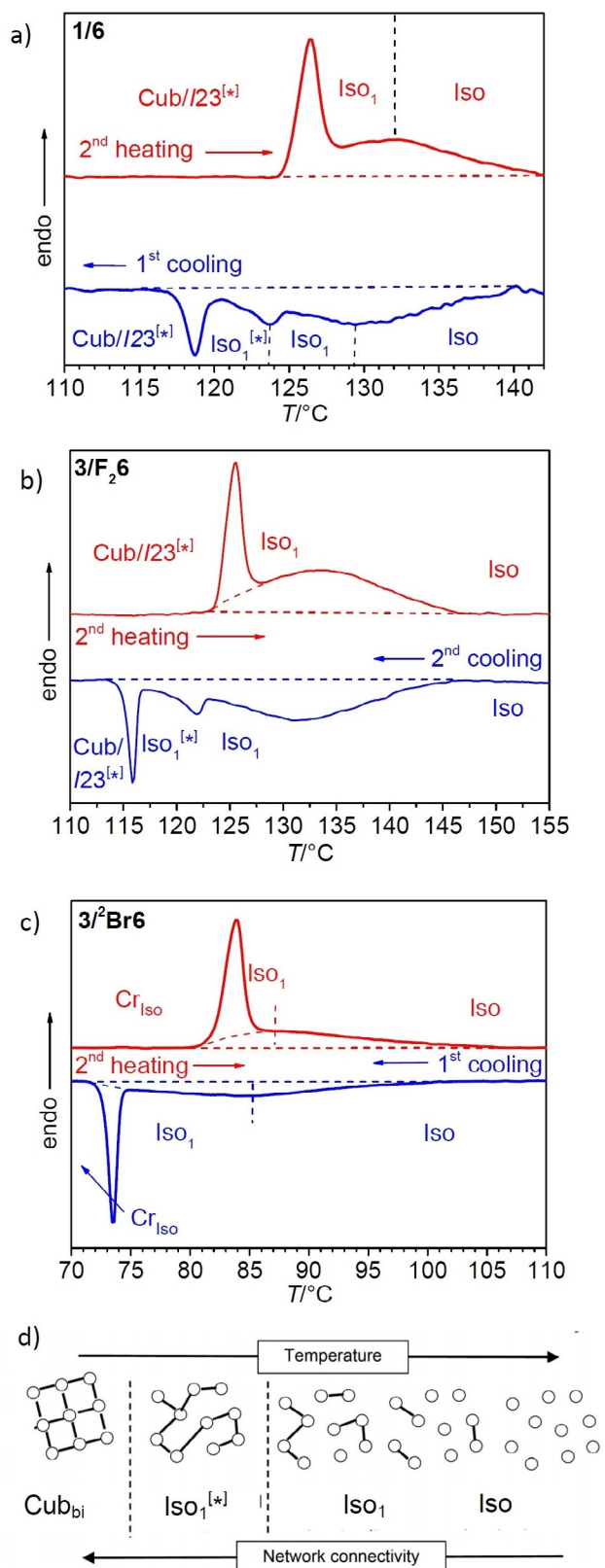


**Figure 8.** a–c) Representative DSC heating and cooling traces of a) compound 1/6 and b,c) the laterally core halogenated compounds 3/Y6;<sup>[44]</sup> a,b) Iso–Iso<sub>1</sub>–Iso<sub>1</sub><sup>[\*]</sup>–Cub<sub>bi</sub>//I23<sup>[\*]</sup> transitions of compounds a) 1/6 and b) 3/F<sub>2</sub>6 and c) Iso–Iso<sub>1</sub>–Cr<sub>Iso</sub> transition of compound 3/Br6; for full scans and the DSC traces of 3/F<sub>2</sub>6 and 3/Br6, see Figure S1 o,q. d) Schematic sketch showing the transition from Iso via a cybotactic and a percolated liquid to Cub<sub>bi</sub> by increasing transient network connectivity, the dots represent locally ordered clusters and the lines indicate the connections between them, the vertical dotted lines indicate phase transitions.

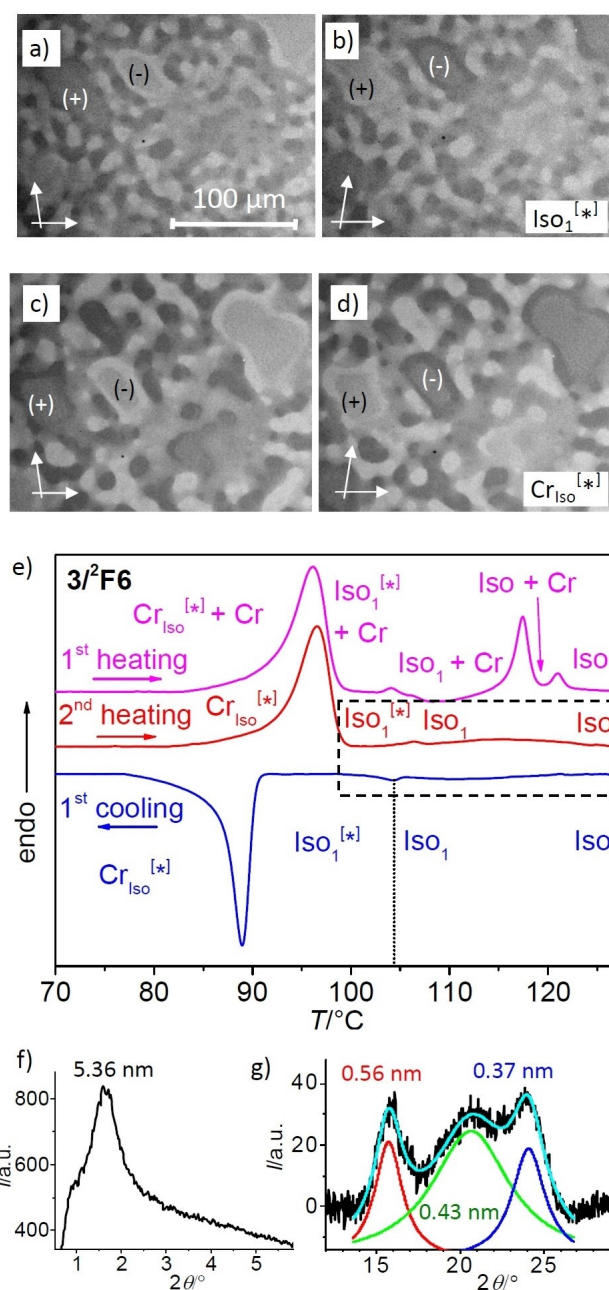


**Figure 9.** Investigation of compound 3/2F6. a,b) optically active domains in the Iso<sub>1</sub><sup>[\*]</sup> phase at 100°C and c,d) in the Cr<sub>Iso</sub><sup>[\*]</sup> phase at 60°C, as observed between slightly uncrossed polarizers after rotation in a), c) anticlockwise and b), d) clockwise direction (contrast enhanced). The different degrees of intermediate brightness result from overlapping with surface films having opposite chirality; e) shows the complete DSC heating and cooling traces (the section indicated by the dashed rectangle is shown in Figure S1 m); f) small angle and g) wide angle X-ray scattering pattern in the Cr<sub>Iso</sub><sup>[\*]</sup> phase at 25°C (see also Figure S5 for the complete pattern).

ments, with the disordered segments of the chains filling the remaining space.<sup>[59,60]</sup> Additional birefringent crystalline phases with melting points at 117 and 121°C (magenta curve in Figure 9e) slowly crystallize from the Iso<sub>1</sub> or Iso phases, meaning that all mesophases of 3/2F6 are metastable.

Either chain elongation (3/2F10) or 2,3-difluorination (3/F26) recovers the I23<sup>[\*]</sup> phase and retains the Iso<sub>1</sub><sup>[\*]</sup> phase, whereas

**Table 4.** Comparison of the phase transitions of compounds **3/Yn** having additional lateral halogen substituents.<sup>[a]</sup>

Compound	<i>n</i>	Y <sup>3</sup>	Y <sup>2</sup>	<i>T</i> [°C] [ $\Delta H$ in kJ mol <sup>-1</sup> ] <sup>[a]</sup>	<i>a</i> <sub>cub</sub> [nm]
<b>1/6</b> <sup>[44]</sup>	6	H	H	H: Cr 118 [64.6] (Cr <sub>Iso</sub> <sup>[*]</sup> 82 [17.3]) <b>I23</b> <sup>[*]</sup> 126 [2.2] Iso <sub>1</sub> 134 [5.7] Iso C: Iso 130 [-7.1] Iso <sub>1</sub> 123 [-0.5] Iso <sub>1</sub> <sup>[*]</sup> 118 [-1.1] <b>I23</b> <sup>[*]</sup> 61 [-15.3] Cr <sub>Iso</sub> <sup>[*]</sup>	18.1
<b>3<sup>3</sup>F6</b>	6	F	H	H: Cr 93 [54.6] <b>I23</b> <sup>[*]</sup> 116 [0.4] Iso <sub>1</sub> 126 [9.5] Iso C: Iso 123 [-7.4] Iso <sub>1</sub> 108 [-0.2] Iso <sub>1</sub> <sup>[*]</sup> 103 [-0.8] <b>I23</b> <sup>[*]</sup> 78 [-17.0] Cr	17.1
<b>3<sup>2</sup>F6</b>	6	H	F	H: Cr 121 <sup>[b]</sup> (Cr <sub>Iso</sub> <sup>[*]</sup> 96 [24.5] Iso <sub>1</sub> <sup>[*]</sup> 106 [0.2] Iso <sub>1</sub> 114 [3.0]) Iso C: Iso 111 [-3.1] Iso <sub>1</sub> 104 [-0.2] Iso <sub>1</sub> <sup>[*]</sup> 89 [-21.5] Cr <sub>Iso</sub> <sup>[*]</sup>	–
<b>3<sup>2</sup>F10</b>	10	H	F	H: Cr 103 [45.5] <b>I23</b> <sup>[*]</sup> 113 [1.5] Iso <sub>1</sub> 121 [4.3] Iso C: Iso 120 [-4.1] Iso <sub>1</sub> 111 [-0.3] Iso <sub>1</sub> <sup>[*]</sup> 101 [-0.5] <b>I23</b> <sup>[*]</sup> 82 [-31] Cr	18.1
<b>3/F<sub>2</sub>6</b>	6	F	F	H: Cr 93 [16.4] <b>I23</b> <sup>[*]</sup> 126 [2.1] Iso <sub>1</sub> 133 [2.4] Iso C: Iso 131 [-2.1] Iso <sub>1</sub> 122 [-0.3] Iso <sub>1</sub> <sup>[*]</sup> 117 [-0.9] <b>I23</b> <sup>[*]</sup> 80 [17] Cr	17.2
<b>3<sup>2</sup>Cl6</b>	6	H	Cl	H: Cr 109 [67.2] (Cr <sub>Iso</sub> 84 [29.0] Iso <sub>1</sub> 93 [3.0]) Iso C: Iso 86 [-2.1] Iso <sub>1</sub> 78 [-0.2] <i>la</i> $\bar{3}$ <i>d</i> <sub>(5)</sub> 73 [-22.3] Cr <sub>Iso</sub>	–
<b>3<sup>2</sup>Br6</b>	6	H	Br	H: Cr 77 [21.0] ( <i>la</i> $\bar{3}$ <i>d</i> <sub>(5)</sub> <sup>[c]</sup> 80 <sup>[d]</sup> ) Cr <sub>Iso</sub> 84 [4.2] Iso <sub>1</sub> 90 [3.4] Iso C: Iso 85 [-4.5] Iso <sub>1</sub> 73 [-2.4] Cr <sub>Iso</sub>	–

[a] DSC peak temperatures on heating/cooling (H/C) at 10 Kmin<sup>-1</sup>; values in brackets give monotropic phase transitions observed in the second heating scan; abbreviations: Cr = birefringent crystalline phase; Cr<sub>Iso</sub> = optically isotropic crystalline solid, Cr<sub>Iso</sub><sup>[\*]</sup> = mirror symmetry broken Cr<sub>Iso</sub> phase; for the other abbreviations, see Table 1 and 3; phases shown in bold and with <sup>[\*]</sup> indicate mirror symmetry broken phases; for DSCs, see Figures 8, 9e and Figure S1; the maxima of the Iso–Iso<sub>1</sub> transitions are given, the corresponding temperature ranges are shown in Table S1. [b] Several crystalline modifications and crystallization processes take place in first heating, only the crystalline phase with highest melting point is given. [c] Due to crystallization no X-ray scattering could be performed. [d] The cubic phase can only be observed in the first heating as long as Cr<sub>Iso</sub> is not formed.

the Cr<sub>Iso</sub><sup>[\*]</sup> phase is removed and replaced by a birefringent crystalline phase (Table 4). Note that the Cub<sub>bi</sub>–Iso<sub>1</sub> transition temperature of the difluorinated compound **3/F<sub>2</sub>6** (Figure 8c, Figure S1 o) is almost the same as that observed for the non-fluorinated compound **1/6**, meaning that the steric mesophase destabilizing effect of 2-substitution is compensated by the additional electron attracting substituent in 3-position, strengthening the intermolecular attraction.

Investigation of the development of the correlation length  $\zeta$  of the clusters in the isotropic phase range by SAXS on cooling was conducted for compound **3/F<sub>2</sub>6** as example. The  $\zeta = f(T)$  curve is characterized by an increase of the slope at around 145–150 °C (Figure 10). This coincides with the onset of the broad DSC feature of the Iso–Iso<sub>1</sub> transition (Figure 8a). The correlation length increases continuously from 13 nm to 36 nm in the Iso<sub>1</sub><sup>[\*]</sup> phase without any distinct jump at the phase transitions. This is in line with the proposed model of the Iso–Iso<sub>1</sub><sup>[\*]</sup> transition. The increase of the *d*-value of the small angle scattering is also continuous, which is mainly attributed to the transition from a diffuse scattering, not following the Bragg law, to a more Bragg-like character of this scattering upon approaching the Cub<sub>bi</sub> phase. Similar observations were made for **3<sup>3</sup>F6**, see Figure S5.

### Non-symmetric tetracatenars with other halogens at the less substituted terminal

The effect of replacing fluorine by the larger halogens Cl or Br was investigated for the series **3<sup>2</sup>Y6** with the halogen in the

2-position (compounds **3<sup>2</sup>Cl6** and **3<sup>2</sup>Br6**, see Table 4). The reason for choosing this position is that changes in this position provide a stronger effect on the self-assembly than in the 3-position. For example, for **3<sup>3</sup>F6** the fundamental phase sequence of **3/6** is retained, whereas the chiral **I23**<sup>[\*]</sup> phase is removed for **3<sup>2</sup>F6**. Interestingly, replacing the fluorine of **3<sup>2</sup>F6** by chlorine restores the Cub<sub>bi</sub> phase, but the space group is changed to the achiral *la* $\bar{3}$ *d* phase, which occurs adjacent to the achiral Iso<sub>1</sub> phase without additional Iso<sub>1</sub><sup>[\*]</sup> range. More-

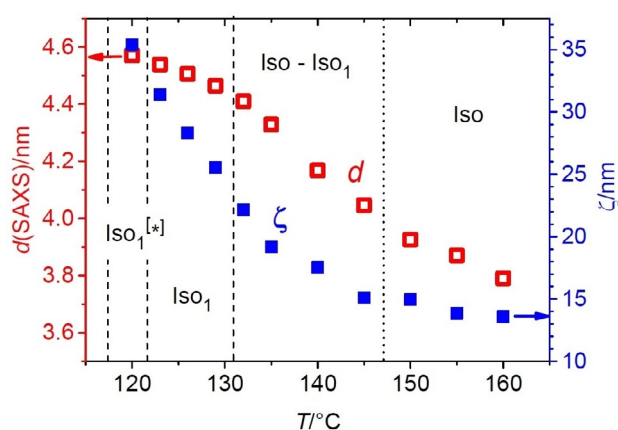


**Figure 10.** Temperature dependence of the *d*-value of the small angle scattering and the correlation length (calculated with the Scherrer equation) of the clusters in the Iso phases of compound **3/F<sub>2</sub>6**, measured on cooling; for the DSC traces see Figure 8b; the lift-off temperature of the broad DSC feature on cooling is around 147 °C, see Figure S5 for the related curve of **3<sup>3</sup>F6**.

over, the  $la\bar{3}d$  phases of  $3/2\text{Cl6}$  and  $3/2\text{Br6}$  are only monotropic and appear in small temperature ranges, observable only on heating (Table 4).<sup>[61]</sup> Though, due to partial crystallization, these  $\text{Cub}_{\text{bi}}$  phases are not accessible to X-ray scattering experiments, they can be investigated by POM. As shown in Figure S2d–f, in the contact region between the (previously confirmed)  $\text{Cub}_{\text{bi}}/la\bar{3}d_{(\text{S})}$  phase of  $1/14$ <sup>[44]</sup> and the  $la\bar{3}d$  phase of compound  $3/2\text{Br6}$  no  $I23^{[*]}$  phase with chiral conglomerate texture is observed, meaning that this  $\text{Cub}_{\text{bi}}$  phase is of the same short pitch  $la\bar{3}d_{(\text{S})}$  type. The increasing size of the lateral 2-substituent in the order  $\text{H} < \text{F} < \text{Cl} < \text{Br}$  obviously changes the cubic space group from  $I23^{[*]}$  to  $la\bar{3}d_{(\text{S})}$ , similar to the effect of alkyl chain elongation in the series  $1/n$ . The crystalline mesophase formed upon further cooling is also optically isotropic as that formed by the fluorinated compound  $3/2\text{F6}$ , but in this case it is achiral ( $\text{Cr}_{\text{Iso}}$ ). It is likely that the network structure in this crystalline mesophase is  $la\bar{3}d$ -like, as in the adjacent cubic phase, which is intrinsically achiral (racemic). Also the chirality synchronization in the liquid state is affected by the size of the halogen. Whereas for the non-fluorinated compound  $1/6$  and all three investigated fluorinated compounds  $3/2\text{F6}$ ,  $3/2\text{Br6}$  and  $3/2\text{Cl6}$  chirality synchronization takes place in the temperature range of the percolated liquid phase ( $\text{Iso}_1^{[*]}$ , see Figure 8b,c) it is not observed for  $3/2\text{Cl6}$  and  $3/2\text{Br6}$ . A possible reason could be that the local network structure in the percolated  $\text{Iso}_1$  phase also becomes  $la\bar{3}d$ -like by the steric effect of these larger halogens and therefore is intrinsically achiral.

### Local versus total mirror symmetry breaking

It is noted that the observed conglomerate formation represents only a local mode of mirror symmetry breaking. Total mirror symmetry breaking with stochastic outcome on a macroscopic length scale can be achieved in the  $I23^{[*]}$  phase if seed formation is slow and growth of the cubic phase is fast and it becomes deterministic in the presence of traces of external sources of chirality.<sup>[8,29a,38,47a]</sup> Related effects were also observed in the mirror symmetry broken soft crystalline phases formed by mesogenic trimers.<sup>[62]</sup> Tiny chirality sources are also assumed to be responsible for “spontaneous” formation of  $I23^{[*]}$  or  $\text{Iso}_1^{[*]}$  phases with uniform chirality, as observed in some cases.<sup>[8]</sup> However, for the benzil-based compounds the tendency to form large homogeneous chiral domains is less developed if compared with related 2,2'-bithiophene based polycatenars<sup>[29a,46]</sup> and formation of relatively small chiral domains is dominating in this class of compounds (see Figures 2a–c and 9a–d). A possible reason could be a higher viscosity or the bent molecular shape, slowing down the growth processes.

### Discussion of the importance of network formation for chirality synchronization

Chirality synchronization of the local helical structure by network formation, suppressing helix reversal defects,<sup>[63]</sup> appears to be the key feature required for mirror symmetry breaking of polycatenar mesogens in the liquid, LC and soft crystalline

states. The helical networks, developing in the  $\text{Iso}_1/\text{Iso}_1^{[*]}$  and  $\text{Cub}_{\text{bi}}/la\bar{3}d/I23^{[*]}$  phases, can obviously be retained after crystallization of the aromatic cores in the optically isotropic crystalline mesophases of compounds  $3/2\text{Yn}$ , where the polyaromatic cores and parts of the alkyl chains assume a crystalline packing in the networks and the disordered segments of the alkyl chains fill the remaining space. These crystalline mesophases are in some respect related to gels (“solvent free gels”),<sup>[43,59,60,62,64–66]</sup> though details of their structures require further investigations. A certain degree of net connectivity is in some cases also retained in the isotropic liquid phases, considered as percolated liquids<sup>[67,68]</sup> and representing dynamic networks, which become chiral after crossing the critical network density required for emergence of chirality synchronization.<sup>[47,38]</sup> These percolated liquids can either transform into chirality synchronized cubic LC phases after assuming long-range periodicity or to disordered crystalline isotropic mesophases by freezing the molecular mobility.

For numerous compounds local clusters and network formation occur in the liquid state prior to the transition to LC and crystalline phases. Often, these transitions take place already at high temperatures outside the investigated (or accessible) temperature range, or do not show up in the DSC traces, because they take place over extremely broad temperature ranges. However, the DSC features of the  $\text{Iso}-\text{Iso}_1$  transitions of the benzil-derived polycatenars appear in relatively narrow temperature ranges close to the phase transition to the  $\text{Cub}_{\text{bi}}$  phase and, therefore, become easily detectable. Similar observations were made for the ANBCs (Scheme 1).<sup>[9b,29a,32b,c,49a]</sup> This kind of polymorphism in the liquid state appears to be associated with network formation and therefore is observed in the vicinity of  $\text{Cub}_{\text{bi}}$  phases. It can also be found if a lamellar or columnar phase separates the  $\text{Iso}_1$  and  $\text{Cub}_{\text{bi}}$  phase (compounds  $2/\text{CN}$  and  $2/\text{NO}_2$ , Figure 7a). It is however not observed at the transition to non-cubic LC phases, which are (with respect to molecular structure or temperature) far away from any  $\text{Cub}_{\text{bi}}$  phase range. Moreover, it appears to require a certain strength of the attractive intermolecular interactions, being strong enough for network formation and sufficiently weak that the networks can be disrupted by mild thermal agitation. Depending on the kind of network structure, the resulting liquid, LC or crystalline mesophases can be optically inactive if a racemic double network ( $la\bar{3}d$ ) is formed, or optically active if a homochiral triple network develops ( $I23^{[*]}$ ). As the local structure can change at the phase transitions also phase sequences combining chiral and achiral phases can occasionally be observed (e.g.  $la\bar{3}d-\text{Iso}_1^{[*]}$ ).

An important point concerns the formation of the  $I23^{[*]}$  structure instead of the usually dominating double gyroid ( $la\bar{3}d$ ) structure, which is only observed if rod-like units are involved in the molecules, leading to a helical twist along the networks.<sup>[29]</sup> Therefore, it can be assumed that this transition is chirality (helicity) induced. One way of thinking considers the matching of the twist at the nodes in the individual nets (intra-network resonance) as important for chirality synchronization.<sup>[29a]</sup> A second important issue concerns the through-space interaction between the nets, that is, the interaction between



adjacent close packed helix segments. Here a slight change of the twist angle of the molecules along the helices could modify the sign and strength of inter-helix interactions at a given angle and distance between the close packed adjacent helices.<sup>[69]</sup> Preferred heterochiral interactions are obviously compatible with the  $la\bar{3}d$  phase structure composed of two enantiomeric networks, leading to chiral extinction (lowest energy racemic state). However, an increasing preference of homochiral helix-helix interaction (lowest energy homochiral state) could destabilize the double gyroid structure and requires a change of the phase structure by retaining the network topology involving exclusively three way junctions. The  $I23^{[*]}$  structure appears to be the best solution for this case, though also non-cubic arrangements of helical networks, as for example in the tetragonal "SmQ phase",<sup>[40]</sup> could have very similar energy and can compete under certain conditions.

The softening of the helix-helix interactions in the liquid state could change the preferred mode of helix correlation and this could explain the transition between an achiral double gyroid cubic phase and a conglomerate type  $Iso_1^{[*]}$  liquid (with assumed local  $I23$  structure) observed in some cases. Though there is a substantial amount of work concerning the investigation of helix-helix interactions in lipid membranes,<sup>[70]</sup> the general understanding of the helix packing depending on the sign and strength of the interaction parameters, the helical twist, and the angle between the interacting helices needs to be studied and simulated in more detail to support this hypothesis.<sup>[69]</sup>

It is noted that there is a strong relation between the  $Cub_{bi}$ - $Iso^{[*]}$  transitions reported here for achiral molecules (with transiently chiral conformations) and the BPI/BPII to BPIII (BP = blue phase) transition observed for permanently chiral rod-like molecules.<sup>[71,72]</sup> The cubic BPII, for example, has a  $la\bar{3}d$  double gyroid structure, whereas the BPIII (blue fog phase) is an isotropic liquid with dynamic network structure.<sup>[71a]</sup> Even the typical DSC features of the BPI/BPII to BPIII transitions resemble those of the  $Cub_{bi}$ - $Iso^{[*]}$  transitions, characterized by a broad diffuse feature in the liquid state.<sup>[49a]</sup> The main difference is that in the case of the Blue Phases the network structure is induced by a permanent molecular chirality, whereas for the achiral polycatenar compounds reported here the network structure leads to chirality synchronization, destabilizing the achiral/racemic states which then spontaneously bifurcate into a conglomerate of chiral liquids due to the emergent cooperativity of chirality transfer provided by the network structure.<sup>[8]</sup>

## Conclusions

It is shown that the 4,4'-diphenylbenzil unit is a universal transiently chiral bent building block for the design of mesogens capable of forming network structures in the liquid, the LC and the crystalline state.  $Cub_{bi}$  network structures with  $la\bar{3}d$  and  $I23^{[*]}$  space groups were obtained for non-symmetric tetracatenars (compounds **1/n**, **4/n** and **3/Yn**) and tricaténars (compounds **2/X**) if the total number of benzene rings incorporated in the core unit is at least five. Polar substituents at the apex (X) were shown to support cubic phase formation, leading to

compounds with high transition temperatures and wide cubic ranges. These polar substituents represent strong electron acceptors which reduce the electron density of the  $\pi$ -system of the cores and this strengthens the attractive core-core interactions, thus stabilizing the cubic phases significantly, even against unfavorable steric effects of these substituents (Table 3). The mesophase stabilizing effect grows in the order  $X = F < OCF_3 < CN < NO_2$ , roughly corresponding to the increasing Hammett constants of these substituents (Figure 11).<sup>[51]</sup> The cubic phases of all these compounds with a relatively small polar apex represent long pitch  $la\bar{3}d_{(L)}$  phases, thus indicating a small helical twist between the molecules along the networks. Larger twist angles, supporting the formation of the mirror symmetry broken  $I23^{[*]}$  phase, were achieved for compounds with longer alkoxy chains at the apex. Halogenation of the monoalkoxylated benzene ring of these tetracatenars further supports the helical twist, leading to a transition from  $I23^{[*]}$  to the achiral short pitch  $la\bar{3}d_{(S)}$  phase for the larger halogens Cl and Br (Figure 11). Especially strong is this effect in the inside directed 2-position. Besides the effect on the twist, there is also a steric mesophase destabilizing effect of the polar substituents X and Y, becoming more important in the sequence of their positions  $4 < 3 < 2$ . Thus, the steric effects of the substituents can override the stabilizing electronic effects, the more they are shifted towards the center of the polyaromatic core.<sup>[73,74]</sup> Figure 11 summarizes the relations between molecular structure and formation of the distinct cubic and accompanying mirror symmetry broken  $Iso_1^{[*]}$  phases gained herein.

Overall, this work contributes to the better understanding of the development of networks and spontaneous mirror symmetry breaking in self-assembled systems, including crystalline helical aggregates,<sup>[43,64-75]</sup> gels,<sup>[60,66]</sup> LC phases<sup>[38,59,60,62,76-79]</sup> and

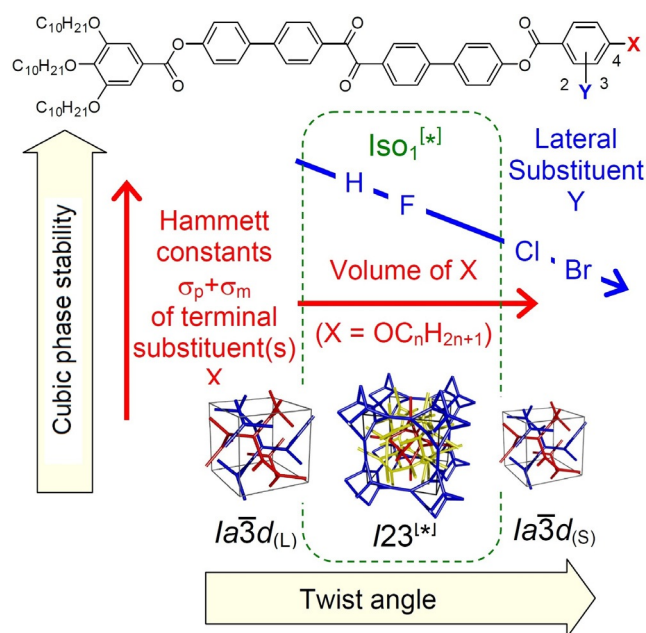


**Figure 11.** Summary of the relations between molecular structure, cubic phase type, cubic phase stability and mirror symmetry breaking in the LC and isotropic liquid phases.



the most intriguing case of mirror-symmetry broken isotropic liquids.<sup>[47]</sup> In general, the nano-structures of the liquid phases and their polyamorphism (liquid–liquid phase transitions and liquid–liquid phase separations) are still less investigated and represent almost unsolved scientific problems with great importance.<sup>[80]</sup> It appears that formation of cybotactic clusters and dynamic networks are important features with relevance for the understanding of the special properties of fluids, especially in the context of prebiotic and biological systems.<sup>[8]</sup> Dynamic network formation in liquids is a prerequisite for development of complexity and obviously provides the basis of the emergence of new features. Among them the bifurcation of achiral and racemic systems into stable homochiral states, thus leading to the transition from achiral to chiral chemical systems, representing the first step of the transition from chemical systems to biogenesis.<sup>[8]</sup>

## Acknowledgements

This Work was supported by the Deutsche Forschungsgemeinschaft (Ts 39/24-2). Open access funding enabled and organized by Projekt DEAL.

## Conflict of interest

The authors declare no conflict of interest.

**Keywords:** chirality · cubic phases · liquid crystals · mirror symmetry breaking · soft matter

- [1] J. Gasteiger, J. Zupan, *Angew. Chem. Int. Ed. Engl.* **1993**, *32*, 503–527; *Angew. Chem.* **1993**, *105*, 510–536.
- [2] S. Kauffman, *At Home in the Universe*, Oxford University Press, Oxford, **1995**, pp. 54–58.
- [3] a) A. S. Y. Wong, W. T. S. Huck, *Beilstein J. Org. Chem.* **2017**, *13*, 1486–1497; b) S. Otto, *Acc. Chem. Res.* **2012**, *45*, 2200–2210; c) B. A. Grzybowski, K. Fitzner, J. Paczesny, S. Granick, *Chem. Soc. Rev.* **2017**, *46*, 5647–5678.
- [4] M. O’Keeffe, O. M. Yaghi, *Chem. Rev.* **2012**, *112*, 675–702.
- [5] T. Kato, J. Uchida, T. Ichikawa, T. Sakamoto, *Angew. Chem. Int. Ed.* **2018**, *57*, 4355–4371; *Angew. Chem.* **2018**, *130*, 4438–4455.
- [6] *Bicontinuous Liquid Crystals* (Eds.: M. L. Lynch, P. T. Spicer), CRC Press, Boca Raton, **2005**.
- [7] A. Guijarro, M. Yus, *The Origin of Chirality in the Molecules of Life*, Royal Society of Chemistry, Cambridge, **2009**.
- [8] C. Tschierske, C. Dressel, *Symmetry* **2020**, *12*, 1098.
- [9] a) G. Ungar, F. Liu, X. B. Zeng in *Handbook of Liquid Crystals, Vol 5* 2nd ed. (Eds.: J. W. Goodby, P. J. Collings, T. Kato, C. Tschierske, H. Gleeson, P. Raynes), Wiley-VCH, Weinheim, **2014**; b) S. Kutsumizu, *Isr. J. Chem.* **2012**, *52*, 844–853.
- [10] C. Tschierske, *Angew. Chem. Int. Ed.* **2013**, *52*, 8828–8878; *Angew. Chem.* **2013**, *125*, 8992–9047.
- [11] K. Borisch, S. Diele, P. Göring, H. Kresse, C. Tschierske, *J. Mater. Chem.* **1998**, *8*, 529–543.
- [12] a) A. J. Meuler, M. A. Hillmyer, F. S. Bates, *Macromolecules* **2009**, *42*, 7221–7250; b) E. L. Thomas, *Sci. China Chem.* **2018**, *61*, 25–32.
- [13] a) J. M. Seddon, R. H. Templer in *Handbook of Biological Physics, Vol. 1* (Eds.: R. Lipowsky, E. Sackmann), Elsevier, Amsterdam, **1995**, pp. 97–160; b) S. T. Hyde in *Handbook of Applied Surface and Colloid Chemistry, Vol 1* (Ed. K. Holmberg), Wiley, New York, **2001**, pp. 299–332; c) L. van ’t Hag, S. L. Gras, C. E. Conn, C. J. Drummond, *Chem. Soc. Rev.* **2017**, *46*, 2705–2731.
- [14] L. Han, S. Che, *Adv. Mater.* **2018**, *30*, 1705708.
- [15] a) C. Tschierske, *J. Mater. Chem.* **2001**, *11*, 2647–2671; b) C. Tschierske, *Annu. Rep. Prog. Chem. Sect. C* **2001**, *97*, 191–267; c) C. Tschierske, *Isr. J. Chem.* **2012**, *52*, 935–959; d) C. Tschierske in *Handbook of Liquid Crystals, Vol. 5*, 2nd ed. (Eds.: J. W. Goodby, J. P. Collings, T. Kato, C. Tschierske, H. F. Gleeson, P. Raynes), Wiley-VCH, Weinheim, **2014**, pp. 1–88.
- [16] a) J.-H. Ryu, M. Lee, *Struct. Bonding (Berlin)* **2008**, *128*, 63–98; b) L.-Y. Shi, Y. Zhou, X.-H. Fan, Z. Shen, *Macromolecules* **2013**, *46*, 5308–5316.
- [17] X. Zeng, M. Prehm, G. Ungar, C. Tschierske, F. Liu, *Angew. Chem. Int. Ed.* **2016**, *55*, 8324–8327; *Angew. Chem.* **2016**, *128*, 8464–8467.
- [18] X. Zeng, S. Poppe, A. Lehmann, M. Prehm, C. Chen, F. Liu, H. Lu, G. Ungar, C. Tschierske, *Angew. Chem. Int. Ed.* **2019**, *58*, 7375–7379; *Angew. Chem.* **2019**, *131*, 7453–7457.
- [19] S. Poppe, X. Cheng, C. Chen, X. Zeng, R.-B. Zhang, F. Liu, G. Ungar, C. Tschierske, *J. Am. Chem. Soc.* **2020**, *142*, 3296–3300.
- [20] C. Chen, R. Kieffer, H. Ebert, M. Prehm, R.-B. Zhang, X. Zeng, F. Liu, G. Ungar, C. Tschierske, *Angew. Chem. Int. Ed.* **2020**, *59*, 2725–2729; *Angew. Chem.* **2020**, *132*, 2747–2751.
- [21] a) F. Liu, M. Prehm, X. Zeng, C. Tschierske, G. Ungar, *J. Am. Chem. Soc.* **2014**, *136*, 6846–6849; b) S. Poppe, C. Chen, F. Liu, C. Tschierske, *Chem. Commun.* **2018**, *54*, 11196–11199.
- [22] A. M. Levelut, M. Clerc, *Liqu. Cryst.* **1998**, *24*, 105–115.
- [23] X. B. Zeng, G. Ungar, M. Imperor-Clerc, *Nat. Mater.* **2005**, *4*, 562–567.
- [24] X.-Q. Jiang, R.-Y. Zhao, W.-Y. Chang, D.-X. Yin, Y.-C. Guo, W. Wang, D.-H. Liang, S. Yang, A.-C. Shi, E.-Q. Chen, *Macromolecules* **2019**, *52*, 5033–5041.
- [25] Y. Sun, P. Padmanabhan, M. Misra, F. A. Escobedo, *Soft Matter* **2017**, *13*, 8542–8555.
- [26] There are only few reports about bicontinuous networks having the aromatic core on the minimal surface, either parallel<sup>[20]</sup> or perpendicular to them.<sup>[27]</sup>
- [27] M. Poppe, C. Chen, F. Liu, S. Poppe, C. Tschierske, *Chem. Eur. J.* **2017**, *23*, 7196–7200.
- [28] S. Andersson, S. T. Hyde, K. Larsson, S. Lidin, *Chem. Rev.* **1988**, *88*, 221–242.
- [29] a) C. Dressel, F. Liu, M. Prehm, X. B. Zeng, G. Ungar, C. Tschierske, *Angew. Chem. Int. Ed.* **2014**, *53*, 13115–13120; *Angew. Chem.* **2014**, *126*, 13331–13336; b) M. Alaasar, S. Poppe, Q. Dong, F. Liu, C. Tschierske, *Chem. Commun.* **2016**, *52*, 13869–13872; c) Y. Cao, M. Alaasar, A. Nallapaneni, M. Salamończyk, P. Marinko, E. Gorecka, C. Tschierske, F. Liu, N. Vaupotič, C. Zhu, *Phys. Rev. Lett.* **2020**, *125*, 027801.
- [30] a) T. Kajitani, S. Kohmoto, M. Yamamoto, K. Kishikawa, *Chem. Mater.* **2005**, *17*, 3812–3819; b) J. M. Wolska, J. Wilk, D. Pocięcha, J. Mieczkowski, E. Gorecka, *Chem. Eur. J.* **2017**, *23*, 6853–6857; c) H. R. Brand, H. Pleiner, *Eur. Phys. J. E* **2019**, *42*, 142.
- [31] X. B. Zeng, G. Ungar, *J. Mater. Chem. C* **2020**, *8*, 5389–5398.
- [32] a) G. W. Gray, B. Jones, F. Marson, *J. Chem. Soc.* **1957**, 393–401; b) S. Kutsumizu, K. Morita, T. Ichikawa, S. Yano, S. Nojima, T. Yamaguchi, *Liq. Cryst.* **2002**, *29*, 1447–1458; c) S. Kutsumizu, M. Yamada, S. Yano, *Liq. Cryst.* **1994**, *16*, 1109–1113.
- [33] a) H. Schubert, J. Hauschild, D. Demus, S. Hoffmann, *Z. Chem.* **1978**, *18*, 256; b) Y. Yamamura, Y. Nakazawa, S. Kutsumizu, K. Saito, *Phys. Chem. Chem. Phys.* **2019**, *21*, 23705–23712.
- [34] S. Kutsumizu, I. Tokiwa, A. Kawafuchi, Y. Miwa, Y. Yamamura, K. Saito, *Phys. Chem. Chem. Phys.* **2016**, *18*, 9013–9020.
- [35] a) H. T. Nguyen, C. Destrade, J. Malthete, *Adv. Mater.* **1997**, *9*, 375–388; b) D. W. Bruce, *Acc. Chem. Res.* **2000**, *33*, 831–840; c) W. Weissflog in *Handbook of Liquid Crystals, Vol. 5* 2nd Ed. (Eds.: J. W. Goodby, J. P. Collings, T. Kato, C. Tschierske, H. F. Gleeson, P. Raynes), Wiley-VCH, Weinheim, **2014**, pp. 89–174.
- [36] In a similar way also silyl groups and perfluorinated alkyl chains could lead to Cub<sub>b1</sub> phases due to the interface curvature provided by these bulky chains.<sup>[15,34,37]</sup>
- [37] a) I. Nishiyama, *Chem. Rec.* **2009**, *9*, 340–355; b) M. Yoneya, *Chem. Rec.* **2011**, *11*, 66–76; c) E. Nishikawa, J. Yamamoto, H. Yokoyama, *J. Mater. Chem.* **2003**, *13*, 1887–1893; d) E. Nishikawa, E. T. Samulski, *Liq. Cryst.* **2000**, *27*, 1463–1471.
- [38] a) C. Tschierske, *Liqu. Cryst.* **2018**, *45*, 2221–2252; b) C. Tschierske, G. Ungar, *ChemPhysChem* **2016**, *17*, 9–26.
- [39] A. H. Schoen, *Interface Focus* **2012**, *2*, 658–668.

- [40] A similar synchronization of the network chirality was found in the non-cubic SmQ phase with 90° four-way junctions, see ref. [41].
- [41] H. J. Lu, X. B. Zeng, G. Ungar, C. Dressel, C. Tschierske, *Angew. Chem. Int. Ed.* **2018**, *57*, 2835–2840; *Angew. Chem.* **2018**, *130*, 2885–2890.
- [42] The effect of the alkyl chains in the LC phases is similar to the contribution of steric effects on helix formation in the case of the crystalline self-assembly in supramolecular polymers, leading to fibres and gels, see ref. [43].
- [43] Y. Dorca, E. E. Greciano, J. S. Valera, R. Gjmez, L. Sanchez, *Chem. Eur. J.* **2019**, *25*, 5848–5864; E. Yashima, N. Ousaka, D. Taura, K. Shimomura, T. Ikai, K. Maeda, *Chem. Rev.* **2016**, *116*, 13752–13990.
- [44] T. Reppe, S. Poppe, X. Cai, F. Liu, C. Tschierske, *Chem. Sci.* **2020**, *11*, 5902–5908.
- [45] T. Reppe, C. Dressel, S. Poppe, C. Tschierske, *Chem. Commun.* **2020**, *56*, 711–713.
- [46] C. Dressel, T. Reppe, S. Poppe, M. Prehm, H. Lu, X. Zeng, G. Ungar, C. Tschierske, *Adv. Funct. Mater.* **2020**, 2004353.
- [47] a) C. Dressel, T. Reppe, M. Prehm, M. Brautzsch, C. Tschierske, *Nat. Chem.* **2014**, *6*, 971–977; b) C. Dressel, W. Weissflog, C. Tschierske, *Chem. Commun.* **2015**, *51*, 15850–15853; c) M. Alaasar, M. Prehm, Y. Cao, F. Liu, C. Tschierske, *Angew. Chem. Int. Ed.* **2016**, *55*, 312–316; *Angew. Chem.* **2016**, *128*, 320–324; d) M. Alaasar, S. Poppe, Q. Dong, F. Liu, C. Tschierske, *Angew. Chem. Int. Ed.* **2017**, *56*, 10801–10805; *Angew. Chem.* **2017**, *129*, 10941–10945.
- [48] a) C. J. Brown, R. Sadanaga, *Acta Crystallogr.* **1965**, *18*, 158–164; b) Q. Shen, K. Hagen, *J. Phys. Chem.* **1987**, *91*, 1357–1360; c) Z. Pawelka, A. Koll, T. Zeegers-Huyskens, *J. Mol. Struct.* **2001**, *597*, 57–66.
- [49] a) J. W. Goodby, D. A. Dunmur, P. J. Collings, *Liq. Cryst.* **1995**, *19*, 703–709; b) A. Gradisek, M. Cifelli, M. Wojcik, T. Apih, S. V. Dvinskikh, E. Gorecka, V. Domenici, *Crystals* **2019**, *9*, 178.
- [50] J. W. Steed, J. L. Atwood, *Supramolecular Chemistry*, Wiley, Chichester, **2000**.
- [51] C. Hansch, A. Leo, R. W. Taft, *Chem. Rev.* **1991**, *91*, 165–195.
- [52] a) K. Kishikawa, *Isr. J. Chem.* **2012**, *52*, 800–808; b) M. Hird, *Chem. Soc. Rev.* **2007**, *36*, 2070–2095.
- [53] S. Kutsumizu, Y. Yamada, T. Sugimoto, N. Yamada, T. Udagawa, Y. Miwa, *Phys. Chem. Chem. Phys.* **2018**, *20*, 7953–7961.
- [54] S. Kutsumizu, S. Miisako, Y. Miwa, M. Kitagawa, Y. Yamamura, K. Saito, *Phys. Chem. Chem. Phys.* **2016**, *18*, 17341–17344.
- [55] As another case of chirality induction by mixing two components, the induction of a chiral N<sub>18</sub> phase was observed by mixing two achiral complementary hydrogen bonding molecules, see ref. [56].
- [56] R. Walker, D. Pocięcha, J. P. Abberley, A. Martinez-Felipe, D. A. Paterson, E. Forsyth, G. B. Lawrence, P. A. Henderson, J. M. D. Storey, E. Gorecka, C. T. Imrie, *Chem. Commun.* **2018**, *54*, 3383–3386.
- [57] Values on heating were used, because the values on cooling tend to be lower due to the slow transitions, which are partly suppressed in the cooling cycle.
- [58] R. Androsch, A. M. Rhoades, I. Stolte, C. Schick, *Eur. Polym. J.* **2015**, *66*, 180–189.
- [59] M. Alaasar, M. Prehm, C. Tschierske, *Chem. Commun.* **2013**, *49*, 11062–11064; M. Alaasar, M. Prehm, M. Brautzsch, C. Tschierske, *J. Mater. Chem. C* **2014**, *2*, 5487–5501; M. Alaasar, M. Prehm, M. Brautzsch, C. Tschierske, *Soft Matter* **2014**, *10*, 7285–7296; M. Alaasar, M. Prehm, C. Tschierske, *Chem. Eur. J.* **2016**, *22*, 6583–6597.
- [60] a) T. Otani, F. Araoka, K. Ishikawa, H. Takezoe, *J. Am. Chem. Soc.* **2009**, *131*, 12368–12372; b) A. Zep, M. Salamonczyk, N. Vaupotic, D. Pocięcha, E. Gorecka, *Chem. Commun.* **2013**, *49*, 3119–3121; c) S. Shadpour, A. Nemati, N. J. Boyd, L. Li, M. E. Prevot, S. L. Wakerlin, J. P. Vanegas, M. Salamonczyk, E. Hegmann, C. Zhu, M. R. Wilson, A. I. Jakli, T. Hegmann, *Mater. Horiz.* **2019**, *6*, 959–968.
- [61] The cubic phase is not observed on cooling due to the delay of the Iso<sub>1</sub>-Cub<sub>bi</sub> transition on cooling, so that only the Cr<sub>iso</sub> phase can be found.
- [62] A. Yoshizawa, Y. Kato, H. Sasaki, Y. Takanishi, J. Yamamoto, *J. Phys. Chem. B* **2016**, *120*, 4843–4851; R. Oikawa, H. Sasaki, Y. Takanishi, M. Sagisaka, J. Yamamoto, A. Yoshizawa, *Soft Matter* **2019**, *15*, 3179–3187; M. Kurata, A. Yoshizawa, *Chem. Commun.* **2020**, *56*, 8289–8292.
- [63] B. Jouvet, B. Isare, L. Bouteiller, P. van der Schoot, *Langmuir* **2014**, *30*, 4570–4575.
- [64] a) J. V. Selinger, M. S. Spector, J. M. Schnur, *J. Phys. Chem.* **2001**, *105*, 7157–7169; b) T. G. Barclay, K. Constantopoulos, J. Matison, *Chem. Rev.* **2014**, *114*, 10217–10291; c) A. Brizard, R. Oda, I. Huc, *Top. Curr. Chem.* **2005**, *256*, 167–218.
- [65] a) M. Liu, L. Zhang, T. Wang, *Chem. Rev.* **2015**, *115*, 7304–7397; b) G. Liu, C. Zhou, W. L. Teo, Ch. Qian, Y. Zhao, *Angew. Chem. Int. Ed.* **2019**, *58*, 9366–9372; *Angew. Chem.* **2019**, *131*, 9466–9472; c) S. Yu, R. Sun, T. Chen, L. Y. Jin, *Soft Matter* **2018**, *14*, 6822–6827.
- [66] a) Z. Shen, T. Wang, M. Liu, *Angew. Chem. Int. Ed.* **2014**, *53*, 13424–13428; *Angew. Chem.* **2014**, *126*, 13642–13646; b) L. Zhang, T. Wang, Z. Dhen, M. Liu, *Adv. Mater.* **2016**, *28*, 1044–1059.
- [67] D. de las Heras, J. M. Tavares, M. M. Telo da Gama, *Soft Matter* **2011**, *7*, 5615–5626.
- [68] a) P. Gallo, K. Amann-Winkel, C. A. Angell, M. A. Anisimov, F. Caupin, C. Chakravarty, E. Lascaris, T. Loerting, A. Z. Panagiotopoulos, J. Russo, J. A. Sellberg, H. E. Stanley, H. Tanaka, C. Vega, L. Xu, L. G. M. Pettersson, *Chem. Rev.* **2016**, *116*, 7463–7500; b) L. Longa, M. Ciesla, H.-R. Trebin, *Phys. Rev. E* **2003**, *67*, 061705.
- [69] a) D. M. Hall, G. M. Grason, *Interface Focus* **2017**, *7*, 20160140; b) G. M. Grason, *J. Chem. Phys.* **2016**, *145*, 110901; c) C. J. Forman, S. N. Fejer, D. Chakrabarti, P. D. Barker, D. J. Wales, *J. Phys. Chem. B* **2013**, *117*, 7918–7928.
- [70] V. Corradi, B. I. Sejdiu, H. Mesa-Galloso, H. Abdizadeh, S. Yu, Noskov, S. J. Marrink, D. P. Tieleman, *Chem. Rev.* **2019**, *119*, 5775–5848.
- [71] a) O. Henrich, K. Stratford, M. E. Cates, D. Marenduzzo, *Phys. Rev. Lett.* **2011**, *106*, 107801; b) S. S. Gandhi, L.-C. Chien, *Adv. Mater.* **2017**, *29*, 1704296; A. Yoshizawa, *RSC Adv.* **2013**, *3*, 25475–25497.
- [72] Z.-G. Zheng, Y.-Q. Lu, Q. Li, *Adv. Mater.* **2020**, *32*, 1905318; H. K. Bisoyi, T. J. Bunning, Q. Li, *Adv. Mater.* **2018**, *30*, 1706512.
- [73] In this context it is noted that polar substituents like F and CN in the center of the rod-like cores of symmetric tetracatenars have been reported to inhibit any cubic phase formation and replace it by lamellar phases, see ref. [74].
- [74] A. I. Smirnova, B. Heinrich, B. Donnio, D. W. Bruce, *RSC Adv.* **2015**, *5*, 75149–75159.
- [75] A. R. A. Palmans, E. W. Meijer, *Angew. Chem. Int. Ed.* **2007**, *46*, 8948–8968; *Angew. Chem.* **2007**, *119*, 9106–9126; C. Kulkarni, E. W. Meijer, A. R. A. Palmans, *Acc. Chem. Res.* **2017**, *50*, 1928–1936.
- [76] S. P. Sreenilayam, Y. P. Panarin, J. K. Vij, V. P. Panov, A. Lehmann, M. Poppe, M. Prehm, C. Tschierske, *Nat. Commun.* **2016**, *7*, 11369; M. Poppe, M. Alaasar, A. Lehmann, S. Poppe, M.-G. Tamba, M. Kurachkina, A. Eremin, M. Nagaraj, J. K. Vij, X. Cai, F. Liu, C. Tschierske, *J. Mater. Chem. C* **2020**, *8*, 3316–3336; A. Lehmann, M. Alaasar, M. Poppe, S. Poppe, M. Prehm, M. Nagaraj, S. P. Sreenilayam, Y. P. Panarin, J. K. Vij, C. Tschierske, *Chem. Eur. J.* **2020**, *26*, 4714–4733.
- [77] D. Chen, Y. Shen, J. Agüero, E. Korblova, D. M. Walba, N. Kapernaum, F. Giesselmann, J. Watanabe, J. E. MacLennan, M. A. Glaser, N. A. Clark, *ChemPhysChem* **2014**, *15*, 1502–1507.
- [78] H. Takezoe in *Topics in Current Chemistry Vol. 318* (Ed.: C. Tschierske), Springer, Berlin, **2011**, pp. 303–330.
- [79] K. V. Le, H. Takezoe, F. Araoka, *Adv. Mater.* **2017**, *29*, 1602737.
- [80] a) J. A. Bollinger, T. M. Truskett, *J. Chem. Phys.* **2016**, *145*, 064902; b) M. B. Sweatman, R. Fartaria, L. Lue, *J. Chem. Phys.* **2014**, *140*, 124508; c) C. A. Angell, Z. Zhao, *Faraday Discuss.* **2013**, *167*, 625–641; d) H. Tanaka, *Eur. Phys. J. E* **2012**, *35*, 113; e) T. S. Ingebrigtsen, T. B. Schröder, J. C. Dyre, *Phys. Rev. X* **2012**, *2*, 011011.

Manuscript received: June 14, 2020

Accepted manuscript online: July 11, 2020

Version of record online: October 29, 2020

# Chemistry–A European Journal

Supporting Information

## **Controlling Mirror Symmetry Breaking and Network Formation in Liquid Crystalline Cubic, Isotropic Liquid and Crystalline Phases of Benzil-Based Polycatenars**

Tino Reppe, Silvio Poppe, and Carsten Tschierske\*<sup>[a]</sup>

## 1. Methods

**Optical and calorimetric investigations.** Phase transitions were determined by polarizing microscopy (Leica DMR XP) in conjunction with a heating stage (FP 82 HT, Mettler) and controller (FP 90, Mettler) and by differential scanning calorimetry (DSC-8000, Perkin Elmer) at heating/cooling rates of  $10 \text{ K min}^{-1}$  (peak temperatures). If not otherwise noted transition temperatures and  $\Delta H$  were taken from the second heating and cooling curve. Optical investigation was carried out under equilibrium conditions between glass slides which were used without further treatment, sample thickness was  $\sim 15 \text{ }\mu\text{m}$ . A full wavelength retardation plate was used to determine the sign of birefringence. Optical micrographs were taken using a Leica MC120HD camera.

**X-ray diffraction.** X-ray investigations (Kristalloflex 760H, Siemens) on powder-like samples were carried out using Ni filtered  $\text{CuK}\alpha$  radiation (15 to 30 min exposure time). The samples were prepared in the isotropic state on a glass plate and cooled (rate:  $5 \text{ K}\cdot\text{min}^{-1}$ ) to the measuring temperature. The samples were held on a temperature controlled heating stage and the diffraction patterns were recorded with a 2D detector (Vantec 500, Bruker); exposure time was 15-20 min. The sample-detector distance for the samples was 9.00 cm for WAXD and 26.90 cm for SAXD measurements. The diffraction patterns obtained were transform to 1D plots using GADDS over the full Chi range.

## 2. Additional Data

### 2.1 DSC traces and textures

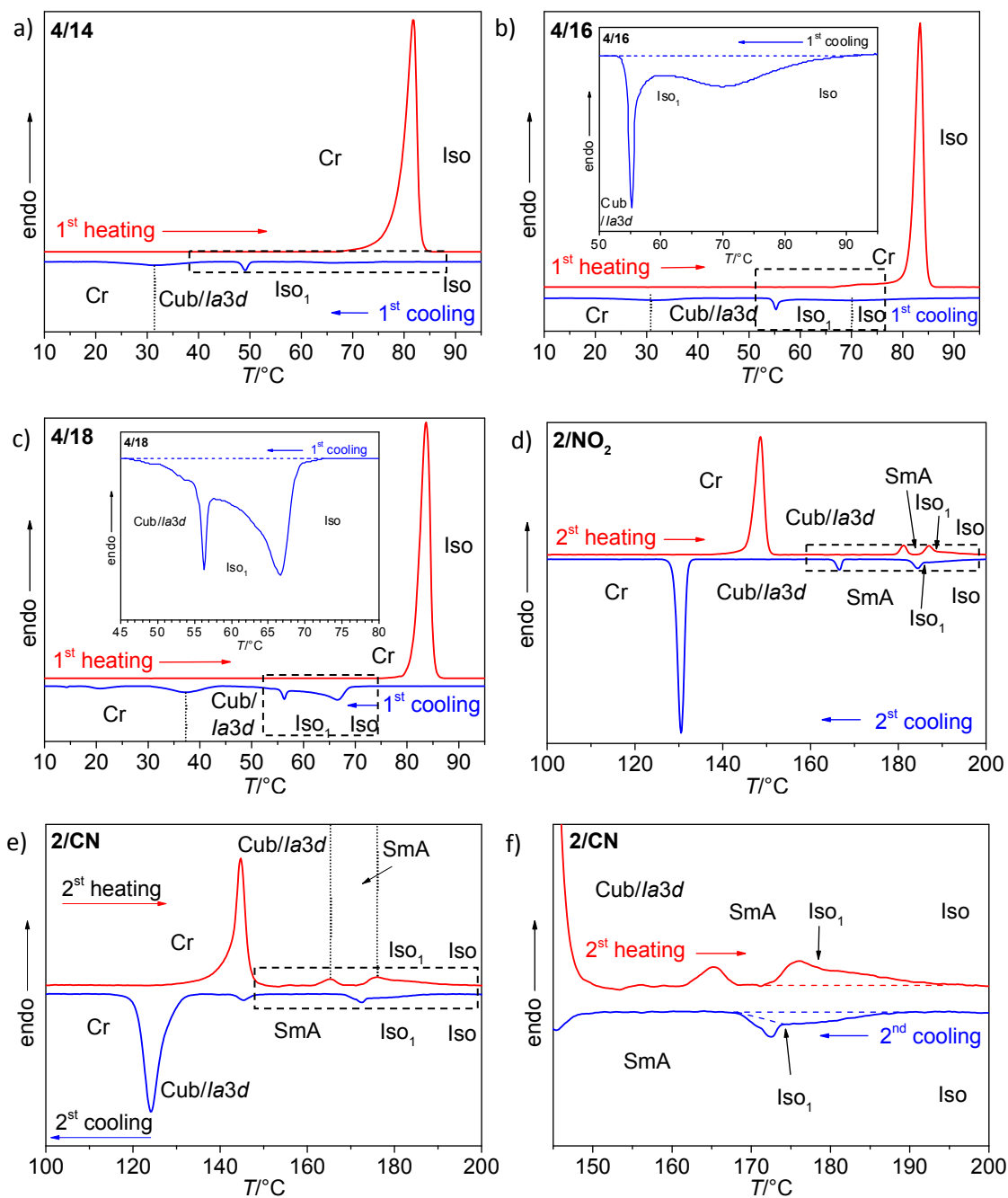


**Figure S1.** DSC heating and cooling traces of compounds  $4/n$  and  $2/X$ , recorded at  $10\text{ K min}^{-1}$ ; the dashed rectangles indicate the expanded sections in Fig. 7a and S1f.

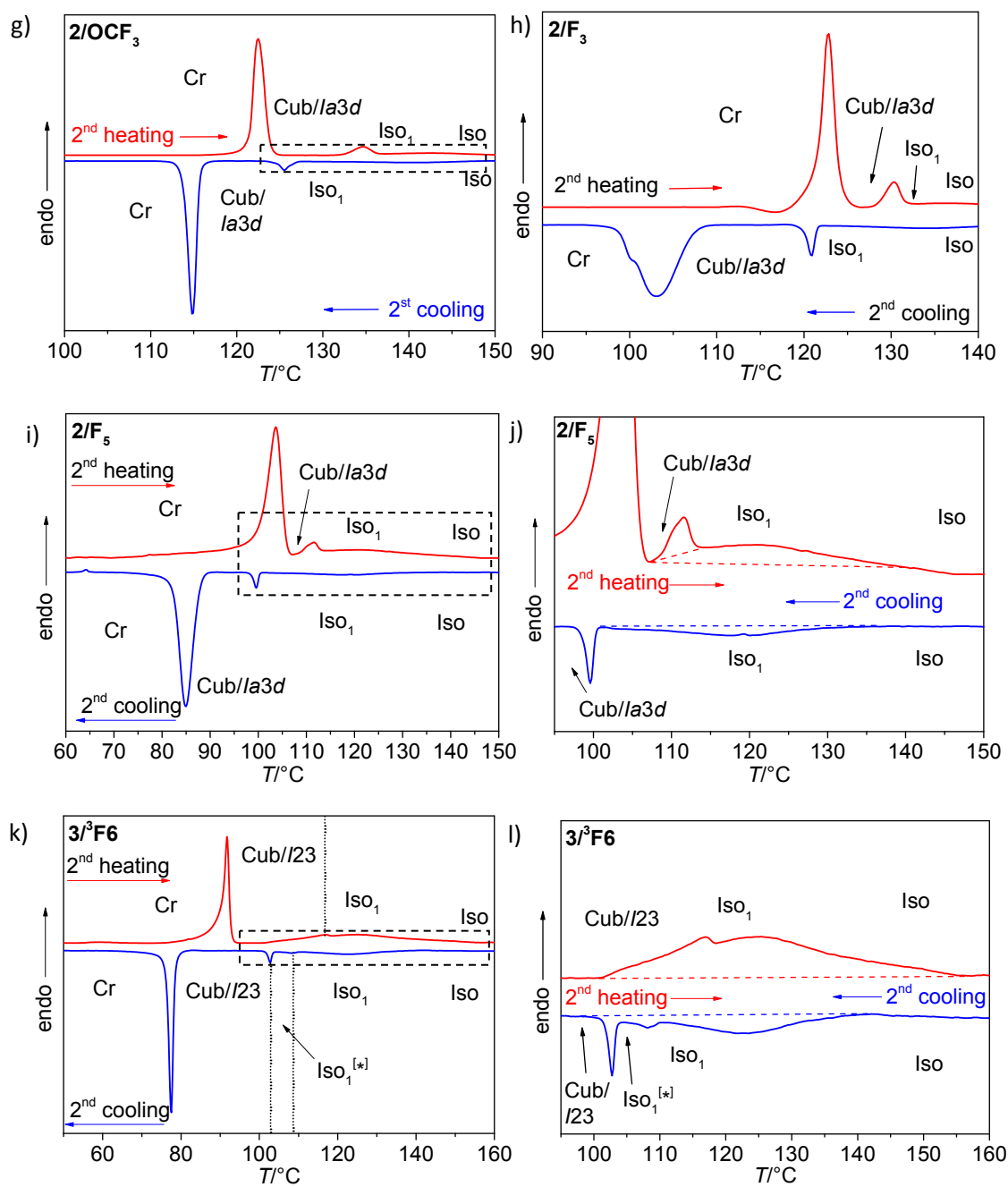


**Figure S1** (continued). DSC heating and cooling traces of compounds  $2/\text{X}$  and  $3^3\text{F6}$ , recorded at  $10 \text{ K min}^{-1}$ ; the dashed rectangles indicate the expanded sections in Fig. 7b and Fig. S1h.



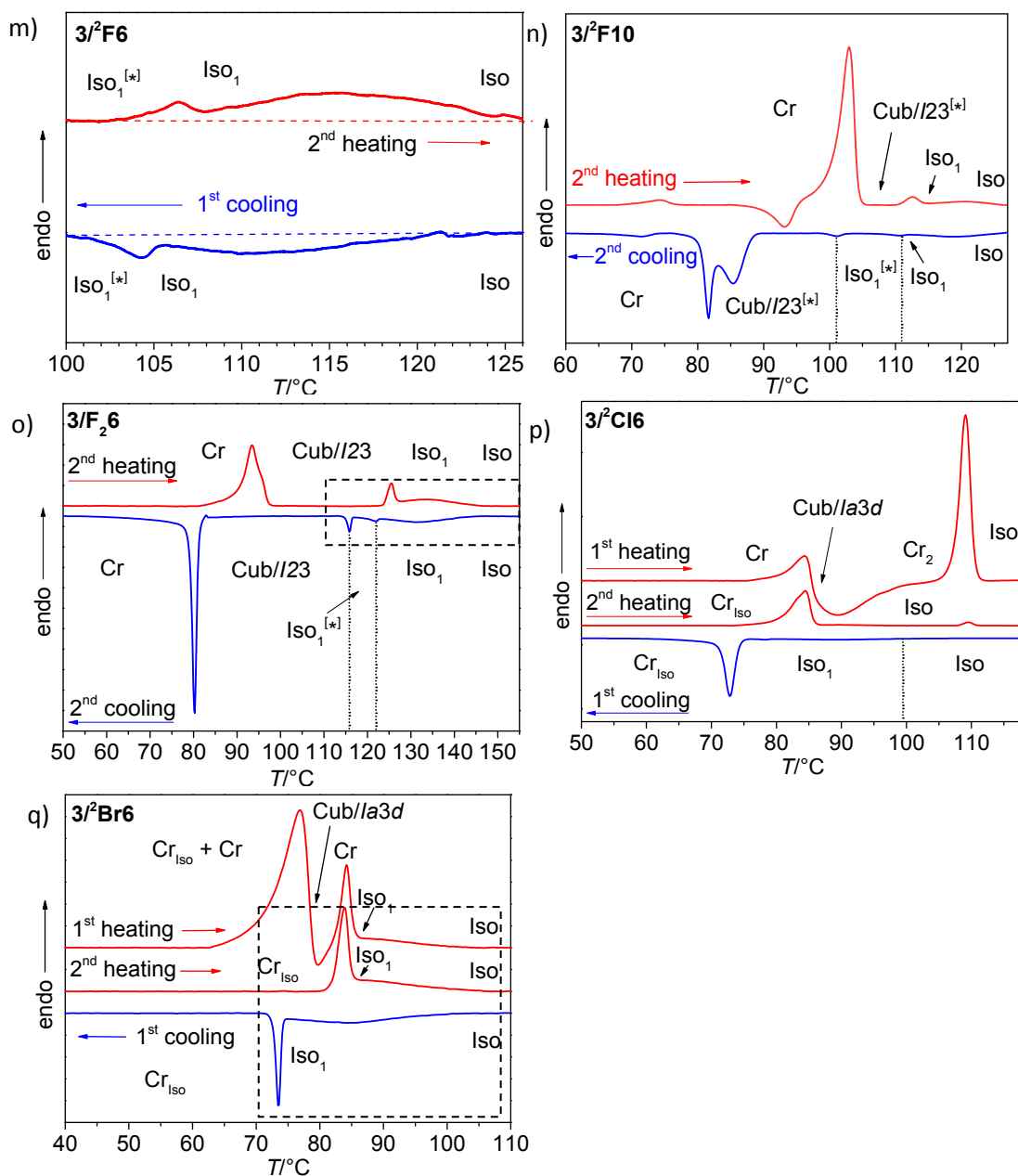


**Figure S1** (continued). DSC heating and cooling traces of compounds  $3/Y_n$  recorded at  $10\text{ K min}^{-1}$ ; the dashed rectangles indicate the expands sections in Fig. 8.

**Table S1.** Temperature ranges of the Iso-Iso<sub>1</sub> transitions.

Compd.	Heating $T/^\circ\text{C}$ [ $\Delta H$ kJ mol <sup>-1</sup> ]	Cooling $T/^\circ\text{C}$ [ $\Delta H$ kJ mol <sup>-1</sup> ]
<b>2/CN</b>	Iso <sub>1</sub> 178-190 [2.2] Iso	Iso 189-174 [2.9] Iso <sub>1</sub>
<b>2/NO<sub>2</sub></b>	Iso <sub>1</sub> 189-200 [2.5] Iso	Iso 199-184 [3.0] Iso <sub>1</sub>
<b>2/OCF<sub>3</sub></b>	Iso <sub>1</sub> 137-153 [4.0] Iso	Iso 148-127 [2.4] Iso <sub>1</sub>
<b>2/F<sub>3</sub></b>	Iso <sub>1</sub> 132-148 [3.4] Iso	Iso 144-122 [3.4] Iso <sub>1</sub>
<b>2/F<sub>5</sub></b>	Iso <sub>1</sub> 113-138 [5.2] Iso	Iso 137-101 [7.7] Iso <sub>1</sub>
<b>3<sup>3</sup>F6</b>	Iso <sub>1</sub> 119-142 [9.5] Iso	Iso 139-109 [7.4] Iso <sub>1</sub>
<b>3<sup>2</sup>F6</b>	Iso <sub>1</sub> 108-124 [3.0] Iso	Iso 121-106 [3.1] Iso <sub>1</sub>
<b>3<sup>2</sup>F10</b>	Iso <sub>1</sub> 115-129 [4.3] Iso	Iso 126-112 [4.1] Iso <sub>1</sub>
<b>3/F<sub>2</sub>6</b>	Iso <sub>1</sub> 128-146 [2.4] Iso	Iso 144-123 [2.1] Iso <sub>1</sub>
<b>3<sup>2</sup>Cl6</b>	Iso <sub>1</sub> 87-99 [3.0] Iso	Iso 98-74 [2.1] Iso <sub>1</sub>
<b>3<sup>2</sup>Br6</b>	Iso <sub>1</sub> 87-105 [3.4] Iso	Iso 100-75 [2.4] Iso <sub>1</sub>
<b>4/14</b>	-	Iso 88-50 [6.5] Iso <sub>1</sub>
<b>4/16</b>	-	Iso 86-56 [6.1] Iso <sub>1</sub>
<b>4/18</b>	-	Iso 72-57 [19.9] <sup>[b]</sup> Iso <sub>1</sub>

<sup>[b]</sup> Transition is accompanied by partial crystallization.

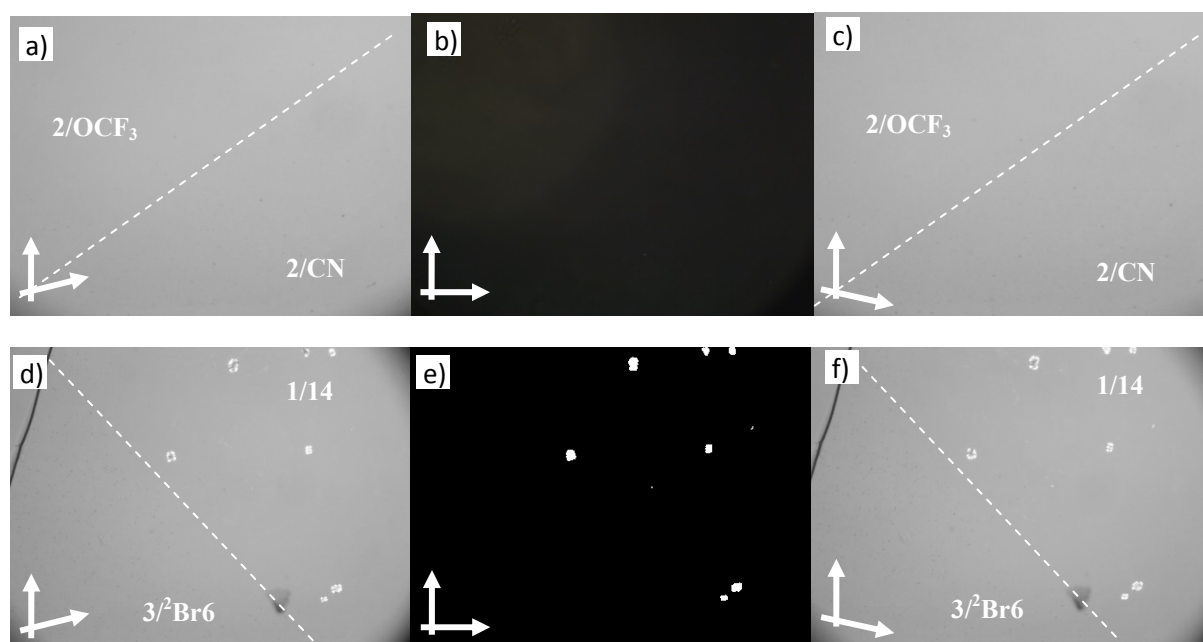


**Figure S2.** POM images of the contact regions a-c) between the  $Ia\bar{3}d$  phase of **2/OCF<sub>3</sub>** and **2/CN** at 135 °C; the absence of any induced  $I23$  phase indicates that the two  $\text{Cub}_{\text{bi}}/Ia\bar{3}d$  phases are the same type ( $Ia\bar{3}d_{(\text{L})}$ ); d-f) show the contact region between **1/14** and **3<sup>2</sup>Br6** at 70 °C (the white dots are due to crystallization); because **3/14** was previously proven to have a  $Ia\bar{3}d_{(\text{S})}$  phase,<sup>S2</sup> the absence of any induced  $I23$  phase indicates that the two  $\text{Cub}_{\text{bi}}/Ia\bar{3}d$  phases are the same type, i. e. that of **3<sup>2</sup>Br6** is also  $Ia\bar{3}d_{(\text{S})}$ .

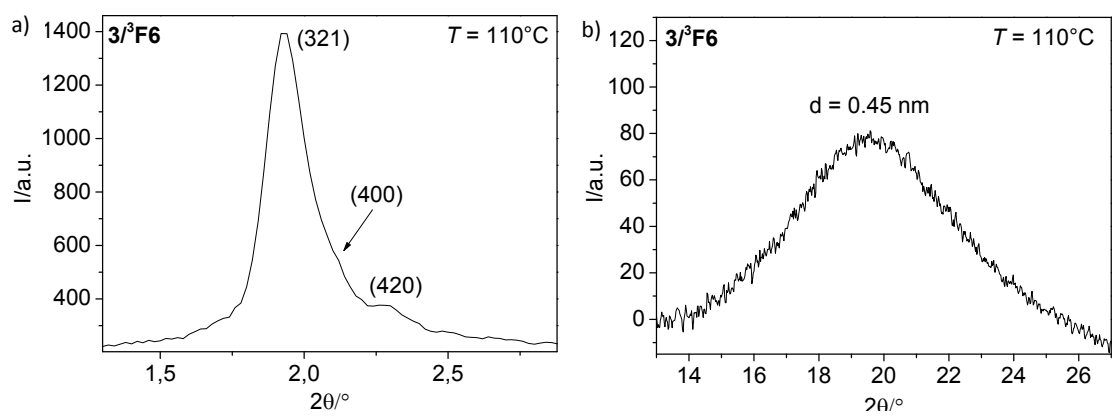
## 2.2 Additional XRD-data

**Table S2.** SAXS data of the  $\text{Cub}_{\text{bi}}/Ia\bar{3}d$  phases of the investigated compounds **2/X**.

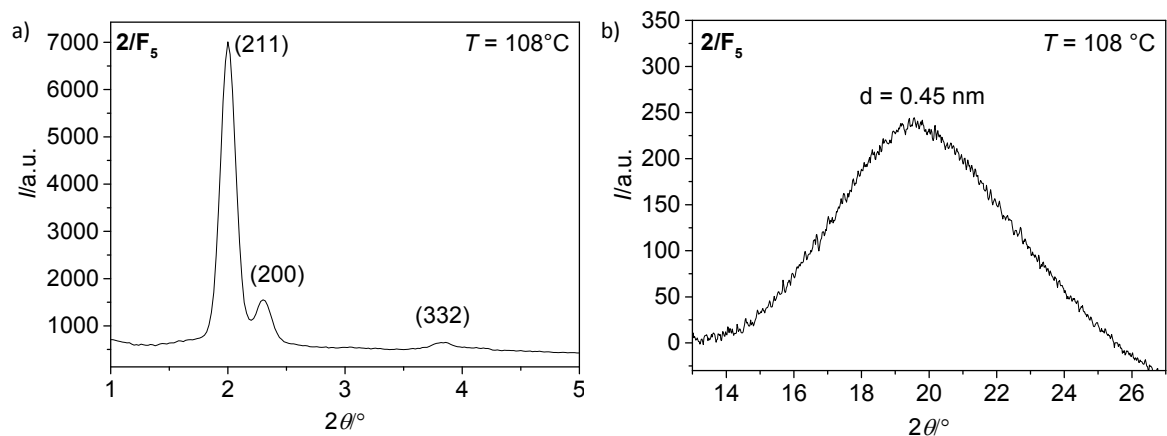
Compd.	(hkl)	$d_{\text{obs}} - \text{spacing/nm}$	$d_{\text{calc}} - \text{spacing/nm}$	$d_{\text{obs}} - d_{\text{calc}}$	$a_{\text{cub}}/\text{nm} (T/^{\circ}\text{C})$
<b>2/F<sub>5</sub></b>	(211)	4.41	4.41	0.00	10.80 (108)
	(220)	3.85	3.82	0.03	
	(332)	2.30	2.30	0.00	
<b>2/CN</b>	(211)	5.07	5.07	0.00	12.44 (155)
	(220)	4.42	4.40	0.02	
<b>2/NO<sub>2</sub></b>	(211)	4.95	4.95	0.00	12.12 (160)
	(220)	4.31	4.28	0.03	
<b>2/OCF<sub>3</sub></b>	(211)	4.60	4.60	0.00	11.26 (125)
	(220)	4.00	3.98	0.02	
	(332)	2.41	2.40	0.01	
<b>2/F<sub>3</sub></b>	(211)	4.46	4.46	0.00	10.94 (125)
	(220)	3.90	3.87	0.03	
	(332)	2.34	2.33	0.01	

**Table S3.** SAXS data of  $\text{Cub}_{\text{bi}}/I23^{[*]}$  phases of the investigated compounds **3/Y<sub>n</sub>**.

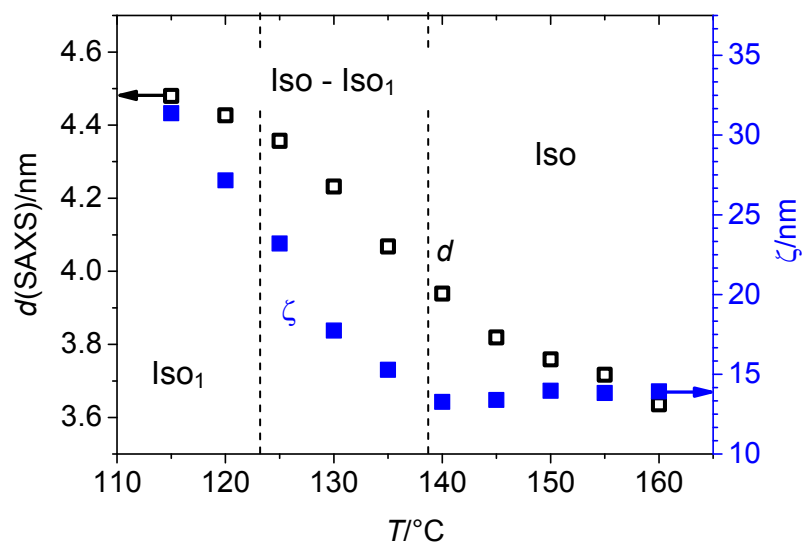
Compd.	(hkl)	$d_{\text{obs}} - \text{spacing/nm}$	$d_{\text{calc}} - \text{spacing/nm}$	$d_{\text{obs}} - d_{\text{calc}}$	$a_{\text{cub}}/\text{nm} (T/^{\circ}\text{C})$
<b>3/<sup>3</sup>F<sub>6</sub></b>	(321)	4.58	4.58	0.00	17.14 (110)
	(400)	4.25	4.28	0.03	
	(420)	3.88	3.83	0.05	
<b>3/F<sub>2</sub>6</b>	(321)	4.58	4.58	0.00	17.15 (115)
	(400)	4.29	4.29	0.00	
	(420)	3.88	3.84	0.04	
	(431)	3.37	3.36	0.01	
	(651)	2.22	2.18	0.04	
<b>3/<sup>2</sup>F<sub>10</sub></b>	(321)	4.84	4.84	0.00	18.09 (110)
	(400)	4.47	4.42	0.05	
	(420)	4.05	4.04	0.01	



**Figure S3.** a) SAXS and b) WAX patterns of the  $\text{Cub}_{\text{bi}}/I23^{[*]}$  phase of  $3^3\text{F6}$ .



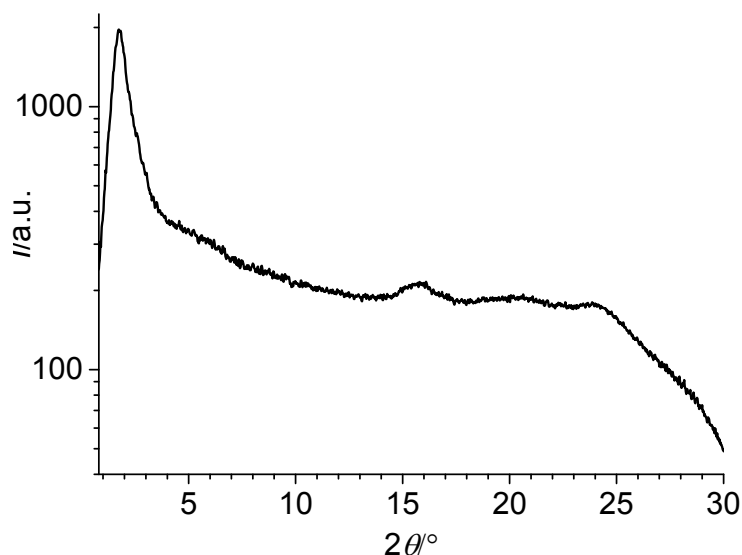
**Figure S4.** a) SAXS and b) WAX patterns of the  $\text{Cub}_{\text{bi}}/Ia\bar{3}d$  phase of  $2/\text{F}_5$ .



**Figure S5.** Temperature dependence of the  $d$ -value of the small angle scattering and the correlation length (calculated with the Scherrer equation) of the clusters in the Iso phases of compound  $3^3\text{F6}$ .

**Table S4.** SAXS data of the smectic phases of the investigated compounds

Compd.	Phase	(hk)	$d/\text{nm}$	$T/^\circ\text{C}$
<b>2/CN</b>	SmA	10	5.52	168
<b>2/NO<sub>2</sub></b>	SmA	10	5.33	185

**Figure S6.** XRD pattern of the crystalline isotropic mesophase ( $\text{Cr}_{180}^{[*]}$ ) of **3<sup>2</sup>F6** at 25 °C (complete scan, for enlarged regions, see Fig. 9f,g).**Table S5.** Structural data of the cubic phases of the investigated compounds.<sup>a</sup>

Compd.	Phase	$a_{\text{cub}}/\text{nm}$	$V_{\text{cell}}/\text{nm}^3$	$V_{\text{mol}}/\text{nm}^3$	$n_{\text{cell}}$	$L_{\text{net}}/\text{nm}$	$n_{\text{raft}}$	$\Phi/^\circ$ <sup>b</sup>
<b>1/2<sup>b</sup></b>	$Ia\bar{3}d_{(L)}$	12.9	2147	1.59	1206	109.5	4.9	6.9
<b>1/6<sup>b</sup></b>	$I23^{[*]}$	18.1	5930	1.69	3133	374.3	3.8	7.7
<b>2/F<sub>5</sub></b>	$Ia\bar{3}d_{(L)}$	10.8	1260	1.56	721	91.6	3.5	8.3
<b>2/CN</b>	$Ia\bar{3}d_{(L)}$	12.4	1907	1.56	1091	105.2	4.6	7.2
<b>2/NO<sub>2</sub></b>	$Ia\bar{3}d_{(L)}$	12.1	1772	1.55	1021	102.7	4.5	7.4
<b>2/OCF<sub>3</sub></b>	$Ia\bar{3}d_{(L)}$	11.3	1443	1.58	816	95.9	3.8	7.9
<b>2/F<sub>3</sub></b>	$Ia\bar{3}d_{(L)}$	10.9	1295	1.55	746	92.5	3.6	8.2
<b>3<sup>3</sup>F6</b>	$I23^{[*]}$	17.1	5000	1.70	2626	353.6	3.3	8.2
<b>3/F<sub>2</sub>6</b>	$I23^{[*]}$	17.2	5088	1.70	2673	355.7	3.4	8.1
<b>3<sup>2</sup>F10</b>	$I23^{[*]}$	18.1	5930	1.79	2960	374.3	3.6	7.7

<sup>a</sup> Abbreviations:  $V_{\text{cell}}$  = volume of the unit cell;  $V_{\text{cell}} = a_{\text{cub}}^3$ ;  $V_{\text{mol}}$  = molecular volume as calculated with the crystal volume increments of Immirzi<sup>S1</sup>;  $n_{\text{cell}}$  = number of molecules in a unit cell; calculated according to  $0.893 V_{\text{cell}}/V_{\text{mol}}$ , where the factor 0.893 is a correction for the different packing density in the crystalline and the LC state;  $L_{\text{net}}$  = total length of the networks per unit cell ( $L_{\text{net}} = 8.485a_{Ia\bar{3}d}$  and  $L_{\text{net}} = 20.68a_{I23}$ , respectively, see <sup>S2</sup>);  $n_{\text{raft}}$  = number of molecules in each 0.45 nm high rafts forming the networks;  $n_{\text{raft}} = n_{\text{cell}}/(L_{\text{net}}/0.45)$ ;  $\Phi$  = twist angle between adjacent molecules in the networks:  $\Phi(Ia\bar{3}d) = 70.5^\circ/[0.354a_{\text{cub}}/0.45\text{nm}]$ ,  $\Phi(I23) = 90^\circ/[0.290a_{\text{cub}}/0.45\text{nm}]$ . <sup>b</sup> only compounds with sufficiently similar molecular structures can be compared directly.

# Publikationsliste

## Publikationen mit Hauptautorenschaft

- 1.) „Controlling spontaneous mirror symmetry breaking in cubic liquid crystalline phases by the cycloaliphatic ring size”, T. Reppe, C. Dressel, S. Poppe, C. Tschierske, *Chem. Commun.* **2020**, *56*, 711–714. DOI: 10.1039/c9cc09206d.
- 2.) „Spontaneous mirror symmetry breaking in benzil-based soft crystalline, cubic liquid crystalline and isotropic liquid phases”, T. Reppe, S. Poppe, X. Cai, F. Liu, C. Tschierske, *Chem. Sci.* **2020**, *11*, 5902–5908. DOI: 10.1039/d0sc01396j.
- 3.) „Helical networks of  $\pi$ -conjugated rods - A robust design concept for bicontinuous cubic liquid crystalline phases with achiral *Ia3d* and chiral *I23* lattice”, C. Dressel, T. Reppe, S. Poppe, M. Prehm, H. Lu, X. Zeng, G. Ungar, C. Tschierske, *Adv. Funct. Mater.* **2020**, *30*, 2004353. DOI: 10.1002/adfm.202004353.
- 4.) „Controlling mirror symmetry breaking and network formation in liquid crystalline cubic, isotropic liquid and crystalline phases of benzil-based polycatenars”, T. Reppe, S. Poppe, C. Tschierske, *Chem. Eur. J.*, **2020**, *26*, 16066–16079. DOI: 10.1002/chem.202002869.
- 5.) „Swallow-Tailed Polycatenars: Controlling Complex Liquid Crystal Self-Assembly and Mirror Symmetry Breaking at the Lamellae-Network Cross-Over“, T. Reppe, C. Dressel, S. Poppe, A. Eremin, C. Tschierske, *Adv. Optical Mater.* **2021**, *9*, 2001572. DOI: 10.1002/adom.202001572.

## Publikationen mit Co-Autorenschaft

- 1.) „Chiral self-sorting and amplification in isotropic liquids of achiral molecules“, C. Dressel, T. Reppe, M. Prehm, M. Brautzsch, C. Tschierske, *Nat. Chem.* **2014**, *6*, 971–977. DOI: 10.1038/nchem.2039.

## Konferenzbeiträge

- 1.) „Mirror symmetry breaking in cubic and isotropic liquid phases of achiral polycatenare molecules”, T. Reppe, M. Prehm, C. Tschierske, Vortrag O17, 1st Joint Meeting of the German & British Liquid Crystal Societies, Edinburgh (Scotland), 21st – 23rd March, 2016.
- 2.) „Influence of molecular chirality on the cubic and isotropic liquid phases of polycatenar molecules”, T. Reppe, S. Poppe, C. Tschierske, Poster P33, 2nd Joint Meeting of the German British Liquid Crystal Societies, Würzburg (Germany), 3rd – 5th April, 2017





# Lebenslauf

---

## Persönliche Angaben

Name	Tino Reppe
Geburtsdatum	06.09.1990
Geburtsort	Halle (Saale)
Staatsangehörigkeit	deutsch
Familienstand	ledig

---

## Berufserfahrung

05/2022 – heute	Wissenschaftlicher Mitarbeiter, Miltitz Aromatics GmbH
05/2020 – 04/2022	Wissenschaftlicher Mitarbeiter, Hochschule Merseburg

---

## Ausbildung/ akademischer Werdegang

11/2015 – 04/2020	Promotion an der Martin-Luther-Universität Halle-Wittenberg, Institut für Organische Chemie, AK Prof. Dr. C. Tschierske
10/2013 – 09/2015	Masterstudium Chemie an der Martin-Luther-Universität Halle-Wittenberg
10/2009 – 10/2013	Bachelorstudium Chemie an der Martin-Luther-Universität Halle-Wittenberg
06/2009	Abitur Gymnasium Südstadt Halle (Saale)

---

## Betreute Abschlussarbeiten

2017	Linda Höhlich, Bachelorarbeit, fachliche Betreuung und Begutachtung
2017	Philipp Melcher, Masterarbeit, fachliche Betreuung und Begutachtung

Halle (Saale), den 18.07.2022

Tino Reppe



# **Eidesstattliche Erklärung**

Hiermit erkläre ich, dass die vorliegende Arbeit selbstständig verfasst und keine anderen, als die von mir angegebenen Quellen und Hilfsmittel verwendet habe.

Diese Dissertation wurde bisher an noch keiner anderen Hochschule oder Universität vorgelegt.

Halle (Saale), den 18.07.2022

Tino Reppe